


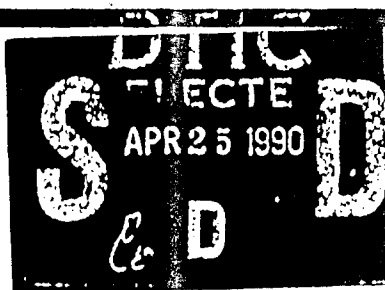
AD-A220 940

DTIC FILE COPY



Optical Society of America 

OSA Proceedings on
**Picosecond
Electronics and
Optoelectronics**



Edited by
T.C.L. Gerhard Sollner
and
David M. Bloom

DISTRIBUTION STATEMENT A

Approved for public release

Distribution Unlimited

March 8-10, 1989 in Salt Lake City, Utah

Volume 4

90 04 22 08

**OSA Proceedings on
Picosecond Electronics
and Optoelectronics**

Volume 4

Technical Program Committee

David M. Bloom, General Chair

Stanford University

Gerhard Sollner, Program Chair

MIT Lincoln Laboratory

David H. Auston

Columbia University

Larry A. Coldren

University of California, Santa Barbara

Lester Eastman

Cornell University

James Harris

Stanford University

Hideki Hasegawa

Hokkaido University, Japan

Ravinder K. Jain

Amoco Research Center

Richard A. Kiehl

IBM Watson Research Center

Fred J. Leonberger

United Technologies Research Center

Chi H. Lee

University of Maryland

Gerard A. Mourou

University of Rochester

James Murphy

Defense Advanced Research Projects Agency

Tadasi Sueta

Osaka University, Japan

Claude Weisbuch

Thomson CSF, France

Jerry Woodall

IBM Watson Research Center

OSA Proceedings on Picosecond Electronics and Optoelectronics

Volume 4

Edited by
T. C. L. Gerhard Sollner and David M. Bloom

Proceedings of the OSA Topical Meeting,
March 8 - 10, 1989,
Salt Lake City, Utah



*This topical meeting was cosponsored
by the Optical Society of America
and by the Lasers and Electro-Optics Society
of the Institute of Electrical and Electronics Engineers*

PRICE-\$69.00 per Optical Society of
America, 1816 Jefferson Place, NW
Washington, DC 20036
TELECON

4/23/90

VG

Optical Society of America
1816 Jefferson Place, N.W.
Washington, DC 20036
(202) 223-8130

| | |
|--------------------|-------------------------------------|
| Accession For | |
| NTIS CRA&I | <input checked="" type="checkbox"/> |
| DTIC TAB | <input type="checkbox"/> |
| Unannounced | <input type="checkbox"/> |
| Justification | |
| By <i>5/69.00</i> | |
| Distribution | |
| Availability Codes | |
| Dist | Avail and/or Special |
| <i>A-1</i> | <i>21</i> |

Articles in this publication may be cited in other publications. To facilitate access to the original publication source, the following form for the citation is suggested:

Name of Author(s), "Title of Paper," in OSA Proceedings on Picosecond Electronics and Optoelectronics, Vol. 4 of the OSA Proceeding Series, T. C. L. G. Sollner and D. M. Bloom, eds. (Optical Society of America, Washington, D.C., 1989), pp. xx-xx.

ISBN 1-55752-110-7

Library of Congress Catalog Card Number 89-61044

Copyright © 1989, Optical Society of America

Individual readers of this proceedings and libraries acting for them are permitted to make fair use of the material in it, such as to copy an article for use in teaching or research, without payment of fee, provided that such copies are not sold.

Permission is granted to quote excerpts from articles in this proceedings in scientific works with the customary acknowledgment of the source, including the author's name, name of the proceedings, and the publisher, year, volume, and page. Reproduction of figures and tables is likewise permitted in other articles and books provided that the same information is printed with them, permission of one of the original authors is obtained, and notification is given to the Optical Society of America. For publication or systematic or multiple reproduction of any material in this proceedings is permitted only under license from the Optical Society of America; in addition, the Optical Society may require that permission also be obtained from one of the authors. In the case of articles whose authors are employees of the United States Government or its contractors or grantees, the Optical Society of America recognizes the right of the United States Government or retain a nonexclusive, royalty-free license to use the author's copyrighted article for United States Government purposes. Address inquiries and notices to Director of Publications, Optical Society of America, 1816 Jefferson Place, N.W., Washington, DC 20036.

The views and conclusions contained in this proceedings are those of the author(s) and should not be interpreted as necessarily representing endorsements, either expressed or implied, of the editors or the Optical Society of America.

Printed in the United States of America

→ Pacific Symposium

Contents

| | |
|---------------|----|
| Preface | xi |
|---------------|----|

Part 1 Lightwave Technology

| | |
|--|---|
| ↪ High-Speed Lightwave Systems <i>Alan H. Gnauck</i> | 2 |
| ↪ Ultrafast All-Optical Multiplexing-Demultiplexing Techniques for Future Optical Communications <i>Masatoshi Saruwatari</i> | 7 |

Part 2 High-Speed Measurement Techniques

| | |
|---|----|
| ↪ Picosecond Pulse Generation and Sampling with GaAs Monolithic Integrated Circuits <i>R. A. Marsland, C. J. Madden, V. Valdivia, M. J. W. Rodwell, and D. M. Bloom</i> | 16 |
| Ultra-high Bandwidth Detachable Optoelectronic Probes <i>M. Scheuermann, R. Sprik, J.-M. Halbout, P. A. Moskowitz, and M. Ketchen</i> | 22 |
| Measurement of Gigahertz Waveforms and Propagation Delays in an InGaAs/InAlAs MODFET Using Phase-Space Absorption Quenching <i>J. M. Wiesenfeld, M. S. Heutmaker, I. Bar-Joseph, D. S. Chemla, J. M. Kuo, T. Y. Chang, and C. A. Burrus</i> | 27 |
| 120-GHz Active Wafer Probes for Picosecond Device Measurement <i>R. Majidi-Ahy and D. M. Bloom</i> | 31 |
| Observation of Low-Power-Level Picosecond Pulses Using a Single-Photon Counting Techniques <i>M. Hamana, A. Kimura, T. Umeda, Y. Cho, and M. Kanda</i> | 36 |
| ↪ Investigation of Picosecond Time-Resolved Photoluminescence in Gallium Arsenide with 3 μ m Spatial Resolution <i>Thomas A. Louis</i> | 39 |
| ↪ Differential Sampling with Picosecond Resolution Using Bulk Photoconductors <i>J. Paslaski and A. Yariv</i> | 46 |

| | |
|---|----|
| Timing Jitter of Colliding Pulse Mode-Locked Lasers | 48 |
| <i>G. T. Harvey, M. S. Heutmaker, P. R. Smith, J. A. Valdmanis and M. C. Nuss</i> | |
| Comparison of Electro-Optic and Photoconductive Sampling Using a 28-GHz Monolithic Amplifier | 52 |
| <i>E. Chauchard, G. Treacy, K. Webb, Chi H. Lee, H.-L. A. Hung, H. C. Huang, and P. Polak-Dingels</i> | |
| Application of Frequency-Domain Techniques for Tuning Pulsed Lasers | 57 |
| <i>J. C. Swartz, F. C. De Lucia, and B. D. Guenther</i> | |

Part 3 Laser Diodes, Amplifiers, and Modulators

| | |
|---|----|
| Picosecond, Spatially Resolved Optical Detection of Charge-Density Modulation in AlGaAs Lasers | 62 |
| <i>H. K. Heinrich</i> | |
| Spectral Filtering of Relaxation Oscillations in Injection-Current-Modulated Diode Lasers | 68 |
| <i>Santanu Basu, Paul G. May, and Jean-Marc Halbout</i> | |
| Ultrafast Nonlinearities in InGaAsP Diode Laser Amplifiers | 73 |
| <i>K. L. Hall, E. P. Ippen, J. Mark, and G. Eisenstein</i> | |
| Spread-Spectrum-Integrated Optic Modulators | 76 |
| <i>David W. Dolfi</i> | |
| Electro-Optical Synthesis of Picosecond Optical Pulses | 81 |
| <i>Tetsuro Kobayashi and Akihiro Morimoto</i> | |
| Subpicosecond Multiple Pulse Formation in Actively Mode-Locked Semiconductor Lasers | 87 |
| <i>P. A. Morton, R. J. Helkey, S. W. Corzine, and J. E. Bowers</i> | |

Part 4 Tunneling and Resonant Tunneling

| | |
|--|-----|
| Ultrafast Optical Studies of Tunneling and Perpendicular Transport in Semiconductor Microstructures | 94 |
| <i>D. Y. Oberli, Jagdeep Shah, B. Deveaud, and T. C. Damen</i> | |
| Fabrication of Resonant Tunneling Diodes for Switching Applications | 101 |
| <i>S. K. Diamond, E. Ozbay, M. J. W. Rodwell, D. M. Bloom, Y. C. Pao, E. Wolak, and J. S. Harris</i> | |
| Time-Resolved Observation of Luminescence from a Charge-Transfer State in Double Quantum Wells | 106 |
| <i>T. B. Norris, N. Vodjdani, B. Vinter, C. Weisbuch, and G. A. Mourou</i> | |

| | |
|---|-----|
| Optical Phonon-Assisted Tunneling in Double Quantum-Well Structures | 111 |
| <i>Y. Oberli, Jagdeep Shah, T. C. Damen, R. F. Kopf, J. M. Kuo, and J. E. Henry</i> | |
| New Equivalent-Circuit Model for Resonant Tunneling Diodes | 115 |
| <i>E. R. Brown, C. D. Parker, T. C. L. G. Sollner, C. I. Huang, and C. E. Stutz</i> | |
| Electric-Field Dependence of the Tunneling Escape Time of Electrons from a Quantum Well | 121 |
| <i>T. B. Norris, X. J. Song, G. Wicks, W. J. Schaff, L. F. Eastman, and G. A. Mourou</i> | |
| Electron Tunneling Time Measured by Photoluminescence Excitation Correlation Spectroscopy | 124 |
| <i>M. K. Jackson, M. B. Johnson, D. H. Chow, J. Soderstrom, T. C. McGill, and C. W. Nieh</i> | |

Part 5 Transistors and Transport

| | |
|--|-----|
| Silicon FETs at 0.1- μ m Gate Length | 132 |
| <i>G. A. Sai-Halasz</i> | |
| GaAs MESFET and HBT Technology in Picosecond Electronics | 139 |
| <i>Kazuyoshi Asai and Tadao Ishibashi</i> | |
| Electron-Hole Effects on the Velocity Overshoot in Photoconductive Switches | 147 |
| <i>R. Joshi, S. Chamoun, and R. O. Grondin</i> | |
| Role of Electron-Electron Scattering on the Ultrafast Relaxation of Hot Photoexcited Carriers in GaAs | 153 |
| <i>M. J. Kann and D. K. Ferry</i> | |
| Intersubband Relaxation of Electrons in $\text{Al}_x\text{Ga}_{1-x}\text{As}/\text{GaAs}$ Quantum Wells During Photoexcitation | 158 |
| <i>Stephen M. Goodnick and Paolo Lugli</i> | |
| Phonons and Phonon Interactions in Layered Semiconductors | 163 |
| <i>G. Mahler, A. M. Kriman, and D. K. Ferry</i> | |
| Mobility and Lifetime Measurements in PECVD and Type IIa Diamond | 170 |
| <i>Don Kania, Otto L. Landen, Lawrence Pan, Piero Pianetta, and K. V. Ravi</i> | |

Part 6 Optical Switches, Detectors, and Applications

| | |
|--|-----|
| Picosecond GaAs-Based Photoconductive Optoelectronic Detectors | 176 |
| <i>F. W. Smith, S. Gupta, H. Q. Le, M. Frankel, V. Diadiuk, M. A. Hollis, D. R. Dykaar, G. A. Mourou, and A. R. Calawa</i> | |

| | |
|--|-----|
| Interdigitated Metal-Semiconductor-Metal Detectors | 184 |
| <i>D. L. Rogers</i> | |
| Coplanar Vacuum Photodiode for Measurement of Short-Wavelength Picosecond Pulses | 189 |
| <i>J. Bokor, A. M. Johnson, W. M. Simpson, R. H. Storz, and P. R. Smith</i> | |
| 20-ps Resolution Single-Photon Solid-State Detector | 194 |
| <i>M. Ghioni, A. Lacaita, S. Cova, and G. Ripamonti</i> | |
| Photoconductive and Photovoltaic Picosecond Pulse Generation Using Synthetic Diamond Film | 201 |
| <i>S. T. Feng, J. Goldhar, and Chi H. Lee</i> | |
| Beryllium-Bombarded $\text{In}_{0.53}\text{Ga}_{0.47}\text{As}$ and InP Photoconductors with High Responsivity and Picosecond Resolution | 206 |
| <i>R. Loepfe, A. Schaelin, and H. Melchior</i> | |
| Photocurrent-Voltage Characteristics of Ultrafast Photoconductive Switches | 210 |
| <i>S. Moss, J. Knudsen, R. Bowman, P. Adams, D. Smith and M. Herman</i> | |
| Use of Tandem Photoconductive Switches for Measuring Picosecond Turn-On Delay of Laser Diodes | 217 |
| <i>P. Blixt, E. Adomaitis, and A. Krotkus</i> | |
| Picosecond Optoelectronic Integrated Antennas for Broadband Dielectric Measurements | 222 |
| <i>Y. Pastol, G. Arjavalingam, J.-M. Halbout, and G. V. Kopcsay</i> | |
| Beams of Terahertz Electromagnetic Pulses | 225 |
| <i>Ch. Fättinger and D. Grischkowsky</i> | |
| Characterization of Optically Pulsed Millimeter-Wave Antennas | 232 |
| <i>Charles R. Lutz and Alfred P. DeFonzo</i> | |
| Ultrafast Optical Switching through Virtual Charge Polarization in dc-Biased Quantum-Well Structures | 239 |
| <i>Masamichi Yamanishi</i> | |

Part 7 Digest Summaries

| | |
|---|-----|
| High-Frequency Laser Modulation | 244 |
| <i>Robert Olshansky</i> | |
| Recent Developments in High- T_c Superconducting Films and Devices | 246 |
| <i>R. A. Buhrman</i> | |
| Optical Detection of Resonant Tunneling of Electrons in Quantum Wells | 247 |
| <i>G. Livescu, A. M. Fox, T. Sizer, W. H. Knox, and D. A. B. Miller</i> | |

| | |
|---|-----|
| Optical Evidence of Charge Accumulation in Double-Barrier Diodes : | 251 |
| <i>N. Vojdani, E. Costard, F. Chevoir, D. Thomas, D. Cote, P. Bois, and S. Delaitre</i> | |
| Tunneling Dynamics and Resonant Coupling of Electrons in GaAs/AlAs Coupled Double Quantum-Well Structures under Electric Fields | 254 |
| <i>T. Matsusue, M. Tsuchiya, and H. Sakaki</i> | |
| Timing Jitter in Repetitively Pulsed Semiconductor Lasers | 258 |
| <i>Ruixi Yuan and Henry F. Taylor</i> | |
| Millimeter Wave AlInAs-GaInAs HEMTs | 260 |
| <i>U. K. Mishra</i> | |
| Picosecond Lasing Dynamics in Quantum-Well Lasers and Its Dependence on the Number of Quantum Wells | 262 |
| <i>Y. Arakawa, T. Sogawa, M. Tanaka, and H. Sakaki</i> | |
| Femtosecond Excitonic Electroabsorption Sampling | 264 |
| <i>W. H. Knox, J. E. Henry, B. Tell, K. D. Li, D. A. B. Miller, and D. S. Chemla</i> | |
| A 10-Gb/s 100-km Optical Fiber Transmission Experiment Using a High-Speed Multiple Quantum Well DFB-LD and a Back-Illuminated InGaAs-APD | 266 |
| <i>S. Fujita, M. Kitamura, T. Torikai, N. Henmi, H. Yamada, T. Suzaki, I. Takano, K. Komatsu, and M. Shikada</i> | |
| Author Index | 269 |
| Subject Index | 271 |

Preface

This volume is composed of papers that were presented at the 1989 Picosecond Electronics and Optoelectronics Topical Meeting. This preface serves as a brief summary of the meeting and as a guide to these proceedings.

Part 1 begins with an introduction to optical communications. Systems considerations of this important application of optoelectronics are used to provide the motivation for many of the papers that follow.

Part 2 is primarily concerned with another important optoelectronic application, the measurement of phenomena that take place on a picosecond time scale. Short optical or electrical pulses are used to sample the parameter of interest, usually electric fields, in electronic or optoelectronic devices and circuits. Several methods of sampling are described, as are improvements to components that make up these systems.

Part 3—Laser Diodes, Amplifiers, and Modulators—is the first of several parts that address the electronic and optoelectronic components that lay the foundation for the systems considered above. Diode laser chirping, picosecond optical pulse amplifiers, a spread-spectrum approach to modulation, and two novel methods of picosecond pulse synthesis are discussed.

In Part 4 papers on tunneling and resonant tunneling are presented. Devices based on these effects have promise in high-speed electronics. Several papers investigate the speed of electron tunneling between two reservoirs and the effect of speed on device performance. Resonant-tunneling diode switches are also considered.

Part 5 covers transistors as well as studies of carrier transport on the picosecond time scale. Excellent results for silicon FETs are given, demonstrating the great flexibility of that established technology. The frontiers of gallium arsenide technology are also highlighted by MESFETs and HBTs. Several papers study electron dynamics in gallium arsenide, including scattering from phonons, electrons, and holes.

Part 6 completes the summary of electronic and optoelectronic components, describing optical switches, detectors, and some of their applications. Several improved switch materials and detectors are discussed, and a novel method for switching using virtual charge polarization is included. Three groups discuss their use of short optical pulses to generate short electromagnetic pulses coupled to free space.

The final part, Part 7, includes summaries of papers that were presented at the meeting, but for which no manuscript was submitted.

Part 1

Lightwave Technology

High-Speed Lightwave Systems

Alan H. Gnauck

AT&T Bell Laboratories, Crawford Hill Laboratory, Holmdel, New Jersey 07733

ABSTRACT

The status of multigigabit direct-detection lightwave systems is reviewed, with an emphasis on the potential and limitations of present system components.

In the past several years lightwave systems have been demonstrated at increasingly higher bit rates. An electrically-time-division-multiplexed (ETDM) system has reached 11 Gbit/s over 81 km (94 km with an optical amplifier) [1], while an optical-time-division-multiplexed (OTDM) systems has been operated at 16 Gbit/s over 8 km [2]. A wavelength-division-multiplexed (WDM) system using ten 2 Gbit/s channels has spanned 68 km [3]. Aggregate bit rates for laboratory systems are shown in Figure 1.

ETDM systems place the most severe demands on electronic and opto-electronic components, but the simplicity and economy of such systems continues to make them attractive. In addition, the ETDM system is a building block for WDM and OTDM systems.

An ETDM system is diagrammed in Figure 2, and the bit rate \times distance products of such systems for the last few years are shown in Figure 3. At the transmitter, either direct or external modulation may be used to perform the electrical-to-optical conversion. Multi-frequency lasers operating near the dispersion zero of the optical fiber may be used in systems operating at speeds less than a few gigabits-per-second or over short distances.

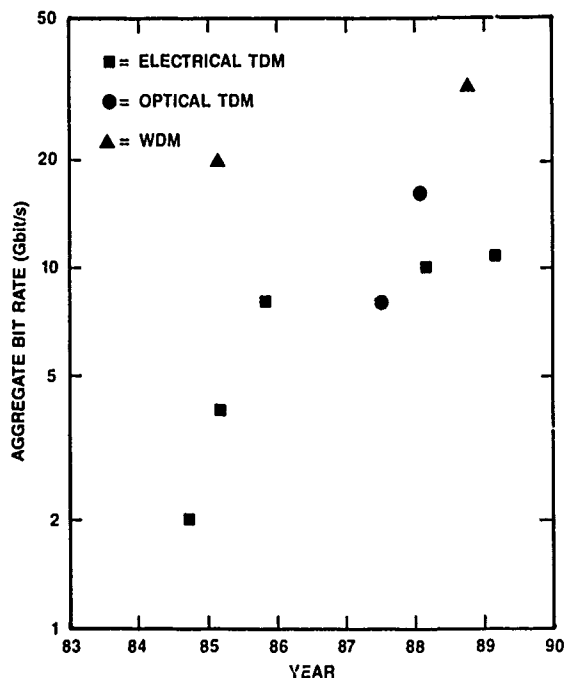


Fig. 1: Demonstrated aggregate bit rates for ETDM, OTDM, and WDM laboratory lightwave systems.

A multifrequency laser with an rms spectral width of ~ 1 nm combined with fiber dispersion of ~ 1 psec/km \cdot nm results in a dispersion-limited bit rate \times distance product of ~ 250 Gbit/s \cdot km. In fact, such a system has been demonstrated at 8 Gbit/s over 30 km of fiber [4], and an error-rate floor was encountered at 40 km, consistent with the above limit. Single-frequency lasers are desired for multigigabit systems to reduce fiber dispersion penalties,

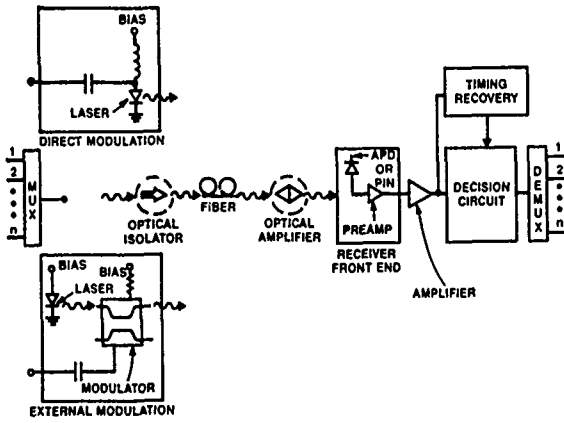


Fig. 2: Diagram of an ETDM lightwave system.

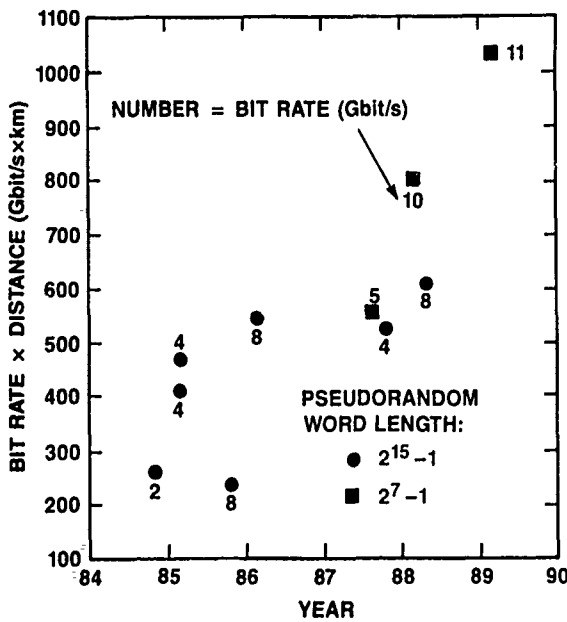


Fig. 3: Bit rate \times distance products obtained in laboratory ETDM systems. The bit rate is given for each point, and the pseudorandom word length is also indicated. Longer word lengths more accurately simulate the random data of commercial systems.

and the distributed feedback (DFB) laser has become the most widely-used source in high bit rate systems. However, even a single-frequency laser suffers "chirp" when modulated, broadening its spectrum according to the formula [5],

$$\Delta\nu(t) = -\frac{\alpha}{4\pi} (kP(t) + \frac{d}{dt}\ln P(t)) \quad (1)$$

where $\Delta\nu(t)$ is the change in optical frequency, and α and k are constants which depend on the laser structure. The spectrum of a laser

undergoing modulation at the rate of a few gigabits per second may widen to a few tens of gigahertz due to chirp. (When combined with fiber dispersion, this broadening can limit transmission distances severely.) Additionally, the laser may not be able to be turned completely off (due to spectral or speed considerations) resulting in an extinction-ratio penalty at the receiver. External modulation allows an information-bandwidth-limited spectrum and good extinction ratio. It also allows uncompromised laser design.

However, external modulation contributes insertion loss and additional complexity to the system. Direct modulation has been demonstrated at 16 Gbit/s [6], while external modulation using a TiLiNbO_3 switch has reached 8 Gbit/s [7]. Small-signal bandwidths of ~ 22 GHz have been reported for both lasers and switches [8,9]. Another type of external modulator is the electroabsorption modulator. This device has the potential for being integrated into a monolithic laser/modulator chip. In fact, such a monolithic chip has been demonstrated in a lightwave system, achieving a small-signal bandwidth of 8.5 GHz and digital modulation at 5 Gbit/s [10]. With either direct or external modulation, an optical isolator is a desirable system component. The isolator protects the laser from reflection-induced amplitude and frequency fluctuations.

High-quality single-mode fiber has a loss of ~ 0.4 dB/km at $1.3\text{-}\mu\text{m}$ wavelength and ~ 0.25 dB/km at $1.55\text{-}\mu\text{m}$ wavelength. Conventional fiber having zero first-order chromatic dispersion at $1.3\text{ }\mu\text{m}$ has dispersion of 15-20 psec/km \cdot nm at $1.55\text{ }\mu\text{m}$. Dispersion-shifted (DS) fiber translates the dispersion zero to the low-loss region at $1.55\text{ }\mu\text{m}$. Figure 4 shows transmission limits for single-mode fiber due to loss (assuming 1 mW launched power and 500 photons/bit receiver sensitivity) and dispersion. Laboratory results are included for comparison. The chromatic dispersion limits shown in Figure 4 assume an information-bandwidth-limited optical spectrum, and indicate the point at which a 1 dB power penalty is incurred. This is given by [11],

$$B^2L \leq \frac{C}{2D\lambda^2} \quad (2)$$

where B is the bit rate, L is the distance, D is the dispersion, and λ is the wavelength.

At $1.55\text{-}\mu\text{m}$ wavelength in conventional fiber, $B^2L \leq 4000(\text{Gbit/s})^2 \cdot \text{km}$. The B^2L product of $4350(\text{Gbit/s})^2 \cdot \text{km}$ and reported dispersion

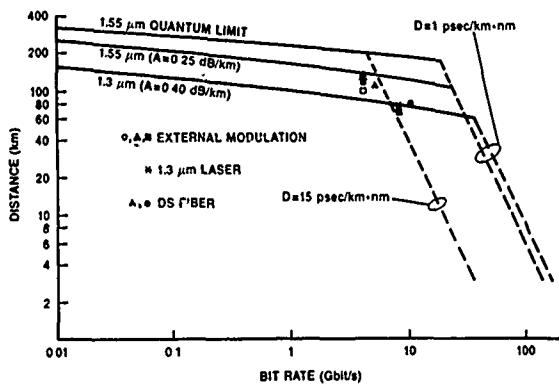


Fig. 4: Transmission limits due to loss (solid lines) and dispersion (dashed lines) in single-mode fiber. Loss limits assume 1 mW launched power and 500 photons/bit receiver sensitivity. Dispersion limits assume an information-bandwidth-limited optical spectrum.

penalty of 1 dB in the external-modulation system of reference [7] agree well with Equation (2). If the laser is operated near the dispersion zero (say, $D = 1 \text{ psec/km} \cdot \text{nm}$) the B^2L limit can be higher by a factor of 15 or more. However, transmission limits may be reduced by polarization dispersion and nonlinear effects such as stimulated Raman scattering, stimulated Brillouin scattering, and four-photon mixing.

Polarization mode dispersion results from fiber birefringence, and corresponds to the difference in propagation time associated with two orthogonal principal states of polarization. This leads to pulse broadening. The differential delay time depends upon the amount of mode mixing that occurs in the fiber, and the mean value appears to increase as the square root of the fiber length [12]. The actual delay has a truncated Gaussian probability distribution, with a maximum value corresponding to the case of no mode coupling. Assuming some mode mixing, the effects of polarization dispersion are expected to become important in a system having a bit rate above 10 Gbit/s and fiber length greater than 100 km [13]. Note that this can be a more severe limitation than chromatic dispersion in a system operating near the fiber chromatic dispersion zero.

Non-linear fiber effects are not expected to be a problem in single-channel intensity-modulated systems with present laser powers of less than ~ 20 milliwatts. In WDM systems,

stimulated Brillouin scattering and four-photon mixing will only be a problem if the channels are closely spaced ($\sim 11 \text{ GHz}$ and counterpropagating for Brillouin scattering, and $\leq 300 \text{ GHz}$ for four-photon mixing). In WDM systems with channel spacings of more than a few nanometers, the dominant nonlinear effect will be stimulated Raman scattering. Consider N channels, equally separated by frequency Δf , and each containing power P , falling within the Raman gain profile ($\sim 15000 \text{ GHz}$). If the power penalty due to stimulated Raman scattering is to be less than $\sim 0.5 \text{ dB}$ in the most strongly affected channel, then [14]:

$$NP \leq \frac{500}{(N-1)\Delta f} \text{ GHz} \cdot W \quad (3)$$

For example, in a system with 4 mW per channel and channel separation $\Delta f = 1300 \text{ GHz}$ ($\Delta\lambda = 10 \text{ nm}$ at $1.5\text{-}\mu\text{m}$ wavelength), the maximum number of channels would be ~ 10 .

Benchmark values for high-speed avalanche photodiode (APD) receiver sensitivities now stand at ~ 450 photons/bit in the 1.3- to $1.55\text{-}\mu\text{m}$ wavelength region [15]. This is still 17 dB away from the quantum limit of 10 photons/bit for direct detection. The limited gain \times bandwidth product of present long-wavelength APD's ($\sim 70 \text{ GHz}$) begins to reduce receiver sensitivity above about 5 Gbit/s, as both optimum gain and bandwidth cannot be simultaneously achieved. In addition, the maximum bandwidth of present devices ($\sim 7\text{-}8 \text{ GHz}$) may limit their use to systems operating below about 15 Gbit/s. Alternatively, p-i-n photodiodes have demonstrated bandwidths above 50 GHz, but lack the internal gain of APD's. Therefore, receivers incorporating p-i-n's suffer a larger preamplifier thermal noise penalty, making them generally less sensitive than APD receivers. An optical amplifier can be used to increase p-i-n receiver sensitivity by boosting the lightwave signal. The generated photocurrent is thereby increased, and the signal-to-noise ratio is improved. The sensitivity of optical preamplifier receivers has been studied by several authors, and the quantum-limited value is estimated to be ~ 40 photons/bit [16]. Already optical preamplifiers used with p-i-n receivers have shown improvements over APD receivers at bit rates as high as 8 Gbit/s [17]. Figure 5 shows champion APD receiver sensitivities at bit rates from 400 Mbit/s to 8 Gbit/s. Optical preamplifier receiver results are shown for comparison.

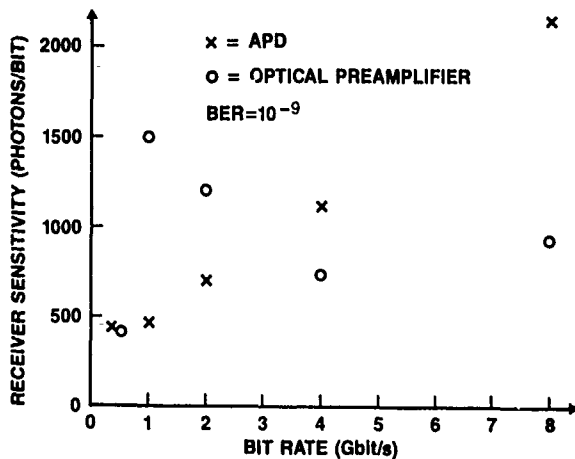


Fig. 5: Comparison of champion APD receiver sensitivities and demonstrated optical preamplifier receiver sensitivities.

Adequate electronic bandwidth and gain flatness become increasingly difficult to obtain as bit rate is increased. Integrated circuits (including amplifiers, multiplexers, demultiplexers, and decision circuits) have been built which would allow the construction of 5-6 Gbit/s systems [18]. Hybrid amplifiers and simple NAND and NOR gates using GaAs FET's have exhibited 10-20 GHz bandwidths. These should allow laboratory demonstrations of ETDM systems operating at bit rates up to about 20 Gbit/s. It is likely that, with present technology, WDM and OTDM will be necessary to obtain aggregate bit rates above 20 Gbit/s.

REFERENCES

- [1] J. L. Gimlett, M. Z. Iqbal, C. E. Zah, J. Young, L. Curtis, R. Spicer, C. Caneau, F. Favire, S. G. Menocal, N. Andreadakis, T. P. Lee, N. K. Cheung, and S. Tsuji, "A 94 km, 11 Gb/s NRZ transmission experiment using a 1540 nm DFB laser with an optical amplifier and a PIN/HEMT receiver", postdeadline paper PD16, OFC '89, Houston, TX (1989).
- [2] R. S. Tucker, G. Eisenstein, and S. K. Korotky, "Optical time-division multiplexing for very high bit-rate transmission", *J. of Lightwave Tech.*, **6**, 1737-1749 (1988).
- [3] N. A. Olsson, J. Hegarty, R. A. Logan, L. F. Johnson, K. L. Walker, L. G. Cohen, B. L. Kasper, and J. C. Campbell, "Transmission with 1.37-Tbit · km/sec capacity using ten wavelength division multiplexed lasers at 1.5 μ m", paper WB6, OFC '85, San Diego, CA (1985).
- [4] A. H. Gnauck, J. E. Bowers, and J. C. Campbell, "8 Gbit/s transmission over 30 km of optical fibre", *Electron. Lett.*, **22**, 600-602 (1986).
- [5] T. L. Koch and R. A. Linke, "Effect of nonlinear gain reduction on semiconductor laser wavelength chirping", *Appl. Phys. Lett.*, **48**, 613-615 (1986).
- [6] A. H. Gnauck and J. E. Bowers, "16 Gbit/s direct modulation of an InGaAsP laser", *Electron. Lett.*, **23**, 801-803 (1987).
- [7] S. K. Korotky, A. H. Gnauck, B. L. Kasper, J. C. Campbell, J. J. Veselka, J. R. Talman, and A. R. McCormick, "8-Gbit/s transmission experiment over 68 km of optical fiber using a TiLiNbO₃ external modulator", *J. of Lightwave Tech.*, **LT-5**, 1505-1509 (1987).
- [8] R. Olshansky, W. Powazinik, P. Hill, V. Lanzisera, and R. B. Lauer, "InGaAsP buried heterostructure laser with 22 GHz bandwidth and high modulation efficiency", *Electron. Lett.*, **23**, 839-841 (1987).
- [9] S. K. Korotky, G. Eisenstein, R. S. Tucker, J. J. Veselka, and G. Raybon, "Optical intensity modulation to 40 GHz using a waveguide electro-optic switch", *Appl. Phys. Lett.*, **50**, 1631-1633 (1987).
- [10] H. Soda, T. Okiyama, M. Furutsu, K. Sato, M. Matsuda, I. Yokota, H. Nishimoto, and H. Ishikawa, "5 Gb/s transmission experiment using a monolithic electro-absorption modulator/DFB laser light source", postdeadline paper PD1, OFC '89, Houston, TX (1989).
- [11] S. E. Miller and I. P. Kaminow, eds., *Optical Fiber Telecommunications II* (Academic Press, San Diego, CA, 1988), p. 808.

- [12] C. D. Poole, "Statistical treatment of polarization dispersion in single mode fiber", *Opt. Lett.*, 13, 687-689 (1988).
- [13] R. E. Wagner and A. F. Elrefaie, "Polarization-dispersion limitations in lightwave systems", paper TU16, OFC '88, New Orleans, LA (1988).
- [14] A. R. Chraplyvy, "Limitations on lightwave communications imposed by optical fiber nonlinearities", invited paper TuD3, OFC '88, New Orleans, LA (1988).
- [15] B. L. Kasper and J. C. Campbell, "Multigigabit-per-second avalanche photodiode lightwave receivers", *J. of Lightwave Tech.*, LT-5, 1351-1364 (1987).
- [16] P. S. Henry, "Error-rate performance of optical amplifiers", paper ThK3, OFC '89, Houston, TX (1989).
- [17] A. H. Gnauck, R. M. Jopson, B. L. Kasper, J. R. Talman, and A. R. Chraplyvy, "8-Gbit/s receiver using an optical preamplifier", paper WN1, OFC '89, Houston, TX (1989).
- [18] R. G. Swartz, "Electronics for high bit rate systems", invited paper WJ2, OFC '89, Houston, TX (1989).

Ultrafast All-Optical Multiplexing-Demultiplexing Techniques for Future Optical Communications

Masatoshi Saruwatari

*NTT Transmission Systems Laboratories, Take 1-2356, Yokosuka-shi,
Kanagawa 238-03, Japan*

Abstract

This paper reviews the all-optical switching techniques, based on the Kerr effect in optical waveguides, which could be applied to time-division multi/demultiplexing of high-speed optical signals. Potential applications are suggested.

1. Introduction

Ultrafast all-optical Kerr switching techniques based on the third optical nonlinearities, are expected to be applied to future ultrahigh-speed optical communication technologies such as optical time-division multi/demultiplexing, optical signal processing, and photonic switching. Particularly, optical Kerr switching using transparent materials such as silica glass, has this potential due to its intrinsically fast (several femtoseconds) response time resulting from non-resonant electronic processes. However, to make Kerr switching a feasible candidate for the above applications, it is necessary to drastically reduce the control optical power which traditionally must be high for the very weak optical nonlinearities of transparent materials. For Kerr switching, therefore, a waveguide structure that confines light in a small area over a long distance, is essential because it can increase optical power density and interaction length, resulting in a reduction of the required optical power. To date, various kinds of all-optical switching using silica optical fibers, fiber couplers and optical waveguides have been investigated to this purpose.

This paper reviews present state-of-the-art all-optical switching techniques based on the Kerr effect in optical waveguides. Included are the principles of optical Kerr switching, configurations and features of various all-

optical switching devices such as interferometric type and directional coupler type, and demonstrations of all-optical switching and time-division multi/demultiplexing of high-speed optical signals [1-2].

2. Principle of Optical Kerr Effect

Any Kerr effect device utilizes an instantaneous refractive index change $\Delta n(t)$ induced by an intense optical pulse given by

$$\Delta n_{ij}(t) = n_2^{ij} I_j(t), \quad (1)$$

where n_2 is nonlinear refractive index, $I(t)$ is input optical pulse intensity (W/m^2), the subscript ij denotes the polarization direction, and the superscript of n_2 denotes the tensor components of nonlinear refractive index. $\Delta n_{ij}(t)$ implies the refractive index change of i -polarization direction induced by j -polarization light. It must be noted that n_2 for self-phase modulation (n_{2s}) is different from that for the Kerr effect (n_{2k}) in which one light influences another. The relationship between them is given by $n_{2s}^{ii} = (1/2) \times n_{2k}^{ii}$; in addition, the tensor components have the relation of $n_{2k}^{ij} (i \neq j) = (1/3) \times n_{2k}^{ii}$ [3]. Therefore, the theoretical optical powers required for switching depend on the switching configurations as cited later.

Total phase change of an input light induced by transmission through $\Delta n(t)$ medium with a length of L is expressed by

$$\Delta \phi_{ij}(t) = (2\pi/\lambda) \Delta n_{ij}(t) \int_0^L I_j(t - \tau L') dL', \quad (2)$$

where, λ is wavelength of signal light, τ is the relative group delay difference (sec/m) between signal and pump lights originating from chromatic dispersion and polarization

dispersion. When $\tau=0$, as in the case for self-phase modulation, the integral, that is, $\Delta\phi_{ij}(t)$ value, is proportional to L as expressed by $I_j(t)L$. Thus the required power to get a certain $\Delta\phi_{ij}(t)$ value can be reduced by increasing the nonlinear guide length: L . On the other hand, when $\tau \neq 0$, the integral tends to be saturated as the length L increases, and becomes independent of the length L if $\tau L \geq$ optical pulse width. Consequently, when using long waveguides like optical fibers as the Kerr medium, the τ value as well as the mode-field diameter must be reduced to achieve lower pump powers [1].

3. All-Optical Switching Devices

Optical Kerr switching devices are roughly classified into two categories; one is the interferometric type, the other is the directional coupler type. In the following, each configuration and its feature will be discussed.

(1) Interferometric type

There are two kinds of all-optical switches using the interferometric type; (a) polarization switching and (b) Mach-Zehnder (M-Z) interferometer devices. In both cases, transmittance is sinusoidal with respect to the phase shift as expressed by $\sin^2(\Delta\phi(t)/2)$, and $\Delta\phi(t)$ must be π for 100% switching.

The polarization switching devices (Fig. 1) operate through the interference between orthogonal polarization components of signal pulse. When polarization directions of pump and signal pulses are offset by 45 degrees, the relative phase shift in orthogonal components is

introduced by the difference between diagonal : n_{2k}^{ii} and nondiagonal : n_{2k}^{ij} components of n_{2k} , as expressed with $\Delta\phi(t) = \Delta\phi_{ii}(t) - \Delta\phi_{ij}(t) \approx (2/3) \times \Delta\phi_{ii}(t)$ (when $\tau=0$) [3]. This shows that the overall phase shift for the polarization switching is 4/3 times larger than that of self-phase modulation. Because polarization fluctuations in the Kerr medium deteriorate switching characteristics, polarization-maintaining single-mode fibers (PANDA-fibers) are preferable when using long fibers. Ultrafast time division demultiplexing with a switching peak power of 3.4 W using 150m long PANDA-fibers [1-2] and optical sampling (gating) [4-5] experiments using single-mode fibers have been demonstrated.

The M-Z devices (Fig. 2) operate essentially like electrooptic M-Z modulators. Here, optically induced phase shift is caused by either n_{2k} component: $\Delta\phi_{ii}(t)$ or $\Delta\phi_{ij}(t)$ depending on polarization direction of the pump light with respect to that of the signal light. Preliminary experiments on all-optical functional gates (inverter, XOR and AND gates) have been conducted using a M-Z-type LiNiO_3 waveguide [6] and single-mode fibers [7-8]. Also, another approach utilizing the signal pulse itself for generating the phase shift has been proposed using the differences in arm-length [9] or waveguide parameters [10] of M-Z interferometer. Except for fiber types [7-8], very intense pump pulses are inherently required for 100% switching due to the short interaction length. Complete switching operation using these M-Z devices has not yet been achieved.

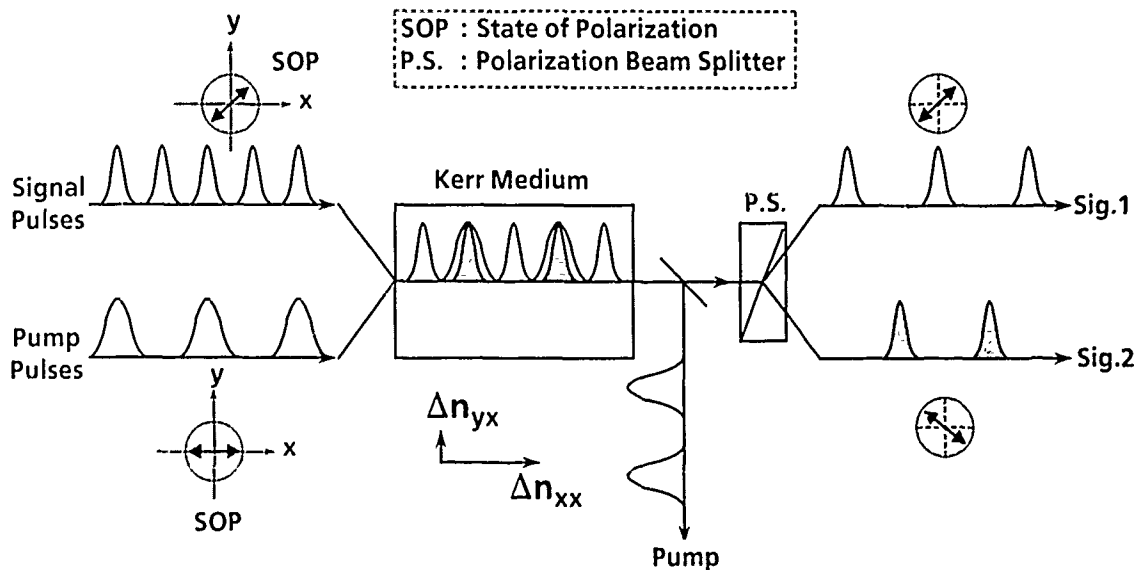


Fig. 1. Configuration of interferometric type all-optical switching (1) Polarization switching

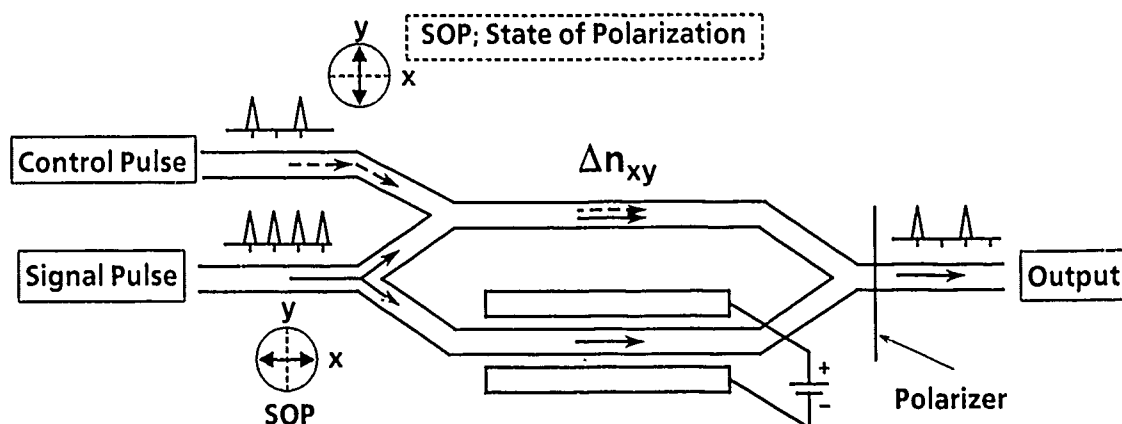


Fig. 2. Configuration of interferometric type all-optical switching (2) Mach-Zehnder interferometer

(2) Directional coupler type

This utilizes a 2×2 directional coupler having two adjacent waveguides, embedded in a nonlinear material, and coupled as shown in Fig. 3 [11]. Switching is based on the coupling coefficient change via $\Delta n_{ij}(t)$ induced by the nonlinear refractive index: n_{2s}^{ii} corresponding to self-phase modulation. Ordinarily, coupling from guide 1 to guide 2 occurs when input light transmits through the coupler. When input power exceeds the critical power, no coupling occurs in the directional coupler, resulting in abrupt switching from cross-state to bar-state [11]. This means that low-power pulses are transferred to guide 2, whereas high-power pulses remain in guide 1 as described in Fig. 3. Several switching experiments have been reported using dual-core fibers [12-14] and GaAs waveguides [15]. Fig. 4 shows the experimental data and theoretical curves of output power versus input power for 2-m nonlinear dual-core fiber coupler. Its somewhat dull switching characteristics are attributed to pulse break-up originating from the pulsewings which still remain in the cross-state due to their

lower phase-shift. Therefore, directional coupler type switching cannot achieve 100 % energy transfer unless ideally rectangular optical pulses are used.

To solve the above problem which originates from the time-dependent phase-shift: $\Delta\phi(t)$ within a pulse, another intriguing approach that applies optical soliton pulses to nonlinear couplers has recently been proposed [16]. This utilizes the phenomena that the soliton pulse in the anomalous dispersion regime maintains its shape unchanged and the Kerr effect imparts a common nonlinear phase to an entire pulse, resulting in complete switching characteristics even for non-square pulses. Fig. 5 shows calculated curves of transmitted optical pulse energy with respect to input peak power, both for ordinary pulses (dashes) and soliton pulses (solid lines). Nearly 100% switching operation may be expected for the soliton pulses by slightly increasing the input power. Recently, with the use of soliton pulses, all-optical high contrast switching has been demonstrated using all-fiber ring-interferometer-type switching [17].

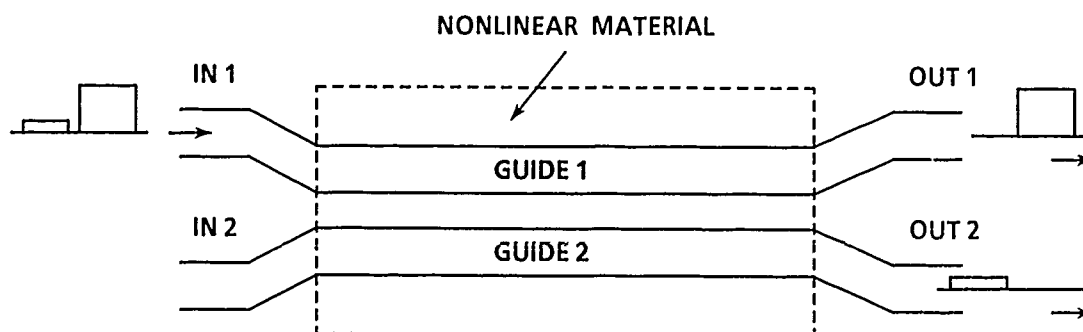


Fig. 3. Configuration of directional coupler type all-optical switching

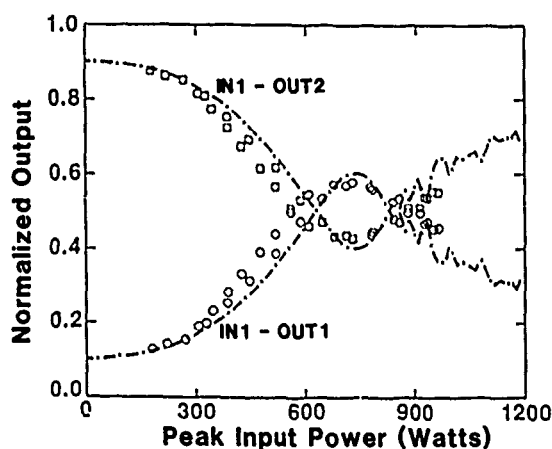


Fig. 4. Output power versus input power for 2-m nonlinear dual-core fiber coupler. Circles (port 1) and squares (port 2); experimental, broken line; theoretical (after Ref.12).

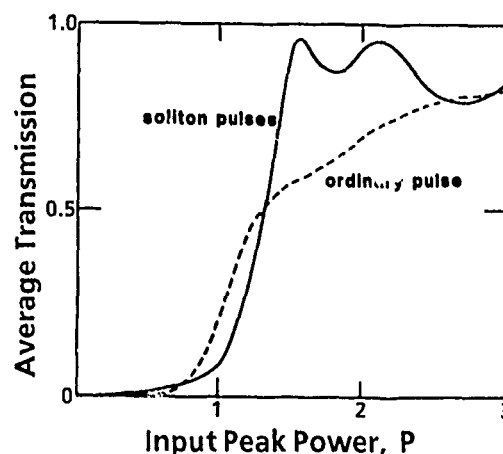


Fig. 5. Calculated curves of transmitted pulse energy versus input peak power. Solid and dashed lines correspond to soliton pulse and ordinary pulse, respectively (after Ref.16).

4. Applications of All-Optical Switching

In the previous Section, operation principles and features have been described for typical all-optical switching devices utilizing the optical Kerr effect. In the following, some applications of these switching devices to optical communication systems and a demonstration on time-division demultiplexing will be described.

(1) Applications of all-optical switching to optical communication systems

One way of realizing ultrahigh-bit rate optical communication is to multiplex several lower bit-rate optical signals into one higher bit-rate signal, and to demultiplex the signal when

needed, all-optically. Fig. 6 shows the conceptual configuration of such optical transmission systems utilizing all-optical MUX/DEMUX [1,2] techniques. This can circumvent bandwidth limitations imposed by conventional electronic/optoelectronic devices such as laser diodes (LDs), photodiodes (PDs) and electrical switching circuits. Here, optical sources must generate ultrashort optical pulses with the relatively high repetition-rates at which external modulators can still function. Recently, less than 10 ps optical pulses have been generated at a 10-40GHz repetition-rate using a monolithic long-cavity mode-locked LD [18] or a gain-switched DFB-LD followed by a

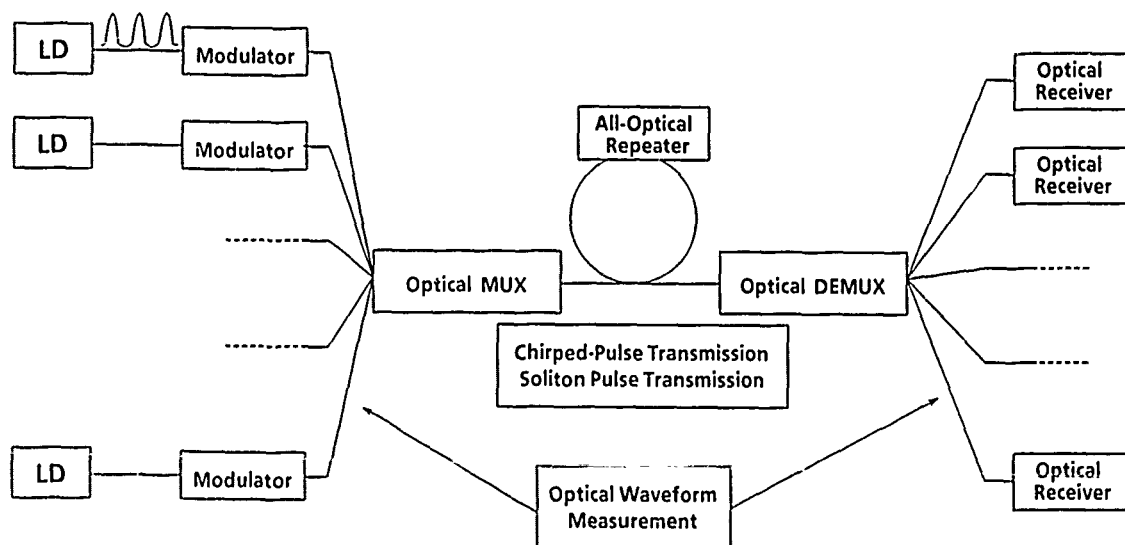


Fig. 6. Conceptual configuration of optical transmission systems utilizing all-optical switching technology.

fiber compression technique [19]. Chirped-pulse transmission using the pulse compression effect in a normal dispersion regime and soliton pulse transmission using the Kerr effect in an anomalous dispersion regime may be promising techniques for such ultrashort pulse transmissions through long fibers. Gate operation with Kerr switching can also be applied to optical sampling [4,20] which can measure an optical waveform with very high resolution. It must be noted that the all-optical MUX/DEMUX requires 100% switching, whereas the optical sampling does not.

(2) Demonstration on all-optical time-domain multi/demultiplexing

Fig. 7 shows the experimental setup for all-optical time-division demultiplexing of an optical pulse train using the Kerr effect in polarization-maintaining (PM) single-mode (SM) fibers. Main fiber parameters are core diameter: 4.6 μm , cutoff wavelength: 1.06 μm , and polarization dispersion: 1 ns/km. Control (pump) pulses and signal pulses are generated from the 1.06 μm mode-locked YAG laser at 82 MHz and the 1.3 μm gain-switched DFB-LD at 2 GHz. The 2 GHz 30 ps signal pulses are synchronized to the 82 MHz 80 ps control pulses using the 48th harmonic of the trigger signals from the mode-locker. Fine phase adjustments between control and signal pulses are accomplished by a mechanical electrical delay line. The control and signal pulses are then coupled into the PM-SM fiber so that the polarization axes of each are parallel

and at 45 degrees to one of the principal axes of the PM fiber. Because only the signal pulses superimposed with the control pulses change their polarization direction by 90 degrees, the signal pulse stream can be demultiplexed with the polarization splitter into two pulse streams according to the control pulse stream.

To stabilize the polarization fluctuations of the signal pulses caused by temperature/ pressure-induced birefringence changes, two birefringent fibers with the same length are spliced so that their fast axes cross at right angles [1,2]. This results in overall birefringence compensation without sacrificing the polarization maintaining property of the fibers. With the control pulses of 30 W at peak, the 2 GHz pulse stream is completely demultiplexed for the 20 m spliced fiber [1,2]. Fig. 8 shows the original gain-switched signal pulses and the two streams of the demultiplexed pulses observed with a PIN photodetector. Channel crosstalk between two demultiplexed streams was measured as better than -20 dB.

The present Kerr-switching duration of about 100 ps is determined by the control pulse width of 80 ps and by the walk-off of 100 ps between signal and control pulses. The latter is caused by the chromatic dispersions between 1.06 μm and 1.3 μm wavelength. It limits the effective interaction fiber length, which is inversely proportional to the required control power [1]. When much shorter control pulses and no-walk-off conditions are adopted, less than 1 ps operation can be expected with much lower

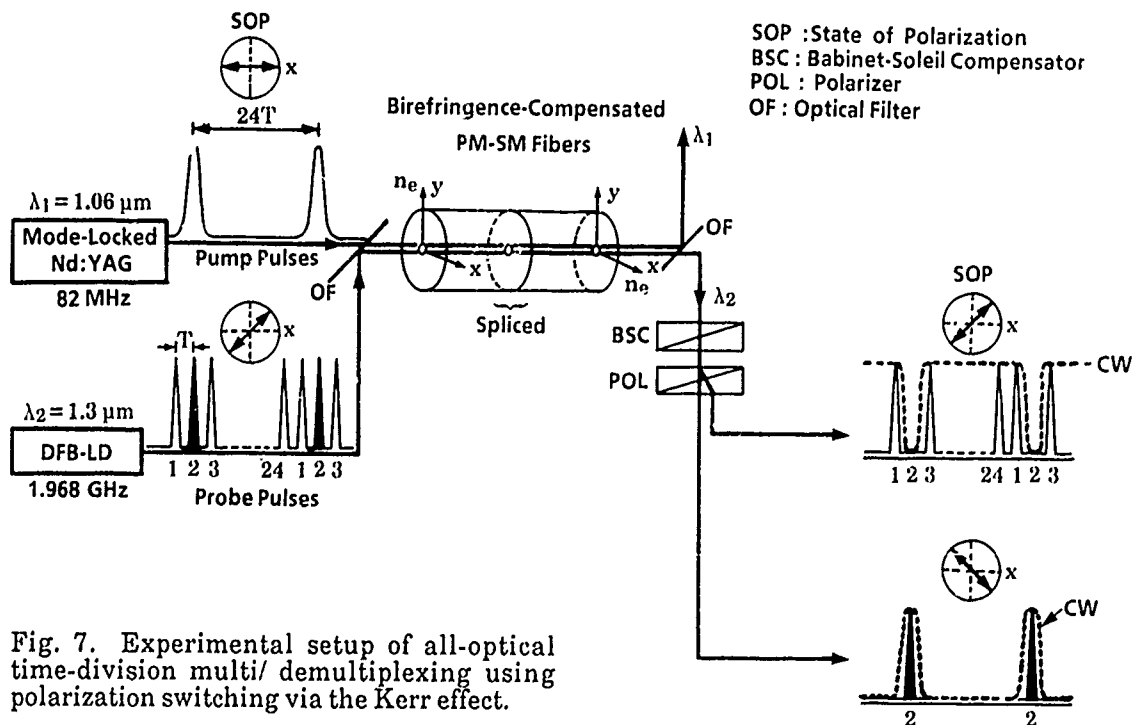
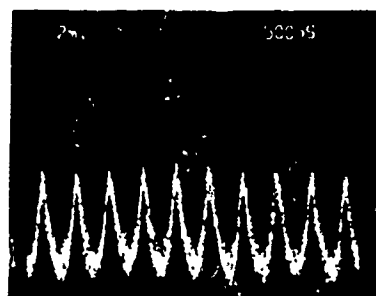
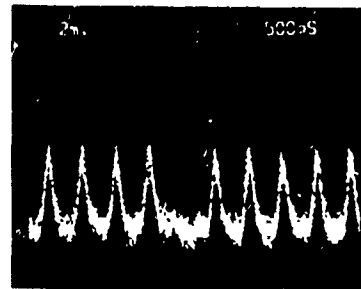


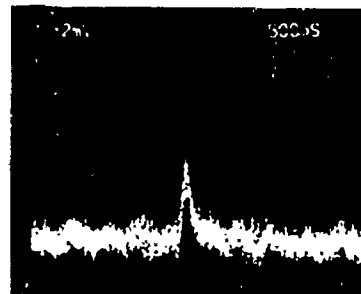
Fig. 7. Experimental setup of all-optical time-division multi/ demultiplexing using polarization switching via the Kerr effect.



(a) Original 2GHz pulse stream



(b) Demultiplexed pulse stream



(c) Demultiplexed pulse stream

Fig. 8. Original and demultiplexed optical pulse trains.

control power. A preliminary experiment using a $1.32 \mu\text{m}$ YAG laser and a 150m long spliced fiber has shown that the required peak control power is decreased to 3.4 W [1]. This was achieved by minimizing the walk-off between pump and probe pulses due to chromatic dispersion. Experimental results for all-optical demultiplexing with and without walk-off are summarized in Table 1.

The required pump power could be reduced further using GeO_2 -doped fibers with extremely small core area ($2 \mu\text{m}^2$) as described in Ref.[18]. The measured data show that the predicted power-length product (P-L) to get π -phase shift is as small as 11Wm . This corresponds to nearly 1/50 th the $3.4 \text{ W} \times 150 \text{ m}$ value for the

present DEMUX experiment, and it would be expected that low-power laser diodes, instead of high-power lasers, could be used for pump sources.

4. Conclusion

Various all-optical switching techniques utilizing the Kerr effect have been reviewed for potential applications to high-speed optical communication systems. Although these techniques are not sufficiently mature to be actually used, they are expected to enhance new conceptual technologies, such as all-optical signal processing, photonic switching, optical computers, and others.

TABLE 1. EXPERIMENTAL RESULTS

| Item | Experiment I | | Experiment II | |
|------------------------------|-----------------------|------|------------------------|------|
| | Probe | Pump | Probe | Pump |
| Optical Source | | | | |
| Wavelength (μm) | 1.30 | 1.06 | 1.31 | 1.32 |
| Repetition rate(MHz) | 1968 | 82 | 2000 | 100 |
| Pulse width (ps) | 35 | 95 | 33 | 175 |
| Fiber | | | | |
| Length | 10+10 m | | 75+75 m | |
| Chromatic dispersion | 5.0 ns/km | | negligible | |
| (Time delay) | (100 ps) | | | |
| Required Pump Power | 30W | | 3.4W | |
| Switching Response | Chromatic disp. limit | | Pump pulse width limit | |

Reference

1. T.Morioka and M.Saruwatari, "Ultrafast All-Optical Switching Utilizing the Optical Kerr Effect in Polarization-Maintaining Single-Mode Fibers," *IEEE J. Selected Area Commun.*, **6**, 1186-1198(1988).
2. T.Morioka, M.Saruwatari and A.Takada, "Ultrafast Optical Multi / Demultiplexer Utilising Optical Kerr Effect in Polarisation-Maintaining Single-Mode Fibres," *Electron.Lett.*, **23**, 453-454(1987).
3. T.Morioka and M.Saruwatari, "Determination of Nondiagonal Component $n_{2\beta\beta}$ of Nonlinear Refractive Index in Polarisation-Maintaining Fibres Utilising Optical Kerr Modulation Scheme," *Electron.Lett.*, **23**, 1330-1332(1987).
4. K.Kitayama, Y.Kimura, K. Okamoto, and S.Seikai, "Optical Sampling using an All-Optical Gate," *Appl.Phys. Lett.* **46**, 623-625(1985).
5. N.J.Halas, D.Krökel, and D.Grischkowsky, "Ultrafast Light-Controlled Optical-Fiber Modulator," *Appl.Phys. Lett.* **50**, 886-888(1987).
6. A.Lattes, H.A.Haus, F.J.Leonberger and E.P.Ippen, "An Ultrafast All-Optical Gate," *IEEE J. Quantum Electron.*, **QE-19**, 1718-1723(1983).
7. M.Shirasaki, H.A.Haus, and D.Liu Wong, "Nonlinear Fiber Interferometer and Logic Gate," in *Technical Digest, Conference on Lasers and Electro-Optics* (Optical Society of America, Baltimore, 1987), *CLEO'87*, paper ThO-1.
8. M.J.LaGasse, D.Liu-Wong, J.G.Fujimoto, and H.A.Haus, "Femtosecond Pump-Probe Interferometry," in *Technical Digest, International Conference on Quantum Electronics* (Japan Society of Applied Physics, Tokyo, 1988), paper WG-4.
9. H.Kawaguchi, "Proposal for a New All-Optical Waveguide Functional Device," *Opt.Lett.*, **10**, 411-412(1985).
10. L.Thylen, N.Finlayson, C.T.Seaton, and G.I.Stegeman, "All-Optical Guided-Wave Mach-Zehnder Switching Device," *Appl. Phys. Lett.*, **51**, 1304-1306(1987).
11. S.M.Jensen, "The Nonlinear Coherent Coupler," *IEEE J. Quantum Electron.*, **QE-18**, 1580-1583(1982).
12. S.R.Friberg, Y.Silberberg, M.K.Oliver, M.J.Andrejco, M.A.Saifi, and P.W.Smith, "Ultrafast all-optical switching in a dual-core fiber nonlinear coupler," *Appl. Phys. Lett.*, **51**, 1135-1137(1987).
13. A.M.Weiner, Y.Silberberg, S.R.Friberg, B.G.Sfez, and P.W.Smith, "Femtosecond All-Optical Switching in Nonlinear Directional Couplers," in *Technical Digest, International Conference on Ultrafast Phenomena* (Japan Society of Applied Physics, Kyoto, 1988), paper FB-1.
14. Y.Silberberg, "All-optical Kerr-effect waveguide devices" in *Technical Digest, International Conference on Quantum Electronics* (Japan Society of Applied Physics, Tokyo, 1988), paper WG-5.
15. L.K.P.Wa et al, "All Optical Multiple-Quantum-Well Waveguide Switch," *Elect. Lett.*, **21**, 26-28(1985).
16. S.Trillo and S.Wabnitz, "Soliton Switching and Modulational Instability in Nonlinear Couplers," in *Technical Digest, International Conference on Quantum Electronics* (Japan Society of Applied Physics, Tokyo, 1988), paper WA-4.
17. N.J.Doran, K.J.Blow, and B.K.Nayar, "Soliton Switching of Entire 400fs Optical Pulses," in *Technical Digest, Optical Fiber Communication Conference* (Optical Society of America, Houston, 1989), paper PD-4.
18. R.S.Tucker, U.Koren, G.Raybon, C.A.Burrus, B.I.Miller, T.L.Koch, G.Eisenstein, and A.Shahar, "40GHz Active Mode-Locking in a Monolithic Long-Cavity Laser," in *Technical Digest, Semiconductor Laser Conference* (Optical Society of America, Boston, 1988), paper PD-5.
19. A.Takada, T.Sugie and M.Saruwatari, "High-Speed Picosecond Optical Pulse Compression from Gain-Switched 1.3- μ m Distributed Feedback-Laser Diode (DFB-LD) through Highly Dispersive Single-Mode fiber," *IEEE J. Lightwave Tech.*, **LT-5**, 1525-1533(1987).
20. Y.Yamabayashi, A.Takada, and M.Saruwatari, "Picosecond Optical Sampling with LiNbO₃ Waveguide and Compressed Laser Diode Pulses," in *Technical Digest, Integrated and Guided-Wave Optics* (Optical Society of America, Santa Fe, 1988), paper WD-5.
21. I.H.White R.V.Penty and R.E.Epworth, "Demonstration of the Optical Kerr Effect in on Sell-Fiber Mach-Zehnder Interferometer at Laser Diode Powers," *Electron.Lett.*, **24**, 340-341(1988).

Part 2
High-Speed Measurement Techniques

Picosecond Pulse Generation and Sampling with GaAs Monolithic Integrated Circuits

R. A. Marsland, C. J. Madden, V. Valdivia, M. J. W. Rodwell,* and D. M. Bloom
Edward L. Ginzton Laboratory, Stanford University, Stanford, California 94305

Abstract

We have developed a GaAs nonlinear transmission line pulse generator capable of producing a 6 V, 1.6 ps falltime electrical transient. We have also developed a monolithic diode sampling bridge which, when driven by a nonlinear transmission line, has a bandwidth in excess of 128 GHz.

Introduction

With integrated circuit speeds of 100 GHz and above made possible by advances in devices in the GaAs and InP material systems, there is an increasing need for accurate, high speed, on wafer measurement of monolithic integrated circuits and devices. Since the technology does not yet exist for capturing these signals in real time, a representation of the signal must be built up over many cycles. This is done by taking a short sample of the signal at progressively later instances in the signal cycle. If a complete cycle is traced out at a relatively slow rate, the sampled output can be low-pass filtered and displayed on a slow oscilloscope. The displayed waveform is the same as the actual waveform except the time axis has been scaled.

This type of "equivalent-time" sampling has a time resolution determined by a convolution of the speeds of the pulse generator and the sampling device which take the samples in addition to any timing jitter between the sampling pulse train and the signal being sampled. An additional speed limitation is imposed by the interconnection between functional blocks. To date, electronic sampling systems have been limited to ~ 20 GHz due to the lack of a fast pulse generator in a compatible technology. The one exception is the Hypres superconducting

sampler which is limited by the coaxial interface to the signal to be sampled. This paper will describe a 6 V, 1.6 ps GaAs Nonlinear Transmission Line (NLTL) pulse generator and a monolithic diode sampling bridge with a bandwidth in excess of 130 GHz. This circuit is small enough to be brought into direct contact with the circuit to be tested, eliminating the coaxial interface.

The Nonlinear Transmission Line

The Nonlinear Transmission Line shown schematically in Fig 1. is a relatively high impedance planar transmission line periodically loaded with reverse biased Schottky diodes serving as voltage-dependent shunt capacitances [1-3]. Because the capacitance decreases with increasing reverse bias, the phase velocity of a small signal will be slower when the line is biased near zero volts than when it is strongly reversed biased. If a large signal is applied to the line, the peak of the waveform near zero will experience a greater delay than the more negative portion. Therefore, the falling edge will tend to steepen as it propagates. The falltime will continue to decrease until spreading due to dispersion just balances the compression arising from the nonlinear capacitance.

Dispersion arises from the line periodicity and device parasitics. Because the line is periodic, there will be a Bragg frequency set by the round-trip time between diodes where small reflections from each diode add in phase. Near the Bragg frequency, the group velocity approaches zero. If the diodes are close enough together, so the Bragg frequency is high, the bandwidth of the line will be limited by the diode cut-off frequency. The final output falltime is achieved when the dispersion arising from diode cut-

* Present address, Department of Electrical and Computer Engineering, University of California at Santa Barbara, Santa Barbara, California 93106.

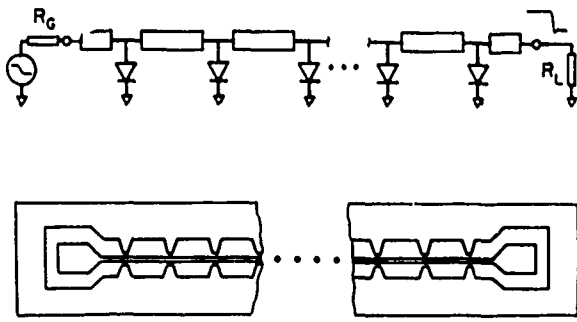


Figure 1. Nonlinear Transmission Line schematic diagram (a) and layout (b).

off and line periodicity just balance the compression arising from the non-linear capacitance.

The circuit is implemented in coplanar waveguide (CPW) to reduce the parasitic inductance of the shunt diode connection. Processing is also simplified since vias and back-side metallization are not required.

The NLTL is fabricated on a semi-insulating GaAs wafer. The active layers are grown by molecular-beam epitaxy. A heavily doped N^+ buried layer provides the diode cathode connection and shorts the two ground planes of the CPW together to suppress the unwanted even CPW mode. The doping profile of the top N^- layer determines the capacitance and resistance per unit area of the diode. This profile is tailored to provide the lowest RC time constant possible, while achieving the desired change in capacitance with voltage. We have fabricated lines with a uniformly doped N^- layer [4] as well as with an exponential hyperabrupt profile [5].

Ohmic contacts are formed by etching down to the N^+ layer and performing a self-aligned liftoff of Au/Ge/Ni/Au. After liftoff, the contacts are annealed. Next, isolation between diodes is achieved with a multienergy proton implant. Finally, Schottky contacts and interconnects are simultaneously formed with a liftoff of Ti/Pt/Au with a total thickness of $1.4 \mu\text{m}$. Schottky diodes are formed where the center conductor crosses over an undamaged active region. To integrate the NLTL with a sampling bridge, 1000 Å PECVD Si_3N_4 metal-insulator metal capacitors, and plated airbridges are added to the process.

Since the final output falltime depends on the Bragg and diode cutoff frequencies, small diodes spaced closely together are desirable. However, because this fine structure is lossy, we first use a large scale structure (with a diode spacing of $160 \mu\text{m}$) and then taper down to the smaller scale structure only near the output where the higher cutoff is needed.

The circuit performance was evaluated by direct electrooptic (EO) sampling [6] of the voltage waveforms launched onto the line through microwave wafer probes. The EO sampling system uses a pulse-compressed, cw mode-locked, Nd:YAG laser to non-invasively probe the internal nodes of GaAs integrated circuits with a time resolution of $\sim 1.9 \text{ ps}$. The EO sampled input and output of a uniformly doped NLTL line is shown in Fig 2. The input is an 8 V, 8 GHz sine wave, the output is a 2 V sawtooth wave with a 3.5 ps fall time. The input sine wave is clipped slightly at the top, due to the diodes going into forward conduction. The overshoot and ringing on the sawtooth wave becomes quite pronounced when the falltime is approaching the Bragg limited value. This result was achieved using 90 large scale diodes and 11 half scale diodes. The total length of the structure was 2 cm.

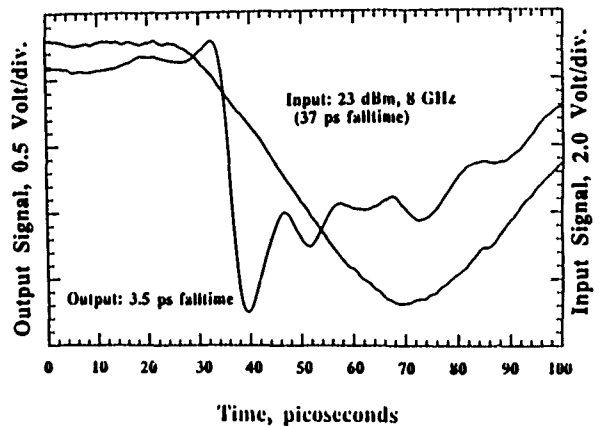


Figure 2. Input and output of a uniformly doped diode nonlinear transmission line measured electrooptically.

Increasing the length of the line will not provide a shorter falltime because large attenuation due to losses in the diode series resistance reduces the amplitude of the waveform which yields a smaller change in capacitance and therefore a smaller change in delay. This process continues until the change in delay can no longer balance dispersion and the falltime begins to increase rather than decrease as a function of length.

Fortunately, tailoring the doping profile of the Schottky diode can solve this problem. The NLTL discussed above used diodes with the uniformly doped profile in Fig 3. The Schottky contact is at $x=0$. The N^- type doping concentration is plotted on a log scale on the y-axis. The x-axis is the distance away from the surface. The N^- layer had a doping of $3 \times 10^{16}/\text{cm}^3$ and a thickness of $0.6 \mu\text{m}$. The N^+ back contact had a doping of $6 \times 10^{18}/\text{cm}^3$ and extended to $1.4 \mu\text{m}$.

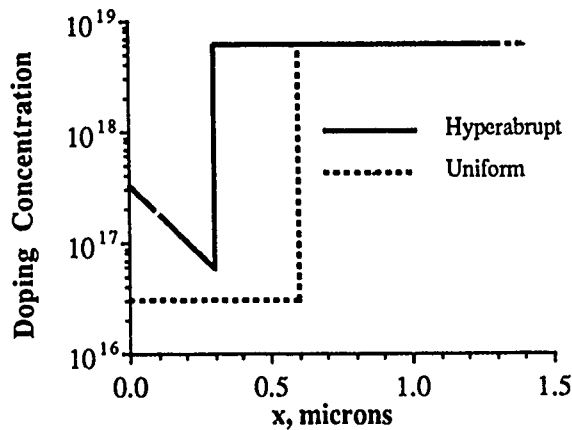


Figure 3. Doping profiles of the diodes used in the uniform doped and the hyperabrupt doped NLTLs.

The hyperabrupt profile raises the surface concentration to $3 \times 10^{17}/\text{cm}^3$ and reduces the N^- layer thickness to $0.3 \mu\text{m}$. The decrease in doping away from the surface increases the fractional change in capacitance and therefore the change in delay per section allowing a shorter line to be used. The increased average doping reduces the resistivity of the N^- layer as well as the thickness required, thus reducing the diode series resistance and thereby the loss per unit length. It was found that an exponential decrease in doping away from the surface gave a good combination of these two properties [7]. In addition, for the hyperabrupt NLTLs the small diodes at the output were scaled to one quarter the size of the large scale diodes.

The EO sampled output of an NLTL using such a hyperabrupt profile is shown in Fig 4. The input is a 10 GHz, 25 dBm sine wave which has a falltime of 30 ps. The output has an amplitude of 6 V and a measured fall time of 2.5 ps. After taking into account the time resolution of the electrooptic sampling system, we believe the falltime of this pulse is 1.6 ps. To our knowledge, this is the fastest electrically generated transition time to date. This is $2\times$ improvement in speed and a $3\times$ improvement in signal amplitude over the uniformly doped NLTL results.

Electronic Sampling

Our first application of these fast waveforms to driving a sampling bridge involved the relatively slow (3.5ps falltime) uniformly doped design. The output of an NLTL is roughly a sawtooth wave, but to drive a sampling device, an impulse function is required. The sawtooth wave can be converted to an impulse while preserving the speed of the waveform by using shorted transmission line as a differentiator [8]. A step function is used here for illustration.

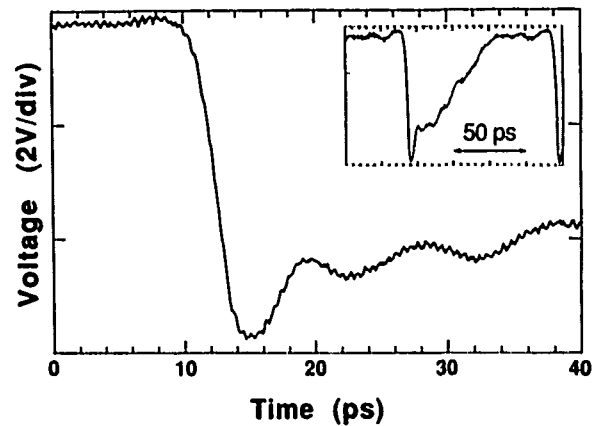


Figure 4. Output of the hyperabrupt-doped NLTL measured with the EO sampling system.

The incident and reflected voltage at three points along the shorted line as well as the total voltage are plotted in Fig. 5 as a function of time. At point (a), the incident wave appears after a time τ . Then, after a round trip time of the remainder of the line, $\Delta\tau$, the reflected wave appears, which is simply the input wave inverted and delayed. The pulse width of the total voltage is approximately equal to the round trip time of the shorted line to the right of this node.

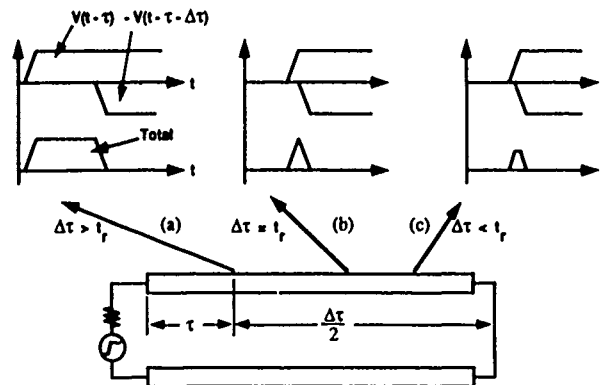


Figure 5. Converting a fast rising step-function into an impulse-like waveform using a shorted transmission line. The load would be attached at point (b) for shortest pulse width without loss of amplitude.

Further down the line, at point (b), the incident and reflected waves are closer together, and the resultant pulse just has time to reach its full value before the reflected wave brings it back down to zero.

Even further down the line, at point (c), the pulse width is no longer determined by round trip time, but rather the risetime of the step. In this limit, the voltage waveform will become proportional to the derivative of the input waveform. However,

the pulse no longer has time to reach its full value. Therefore, to make a pulse from a step function, the shorted line section should have a round trip time equal to the risetime of the step. This achieves the smallest pulse width without loss of amplitude. For a step function with a 3.5 ps risetime, the length required for a coplanar line on GaAs is approximately, $180\text{ }\mu\text{m}$. Because the line is so short, loss and dispersion can readily be neglected.

Fig. 6 shows the sampling bridge structure used by Grove in Hewlett-Packard's 12 GHz sampling oscilloscope in 1966 [8]. The signal to be sampled is input from the left and travels through the sampling structure. The ground of the signal line is split and the sampling diodes are placed across the gap in series with two coupling capacitors. The step which is to drive the sampling diodes, is applied across this split in the signal ground which acts as a balanced transmission line that is shorted at both ends. This shorted transmission line differentiates the input step function so that the voltage applied across the diodes is impulse like. Since the impedance to ground from each of these nodes for frequencies of interest is relatively high, the pulses are well balanced with respect to the signal line so that there is little coupling between the strobe generator line and the signal line.

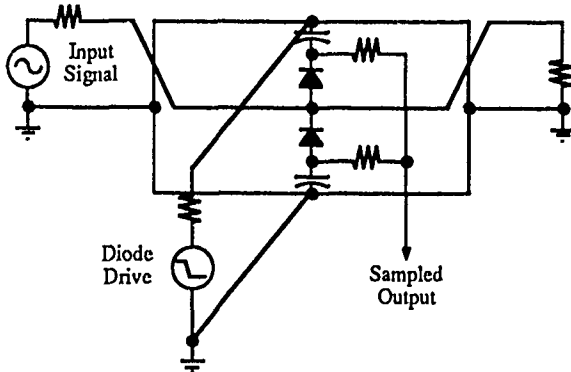


Figure 6. Two diode sampling bridge structure with split ground differentiator.

If the same point in the input signal cycle is sampled repeatedly, the voltage at the output node will eventually charge up to the full RF voltage at that point in the cycle. If the delay is increased between samples, the output voltage will slowly map out the input signal in equivalent time.

The problem with this structure is that, even in more modern implementations [9,10], it is highly three dimensional and requires hybrid assembly. By using coplanar waveguide for the transmission lines, we have collapsed it into one plane so that it can be monolithically integrated with a nonlinear transmission line strobe signal generator [11].

A drawing of the layout of the sampler and portions of two nonlinear transmission lines is shown in Fig. 7. The signal to be sampled is input from a coplanar probe and travels vertically down past the sampling diodes. The nonlinear transmission line on the left provides the sawtooth wave that is applied to the sampling diodes. The nonlinear transmission line at the bottom is attenuated 35 dB down to 40 mV to provide a test signal for the sampler. The attenuator also provides a good termination for the external input at the top figure if the test signal is not used. The equivalent time output of the sampler is filtered by two $1\text{ k}\Omega$ resistors and brought out at the right.

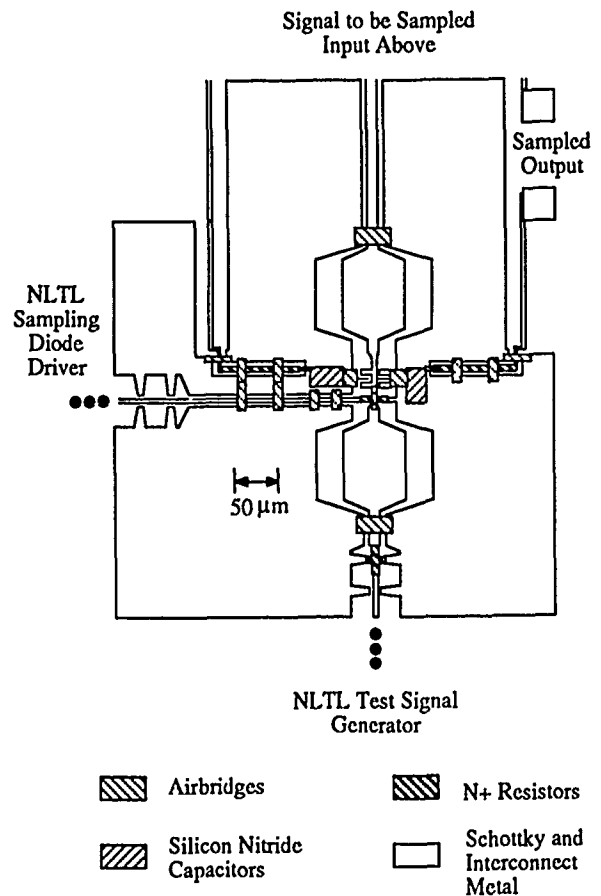


Figure 7. Layout drawing of monolithic GaAs sampling head and portions of two NLTL pulse generators.

The sawtooth strobe signal is applied across the split in the signal ground in the center of the structure through a $40\text{ }\Omega$ resistor which provides a DC termination for the nonlinear transmission line. The wave then propagates on the slot-line [12] type mode of the split ground until it reaches the airbridge short circuits $180\text{ }\mu\text{m}$ from the center. The reflected pulse

then returns to the center to terminate the sampling interval. This is the transmission line differentiator described earlier. The split in the signal ground is narrow at the center to minimize the inductance of the strobe pulse connection but widens out to $130\text{ }\mu\text{m}$ to increase the wave impedance across the split ground, increasing the voltage that is developed across the diodes. The center conductor is also widened to maintain a $50\text{ }\Omega$ impedance for the signal line. The round trip time from the center to the air-bridge shortcircuits and back is approximately 3.5 ps.

To evaluate the sampler performance, we electrooptically sampled under each coupling capacitor to look at the strobe pulse shape and under the RF signal line to compare the waveform measured with the electrical sampler with that obtained from the optical measurement.

Fig. 8 shows the electrooptically sampled diode gating pulses for the sampler. The diodes are fully conducting for only about the last 25% of this pulse, so the aperture time can be less than 4ps. Although the pulses have some ringing, the voltage never returns to the value necessary to turn the diodes back on. The pulses are remarkably well balanced which reduces kick-out of the sample pulse onto the signal line. The width of the pulse is probably closer to 3.5 ps due to the finite time resolution of the EO sampling system.

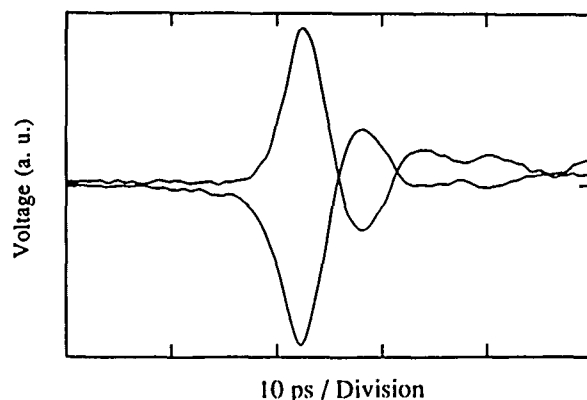


Figure 8. Electrooptically measured voltage at the anode (positive going trace) and cathode (negative going trace) of the sampling diode pair.

To measure the speed of the sampler, we used the attenuated NLTL as a test signal generator. With a sampling rate of 4.5 GHz and a measurement bandwidth of 70 kHz, the diode sampler was able to measure the 40 mV, 4 ps falltime signal of the attenuated NLTL (Fig. 9). The ringing is due to the underdamped response of the 35 dB attenuator. The actual falltime is most likely on the order

of 3.5 ps, however, this could not be verified since the signal is too small to be reliably electrooptically sampled.

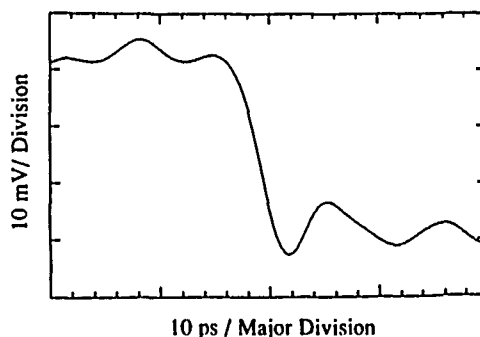


Figure 9. Output of an attenuated NLTL measured by the Schottky diode sampling bridge.

To get a better measure of the speed of this sampler, we used a 5 times frequency multiplier probe which has measurable power from 80 to 128 GHz [13].

With the multiplier probe providing the input test signal, the node being electrically sampled was simultaneously probed by the electrooptic sampler. The power computed from the voltage measured by the sampling head was divided by that measured with the optical probe. The result is shown in Fig. 10. Here 0 dB corresponds to the video response at 82 MHz. The graph shows that the response is relatively flat up to 128 GHz. If the phase is linear up to this frequency, the time resolution of this all electrical sampler is better than 2.7 ps.

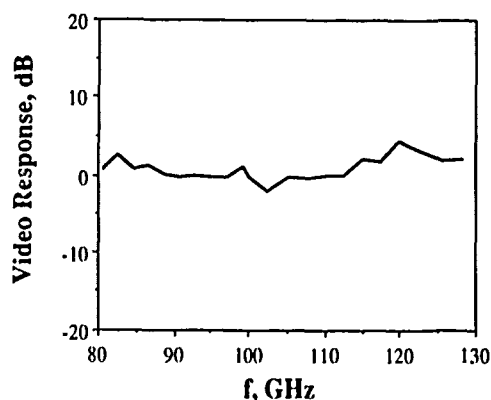


Figure 10. Video response of the Schottky diode sampling bridge from 80 to 128 GHz.

Even at 3.5 ps, the speed of the pulse generator driving the diodes is still the speed limiting factor. Using a hyperabrupt doped nonlinear transmission line to switch the sampling diodes would greatly improve performance, possibly to over 300 GHz. While the large diodes in the nonlinear transmission lines

have an RC cut-off frequency of 900 GHz, the sampling diodes cut-off is only 300 GHz due lithography limits encountered in scaling. The sampling diodes are connected in series at the output of the nonlinear transmission line so it must charge 4 fF of diode capacitance through 120 Ω of diode resistance thus degrading the strobe pulse. With improved lithography and diode design, diode series resistance can be reduced below 20 Ω allowing switching times well below 1 ps.

With improved sampling diodes driven by the hyperabrupt nonlinear transmission line, sub-picosecond time resolution should be obtainable.

Conclusion

In conclusion, we have fabricated a nonlinear transmission line using hyperabrupt-doped Schottky diodes capable of producing 1.6 ps falltime electrical shock-waves with an amplitude of 6 V. This improved design also consumed half of the area of the previous uniformly doped lines. We have used the uniformly doped lines to produce 4 ps FWHM gating pulses to drive a pair of 300 GHz sampling diodes. The pulses were obtained using a coplanar waveguide differentiator that also provides balance. With this design we have demonstrated a sampler bandwidth in excess of 130 GHz using no optical components. We believe bandwidths in excess of 300 GHz should be readily obtained with an improved diode process.

Acknowledgments

The authors would like to thank Yi-Ching Pao for the MBE growth and Gerald Li for performing the nitride deposition. This work was supported by Office of Naval Research (ONR) contract N00014-85-K-0381 and Air Force Office of Scientific Research contract F49620-88-C-0103. R. A. Marsland acknowledges an ONR fellowship, and C. J. Madden acknowledges a Newport Research Award.

References

- [1] R. Landauer, "Parametric amplification along nonlinear transmission lines," *J. Appl. Phys.* **31**, 479 (1960).
- [2] M.J.W. Rodwell, D.M. Bloom, and B.A. Auld, "Nonlinear transmission line for picosecond pulse compression and broadband phase modulation," *Elect. Lett.* **23**, 109 (1987).
- [3] M.J.W. Rodwell, C.J. Madden, B.T. Khuri-Yakub, D.M. Bloom, Y.C. Pao, N.S. Gabriel, and S.P. Swierkowski, "Generation of 7.8 ps electrical transients on a monolithic nonlinear transmission line," *Elect. Lett.* **24**, 100 (1988).
- [4] C.J. Madden, M.J.W. Rodwell, R.A. Marsland, D.M. Bloom, and Y.C. Pao, "Generation of 3.5 ps fall-time shock waves on a monolithic nonlinear transmission line," *IEEE Elec. Dev. Lett.* **9**, 303 (1988).
- [5] C.J. Madden, R.A. Marsland, M.J.W. Rodwell, D.M. Bloom, and Y.C. Pao, "Hyperabrupt-doped GaAs nonlinear transmission line for picosecond shockwave generation," *Appl. Phys.* **54**, 1019 (1989).
- [6] K.J. Weingarten, M.J.W. Rodwell, and D.M. Bloom, "Picosecond optical sampling of GaAs integrated circuits," *IEEE J. Quant. Elect.* **QE-24**, 198 (1988).
- [7] K. Lundien, R.J. Matlack, J. Archer, and R. Malik, "Hyper-abrupt junction varactor diodes for millimeter-wavelength harmonic generation," *IEEE Trans. Microwave Theory Tech.* **MTT-31**, 235 (1983).
- [8] W.M. Grove, "Sampling for Oscilloscopes and Other RF Systems: Dc Through X-Band," *IEEE Trans. Microwave Theory Tech.* **MTT-14**, 629 (1966).
- [9] J. Merkelo and R.D. Hall, "A dc-to-20-GHz Thin-Film Signal Sampler for Microwave Instrumentation," *IEEE J. Solid-State Circuits* **SC-7**, 50 (1972).
- [10] S.R. Gibson, "Gallium Arsenide Lowers Cost and Performance of Microwave Counters", *Hewlett-Packard Journal*, February 1986, p 4.
- [11] R.A. Marsland, V. Valdivia, C.J. Madden, M.J.W. Rodwell, and D.M. Bloom, "130 GHz Gallium Arsenide Monolithic Integrated Circuit Sampling Head", to be published in *Applied Physics Letters*.
- [12] K.C. Gupta, R. Garg, and I.J. Bahl, *Microstrip Lines and Slotlines*, (Artech House Inc., Norwood, 1979), p 356.
- [13] R. Majidi-Ahy, and D.M. Bloom, "120-GHz active probes for picosecond device measurement," in this volume.

Ultra-High Bandwidth Detachable Optoelectronic Probes

M. Scheuermann, R. Sprik, J.-M. Halbout, P. A. Moskowitz,
and M. Ketchen

*IBM Research Division, T. J. Watson Research Center, Box 218,
Yorktown Heights, New York 10598*

ABSTRACT

Ultra-high bandwidth detachable optoelectronic sampling probes have been fabricated and characterized. Electrical pulses having a correlation FWHM of 3.5 picoseconds can propagate across the probe contacts. The bandwidth of these probes is greater than 200 GHz. Pulses have been launched from a probe to a short transmission line and detected with a second probe. A single probe configuration has been used to characterize the optical response of a GaAs photodetector.

INTRODUCTION

In the past few years there has been considerable interest in using optoelectronic sampling techniques to study the response of high speed electrical devices, packages, and interconnects [1-3]. Picosecond electrical pulses are routinely produced and detected using photoconducting switches activated by short laser pulses. Because these switches have such high bandwidths, it is difficult to make reproducible and calibrated connections to a device under test (DUT). This difficulty can be avoided if the photoconducting switches are integrated on the same chip as the DUT. This has been done to study pulse propagation on passive transmission line structures. In general, switch fabrication is not compatible for integration with devices, although some progress has been made in process compatibility by fabricating polysilicon switches on SiO₂. In addition substantial real estate is required to launch and detect clean signals. A second technique

used to characterize devices is to wirebond chips with photoconducting switches to chips with the DUT. It has been demonstrated that under ideal geometrical conditions electrical pulses having a FWHM as short as 3 picoseconds can propagate across short wirebonds [3]. However, significant ringing was observed even under well controlled conditions. Furthermore, although wire bonds may be adequate to study a small number of devices, probing a larger number of devices is impractical. Once optoelectronic chips with the generating/sampling gaps are bonded to a device, it is virtually impossible to remove them without permanent damage to both the transmission lines as well as the bonding pads of the device. A probe which can repeatedly and nondestructively contact and detach from the bonding pads of a test site is needed. In this paper the design, fabrication and characterization of such a probe is discussed.

DESIGN AND FABRICATION

A schematic cross-section of the probe is shown in Fig. 1. The photoconducting layer and the metal pattern defining the transmission lines are on the bottom side of the probe. Photoconducting switches are illuminated from the top by focusing the optical pulses through the transparent substrate. Contacts from the probe to the DUT are made through gold contacts located at the end of the transmission lines. The geometry of the probe is shown in Fig. 2. A balanced 120 ohm coplanar transmission line is used to carry the signals to/from the contacts to photoconducting detector/generator sites. Tapers at the end of the transmission lines are

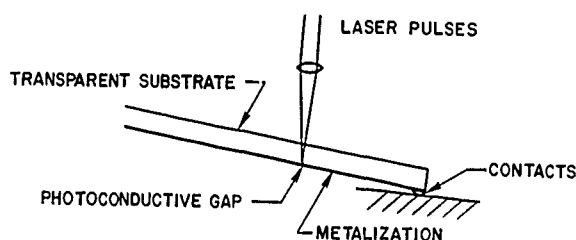


Figure 1. Cross-section of the probe. Optical pulses are focused through the probe onto a photoconducting switch. The electrical pulse propagates to or from the DUT through the contacts at the end of the probe.

used to match the pad configuration of the device. The transmission line is approximately 2 cm long so that reflections from the far end of the lines will not interfere with the waveform being generated or detected for several hundred picoseconds. Pads at the far end of the lines are used to bias the lines and detect the sampled output. The side probe tapers away from the transmission-line quickly to minimize the impedance mismatch. Since the entire substrate is optically active, pulses can be generated by shorting between the side gap and the transmission line (side gap excitation) or anywhere between the two lines (sliding contact excitation). Waveforms can be detected in a similar manner. Probes have been fabricated on SOS (silicon on sapphire) substrates. SOS was chosen because it is mechanically strong, optically transparent, and high-speed photoconducting switches can be easily fabricated on this substrate. The substrate is 15 mils thick with $0.5\ \mu\text{m}$ of intrinsic silicon on one side and the other side is optically polished. Wafer processing is relatively simple consisting of one level of metal and one implant. The transmission lines are $1\ \mu\text{m}$ thick sputtered aluminum and defined by liftoff. An oxygen implant is needed to shorten the lifetime of the carriers in the silicon. The probes are diced from the wafer and gold contacts are bonded at the ends of the tapers. Reliable and reproducible contacts can be achieved by ball bonding gold wires onto the tapers and then breaking the wire from the ball. The gold contacts are approximately $80\ \mu\text{m}$ in diameter, substantially shorter than wire bonds. Hence, a much smaller inductive discontinuity is possible between the transmission lines and the DUT. Because the waveform is sampled on the probe, all other connections are either lowspeed or dc, so wire bonded connections are adequate. The

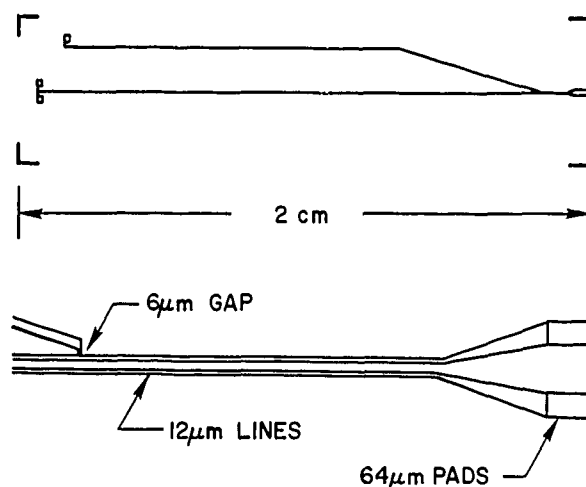


Figure 2 a) Metal pattern on the bottom of the probe. The length of the line is nearly 2 cm long. A third line is used to provide electrical contact for the side gap probe. b) plot of the probe end showing taper. The side probe is 10 microns long and 6 microns from the transmission lines. Gold contacts are bonded to the end of the tapers.

optoelectronic probe is supported by a PC board and mounted on the arm of an x-y-z translation stage so that the probe can be accurately positioned and placed on the pads of a test site. In addition, the probe also has the rotational degree of freedom about the transmission line so that both contacts hit the DUT simultaneously. The translation stage is designed to mount on a probe station so that positioning is aided by independent wafer control and a microscope.

PROBE CHARACTERIZATION

Standard optical sampling techniques have been used to characterize the bandwidth of these probes. The technique is shown schematically in Fig. 3. A laser generating 150 femtoseconds optical pulses at 100 MHz is used to trigger the photoconducting switches. The beam is split into two synchronous beams, one to trigger or generate the electrical signal, the second to sample the electrical signal of interest. Typically, the trigger beam is chopped at low frequencies so lockin detection can be used. As the delay of the sampling beam is increased, the amplitude of the measured waveform is obtained. To generate the electrical pulse, a dc bias is placed across the line to be shorted. At the detector, the bias is produced by the waveform which is being

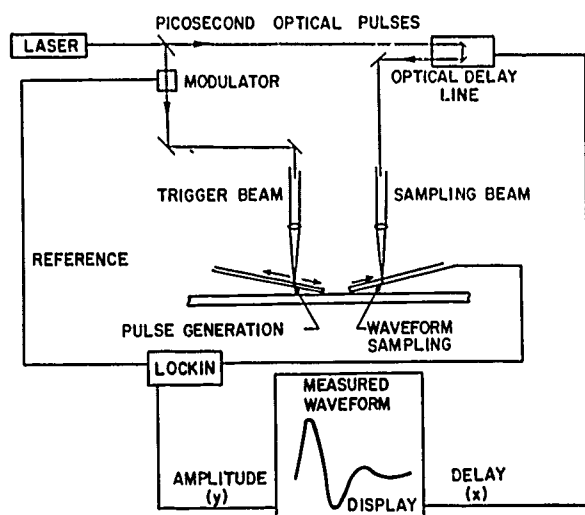


Figure 3. Schematic of optical sampling apparatus.

sampled. It should be pointed out that the measured electrical pulse is the correlation between the actual electrical pulse and the electrical response of the sampling switch.

To characterize the probe a pulse was generated on the probe via sliding contact excitation. The pulse propagated through a taper, the contacts and was detected on a SOS wafer with a matching taper and transmission line. The final waveform shown in Fig. 4 had a FWHM of approximately 3.5 picoseconds and a corresponding bandwidth greater than 250 GHz. The amplitude of the pulse is estimated to be 1 mV. The pulse is very clean with no significant ringing observed. The pulse width is most likely limited by the response of the photoconductor and may be improved by optimization of the implant and processing. This measurement is reproducible after repositioning the probe. The probes were tested in a dual probe configuration. A signal was launched on one probe, propagated through a contact, 1 mm of transmission line (DUT) and then through the contacts on a second probe, 2 mm of transmission line and then sampled using side gap detection. The detected waveform shown in Fig. 5 has a FWHM of 5.7 picoseconds. Some ringing is observed, however it is not inherent to the probe or the contacts since it was not observed in Fig. 4. Instead it is associated with ringing in the 1 mm transmission line which is consistent with the period of the ringing.

The gold contacts survive well over a hundred hits if used carefully. Care must be taken to insure

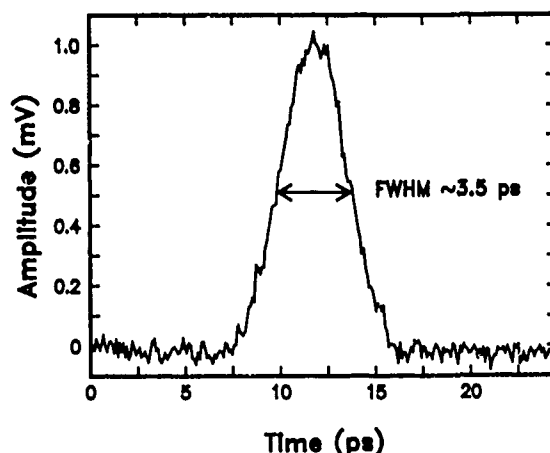


Figure 4. Pulse detected after propagation through contact and 1 mm of transmission line.

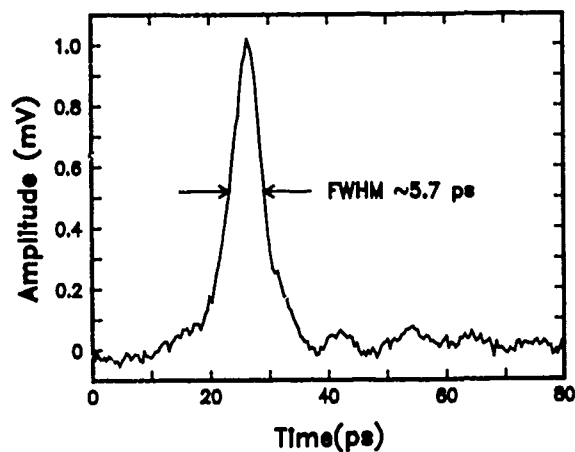


Figure 5. Pulse detected after propagation through two contacts and 4 mm of transmission line.

both contacts hit simultaneously. Approximately two mils of horizontal skating is required to insure good electrical contact. No probe has failed due to the contacts. The major failure of the probes is due to electrical breakdown or shorting between the side probe and the closest line. This problem is accentuated in dry weather when static charge is worst. Future designs will minimize this problem. It is relatively easy to align the contacts to the pads of the DUT, although the best geometry for observation is at an angle facing the contact side of the probe. In this configuration the reflection of the contacts can be observed on the pads so the precise location of contact is known.

PHOTODETECTOR CHARACTERIZATION

The response of a GaAs photodetector was meas-

ured to demonstrate the capabilities of the probe. Details of the diode structure and fabrication are given elsewhere [4]. A reverse bias was applied across the photodetector by applying a voltage between the two transmission lines. One beam of the sampling system was used to excite the photodetector. The second beam triggered a sampling gap on the probe. Figure 6a-b show results obtained by varying the power of the pulses illuminating the photodetector. In both cases a rise time of approximately 10 picoseconds was observed. Increasing the power by a factor of 32 resulted in an increase of 25 in the maximum amplitude of the pulse. At higher power the falltime of the detector was nearly twice as long due to carrier saturation effects. Figure 7a-b show the response of the photodiode at two bias voltages under the same illumination conditions. In both cases a similar risetime is measured. The amplitude increased with the bias voltage indicating more carriers were col-

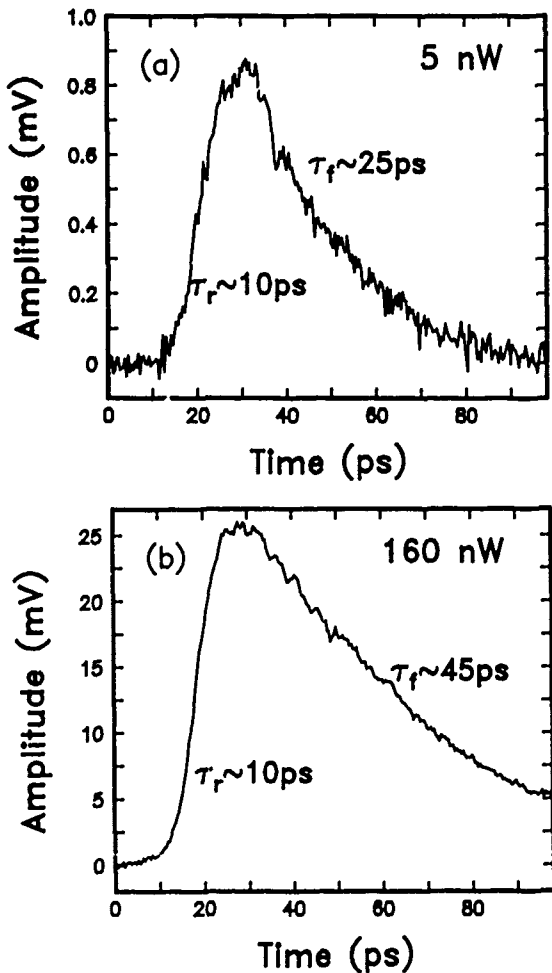


Figure 6. Power dependence of GaAs photodetectors a) 5 nW, b) 160 nW.

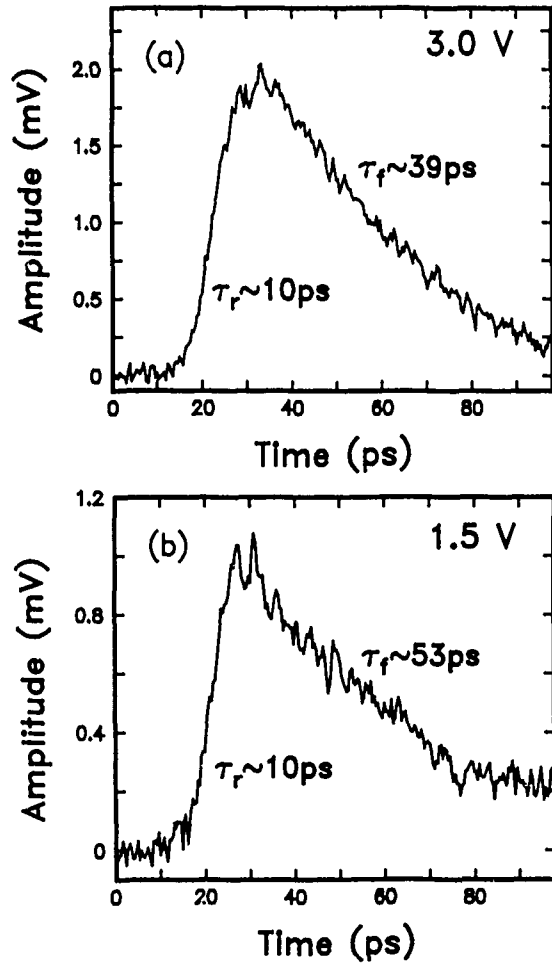


Figure 7. Bias dependence of GaAs photodetectors a) 3.0 V, b) 1.5 V.

lected. Furthermore, the falltime of the pulse decreases with increasing bias voltage because of the larger drift field at higher bias. These results demonstrate how the probes can be used to examine the detailed electrical behavior of the photodiode.

CONCLUSIONS

We have fabricated and characterized ultra-high speed detachable sampling probes. These probes have the highest bandwidth of any probe available. Contact to the DUT is controlled, reproducible and nondestructive. In addition, since the probe is used many times it can be well characterized. We have demonstrated the use of this probe for high speed device, and package characterization. A number of design improvements are being made including fiber coupling, lithographically defined contacts, step function generation, ac coupling with dc bias and multi-connector probes.

ACKNOWLEDGMENTS

We would like to thank R. McIntosh for help in fabrication, D. Grischkowsky for generous use of his laser facilities and D. Rogers for the GaAs photodiodes.

R. Sprik's present address: Natuurkundig Laboratorium, Valckenierstraat 65, 1018 XE, Amsterdam, Netherlands, 20-5255661.

REFERENCES

1. D. H. Auston, "Picosecond Photoconductors," in Picosecond Optoelectronic Devices, C. H. Lee, ed. (Academic Press, London 1984), p 73.
2. B. J. Van Zeghbroeck, W. Patrick, J.-M. Halbout, and P. Vettiger, "105-GHz Bandwidth Metal-Semiconductor-Metal Photodiode," IEEE Electron Device Letters, EDL-9 No. 10, p. 527 (1988).
3. P. G. May, G. P. Li, J.-M. Halbout, M. B. Ketchen, C. C. Chi, M. Scheuermann, I. N. Duling III, D. R. Grischkowsky and M. Smyth, "Picosecond Electrical Pulses in Microelectronics," proceedings of the conference on Ultrafast Phenomena, June 1986, Snowmass Colorado.
4. D. L. Rogers, "Monolithic Integration of a 3-GHz Detector/Preamplifier Using a Refractory Ion Implanted MESFET Process," IEEE Electron Device Letters, EDL-7, No.11, p. 600 (1986).

Measurement of Gigahertz Waveforms and Propagation Delays in an InGaAs/InAlAs MODFET Using Phase-Space Absorption Quenching

J. M. Wiesenfeld,* M. S. Heutmaker,[†] I. Bar-Joseph,[‡] D. S. Chemla,[‡] J. M. Kuo,[‡]
T. Y. Chang,[‡] and C. A. Burrus*

*AT&T Bell Laboratories, Crawford Hill Laboratory, Box 400, Holmdel New Jersey 07733

[†]AT&T Bell Laboratories, Box 900, Princeton, New Jersey 08540

[‡]AT&T Bell Laboratories, Holmdel, New Jersey 07733

Abstract

We use the phase-space absorption quenching (PAQ) effect as a high-speed optical probe of the carrier density in the channel of an InGaAs/InAlAs modulation-doped FET (MODFET). This effect is caused by the presence of carriers in the quantum well that forms the MODFET channel, which suppresses the optical absorption of the 10 - 20 ps probe pulses at wavelengths near the first subband edge due to Pauli exclusion. Because the technique probes the carrier density in the gate, it can determine the logic state of the MODFET. We combine the charge-sensitive PAQ technique with voltage-sensitive electro-optic sampling to study internal dynamics of the MODFET. A channel charging time of 11 ps and a gate to drain propagation delay of 15 ps are measured.

The high mobility of electrons in modulation-doped quantum wells (MD QW) has been exploited in the fabrication of high-speed modulation-doped field effect transistors (MODFETs) in several material systems. [1,2] Modulation doping spatially separates the free carriers from the ionized donor impurities, which increases the carrier mobility by reducing impurity scattering of the carriers. [3] In a MODFET, the free carriers in the QW form the conducting channel beneath the gate, and the conductivity of the channel is proportional to the carrier density, which can be controlled by a reverse bias applied to the gate. The

optical absorption spectrum of the MD QW changes significantly with the carrier density, and this effect allows us to optically probe the carrier density in the channel of the MODFET as the gate voltage varies. [4-6] The presence of a free electron plasma in the QW fills states in the first conduction subband, and the Pauli exclusion principle inhibits optical absorption transitions into these states. Thus the absorption at wavelengths near the band edge is quenched when the channel contains carriers, and the absorption is recovered when the channel is depleted. This phenomenon, phase space absorption quenching (PAQ), is the two-dimensional analogue of the Burstein-Moss effect. For a carrier density in the QW of 10^{12} cm⁻², the width of the quenched spectral region can exceed 60 meV, and fractional modulation of a probe beam in this wavelength range may be as large as several percent. [5]

In this work we report the application of phase-space absorption quenching (PAQ) to the measurement of gigahertz frequency waveforms in an InGaAs/InAlAs modulation-doped quantum well FET (MODFET). We combine the PAQ sampling technique, which is charge-sensitive, with electro-optic sampling, [7,8] which is voltage-sensitive, to study device operation.

PAQ sampling relies on changes in the absorption of a probe beam by the device under test. In contrast, other optical probing techniques which are sensitive to charge density are based on the refractive index variation caused by the variation of the carrier density in the device. The refractive index changes

are transformed into probe beam intensity variation by interferometric techniques. [9-11]

A schematic of the experimental arrangement for measuring gigahertz waveforms using the PAQ effect is shown in Fig. 1. This arrangement is nearly identical to that used in previous work for electro-optic sampling of integrated circuits. [12,13] Three frequency synthesizers are locked to a common reference frequency. Synthesizer #1 drives a modelocked, external cavity semiconductor laser, which produces pulses of 10 - 20 ps duration over the wavelength range from 1.48 - 1.56 μm , at repetition rate f_1 . The gate of the MODFET is driven at frequency f_2 by synthesizer #2. Pulses from the laser are incident on the MODFET from the rear, pass through the quantum well channel under the gate, reflect off the gate electrode, and after a second pass through the quantum well channel are reflected by a beamsplitter into a receiver. The presence of carriers in the channel causes an increase in the transmission of the probe beam, which is detected by the receiver. f_2 is slightly larger than f_1 , so the pulse train from the laser sweeps through the current waveform at the rate $\Delta f = f_2 - f_1$. Synthesizer #3 is set to Δf and triggers the data acquisition electronics, which records changes in probe beam transmission.

The device studied is a depletion mode InGaAs/InAlAs MODFET made by molecular beam epitaxy on an InP substrate. [4] The

MODFET is configured as a 50 Ω common source inverter, as shown in the insert in Fig. 1. V_{DD} provides the drain-source bias and V_{GS} is the dc gate bias. For this device, pinch-off occurs at $V_{GS} = -1.0$ V.

Waveforms were measured by PAQ sampling at a variety of wavelengths between 1.48 μm and 1.56 μm . The shapes of the measured waveforms depend on the probing wavelength and on the bias conditions. Figure 2 shows waveforms measured at 1.557 μm for input of a 500 mV peak to peak sine wave at 3.96 GHz, for several values of the gate bias V_{GS} . The positive vertical direction in Fig. 2 represents increasing transmission and, hence, increasing carrier concentration in the QW. The fractional modulation of the probe beam is as large as 0.4% for values of V_{GS} between -0.5 V and 0 V. As V_{GS} approaches pinch-off, the PAQ signal becomes smaller and the waveform flattens at the bottom. The distortion near pinch-off occurs because carriers are present in the channel only when the gate voltage ($V_{GS} + \text{signal}$) is above -1.0 V. This will occur only for a small positive portion of the input sine wave. Therefore, the PAQ signal, which is caused by the presence of free carriers in the channel, will be nonzero only for a small portion of the sinusoid, as the experiment shows. The waveform at 0V gate bias is also slightly distorted, flattening at the top. This is caused by the approach to complete bleaching of the absorption at the probe wavelength as the

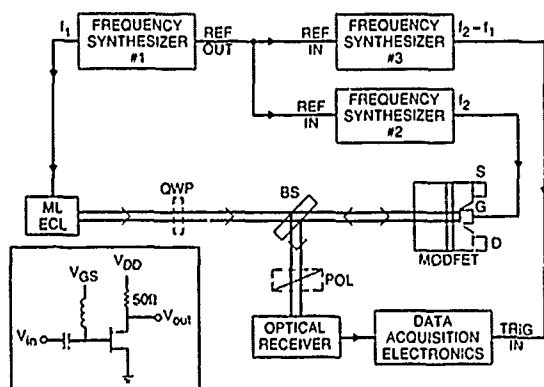


Figure 1: Experimental schematic. MLECL = modelocked external cavity semiconductor laser, BS = beamsplitter. The quarter-wave plate (QWP) and polarizer (POL) are used for the electro-optic sampling measurement.

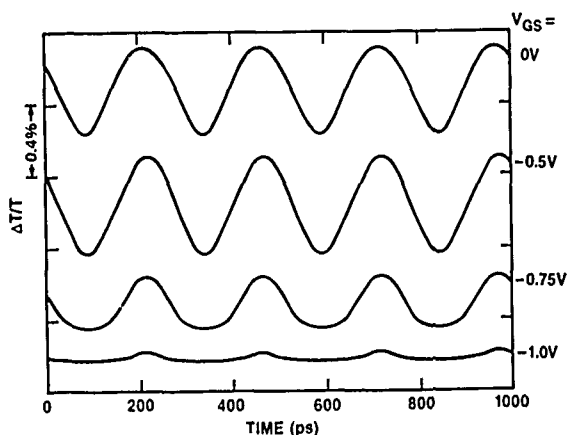


Figure 2: Waveforms measured by PAQ sampling for 3.96 GHz input sine wave. Probe wavelength is 1.557 μm , V_{DD} is 1.0V, and V_{GS} values are indicated. For clarity, the waveforms are offset arbitrarily.

carrier density in the quantum well becomes very large. Data qualitatively similar to that shown in Fig. 2 is obtained for other values of V_{DD} and for other probe wavelengths near the band edge. The PAQ sampling technique can measure very high frequency waveforms. Figure 3 shows waveforms measured for frequencies up to 20 GHz. The absolute magnitude of the signal measured at 19.68 GHz is small because of attenuation near 20 GHz in the cables and directional couplers used between synthesizer #2 and the MODFET.

The temporal resolution of PAQ sampling is determined by the intrinsic speed of PAQ, the transit time of the probe pulse through the QW, and the duration of the probe pulse. The first two effects have subpicosecond time scales, so for the present experiments the limitation to the temporal response is the 10-20 ps duration of the probe pulse.

Because the probe is tuned to a wavelength of absorption of the empty QW, the PAQ sampling technique is potentially invasive. Indeed, there is a tradeoff between invasiveness and sensitivity. For shot-noise limited detection, the sensitivity, expressed in terms of the minimum detectable sheet charge density, $\Delta\bar{N}_{min}$ (which is the density that produces a signal-to-noise ratio of unity for a 1 Hz detection bandwidth) is

$$\Delta\bar{N}_{min} = \frac{2}{\sigma} \sqrt{q/i_{avg}} \text{ carriers/cm}^2\sqrt{\text{Hz}},$$

where q is the electron charge, i_{avg} is the

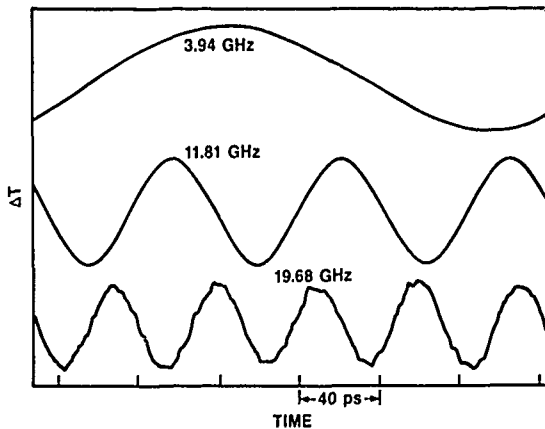


Figure 3: Waveforms measured for various frequencies. Probe wavelength is $1.489 \mu\text{m}$, $V_{DD} = 1.5\text{V}$, and $V_{GS} = -0.3\text{V}$. The waveforms are arbitrarily scaled in the vertical direction.

average received photocurrent, and $\sigma \approx 1 \times 10^{-14} \text{ cm}^{-2}$ is the absorption cross section at the probe wavelength. The power from the laser is adjusted as a compromise between sensitivity and invasiveness. The average power incident on the MODFET is $6 \mu\text{W}$ at a 2 GHz repetition rate, which produces a received photocurrent of about $0.3 \mu\text{A}$. For this photocurrent, the predicted $\Delta\bar{N}_{min}$ is $1.4 \times 10^8 \text{ carriers/cm}^2\sqrt{\text{Hz}}$. Experimentally, we estimate $\Delta\bar{N}_{min}$ to be $1 \times 10^9 \text{ carriers/cm}^2\sqrt{\text{Hz}}$. A factor of three difference between the experimental and theoretical $\Delta\bar{N}_{min}$ is due to the $3 \mu\text{m}$ diameter of the focused probe beam, which is three times larger in one dimension than the $1 \mu\text{m}$ width of the gate; the remaining factor is excess laser noise. At the level of probe power used, invasiveness is minimal. The source-drain current is changed by less than 0.7% by probe beam irradiation under all experimental conditions.

The PAQ sampling of the MODFET can be combined with the technique of direct electro-optic sampling to measure propagation delays in the FET. While PAQ sampling is sensitive to charge, electro-optic sampling is sensitive to longitudinal electric fields in the InP substrate of the MODFET and converts electric field (i.e. voltage differences) across the substrate into birefringence along the optical path of the probe beam. Thus, the voltage present at the position of the probe beam is detected as a change in state of polarization of the probe beam. The electro-optic sampling measurement is implemented using the quarter-wave plate (QWP) and analyzer shown by dashed lines in Fig. 1. To measure propagation delays, a ~ 50 ps electrical pulse produced by a comb generator [12] operating at 2 GHz is coupled into the gate. The peak amplitude of the electrical pulse is 500 mV. Input and output voltage waveforms are measured by electro-optic sampling under the gate and drain bonding pads, respectively, and the charge in the gate channel is measured by PAQ sampling. The fractional modulation of the probe beam measured by electro-optic sampling is about ten times smaller than that for PAQ sampling. Results are shown in Fig. 4 for $V_{DD} = 1.0\text{V}$ and $V_{GS} = -0.5\text{V}$. Propagation delays are determined by measuring shifts in the arrival time of the peak of the measured waveform,[13] and are 11 ± 3 ps for gate voltage to PAQ delay

and 15 ± 3 ps for the gate voltage to drain voltage delay. The 11 ps delay for the appearance of charge in the gate channel is the gate charging time, while the 4 ps subsequent delay for the arrival of the pulse at the drain reflects the drain capacitance. It is clear that the combination of charge and voltage sensitive probing techniques is a powerful tool for investigating detailed dynamics of semiconductor devices.

The details of the PAQ signal depend on probe wavelength [4-6] and device operating conditions. This could be exploited to obtain other information on the conducting channel (field inside the QW for example) which is important in understanding the physics of these devices. We have shown, however, that the logic state of the MODFET is probed directly, so PAQ sampling should find significant application to the study of integrated circuits fabricated with MODFET devices. The relatively large changes in probe beam transmission observed in PAQ sampling enables measurement of the temporal variation of carrier density in the gate channel of MODFETs with excellent signal-to-noise ratio. The temporal resolution reported here is limited by the 10 - 20 ps duration of the optical probe pulse, but with shorter pulses it could be extended into the subpicosecond time domain.

We thank J. R. Talman and J. S. Perino for technical assistance.

The present address for I. Bar-Joseph is

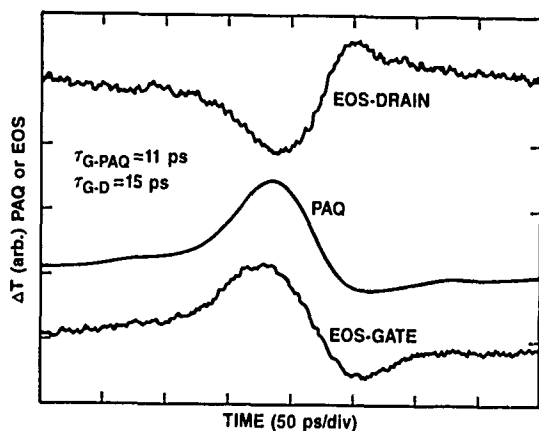


Figure 4: Measured propagation delays. Probe wavelength is $1.489 \mu\text{m}$, $V_{DD} = 1.0\text{V}$, and $V_{GS} = -0.5\text{V}$. The traces are arbitrarily scaled in the vertical direction.

Department of Physics, Weizmann Institute of Science, Rehovot, Israel. The present address for J. M. Kuo is AT&T Bell Laboratories, Murray Hill, NJ 07974.

References

1. N. J. Shah, S. S. Pei, C. W. Tu, and R. C. Tiberio, *IEEE Trans. Electron Dev.*, **ED-33**, 543 (1986).
2. U. K. Mishra, J. F. Jensen, A. S. Brown, M. A. Thompson, L. M. Jelloian, and R. S. Beaubien, *IEEE Electron Dev. Lett.*, **EDL-9**, 482 (1988).
3. H. L. Stormer, *Surf. Sci.*, **132**, 519 (1983).
4. D. S. Chemla, I. Bar-Joseph, J. M. Kuo, T. Y. Chang, C. Klingshern, G. Livescu, and D. A. B. Miller, *IEEE J. Quantum Electron.*, **QE-24**, 1664 (1988).
5. D. S. Chemla, I. Bar-Joseph, C. Klingshern, D. A. B. Miller, J. M. Kuo, and T. Y. Chang, *Appl. Phys. Lett.*, **50**, 585 (1987).
6. I. Bar-Joseph, J. M. Kuo, C. Klingshern, G. Livescu, D. A. B. Miller, T. Y. Chang, and D. S. Chemla, *Phys. Rev. Lett.*, **59**, 1357 (1987).
7. J. A. Valdmanis and G. A. Mourou, *IEEE J. Quantum Electron.*, **QE-22**, 69 (1986).
8. B. H. Kolner and D. M. Bloom, *IEEE J. Quantum Electron.*, **QE-22**, 79 (1986).
9. H. K. Heinrich, D. M. Bloom, and B. R. Hemenway, *Appl. Phys. Lett.*, **48**, 1066 (1986).
10. U. Keller, S. K. Diamond, B. A. Auld, and D. M. Bloom, *Appl. Phys. Lett.*, **53**, 388 (1988).
11. G. N. Koskovich and M. Soma, *IEEE Electron Dev. Lett.*, **EDL-9**, 433 (1988).
12. A. J. Taylor, R. S. Tucker, J. M. Wiesenfeld, C. A. Burrus, G. Eisenstein, J. R. Talman, and S. S. Pei, *Electron. Lett.*, **22**, 1068 (1986).
13. J. M. Wiesenfeld, R. S. Tucker, A. Antreasyan, C. A. Burrus, A. J. Taylor, V. D. Mattera, and P. A. Garbinski, *Appl. Phys. Lett.*, **50**, 1310 (1987).

120-GHz Active Wafer Probes for Picosecond Device Measurement

R. Majidi-Ahy and D. M. Bloom

Edward L. Ginzton Laboratory, Stanford University, Stanford, California 94305

Abstract

We have developed frequency-multiplier and harmonic mixer active wafer probes for picosecond device measurements to 120 GHz. All-electronic 100 GHz on-wafer frequency-response measurements have been demonstrated using these probes.

Introduction

On-wafer frequency domain electronic measurements of high speed devices are presently limited to 40 GHz. For higher frequency analysis and circuit design with these devices, equivalent circuit models derived from measurements below 40 GHz are typically used. However due to frequency-dependent elements in the equivalent circuit models of the devices, these extrapolations to higher frequencies are not accurate. Therefore direct measurements at the operating frequencies above 40 GHz are essential to accurately characterize and understand high speed devices and IC's.

Optical techniques for picosecond device measurements have been demonstrated. Time-domain approaches using photoconductive element (PCE) pulsers in conjunction with PCE or electrooptic samplers provide a broad bandwidth, but have limited accuracy and dynamic range due to the discontinuities in the circuit created by the PCE's and low PCE pulser power[1]. Frequency-domain approaches such as direct electrooptic sampling in conjunction with CW electronic sources have also been demonstrated up to 100 GHz[2]. However currently all these optical techniques require addition of external elements such as transmission lines or PCE's to the device under test and therefore devices and IC's in their standard layout configurations can not be tested.

Conventional millimeter-wave sources and harmonic mixers have their output in waveguide configuration[3]. On-wafer testing of picosecond

devices and IC's however, requires a probe with planar output configuration to contact the device or IC pads. At these frequencies, signal transfer between a waveguide port to a probe with planar tip configuration cannot be accomplished easily over broad bandwidth with low loss and single mode operation. An alternative approach is to generate and down-convert the millimeter-wave signal in the probe itself, where the probe incorporates the nonlinear circuit.

We have developed active electronic wafer probes as shown in Figure 1 for 80-120 GHz measurements of ultrafast devices. An active probe frequency-multiplier generates the stimulus signal and supplies it to the device under test. An active probe harmonic mixer down-converts the output signal from the device under test. Both probes have coplanar waveguide (CPW) tips which contact the device pads on wafer. These probes are interfaced with external instrumentation via their coaxial connectors.

Active Probe Frequency-Multiplier

The active probe frequency-multiplier has a coaxial input and a CPW output and converts an input microwave signal to its fifth harmonic at millimeter-wave frequencies and delivers it to the device or circuit under test. A 16-25 GHz input signal to the active probe quintupler, provided by a commercially available microwave source and a power amplifier, is multiplied by five to generate the 80-125 GHz output signal supplied to the device under test by contacting its input pads.

The frequency-multiplier circuit consists of an input low-pass filter and matching network, a nonlinear element, and an output bandpass filter and matching network. The schematic circuit diagram of the quintupler is shown in Figure 2. The circuit design was implemented in CPW. The device used as the nonlinear element in the

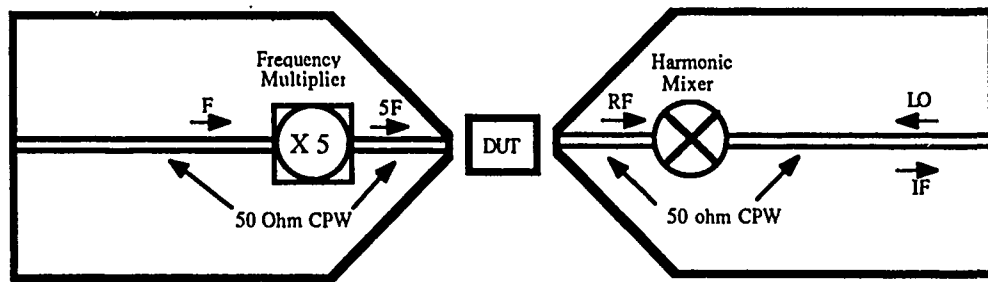


Figure 1. The general schematic of the millimeter-wave active electronic wafer probes for frequency response measurements.

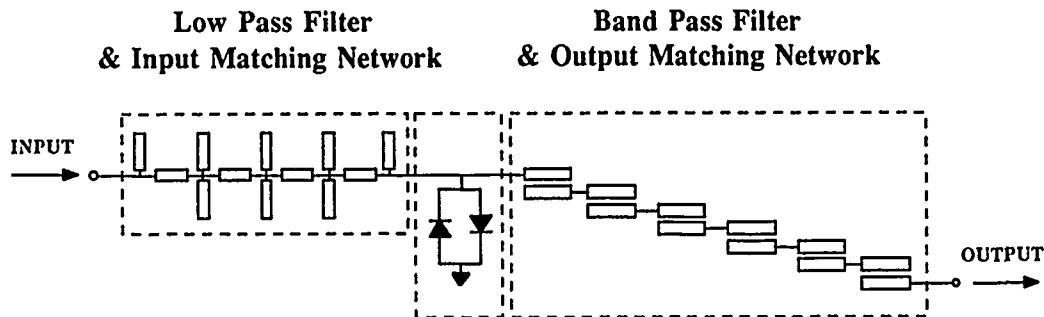


Figure 2. The schematic circuit diagram of the active probe frequency-multiplier.

frequency-multiplier was a beam lead antiparallel pair of double-stacked GaAs Schottky barrier diodes manufactured by Hewlett-Packard Company. Using an antiparallel diode pair results in a symmetrically distorted waveform and suppression of the even harmonics of the pump signal. Lower conversion loss is therefore obtained for odd harmonic generation. Each Schottky diode consisted of two parallel 10 micron long fingers and had a zero-bias junction capacitance of 30 fF, a series resistance of 10 ohms, a built-in potential of 0.68 volts and a breakdown voltage of 10 volts. The intrinsic zero-bias cut-off frequency of the antiparallel diode pair was in excess of 1 THz.

The input filter and matching network was a five section direct-coupled low pass circuit implemented in CPW with its first cut-off frequency at 30 GHz. The output filter and matching network was a six section coupled-line CPW band-pass circuit. Bond wires were used to connect the ground planes to suppress the undesired zero-cutoff fundamental modes of CPW and coupled CPW's.

The active probe quintupler performance was measured by equivalent-time sampling. A recently reported electrical sampler[4] measured the output time-waveform of the quintupler from which the spectral content and the power in each harmonic was determined. The time-waveform of a 95 GHz signal generated by the active probe

frequency multiplier, and measured by the electrical sampler is shown in Figure 3. An output voltage of 180 mV peak-to-peak was generated by the active probe quintupler at 95 GHz. Due to the finite rejection of the quintupler output filter a small amount of the fundamental pump signal at 19 GHz, can be observed as an envelope to the fifth harmonic waveform in Figure 3. The spectral content of this waveform is shown in Figure 4. Although the fifth harmonic was more than 12 dB above all other undesired harmon-

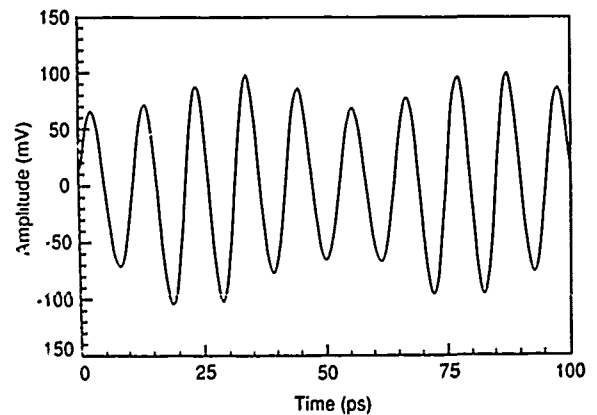


Figure 3. A 95 GHz waveform generated by the active probe quintupler.

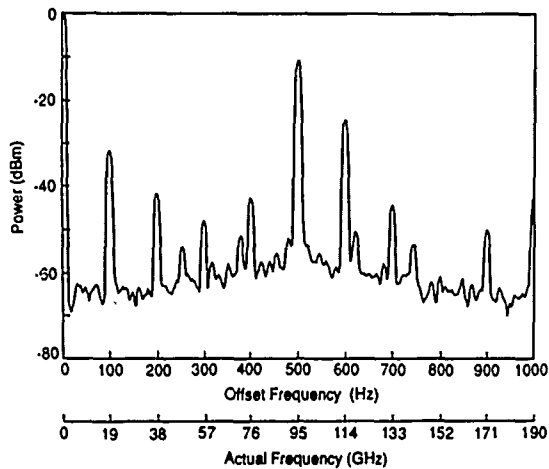


Figure 4. Spectral content of the active probe quintupler 95 GHz waveform.

ics, due to the hybrid construction of the active probe quintupler and increasing imperfection of the antisymmetry in the nonlinear element with increasing frequency, sixth harmonic power level was closest to the desired fifth harmonic output as shown in Figure 4. The measured quintupler

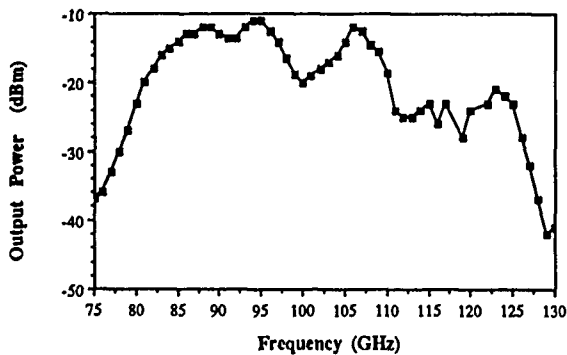


Figure 5. Active probe quintupler power output vs frequency.

output power versus frequency is shown in Figure 5. The quintupler bandwidth was from 80 to 125 GHz with a maximum power of -11 dBm. An average conversion loss of 38 dB was obtained which is comparable to the commercially available W-band waveguide quintuplers that benefit from significantly lower conduction losses of the waveguide medium[3].

Active Probe Harmonic Mixer

The active probe harmonic mixer has a coaxial LO (Local Oscillator)/IF (Intermediate Frequency) port and CPW RF (Radio Frequency) input port and converts a millimeter-wave signal at the output of the device under test to an IF signal. The harmonic mixer was designed to operate with an LO in the frequency range of 3.75-6 GHz chosen such that the mixing product of the 20th harmonic of the LO with the RF signal in the 75-120 GHz frequency range, produced a fixed 20 MHz IF signal.

The harmonic mixer circuit consists of a diplexer, a LO/IF filter and matching network, a nonlinear element and an RF filter and matching network. The schematic diagram of the harmonic mixer circuit is shown in Figure 6. An unbiased anti-parallel beam-lead GaAs Schottky diode pair in series, was used as the nonlinear element in the harmonic mixer. The antisymmetry in the I/V characteristics of the diode pair results in the suppression of the even order LO harmonics and odd order mixing products and therefore a lower conversion loss[5]. Each diode had a zero-bias junction capacitance of 20 fF and a series resistance of 6 ohms, and each beam lead had an inductance of 100 pH.

The signal path for the LO and IF were on the same side of the diode pair and these signals were separated by a diplexer and a commercially available diplexer separates the 3.75-6 GHz LO and the 20 MHz IF external to the probe. A CPW lowpass filter and matching network was designed to present 50 ohm to the LO and IF signals, and to terminate RF and most significant idlers in a short by a lumped chip capacitor

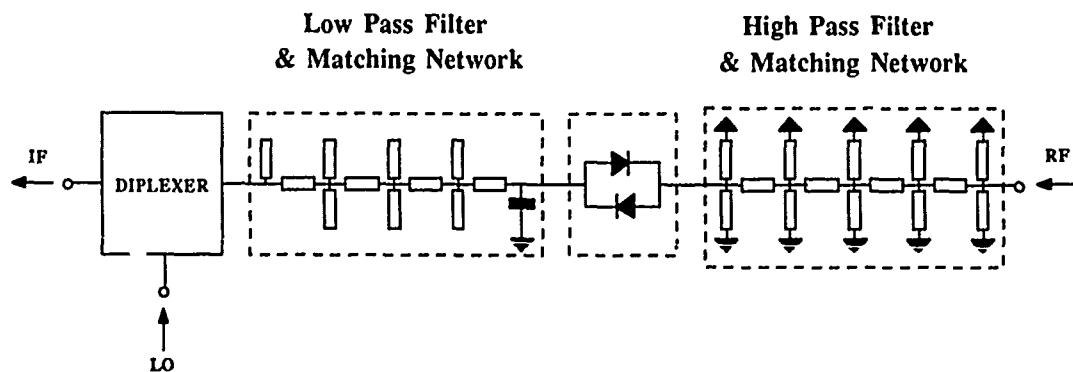


Figure 6. Schematic diagram of the 80-120 GHz active probe harmonic mixer circuit.

as the first circuit element at the diode input plane. A CPW high pass filter was designed to present 50 ohm to the RF and short circuit LO, IF and lower LO harmonics and mixing products at the diode output plane. Proper termination of the idlers was essential in obtaining low conversion loss and effective decoupling of the RF and LO/IF circuits.

The performance of the harmonic mixer was measured using an active probe frequency-multiplier with known output power to supply the 75-120 GHz RF signal. The measured conversion loss of the harmonic mixer is shown in Figure 7. The average conversion loss was approximately 48 dB, which is comparable to W-band waveguide harmonic mixers that benefit from low loss waveguide environment for their high frequency RF circuit[6].

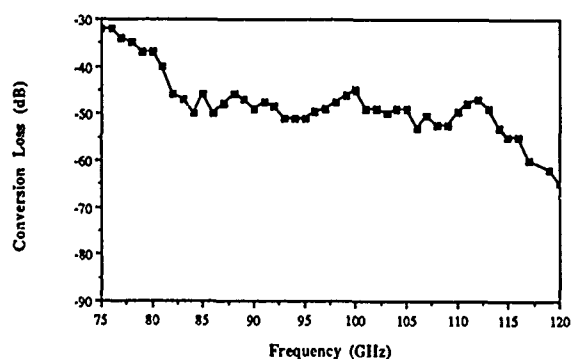


Figure 7. Measured conversion loss of the 80-120 GHz active probe harmonic mixer.

100 GHz On-Wafer Measurements

The frequency-multiplier and harmonic mixer active probes were used in conjunction with an HP 8510 automatic network analyzer for 100 GHz on-wafer frequency response measurements. The active probe quintupler supplied the 75-100 GHz signal to the device under test and the signal at the output of the device under test was down-converted by the active probe harmonic mixer. The 20 MHz IF output of the active probe harmonic mixer was then interfaced with HP85102, the signal processing section of an HP 8510 network analyzer, for a second stage down-conversion to 100 KHz and data display by HP85101. A modified HP software program was used to control the frequency and power settings of the two synthesizers and the display of the HP8510 to obtain swept frequency response measurements.

An example of such measurements is shown in Figure 8. A matched CPW 20 dB attenuator on a GaAs wafer was measured using the active probes from 75 to 100 GHz. At frequencies below 80 GHz the measurement accuracy was reduced due to a degradation in the output match of the active probe quintupler.

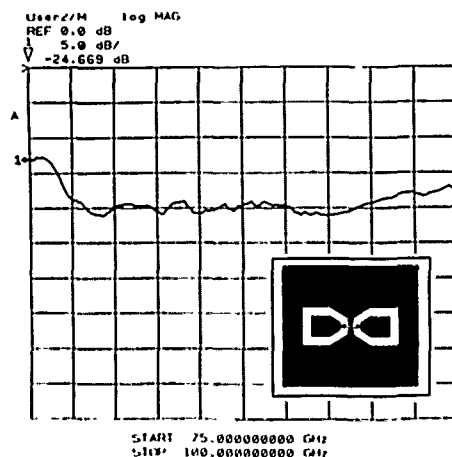


Figure 8. 75-100 GHz measured insertion loss of a matched CPW 20 dB attenuator by active electronic wafer probes.

Conclusion

We have reported the development of millimeter-wave active electronic wafer probes for characterization of picosecond devices and IC's. An active probe quintupler generates the 80-125 GHz signal and supplies it to the device or circuit under test on the wafer. An active probe harmonic mixer down-converts the 80-120 GHz signal from the output of the device under test to an IF frequency. These wafer probes together were used in conjunction with an HP 8510 automatic network analyzer to demonstrate 100 GHz all-electronic on-wafer frequency-response measurements.

Acknowledgments

The authors wish to thank Pauline Prather for her work in assembling the probes, Mohammad Shakouri and Reed Gleason for their help and suggestions. We acknowledge the generous measurement equipment donations by the Hewlett-Packard Company, Tektronix Inc. and Cascade Microtech Inc. This work was supported in part by Air Force Office of Scientific Research contract F49620-85K-0016. Reza Majidi-Ahy acknowledges a Rockwell Science Center/Stanford Center for Integrated Systems fellowship.

References

- [1]- Halbout J.-M. et al: "Picosecond Electrical Pulse for VLSI Electronics Characterization", *Picosecond Electronics and Optoelectronics II*, Springer-Verlag 1987, pp. 36-39.
- [2]- Majidi-Ahy R. et al: "Millimeter-Wave Active Probe Frequency-Multiplier for On-Wafer Characterization of GaAs Devices and IC's", *Electronics Letters*, Vol. 25, No.1, January 1989, pp.6-8.

[3]- Sayed M. M. et al: "Millimeter-Wave Sources and Instrumentation", HP Journal, April 1988, pp. 6-11.

[4]- Marsland R. A. et al: "Picosecond Pulse Generation and Sampling with GaAs Integrated Circuits", in this volume.

[5]- Kohn M. et al: "Harmonic Mixing with an Anti-Parallel Diode Pair", IEEE Trans, August 1975, MTT-23, pp. 667-673.

[6]- Matreci B. et al: "Unbiased Harmonic Mixers for Millimeter-Wave Spectrum Analyzers", HP Journal, November 1986, pp. 22-26.

Observation of Low-Power-Level Picosecond Pulses Using Single-Photon Counting Techniques

M. Hamana, A. Kimura, T. Umeda, and Y. Cho

*The Institute of Scientific and Industrial Research, Osaka University, Mihogaoka 8-1,
Ibaraki, Osaka 567, Japan*

M. Kanda

*Research and Development Group, Basic High Technology Laboratory, Sumitomo
Electric Industries, Ltd., Shimaya 1-1, Konohana-ku, Osaka 554, Japan*

ABSTRACT

Picosecond measurement capability using low power-level pulses from semiconductor lasers based on a combination of nonlinear process and single-photon counting technique was tested and the preliminary result showed sensitivities of μW range.

INTRODUCTION

In recent years, reliable and stable picosecond pulses became available from semiconductor lasers with mode-lockings by forming an absorbing section in the active layer [1] or by inserting a saturable absorber such as an MQW platelet into the external cavity [2], or chirp-compensation technique [3]. Semiconductor laser may offer a unique regime in the field of ultrafast measurements, because of its compactness and reliability. Peculiarity of ultrafast measurements using those picosecond pulses available from semiconductor lasers is its associated low level power. Corresponding to this low handling power level, pulse detection process must be reconsidered. For example, if we attempt to make a time-resolved measurement utilizing the correlation or sampling technique by a certain nonlinear process with using pulses from semiconductor lasers, signal levels inevitably become low because the conversion efficiency of the nonlinear process drops excessively. Here in this paper, we report a preliminary result of our investigation of finding out the possibility of application of single-photon counting technique onto a low level picosecond pulse measurement based on the cross-correlation or sampling scheme using a nonlinear crystal.

EXPERIMENTAL SETUP

To measure the sensitivity of cross-correlation

measurements using single-photon counting technique, we tested an "unbalanced autocorrelation" measurement as shown in Fig.1. A picosecond pulse (pulsewidth 18 - 25 ps) train from a mode-locked semiconductor laser ($\lambda=830\text{ nm}$) was split into two unbalanced pulse trains. Smaller one served as a signal I_s , while larger one served as a pump I_p . After receiving a mutual variable delay τ , they were focused onto a nonlinear crystal of LiIO_3 with a non-collinear configuration. Second harmonic signal generated in the bisectinal direction between I_s and I_p , which is proportional to $I_s \cdot I_p$, producing the unbalanced autocorrelation signal, was lead through a guiding fiber to a single-photon counting photomultiplier (Hamamatsu Photonix 2757 kept at room temperature). The single-photon counting rate as a function of τ

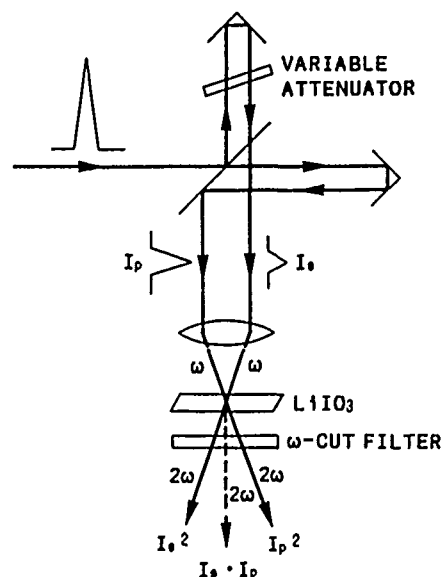


Figure.1 Experimental setup

gave unbalanced autocorrelation traces such as shown in Fig.2. In this example, correlation pulse width is 30 ps and corresponding actual pulse width is 22 ps assuming a Gaussian pulse shape. The signal to noise ratio S/N of this detected correlation trace was measured with a definition of S/N as $S/N = (C_s - C_b)/\Delta C_s$, where C_s is the average count during the gate time t_g at the correlation trace peak, C_b is the averaged background (at the flat outskirts part of the trace) count during the gate time t_g , and ΔC_s is the value of the standard deviation of the count during the gate time t_g at around the correlation trace peak.

EXPERIMENTAL RESULT

From those traces as shown in Fig.2, with having the gate time t_g for photon counting as a parameter and keeping the pumping power level I_p (peak value) constant, signal to noise ratio S/N as a function of input signal level I_s (also peak value) was plotted. The result is shown in Fig.3. It is seen that, while the signal level is small, S/N is proportional to I_s (slope 1), and for sufficiently large signal levels, it becomes proportional to the square root of I_s (slope 1/2).

FACTORS DETERMINING THE S/N RATIO

The observed result shown in Fig.3 means that the main cause of the noise was shot noise (proportional to $I_s^{1/2}$) at high signal levels (around $10^3 - 10^4 \mu W$) and it was masked out by noise which was independent of signal levels (hereinafter, called as level-independent noise) at low signal levels (around $10^2 - 10^3 \mu W$). Improvements of S/N by lengthening the gate time t_g is approximately proportional to the square root of t_g as it is usually the case in the signal averaging process.

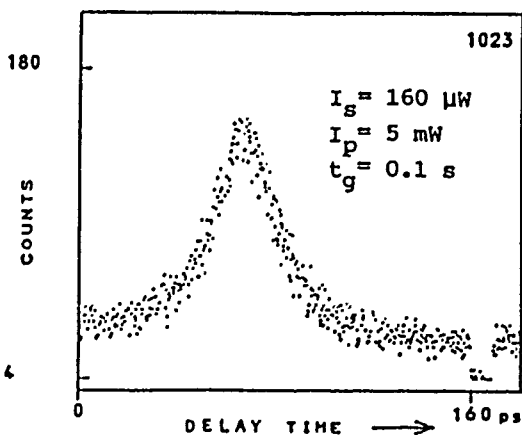


Figure.2 An example of single-photon counted unbalanced autocorrelation trace

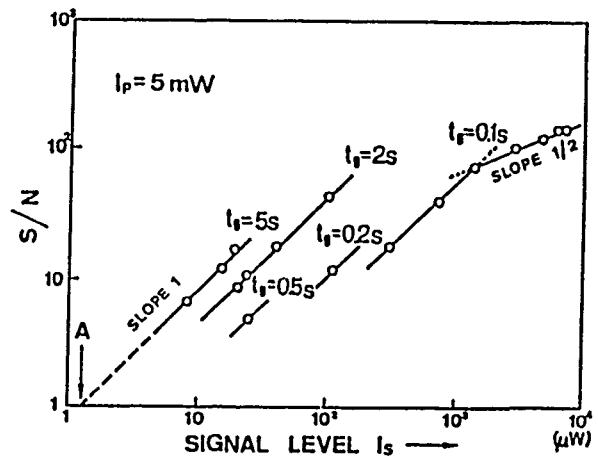


Figure.3 Variations of signal to noise ratio as functions of input signal level

Main cause of this level-independent noise is considered to be the following two; the one originated from the photon counting process and the one that from the optical nonlinear process. The former is comprised of thermal dark counts from the photocathode and its associating partition fluctuations in the electron-multiplication process, either of which take place even in dark, while the latter is caused by direct photo-excited counts proportional to I_p^2 , which is induced by second harmonic of the pump light I_p , giving constant background counts and their accompanying fluctuations. In the non-collinear configuration we employed, since the I_p^2 -component have only a poor phase matching in the crystal and also its output delivering direction is different from that of the $I_s \cdot I_p$ -component which constitutes the signal, its mixing into the $I_s \cdot I_p$ -signal component is considered very little, but usually I_p is taken as $I_p \gg I_s$ in order to keep the conversion efficiency to the second harmonic high particularly when I_s is in low levels, the I_p^2 -component mixed into the $I_s \cdot I_p$ -signal direction becomes non-negligible, and causes counts comparable with that by the $I_s \cdot I_p$ -signal component. In this respect, care must be taken on reducing the scattering of I_p^2 -component at the output-side surface of the crystal or the imperfection of the beam alignment in the crystal. In our experiment, with $I_p = 5$ mW, main cause of the level-independent noise was the pump light origin mentioned above.

In Fig.3, solid lines indicate theoretical estimations described below: Here denoting the signal count rate (per sec.) by c_s and the background count rate (per sec.) by c_b , $C_s = c_s t_g$, and $C_b = c_b t_g$ with having the gate time t_g .

At high signal levels, since the shot noise dominates, ΔC_s is given by $(c_s t_g)^{1/2}$, then the S/N is expressed by $S/N = (c_s^{1/2} - c_b c_s^{-1/2}) t_g^{1/2}$, giving an approximate expression of $S/N \approx (c_s t_g)^{1/2}$ for the case of $c_s \gg c_b$, i.e., for high signal levels. The signal count rate c_s is expressed by

$c_s = \lambda_{2\omega} (hc)^{-1} \eta_c \eta_{pm} I_s$ where h is Planck's constant, c is the light velocity, $\lambda_{2\omega}$ is the second harmonic wavelength, η_c is the conversion efficiency of the crystal to the second harmonic, η_{pm} is the quantum efficiency of the photomultiplier. The conversion efficiency η_c is given by, assuming that the phase matching condition is fulfilled, $\eta_c = (\mu_o/\epsilon_o)^{3/2} \times (2\pi c/\lambda_{2\omega})^2 (Ld)^2 (2n^3 A)^{-1} I_p$ [4], where $(\mu_o/\epsilon_o)^{1/2}$ is the free space impedance, n is the refractive index of the crystal, d is the nonlinear coefficient of the crystal, A is the beam cross-sectional area in the crystal, L is the effective cross-over length between mutually non-collinear signal and pump beams in the crystal, and I_p is the pumping power. For our experiment, using values; $\lambda_{2\omega}=415$ nm, $n=1.8$, $d=5 \times 10^{-24}$ MKS (for LiIO_3), $L=20$ μm , $A=60$ μm^2 , $I_p=5$ mW, η_c becomes $\eta_c=1.6 \times 10^{-8}$. The quantum efficiency η_{pm} of the photomultiplier we used is about 15 % at around $\lambda_{2\omega}$. Using these values and with $t_g=0.1$ s, the estimated slope-1/2 line becomes $S/N \approx 1.8 \times 10^3 I_s^{1/2}$ (I_s in Watts), which shows a good agreement with observed plot.

Meanwhile, at lower signal level, where the level-independent noise is dominant, the S/N can be expressed by $S/N = (c_s t_g - c_b t_g) / (c_b t_g)^{1/2} = (c_s c_b^{-1/2} - 1) t_g^{1/2}$, giving an approximate expression $S/N \approx c_s c_b^{-1/2} t_g^{1/2}$ for $c_s > c_b$. This means the slope-1 dependence of S/N on I_s for constant c_b (level-independent noise), the situation met in the low signal levels. Estimated slope-1 lines become $S/N \approx 2 \times 10^5 I_s t_g^{1/2}$.

MINIMUM DETECTABLE POWER

In case that the S/N ratio at low signal levels is masked by the level-independent noise, as is in the present experiment, the sensitivity (minimum detectable input signal level determined as a input power level giving unity S/N) is hence determined solely by the magnitude of the level-independent noise. Although we didn't take particular care on the reduction of those noises composing the level-independent noise so far, the sensitivity we could get was as low as $1 \mu\text{W}$ with a pump-

ing peak power I_p of 5 mW and a gate time t_g of 5 seconds as seen at point A on the extended (dashed) line.

Since the level-independent noise was mainly caused by the pump light itself, discrimination of this component from the output signal is essential to improve the sensitivity of the system for operation ranges such as in the present experiment. Further improvement will be gained by cooling the photocathode of the photomultiplier.

CONCLUSION

Responding to the recent availability of picosecond pulses from semiconductor lasers, the measurement capability utilizing low power level pulses based on a combination of nonlinear process and single-photon counting technique has been tested and μW order sensitivity was achieved. There is still much room to improve this sensitivity.

REFERENCES

1. P. P. Vasil'ev, V. N. Morozov, Y. M. Popov, and A. B. Sergev, "Subpicosecond pulse generation by tandem-type AlGaAs DH laser with colliding pulse mode locking", *IEEE J. Quantum Electron.* QE-22, 149-151(1986).
2. Y. Silberberg, P. W. Smith, D. J. Eilenberger, D. A. B. Miller, A. G. Gossard, and W. Wiegmann, "Passive mode locking of a semiconductor diode laser", *Optics Lett.* 9, 507-509 (1984).
3. A. Takada, T. Sugie, and M. Saruwatari, "High-speed picosecond optical pulse compression from gain-switched 1.3- μm distributed feedback-laser diode through highly dispersive single-mode fiber", *J. Lightwave Technology* LT-5, 1525-1533 (1987).
4. For example, A. Yariv and P. Yeh *Optical Waves in Crystals*, John Wiley and Sons, N.Y., Chap.12 (1984).

Investigation of Picosecond Time-Resolved Photoluminescence in Gallium Arsenide with 3- μ m Spatial Resolution

Thomas A. Louis

*Physics Department, Heriot-Watt University, Riccarton, Edinburgh EH14 4AS,
United Kingdom*

ABSTRACT

A novel instrument has recently been developed for picosecond time-resolved photoluminescence (TRPL) investigation of GaAs with 3 μ m spatial resolution: the Photoluminescence Lifetime Microscope Spectrometer (PL μ S). The PL μ S is based on time-correlated single photon counting (TCSFC) with a single photon avalanche diode (SPAD) detector. Sensitivity of the PL μ S, especially in the near infrared wavelength region (800–1000nm), is several orders of magnitude better than for synchroscan streak cameras. A signal-to-noise ratio of better than 1000:1 is typically obtained from a GaAs sample region of 3 μ m diameter at room temperature and at excess carrier densities (at peak excitation) as low as 10^{15}cm^{-3} . As a result of the very low optical power requirements, a pulsed diode laser can be used as the excitation source. All signals are conveniently handled via optical fiber, which makes the PL μ S a unique instrument for routine assessment of semiconductor materials and devices in an industrial environment.

1. INTRODUCTION

It is well known that, at present, all commercial gallium arsenide (GaAs) and indium phosphide (InP) substrates for the electronics and optoelectronics industry show some degree of material inhomogeneity [1]. These inhomogeneities lead to an undesirable scatter in the performance of directly implemented devices (e.g. FETs) and they affect the quality of subsequently grown epitaxial layers. This is a particularly severe problem in the manufacturing of complex electrical and optoelectronic integrated

circuits (ICs, OEICs), because it reduces the production yield and imposes practical limits on IC and OEIC chip complexity.

In order for III-V device technology to reach a modest level of integration, say compared with silicon VLSI technology today [2], the nature of these inhomogeneities must be better understood so that GaAs and InP substrate technology can improve. Novel experimental techniques are needed for the investigation of spatial fluctuations in the value of fundamental material parameters on a diffusion length scale. The experimental techniques with which this has been attempted in the past are photoluminescence (TRPL, CWPL), cathodoluminescence (TRCL, CWCL), electron beam induced current (EBIC), optical beam induced current (OBIC), near infrared absorption (NIR) and etch pit density (EPD). Generally, the information content of a single measurement in a time-resolved experiment is higher than in a CW experiment. On the other hand, the sensitivity of traditional experimental setups with very fast detection systems, such as e.g. single shot streak cameras, non-linear optical gates etc., is rather poor. The problem here lies in the interpretation of data from such experiments, which normally requires complex analytical models in order to account for non-linear effects at the typical high excitation densities. So far, no single method provides accurate enough information in order to unambiguously explain the origin of the observed microstructures.

Picosecond time-resolved photoluminescence (TRPL) is the most powerful and most widely used experimental technique for investigating the fast carrier dynamics in GaAs. The popularity of this method has grown rapidly since synchronously pumped picosecond dye laser sources and

ultrafast streak camera detection systems have become commercially available.

Yet, despite the successful usage of synchronously pumped dye lasers and streak cameras in many areas of fundamental research, these systems have significant drawbacks: streak cameras suffer from the lack of good photocathode materials in the technologically important near infrared wavelength range (800–1500nm) and picosecond dye laser systems are still far too complex and unreliable in order to be suitable for routine applications in an industrial environment.

In this paper, we present the novel Photoluminescence Lifetime Microscope Spectrometer (PLuS) [3]. The PLuS is based on time-correlated single photon counting (TCSPC) [4] with a single photon avalanche diode (SPAD) [5] detector. Figure 1 shows the complete PLuS system and labels individual components. Typical results are shown for TRPL measurements on a GaAs substrate and, as an example of a simple p-n junction device, a homojunction GaAs solar cell.

2. EXPERIMENTAL TECHNIQUE

It has recently been demonstrated that a TCSPC setup with an instrumental response width of 70 ps (FWHM) can resolve fluorescence decay times of the order of 10 ps with ± 2 ps accuracy [6]. These results were obtained on a synchronously pumped laser based TCSPC system with a silicon SPAD detector of the first generation.

Continuous improvements in the timing characteristics of subsequent generations of SPADs and careful analysis of the jitter contribution from associated electronic circuitry showed the time resolution of the SPAD itself to be only twenty picoseconds (FWHM) [7]. This is comparable to the time resolution of the fastest micro-channelplate (MCP) detectors in similar TCSPC setups, below 30 ps (FWHM) [8,9].

The overall time resolution (=instrumental response width) of systems with a synchroscan streak camera is around 8–10 ps (FWHM) [10], compared with 40–45 ps (FWHM) for TCSPC systems [6–9]. However, the higher statistical accuracy of TCSPC data, the

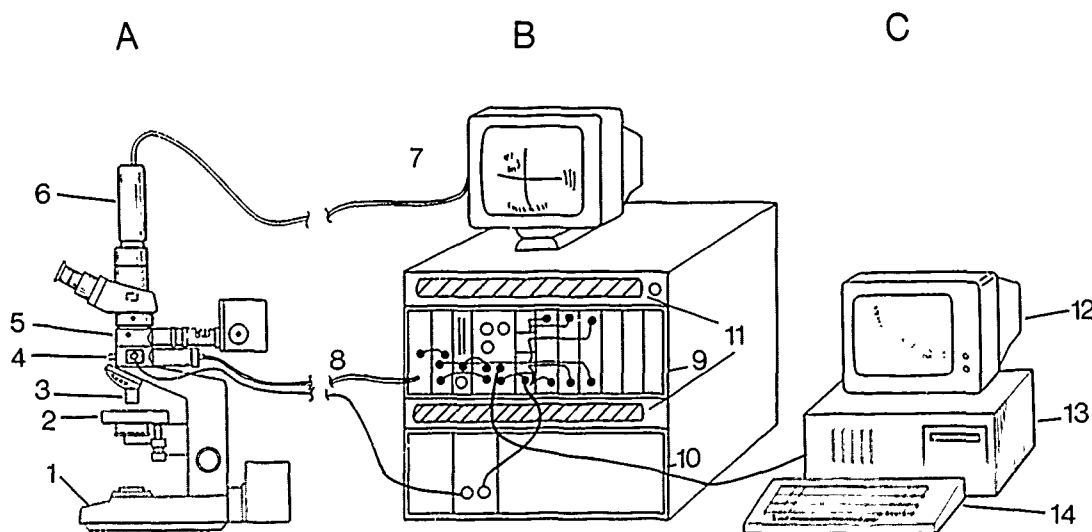


Fig.1: Photoluminescence Lifetime Microscope Spectrometer (PLuS) consisting of microscope spectrometer (A), instrument rack (B), data station (C). The labeled components are: (1) stable microscope base (optional autofocus drive, cassette wafer handling system and motorized and computer controlled XY-stage not shown), (2) manual sample stage (standard version), (3) reflecting objective, (4) customized optical routing module, (5) illuminator, (6) high resolution CCD camera, (7) video monitor for sample inspection, (8) singlemode/multimode fiberoptic links, (9) NIM timing electronics, (10) PFOS diode laser excitation source, (11) forced ventilation, (12) PC monitor and MCA display, (13) IBM PC/XT/AT, PS/2 or compatible PC for automated data collection and analysis, (14) keyboard (optional stage control).

excellent differential linearity and the larger dynamic range of TCSPC systems permit sophisticated non-linear least squares convolution analysis techniques to be applied for data reduction [11,12]. Thus, the timing accuracy of extracted decay time constants is, under favourable conditions, improved by a factor of 10-15 w.r.t. the instrumental response width or, in other words, the actual timing accuracy of the extracted (reduced) data is much better than indicated merely by the hardware time resolution.

The spectral sensitivity of the silicon SPAD is better than that of S20, S25 and S1 photocathodes in the near infrared up to about 1000 nm. Moreover, the Burstein-Moss shift of the absorption edge in the heavily doped SPAD junction and the influence of large local electric fields due to ionized impurities in the high field junction region (tunneling assisted transitions, known as the Franz-Keldysh effect [13]) effectively lower the absorption edge. For this reason, the spectral sensitivity of the silicon SPAD will faintly extend beyond the absorption edge of silicon and into the important 1300/1550nm telecommunication wavelength region. Cova recently suggested [14] that this might allow InGaAsP (Telecom) laser diode waveform measurements, as was already successfully demonstrated with an MCP based TCSPC system with S1 photocathode [15]. Whether future InGaAs-SPADs or Si-SPADs with Ge-enriched (Si/Ge graded superlattice) absorption region can extend the range of TRPL applications with the PLuS from visible and near infrared wavelengths up to 1000 nm into the 1.3/1.55 μm region remains yet to be shown.

The minimum detectability of the PLuS' TCSPC detection system is better than one photogenerated event per 10^7 pulses [16], whereas for synchroscan streak cameras this is around 1 photoelectron per 2.4×10^4 pulses [10]. In other words, the sensitivity of the PLuS at around 870 nm is such that TRPL in bulk GaAs samples can be investigated at room temperature with 3 μm spatial resolution and excess carrier densities as low as 10^{10} - 10^{12} cm^{-3} .

A compilation of the minimum performance requirements for high resolution spatial mapping of the minority carrier lifetime in GaAs and a comparison of presently available experimental techniques showed, that time-correlated single photon counting (TCSPC) with a SPAD detector was the ideal method [17].

A number of practical advantages result directly from the PLuS system's ability to operate at very low excitation densities in the range 10^{11} - 10^{13} cm^{-3} . Under low excitation conditions, bulk recombination is dominantly non-radiative, hence linear, in all but very

pure, undoped GaAs samples. Unless saturable surface/interface centers play an important role as a recombination mechanism, the overall luminescence response of the sample will be proportional to the excitation density, hence the shape and finite width of the diode laser pulse, typically several 10 ps (FWHM) for gain-switched diode lasers, are explicitly taken into account through convolution analysis of the TCSPC data.

As a result, excess minority carrier lifetimes in doped GaAs can be measured with picosecond timing accuracy even though the diode laser pulse is several ten picoseconds (FWHM) long !

3. DATA ANALYSIS

The principles of TCSPC, data reduction by non-linear least squares convolution analysis, sources of systematic instrumental error, criteria for assessing the quality of the fit etc. are discussed in detail elsewhere [18] and will not be reviewed here.

A fundamental requirement in order for convolution analysis to perform well is the availability of a proper kinetic model for fitting the raw TCSPC data. Ideally, this kinetic model should represent the analytical solution of the transient diffusion equation and appropriate boundary conditions for the sample under investigation. The experimental decay data can then be interpreted directly in terms of the fitted values for the physical parameters contained in the model.

In general, numerical solutions for the time-dependence of the external photoluminescence signal may be found, provided the structure of the (complex) sample is accurately known. Numerical solutions need to be subjected to a sensitivity analysis and suitably parametrized in order for the dominant physical parameters to be extracted.

Finally, if the structure of the sample is not known at all, convolution analysis and fitting of the raw data is still meaningful. Mathematically this is equivalent to expanding (approximating) the unknown decay function as a truncated series in terms of some basic function. A perfect numerical fit, e.g. with a multi-exponential function, should therefore be seen as a success, at least from the point of view of data reduction, although the parameters themselves are physically meaningless.

Whatever the choice of kinetic model, analytical, semi-analytical or purely phenomenological, a good fit, as assessed by the sensitive criteria of chi-square, residual distribution, autocorrelation of residuals etc., always represents the complete set of information contained in both the photoluminescence decay and the instrumental response data. The impulse response, extracted from

the raw TCSPC data by fitting over the complete decay, therefore contains the full information obtained in the experiment. Note that this information relates only to the sample itself, as it is stripped off any instrumental characteristics to a much higher degree, as compared to simple deconvolution with the instrumental response width (FWHM) [19].

4. RESULTS

The results from the TRPL measurements of two different types of sample, a GaAs substrate and a homojunction GaAs solar cell, are given in Table 1 and in Figures 1 to 6. Table 2 gives details of the two excitation sources used, a pulsed diode laser for measuring the GaAs substrate and a synchronously pumped dye laser for measuring the GaAs solar cell.

The solar cell has also been measured with the pulsed diode laser source, which gave very similar results. Generally, the advantage of the synchronously pumped dye laser over the pulsed diode laser is the availability of higher peak power (typically up to 10^4 more) and wavelength tunability. In the experiments reported here, the excitation conditions were chosen very similar for both samples, only the excitation pulse width was significantly different.

4.1 GaAs substrate

The GaAs substrate was LEC grown and n-doped (Si) at 10^{17}cm^{-3} . The sample was measured at room temperature (293 K). A gain-switched commercial AlGaAs laser diode [20] at 785nm, pigtailed with a polarization preserving single mode fiber, was used as the

excitation source (Table 2). The excitation spot size on the sample was 6 μm diameter, the spatial resolution, as defined through the detector field of view, 3 μm . The estimated maximum excited carrier density in the sample was less than 10^{15}cm^{-3} and linear non-radiative recombination prevailed in this experiment. The 5 μm diameter SPAD detector was operated uncooled (293 K) with a bias voltage of 2.0 V above breakdown.

The overall instrumental response width was 68 ps (FWHM). A three-exponential decay model

$$I_{PL}(t) = A_0 + A_1 \exp(-t/\tau_1) + A_2 \exp(-t/\tau_2) + A_3 \exp(-t/\tau_3) \quad (1)$$

was used for fitting the data. The values of these fitted parameters are given in Table 1.

Figure 2A shows the instrumental response, the TRPL decay data and the 3-exponential fit. Figure 2B shows the residual distribution and the autocorrelation function of the residuals. Figure 2C shows the impulse response function, which represents the 3-exponential model with fitted parameters as extracted from the raw data in Fig.2A by non-linear least squares analysis using iterative convolution.

The quality of the fit in terms of the value of normalized chi-square, $\chi^2=1.23$, (Table 1A) is good. However, the residual distribution reveals some systematic misfit in the rising edge of the decay. This indicates some non-linearity in the sample's luminescence response to the finite width excitation pulse. There is also some slow periodic structure in the autocorrelation plot,

Table 1 : Values of fitted parameters for the 3-exponential decay model :

$$I_{PL}(t) = A_0 + A_1 \exp(-t/\tau_1) + A_2 \exp(-t/\tau_2) + A_3 \exp(-t/\tau_3)$$

| | GaAs substrate | GaAs solar cell |
|---------------|-----------------------|-----------------------|
| τ_1 (ps) | 50.8 | 36.0 |
| τ_2 (ps) | 342 | 345 |
| τ_3 (ps) | 1101 | 1439 |
| A_0 | 57.03 | 4.51 |
| A_1 | $8.838 \cdot 10^{-2}$ | $1.915 \cdot 10^{-1}$ |
| A_2 | $2.939 \cdot 10^{-2}$ | $2.871 \cdot 10^{-3}$ |
| A_3 | $7.086 \cdot 10^{-3}$ | $4.597 \cdot 10^{-4}$ |
| XSQ | 1.23 | 1.16 |

Table 2 : Experimental conditions, data collection rate, signal-to-noise ratio and related data.

| | | GaAs substrate | GaAs solar cell |
|-------------------|---------------|-------------------|-----------------------|
| excitation WL | nm | 785 | 801.5 |
| PL detection WL | nm | 870 | 860 |
| filter halfwidth | nm | 12 | 11 |
| repetition rate | MHz | 50 | 80 |
| pulse FWHM | ps | 40 | 8 |
| average power | μW | 5 | 5 |
| signal count rate | kcps | 44 | 25 |
| data coll. time | s | 7.8 | 19.2 |
| count sum | $\times 10^3$ | 1,060 | 310 |
| peak count | | 9,996 | 11,126 |
| background | | 57.0 | 4.5 |
| s/n ratio | | 175:1 | 2,472:1 |

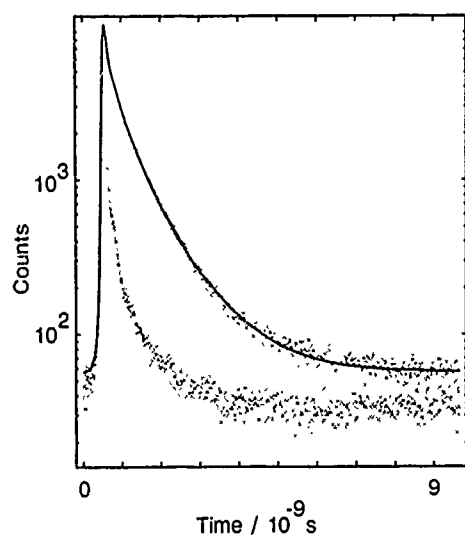


Fig.2A: Instrumental response, TRPL data (dots) and fit (line) for GaAs substrate.

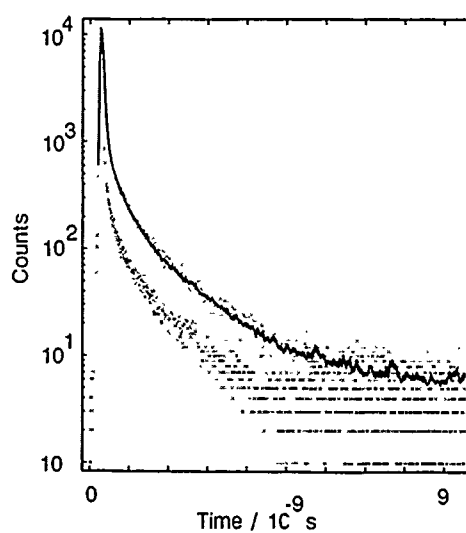


Fig.3A: Instrumental response, TRPL data (dots) and fit (line) for GaAs solar cell.

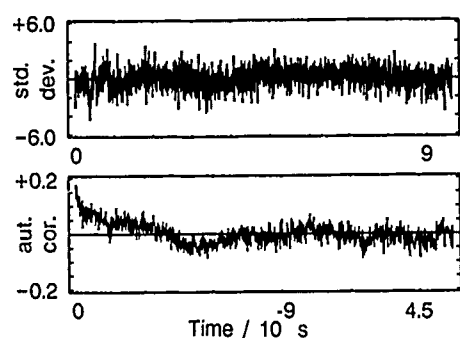


Fig.2B: Residual distribution and autocorrelation of residuals for GaAs substrate.

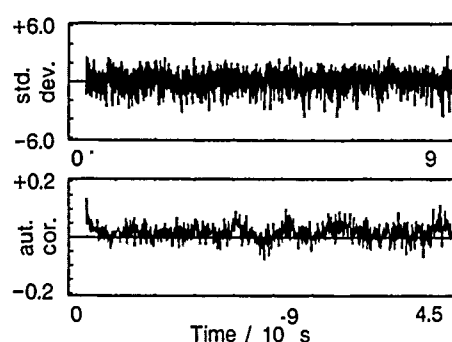


Fig.3B: Residual distribution and autocorrelation of residuals for GaAs solar cell.

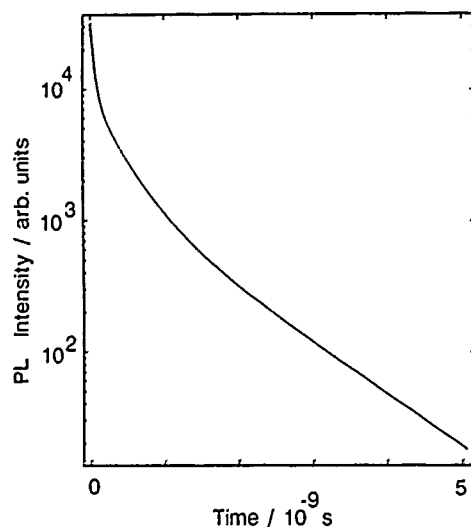


Fig.2C: Impulse response for GaAs substrate.

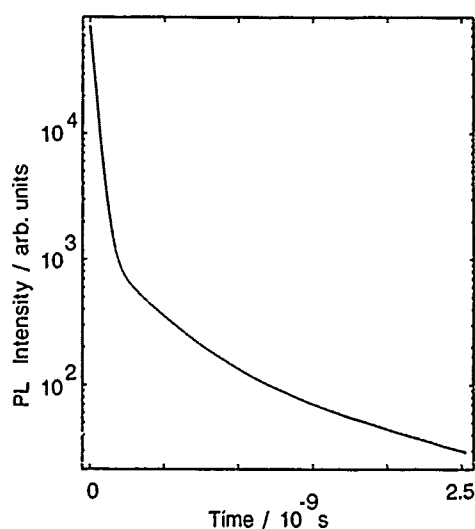


Fig.3C: Impulse response for GaAs solar cell.

which is due to degradation of the linearity of the time-to-amplitude converter (TAC), when used with a high repetition rate laser source (50 MHz) without a START/STOP rate reducer circuit [17].

4.2 GaAs solar cell

The homojunction GaAs solar cell was directly implemented on a n-doped (Si) LEC grown GaAs substrate. The $\text{Al}_x\text{Ga}_{1-x}\text{As}$ ($x \geq 0.9$) window layer was grown and the shallow emitter (0.3 μm) diffused simultaneously by LPE isothermal overgrowth with an AlGaAs:Zn melt. TRPL was measured under similar conditions as for the GaAs substrate, except that the excitation source was a suitably attenuated synchronously pumped dye laser of 8 ps (FWHM) pulse width. The overall instrumental response width was therefore slightly less, 60 ps (FWHM).

As before, a 3-exponential model was used for convolution analysis and the values of the fitted parameters are listed in Table 1B. Figure 3A shows the instrumental response, the TRPL decay data and the 3-exponential fit, Figure 3B the residual distribution and the autocorrelation of residuals, Figure 3C the impulse response function.

This time, the quality of the fit in terms of the value of normalized chi-square, $\chi^2=1.16$, is excellent and no systematic misfit is seen in the residual distribution and autocorrelation plot. Although a non-linearity in the sample's luminescence response is known to occur due to saturation of residual trap states at the passivated AlGaAs/GaAs interface, this does not lead to a misfit along the rising edge of the decay (as indeed observed with laser diode excitation), because of the very short duration of the excitation pulse.

It is interesting to note the very rapid initial decay with a slope of 36 ps (Table 1B. This is due to very efficient collection of excess minority carriers by the shallow homojunction - rather than bad material quality! - and is typical for a well designed solar cell.

5. CONCLUSION

We have described the Photoluminescence Lifetime Microscope Spectrometer (PLuS) as a novel time-correlated single photon counting instrument, based only on solid state components, i.e. diode laser excitation and SPAD detection, for use in the investigation of picosecond time-resolved photoluminescence of GaAs materials and devices.

Despite its larger instrumental response width (≈ 70 ps), the timing accuracy obtained with the PLuS (± 2 ps) is comparable with the time resolution of a synchronously

pumped dye laser based TRPL setup with synchroscan streak camera detection. The PLuS' sensitivity is, however, orders of magnitude better, especially in the near infrared wavelength range from 800-1000 (1500) nm. This allows investigation of inhomogeneous samples with microscopic spatial resolution (3 μm) even at very low excitation densities ($\leq 10^{15}\text{cm}^{-3}$).

The rugged all solid state design of the PLuS and the simplicity of use make it the first instrument of its kind compatible with routine operation in an industrial environment. Applications such as substrate wafer testing and laser diode quality control are currently being investigated.

ACKNOWLEDGMENTS

The PLuS was developed in close collaboration with Edinburgh Instruments Ltd. The prototype SPAD detector was generously provided by Prof. Sergio Cova from the Polytechnical University of Milan.

The author is a consultant to Edinburgh Instruments Ltd. (Research Park, Riccarton, Edinburgh, UK, Tel. (031) 4485944, Fax (031) 4485848).

REFERENCES AND NOTES

- [1] R.N. Thomas, S. McGuigan, G.W. Eldridge and D.L. Barrett, "Status of device quality GaAs substrate technology for GaAs integrated circuits", *Proceedings of the IEEE* **76**, 778-791 (1988)
- [2] C.G. Kirkpatrick, "Making GaAs integrated circuits", *Proceedings of the IEEE* **76**, 792-815 (1988)
- [3] The PLuS was developed in collaboration with and is now manufactured by Edinburgh Instruments Ltd, UK. Patents pending.
- [4] For a detailed description of the TCSPC technique see e.g. D.V. O'Connor and D. Phillips, "Time-correlated Single Photon Counting" (Academic, New York, 1983)
- [5] S. Cova, G. Ripamonti and A. Lacaita, "Avalanche semiconductor detector for single optical photons with a time resolution of 60 ps", *Nucl.Instrum. Methods* **A253**, 482-487 (1987)
- [6] T.A. Louis, G.H. Schatz, P. Klein-Bölting, A.R. Holzwarth, G. Ripamonti and S. Cova, "Performance comparison of a single photon avalanche diode with a micro-channelplate photomultiplier in time-correlated single photon counting", *Rev.Sci.Instrum.* **59**, 1148 (1987)

- [7] S. Cova, A. Lacaita, M. Ghioni, G. Ripamonti and T.A. Louis. "Twenty-picosecond timing resolution with single photon avalanche diodes", *Rev.Sci.Instrum.* (to be published)
- [8] D. Bebelaar, *Rev.Sci.Instrum.* 57, 1116 (1986)
- [9] H. Kume, K. Koyama, K. Nakatsugawa, S. Suzuki and D. Fatlowitz, *Appl.Opt.* 27, 1170-1178 (1988)
- [10] Y. Tsuchiya, "Advances in streak camera instrumentation for the study of biological and physical processes", *IEEE J.Quant.Electron.* QE-20, 1516-1528 (1984)
- [11] P.R. Bevington, "Data and Error Reduction for the Physical Sciences" (McGraw-Hill, New York, 1969) pp. 204-242
- [12] L.J. Dowell and G.T. Dillies, "Precision limits of lifetime estimation algorithms as determined by Monte Carlo simulation : A comparison of theory and experiment", *Rev.Sci.Instrum.* 59, 1310-1315 (1988)
- [13] see M. Gershenson, "Radiative recombination in the III-V compounds" in Semiconductors and Semimetals, R.K. Willardson and A.C. Beer, eds. (Academic, New York, 1969) Vol.2, p. 330 and refs 182-185.
- [14] S. Cova (private communication, 1988)
- [15] Hamamatsu Technical Information No. ET-03/OCT 1987, "Application of MCP-PMTs to Time Correlated Single Photon Counting and Related Procedures", p.11:
- [19] "Deconvolution" usually refers to quadratically subtracting the instrumental response width (FWHM) from the measured signal and taking the square root thereof.
- [20] Opto-Electronics Ltd., Canada, Picosecond Fiberoptic System (PFOS), laser diode module PPL50M785 fig.14 shows a laser diode waveform measurement at 1.55 μ m using a MCP with S1 photocathode in TCSPC mode. Note that the quantum efficiency of the S1 photocathode at this wavelength is only 0.00001 %, the dark count rate is typically much higher than for a SPAD detector, yet the subnanosecond structure of the waveform is perfectly resolved.
- [16] A S/N ratio of 10⁴:1 at 100 MHz excitation repetition rate and 50 kHz signal rate corresponds to a minimum detectability limit (S/N=1) of better than 1x10⁻⁷ photogenerated events per pulse.
- [17] T.A. Louis, G. Ripamonti and A. Lacaita, "Photoluminescence Lifetime Microscope Spectrometer based on time-correlated single photon counting with a single photon avalanche diode detector", *Rev.Sci.Instrum.* (to be published)
- [18] see e.g. review article by B.H. Candy, "Photomultiplier characteristics and practice relevant to photon counting", *Rev.Sci.Instrum.* 56, 183-193 (1985)

Differential Sampling with Picosecond Resolution Using Bulk Photoconductors

J. Paslaski and A. Yariv

California Institute of Technology, 128-95, Pasadena, California 91125

Abstract

A photoconductive sampling technique is demonstrated whose resolution is independent of carrier lifetime and is in principle limited only by the RC charging time of the photoconductor.

The success of photoconductive sampling has critically depended on the ability to reduce carrier lifetimes to attain sufficiently short temporal resolution. We present an alternate approach which achieves a sampling resolution limited only by the RC circuit response of charging the photoconductive gap.

The result of a typical sampling measurement, $V_{meas}(\tau)$, can be expressed as the correlation between the signal to be measured, $V_{sig}(t)$, and a sampling function, $f_{samp}(t)$ ^[1]:

$$\begin{aligned} V_{meas}(\tau) &\equiv V_{sig} \circ f_{samp} \\ &= \int dt V_{sig}(t) f_{samp}(t - \tau) \end{aligned} \quad (1)$$

For photoconductive sampling—and neglecting the finite optical pulse width and mobility transients— f_{samp} is itself a correlation between the gap conductivity $G(t)$ and a gap charging transient $h(t)$ which is typically fast (a few ps at most). If the conductivity $G(t)$ is very short, then $V_{meas} \simeq V_{sig}$ to the extent that f_{samp} approximates a delta function. If instead, the conductivity has a slow decay, then V_{meas} will be approximately the integral of V_{sig} (for sufficiently short V_{sig}) and it is recovered by a derivative operation. As such, consider the following:

$$\begin{aligned} \Delta V_{meas}(\tau) &\equiv V_{meas}(\tau) - \alpha V_{meas}(\tau + \Delta\tau) \\ &= V_{sig} \circ [h \circ (G(t) - \alpha G(t - \Delta\tau))] \end{aligned} \quad (2)$$

The expression in square brackets is a new effective sampling function composed of a sharp "spike" followed by an equal area negative tail which becomes negligible if it is much longer than the signal being measured. In the special case that $G(t)$ is an exponential decay, this tail can be eliminated altogether by an appropriate choice of the factor α . This effective sampling function is plotted in Fig. 1 for various values of $\Delta\tau$, using exponential decays for $h(t)$ and $G(t)$ (dotted line) with respective time constants of 2ps and 150 ps. It is seen that very short sampling windows can be achieved which are independent of the carrier decay, and limited only by the circuit transient $h(t)$.

We have implemented the difference operation of Eq. 2 by a double gap circuit which is similar to those used for correlation measurements of photoconductors^[1]. The experimental set-up used is diagrammed in Fig. 2. The electrical signal to be measured is fed to a microstripline and two opposing photoconductors sample it with a relative delay, $\Delta\tau$, set by the positioning of mirror M_2 . The correlation variable τ is swept by moving mirror M_1 . The low frequency average currents from the two sampling electrodes are then subtracted with the balancing factor α , and the result is synchronously detected with a lock-in amplifier. The simultaneous measurement of the two sampling signals minimizes effects due to low frequency noise of the optical pulse source which degrade simpler schemes such as just shifting the stored result of a single gap measurement and subtracting it from itself (this does work rather well). The center microstripline and two sampling electrodes were designed for 50 Ω impedance and were separated by 50 μm gaps which had a dark resistance of 80M Ω . The substrate was ordinary semi-insulating InP:Fe and the metallization was AuGe:Fe with a 5 minute anneal at 340

°C. A modelocked dye laser operating at 100 MHz, $\lambda=600$ nm, and a pulse width of 2ps illuminated the photoconductors as well as a *pin* photodiode which generated the electrical signal.

The result of a sampling measurement of the *pin* photodiode is shown in Fig. 3. A sampling oscilloscope measurement of the same signal confirms the shape and calibrates the amplitude with a peak signal level of 60 mV. The resolution is believed to be a little over the fixed delay, $\Delta\tau$, which is 10 ps here; although it is unfortunately not demonstrated here, presumably due to the lack of fast features in the measured signal. This is a substantial improvement over the single gap capabilities which had a photoconductive decay of 150 ps. Also, the optical power incident on each photoconductor was only $5\mu\text{W}$ which is quite low for typical optoelectronic sampling.

A major advantage of this scheme is that it achieves picosecond resolution without the need for a technique to reduce carrier lifetimes. This is es-

pecially useful in situations where such techniques (usually involving material damage) are undesirable or for materials for which such techniques are not developed. It also means that mobility, and dark resistance do not have to be sacrificed which can improve sensitivity in most cases, although the long carrier lifetimes cause increased Johnson noise from the illuminated photoconductors. Another feature is that the adjustment of $\Delta\tau$ offers a selectable trade-off between resolution and sensitivity since a wider sampling window gives a stronger signal. Finally, the application of this scheme to a coplanar, "sliding contact" geometry^[2] could result in resolutions well below a picosecond.

References

1. D. H. Auston, IEEE J. Quant. Electron., QE-19, 639, (1983)
2. D. R. Grischkowsky, M. B. Ketchen, C.-C. Chi, I. N. Duling, III, N. J. Halas, J.-M. Halbout, and P. G. May, IEEE J. Quant. Electron., QE-24, 221, (1988)

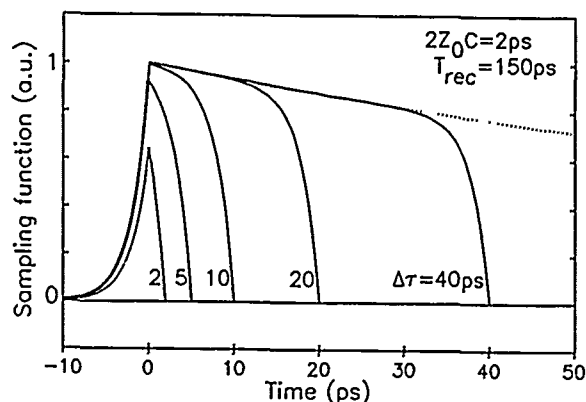


Figure 1. Effective sampling function curves.

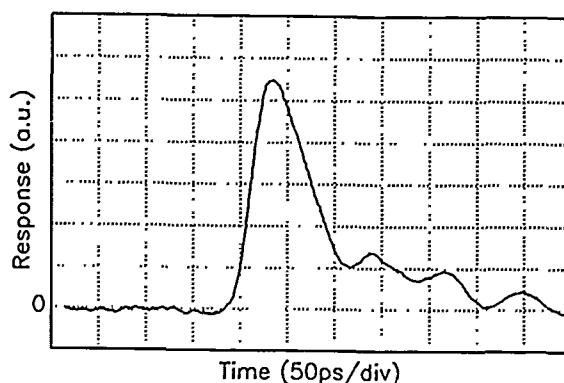


Figure 3. Differential sampling measurement of *pin* photodiode response.

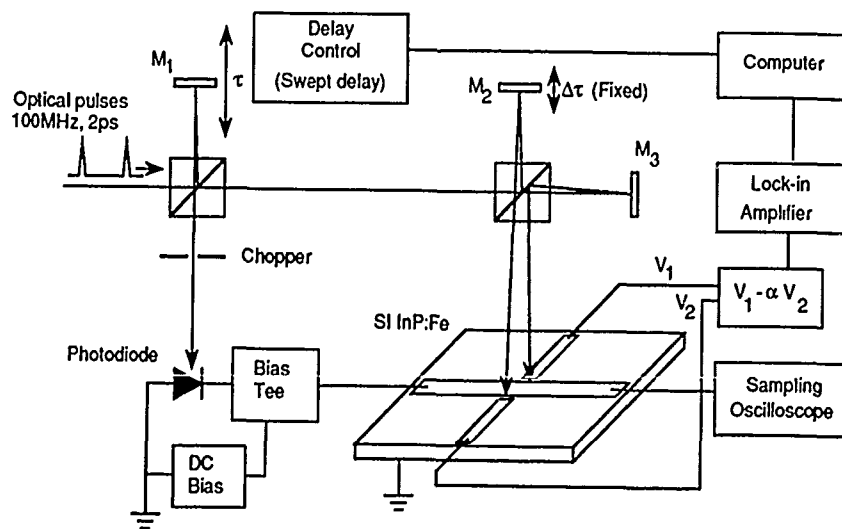


Figure 2. Experimental set-up.

Timing Jitter of Colliding Pulse Mode-Locked Lasers

G. T. Harvey and M. S. Heutmaker

AT&T Bell Laboratories, P.O. Box 900, Princeton, New Jersey 08540

P. R. Smith

AT&T Bell Laboratories, Murray Hill, New Jersey 07974

J. A. Valdmanis

University of Michigan, Ann Arbor, Michigan 48109

M. C. Nuss

AT&T Bell Laboratories, Holmdel, New Jersey 07733

ABSTRACT

The colliding pulse modelocked (CPM) laser is an attractive source of subpicosecond pulses for electro-optic sampling, but the time resolution of electro-optic sampling also depends on the timing jitter of the optical pulse train. We find that the jitter of the CPM running alone (the absolute jitter) is about 5 ps at 100 MHz, while the jitter between the CPM and a phase-locked RF synthesizer (the relative jitter) is about 1.8 ps.

INTRODUCTION

The balanced colliding pulse modelocked [1,2] (CPM) dye laser produces a stable train of subpicosecond pulses and is an attractive source for electro-optic sampling [3]. The time resolution of electro-optic sampling, however, is not determined solely by the duration of the optical pulse, but also depends on the timing jitter [4,5] between the optical pulse train and the electrical signal of interest. Since the CPM is a free-running laser, it is convenient to use the laser as the master oscillator of the electro-optic sampling system, and lock electrical signals to the CPM repetition rate. In actively modelocked lasers, on the other hand, the repetition rate of the optical pulse train is set by an external oscillator that modulates the gain or loss of the cavity. In this case the oscillator that modulates the laser is also the master clock for electrical signals.

In this work we calculate the timing jitter of the CPM from frequency-domain measurements of phase noise under two different conditions. We refer to the timing jitter of the CPM alone as absolute jitter, and

we refer to the jitter between the CPM and a phase-locked RF synthesizer as relative jitter. In electro-optic sampling, the relative timing jitter between the optical pulses and the electrical signal is the relevant quantity that must be minimized for optimum time resolution.

Fig. 1 shows the cavity of the CPM laser [2] studied here. In typical operation, the laser produces pulses of about 100 fs duration at an average power of 25 mW per beam, at a wavelength of 620 nm. The prism sequence in the cavity provides group velocity dispersion that balances the self phase modulation of the cavity to produce short pulses.

ABSOLUTE TIMING JITTER

We have used a high-speed photodetector and RF spectrum analyzer, as shown in Fig. 2, to measure the absolute timing jitter [6,7] of pulses from the CPM laser. We distinguish phase noise from amplitude noise by the fact that phase noise power in a sideband grows as the square of the harmonic number, while the amplitude noise is constant. Fig. 3 shows the spectrum of the photodetector pulses at

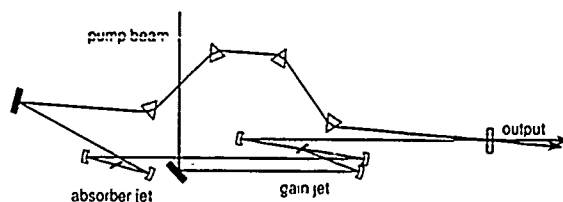


Figure 1. The cavity of the balanced CPM laser.

the fundamental (100 MHz) and the tenth harmonic. The fundamental spectrum contains a noise continuum and a set of peaks spaced by 60 Hz around the central (carrier) peak. At 1 GHz, the noise continuum within about 500 Hz of the carrier has increased markedly, and rises sharply with decreasing frequency offset. The resolution bandwidth of the spectrum analyzer (Hewlett-Packard 8566B) is 10 Hz in these measurements.

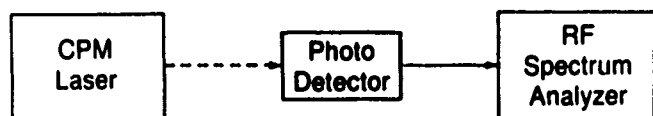


Figure 2. Experimental configuration for measurement of the absolute jitter.

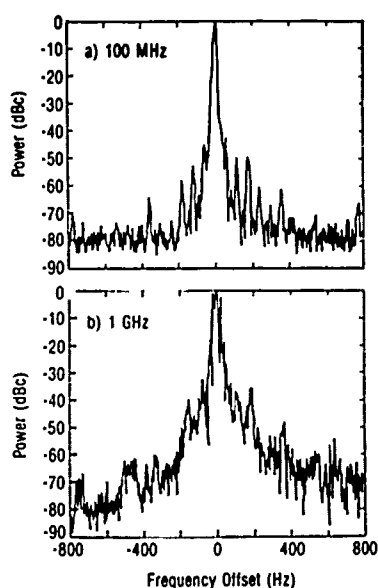


Figure 3. Power spectrum of the fundamental (100 MHz) and the tenth harmonic.

We calculate the timing jitter on the fundamental by integrating the power in the phase noise continuum at the n th harmonic, and dividing by n^2 [2]. From the ratio of integrated phase noise power to the carrier power, we find the rms phase jitter and convert it to timing jitter. From measurements on the fundamental, the fifth harmonic, and the tenth harmonic the jitter (integrated from 50 Hz to 500 Hz) is found to be 3.5 ± 1.5 milliradian rms, or about 5 ps at 100 MHz. We have measured the absolute jitter on

two different CPM lasers of the same balanced cavity design, and found it to be of the same magnitude in both cases.

The measured absolute timing jitter is consistent with submicron variations in cavity length occurring in the frequency range of 50-500 Hz. A small and slow change in cavity length leads to significant variation in the phase of the laser pulse train because the phase change accumulates over many round trip times of the cavity. The fractional change in cavity frequency due to phase modulation of $\Delta\phi$ at frequency f_{mod} is

$$\frac{\Delta f}{f_{cavity}} = \frac{f_{mod} \Delta\phi}{f_{cavity}}$$

Since the fractional change in cavity length $\Delta L/L$ is equal to the fractional change in cavity frequency, we can compute the length change ΔL that corresponds to a given amount of phase modulation. For $\Delta\phi = 3.5 \times 10^{-3}$ radian, $f_{mod} = 300$ Hz, and $f_{cavity} = 100$ MHz, $\Delta L = 0.03 \mu\text{m}$. These cavity length variations may arise from relative motion of optical elements, or from fluctuations in the dye jets.

RELATIVE TIMING JITTER

To measure the relative phase noise between a CPM and an external oscillator we use the phase detector method [8]. Fig. 4 shows the experimental configuration. The divider generates a 10 MHz square wave from the 100 MHz output of a PIN detector monitoring the laser pulses. The divider output is used as an external reference for a low phase noise RF synthesizer. To test the synchronization between the synthesizer and the laser, another part of the PIN signal is attenuated and low pass filtered, and combined with a 100 MHz signal from the synthesizer in a double-balanced mixer. The signal from the PIN is attenuated to prevent harmonic generation in the mixer, in order to reduce the amount of amplitude to phase (AM-PM) conversion [5]. A low pass filter eliminates the high frequency components of the mixer output, and the amplified signal is viewed on a low frequency spectrum analyzer and an oscilloscope. For proper phase detection, the phase shifter in the synthesizer arm is adjusted for quadrature by nulling the DC mixer output on the oscilloscope.

The low frequency spectrum analyzer takes the Fourier transform to calculate the power spectral density of the phase noise. To find the mean square phase noise density (both side bands), the power spectral density is divided by the carrier power and by a factor of 2 to account for the base band conversion. Integrating and taking the square root gives the rms phase noise which is used to calculate the jitter.

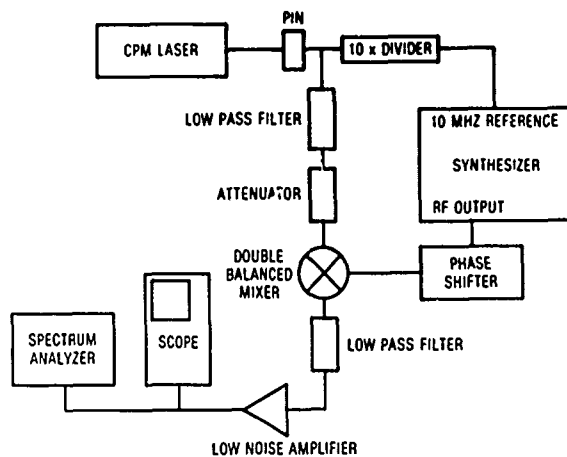


Figure 4. Experimental configuration for measurement of the relative jitter.

The upper trace in Fig. 5 shows the relative phase noise from 1 Hz to 100 Hz, using a Programmed Test Sources Model 160 synthesizer. The lower trace shows the noise floor of the phase detection system when the CPM beam is blocked. Discrete spurious signals, such as the signal at 60 Hz in Fig. 5, were excluded from the integration of the phase noise. A number of synthesizers were tested with the CPM, and the PTS synthesizer had the lowest relative phase noise, calculated at 1.1 milliradian rms over a 2 Hz to 1 kHz band. This phase jitter corresponds to timing jitter of 1.8 ps at 100 MHz.

DISCUSSION AND CONCLUSION

We have measured the absolute jitter of the CPM to be about 3.5 milliradian, (or 5 ps at 100 MHz), in the band from 50 Hz to 500 Hz. It is interesting to note that the absolute phase noise of a CPM laser

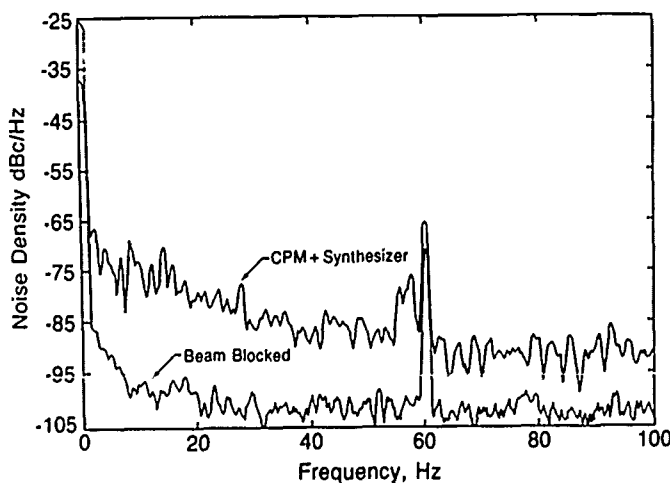


Figure 5. Relative phase noise sideband (upper trace) and noise floor of measurement system (lower trace).

has been measured previously (Ref. 7), and the earlier results differ significantly from our data. In Ref. 7 an upper limit of 50 fs at 100 MHz, or .03 milliradian, was measured for the absolute jitter, and no phase noise was visible on harmonics up to 15th order (for a resolution bandwidth of 30 Hz on the spectrum analyzer). We are presently exploring possible reasons for the difference between these measurements.

In electro-optic sampling, the relative timing jitter between the optical pulse and the electrical signal will degrade time resolution. We find relative jitter of 1.8 ps at 100 MHz (or 1.1 milliradian) between the CPM and a phase-locked RF synthesizer. We measured the relative jitter using several different synthesizers, and the lowest jitter we achieved was 1.8 ps at 100 MHz (1.1 milliradian) using the Programmed Test Sources Model 160 synthesizer.

When the CPM is the master oscillator in the system, several possible sources of relative jitter can be identified. The absolute jitter of the CPM produces phase variations in the time base of the synthesizer, and the ability of the synthesizer to track these variations will affect the relative jitter. For example, a synthesizer with a phase-locked loop at the reference input will not be able to track phase noise that lies outside the loop bandwidth. Also, any jitter introduced by the synthesizer in addition to that present on its clock reference will appear as relative jitter. Another source of relative jitter is amplitude-to-phase (AM-PM) conversion in the divider circuit (or at the synthesizer input if the synthesizer can use a 100 MHz reference). Some of these sources of relative jitter are independent of the absolute jitter of the CPM, and thus the relative jitter could exceed the absolute jitter if the absolute jitter is sufficiently small. In our experiment, the relative jitter was less than the absolute jitter of the CPM, presumably due to effective tracking of the CPM absolute jitter by the synthesizer.

ACKNOWLEDGMENTS

We acknowledge useful discussions with M.J.W. Rodwell and J.M. Wiesenfeld.

REFERENCES

1. R.L. Fork, B.I. Greene, and C.V. Shank, "Generation of Optical Pulses Shorter than 0.1 psec by Colliding Pulse Mode Locking", *Appl. Phys. Lett.* **38**, 671 (1981).
2. J.A. Valdmanis and R.L. Fork, "Design Considerations for a Femtosecond Pulse Laser

- Balancing Self Phase Modulation, Group Velocity Dispersion, Saturable Absorption, and Saturable Gain", IEEE J. Quant. Elect. QE 22 112 (1986).
3. J.A. Valdmanis, "1-THz Bandwidth Prober for High-Speed Devices and Integrated Circuits", Electron. Lett. 23, 1308 (1987).
 4. B.H. Kolner and D.M. Bloom, "Electrooptic Sampling in GaAs Integrated Circuits", IEEE J. Quant. Elect. QE 22, 79 (1986).
 5. M.J.W. Rodwell, D.M. Bloom, and K.J. Weingarten, "Subpicosecond Laser Timing Stabilization", to be published in IEEE J. Quant. Electron.
 6. J. Kluge, D. Wiechert, and D. Von Der Linde, "Fluctuations in Synchronously Mode-Locked Dye Lasers", Optics Comm. 51, 271 (1984).
 7. D. von der Linde, "Characterization of the Noise in Continuously Operating Mode-Locked Lasers", Appl. Phys. B 39, 201 (1986).
 8. "Phase Noise Characterization of Microwave Oscillators: The phase detector method", Hewlett Packard Product Note 11729B-1.

Comparison of Electro-Optic and Photoconductive Sampling Using a 28-GHz Monolithic Amplifier

E. Chauchard, G. Treacy, K. Webb, and Chi H. Lee

*Department of Electrical Engineering, University of Maryland,
College Park, Maryland 20742*

H.-L. A. Hung and H. C. Huang

COMSAT Laboratories, Clarksburg, Maryland 20871-9475

P. Polak-Dingels

University Research Foundation, 6411 Ivy Lane, Suite 110, Greenbelt, Maryland 20770

Abstract

The performance of a 28-GHz monolithic amplifier is evaluated using electro-optic sampling, photo-conductive sampling and network analyzer. The advantages and limitations of each technique are discussed.

Introduction

Electro-optic sampling (EO) and photoconductive sampling (PC) have been used by different groups [1-3] to evaluate the performance of high speed electronic circuits. Photoconductive sampling can be performed on any type of substrate but requires the fabrication of a sampling port at every position where the circuit needs to be tested. Electro-optic sampling in the chip substrate can only be performed on an electro-optic substrate like GaAs but a measurement can be performed "in situ" anywhere in the circuit. Electro-optic sampling can also be performed in an external modulator like LiTaO₃, which can be cut in the shape of a probe tip. Both techniques are essentially non-invasive; they do not require the use of a microwave probe which makes them potentially much faster than network analyzer measurements.

No one has yet quantitatively compared the two techniques using the same device. In this paper, we evaluate the performance of a 28-GHz monolithic microwave integrated circuit (MMIC) using both techniques and compare the results to frequency domain network analyzer measurements. We utilize a unique approach for characterizing the MMIC. A short electrical pulse with wide frequency content is measured in the time domain before and after passing through the

device. The transfer function of the MMIC is then obtained from the ratio of the Fourier Transforms of the sampled signals. A network analyzer was used to determine the loss and phase shift of a GaAs transmission line and this correction was applied to the data.

Experimental Technique

The device evaluated consisted of a 28-GHz MMIC mounted between two sets of photoconductive switches fabricated on a GaAs substrate. The GaAs substrate was proton implanted to minimize the carrier recombination time. The best proton implantation level (10^{14} /cm²) was determined previously by using photoconductive sampling to test a series of switches [4]. Figure 1 is a schematic diagram of the device. This design permits both techniques to be utilized to study the performance of the MMIC.

The laser system is a Quantronix CW mode-locked Nd:YAG laser followed by a fiber-grating pulse compressor and a KTP frequency doubler. This system generates pulse trains at 0.532 and 1.06 micron having a typical pulse duration of 5-6 psec and a repetition rate of 100 MHz.

For photoconductive sampling, the 0.532 micron pulse train is split into two separate pulse trains. One is directed to Port a of the device to generate a voltage pulse on the input microstrip line; the second pulse train is used to sample both the input waveform to the MMIC and the reflected waveform at Port b or the output waveform of the MMIC at Port d. For electro-optic sampling, the input waveform is also generated at Port a using the 0.532 micron laser pulse train. The sampling of the waveforms is performed with the 1.06 micron pulse train using the electro-optic

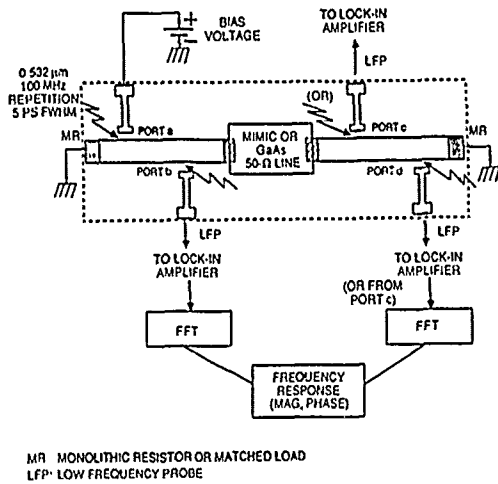


Figure 1: Schematic diagram of the device.

effect in GaAs. For a valid comparison of the two techniques, the input, reflected and output waveforms were sampled at the same positions on the microstrip line.

Results and Discussion

Figures 2 and 3 show the input and output waveforms as sampled by these two techniques. The main peak of the input waveforms which reflects the photoconductive switch response time were very short (10 ps for electro-optic sampling and 15 ps for photoconductive sampling) because of the short carrier recombination time in the GaAs substrate. The Fourier transforms of the input and output waveforms were performed using a numerical FFT routine. The transfer function of the MMIC, both magnitude and phase,

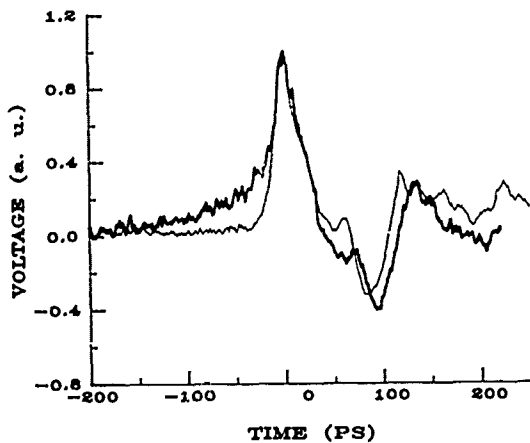


Figure 2: Temporal waveform measured at Port b by EO sampling (light) and PC sampling (bold).

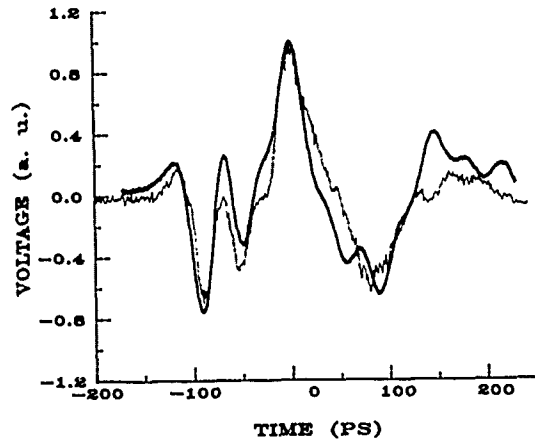


Figure 3: Temporal waveform measured at Port d by EO sampling (light) and PC sampling (bold).

were calculated by a ratio of the output and input Fourier transforms and corrected for the RF loss and phase shift of the GaAs transmission lines, so that the reference planes are at the input and output of the MMIC. The RF loss and phase shift of the GaAs transmission line were determined by network analyzer measurement [5]. The speed of the gap generating the incoming pulse is the limiting factor for the highest frequency of the transfer function calculation. In this case, the calculation is limited to approximately 60 GHz. Since the device chosen operates at 28 GHz, we have displayed the results only to 32 GHz.

Figure 2 shows an important difference between the two techniques, the time response measured by electro-optic sampling is shorter. In photoconductive sampling, the waveform is sampled by a gate whose temporal characteristics are dominated by the switch response time. For the input waveform, this results in an autocorrelation of the switch response time. In electro-optic sampling, the waveform is sampled by a gate whose shape is that of the laser pulse. Therefore the temporal resolution of electro-optic sampling is better than that obtained by photoconductive sampling.

Figures 4 and 5 show the S_{11} parameter measurements obtained by the Fourier transform of the temporal waveforms. The magnitude and phase of S_{11} measured by these two techniques shows good agreement, although some differences exist. The phase of S_{11} is determined by separating the incoming pulse from the reflected pulse on the measured temporal waveform. There is some inaccuracy associated with the choice of the separation point, which explains the discrepancy between the phase shift data from the two optical techniques. The phase shift is much more sensitive than the

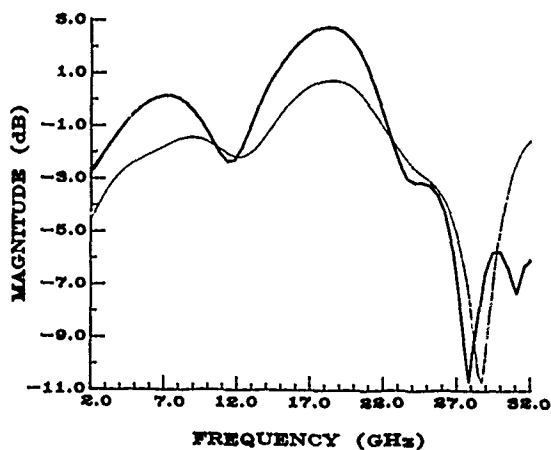


Figure 4: S_{11} magnitude determined by EO sampling (light) and PC sampling (bold).

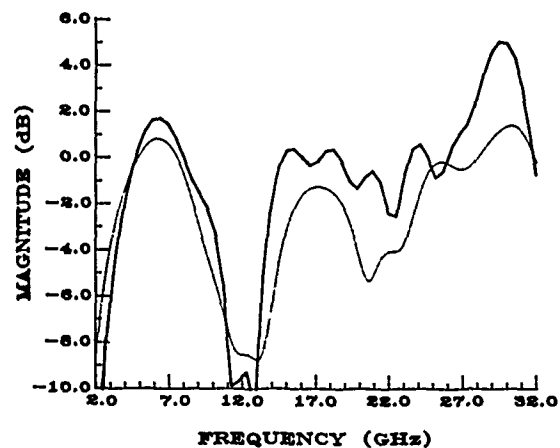


Figure 6: S_{21} magnitude determined by EO sampling (light) and PC sampling (bold).

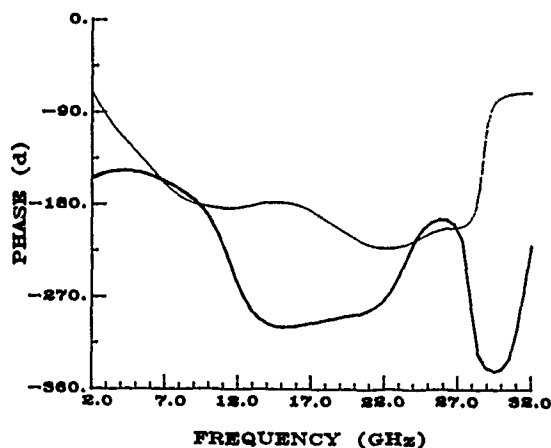


Figure 5: S_{11} phase determined by EO sampling (light) and PC sampling (bold).

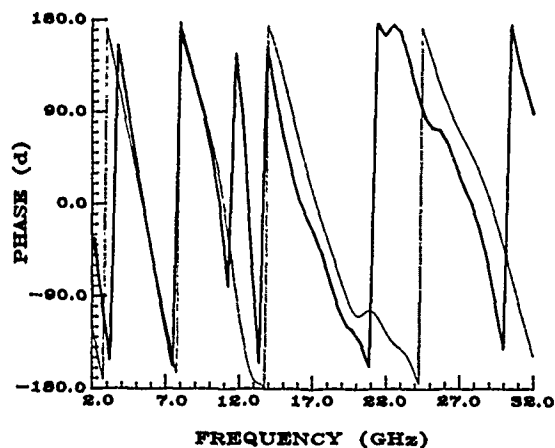


Figure 7: S_{21} phase determined by EO sampling (light) and PC sampling (bold).

magnitude to the choice of separation point.

The inaccuracy is larger for photoconductive sampling since some of the reflected pulse temporal waveform is embedded in the incoming pulse waveform. In order to do a valid S_{11} measurement with photoconductive sampling, it is necessary to design the switch layout so that there is a sufficient distance between the second gap (port b) and the device. With electro-optic sampling, it is possible to move the sampling point to a position on the line where there is sufficient time resolution between the input and reflected pulse.

Figures 6 and 7 show the S_{21} parameter measurements obtained by the two techniques. The magnitude measured by these two techniques agrees quite well. The magnitude measured by the electro-optic

technique is low and may be due to a calibration problem. In order to obtain a quantitative measurement of the voltage on the line, a calibration of the sampling configuration is necessary. For photoconductive sampling, the calibration of both sampling ports b and d can be done by generating a pulse at port a and port c respectively. We found this calibration more difficult to obtain with electro-optic sampling because the signal is very sensitive to the position of the sampling beam next to the microstrip line. The calibration is only needed for S_{21} measurements where the sampling is done at two different positions. S_{21} measurements by electro-optic sampling should thus be regarded as less reliable. The phase measured by the photoconductive technique should also be considered more

reliable since the time delay between the input and output waveforms can be accurately determined.

In comparing both methods, we found that it is more difficult to implement electro-optic sampling because of its lower sensitivity. For our device, the ratio of the detected signal voltage to the sampled voltage is 2×10^{-5} for electro-optic sampling and 3×10^{-3} for photoconductive sampling. The lowest measurable signals were 6 mV for electro-optic sampling and .2 mV for photoconductive sampling. The largest measurable signal is in theory very large for both methods. The practical upper bound on the largest signal is given by the peak voltage that the switch is able to generate when activated by this laser system. For this device the peak voltage was 300mV. This gives a dynamic range of 34 dB for electro-optic sampling and 63 dB for photoconductive sampling. Other switches could generate pulses up to 1.5V. Of course, low input voltages are necessary if one is interested in observing the response of the device in the linear regime. For these experiments, the applied voltage was never greater than 300 mV.

Figures 8 - 11 show S_{11} and S_{21} , both magnitude and phase, as determined by network analyzer measurements (Hewlett Packard Model 8510B/8516A). The network analyzer results show the same main features as the optical techniques, but some differences appear. For example, there is an additional resonance dip at low frequency for the magnitude of S_{11} and less phase shift for S_{21} . These differences may be partly due to the network analyzer measurement technique. The data were obtained by measuring the response of the package consisting of two photoconductive switches, the MMIC, and the K connectors, as shown in Figure 1. In order to compare these results

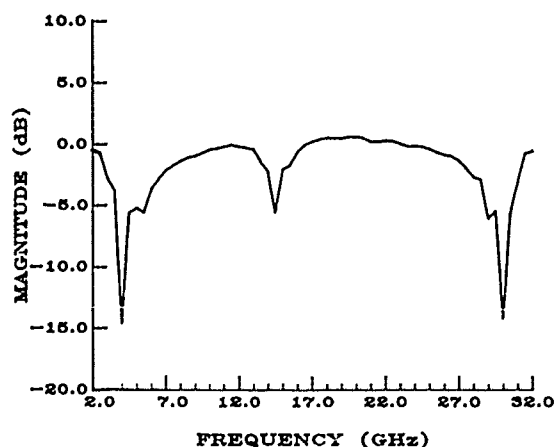


Figure 8: S_{11} magnitude measured with network analyzer, HP8510.

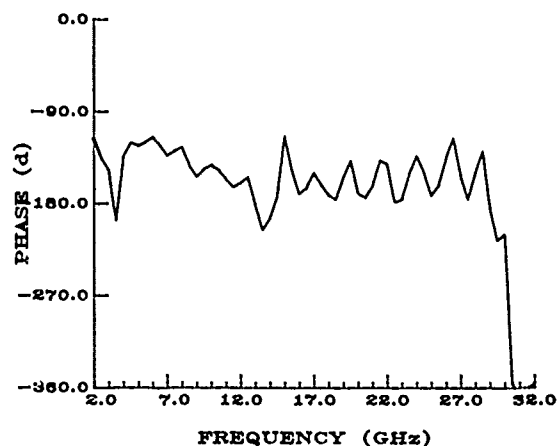


Figure 9: S_{11} phase measured with network analyzer, HP8510.

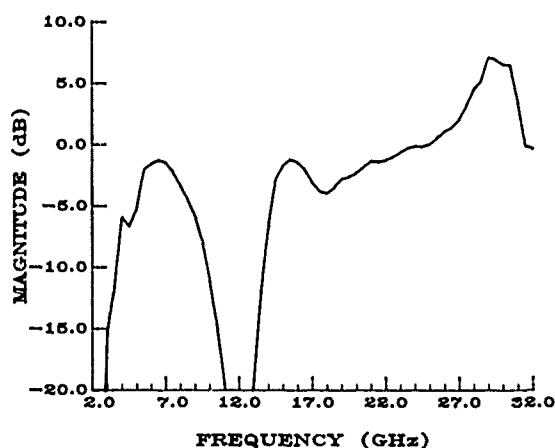


Figure 10: S_{21} magnitude measured with network analyzer, HP8510

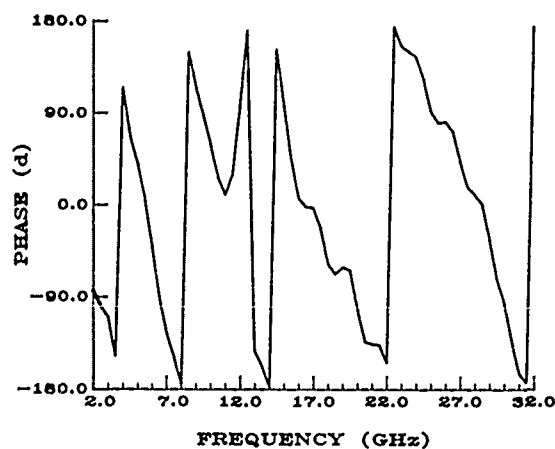


Figure 11: S_{21} phase measured with network analyzer, HP8510.

with the optical techniques, it was necessary to correct for the loss and phase shift due to the 50 ohm line of the switches and the effect of the K connectors. This de-embedding process may introduce some errors into the network analyzer measurements. The effect of the K connectors is determined by measuring the S parameters for a separate test structure. Since the performance of the K connectors is dependent upon the way the connectors are assembled, this term may be a source of error.

Laser performance is an important problem associated with these optical techniques and needs to be addressed. Any laser drift will affect data taken at consecutive data points. In order to quantify this error, the variance between successive temporal waveforms was measured. For the data reported here, the variance was about 10% and will be an additional source of error in the results.

Conclusions

Electro-optic sampling requires only one photoconductive switch for the pulse generation since sampling can be done anywhere along the microstrip line and even "on-chip", within the integrated circuit. However photoconductive sampling can be performed on any substrate while electro-optic sampling when performed directly in the substrate is limited to GaAs. Our results

indicate that the transfer functions obtained by these two techniques and network analyzer measurements show the same main features, for example gain at 28 GHz. However, some differences exist which determine the range of applicability of each technique. A calibration can be obtained by measuring a known dc voltage at the sampling port prior to each measurement. Laser stabilization or the use of a different type of laser would greatly improve the accuracy of these measurements. Both techniques can be of great value for testing microwave devices.

References

1. K. J. Weingarten, M. J. W. Rodwell and D. M. Bloom. *IEEE J. Quantum Electronics* **QE-24**, (1988), 198.
2. D. A. Auston. *IEEE J. Quantum Electronics*. **QE-19**, (1983), 639.
3. J. A. Valdmanis and S. S. Pei. *Tech. Digest, Conf. on Lasers and Electro-Optics* (OSA, Washington, D.C., 1984), p. 352.
4. H. L. Hung, P. Polak-Dingels, K. J. Webb, T. Smith, H. C. Huang and C. H. Lee. To be published in *IEEE Trans. Microwave Theory Tech.*, 1989.
5. H. L. Hung, T. Smith, H. C. Huang, P. Polak-Dingels, K. J. Webb and C. H. Lee, *Digest, 12th Inter. Conf. on Infrared and Millimeter Waves* (IEEE, New York, NY, 1987), paper T3-2.

Application of Frequency-Domain Techniques for Tuning Pulsed Lasers

J. C. Swartz, F. C. De Lucia, and B. D. Guenther

Department of Physics, Duke University, Durham, North Carolina 27706

Abstract

We demonstrate an alternative technique to the use of an autocorrelator for accurately tuning pulsed lasers. This technique is based upon the use of frequency domain information in place of the time domain information to obtain the optimum modelocked condition.

I. INTRODUCTION

This paper introduces a simple device to tune picosecond lasers and to measure the laser pulse width.

The device is based on the conversion of a picosecond optical pulse train to a train of electron bunches by a photocathode. The spatially bunched electrons produce microwave radiation which contains all the information needed to reconstruct the pulse shape.^{1,2}

The photocathode response time is less than 10^{-12} seconds resulting in a temporal resolution of at least one picosecond. The exact limit is determined by the wavelength and the photocathode material. The electron bunches created by the optical pulses are accelerated across a microwave structure by a dc field and the kinetic energy of the electrons is converted into an electromagnetic wave whose spectral content is equal to the Fourier transform of the optical pulse. An analysis of the spectrum will yield the optical pulse shape.

We have observed that it is possible to adjust a mode locked laser for optimum performance by simply monitoring the average rf power contained in a fixed bandwidth.

This technique offers a number of advantages. It can operate at relatively low light levels. The detector does not need readjustment when the wavelength of the source is changes and its performance improves as one moves from the red into the blue spectral region. The components required to construct the detector are low cost, small and easily to assemble.

II. EXPERIMENTAL

Our experimental setup, shown in Fig. 1, is based on a synchronously pumped picosecond dye laser system, a Spectra Physics 375 dye laser with an extended cavity pumped by a mode locked Spectra Physics 171 argon ion laser. The laser output is monitored by an autocorrelator (Spectra Physics model 409) and a portion of the beam is also sent to the picosecond demodulator. The picosecond demodulator is a device which generates the Fourier spectrum of the time envelope of the light pulses. This setup allows easy comparison of the time and frequency domain signals.

In this work, the time to frequency transform is performed by the phototube and microwave coupling structure, shown in Fig. 2. The vacuum photodiode (ITT FW114A) has planar electrodes, S-20 spectral sensitivity, and is enclosed by a glass envelop. The microwave structure is a reduced height TE_{01} waveguide, with an opening to hold the phototube. The left and right faces of the waveguide are coplanar with the photodiode anode and cathode respectively. Together the phototube and the

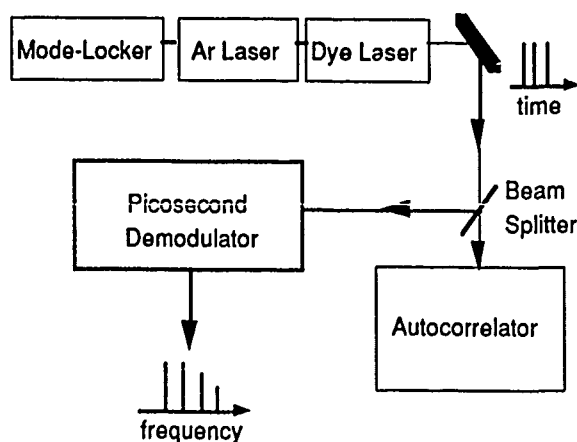


Figure 1: Experimental setup.

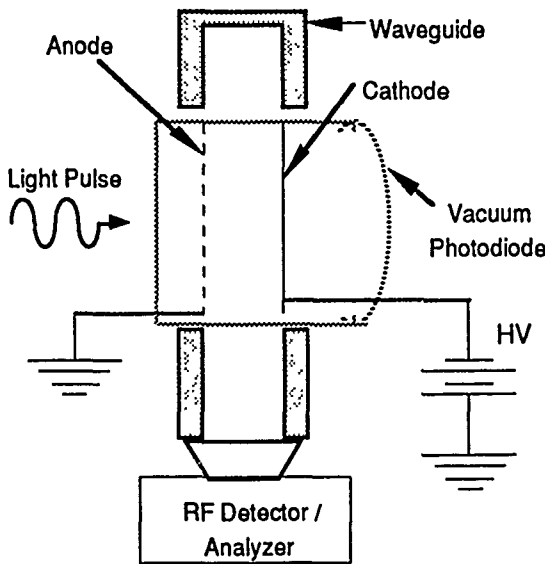


Figure 2: Picosecond demodulator

waveguide form a closed structure to propagate microwaves to the analyzer.

In operation, the picosecond optical pulses strike the photocathode and photoelectrons are emitted, their number being proportional to the optical intensity. The high voltage supply accelerates the electrons from the cathode to the anode. As they traverse the waveguide structure, the electron bunches produced by the picosecond optical pulses radiate microwaves which propagate through the waveguide. These microwaves are subsequently detected either by a spectrum analyzer or a waveguide mounted crystal detector.

III. THEORY

Consider the optical pulse train shown in Fig. 3 with pulse width τ and pulse repetition period T . The Fourier components of this pulse train are

$$f(t) = \frac{\tau}{T} + \frac{2}{\pi} \sum_{n=1}^{\infty} \frac{(-1)^n}{n} \sin \frac{n\pi\tau}{T} \cos \frac{n2\pi}{T} \quad (1)$$

In the limit $\tau/T \ll 1$ (i. e. the width of the picosecond pulse is very small in comparison to the time between pulses)

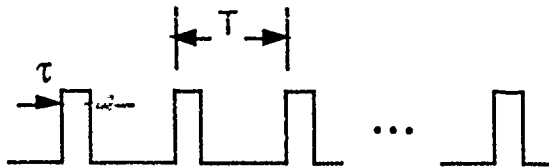


Figure 3: The optical pulse train.

$$f(t) = \frac{\tau}{T} + \frac{2}{\pi} \sum_{n=1}^{\infty} (-1)^n \frac{n\pi}{T} \cos \frac{n2\pi}{T} \quad (2)$$

and each frequency component is given by

$$f_n(t) = \frac{2\tau}{T} \cos \frac{n2\pi}{T} \quad (3)$$

A photocathode is used to convert the optical pulse train into bunches of electrons which are subsequently accelerated through a microwave structure. Since at a photocathode the current produced is proportional to the optical power, the current in the n^{th} Fourier component is

$$i_n(t) = i_n \cos \frac{n2\pi}{T} = 2i_a \cos \frac{n2\pi}{T} \quad (4)$$

where i_a is the average current.

For the envelope of the current to be a faithful representation of the optical pulse train, the speed of the photoelectric process must be fast compared to the microwave period. Although the photoelectric process is an electronic process and the fundamental emission time scales are characteristic of electronic speeds ($<10^{-14}$ sec), some photo materials (especially semiconductors) are more properly characterized as volume rather than surface photoemitters. In these cases the emitted electrons must random walk their way to the surface and the photoemission is characterized by a rapid rise followed by a much longer decay as the more deeply emitted electrons reach the surface. However, the photocathode used in this work (S-20) is a metallic photocathode and can be characterized as either a surface or shallow volume emitter. Characteristic speeds for such photocathodes are typically 10^{-12} seconds.

The kinetic energy of bunched electrons is converted into the energy of an electromagnetic field in a microwave structure by insuring that the phase of the microwave field is such that it decelerates the electrons. A simple (and relatively inefficient) coupling structure consists of a section of TE_{01} waveguide of height a , width b , with electrons emanating from a photocathode on the bottom of the waveguide and accelerated by a voltage V_0 which is applied across the narrow dimension of the waveguide. This geometry is a good approximation of the geometry of the device which is the subject of this paper and shown in Fig. 2.

Simple calculations show that the transit time t_r for this waveguide geometry is given by

$$t_r = \sqrt{\frac{2ma^2}{V_0 e}} \quad (5)$$

where e is the charge on the electron, m its mass and a the height of the waveguide. The coupling of the beam to the waveguide can be characterized by a coupling impedance R with the power in each component given by^{4,5}

$$P_n = i_n^2 R \quad (6)$$

In the limit of zero transit time, it can be shown for a TE_{01} mode waveguide coupling structure that the coupling impedance is²

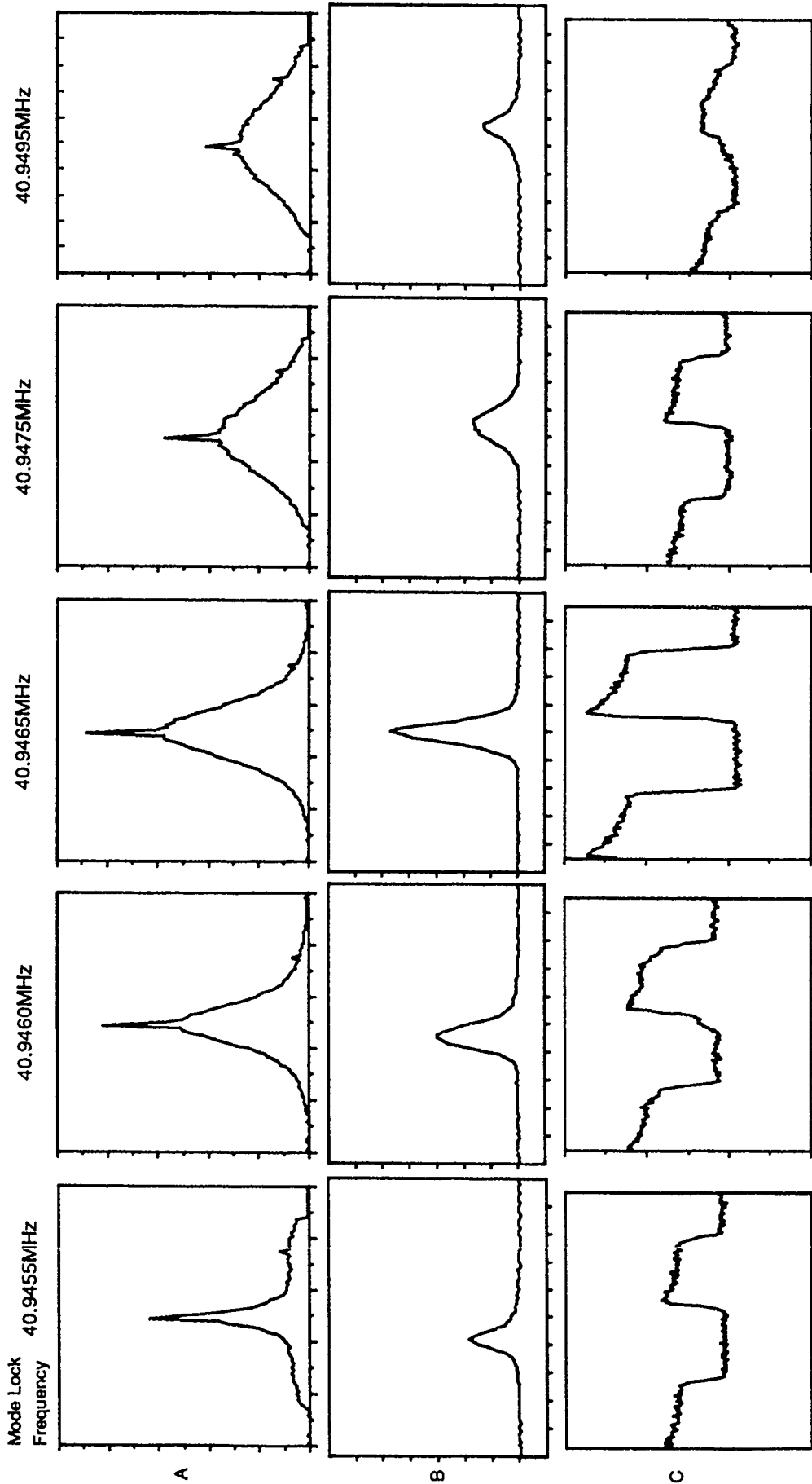


Figure 4. The Experimental Results. Row A is the autocorrelator signal, 15pS/div horizontally, relative intensity vertically. Row B in the spectrum analyzer output centered at 8.936GHz, .2MHz/div horizontally, relative amplitude vertically. Row C is the crystal detector output, 25mS/div horizontally, relative amplitude vertically.

$$R = \frac{2Z_0 a}{b} \quad (7)$$

where Z_0 is the impedance of free space. If transit time effects are included the microwave power produced in the n^{th} Fourier component is¹

$$P_n = \frac{i_n^2 R}{(\omega t_r)^2} \quad (8)$$

where ω is the microwave frequency.

With finite pulse lengths the term

$$\frac{1}{n} \sin \frac{n\pi\tau}{T} \quad (9)$$

in Eqn. 1 must be retained and the roll off in power due to finite pulse width predicts that the power in the n^{th} mode will be reduced by the factor

$$\left[\frac{\frac{1}{n} \sin \frac{n\pi\tau}{T}}{\frac{\pi\tau}{T}} \right]^2 \quad (10)$$

This relation describes the decrease in Fourier component amplitude that occurs as the pulse width approaches the reciprocal of the frequency of the n^{th} component.

IV. RESULTS

In these experiments the laser pulse width was varied by changing the mode lock frequency of the argon ion laser. The time domain pulse width was measured using an autocorrelator. The first row of images in Fig. 4 shows the autocorrelation of the optical pulses as the mode lock frequency was varied.

As discussed in Section II, several devices may be used to analyze the microwave radiation produced by the photoelectrons. Using a spectrum analyzer, the second row of images in Fig. 4 shows a single frequency component (at 8.936GHz) of the microwave spectrum. The amplitude of the microwave frequency component varies with the picosecond pulse width. In order to make maximum use of this technique, the average photocurrent (which is a measure of the average laser power) must be used to normalize the observed microwave power. The third row of images in Fig. 4 shows the signal from a crystal detector mounted in a X-band horn (the signal is chopped at 20Hz to give a zero reference). The oscilloscope output again shows that there is a strong correlation between average microwave power in the waveguide band and the optical pulse width measured by the autocorrelator.

In addition, similar observations can be used to measure the width of the picosecond pulse. Figure 5 shows the microwave output as measured by a K band (~25 GHz) detector system coupled to the device shown in Fig. 4 by a microwave horn. In these measurements the pulse width of the laser system was

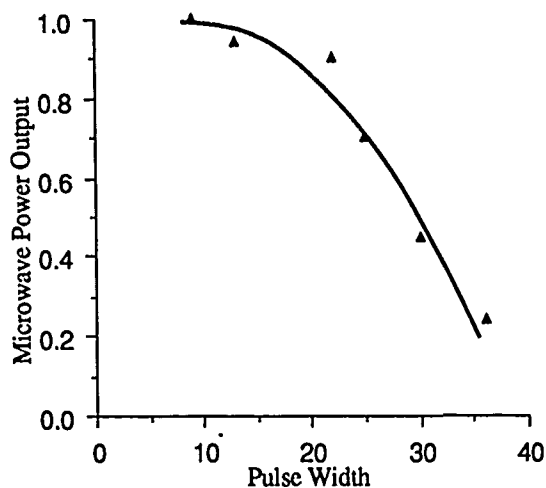


Figure 5: Microwave power vs pulse width.

increased by offsetting the dye laser length. The pulse width shown on the horizontal axis was measured by the autocorrelator. Also shown on this figure is the theoretical roll off as predicted by Eqn. 10.

V. DISCUSSION

It is important to note that the coupling efficiency of the microwave structure to the electron beam affects only the absolute microwave power and that the contribution from the pulse width to the strength of a Fourier component is a separate, multiplicative factor. Thus, it is possible to measure pulse lengths via Eqn. 1 by use of simple microwave coupling structures and without a detailed knowledge (which depends not only on the geometry of the microwave structure, but also on the geometry of the electron trajectories) of the coupling impedance R and the transit time t_r .

A quantitative measurement of pulse length via relations such as Eqn. 1 (which assumed for the sake of simplicity a square pulse) requires knowledge of the pulse shape. However, measurement of the roll off at several different microwave frequencies can provide information about this shape as can experience with the laser type being evaluated. This is the common practice in interpreting measurements based on autocorrelators.

References

1. F. C. De Lucia, B. D. Guenther, and Todd Anderson, *Appl. Phys. Lett.* **47**, 894 (1985).
2. F. C. De Lucia, Night Vision and Electro-Optics Laboratory Laboratory report DAAK 70-79-C-0121 (1982).
3. W.E. Spicer and F. Wooten, *Proc. IEEE*, **51**, 1119-1126, (1963).
4. P. D. Coleman, *J. Appl. Phys.* **28**, 927 (1957).
5. A. E. Siegman, S. E. Harris, and B. J. McMurtry, Third International Symposium on Quantum Electronics, Paris, France, 1963.

Part 3
Laser Diodes, Amplifiers, and Modulators

Picosecond, Spatially Resolved Optical Detection of Charge-Density Modulation in AlGaAs Lasers

H. K. Heinrich

IBM T. J. Watson Research Center, Yorktown Heights, New York 10598

Abstract

This paper presents the first application of a modified confocal optical probing system to spatially-resolving picosecond charge-density modulation along the cavity of an AlGaAs semiconductor laser. The measurements show that the internal charge concentration overshoots and then clamps at the threshold level in response to an input current pulse. The amount of overshoot was found to be proportional to the current pulse amplitude, and appears to agree with previous theoretical analyses.

Introduction

The performance of a semiconductor laser is determined by the interaction of three parameters: the pumping current through the laser; the charge-density within the laser cavity; and the intercavity photon density. The ability to spatially resolve internal charge-density modulation within the laser could be used to better understand the ac, dc, spectral, and reliability performance of the laser. For example, the transient interaction between electrons and photons, in response to an input current step, determines the amount of ringing present in the optical output of the laser in switching applications. During dc operation, when the laser reaches its threshold, the carrier lifetime changes from the spontaneous to the stimulated value, which is several orders of magnitude less. This process clamps the internal carrier density at the threshold level. Spatial variations in the internal carrier threshold level could reveal low gain regions of the laser cavity. This information could be used to improve the laser design or reveal

internal defects within the laser, which could adversely impact the laser reliability. Multilongitudinal or multitransverse mode operation of the laser could also be observed by measuring the internal carrier concentration along or transverse to the laser cavity.

Previously, researchers have used the photoluminescence perpendicular to the laser cavity to spatially resolve defects[1], and observe spatial hole burning and gain saturation[2]. However, since photoluminescence is generated by the spontaneous recombination of charge in the laser cavity, this system can not detect picosecond transient interactions between the cavity photons and free-carriers. In addition, this approach generally can not be used to probe lasers packaged with the active region next to the heat-sink, since the photoluminescence is absorbed in the substrate. By guiding dye laser pulses along a semiconductor laser cavity, researchers[3,4] have probed femtosecond nonlinear carrier dynamics. However, this approach measures carrier temporal fluctuations by averaging over the entire length of the laser, which obscures information about spatially dependent charge-dynamics.

Recently, an optical probing system has been demonstrated that can detect charge-density modulation in pn junctions in Silicon[5,6] and GaAs[7,8] integrated circuits. By pulsing the probing laser, researchers[9] were able to use it to sense picosecond charge-density modulation in a high-speed silicon bipolar-junction transistor. This charge-sensing system used two beams, a probe and reference beam, to interferometrically detect the free-carrier induced index perturbation in the material. However, it required that the semiconductor device in the integrated circuit be very close to the front surface met-

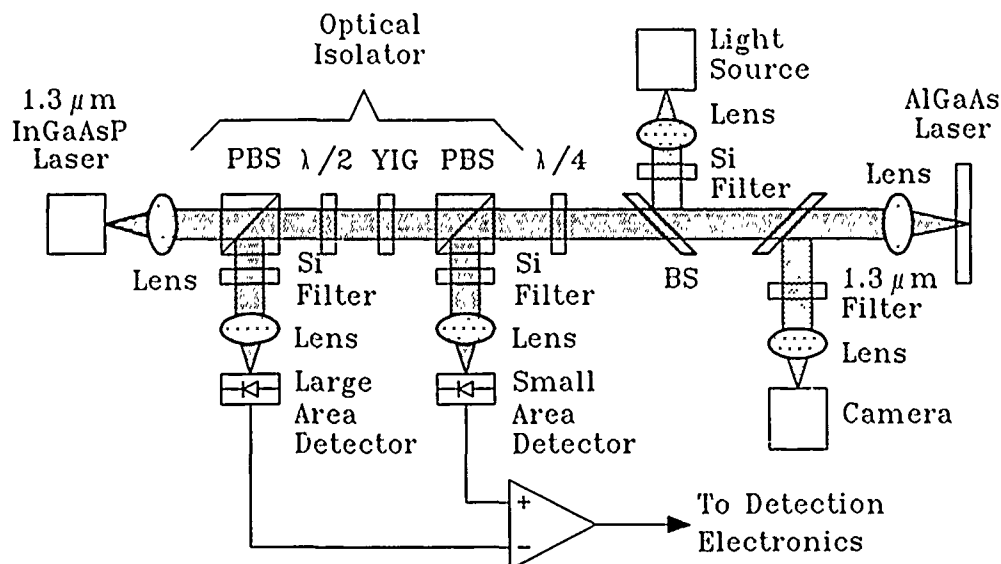


Figure 1: Optical schematic diagram of the modified differential phase-contrast confocal optical probing system.

alization, which was used as a reflector for the two optical beams. Unfortunately, many semiconductor lasers have the active region of the device near an exposed top surface, which is far from the metallized back surface of the device. Hence, these laser structures could not be probed with this previous optical probing system.

This paper describes a modified differential phase-contrast confocal optical probing system[10]. This simple optical system uses a single optical probe spot to detect charge-density modulation in the cavity of a top-surface semiconductor laser, and we have used this optical probing system to spatially resolve picosecond variations in the free-carrier density in a crank transverse-junction(TJS) stripe AlGaAs semiconductor laser[11].

Experimental System

Fig. 1 shows a schematic diagram of the optical probing system used to observe charge-density modulation in an AlGaAs semiconductor laser. In this system, the AlGaAs laser sample is imaged onto a small area photodetector. This system is referred to as a confocal imaging system[10]. Index variations or axial translations of the sample move the focus position of the AlGaAs laser image in the optical probing system. This defocuses the laser image on the small area detector, which reduces the observed photocurrent. By using polarization optics, we can split the return optical beam between a large and a small area photodetector. Because of the large area photodiode's size, the previous image defocusing does not generate any photocurrent vari-

ation. However, intensity variations in the probing laser source generate correlated noise photocurrents in both the small and the large area photodiodes. By differencing the signals from these two photodiodes, we can cancel this noise source, which improves the measurement system sensitivity.

The optical source for this probing system was a $1.3\mu\text{m}$ semiconductor laser. This laser was gain switched with 100ps wide electrical pulses at 100MHz using a comb generator. The laser produced an average output power of approximately $100\mu\text{W}$ and had a pulsewidth of 43ps. This optical pulsewidth gave the probing system a sampling bandwidth of 8GHz. Unfortunately, the limited optical power prevented us from achieving the theoretical shot-noise limited sensitivity.

A conventional 2800°K Tungsten light source illuminated the AlGaAs semiconductor laser sample. A narrow linewidth optical filter in front of the infrared camera passed the illumination of the light source and partially attenuated the $1.3\mu\text{m}$ wavelength probing laser. This allowed us to image both the AlGaAs laser sample and the probing laser spot without the problems of objective lens chromatic aberration or camera damage.

Fig. 2 shows a schematic diagram of the electrical portion of the optical probing system. In this system, the gain switching signal applied to the $1.3\mu\text{m}$ wavelength probing laser was synchronized with the current switching signal applied to the AlGaAs semiconductor laser. A slight difference in the frequency(Δf) of these two signals stroboscopically maps out the picosecond charge-density modulation in the AlGaAs laser at the low bandwidth, small area

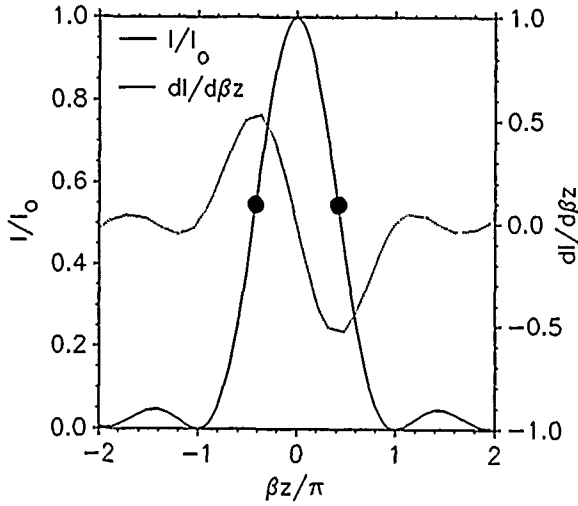


Figure 3: Optical transfer function between index variations in the sample, β , the normalized photocurrent, and the small-signal photocurrent, $dI/d\beta z$. The dots denote the peaks in the magnitude of the small-signal sensitivity.

shot-noise limited, the noise fluctuations present at the photodetector will be given by

$$\delta I = \sqrt{2qKI_0B}, \quad (5)$$

where KI_0 is the sum of the average photocurrent from both detectors, $K = 1.0954$, and B is the bandwidth of the detection system. Solving Eqs. (4) and (5) for the minimum detectable charge-density modulation, we get

$$\delta N_s = 13.82 \frac{4\pi n_0 \epsilon_0 m^* c^2}{q^2 \lambda} \sqrt{\frac{2qKB}{I_0}}, \quad (6)$$

where δN_s is the equivalent sheet-charge density seen by the optical probing beam as it integrates the effects from the volume charge density, δN , while passing through the AlGaAs laser cavity depth, L ($\delta N_s \equiv \delta NL$). Assuming a photocurrent of $I_0 = 1\text{mA}$, we arrive at a theoretical system sensitivity of

$$\frac{\delta N_s}{\sqrt{Hz}} = 1.6 \times 10^9 \frac{e}{\text{cm}^2 \sqrt{Hz}}. \quad (7)$$

The present optical probing system operated with a photocurrent of $I_0 = 10\mu\text{A}$, and was thermal noise limited approximately 20dB above the shot-noise floor. This gave our experimental probing system a minimum detectable charge-sensing level of

$$\frac{\delta N_s}{\sqrt{Hz}} \approx 2 \times 10^{11} \frac{e}{\text{cm}^2 \sqrt{Hz}}. \quad (8)$$

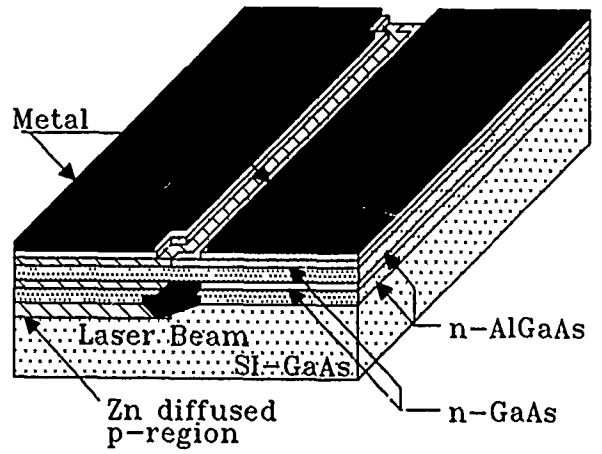


Figure 4: The cross-section of the AlGaAs semiconductor laser.

AlGaAs Semiconductor Laser Sample

A cross-section of the AlGaAs semiconductor laser is shown in Fig. 4[11]. This laser consisted of a series of GaAs and AlGaAs epitaxial layers grown on the surface of a $\langle 100 \rangle$ semi-insulating GaAs substrate. A Zn diffusion was introduced into half of the laser structure, and driven into the semi-insulating substrate. Anode and cathode metal contacts were then placed on the two halves of the laser structure, but approximately $10\mu\text{m}$'s on either side of the laser cavity (pn junction) was left unmetallized. Fig. 5 shows a top-view picture of the AlGaAs laser sample during operation. The light stripe down the center of the exposed region of the laser is photoluminescence from the laser cavity. Notice that near the edges of the junction, the photoluminescing gain region is bent back. This structure prevents carriers from diffusing to the laser facets, which could cause facet damage, and thereby degrade the laser reliability. Because of the shape of laser cavity, it is referred to as a "crank" structure. Measurements were made on this device by focusing the $1.3\mu\text{m}$ wavelength probing laser directly onto the white stripe region (cavity) of the laser sample.

This particular laser structure was convenient to probe, since the semi-insulating substrate eliminated capacitance and stray electric fields to the substrate. Hence, all the internal electric fields in this structure lie parallel to the surface of the device. Because of this configuration, electrooptic effects from the electric field across the junction should not generate a signal in the optical probing system. We experimentally verified this by applying a signal to the laser while it was reverse biased. Under this condition, no signal was observed from the optical probing system.

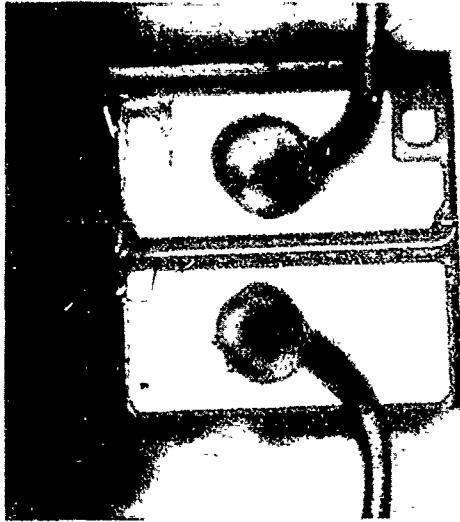


Figure 5: A top-view picture of the crank transverse-junction stripe AlGaAs semiconductor laser during operation.

Experimental Results

We have used this optical probing system to spatially resolve picosecond carrier dynamics within the AlGaAs semiconductor laser sample. Fig. 6 shows a set of measurements taken with the confocal charge-sensing optical probing system. In this experiment, the $1.3\mu\text{m}$ wavelength optical probe spot was focused to the center of the AlGaAs laser cavity. The laser sample was biased just below threshold ($I_b = 18\text{mA}$, $I_{th} = 23\text{mA}$), and pulsed differing amounts above threshold by varying the RF power to an attenuated comb-generator. The output from the attenuated comb generator consisted of 100ps FWHM current pulses at a 100MHz repetition rate, which was used to gain switch the 50Ω terminated AlGaAs laser sample. Curve A in this measurement is the optically detected charge-density modulation in the AlGaAs laser sample in response to a 10mA current pulse. Curve B is a measurement at a 15mA current pulse, and curve C corresponds to a measurement at a 30mA current pulse. This result shows two interesting features: 1) the charge-density within the laser cavity clamps to the threshold level following an initial transient; and 2) during the switching transient the charge-density overshoots the threshold level by an amount that depends upon how hard the laser sample has been driven.

Previous theoretical calculations [14,15] predict that the internal charge-density level should overshoot and clamp at the threshold level in response to an input current pulse in a manner similar to what is observed here. In addition, the theoretical analyses suggest that above $I_p/I_{th} = 7$ the laser should de-

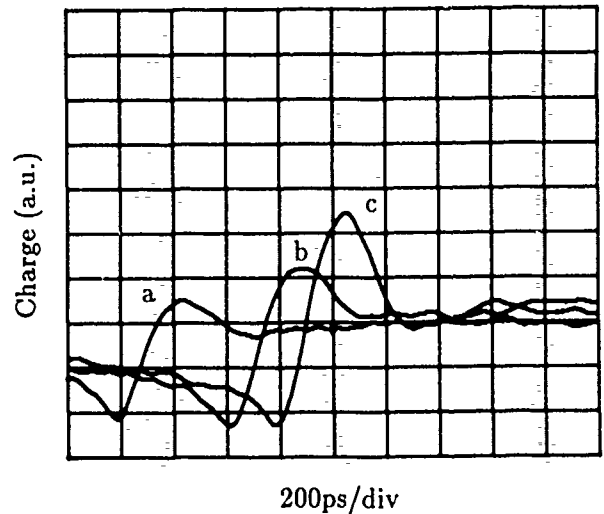


Figure 6: Picosecond optical detection of charge-density modulation in the crank transverse-junction stripe AlGaAs semiconductor laser in response to the following peak current pulses: a.) 10mA ; b.) 15mA; and c.) 30mA.

velop ringing within the charge-density modulation. However, since this would require driving this laser with over 175mA, we did not explore this regime for fear of damaging the laser. At the lower drive conditions used in this experiment, there is no clear evidence of ringing.

The experiment also shows an increasing phase shift between the three measurements. In the present experimental system, variations in the RF power to the comb generator produced phase delays in the pulse-output of the comb generator. Future measurements with a constant-phase pulse amplitude control should allow us to observe variations in the time delay of charge buildup in the laser cavity. The dip in the traces just prior to the rise of the charge is the response of the cavity charge-density to the 100MHz feedthrough from the comb generator.

In an effort to guarantee that these measurements were not the result of a thermally generated index perturbation within the laser cavity, we again biased the laser sample just below threshold ($I_b = 18\text{mA}$), and applied a 100MHz, $\pm 10\text{mA}$ sine wave to the device. Since the temperature of the sample is proportional to its power dissipation ($T_j = P_j/\theta_j$, where P_j is the power dissipation at the junction, and θ_j is the thermal resistivity of the sample), we would expect that beyond the threshold of the sample, the thermal signal would continue to increase, while the charge signal would be clamped. The measurements taken with the charge-sensing optical probing system strongly clamped in this experiment, and no evidence of a thermally generated signal was observed.

beyond threshold. Therefore, since no electric field effects and no thermal effects were observed, we believe that these measurements represent spatially-resolved charge dynamics within the laser cavity.

Conclusions

This paper has presented a noninvasive, noncontact optical probing system for temporally and spatially resolving charge-density modulation in an AlGaAs semiconductor laser diode. The present system has a 43ps temporal resolution, which was sufficient to allow us to observe charge overshoot and clamping at the internal threshold level. Future improvements to the temporal response of this probing system should give us the capability of observing subpicosecond carrier dynamics within the laser. The measurements were made with a 2.5 μ m spatial resolution. This spatial resolution should be sufficient to allow us to temporally resolve spatially dependent effects — such as spatial hole burning, and defects — within the laser cavity. Therefore, this optical probing system should provide a powerful technique for characterizing the performance of AlGaAs semiconductor lasers.

Acknowledgments

I would like to thank G. Arjavalingam, M. Kesler, and D. McBride for thought provoking discussions on this optical probing system and the associated measurements. In addition, I would like to thank D. McBride for reading this document and for suggesting ways that it could be better written.

References

- [1] W. Both, R. Rimpler, G. Erbert, G. Stadermann, A. Klehr, U. Zeimer, "Catastrophic optical damage in GaAlAs/GaAs laser diodes", *IEEE Proc. J.* **134**, 95 (1987)
- [2] H. Kawaguchi, K. Takahei, "Direct Observation of the Spatial Hole Burning and the Saturation of the Spontaneous Emission in InGaAsP/InP Lasers", *IEEE J. Quantum Electron.* **QE-16**, 706 (1980)
- [3] M.P. Kesler, and E.P. Ippen, "Subpicosecond gain dynamics in GaAlAs laser diodes", *Appl. Phys. Lett.* **51**, 1765 (1987)
- [4] T.L. Koch, L.C. Chiu, Ch. Harder, and A. Yariv, "Picosecond carrier dynamics and laser action in optically pumped buried heterostructure lasers", *Appl. Phys. Lett.* **41**, 6 (1982)
- [5] H.K. Heinrich, D.M. Bloom, B.R. Hemenway, "Noninvasive sheet charge density probe for integrated silicon devices", *Appl. Phys. Lett.* **48**, 1066 (1986)
- [6] B.R. Hemenway, H.K. Heinrich, J.H. Goll, Z. Xu, and D.M. Bloom, "Optical Detection of Charge Modulation in Silicon Integrated Circuits Using a Multimode Laser-Diode Probe", *Electron. Dev. Lett.* **EDL-8**, 344 (1987)
- [7] U. Keller, S.K. Diamond, B.A. Auld, D.M. Bloom, "Noninvasive optical probe of free charge and applied voltage in GaAs devices", *Appl. Phys. Lett.* **53**, 388 (1987)
- [8] G.N. Koskovich, M. Soma, "Voltage Measurement in GaAs Schottky Barriers Using Optical Phase Modulation", *IEEE Electron Dev. Lett.* **EDL-9**, 433 (1988)
- [9] A. Black, C. Courville, G. Schultheis, H.K. Heinrich, "Optical Sampling of GHz Charge Density Modulation in Silicon Bipolar Junction Transistors", *Electron. Lett.* **23**, 783 (1987)
- [10] T. Wilson, D.K. Hamilton, "Difference confocal scanning microscopy", *Optica Acta* **31**, 453-465 (1984)
- [11] K. Isshiki, N. Kaneno, H. Kumabe, H. Namizaki, K. Ikeda, and W. Susaki, "Ten-Thousand-Hour Operation of Crank Transverse-Junction-Stripe Lasers Grown by Metal-Organic Chemical Vapor Deposition", *J. Light-wave Tech.* **LT-4**, 1475-1481 (1986)
- [12] T.R. Corle, C.-H. Chou, and G.S. Kino, "Depth response of confocal optical microscopes", *Optics Letters* **11**, 770 (1986)
- [13] F. Wooten, "Optical Properties of Solids", (Academic Press, New York, 1972), pp.52-55
- [14] P. Paulus, R. Langenhorst, D. Jäger, "Generation and Optimum Control of Picosecond Optical Pulses from Gain-Switched Semiconductor Lasers", *IEEE J. Quantum Electron.* **QE-24**, 1519 (1988)
- [15] D. Bimberg, K. Ketterer, E.H. Böttcher, and E. Schöll, "Gain modulation of unbiased semiconductor lasers: ultrashort light-pulse generation in the 0.8 μ m-1.3 μ m wavelength range", *Int. J. Electron.* **60**, 23 (1986)

Spectral Filtering of Relaxation Oscillations in Injection-Current-Modulated Diode Lasers

Santanu Basu, Paul G. May, and Jean-Marc Halbout

*IBM Research Division, T. J. Watson Research Center,
Yorktown Heights, New York 10598*

Abstract

Spectrally resolved pulse shapes from injection current modulated Fabry-Perot diode lasers have been obtained using a streak camera. The results indicate that the relaxation oscillations are spectrally separated from the primary pulse. Spectral filtering was carried out to produce single-longitudinal-mode output free of relaxation oscillations.

Introduction

Gain switching by current pulse injection is an established technique to generate short optical pulses from diode lasers[1 - 4]. The gain-switched output from Fabry-Perot laser diodes is accompanied by relaxation oscillations and spectral broadening. For communication applications, the spectral width, $\Delta\lambda$ of the short-pulse optical source determines the bit rate-distance product[5] according to

$$BL \leq (4D\Delta\lambda)^{-1} \quad (1)$$

where, B is the bit rate, L is the length of the optical fiber of dispersion D. The spectral bandwidth of the gain-switched pulse output from Fabry-Perot laser diodes far exceeds the transform limited bandwidth which makes them unsuitable for high bit rate communication applications. In this paper, we investigate the temporal evolution of the spectral components of the gain-switched laser diode.

The injection current modulated laser operation is best described by a set of nonlinear rate

equations for the carrier density, N and the photon density, S. These are[3,4,6]

$$\frac{dN}{dt} = \frac{I}{qV} - g(N - N_t)S - \frac{N}{\tau_n} \quad (2)$$

and,

$$\frac{dS}{dt} = g\Gamma(N - N_t)S - \frac{S}{\tau_p} + \beta\Gamma\frac{N}{\tau_n} \quad (3)$$

where I is the current in the active region of volume V, and q is the electronic charge. The gain coefficient, g takes into account the effect of gain compression at high optical power density[3], and the band filling effect[6]. N_t is the electron concentration at the transparency point, τ_n and τ_p are the electron and the photon lifetimes, Γ is the modal confinement factor and β is the fraction of the spontaneous emission which is coupled into the lasing mode. The numerical solutions of the rate equations for current pulse modulation have been reported in the literature without taking into account band filling[2 - 4]. The results indicate that the both the electron density and the photon density undergo relaxation oscillations in gain-switched operation. The overshoot of the electron density is greater in the first oscillation than in the subsequent ones. The primary pulse from the gain-switched laser diode is also emitted during the first electron density oscillation. The effect of the rapidly changing carrier density are twofold. It has been shown both experimentally and theoretically, that with increasing carrier density, the gain spectrum shifts to shorter wavelength because of the band filling effect[7,8]. The change in the carrier density also causes longitudinal mode shift and change in the mode spacing[9] due to a change in the modal refractive index.

Spectral and Temporal Measurements

The experimental configuration is shown in Fig. 1. A commercial crank transverse junction stripe laser diode (Mitsubishi ML 5101A) with an emission wavelength of 820 nm was used in this experiment. The characteristics of these types of laser diodes are given in Ref. 10. The laser diode was biased at various current levels and was gain-switched by the application of a voltage pulse from a step recovery diode. The step recovery diode was driven by a 100-MHz sinusoidal rf signal and the output voltage had a peak value of 15.2 V and a duration of 70 ps. The laser diode output was collimated and was incident on a diffraction grating with 1700 lines per mm which spatially separated the longitudinal modes of the laser diode. An aperture was used to select any wavelength region and the apertured output was characterized by a 0.35-m grating monochromator of approximately 0.5 Å resolution and a Hamamatsu synchroscan streak camera of 10-ps resolution.

The threshold current for this laser diode was 28 mA. The output optical pulse duration was measured at different bias currents. It was noted that with 15.2-V voltage pulse applied to the laser diode, the minimum pulse duration of 25 ps was obtained at a bias current of 6 mA. Significant relaxation oscillations were noted at the laser output. The bias current required for the minimum pulse duration depended on the applied voltage pulse, and when the laser was biased below threshold, the required bias current decreased as the voltage pulse was increased.

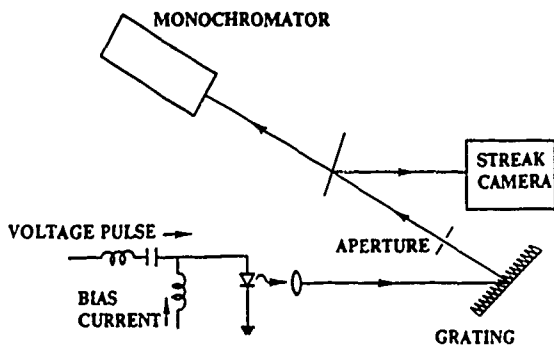


Figure 1. A schematic of the experimental configuration

The laser diode spectrum under pulsed excitation at various bias levels are shown in Fig. 2. The parameter r used in these figures is defined as the ratio of the bias current and the current at

the lasing threshold. When the laser was biased above threshold, the gain-switched spectrum was significantly broader than the cw spectrum in absence of the voltage pulse. When the laser was biased below threshold, the broadening of the spectrum was even greater and the spectrum exhibited a spontaneous emission background on the short wavelength side. The spontaneous emission background is an indication of band filling. When the laser oscillation builds up in the cavity, the carrier density is near its maximum value and the gain spectrum is shifted to

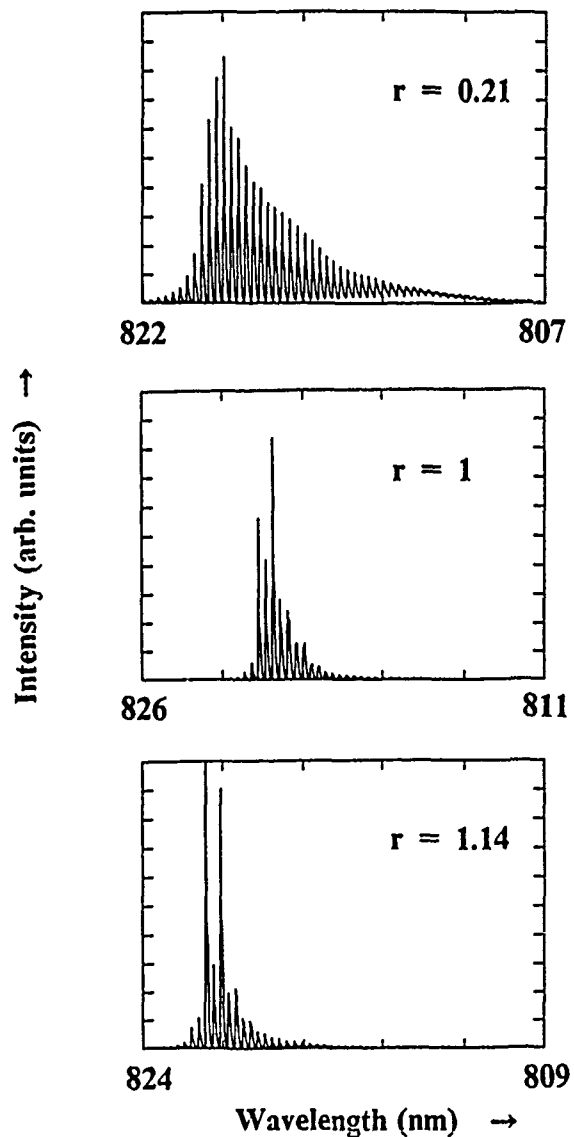


Figure 2. Gain-switched laser spectrum

the short wavelength side[7]. At later times, the peak of the gain spectrum shifts to longer wavelength, and hence the ratio of spontaneous emission to stimulated emission decreases at longer wavelength. At all bias levels, the spectrum was asymmetric with a longer tail on the short wavelength side.

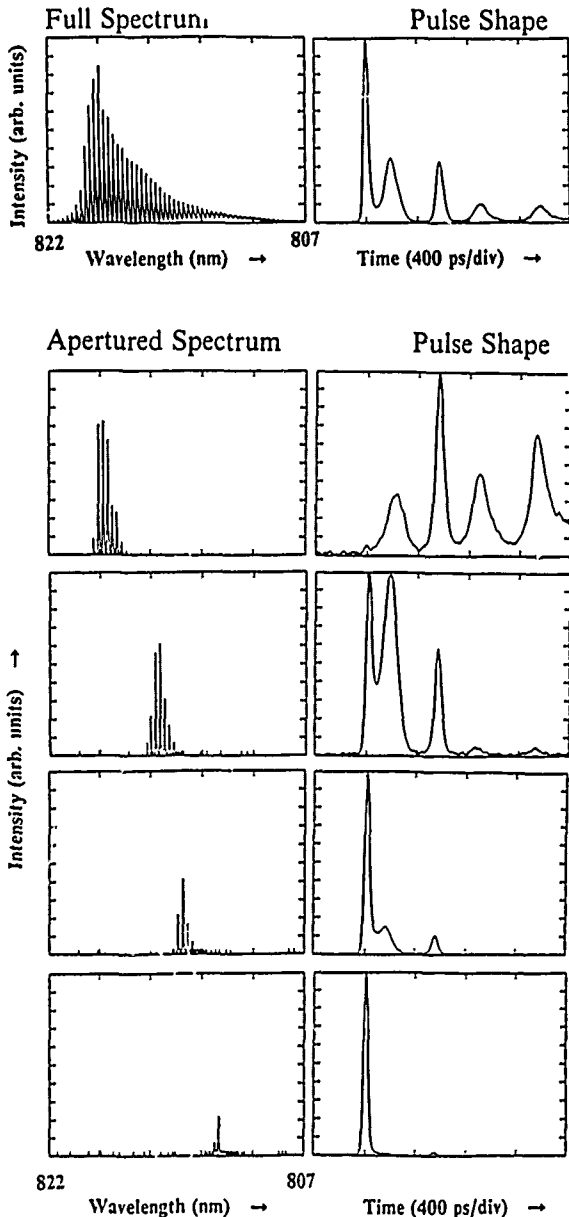


Figure 3. Simultaneous measurement of gain-switched Fabry-Perot laser diode spectrum and pulse shape

The temporal characteristics of various parts of the output spectrum are shown in Fig. 3. The spectrum and the pulse shape of the laser diode output are shown in the top section. For this experiment, the laser diode was gain switched by a 15.2-V pulse in presence of 6 mA of bias current. The external grating-aperture combination as shown in Fig. 1 was used to spectrally resolve the laser diode output. The apertured spectrum and the corresponding pulse shape for different wavelength regions are shown in the bottom part of Fig. 3. It is seen that the primary optical pulse is absent in the longest wavelength part of the spectrum. In the shorter wavelength region, the output consisted of the primary laser pulse followed by relaxation oscillations. The laser output in the shortest wavelength region was free of relaxation oscillations. The minimum duration noted for pulses free of relaxation oscillations was 22 ps with rise and fall times of 14 ps. By replacing the aperture with a knife edge, the longitudinal modes present in the relaxation oscillations could be filtered out. The fraction of energy contained in the filtered spectrum was estimated to be 12.5% when the laser was biased below threshold. Similar data was taken at various bias conditions, both below and above threshold and the results confirmed the spectral separation of the primary pulse from the relaxation oscillations.

Fig. 4 shows the results of spectral aperturing to select one longitudinal mode from the gain-switched laser output. For this experiment, a different laser diode of the same type as in the previous experiment was used. The lasing threshold for this particular diode was 24 mA, and 33-ps and 32-ps pulses were obtained when the laser was biased at 15 mA and 30 mA respectively. The voltage pulse applied was 13.8 V in amplitude and 90 ps in duration. In Fig. 4, it is demonstrated that relaxation oscillation-free pulses containing essentially one longitudinal mode of the laser diode could be produced by spectral aperturing. The percentage of output energy which was contained in one longitudinal mode was 0.8% when the laser was biased at 15 mA, and it was 2.5% when the laser was biased at 30 mA. The energy per gain-switched and spectrally-apertured pulse is estimated to be 0.45 pJ for 30 mA of bias current, and the peak power in the spectrally apertured pulse is estimated to be 15 mW corresponding to a pulsewidth of 30 ps.

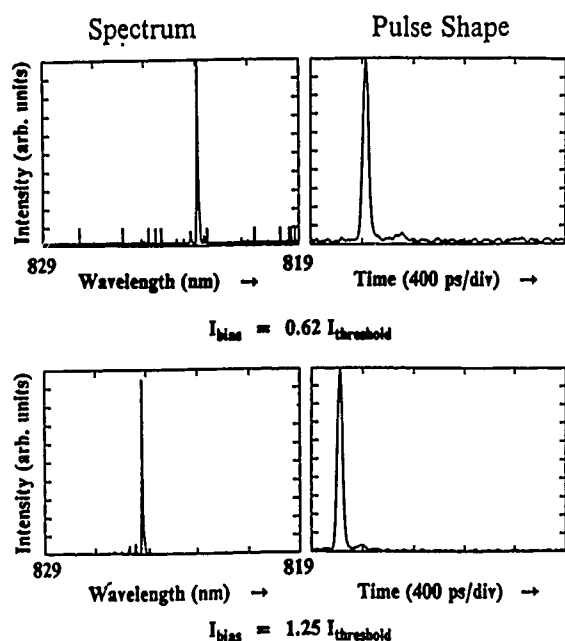


Figure 4. Spectral aperturing to produce relaxation oscillation-free pulses containing one longitudinal mode of the laser cavity. The top curves are for 15 mA of bias current and the bottom curves are for 30 mA of bias current.

The longitudinal modes in the gain-switched laser diode output are chirped because of carrier density induced refractive index change[9,11]. However this chirp may not be linear and the pulse broadening inside the laser cavity may not be completely compensated for by using a fiber or a grating external to the laser cavity. To examine this effect, we used a grating-aperture combination to generate a 27 ps long pulse with 22 ps rise and fall times. When the laser diode output was coupled into a 25-m-long single-mode fiber with positive group velocity dispersion, spectral aperturing of the fiber output produced asymmetric pulses of 21 ps duration and 14 ps fall time. The chirp due to the carrier density change is dependent on the relative delay between the current density maximum and the photon density maximum and is dependent on the bias level. Experimentally it was found that the asymmetry of the pulse shape from the output of the fiber was dependent on the bias current level.

Discussion

We simultaneously measured the output pulse shape and the spectrum of an injection current modulated laser diode. We have shown that the relaxation oscillations from the laser diode are at a longer wavelength than the primary pulse. A simple grating-aperture combination was used to spatially separate the primary pulse from the relaxation oscillation. The shortest pulses free of relaxation oscillations which were produced in this manner were 22 ps in duration. Much shorter pulses are expected for laser diodes designed for high frequency modulation as were used in Ref. 3. With suitable spectral aperturing, short pulses free of relaxation oscillations were generated with a spectral width much less than the longitudinal mode-spacing of 2.7 Å for this laser diode cavity. The width of the longitudinal mode was measured to be less than 0.62 Å. When the laser was biased above threshold, an estimated peak power of 15 mW was obtained in a single longitudinal mode, free of relaxation oscillations. It is to be mentioned that in gain-switched multiple quantum well lasers, it has been very recently shown that the primary pulse contains 50% of the longitudinal modes which appear in the time-averaged spectrum [12].

The results presented in this paper have several practical applications. It is possible to make an integrated single-longitudinal-mode, short-pulse optical source for optical communication. The design would consist of a Fabry-Perot laser followed by an integrated grating-aperture combination and an amplifier. The bit rate-distance product corresponding to such an integrated light source will be suitable for optical communication especially in the 1.3-1.5 μm region where the fiber dispersion is less. The single-longitudinal-mode operation of this proposed laser configuration is due to external wavelength selecting elements as compared to distributed feedback lasers, where the wavelength selection is carried out inside the cavity. In situations where short pulses of high peak power are required for spectroscopic applications, it may be possible to use a diode laser-amplifier combination, with the amplifier gain spectrum shifted to shorter wavelength for enhancing the primary pulse in the laser output. It is also apparent from the results in this paper that a theory of spectral characteristics of gain-switched laser diodes should include the effect of band filling.

References

1. C. Lin, P.L. Liu, T.C. Damen and D.J. Eilenberger, "Simple picosecond pulse generation scheme for injection lasers", *Electron. Lett.*, **16**, 600-601, 1980.
2. D. Bimberg, K. Ketterer, E.H. Bottcher and E. Scholl, "Gain modulation of unbiased semiconductor lasers: ultrashort light-pulse generation in the 0.8 μm - 1.3 μm wavelength range", *Int. J. Electronics*, **60**, 23-45, 1986.
3. P.M. Downey, J.E. Bowers, R.S. Tucker and E. Agyekum, "Picosecond dynamics of a gain-switched InGaAsP laser", *IEEE J. Quantum Electron.*, **QE-23**, 1039-1047, 1987.
4. P. Paulus, R. Langenhorst and D. Jager, "Generation and optimum control of picosecond optical pulses from gain-switched semiconductor lasers", *IEEE J. Quantum Electron.*, **24**, 1519-1523, 1988.
5. N.K. Dutta, N.A. Olsson, L.A. Koszi, P. Besomi, R.B. Wilson and R.J. Nelson, "Frequency chirp under current modulation in InGaAsP injection lasers", *J. Appl. Phys.*, **56**, 2167-2169, 1984.
6. S. Tarucha and K. Otsuka, "Response of semiconductor laser to deep sinusoidal injection current modulation", *IEEE J. Quantum Electron.*, **QE-17**, 810-816, 1981.
7. B.W. Hakki and T.L. Paoli, "Gain spectra in GaAs double-heterostructure injection lasers", *J. Appl. Phys.*, **46**, 1299-1306, 1975.
8. F. Stern, "Calculated spectral dependence of gain in excited GaAs", *J. Appl. Phys.*, **47**, 5382-5385, 1976.
9. J. Manning, R. Olshansky and C.B. Su, "The carrier-induced index change in AlGaAs and 1.3 μm InGaAsP diode lasers", *IEEE J. Quantum Electron.*, **QE-19**, 1525-1530, 1983.
10. K. Isshiki, N. Kaneno, H. Kumabe, H. Namizaki, K. Ikeda and W. Susaki, "Ten-thousand-hour operation of crank-transverse-junction-stripe lasers grown by metal-organic chemical vapor deposition", *J. Lightwave Tech.*, **LT-4**, 1475-1481, 1986.
11. R.A. Linke, "Modulation induced transient chirping in single frequency lasers", *IEEE J. Quantum Electron.*, **QE-21**, 593-597, 1985.
12. K. Ketterer, E.H. Bottcher and D. Bimberg, "Picosecond spectra of gain-switched AlGaAs/GaAs multiple quantum well lasers", *Appl. Phys. Lett.*, **53**, 2263-2265, 1988.

Ultrafast Nonlinearities in InGaAsP Diode Laser Amplifiers

K. L. Hall and E. P. Ippen

Department of Electrical Engineering and Computer Science and Research Laboratory of Electronics, Massachusetts Institute of Technology, Cambridge, Massachusetts 02139

J. Mark

Telecommunications Research Laboratory, Lyngso Alle 2, DK 2970 Horsholm, Denmark

G. Eisenstein

AT&T Bell Laboratories, Crawford Hill Laboratory, Holmdel, New Jersey 07733

Abstract

Using femtosecond pulses at $1.5\ \mu\text{m}$ we study ultrafast gain and loss nonlinearities in InGaAsP optical amplifiers. Suo-picosecond pump-probe dynamics are observed.

Semiconductor optical amplifiers are receiving increasing attention for possible applications to broadband optical communication and switching systems. Of particular interest are InGaAsP devices that can be tailored to the communication bands of 1.3 and $1.5\ \mu\text{m}$. Much is known about their linear and small signal characteristics, much less about their nonlinear and ultrafast dynamical properties. Studies of diode laser modulation characteristics^[1], wave mixing^[2,3], and picosecond pulse amplification^[4,5] have provided information about nonlinearities and gain compression due to population dynamics. In this paper we present results from the first femtosecond investigations of InGaAsP laser amplifiers. They reveal strong nonlinearities due to nonequilibrium carrier distributions.

We perform our pump-probe experiments using femtosecond pulses from an Additive Pulse Modelocked (APM) KCl:Ti color center laser^[6]. The laser is tunable from 1.48 to $1.54\ \mu\text{m}$ and produces pulses of 100 - 200 fsec duration. Figure 1 shows the experimental arrangement. The input from the color center laser is divided into two paths by a beamsplitter. One arm, the so-called "probe" arm passes through a half-wave plate where the polarization is rotated by 90° with respect to that in the "pump" arm. The pump arm includes a retroreflector mounted on a precision stepping stage that is used to set the delay between the pump and probe beams. The pump and probe are recombined at a beamsplitter and are coupled into a short length of dispersion-shifted fiber. The fiber is terminated with a microlens which is used to couple light into the diode. The fiber is used

to insure collinearity of the pump and probe beams and to increase coupling to the active region of the diode. After the diode, a polarizer selects the probe beam for detection.

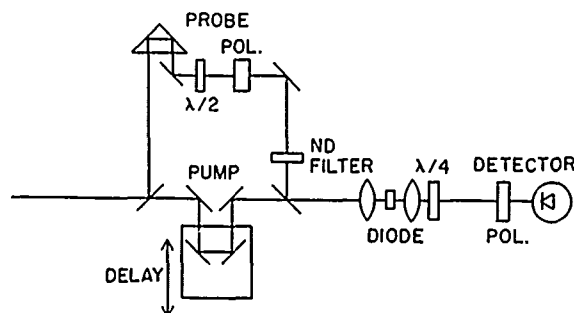


Figure 1. Experimental configuration used to perform pump-probe measurements.

The InGaAsP diodes are $1.5\ \mu\text{m}$, channelled-substrate buried-heterostructure V-groove lasers that have been antireflection coated. The active region length is approximately $250\ \mu\text{m}$ and the threshold current before coating is $18\ \text{mA}$. As we vary either the bias current to the amplifier or the wavelength of the color-center laser, we observe differing effects of the pump pulse on the transmission of the probe. Consider first the long-lived (nanosecond) population effects. Under conditions of gain at the pump-probe wavelength, stimulated emission results in a net decrease of gain ($-\Delta T/T$ observed by the probe) that persists until the carrier population is restored by current injection. Under conditions of loss at the pump-probe wavelength, absorption of pump photons produces an increase in population ($+\Delta T/T$ observed by the probe) that persists until recovery. Between these two conditions is a point we refer to as nonlinear transparency: the point at which there is no

net change in carrier population and there is no persistent change following the pump pulse. By running our pump-probe experiment under these three distinctly different conditions, we are able to separate the other, faster gain dynamics into those (such as spectral hole burning) which have the same sign as that produced by the population change and those (such as carrier heating) which do not. Experimentally we can survey these different regions of nonlinearity by either varying the wavelength of the color-center laser as discussed above or by remaining at a fixed wavelength and changing the current to the diode.

Figure 2 shows probe transmission as a function of delay relative to the pump for various injection current levels. Neglecting the transients at zero delay for a moment, notice that at low injection current the persistent transmission change is positive, indicating that we are in the absorption regime. At 10 mA, we reach transparency and for injection currents higher than 10 mA, we see a negative transmission step, indicating that we are in the gain regime. Figure 3 shows probe transmission versus delay for various pump-probe wavelengths. It is immediately evident that the evolution of the pump-probe signal from short to long wavelengths is the same as that from low to high current.

In all the traces of Figures 2 and 3, sub-picosecond dynamics are evident near zero time delay. It also appears that these dynamics are more complex functions of experimental conditions than those observed in AlGaAs diodes^[7]. In AlGaAs, the initial transient varied in amplitude but had the same (gain compressing) form under all pump-probe conditions: gain, loss and nonlinear transparency. Those data were interpreted to imply that quasi-equilibrium carrier distributions were established in less than 50 fs (too fast to be detected) and that the observed gain compression resulted from a temporary elevation of carrier temperature. Relaxation of the transient then corresponded to equilibration between the carrier and lattice temperatures.

Our present data for InGaAsP diodes change in both amplitude and shape with variations in current or wavelength. To evaluate these changes we have analyzed our data in terms of a sum of responses with different time constants. The total signal $S(\tau)$ measured in our experiment can be written as

$$S(\tau) = \int_{-\infty}^{\infty} h(\tau - t) \cdot G^{(2)}(t) dt$$

where $G^{(2)}(t)$ is the intensity autocorrelation function of our pulses, $h(t)$ is the small signal response of transmission to an impulse of light, and τ is the relative delay between pump and probe. We find that our data can be fit by assuming

$$h(t) = u_{-1}(t)[a_0 + a_1 e^{-t/\tau_1} + a_2 e^{-t/\tau_2}] + a_3 \delta(t)$$

where $u_{-1}(t)$ is the unit step function, $\delta(t)$ is an impulse and the a_i 's are constants. Although the overall shapes

of the experimental curves vary significantly from trace to trace, we are able to fit them all with similar time constants, τ_1 and τ_2 , if we simply vary the amplitudes, a_i . In other words, best fit of $h(t)$ to each curve yields approximately the same time constants: $\tau_1 \cong 650$ fs and $\tau_2 \cong 200$ fs. An example of one of these fits is shown in Fig 4.

In the deduced impulse response $h(t)$, the first term, a_0 , is the amplitude of the step-like change in transmission due to the decrease (or increase) in carrier population caused by stimulated emission (or absorption).

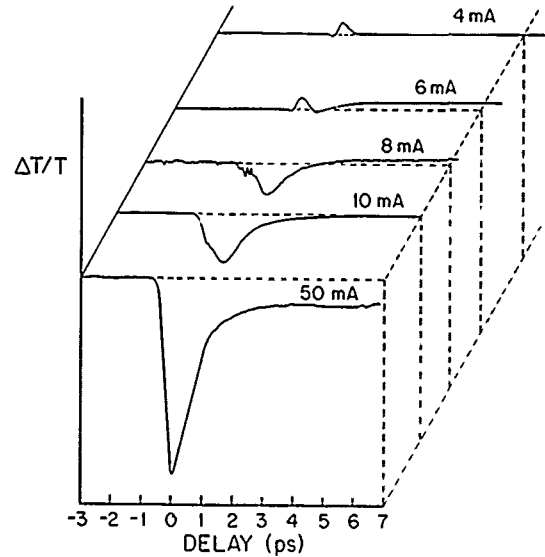


Figure 2. Probe transmission as a function of delay relative to the pump for various injection current levels.

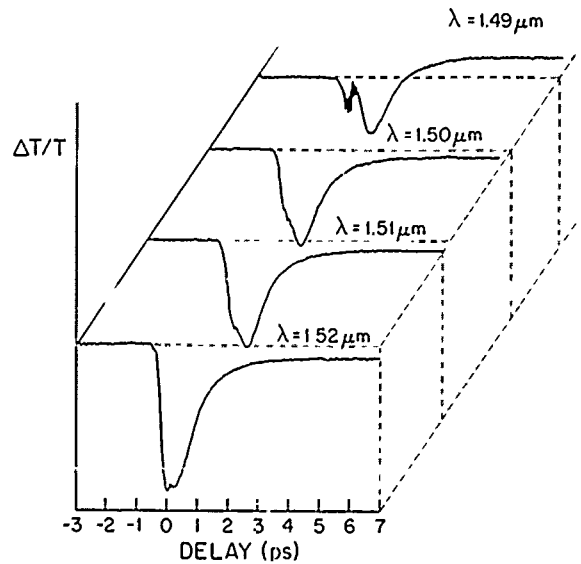


Figure 3. Probe transmission versus delay for various pump-probe wavelengths.

The sign of a_0 reverses as the pump-probe wavelength is varied through the point of nonlinear transparency. The second term, a_1 , the amplitude of the 650 fs component, changes magnitude relative to a_0 but remains negative, corresponding to gain compression, over the entire range of our experiments. We believe that this term reflects carrier heating similar to that seen in the previous AlGaAs diode experiments. The third term, a_2 , is always positive, opposing the effect of a_1 as discussed below. The last term, a_3 , appears to represent either an instantaneously recovering induced absorption or a small, constant coupling term. It is always negative.

A further comparison of the relative magnitudes of a_1 and a_2 may provide some insight into the origin of the initial dynamic. For example, to the extent that they are equal (and opposite), the a_2 term might simply be explained as a delay in the rise of the carrier heating effect, a_1 . Thus, we investigated the behavior of their sum, $a_1 + a_2$. This sum was found to change sign as the pump-probe wavelength moved from the loss regime to the gain regime, revealing an excess 200 fs component that roughly follows the direction of the population change a_0 . Such a component might be indicative of nonequilibrium carrier distribution changes occurring on this timescale, but we have no additional experimental evidence to support such a claim. Finally, it is important to note that the form of the fit we have chosen is strictly ad hoc. Including a pulse-derivative-like coherent coupling term in the analysis, for example, would modify both amplitudes and time constants. At low gains especially, nonlinear interference between guided and unguided components might also contribute to the data.

In summary, there are striking differences between the ultrafast nonlinearities that are observed in InGaAsP laser diodes and those that have been seen in AlGaAs. Under normal (amplifier) conditions of gain, the dominant sub-picosecond nonlinearity in InGaAs diodes is still that of nonequilibrium carrier heating. Nevertheless, there are more rapid pump-probe dynamics that cannot be neglected. They become increasingly apparent as one approaches nonlinear transparency or loss. Other spectroscopic measurements of intraband transition strengths and recovery times in both the valence and conduction bands are needed to clarify the underlying mechanisms.

We gratefully acknowledge collaboration with L.Y. Liu on the femtosecond color-center laser and with G. Raybon on the anti-reflection coating of the InGaAsP laser diodes. This work was supported in part by the A.F.O.S.R. under Contract F49620-88-C-0089 and by the Joint Services Electronics Program under Contract DAAL03-89-6-001.

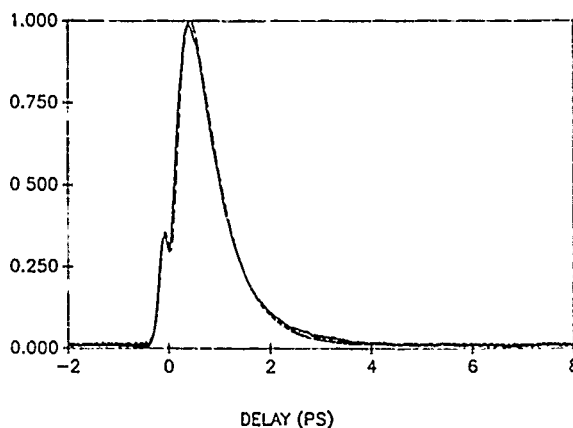


Figure 4. Theoretical fit of $h(t)$, (dashed line) and experimental pump-probe curve (solid line) with the nanosecond response removed. (Note that the traces have been inverted for this figure.)

References

1. R.S. Tucker, "High-speed modulation of semiconductor lasers," *J. Lightwave Technol.* **LT-3**, 1180-1192 (1985).
2. K. Inoue, T. Mukai and T. Saitoh, "Nearly degenerate four-wave mixing in a traveling-wave semiconductor laser amplifier," *Appl. Phys. Lett.* **51**, 1051-1053 (1987).
3. R.M. Jopson, T.E. Darcie, K.T. Gayliard, R.T. Ku, R.E. Tench, T.C. Rice and N.A. Olsson, "Measurement of carrier-density mediated intermodulation distortion in an optical amplifier," *Electron. Lett.* **23**, 1394-1395 (1987).
4. I.W. Marshall, D.M. Spirit and M.J. O'Mahoney, "Picosecond pulse response of a travelling-wave semiconductor laser amplifier," *Electron. Lett.* **23**, 818-819 (1987).
5. G. Eisenstein, P.B. Hansen, J.M. Wiesenfeld, R.S. Tucker and G. Raybon, "Amplification of high repetition rate picosecond pulses using an InGaAsP traveling-wave optical amplifier," *Appl. Phys. Lett.* **53**, 1539-1541 (1988).
6. J. Mark, L.Y. Liu, K.L. Hall, H.A. Haus and E.P. Ippen, "Femtosecond pulse generation in a laser with a nonlinear external resonator," *Opt. Lett.* **14**, 48-50 (1989).
7. M.P. Kesler and E.P. Ippen, "Subpicosecond gain dynamics in GaAlAs laser diodes," *Appl. Phys. Lett.* **51**, 1765-1767 (1987).

Spread-Spectrum-Integrated Optic Modulators

David W. Dolfi

Hewlett-Packard Laboratories, 1651 Page Mill Road, Palo Alto, California 94303

Abstract

Integrated optic modulators have been developed which incorporate spread spectrum concepts in their design in order to achieve high bandwidths. We review their operating principles, limitations, and applications.

Modulator Bandwidth Limitations

In the design of conventional integrated optic modulators, a trade-off exists between the drive voltage and bandwidth, due to the velocity mismatch between the modulating microwave voltage and the optical wave. This trade-off is normally controlled by the device length, whereby extended bandwidth can only be achieved by shortening the device active length, thereby increasing the drive voltage [1]. One approach for overcoming this limitation involves the use of phase reversals in the microwave field to artificially advance its phase. In this paper, we review the extension of this concept to the design of very wide band modulators whose phase reversals are patterned after spread spectrum sequences [5,6].

Figure 1 shows a traveling wave electro-optic modulator of the Mach-Zehnder variety. The single mode optical waveguides form an interferometer, whose output intensity depends on the relative phase retardation in the two arms. This can be controlled electro-optically by applying voltage to the electrodes, which, along with the optical guides, are patterned lithographically on the device. For high frequency operation, the electrode structure is fabricated as a coplanar transmission line as shown,

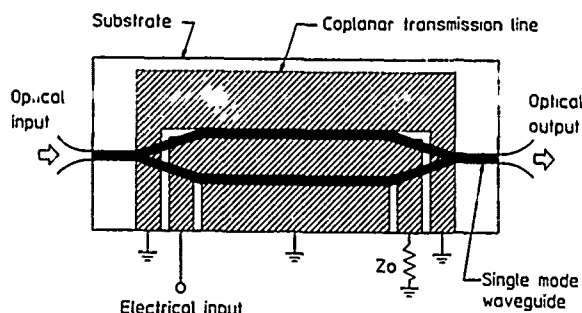


Figure 1. Schematic of a Mach-Zehnder modulator.

so that the electro-optic interaction is between two traveling waves - one optical and one microwave - each in their respective waveguides. In this configuration, the bandwidth of the device is primarily limited by the velocity difference of these two waves, and their resultant walk-off. Clearly, this becomes more severe as the device length increases. On the other hand, an increase in the device length reduces the drive voltage, due to the cumulative nature of the optical retardation induced by the microwave field. This gives rise to the voltage-bandwidth trade-off mentioned previously. A length-independent figure of merit reflecting this trade-off in a given device design is the bandwidth to drive voltage ratio. While we will concentrate on Mach-Zehnder devices in this paper, it should be emphasized that this phenomenon affects all traveling wave electro-optic modulators.

Spread Spectrum Electrode Patterns

One solution to the walk-off problem has been in the use of phase reversed electrodes to artificially ad-

vance the phase of the microwave field, allowing it to overcome - in an artificial manner - the velocity mismatch. Various phase reversal structures have been proposed, both periodic [2] and aperiodic [3,4]. Devices with periodic structures have been fabricated [7,8]. However, periodic phase reversals do not provide mismatch compensation over a broad frequency range, but only at discrete frequencies determined by the periodicity.

We have recently shown [5,6] that these devices can be best understood and hence optimized by interpreting the phase reversal electrode patterns as representations of coded sequences. Optimization of device performance is achieved by choosing for the electrode pattern pseudo-random sequences with good spread spectrum properties (low autocorrelation sidelobes in the time domain and reduced spectral ripple). A particular example of such a spread spectrum modulator - based on the Barker code [9] of length 13 - is shown in Fig. 2a. This figure illustrates the correspondence between the actual electrode pattern and the code from which it derives (Fig. 2b). The fundamental length, or bit length, of the code is the largest length of which the actual phase reversal sections are integer multiples. In Fig. 2, this is one thirteenth of the total device length. It is also obvious that any phase reversal device, periodic or aperiodic, can be associated with a coded sequence in this way. The advantage of the code concept is best illustrated by considering the behavior of these devices in the time domain. It can be easily shown [5] that the impulse response of these devices (ie: the phase retardation or small signal intensity modulation at quadrature induced by a delta function microwave pulse) has the following properties:

1) It's total duration in time is equal to the time of flight difference of the microwave and optical fields through the entire device length. Thus, the time duration of the impulse response is the same for a conventional and phase reversal modulator of the same length.

2) In the absence of microwave loss and other non-idealities, it's shape is an exact scaled replica of the electrode pattern (Fig. 2c), with each lobe having a duration equal to the microwave/optical transit time difference through the corresponding phase reversed section of the actual device. The delay difference through a single bit's length is denoted T_0 .

The first property precludes the widespread use of these devices for applications such as optical communication. It is the second property which, for the proper choice of code, leads to improved performance in the frequency domain, where more obvious applications lie. The impulse response, denoted $h(t)$ in Fig. 2, and the complex frequency response

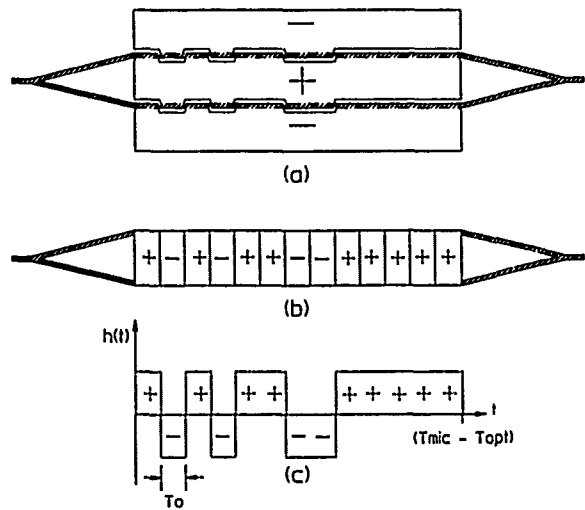


Figure 2. 13-bit Barker code modulator. Electrode structure (a), corresponding code (b), and retardation impulse response (c).

$H(f)$, form a Fourier transform pair. For many applications, however, it is not $H(f)$, but $\|H(f)\|^2$, the power spectrum of $H(f)$, which matters. This quantity is the Fourier transform not of $h(t)$, but of its autocorrelation function, given by:

$$h(t) * h(t) = \int_{-\infty}^{\infty} h(t-t')h(t')dt' \quad (1)$$

Since the impulse response is a scaled replica of the electrode pattern, which in turn embodies the code, the magnitude of the device frequency response is therefore determined by the autocorrelation function of the code itself. The main lobe of the autocorrelation (centered at $t=0$) will have a width $\approx T_0$. It's Fourier transform will correspond to a bandwidth $\approx T_0^{-1}$; that is, to a device with a length corresponding to a single bit. However, it's drive voltage will be substantially reduced provided that a significant imbalance exists between positive and negative phase reversal sections. The autocorrelation will also contain side lobe contributions, which distort the main lobe frequency response with ripple. However, *to the extent that the side lobes of the autocorrelation are small compared to the main lobe, this distortion will be small, and the extended frequency response will be preserved.* This property, a small side lobe to main lobe ratio in the autocorrelation function, is exactly a defining property of spread spectrum sequences [9]. Thus, optimal phase reversed patterns are likely to be found among sequences of this type. Note that the voltage/bandwidth trade-off has not been eliminated. The opposite polarity sections of the device which produce the code, and the corresponding bandwidth expansion, also degrade the

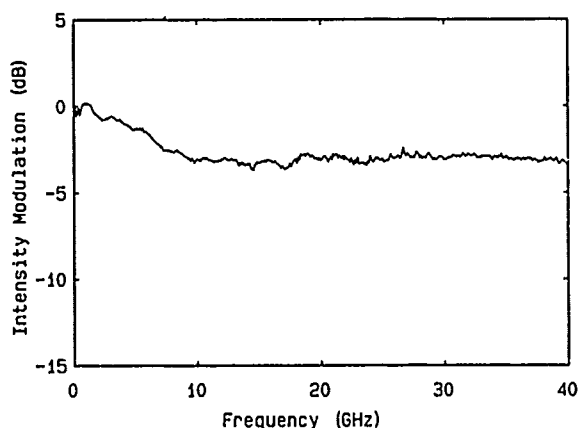


Figure 3. Measured modulation frequency response of the device of Fig. 2. (Reproduced with permission from Ref. 12, Copyright 1988, IEE).

d.c. response by inducing negative phase retardation. However, spread spectrum codes can be found for which this residual trade-off is significantly better than for a conventional device.

Barker Code Modulators

The Barker codes [9] are a family of spread spectrum codes with the property that the autocorrelation main lobe is N times larger than any of the side lobes, where N is the number of bits of the code. Several codes of this type exhibit a good compromise between adequate d.c. response and a wide spectral bandwidth. We have fabricated Mach-Zehnder traveling wave electro-optic modulators based on several of these codes [10-12], which exhibit bandwidths well in excess of conventional devices of the same length. In addition, while the d.c. response is somewhat degraded, their bandwidth to drive voltage ratios exceed that of conventional devices by factors of two to four. Results [12] for a modulator based on the 13-bit Barker code of Fig. 2 is shown in Fig. 3. After an initial roll-off of ≈ 3 dB, the modulation frequency response remains essentially flat to ≥ 40 GHz. This device has an active length of 2 cm, and a drive voltage of 7.5 volts. A conventional device with comparable bandwidth would need to be shortened to a few millimeters, and would require a drive voltage of ≥ 25 volts [13,14].

Applications

The rapid reversals in the impulse response of coded modulators (Fig. 2c) results in a non-linear phase response of $H(f)$ in the frequency domain [4-6]. How-

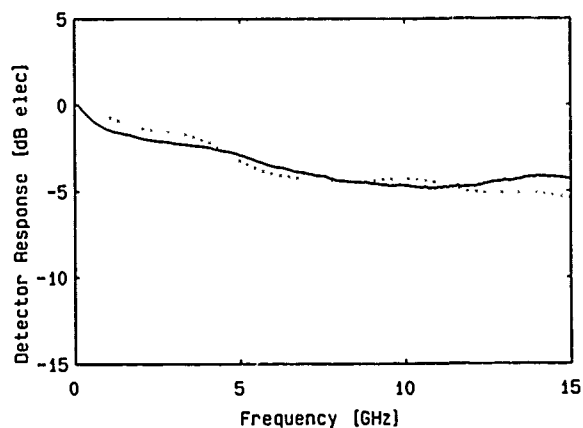


Figure 4. Photodiode calibration, using coded modulator (solid) and heterodyne technique (dotted).

ever, for many measurement applications, this non-linearity can be ignored or calibrated out, whereupon the full bandwidth of the modulators can be utilized. Examples of such applications include component calibration, microwave mixing, and optical network analysis. As an example of the first, a wide bandwidth coded modulator can be utilized to calibrate the frequency response of a fast photodiode, provided that the modulator's frequency response is known. An example of this is shown in Fig. 4, which exhibits the response to 15 GHz of a InP/GaInAs/InP PIN photodiode [15]. The solid curve represents the calibration performed with a 13-bit Barker code modulator similar to that shown in the previous figure. The comparison curve (dotted) shows the same photodiode calibrated using an optical heterodyne technique [16]. Good agreement between these very different methods is achieved over the full bandwidth of the measurement.

An experiment demonstrating the other two applications, microwave mixing and optical network analysis, is shown in Fig. 5, which demonstrates a recently reported [17] optical frequency domain reflectometry (OFDR) experiment. Here, two frequency synthesizers drive two coded modulators, between which is inserted an optical network under test. In this particular test, it consists of a 3 dB fiber directional coupler, the output ports of which are extended by two unequal lengths of fiber. The first modulator is used as a source of modulated light to probe the network at microwave frequencies. The second, driven at a slightly offset (by 50 KHz) frequency, acts as an optical/microwave mixer, generating an optical signal at the 50 KHz intermediate frequency which is proportional to the network

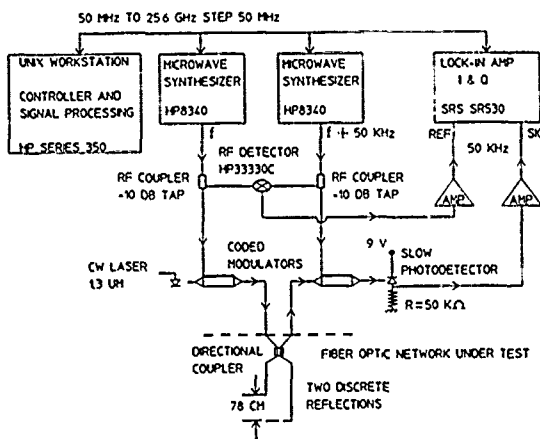


Figure 5. Optical network analysis - experimental set-up. (Reproduced with permission from Ref. 17, Copyright 1989, IEE).

response at the much higher microwave frequency of the source. This low frequency signal is measured with very high sensitivity by a slow detector and narrow-band lock-in amplifier. The dual channel lock-in measures both in-phase and quadrature components of the signal, enabling the full vector response of the network to be measured. This allows one to obtain the corresponding time domain response of the network.

Calibration of the measurement system is accomplished by replacing the network under test by a short length of connecting fiber and measuring the response over the same frequency range. The broadband response and low required drive power of the coded modulators enables their (complex) frequency response $H(f)$ to be measured with high accuracy. Thus, the non-linear phase of the devices can be completely calibrated out of the measurement over the full frequency range. This results in a time resolution limited only by the frequency range of measurement, and not by the phase non-linearity of the modulators or their temporal behavior. The impulse response of the network under test can be obtained by inverse FFT of the measured complex frequency domain data. This is shown in Fig. 6 for the particular network above. The two discrete spikes correspond to the two discrete reflections from the free fiber ends of the coupler. The time resolution is ≈ 40 psec, corresponding to 4 mm distance resolution in fiber.

Summary and Conclusion

Phase reversal electrode modulators based on Spread Spectrum coded sequences have been reviewed. Their operating principles and properties have been

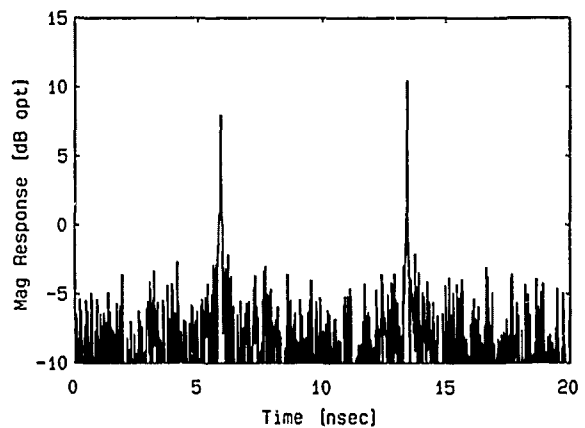


Figure 6. Time domain response of network under test in Fig. 5. (Reproduced with permission from Ref. 17, Copyright 1989, IEE).

discussed, and experimental results have been presented which confirm these theoretical predictions. The non-linear phase vs frequency which these devices exhibit result in a complicated time domain response. Nevertheless, they are ideal candidates for measurement applications where such non-linearity can be ignored or calibrated out, and several examples of these measurements have been demonstrated.

References

- [1] See, for example, R.C. Alferness, "Waveguide electro-optic modulators", *IEEE Trans. Microwave Theory Tech.*, vol. MTT-30, pp. 1121-1137, (1982).
- [2] R.C. Alferness, S.K. Korotky, and E.A. Marcatilli, "Velocity matching techniques for integrated optic traveling wave switch/modulators", *IEEE J. Quant. Electron.*, vol. QE-20, pp. 301-309, (1984).
- [3] A. Djupsjobacka, "Novel type of broadband traveling wave integrated-optic modulator", *Electronics Lett.*, vol. 21, pp. 908-909, (1985).
- [4] D. Erasme and M.G.F. Wilson, "Analysis and optimization of integrated-optic traveling wave modulators using periodic and non-periodic phase reversals", *Opt. and Quant. Electr.*, 18, pp. 203-211, (1986).
- [5] M. Nazarathy, D.W. Dolfi, and R.L. Ungerman, "Velocity-mismatch compensation in traveling wave modulators using pseudorandom switched-electrode patterns", *J. Opt. Soc. Amer.*, 4, pp. 1071-1079, (1987).
- [6] M. Nazarathy, D.W. Dolfi, and R.L. Ungerman, "Spread spectrum frequency response of coded phase

reversal traveling wave modulators", *J. Lightwave Technol.*, **LT-5**, pp. 1433-1443, (1987).

[7] S.C. Hiser, et. al., "Lithium Niobate bandpass response microwave modulator with phase reversal electrodes", in *Tech. digest, IGWO '88*, Santa Fe, N.M., (OSA - LEOS, Washington, D.C., 1988), paper WD-3.

[8] G.E. Betts, "Microwave bandpass modulators in Lithium Niobate", in *Tech. digest, IGWO '89*, Houston, Tx., (OSA - LEOS, Washington, D.C., 1989), paper MAA-4.

[9] See, for example, R.C. Dixon, *Spread Spectrum Systems*, (New York, Wiley, 1984).

[10] D.W. Dolfi, R.L. Jungerman, and M. Nazarathy, "1.3 μm LiNbO₃ modulator with bandwidth greater than 24 GHz", presented at *OFC/IOOC '87*, Reno Nv., post-deadline paper PDP4.

[11] R.L. Jungerman, C.A. Johnsen, D.W. Dolfi, and M. Nazarathy, "Coded phase reversal LiNbO₃ modulator with bandwidth greater than 20 GHz", *Elec. Lett.*, vol. 23, pp. 172-174, (1987).

[12] D.W. Dolfi, M. Nazarathy, and R.L. Jungerman, "40 GHz electro-optic modulator with 7.5 V drive voltage", *Elec. Lett.*, vol. 24, pp. 528-529, (1988).

[13] S.Y. Wang, S.H. Lin, and Y.M. Houn, "GaAs traveling wave polarization electro-optic waveguide modulator with bandwidth in excess of 20 GHz at 1.3 μm ", *Appl. Phys. Lett.*, **51**, pp. 83-85, (1987).

[14] S.K. Korotky, et. al., "Optical intensity modulation to 40 GHz using a waveguide electro-optic switch", *Appl. Phys. Lett.*, **50**, pp. 1631-1633, (1987).

[15] S.Y. Wang and K.W. Carey, "InP/GaInAs/InP PIN photodiode with FWHM \leq 18 psec.", in *Tech. digest, Picosecond Optics & Optoelectronics, 1987*, Incline Village, Nv., (Optical Society of America, Washington, D.C., 1987), paper THA-3.

[16] See, for example, E.R. Ehlers, R.L. Jungerman, and M.P. Zurakowski, "Comparison of frequency response calibration techniques for wide-bandwidth photodetectors", in *Tech. digest, OFC '88*, New Orleans, La., (OSA - LEOS, Washington, D.C., 1988), paper WQ-22.

[17] D.W. Dolfi and M. Nazarathy, "Optical frequency domain reflectometry with high sensitivity and resolution using optical synchronous detection with coded modulators", *Elec. Lett.*, vol. 25, pp. 160-162, (1989).

Electro-Optical Synthesis of Picosecond Optical Pulses

Tetsuro Kobayashi and Akihiro Morimoto

Engineering Science, Osaka University, Toyonaka, Osaka 560, Japan

Abstract

We demonstrate three new electrooptical pulse synthesizing methods to generate arbitrarily shaped optical pulses in the picosecond range from cw lasers using an electrooptic modulator or a deflector. They utilize (1) separation, control, and composition of each sideband component of the phase-modulated light using two gratings and a spatial filter, (2) selection of produced sidebands using an FP filter, and (3) control of near-field pattern of an electrooptically deflected beam using a spatial filter and composition using a grating or a slit. Using these methods picosecond pulses at 9.4-75GHz repetition frequency have been generated.

1. INTRODUCTION

For generating ultrashort optical pulses, passive modelocking of wideband lasers and fiber-grating pulse compression are ordinarily used. They are excellent methods and at present make it possible to generate femtosecond pulses. At the same time, however, they have some disadvantages such as 1) the pulse width depends strongly on laser power and linewidth, 2) electrical control of pulse position, width, shape is difficult, and 3) their application is limited to few kinds of lasers.

On the other hand, electrooptic methods have inherent advantages in stability and controllability, although their application is difficult in the femtosecond range. If we can generate arbitrarily shaped optical pulses even in the picosecond range by purely electrooptic methods, the application area of optical pulse technology, of course, including high speed electronics must be extended more.

One of the typical electrooptic method to generate short optical pulses is to modulate directly light by short electric pulses making use of a

broad-band modulator. In the picosecond range, however, realization of such a broad-band electrooptic modulator is difficult. Another approach is to synthesize the optical pulse utilizing frequency-domain control of optical sidebands produced by electrooptic modulation [1]. For this case, what is required is not a broad-band modulator but widely spread sidebands. Fortunately it is possible to obtain the wide sideband as wide as 1THz by using even a narrow-band electrooptic modulator with the high modulation index [2]. This method should have potentialities to be applied to the subpicosecond range.

Here, we demonstrate three types of synthesizing : 1) by separation, control, and composition of each sideband component of the phase-modulated light using two gratings and a spatial filter, 2) by selection of produced sidebands using an FP filter, and 3) by control of near-field pattern of an electro-optically deflected beam using a spatial filter and composition using a grating or a slit.

2. BASIC CONSIDERATION

Figure 1 shows the basic steps of the proposed synthesizing process [3]. The first step is to produce frequency components (sidebands) distributed in a wide range by electrooptic modulation or deflection. The second step is to separate (demultiplex) the each frequency component. Third one is to control the amplitude and phase of each frequency component. The final step is to compose (multiplex) the frequency components and to form desired pulse shape.

Electrooptic modulation and deflection, as well known, utilize optical phase modulation based on electrooptic effect. For the case of the sinusoidal phase modulation at modulation frequency f_m and with an index $\Delta\theta$, a series of sideband components are produced at intervals of the modulation frequency. They have the Bessel function amplitudes ($\propto J_n(\Delta\theta)$) and are phase-locked with

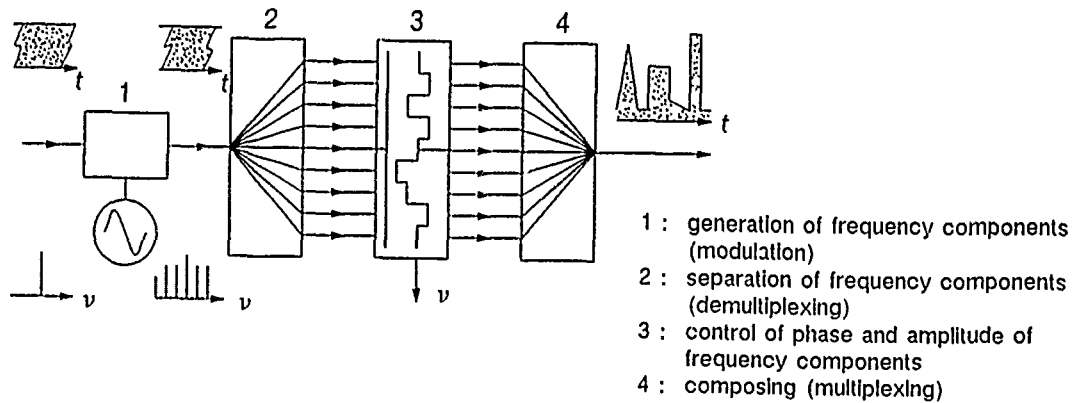


Fig.1 Basic principle of our optical synthesizing.

the relative phases of 0 or π , each other. The spread of sidebands in frequency space (namely spectral width $\Delta\nu$) becomes $2\Delta\theta f_m$, approximately. Accordingly, it is possible to produce wide sideband even for relatively low modulation frequency, provided that high modulation index, i.e. large $\Delta\theta$, is used. Consider the case of $f_m=20\text{GHz}$ and $\Delta\theta=20\pi$ as an example, then $\Delta\nu$ is estimated to be 2.5 THz. When the sidebands are efficiently utilized, the pulse as short as $a/\Delta\nu$ ($a=0.1-1$) is obtainable. For narrow-band modulator, the modulation depth can be enhanced by employing the electrical resonant cavity and such high index as mentioned above becomes very realistic. Actually, we already succeeded in producing 640GHz-width optical sidebands by the electrooptic phase modulation: shown in Fig.2 [2] and in generating a few picosecond pulses using together with a chirping compression technique [4].

The synthesization of ultrashort optical pulse signals is typically accomplished by separating the frequency components spatially and by control their amplitudes and phases. In this point of view, we proposed the pulse synthesizer and compressor using an electrooptic deflector on early days, and succeeded in generating various shaped pulses in the subnanosecond range using them [5]. After that, we also proposed the method using control of the modulation sidebands separated spatially by diffraction gratings with Fourier transform optics [6]. Similar approaches using continuous spectra of femtosecond pulses have recently been reported by other authors [7,8].

3. METHOD UTILIZING SPATIAL CONTROL OF THE SIDEBANDS PRODUCED BY PHASE MODULATION

Figure 3 shows the basic construction of the synthesizing method using spatial control of sidebands [3,4], which is essentially equivalent to the synthesizer using the electrooptic deflector [5] and analogous to a phased-array antenna or a fre-

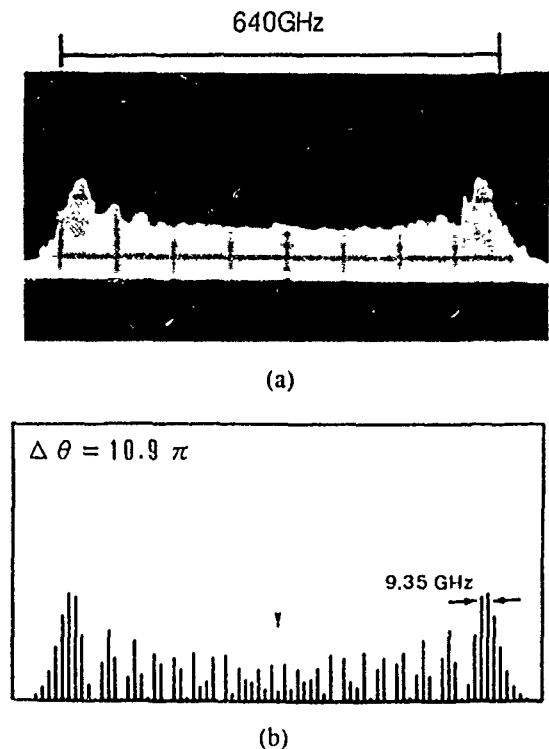


Fig.2 Generation of wide Optical sideband

quency-domain multiplexer in the optical communication system.

Optical sidebands are produced by an electrooptic phase modulator and separated spatially by a diffraction grating with optical Fourier transform system without any overlap. Their amplitudes and phases are controlled individually by a spatial filter, or a modulator array (It contrasts well with the case of single shot pulse input with continuous frequency spectra [7,8], where

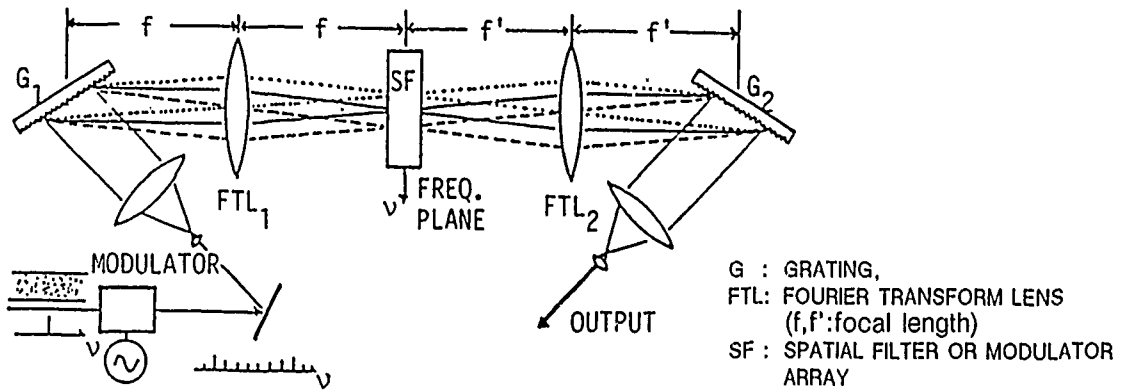


Fig.3 Basic construction of optical synthesizer[3].

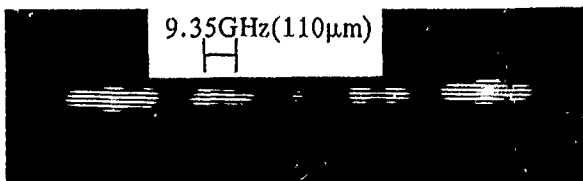


Fig.4 Spatially separated optical sidebands produced by EO modulation.

neighboring frequency components overlap each other and individual control of the frequency components is impossible). Then the synthesized output is obtained after multiplexing with another set of Fourier transform optics and a grating. The necessary amount of the phase control is at most 2π (corresponds to one wavelength). The shortest pulsewidth or the shortest temporal structure of the synthesized output is limited by the width of the sideband spread.

We have done preliminary pulse synthesis experiments using this construction. An argon laser was used as a light source. Optical sidebands were produced by a 9.35GHz LiTaO₃ phase modulator [2]. Figure 4 shows spatially separated FM sidebands after demultiplexing by a grating (the frequency intervals are 9.35GHz). Figure 5 shows the examples of the streak traces of synthesized signals obtained (a) by eliminating central seven sidebands and (b) by giving parabolic phase shift to every sideband. Both results agree well with theoretical ones.

Figure 6 shows the examples of calculated binary signals formed by controlling the sidebands using a 15 segment modulator array. These examples suggest that this method is applicable to construct the high-bit rate optical word generator. We are now planning to synthesize such binary signals using a liquid-crystal modulator array.

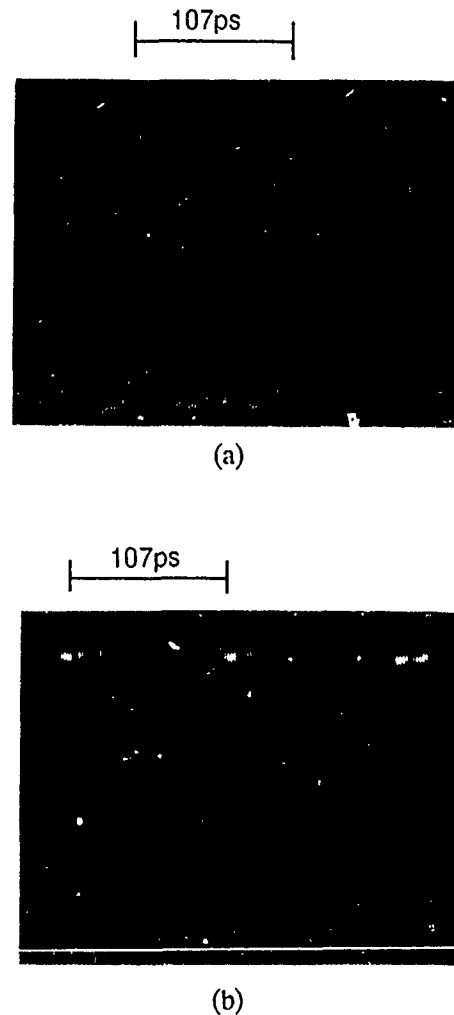


Fig.5 Streak traces of synthesized output. Obtained (a) by eliminating central 7 sidebands and (b) by putting parabolic phase shift.

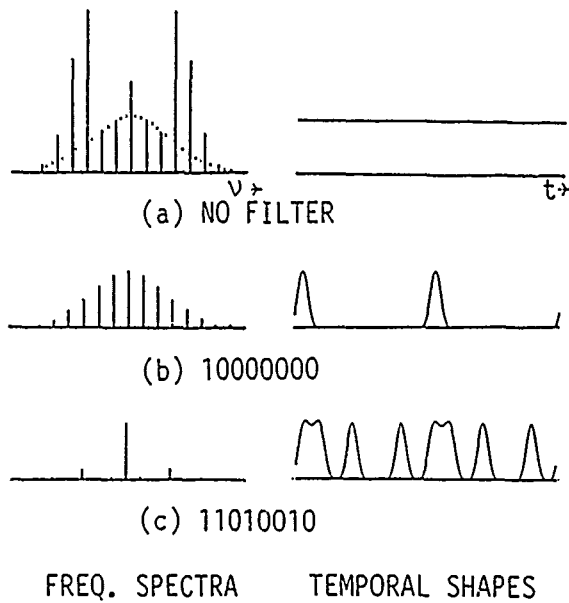


Fig.6 Typical examples of synthesizing word pattern (calculation).

4. METHOD WITH A FABRY-PEROT FILTER [9]

We also proposed a new electrooptic method of generating picosecond optical pulses at very high repetition rate. This method utilizes a phase modulator together with a Fabry-Perot interference filter. A Fabry-Perot filter (FP filter) plays at once the roles of the last three steps in Fig.1.

Pulse generation methods using an FP filter as a slicer for frequency modulated or frequency chirped light have previously been proposed [10,11]. These methods are, however, in a dilemma; the bandwidth of the filter should be narrow as compared with the frequency deviation to obtain short pulses, while a narrow bandwidth filter broadens the pulse according to the property of Fourier transform. Consequently, the wide bandwidth $\Delta\nu$ of the input signal (the order of the total frequency deviation) is not used effectively.

Figure 7 shows a basic setup of our proposed method. It utilizes multi-passbands (windows) of the FP Filter, which are equally spaced in frequency. Through the pass-bands, suitable frequency components to produce short pulses are selected out from the widely spread optical sidebands of an input FM light. We can obtain an output spectrum as wide as the input spectrum. As a result, the pulse as short as $1/\Delta\nu$ is obtainable. The method can not apply to arbitrary shaping, but is suitable to get high-repetition rate pulse trains.

Examples of calculated pulse-waveform are

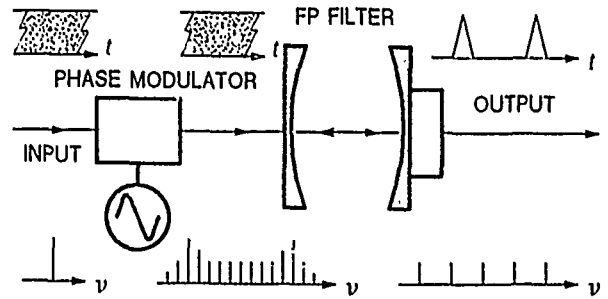


Fig.7 Optical pulse generation by selection of PM sideband using an FP filter.



(a) 20π , $c/2L > \Delta\theta_{fm}$



(b) 2.1π , $c/2L = 4f_m$



(c) 4.2π , $c/2L = 8f_m$

Fig.8 Examples of output pulse shapes (theoretical ones without detuning).

shown in Fig.8. Figure 8(a) is for the before-mentioned frequency-slice method using a single passband ($\Delta\nu \sim 2\Delta\theta_{fm} \ll c/2L$, where L is the length of the filter). In this case, the pulse width is limited by the FP filter bandwidth. Figure 8(b) and (c) are for the proposed method selecting appropriate frequency components using the multiple windows of the FP filter. In these figures, pulse repetition rates are (a) $2f_m$, (b) $4f_m$, and (c) $8f_m$, respectively. For (b) and (c), which are practically useful, the pulse widths are of the order of $1/(2\Delta\theta_{fm})$ and the duty factors are 0.2 - 0.3. These results show that this method is suitable to generate optical clock pulses in optical circuits or carrier pulses in PCM.

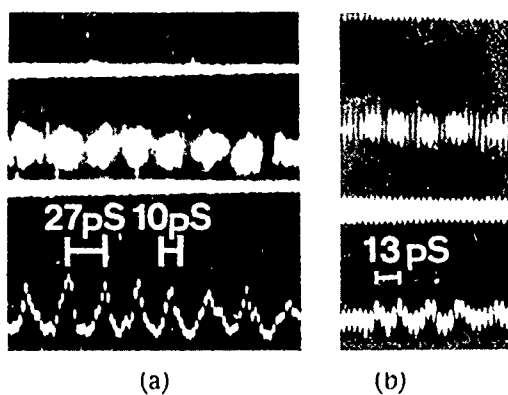


Fig.9 Experimentally obtained pulse shapes
(a) $\Delta\theta=2.1\pi$, $4\text{fm}=(c/2L)$, and
(b) $\Delta\theta=1.15\pi$, $8\text{fm}=(c/2L)$.

In the experiment, an Ar laser light source, a LiTaO_3 EO phase modulator ($f_m=9.35\text{GHz}$), and a Fabry-Perot filter (finesse 10) are used. Examples of the streak traces of the obtained pulses are shown in Fig.9, where the repetition rates are (a) 4fm (38GHz) and (b) 8fm (75GHz), respectively. These pulsewidths are limited by the detector resolution 8ps . Their theoretical values are 5.9 and 5.4ps , respectively. With this method, generation of $200\text{-}300\text{GHz}$ repetition rate pulses would be possible.

5. 10GHz EO DEFLECTOR AND ITS APPLICATION TO SYNTHESIZE SHORT PULSES

It is known that the instantaneous optical frequencies at the output plane of an electrooptic deflector depend linearly on the spatial positions in the beam cross section [5]. Accordingly, the

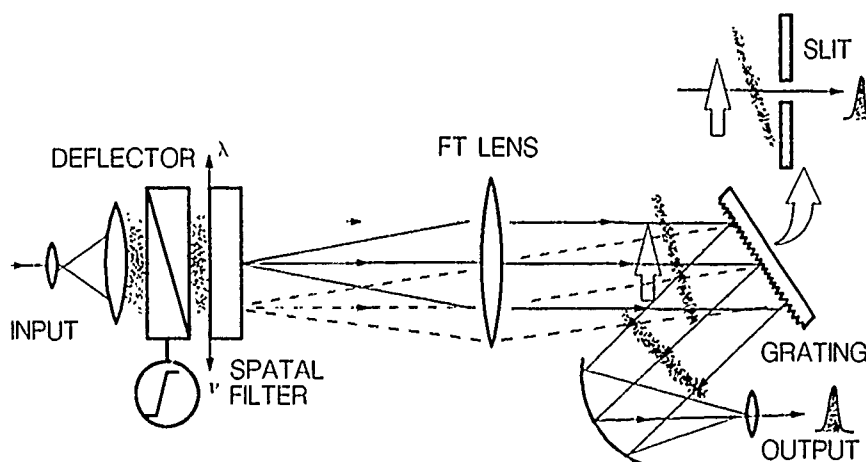


Fig.10 Pulse generation / compression / shaping by an EO deflector.

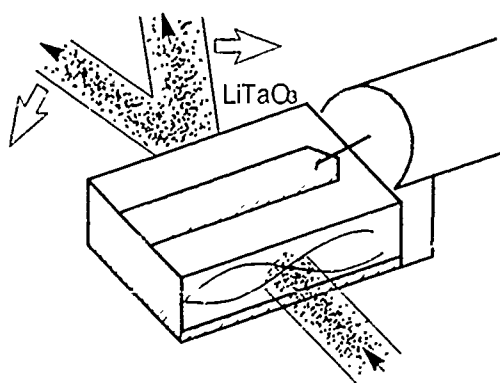


Fig.11 Ultrafast electrooptic deflector

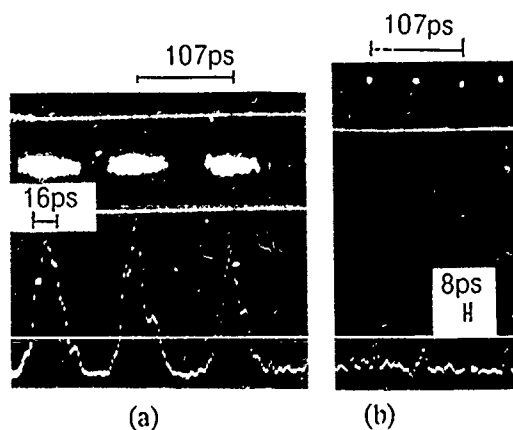


Fig.12 Example of the output pulses obtained by a new deflector.

output plane of the deflector corresponds to the frequency plane in Fig.3, then a type of optical synthesizing is realized by using the construction shown in Fig.10. Through control of the near field (equivalent to frequency-domain control), the output temporal shape corresponding to the spatial far-field pattern (Fourier transform of the near field) are also controlled. It is known that this method has the function as a pulse compressor [5]. Simple pulse synthesizing is also possible when the grating is replaced by a slit at the cost of efficiency as shown in the figure. In the experiment, we used a new scheme of an electrooptic deflector at the highest record driving frequency of 9.35GHz as shown in Fig.11, where an optical beam passes through at the node of the standing electric wave. As results, 8-16ps pulse trains at (a) 9.35GHz and (b) 18.7GHz repetition rates were obtained by using the grating and the slit, respectively, as shown in Fig.12.

6. DISCUSSIONS

Now we discuss the speed-limitation of our methods. For narrow-band / single frequency modulation as in our methods, it is possible to establish the velocity matching between the driving electric signal and the modulated light signal. Accordingly, we can use the relatively long electrooptic interaction length. If we employ 10cm interaction length (that is 10 times longer than the present modulator we used), the modulation index of 100π is expected. For $\Delta\theta=100\pi$ and $f_m=20\text{GHz}$, $\Delta\nu$ is estimated to be 12.6THz, which yields 60-80fs pulses are obtainable. Under such wide optical spectra, however, group velocity dispersion of the light in an electrooptic material must be considered. We roughly estimate several tens of femtosecond are reasonable shortest limit in our purely electrooptical method.

Finally we touch on the problem of reduction of the system size. The system size of our synthesizer is of the order of a couple of meters which is still large for application to opto-electronics, although smaller than ordinary CPM laser system. We expect that integration of a laser diode, a waveguide-type modulator, and compact-size gratings will bring smaller system, in the near future. We are now planning to decrease the size from meter to 10cm.

ACKNOWLEDGMENTS

The authors wish to thank Prof. T. Sueta and Mr. S. Nishimura of Osaka University for stimulating

discussions, M. Doi and B. Y. Lee of Osaka University for considerable assistance, and prof. D. M. Bloom and A. E. Siegman of Stanford University for helpful support.

REFERENCES

1. T. Kobayashi and T. Sueta: "Picosecond Electrooptic Devices," CLEO '84, Anaheim, WG-1(1984).
2. K. Amano, T. Kobayashi, H. Yao, A. Morimoto and T. Sueta: "Generation of 0.64-THz-Width Optical Sidebands by a Novel Electrooptic Modulator for the purpose of Forming Ultrashort Optical Pulses," J. Lightwave Technology LT-5, 1454-1458 (1987).
3. T. Kobayashi, M. Doi, B. Y. Lee, A. Morimoto, and T. Sueta: "Picosecond to Femtosecond Optical Synthesizer," in *Ultrafast phenomena VI* eds. T. Yajima, K. Yoshihara, S. Shionoya, and C. B. Harris (Springer Verlag, Berlin, 1988) 135-138.
4. T. Kobayashi, Y. Fukushima, H. Yao, K. Amano, A. Morimoto, and T. Sueta: "Optical Pulse Compression Using High-Frequency Electrooptic Phase Modulation," IEEE J. Quantum Electron. 24, 382-388 (1988).
5. T. Kobayashi, H. Ideno, and T. Sueta: "Generation of Arbitrarily Shaped Optical Pulses in the Subnanosecond to Picosecond region Using a Fast Electrooptic Deflector," IEEE J. Quantum Electron. QE-16, 132-136 (1980) / T. Kobayashi: Japan Patent, No.1268338 (1977).
6. T. Kobayashi, H. Yao, K. Amano, Y. Fukushima, A. Morimoto, and T. Sueta: "Generation of Ultrashort Optical Pulses Using Diode Laser Synthesizer" *Proc. Meeting Jpn Soc. Appl. Phys.* 27p-F-12 (1986) / "Terahertz Optical Pulse Synthesizer," 30p-ZG-14 (1987).
7. J. P. Heritage and A. M. Weiner: "Fourier-Transform Picosecond Pulse Shaping and Spectral Phase Measurement in a Grating Pulse-Compression," *Ultrafast Phenomena V* (Springer-Verlag, Berlin, 1986) 34-37.
8. A. M. Weiner, J. P. Heritage, and E. M. Krishner: "High-resolution femtosecond pulse shaping," J. Opt. Soc. Am. B 5, 1563-1572 (1988).
9. A. Morimoto, H. Yao, T. Kobayashi, and T. Sueta: "Generation of High Repetition Rate Picosecond Optical Pulses Using an Electrooptic Phase Modulator and a Fabry-Perot Filter," IQEC '88, ThII-6 (1988).
10. A. E. Siegman and D. J. Kuizenga: "Active mode-coupling phenomena in pulsed and continuous lasers," *Opto-Electronics* 6, 43-66 (1974).
11. N. Kagi, K. Ema, and F. Shimizu: "Optical Pulse Narrowing By a Fabry-Perot Interferometer," *Annual Meeting of Jpn Soc. Appl. Phys.* 18p-7C-11 (1987).

Subpicosecond Multiple Pulse Formation in Actively Mode-Locked Semiconductor Lasers

P. A. Morton, R. J. Helkey, S. W. Corzine, and J. E. Bowers

*Department of Electrical and Computer Engineering, University of California,
Santa Barbara, California 93106*

Abstract

Theoretical results for active mode locked semiconductor lasers explain the multiple pulse phenomena seen for all experimental results to date showing subpicosecond pulses. Dynamic detuning, due to gain saturation, causes multiple pulse output by moving the main pulse away from the peak in the gain waveform. This mechanism also limits the inherent pulse width achievable with a given modulation waveform.

Introduction

Mode locked semiconductor laser diodes are a compact source of stable, ultrashort optical pulses. They can be used in telecommunications systems for time division multiplexing or for high bit rate systems using an external modulator. The small size and low cost of semiconductor lasers make them an ideal source for electro-optic sampling, and because many lasers can be driven from the same r.f. synthesizer with low timing jitter they can provide sources of ultra short pulses at different wavelengths for pump/probe and other physics experiments.

Subpicosecond pulses have been obtained using passive [1,2] and active [3] mode locking with the shortest pulses to date of 0.56 ps being obtained using active mode locking [3]. All results published to date showing mode locking of semiconductor lasers with pulse widths below one picosecond have a second harmonic intensity autocorrelation trace with multiple peaks. These multiple peaks are always spaced in time by the round trip time of the laser diode which is typically 5-10 picoseconds. The extra peaks are therefore built up from reflections internal to the laser diode, so the small reflectivity of the anti-reflection coated facet still contributes to the output waveform. A background free second harmonic intensity autocorrelation trace from [3] is shown in Fig. 1. This trace shows a central peak with a FWHM of 0.89 ps,

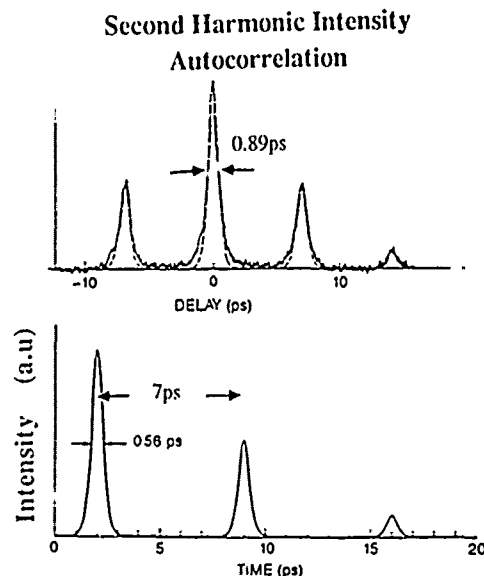


Figure 1. (a) Background free second harmonic intensity autocorrelation, (b) example of possible output pulse train.

with peaks on either side spaced by 7 ps which is the round trip time of the laser diode used in these experiments. One possible example of the output pulse train is also shown in Fig. 1. Assuming a sech² pulse shape the initial pulse has a FWHM of 0.56 ps, followed by decaying versions of this pulse separated by the round trip time of the laser diode. This kind of multiple pulse phenomena cannot be explained by previous theories for active mode locking of laser diodes [4] which make the approximations of a sinusoidal gain waveform and low modulation depth.

We describe a new theoretical model using the traveling wave approach to include spatial variations of the electron and photon densities within the laser diode, together with a non-zero reflectivity for the

anti-reflection coated facet. This model is shown to agree well with experimental observations of picosecond pulses, multiple pulses and pulse powers under all operating conditions, and is used to explain the operation of these devices. The theory is used to explore ways of producing even shorter pulse widths and the production of a single output pulse.

Fig. 2 shows a schematic diagram of the experimental layout used to obtain subpicosecond output pulses. A 1.3 μm GaInAsP high speed Polyimide Semi Insulating Planar Buried Heterostructure (SIPBH) laser diode is used, with a high reflectivity coating on one facet and an anti-reflection (AR) coating on the other. The output from the AR coated facet is coupled into the external cavity using an anti-reflection coated Graded Index Rod (GRINROD) and a high reflectivity mirror is used to form the external cavity. The d.c. bias and r.f. current are combined in a bias 'T' and applied through a high speed mount to the laser diode.

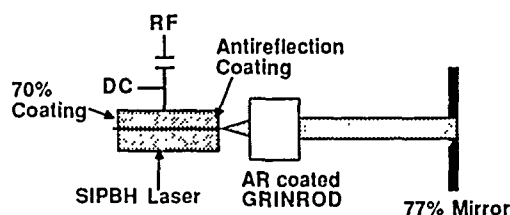


Figure 2. Schematic diagram of experimental layout.

Theoretical Model

The theoretical model is based on the traveling wave rate equations for electron density $N(x,t)$ and forward and backward travelling photon fluxes $S^+(x,t)$ and $S^-(x,t)$:

$$\frac{\partial N}{\partial t} = \frac{J(t)}{e} - \frac{N}{\tau_n} - g(N - N_t)(S^+ + S^-) \quad (1)$$

$$\frac{\partial S^\pm}{\partial t} \pm v_g \frac{\partial S^\pm}{\partial x} = \Gamma g(N - N_t) S^\pm - \alpha_i S^\pm + \frac{\Gamma \beta M N}{\tau_n} \quad (2)$$

where $J(t)$ is the applied current density waveform, e the electronic charge, d the active layer thickness, τ_n the electron lifetime, g the differential gain coefficient, N_t the electron transparency density, v_g the group velocity, Γ the confinement factor, α_i the internal loss, β the spontaneous emission coupling into each external cavity mode, and M the number of external cavity modes oscillating (given by $M = \text{Round trip time} / \text{Pulse width}$). These rate equations are integrated numerically using finite difference approximations, with boundary conditions at the laser facets of:

$$S^+(0,t) = R_1 S^-(0,t) \quad (3)$$

$$S^-(L,t) = R_A S^+(L,t) + R_2 C^2 S^+(L,t - \tau_{ext}) \quad (4)$$

where R_1 and R_2 are the power reflectivities of the left and right mirrors, R_A is the power reflectivity of the anti-reflection coated facet, C is the coupling from laser to external cavity, and τ_{ext} is the external cavity round trip time. The applied current density waveform $J(t)$ is made up of a d.c. bias plus a large sinusoidal component at the reciprocal of the round trip time of the combined cavity. High frequency modulation and a large r.f. power are necessary to produce subpicosecond pulses [3].

Typical values used in the simulations are shown in Table 1. Experimental second harmonic intensity autocorrelation traces are compared with autocorrelation results calculated from the simulations in Fig. 3 for three different levels of r.f. current. For a low r.f. level, a broad peak is seen with a FWHM of over 10 ps. As the r.f. level is increased and the coupling to the external cavity optimized, a subpicosecond multiple peak trace is found, with the spacing between peaks being the round trip time of the laser diode. If the r.f. level is increased further a second set of peaks is seen in the second harmonic intensity autocorrelation trace. The calculated autocorrelation traces show very good agreement with the experimental results at all three r.f. current levels, which gives confidence to the theoretical model used in the simulations. The three r.f. current levels used are 2 mA, 40 mA and 80 mA.

Table 1

| Variable | Symbol | Value | Unit |
|--------------------------------|------------|---------------------|------------------------|
| Waveguide Thickness | d | 0.15 | μm |
| Waveguide Width | W | 1.0 | μm |
| Laser Diode Length | L | 260 | μm |
| Spontaneous Lifetime | τ_n | 1.0 | ns |
| Gain Coefficient | g | $1.8 \cdot 10^{-6}$ | cm^3/s |
| Transparency Density | N_t | $1.2 \cdot 10^{18}$ | cm^{-3} |
| Confinement Factor | Γ | 0.34 | |
| Internal Loss | α_i | 25 | cm^{-1} |
| Spontaneous Emission Coupling: | | | |
| Uncoated Laser | | $1.0 \cdot 10^{-4}$ | |
| In External Cavity | β | $2.5 \cdot 10^{-6}$ | |
| Mirror Reflectivities | R_1, R_2 | 0.7 | |
| AR Coating Reflectivity | R_A | 0.005 | |
| Coupling to External Cavity | C | 0.42 | |
| D.C Bias above threshold | I_{dc} | 4.0 | mA |
| R.F. Current | I_{rf} | 40.0 | mA |
| Modulation Frequency | f | 16.0 | GHz |

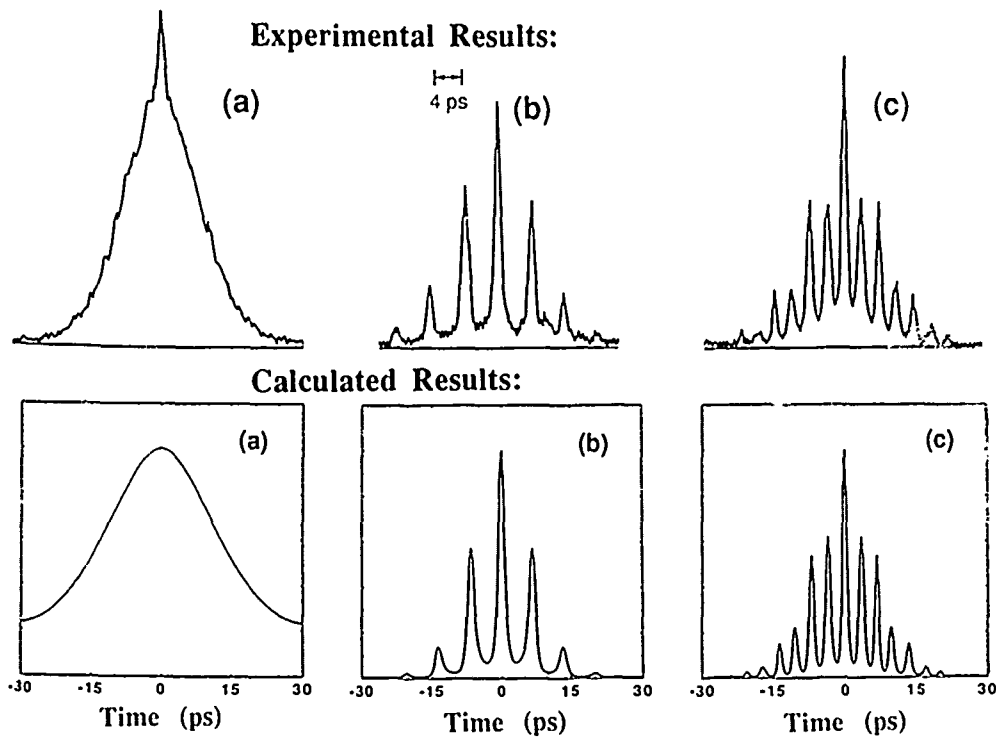


Figure 3. Comparison of experimental and calculated second harmonic autocorrelation traces for increasing levels of r.f. current (a - c).

The build up of a mode locked pulse train over many round trips is shown in Fig. 4. The first trace shows the applied current density waveform during one modulation period which it is clipped in the negative direction by the laser diode. The two other traces show the electron density and optical output waveforms at the anti-reflection coated facet of the laser diode after 25, 75 and 1000 periods of modulation. Initially a gain switched pulse is produced, which travels around the external cavity and returns to seed the output of the next modulation period. After 25 periods the output pulse is still fairly broad (14 ps) and has a peak power of only 3 mW. As the pulse builds up in power the front of the pulse starts to deplete the carriers (and therefore the gain) as it passes through the laser diode, and so the trailing part of the pulse sees less gain and reduces in power. After 75 round trips this process is starting to occur, and as can be seen the effect is to move the pulse to an earlier point in the modulation period. As this initial pulse moves earlier in the modulation period it moves away from the peak in the gain waveform which would occur at the center of the modulation period. Therefore, the gain can rise up again after the initial pulse passes through the laser and so the small reflections from the AR coated facet can be amplified. These reflections build up after many passes through the laser diode until they become much larger than the initial reflection. After steady state conditions have been reached (1000 periods), a subpicosecond pulse

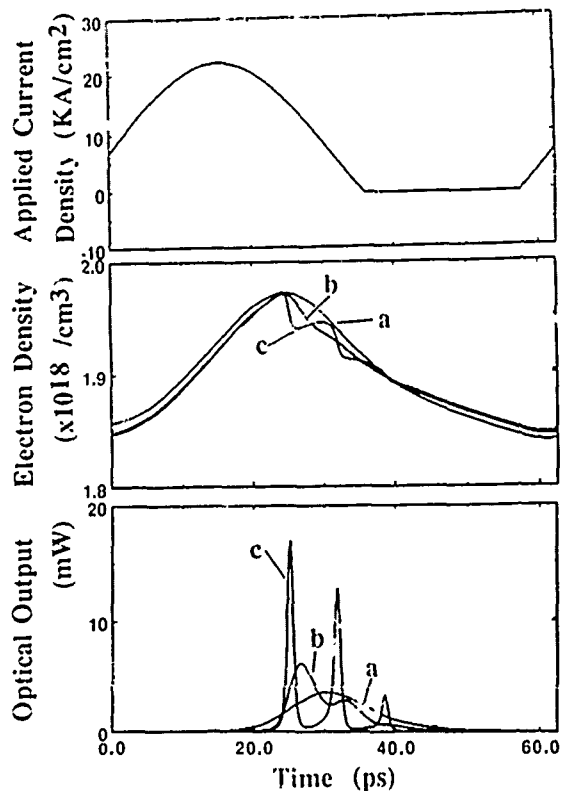


Figure 4. The build up of a mode locked pulse after (a) 25, (b) 75 and (c) 1000 modulation periods.

train is seen. This has a powerful initial pulse followed by pulses built up from the reflections off the AR coated facet, and so they are separated by the round trip time of the laser diode. The initial pulse has moved to an earlier point in the modulation period.

If the r.f. current is increased to higher levels than in Fig. 4, eventually the gain will rise up enough between the initial and first reflected pulses for a separate mode locked pulse to be sustained between them. This new mode locked pulse will itself cause reflections from the AR coated facet and so a second set of pulses will build up in the output waveform. There is no particular time separation between the two sets of pulses, in fact the time difference changes as parameters such as the r.f. current are varied. For very high levels of r.f. current many sets of pulses are observed in the output waveform.

We have called the pulse stabilization mechanism 'Dynamic Detuning' as it is a dynamic process which detunes the position of the pulse away from the peak in the gain waveform. The multiple pulse output is formed because the pulse is detuned away from the gain peak which allows reflections to be amplified and build up. The dynamic detuning process has only one stable solution which defines the pulse width, peak power and shape of the pulse. This mechanism is a limiting factor on the minimum pulse width achievable from mode locked semiconductor lasers, independent of the finite gain linewidth of the laser material and dispersion in the cavity. The dynamic detuning mechanism accounts for the long (0.56 ps) pulses seen from mode locked semiconductor laser diodes compared to the theoretical limits of about 50 fs for the gain linewidth and 100 - 200 fs for dispersion.

The dynamic detuning mechanism moves the mode locked pulse earlier in the modulation period to a stable position at which each part of the pulse sees the same value of gain for one pass through the laser diode. This occurs at a position where the effects of gain saturation (increases gain at front of pulse) are balanced by the slope of the carrier density waveform (increases gain at back of pulse). For sinusoidal modulation the peak slope in the carrier density waveform occurs at one quarter of the modulation period, and so as the initial pulse becomes shorter and higher in power it will move towards this point of maximum slope in order to balance the higher levels of gain saturation that occur. In order to produce a system with a single output pulse it is necessary to use a modulation waveform that has a high slope in the carrier density waveform near the peak in carrier density.

The effects of varying the r.f. current into the laser diode on the main pulse parameters are shown in Fig. 5. For a low value of r.f. current, broad pulses of 10 ps to 20 ps are seen. These pulses have a low peak power and occur near the center of the modulation period. This kind of behavior is well described by previous theories of mode locking [4] which assume a sinusoidal modulation of the gain and small modulation depths. As the r.f. current is increased the pulses become narrower with a corresponding increase in peak power. The pulses can be seen to move towards an earlier position in the modulation

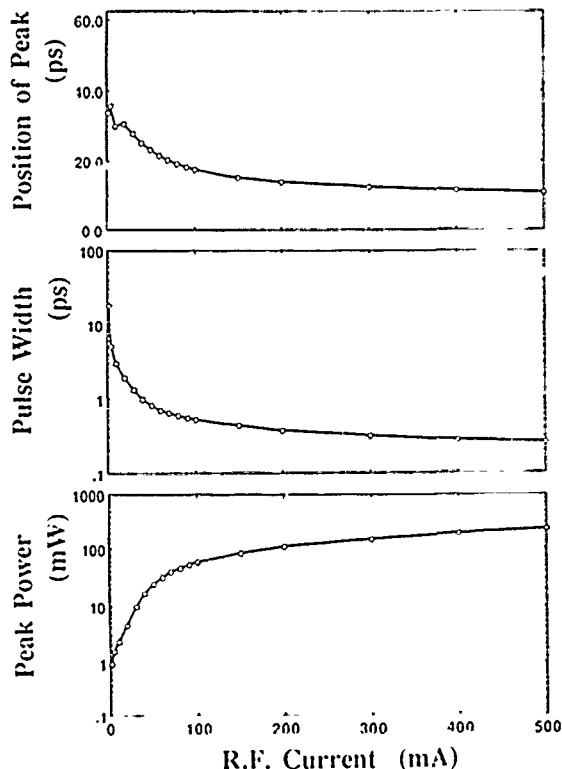


Figure 5. Effect of r.f. current level on the pulse position, pulse width and peak power.

period. For an r.f. current of 40 mA, subpicosecond pulses are seen, with a peak power of about 20 mW. It must be noted that for a modulation frequency of 16 GHz as in this case, it is not a trivial problem to push 40 mA of current into the active region of a laser diode. A very high speed laser diode is necessary to carry out such an experiment, the devices used in [3] being Polyimide Semi Insulating Planar Buried Heterostructure lasers with room temperature small signal bandwidths of up to 19 GHz[5].

We have modelled the effect of having a perfect anti-reflection coated facet, as it has been thought that such a device will provide the shortest mode locked pulses. If the reflectivity of the AR coating is zero, no reflected pulses occur. Fig. 6 shows schematically an example of how the output waveform can build up in such a case. The modulation is started at $t=0$ and traces of the output waveform are shown at different times. An initial mode locked pulse starts to build up, becoming shorter and more powerful and so moving to an earlier point in the modulation period. As it moves, the gain starts to rise to higher levels later in the modulation period and eventually a second mode locked pulse starts to build up. This second mode locked pulse starts to increase in power at the expense of the first pulse, so that eventually it moves to an earlier position in the modulation period and takes over from the first pulse. This whole process repeats itself as the pulses oscillate in position around the modulation period, and so the output is unstable. In

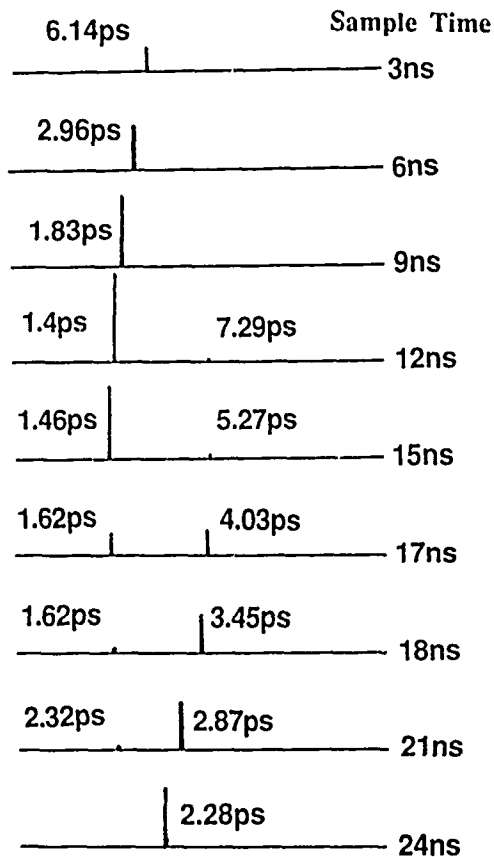


Figure 6. Output waveforms during one modulation period, for various times after starting modulation.

such a case the second harmonic intensity autocorrelation trace will show a stable single peak of a few picoseconds in duration, however, if the output is used in a practical system the timing jitter between pulses will be enormous. This instability may be overcome under certain bias conditions by detuning the modulation frequency slightly.

The instability shown in Fig. 6 for perfect AR coatings could be stopped by increasing the cavity round trip time to be much longer than the carrier recombination time (a few ns). In this case the second mode locked pulse cannot effect the gain of the first pulse and so the first pulse will not decrease in power. This decouples the effects of the optical output on subsequent carrier density waveforms as the carrier density always starts from the same value.

Our simulations show that the unstable outputs seen for devices with perfect anti-reflection coatings can also occur for coatings with power reflectivities of less than 0.1%. The subpicosecond multiple pulse output is seen for AR coating reflectivities of between 0.1% and 3%, with coatings of 5% and more showing much broader pulses (20-30 ps).

We have included the effects of dynamic carrier heating[6] in the simulations using an assumed value for the gain reduction constant and a single exponential time constant. Initial results using the conditions in Table 1 show an increase in pulse width

of 15%, with a corresponding decrease in peak power. Further simulations will be carried out when results for gain dynamics in GaInAsP material are published.

Conclusions

We have described the dynamic detuning mechanism, which is due to gain saturation caused by stimulated emission. This mechanism causes the optical pulse to move within the modulation period to the only possible stable position. This stable solution defines all the pulse parameters such as FWHM, peak power and pulse shape and is therefore a limiting factor on the shortest achievable pulse width for a given modulation waveform. The dynamic detuning mechanism sets limits on the achievable pulse widths which are comparable with experimental measurements, whereas the effects of finite gain linewidth and dispersion have limits much lower than seen in practice. Dynamic detuning is therefore, at present, the major limiting factor to short pulse generation in mode locked semiconductor lasers.

Dynamic detuning moves the initial mode locked pulse to an earlier position in the modulation period. This causes multiple pulse output because the gain rises up again after the passage of the initial pulse, and the small reflections from the AR coated facet are amplified, building up to large values over many round trips. For the case of perfect AR coatings, reflections do not occur, but for high r.f. currents a second, separate mode locked pulse will build up. In this case the output waveform is generally unstable. A range of AR coating reflectivities from 0.1% to 3% were found to give stable subpicosecond multiple pulse output. The unstable output seen for perfect AR coatings was also found for reflectivities below 0.1%, and for reflectivities of 5% and above very broad pulses occur.

The use of a modulation waveform giving a large change in gain near the peak value of gain should help reduce the multiple pulse output. By applying all the injected charge to just one output pulse it should then be possible to produce much shorter and higher power pulses.

Acknowledgments

This work was supported by the Office of Naval Research under contract N00014 88K 1482.

References

- [1] J. P. van der Ziel, "Active Mode Locking of Double Heterostructure Lasers in an External Cavity", *J. Appl. Phys.* **52**, 4435-4446 (1981).
- [2] Y. Silberberg, P. W. Smith, "Subpicosecond Pulses from a Mode-Locked Semiconductor Laser", *IEEE J. Quantum Electron.* **QE-22**, 759-761 (1986).
- [3] S. W. Corzine, J. E. Bowers, G. Przybylek, U. Koren, B. I. Miller, and C. E. Socolich, "Active Mode Locked GaInAsP Laser with Subpicosecond Output", *Appl. Phys. Lett.* **52**, 348 (1988).
- [4] For example, H. A. Haus, "A Theory of Forced Mode Locking", *IEEE J. Quantum Electron.* **QE-11**, 323-330 (1975).

- [5] J. E. Bowers, U. Koren, B. I. Miller, C. Socolich, and W. Y. Yan, "High Speed Polyimide Based Semi-Insulating Planar Buried Heterostructures", *Electron. Lett.* **24**, 1263-1265 (1988).
- [6] M. P. Kesler, E. P. Ippen, "Subpicosecond Gain Dynamics in GaAlAs Laser Diodes", *Appl. Phys. Lett.* **51**, 1765 (1987).

Part 4
Tunneling and Resonant Tunneling

Ultrafast Optical Studies of Tunneling and Perpendicular Transport in Semiconductor Microstructures

D. Y. Oberli, Jagdeep Shah, B. Deveaud,* and T. C. Damen
AT&T Bell Laboratories, Holmdel, New Jersey 07733

Ultrafast optical techniques provide a powerful means of investigating the dynamics of carrier transport and tunneling in semiconductor microstructures. We present a brief review of the basic concepts and various all-optical techniques. We then discuss our results on the direct determination of the dynamics of perpendicular transport using subpicosecond luminescence spectroscopy. Finally, we discuss our recent results on the direct determination of resonant and non-resonant tunneling times in asymmetric double quantum well structures.

1. INTRODUCTION

Transport of carriers in the direction perpendicular to the planes of a semiconductor superlattice was first considered by Esaki and Tsu [1], who predicted many interesting properties, including negative conductance and Bloch oscillations. The considerable activity in the field of superlattices in the early and mid 1970's has been reviewed recently by Esaki [2]. After this initial flurry of activity, the emphasis shifted towards the study of quantum wells, and the quasi-two-dimensional electron gas (2DEG) at hetero-interfaces and in quantum wells. These investigations have led to a number of exciting discoveries in the transport and optical properties of 2DEG.

In recent years, there has been a dramatic increase in research on resonant tunneling and perpendicular transport in semiconductor microstructures, spurred by advances in the growth of high quality semiconductor microstructures. The microwave experiments of Sollner and coworkers [3] were followed by intense experimental and theoretical activities in the field. Many aspects of this research have been discussed in excellent review articles by Esaki [2] and Capasso et al [4] in 1986.

The vast majority of studies on tunneling and perpendicular transport in superlattices have used current-voltage measurements as their primary technique. During the past two years, carrier tunneling and transport in semiconductor microstructures have also been investigated using *optical techniques*. These optical studies provide

information that can not be obtained from electrical measurements and therefore complement the electrical studies. The purpose of this article is to review these optical techniques briefly (Sec. 2) and then present some recent measurements (using *subpicosecond luminescence spectroscopy*) which have directly determined dynamics of perpendicular transport (Sec. 3) as well as non-resonant and resonant tunneling times of electrons in coupled quantum well structures (Sec. 4).

2. BASIC CONCEPTS

Recently developed picosecond and femtosecond lasers have been used to investigate tunneling and transport in a number of different ways. The most direct method is to use an ultrafast laser to generate free carriers and measure the time evolution of the electrical current to determine the transport of carriers. This hybrid time-of-flight technique has been used to study transport in bulk semiconductors [5], parallel transport in inversion layers and quantum wells [6,7], and also perpendicular transport in GaAs/AlGaAs superlattices [8,9]. While this technique is very useful, the time resolution available in measuring electrical transients directly is much longer than the pulsewidths of the ultrashort laser pulses.

The time resolution in the measurement of the electrical transients can be improved considerably by using one of the optical sampling techniques (e.g. electro-optic or photoconductive sampling). This is a promising approach and has been recently applied to investigate resonant tunneling diodes [10] and other semiconductor devices [10]. The strength of this technique is that it allows a direct measurement of devices.

* permanent address : CNET, Lannion, FRANCE

The physics of carrier transport can be more directly explored by applying all-optical techniques to specially designed microstructures. A technique that deserves mention in this context makes use of the fact that the electric field in a semiconductor following its excitation by an ultrashort pulse changes as a function of time because of the motion of photoexcited electrons and/or holes. The time evolution of the field can be measured by monitoring a field-sensitive optical property such as absorption. Since the change in the field is related to the motion of the carriers, information about carrier transport can be obtained from such measurements. This technique was first used by Shank et al [12] to measure velocity overshoot effects in GaAs and has been recently applied to study the transport of carriers in multiple quantum well structures [13].

We will concentrate on a different all-optical technique which provides the means for a *direct measurement of the transport and tunneling of carriers in semiconductor microstructures*. This technique involves the use of an optical "marker" [14] i.e. a thin region of the sample with optical properties different from the rest of the sample. The marker can be a different semiconductor, the same semiconductor with different doping characteristics, or a more complicated microstructure. Such a structure is schematically illustrated in Fig. 1. If carriers are created near the surface by photoexcitation, then their transport to the interior of the sample can be monitored by measuring some optical property of the marker region that is modified when the photoexcited carriers arrive in the marker region. For example, transport in Si was investigated by monitoring the luminescence from a thin doped region in the interior of the Si sample [15]. More generally, the marker region has a different bandgap than the rest of the sample, as illustrated in Fig. 1, and any optical property specific to the marker region can be monitored. As an example, the transport of carriers in bulk InP was investigated by incorporating InGaAs quantum well markers in the interior of the sample [16].

The first application of this concept to semiconductor microstructures was demonstrated by Chomette et al [17]. They introduced an enlarged quantum well in the interior of a superlattice sample. The enlarged well has a different energy bandgap and hence a distinct luminescence spectrum. The dynamics of the transport of carriers photoexcited near the surface of the sample to the enlarged well in the interior of the sample can be explored using such structures. This technique can be obviously extended to use multiple markers in the sample to provide more detailed information on carrier transport.

SINGLE MARKER FOR OPTICAL STUDIES OF TRANSPORT

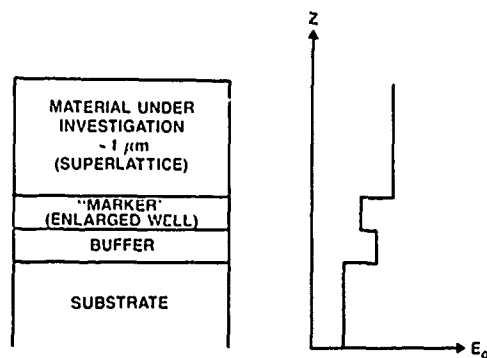


Fig. 1: Schematic diagram illustrating the concept of an optical "marker".

3. ULTRAFAST OPTICAL STUDIES OF PERPENDICULAR TRANSPORT

The concept of multiple markers in a semiconductor microstructure was used to investigate directly the dynamics of carrier transport in GaAsAlGaAs superlattices [18]. The well and the barrier thicknesses in the superlattice were kept constant for a given sample but the barrier height was changed every 800 Å by varying the Al concentration in the barrier. The total superlattice thickness was 8000 Å, so that there were 10 steps with different optical bandgaps (10 optical markers). An enlarged well was grown between the buffer and the superlattice, giving an additional marker.

The dynamics of carrier transport in GaAs/AlGaAs superlattices with multiple markers was investigated using subpicosecond time resolved luminescence spectroscopy [19]. The results of the experiment as a function of superlattice lattice period clearly showed that the transport is Bloch-like for small periods ($d \leq 40$ Å), but the nature of the transport changes drastically as the superlattice period is increased to 60 Å. These studies provided the first measurement of the mobility for perpendicular transport in superlattices.

These results were discussed earlier and will not be reproduced here. However, we will comment on a new aspect of these results. Fig. 2 shows the mobility of the holes in these superlattice samples as a function of the superlattice period. The variation of the mobility expected from a simple model based on the miniband widths does not give a good agreement with the data as shown in Fig. 2. Yang and Das Sarma [20] have examined this problem more closely and argued that a number of different effects must be considered in such a case. These effects arise from the fact that, in contrast to the usual transport, a number of parameters such as the miniband width, the Fermi energy, the inverse of the scattering times, and the temperature of the carriers are approximately of the same order of magnitude in the case of miniband transport. Therefore, some of the usual assumptions of the transport break down in superlattice transport. They have taken into account some of these factors and calculated the variation of the mobility as a function of the superlattice period. The results of their calculations gives a reasonably good agreement with the experimental results, as shown in Fig. 2.

While much more work remains to be done to understand the precise nature of carrier transport in superlattices, these results show the value of all-optical ultrafast studies in elucidating the nature of carrier transport in semiconductor superlattices.

4. TUNNELING IN SEMICONDUCTOR MICROSTRUCTURES

Tunneling in semiconductor microstructures such as double barrier diodes and multiple quantum well structures is currently a very active field of scientific research. Such phenomena have been investigated primarily by cw current-voltage measurements [3]. These studies have clearly established the existence of tunneling in such structures but the dynamical aspects of tunneling remain largely unexplored. Transient current-voltage measurements have been performed on multiple quantum well structures to investigate the dynamics of carrier transport [8,9]. Escape rates for electrons in double barrier diodes have been investigated by recent photoluminescence studies [21-23]. We present in this section our direct measurement of *resonant and non-resonant tunneling times for electrons in asymmetric double quantum well structures*.

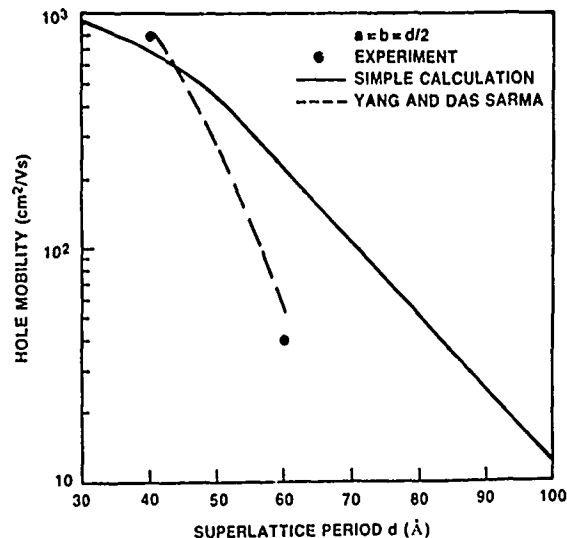


Fig. 2: Hole mobility as a function of superlattice period. Experimental points were obtained from optical transport measurements (Deveaud et al [18], the solid curve was calculated from a simple model of mobility as a function of miniband width and the dashed curve was calculated by Yang and Das Sarma [20].

MULTIPLE DOUBLE WELL STRUCTURE

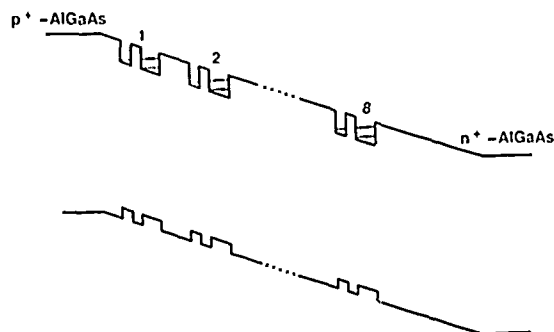


Fig. 3: Schematic diagram of the sample structure used in the experiments on tunneling.

Information about tunneling can be best obtained by investigating an isolated tunneling structure rather than by investigating transport across a superlattice. We accomplished this by studying electron tunneling from the narrow to the wide quantum well in an asymmetric, coupled double well structure. Each double well structure is isolated by a thick AlGaAs barrier on either side of it, as shown in Fig. 3. The recently developed luminescence upconversion technique was used to measure time resolved luminescence spectra with sub-picosecond time resolution. Near resonant excitation with an infrared dye laser was used in these experiments. Experimental details have been discussed earlier [24].

The basic idea behind the experiment is to investigate the decay and rise times of luminescence from each well. Since tunneling provides an additional decay channel, the luminescence decay time of the well from which electrons tunnel out is smaller than the decay time of the other well. Therefore, a comparison of the decay times of the two wells gives a direct measure of the tunneling time.

The eight period structure was embedded in the i-region of a p-i-n structure so that an electric field may be applied to change the relative alignment of energy levels in the two wells. The effect of electric field on the tunneling processes is schematically shown in Fig. 4. Under flat-band conditions, the $n=1$ electron level of the narrow well lies at an energy between the $n=1$ and the $n=2$ electron levels of the wide well. For this *non-resonant* condition, tunneling of electron from the $n=1$ level of the narrow well to the $n=1$ level of the wide well can take place with the help of a momentum conserving collision (collision with an impurity/defect or emission of an LO phonon). By applying an appropriate reverse bias to the structure, the $n=2$ level of the wide well may be brought into *resonance* with the $n=1$ level of the narrow well. Therefore, *both non-resonant and resonant tunneling times can be measured directly using this structure.*

We have investigated three different samples with different barrier thickness and well thickness of 60 Å for the narrow well and 88 Å for the wide well. The thicknesses were checked by TEM as well as by extensive optical studies. The time resolved luminescence spectra from a 65 Å barrier sample for two different delay are shown in Fig. 5. Both the narrow well and the wide well luminescence are clearly resolved. The narrow well luminescence decreases rather quickly with time whereas the wide well luminescence increases during this time.

RESONANT AND NONRESONANT TUNNELING IN COUPLED QUANTUM WELLS

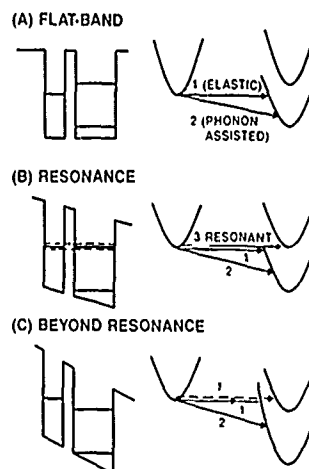


Fig. 4: Schematic diagram of the coupled double well structure at three different electric fields, showing various resonant and non-resonant tunneling processes.

TIME RESOLVED LUMINESCENCE SPECTRA OF COUPLED QUANTUM WELLS

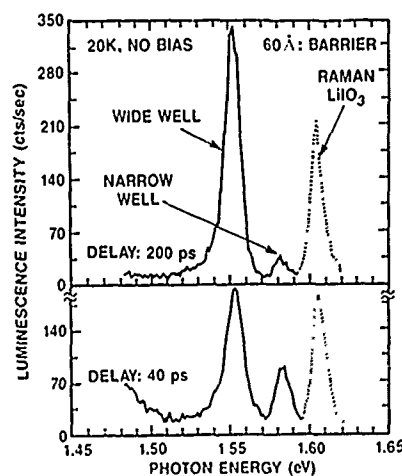


Fig. 5: Luminescence spectra of the 60 Å barrier sample at two different time delays, showing a rapid decay of the narrow well luminescence and a gradual rise of the wide well luminescence.

We first consider zero applied bias so that the electric field is small and there is no resonance between the electron levels of the two wells. The luminescence decay times for the wide well are longer than 500 ps for all samples under these conditions. However, the luminescence decay times for the narrow well are considerably shorter. This is a result of tunneling of electrons from the narrow well to the wide well. Note that the hole tunneling times are expected to be much longer and hole tunneling is not expected to play any part in these experiments.

Fig. 6 shows the non-resonant tunneling times of electrons for the three samples investigated as a function of the barrier widths in these samples. There is a strong increase in the non-resonant tunneling times as the barrier thickness increases. Fig. 6 also shows the tunneling times for optical phonon (LO) assisted transitions between the two wells calculated using a simple model. Although the general trend is similar, the measured values are somewhat shorter than those calculated. We are currently refining our calculations for the phonon-assisted tunneling rates and investigating whether the difference noted above can be attributed to impurity-assisted tunneling processes.

The variation of the luminescence decay time with applied bias is shown in Fig. 7. The decay time decreases strongly as the bias voltage is increased. This results from the increase in the tunneling rate as the $n=1$ level of the narrow well and the $n=2$ level of the wide well are brought into resonance. These results are summarized in Fig. 8 for the sample with 50 Å barrier width. The tunneling time remains nearly constant at low bias voltages; this is the *non-resonant tunneling time*. With increase in the reverse bias, there is first a *sharp reduction* in the tunneling time, followed by an *increase* in the tunneling time. This *non-monotonic* behavior of the tunneling time is a clear evidence for the tunneling resonance. Additional evidence for the resonance has been discussed earlier [24]. We note that the system time resolution for these measurements was ≈ 0.7 ps, so that the measured resonant tunneling time of 7 ps is not limited by the instrument.

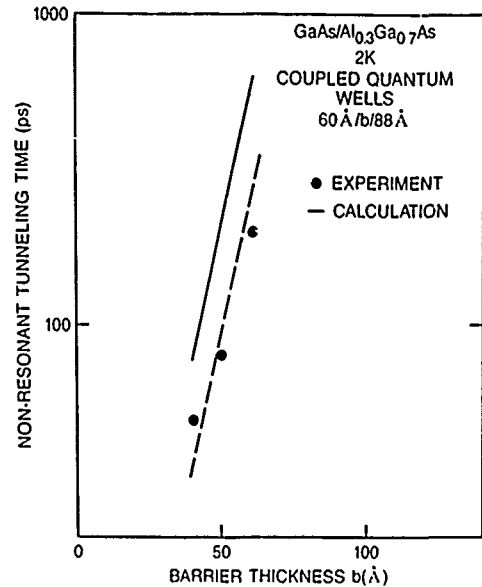


Fig. 6: Dependence of tunneling time on barrier thickness in GaAs/Al_{0.3}Ga_{0.7}As asymmetric double well structure. The points are experimental and the solid line is a calculation based on a simple model.

NARROW WELL LUMINESCENCE

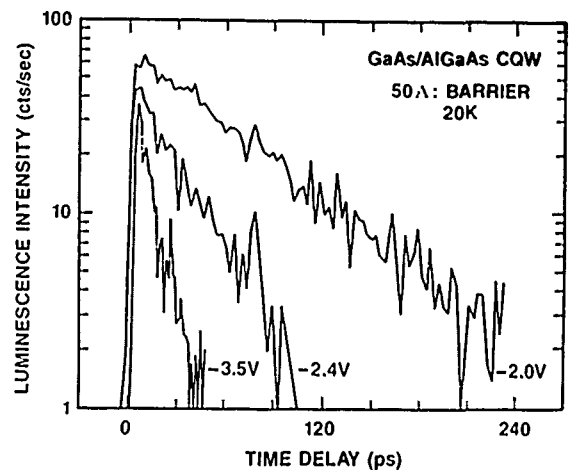


Fig. 7: Decay of the luminescence intensity of the narrow well in the asymmetric double well structure as a function of the applied bias. The decrease in the decay time is a result of resonant tunneling.

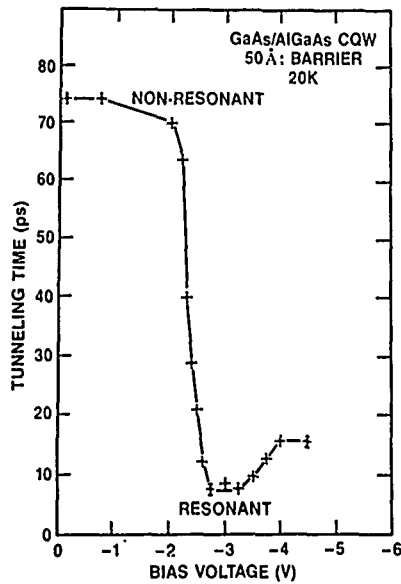


Fig. 8: The measured dependence of the electron tunneling times as a function of the applied electric field. The non-monotonic behavior of the tunneling times demonstrates that the decrease is caused by a resonant process. The time resolution of the measurement system was ≈ 0.7 ps.

These measurements represent the first direct measurements of non-resonant and resonant tunneling times. We stress again the importance of working with isolated structures to separate the effects of transport from tunneling. These direct measurements allow us to address a number of important questions. For example, what is the significance of the tunneling time measured at resonance and how does it compare with the coherent tunneling time? This question has been discussed at length in our earlier publication [24]. That discussion may be summarized as follows: inhomogeneities in the well widths as well as in the electric field in the multiple double well structure contribute to the width of the resonance and may restrict the shortest tunneling time that we observe. However, the coherent tunneling time is expected to be ≈ 1 ps, considerably shorter than the measured resonant tunneling time. We believe that inter-subband scattering in the wide well may make an important contribution to the measured resonant tunneling time. If this is indeed correct, this technique may also shed some light on the currently

controversial question of inter-subband scattering rates in quantum wells.

Another aspect of the data that can provide potentially useful information is the non-resonant tunneling time and the contribution of phonon-assisted processes to this time. Experiments are currently under way to determine directly the phonon-assisted rates by using a slightly modified structure in which the order of growth of the wide and the narrow wells is reversed; i.e. the narrow well is closer to the substrate. Applying a reverse bias lowers the $n=1$ electron level in the narrow well below that in the wide well and the separation can be tuned through an optical phonon energy to investigate the role of phonon processes. Our preliminary results on this structure indicate a strong reduction in the tunneling time at the phonon resonance. This investigation is continuing and promises to give direct information on phonon-assisted tunneling processes.

5. SUMMARY

We have reviewed how *all-optical* studies on picosecond and sub-picosecond timescales provide valuable information about carrier transport in semiconductor microstructures. In particular, the use of optical markers allows one to investigate directly the perpendicular transport of *carriers* in microstructures. Finally, we have presented recent results on direct measurements of resonant as well as non-resonant tunneling times in asymmetric double quantum wells using optical techniques. These measurements provide new insights into the physics of tunneling in such systems and once again illustrate the usefulness of optical techniques in investigating perpendicular transport and tunneling in microstructures.

6. ACKNOWLEDGMENTS

It is a pleasure to acknowledge that the many excellent samples which formed the basis of the work described here were grown by T. Y. Chang, R. F. Kopf, A. Regreny, N. J. Sauer and C. W. Tu. We thank J. E. Henry for processing the wafers into mesas appropriate for electric field work and D. A. B. Miller for helpful discussions on various aspects of the tunneling work.

REFERENCES

- [1] L. Esaki, and R. Tsu, IBM J. Res. Dev. **14**, 61 (1970).
- [2] L. Esaki, IEEE J. of Quantum Electronics QE-22, 1611-1624 (1986).
- [3] T. C. L. G. Sollner, W. D. Goodhue, P. E. Tannenwald, C. D. Parker and D. D. Peck, Appl. Phys. Lett. **43**, 588-590 (1983); and T. C. L. G. Sollner, P. E. Tannenwald, D. D. Peck and W. D. Goodhue, Appl. Phys. Lett. **45**, 1319-1321 (1984).
- [4] Federico Capasso, Khalid Mohammed and Alfred Y. Cho, IEEE J. of Quantum Electronics QE-22, 1853-1869 (1986).
- [5] A. G. R. Evans and P. N. Robson, Solid State Electronics **17**, 805 (1974)
- [6] D. F. Nelson, J. A. Cooper, Jr. and A. R. Tretola, Appl. Phys. Lett. **41**, 857-859 (1982).
- [7] R. A. Höpfel, Jagdeep Shah, D. Block and A. C. Gossard, Appl. Phys. Lett. **48**, 148-150 (1986).
- [8] C. Minot, H. Le Person, F. Alexandre and J. F. Palmier, Physica **134B**, 514-518 (1985).
- [9] H. Schneider, K. von Klitzing and K. Ploog, presented at the Fourth Int'l conf. on Superlattices, Microstructures and Microdevices, Trieste, Italy (1988).
- [10] J. F. Whittaker, G. A. Mourou, T. C. G. Sollner and W. D. Goodhue, Appl. Phys. Letters **53**, 385 (1988).
- [11] K. J. Weingarten, M. J. Rodwell and D. M. Bloom, IEEE J. of Quantum Electronics QE-24, 198 (1988).
- [12] C. V. Shank, R. L. Fork, B. I. Greene, F. K. Reinhart, and R. A. Logan, Appl. Phys. Letters **38**, 104 (1981).
- [13] G. Livescu, D. A. B. Miller, T. Sizer, D. J. Burrows, J. E. Cunningham, A. C. Gossard and J. H. English, Appl. Phys. Letters **54**, 748 (1989).
- [14] B. Deveaud, Jagdeep Shah, T. C. Damen, B. Lambert, A. Chomette and A. Regreny, IEEE J. of Quan. Electronics QE-24, 1641 (1985).
- [15] A. Forchel, B. Laurich, H. Hillmer, G. Tränkle and M. Pilkuhn, J. of Luminescence **30**, 67-81 (1985).
- [16] D. J. Westland, D. Mihailovic, J. F. Ryan and M. D. Scott, Appl. Phys. Lett. **51**, 590-592 (1987).
- [17] A. Chomette, B. Deveaud, J. Y. Emery, A. Regreny and B. Lambert, Solid State Commun. **54**, 75-78 (1985).
- [18] B. Deveaud, Jagdeep Shah, T. C. Damen, B. Lambert and A. Regreny, Phys. Rev. Lett. **58**, 2582-2585 (1987).
- [19] Jagdeep Shah, IEEE J. of Quan. Electronics QE-24, 276 (1988).
- [20] S. -R. Eric Yang and S. Das Sarma, Phys. Rev. **B37**, 10090 (1988).
- [21] M. Tsuchiya, T. Matsusue, and H. Sakaki, Phys. Rev. Letters **59**, 2356 (1987).
- [22] T. B. Norris X. J. Song, W. J. Schaff, L. F. Eastman, G. Wicks and G. A. Mourou, Appl. Phys. Letters **54**, 60 (1989).
- [23] M. K. Johnson, M. B. Johnson, D. H. Chow and T. C. McGill, Appl. Phys. Letters **54**, 552 (1989).
- [24] D. Oberli, Jagdeep Shah, T. C. Damen, C. W. Tu, T. Y. Chang, D. A. B. Miller, J. E. Henry, R. F. Kopf, N. Sauer, A. E. DiGiovanni, to be published.

Fabrication of Resonant Tunneling Diodes for Switching Applications

S. K. Diamond, E. Ozbay, M. J. W. Rodwell, and D. M. Bloom

*Edward L. Ginzton Laboratory, Stanford University,
Stanford, California 94305-4085*

Y. C. Pao, E. Wolak, and J. S. Harris

*Department of Electrical Engineering, Stanford University,
Stanford, California 94305-4055*

Abstract

Resonant tunneling diodes have been fabricated in a microwave compatible process. Current densities in excess of 10^5 A/cm² were achieved. Scattering matrix parameter measurements were performed to validate the equivalent circuit model used. Pulse forming structures were fabricated on chip and rise times from 6-10 ps were obtained.

Introduction

Several researchers have investigated resonant tunneling transistor structures [1] [2]. Because of the small device dimensions and short transit times it is hoped that these devices will operate at high speeds. Transistors have been fabricated with current gains above 50, however, a microwave compatible fabrication process has not yet been developed for three terminal devices and published results have been limited to low frequency operation.

Significant process development remains before device speed is limited by the intrinsic device parameters instead of extrinsic, process related, parasitic capacitances and resistances. In an effort to determine the intrinsic device speed of resonant tunneling devices we have focused our effort on diode pulse forming structures. Because only two contacts need to be made to the device, it was felt that these structures could be fabricated without introducing significant parasitics, and the device operation would only be limited by intrinsic device parameters. Pulse forming circuits provide a useful benchmark for device performance because large signal switching of the device is seen as would be seen in transistor logic circuits. Pulse forming cir-

cuits also require a microwave compatible process which has top side ohmic contacts, device isolation and low parasitic capacitance interconnects. These process features will be essential in a resonant tunneling transistor process.

Pulse Forming Circuit

A RTD pulse forming circuit is shown in Fig. 1a. The pulse forming circuit consists a resonant tunneling diode shunted to ground in the middle of a transmission line. In this work, the diode and transmission line were monolithically integrated on chip. In Fig. 1b the circuit has been simplified to its Thevenin equivalent and the diode has been replaced by its equivalent circuit. Note that the output voltage is equal to the voltage across the diode.

Other researchers have proposed more complicated equivalent circuits including the effects of space charge build up and the transit time in the depletion layer[3]. As shown in reference 4, for depletion lengths less than 1000 Å, these effects can be modeled to first order by the small signal equivalent circuit of Fig. 1c.

Fig. 2 demonstrates the large signal switching operation of the circuit. The device I-V curve and the source load line at two different bias points are shown. The operating point of the diode is given by the intersection of the load line and device curve. If the source voltage is increased from 0 to V_{m1} then the device will be operating at point A. A small increase in the source voltage will shift the load line to the higher line and the operating point of the device will move to point B. Looking at the output node of the transmission line a step would be

observed of magnitude $V_f - V_p$.

Esaki diodes are used in this manner to generate step-function waveforms used for time domain reflectometry instruments. Esaki diodes can generate a 300 mV voltage step with a 20 ps risetime. Step recovery diodes (SRD) are also used for step generation. SRD's can produce voltage swings of up to 10 volts, however risetimes are limited to about 30ps and the waveform generally exhibit ringing and are not suitable for time domain reflectometry applications.

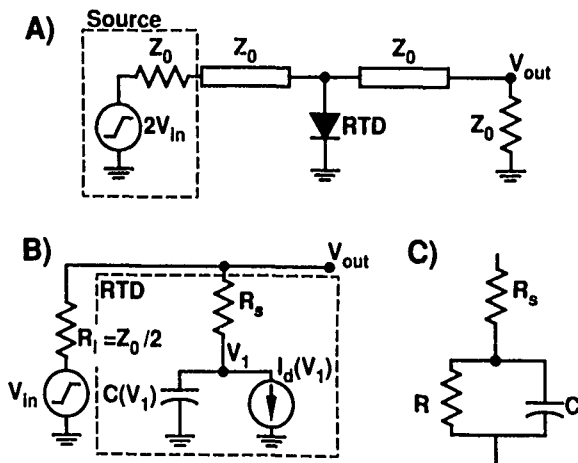


Figure 1: (a) High speed RTD pulse forming circuit. The RTD is shunted to ground across a 50 Ω transmission line. In (b) the matched transmission lines and source has been replaced by a Thevenin equivalent, and the equivalent circuit for the RTD is used. For small signal applications the RTD equivalent circuit in (c) is used.

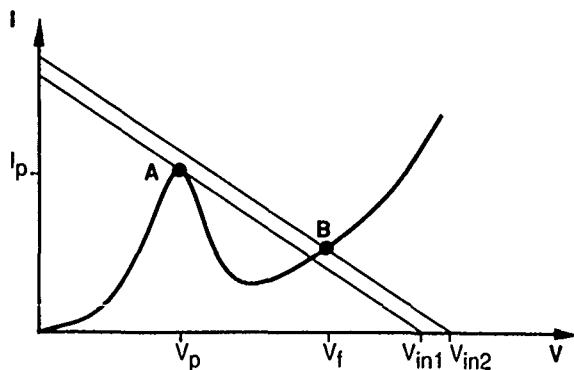


Figure 2: Large signal switching behavior of a resonant tunneling diode is observed as the device switches from state A to state B

The switching speed for RTD's is limited by the device capacitance and current density. As the voltage switches, additional charge is stored on the device capacitance, $\Delta Q = C(V_f - V_p)$. The current which is available for charging this capacitance is indicated by the shaded region in Fig. 3. The greater the area of the shaded region, or the smaller the capacitance, the faster the device will switch. From this graphical analysis, it is apparent that there are diminishing returns for improving the peak to valley ratio (PVR) beyond approximately 2. If the PVR is increased from 2 to 100, then the area of the shaded region increases by a factor of two: resulting in a reduction in switching speed by only a factor of 2. Increasing the device current density has the effect of scaling Fig. 3 upward by an amount equal to the increase in current density. Thus, the areas of the shaded region is proportional to the current density and the switching time is inversely proportional to the current density.

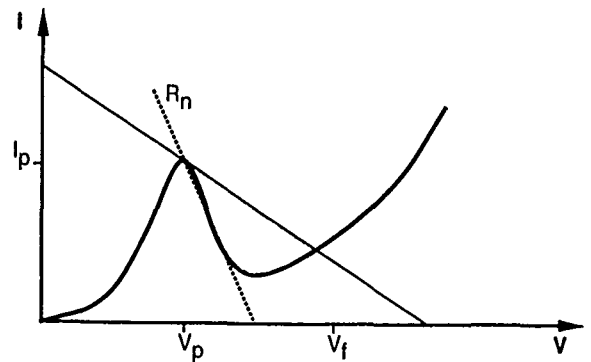


Figure 3: The excess current for charging the device capacitance is shown in the shaded region. The average negative resistance, R_n , is shown by the dashed line

The 10-90% switching transition time can be expressed exactly in the integral form.

$$T_{rise} = \int_{V_p + 0.1(V_f - V_p)}^{V_f - 0.1(V_f - V_p)} \frac{C(v)}{I_l(v) - I_d(v)} dv \quad (1)$$

This form can be difficult to work with and does not emphasize the key device parameters. The minimum possible switching time can be approximated accurately by $5|R_n|C$. R_n is the average negative resistance throughout the negative differential resistance region as shown in Fig. 3. The capacitance is estimated as $C = \epsilon A/d$ where A is the area of the device and d is the combined thickness of double barrier structure the depletion layer thickness at

the resonance voltage [4]. This minimum risetime can only be achieved if a load of resistance equal to $2.5|R_n|$ can be applied to the device.

In the above analysis, the only limitations to switching speed is the current density and device capacitance. The resonant build up times have been assumed to be infinitely fast. If the resonant build up times are estimated from $\delta t \geq \hbar/2\delta E$, where δE is the width of the resonant state, then resonant build up times for high switching speed devices are typically on the order of 150 fs. As shown later, this time constant is negligible compared to the several picosecond switching time from the $|R_n|C$ time constant.

Design and Fabrication

As pointed out in the previous section, high speed devices should have a high current density and small capacitance. Current density can be increased in two ways. First, by degenerately doping the emitter, more electrons are available for tunneling at the resonance condition. Doping levels should be greater than $1 \times 10^{18} \text{ cm}^{-3}$. Second, by increasing the width of the resonant state more electrons can tunnel through at resonance. A broad resonance width is achieved with narrow barriers, ideally the barriers should be less than 6 monolayers thick.

The device capacitance can be controlled in the growth process. If after the double barrier structure, an undoped spacer layer is grown followed by a heavily doped n^+ layer, then the depletion layer will be fixed by the thickness of the spacer layer. Low capacitance devices are desired, so this would suggest the use of long undoped spacer layers. However, the spacer layer has the effect of stretching out the I-V curve and thus increasing $|R_n|$ [4]. To first order, a decrease in the capacitance is matched by an increase in the average negative resistance, $|R_n|$, and the $|R_n|C$ time constant of the device remains invariant. The net effect is that the capacitance can be lowered, however because $|R_n|C$ remains invariant, the device switching will not be improved, but will have larger voltage swings.

Two generations of devices were fabricated. GEN1 had 700 and 100 Å spacer layers while GEN2 had a 350 and 100 Å spacer layers. Typical I-V curves for both generation devices are shown in Fig. 4, note the stretching of the I-V curve for the thick spacer layer devices. Both generations exhibited current densities greater than $1 \times 10^5 \text{ A/cm}^2$ and room temperature PVR's greater than 2.5. Because

of the high resonance voltage of the GEN1 devices, significant power was dissipated and many of the larger area device were destroyed during switching measurements. This problem was eliminated with the GEN2 devices.

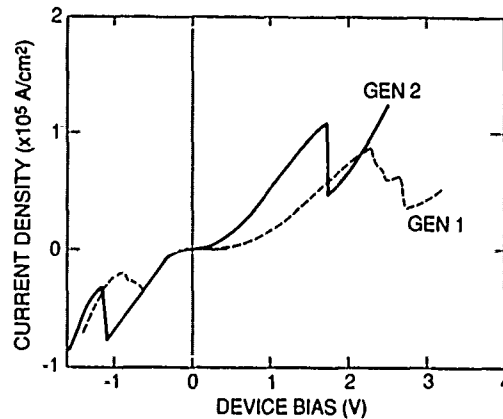


Figure 4: I-V curves for two generations of devices fabricated.

Monolithic integration of transmission lines on wafer requires a microwave compatible fabrication process. A cross section of device is shown in Fig. 5 to illustrate the fabrication process. This process has been reported in detail elsewhere [5]. Only a small fraction of the wafer is etched and the wafer remains planar throughout the process, allowing high resolution lithography at later steps if desired. Topside ohmic contacts are utilized and the devices are well isolated. This allows diodes to be connected in arbitrary circuit configurations. The proton implantation renders the substrate nonconducting and allows the fabrication of low-loss, low parasitic capacitance transmission lines.

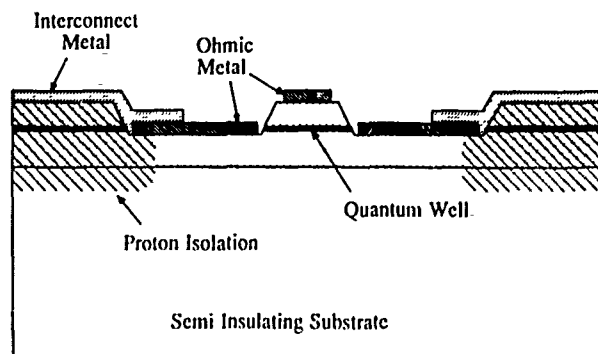


Figure 5: Device cross section of proton implanted, microwave compatible RTD. Proton isolation provides a nonconducting low-loss dielectric for transmission lines and provides device isolation.

For the above process, current must flow vertically through the top ohmic contact and then laterally to the bottom ohmic contact. If the current density is too high or the width of the top ohmic contact is too large, there can be a significant difference in applied voltages between the center of the device and the edge of the device. For this reason, a stripe geometry is used and the width of the active area is kept to a minimum. The width of the active area is kept to less than $8\text{ }\mu\text{m}$'s, larger area devices are obtained by extending the stripe.

In a more standard mesa-isolated process a similar spreading resistance and an additional series resistance can occur at high frequencies. At high frequencies, current is limited to within a skin depth of the surface. At 200 GHz the skin depth is close to 7 microns in heavily doped GaAs. If backside ohmic contacts are used, this can result in a significant series resistance since the current is restricted to the flowing within 7 microns of the surface of the wafer.

Testing

A microwave compatible fabrication process allows the incorporation of devices connected to low capacitance bond pads for S-parameter measurements. S_{11} measurements were performed from 45 MHz to 26.5 GHz. Fig. 6 shows the measured S-parameter measurement and the theoretically predicted S-parameter measurements at three different bias points. No circuit parameters were varied to fit the theoretical results to the data. For the theoretically predicted S-parameters, the series resistance was calculated from on wafer ohmic contact test patterns. The device capacitance was calculated from the spacer layer thickness specified in the growth. The small signal device resistance was estimated by the best linear approximation to the I-V curve at each bias point. In addition, a parasitic capacitance from the bond pad was estimated from separate measurements of blank test pads included on the wafer. Four circuit elements were measured and calculated, and the values were not altered to fit to the data. The close match between theory and experiment indicates that the simplified circuit model shown in Fig. 1c is appropriate for modeling these devices.

From the S parameter measurements, the series resistance, R_s , was confirmed to be $230\text{ }\Omega - \mu\text{m}^2$ and the capacitance was confirmed as $1.3\text{ fF}/\mu\text{m}^2$. The average negative resistance, R_n , was approximated from the I-V curve to be $-650\text{ }\Omega - \mu\text{m}^2$. The pre-

dicted minimum switching time with an ideal load is 4 ps.

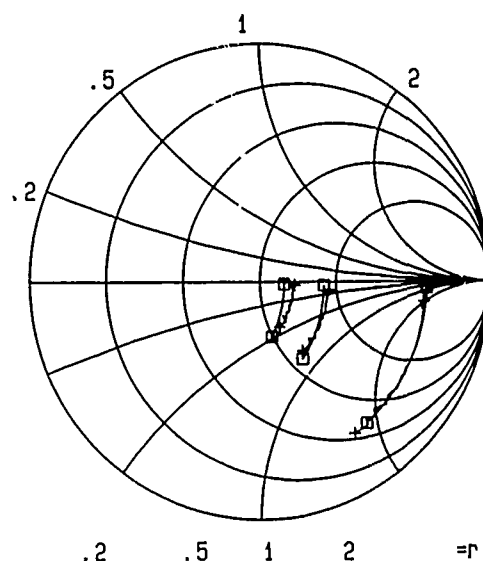


Figure 6: S_{11} measurements and theory at three bias point. The experimental data curves have plus mark endpoints. The predicted curves have box endpoints.

In practice, a 2 GHz sine wave and DC bias was applied to the input transmission line shown in Fig. 1a. If the device is to be reset, the amplitude of the sine wave must be sufficient to switch the load line above the peak voltage, V_p and move the load line back down to less than the valley voltage V_v . Fig. 7 illustrates the expected waveforms for a sinusoidal input voltage. For the devices tested, and the applied sinusoidal voltages, the switching transition were typically less than 70% of the total output voltage swing.

As the device switches, a step waveform travels down the output transmission line. The waveform is measured by electro-optically sampling the voltage at a point just past the device [6]. The transmission line is designed to be long enough to allow measurement of the pulse risetime before any reflections from the output bond pad can interfere with the measurement. Shown in Fig. 8 is a typical electro-optically measured pulse. Switching times of 6-10 ps were measured with voltage swings of 400-500 mV. The measured risetimes are 2 ps greater than the theoretically predicted minimum risetime. The cause of discrepancy has not been fully investigated, however it may be due to jitter in the device switching or variations in device capacitance.

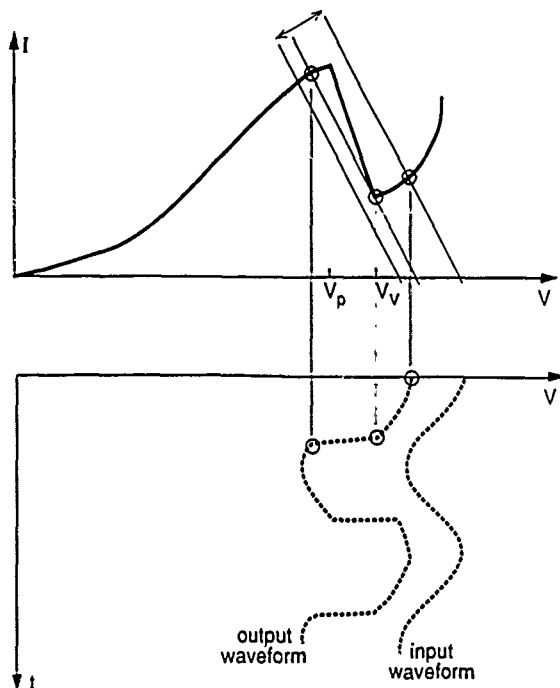


Figure 7: Expected switching waveforms with a sinusoidal input.

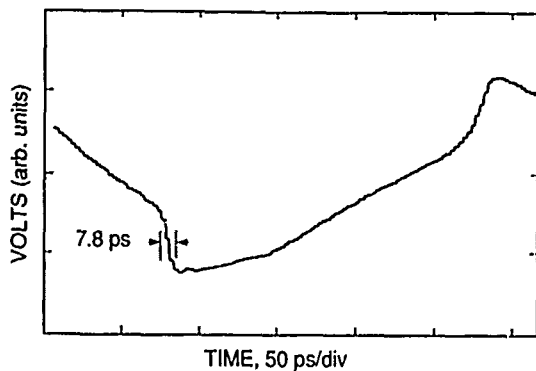


Figure 8: Measured switching waveform with electrooptic sampling. The quantization in the time axis is due to the measurement system

Conclusion

For switching applications, resonant tunneling diodes can be modeled by a resistance, R_s , in series with the parallel combination of a capacitor and nonlinear current source. The switching speed for these device is not being limited by the quantum mechanical time constants but is instead limited by the RC time constants associated with the device. We have demonstrated minimum switching times of 6 ps. Further improvement in switching time will not result from improvements in peak to valley ra-

tio, but will instead result from increasing device current density.

Acknowledgments

The authors wish to thank A. Black for his assistance in the electro-optic device measurements. This work was supported under ONR contract N00014-86-0530.

References

- [1] F. Capasso and R.A. Kiehl "Resonant tunneling transistor with quantum well base and high-energy injection: a new negative differential resistance device," *Appl. Phys. Lett.* **58**, 1366-1368 (1985).
- [2] M.A. Reed, W.R. Frensley, R.J. Matyi, J.N. Randall and A.C. Seabaugh "Realization of a three-terminal resonant tunneling device: The bipolar quantum resonant tunneling transistor," *Appl. Phys. Lett.* **54**, 1034-1036 (1989).
- [3] V.P. Kesan, D.P. Neikirk, P.A. Blakey, B.G. Streetman and T.D. Linton Jr. "The influence of transit-time effects on the optimum design and maximum oscillation frequency of quantum well oscillators," *IEEE Trans. Electr. Dev* **35**, 405-413 (1988).
- [4] S.K. Diamond, E. Özbay, M.J.W. Rodwell, Y.C. Pao, J.S. Harris and D.M. Bloom "Resonant tunneling diodes for switching applications," *Appl. Phys. Lett.* **52**, 2163-2165 (1989).
- [5] S.K. Diamond, E. Özbay, M.J.W. Rodwell, Y.C. Pao, E. Wolak, J.S. Harris and D.M. Bloom "Fabrication of 200-GHz f_{max} resonant-tunneling diodes for integrated circuit and microwave applications," *IEEE Electron Device Lett.* **EDL-10**, 104-106 (1989).
- [6] K.J. Weingarten, M.J.W. Rodwell and D.M. Bloom "Picosecond optical sampling of GaAs integrated circuits," *IEEE J. of Quant. Electr.* **QE-24**, 198-220 (Feb. 1988).

Time-Resolved Observation of Luminescence from a Charge-Transfer State in Double Quantum Wells

T. B. Norris*

*Laboratory for Laser Energetics and Department of Physics and Astronomy,
University of Rochester, 250 E. River Road, Rochester, New York 14623*

N. Vojdani, B. Vinter, and C. Weisbuch

*Thomson-CSF, Laboratoire Central de Recherches, Domain de Corbeville, BP 10,
Orsay, France*

G. A. Mourou*

Laboratory for Laser Energetics, University of Rochester, Rochester, New York 14623

ABSTRACT

We have directly observed the buildup of a charge-transfer state in double quantum well structures due to electron and hole tunneling in opposite directions.

Time-resolved techniques have lately been applied to the study of the dynamics of tunneling in semiconductor quantum well (QW) structures [1-3]. The physics of tunneling in coupled QW structures has also been a topic of much recent interest [3,4]. We have applied the technique of time-resolved photoluminescence (PL) spectroscopy to investigate tunneling in a novel asymmetric GaAs/AlGaAs double QW structure. We report in this paper the direct observation of PL from a "charge-transfer" (CT) state, which is built up by electron and hole tunneling in opposite directions between the QW's.

The double-QW's are designed so that under flat band conditions the electron levels of the two wells are close to resonance, but the hole levels are sufficiently different that the PL energies of the two wells are well separated. This is accomplished by using an asymmetric double QW, where the wider QW has an Al composition that is adjusted so that the electron levels will be close to resonance [5]. Specifically, a 58 Å $\text{Al}_{0.15}\text{Ga}_{0.85}\text{As}$ QW (QW1) is coupled to a 26 Å GaAs QW (QW2) through a 43 or 86 Å $\text{Al}_{0.45}\text{Ga}_{0.55}\text{As}$ barrier. For the thin barrier sample, the electrons are somewhat delocalized over the two wells; for the thick barrier they are strongly localized in each well. There is a semitransparent Schottky contact on the top surface so the effect of an electric field could be studied. The calculated band diagram and electron and hole states for the thin barrier sample are shown in Fig. 1 for both flat-band and strong field conditions.

The samples were held in a cryostat at a temperature of 6 K. Electron-hole pairs were generated in each QW at $t=0$ by picosecond pulses from a synchronously pumped (Pyridine 1) dye laser. The injected carrier density was approximately 10^{11} cm^{-2} . The time-dependent PL spectrum was dispersed through a 0.32-m monochromator with 300 lines/mm grating and monitored on a 100-MHz synchroscan streak camera with 2-D detector. The spectral resolution of the system was about 3 meV and the temporal resolution about 20 ps.

Continuous-wave PL spectra were taken on a separate system with sub-meV resolution. Continuous-wave spectra for both samples are shown in Fig. 2 for both samples at zero applied bias. For the thick barrier sample the transition strengths of the QW1 (1.765 eV) and QW2 (1.73 eV) lines are approximately the same. For the thin barrier sample, the QW2 line is much weaker, indicating stronger tunneling processes for this sample, as will be discussed below.

Time-resolved spectra for the thin (43 Å) barrier sample are shown in Fig. 3 for applied bias voltages of 0, -3, and -4.75 V. The low field spectrum shows the scattered pump light, a PL line corresponding to transitions in QW1, and at lower energy, a line from QW2. The high-field spectra reveal a third PL line that is strongly Stark shifted to lower energy. The decay time of the third PL component is extremely long, it exceeds the 10 ns time interval between pump pulses and synchroscan sweep cycle time, (hence the signal that appears at " $t < 0$ "). The Stark shifts of the three lines are shown in Fig. 4. The QW1 and QW2 transitions show a red shift of a few meV typical of single-QW spectra [6-8]. The long-lived component shows a strong red shift of up to 25 meV at the maximum attained field (approximately $2.5 \times 10^4 \text{ V/cm}$). This Stark shift is

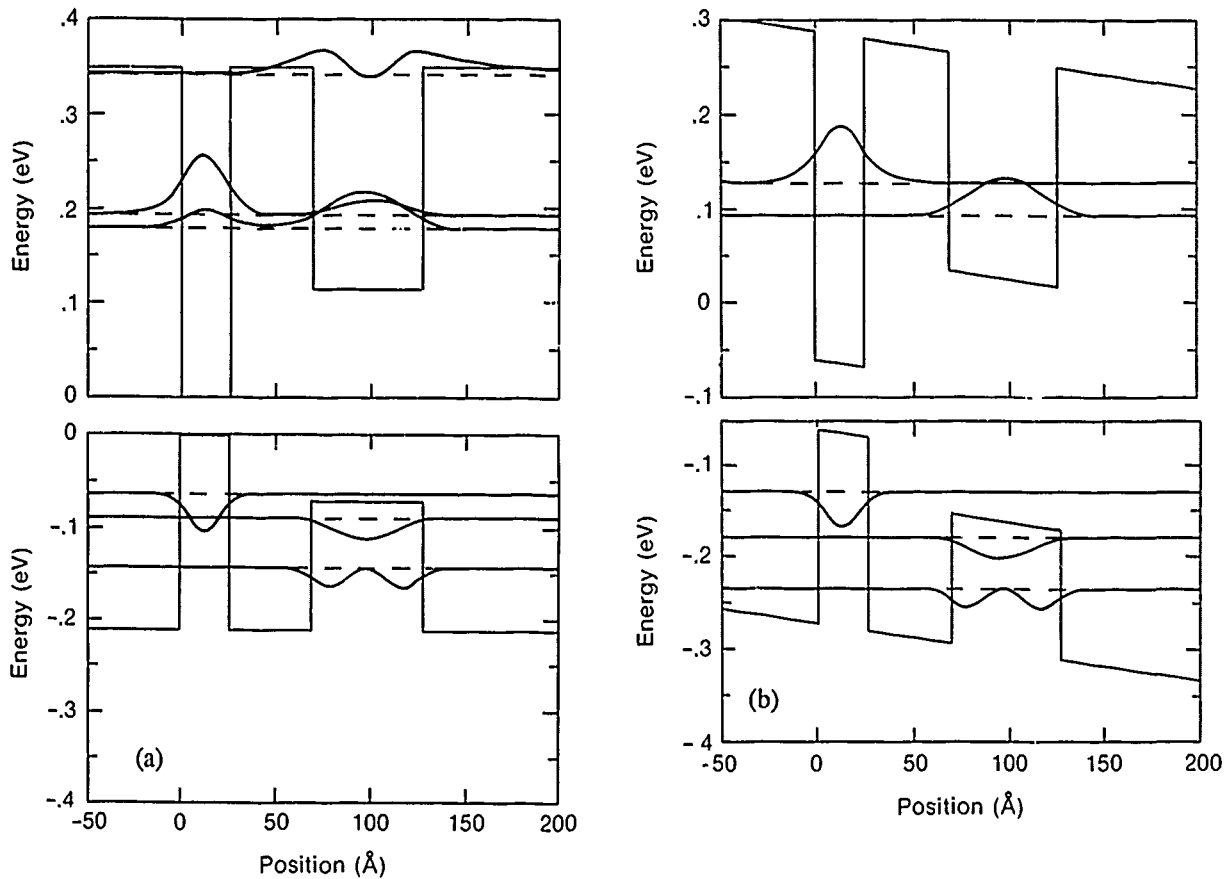


Figure 1. Calculated band diagrams and electron and heavy hole wave functions for the thin barrier sample: (a) under flat-band conditions, and (b) with an electric field of 30 kV/cm. The states for sample B are similar, except the electron states are always strongly localized in each well.

roughly linear with applied field at high bias. These observations lead us to the conclusion that this PL line originates from radiative recombination of electrons in QW1 with holes in QW2, which we refer to as the CT state. The long lifetime is due to the small overlap of the electron and hole wavefunctions of the CT state. The charge separation occurs by electron and hole tunneling in opposite directions. The QW1 decay time, which at high field corresponds to the hole tunneling time from QW1 to QW2, is shown as a function of bias in Fig. 5. This hole tunneling rate is substantially faster than one would expect from simple calculations of the tunneling escape rate of heavy holes from a QW through a thin barrier. It is not possible to assign a decay time to the QW2 luminescence, because the QW2 and CT lines are not spectrally well separated except at high-bias voltage. At the highest bias the decay times of the PL lines corresponding to both QW1 and QW2 are streak-camera-limited. It is this rapid charge separation that enables the observation of luminescence from the CT state in the time-resolved spectra, despite the low instantaneous intensity of the CT luminescence.

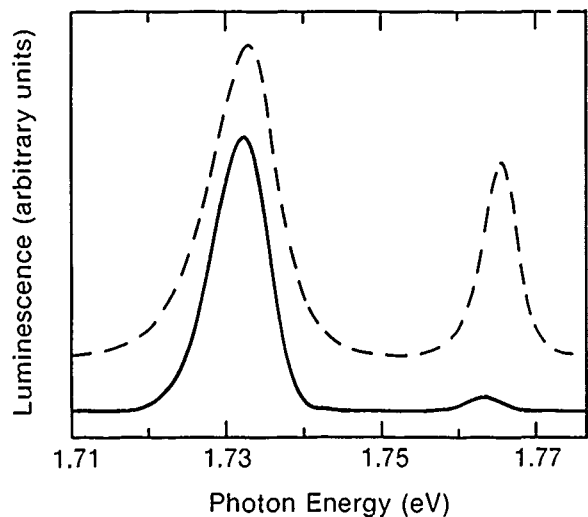


Figure 2. Time-integrated (cw) luminescence spectra for the two samples with no applied bias; the solid (dashed) line is for the thin (thick) barrier sample. The peak near 1.765 eV corresponds to the QW1 transition, and the peak near 1.73 eV to the QW2 transition.

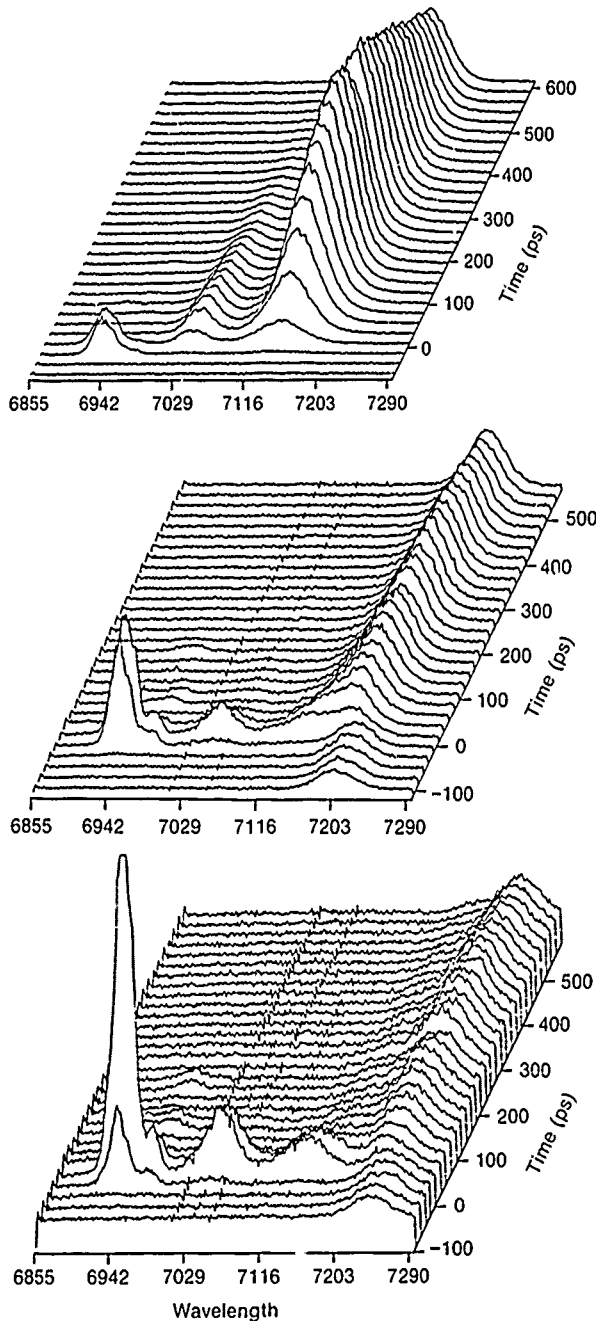


Figure 3. Time-resolved spectra for the thin barrier sample with (a) 0 V, (b) -3 V, and (c) -4.75 V applied bias.

The time-dependent PL spectra for the thick (86 Å) barrier sample do not show the development of a CT state. The spectra show only the two PL lines corresponding to transitions within QW1 and QW2, as can be seen in Fig. 6. The Stark shifts of these lines are a few milli-electron-volts to the red as expected for single QW's in an electric field. Time-integrated (cw) PL spectra of this sample, shown in Fig. 7, reveal that

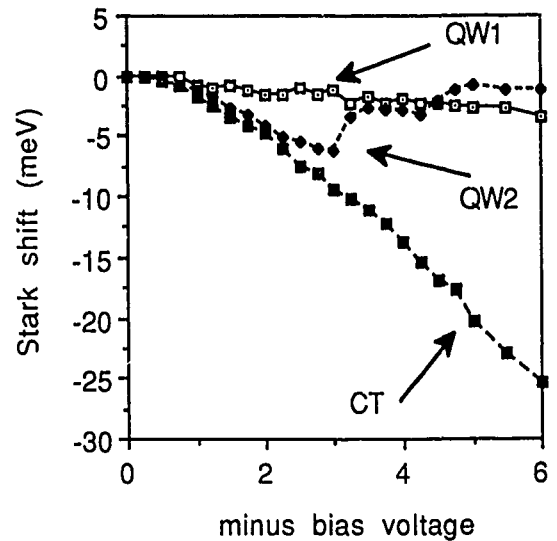


Figure 4. Stark shifts of the luminescence lines versus bias voltage for the thin barrier sample.

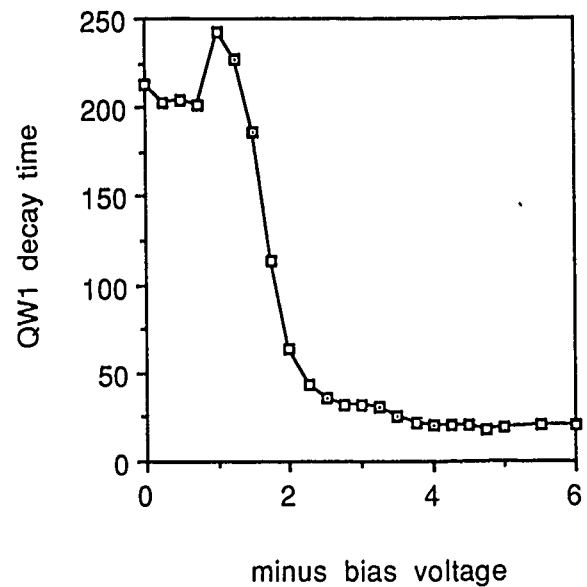


Figure 5. Decay time of the QW1 luminescence versus bias voltage for the thin barrier sample.

there is in fact some charge separation occurring, manifested by the strongly red-shifted component appearing at high fields. In this case only the electrons tunnel, and the holes remain in each QW. The CT luminescence is not observable on the time-resolved spectra because incomplete charge separation takes place, so the instantaneous intensity of the CT PL is much less than that of QW1 and QW2.

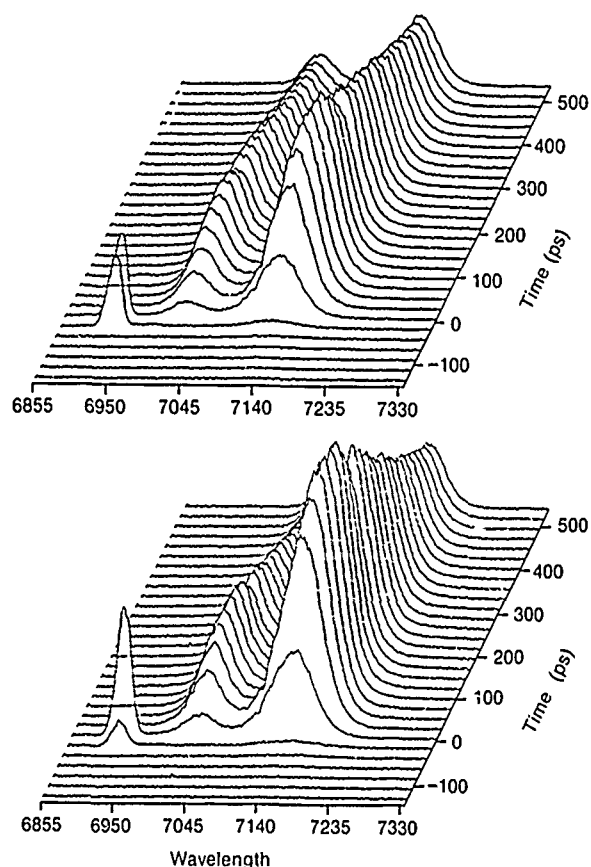


Figure 6. Time-resolved spectra for the thick barrier sample with (a) 0 V and (b) -8 V applied bias.

We further note that the long decay time of the CT state causes a d.c. charge buildup in each well, which screens the applied field and reduces the Stark shift of the CT PL line. Thus by comparing the CT Stark shift with the calculated value from the external field, we have been able to estimate the separated charge density and hence the CT state lifetime. We find that this lifetime depends strongly on the injected carrier density, and ranges from 20 ns to 1 μ s for our experiments on the 43 Å barrier sample. The observed CT decay time is most likely due to nonradiative recombination.

ACKNOWLEDGMENTS

This work was supported by the sponsors of the Laser Fusion Feasibility project at the Laboratory for Laser Energetics and by the U.S. Air Force under contract F49620-87-C-0016.

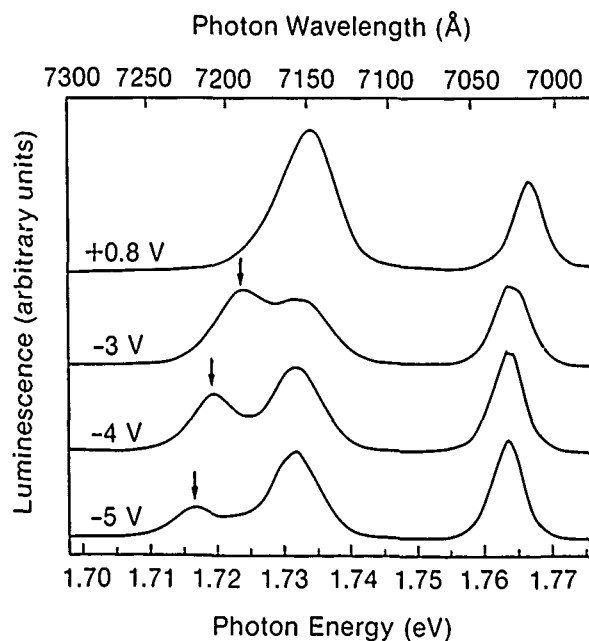


Figure 7. Time-integrated (cw) luminescence spectra for the thick barrier sample at various applied bias voltages.

* Dr. Norris is at the Department of Electrical Engineering and Computer Science and the Department of Applied Physics, University of Michigan, Ann Arbor, MI 48109-2122 and at Thomson-CSF Laboratoire Central de Recherches, Domaine de Corbeville BP10, Orsay, France. Dr. Mourou is at Department of Electrical Engineering and Computer Science, University of Michigan, Ann Arbor, MI 48109-2122.

REFERENCES AND NOTES

1. M. Tsuchiya, T. Matsusue, and H. Sakaki, *Phys. Rev. Lett.* **59**, 2356 (1987).
2. T. Tada, A. Yamaguchi, T. Ninomiya, H. Uchiki, T. Kobayashi, and T. Yao, *J. Appl. Phys.* **63**, 5491 (1988).
3. T. B. Norris, X. J. Song, W. J. Schaff, L. F. Eastman, G. Wicks, and G. A. Mourou, *Appl. Phys. Lett.* **54**, 60 (1989).
4. R. Sauer, K. Thonke, and W. T. Tsang, *Phys. Rev. Lett.* **61**, 609 (1988).
5. G. Wicks, private communication (1986).
6. D. A. B. Miller, D. S. Chemla, T. C. Damen, A. C. Gossard, W. Wiegmann, T. H. Wood, and C. A. Burrus, *Phys. Rev. Lett.* **53**, 2173 (1984).
7. C. Albert, S. Gaillard, A. Brun, G. Bastard, P. Frijlink, and M. Erman, *Solid State Commun.* **53**, 457 (1985).
8. E. J. Austin and M. Jaros, *Appl. Phys. Lett.* **47**, 274 (1985).

Optical Phonon-Assisted Tunneling in Double Quantum-Well Structures

D. Y. Oberli, Jagdeep Shah, T. C. Damen, R. F. Kopf, J. M. Kuo, and J. E. Henry

AT&T Bell Laboratories, Holmdel, New Jersey 07733

Using subpicosecond time-resolved luminescence spectroscopy, we have investigated tunneling of electrons in a double quantum well structure. The sample is a p-i-n diode, which contains two GaAs quantum wells of different thicknesses separated by a 55 Å $\text{Al}_{0.65}\text{Ga}_{0.35}\text{As}$ barrier layer. We observe a large increase of the tunneling rates when the two lowest energy subbands of the coupled wells are separated by more than an optical phonon energy. These results demonstrate that phonon-assisted tunneling play a significant role in this structure and in the carrier transport of related multiple quantum well structures.

The investigation of tunneling of electrons and holes through potential barriers in semiconductor heterostructures is an area of active research. Recently, Goldman, Tsui and Cunningham [1] have identified a shoulder in the valley current of a double barrier resonant tunneling structure to the existence of phonon-assisted resonant tunneling. This observation was then confirmed by a theoretical calculation of the tunneling transmission probability for an electron incident on such a structure [2]. In this paper, we present preliminary results of an optical study of optical phonon-assisted tunneling by subpicosecond luminescence spectroscopy.

The idea of the present study is to investigate the rate of electron tunneling across a single potential barrier separating two quantum wells of different thicknesses. The advantage of this structure is twofold: we can identify the luminescence of each well by its spectral position, thereby monitoring the concentration of electrons in each well separately, and we can restrict

the tunneling of carriers to a single barrier by surrounding the two wells with thick AlGaAs layers.

Previous studies of tunneling in semiconductor structures have been performed in superlattices for which tunneling of carriers could not be separated from carrier transport through the whole structure [3].

The double quantum well structure is placed inside the intrinsic region of a p-i-n diode; thus, the relative energy position of the electronic subbands in adjacent wells can be tuned by applying an external bias voltage. When a bias voltage is applied to the diode, the subband state localized mainly in the narrow well ($n=1'$) may be brought into resonance with the subband state localized mainly in the wide well ($n=1$) and then below it. Optical phonon assisted transitions between these two states are expected to contribute to tunneling if the energy separating them exceeds one optical phonon energy (see Fig.1).

The sample studied was grown at 600 °C by molecular beam epitaxy on (100) n-type GaAs substrate. Eight

periods of an asymmetrical double quantum well structure are placed inside the intrinsic region of a p-i-n diode structure; a 150 Å thick layer of $\text{Al}_{0.35}\text{Ga}_{0.65}\text{As}$ separates each period. Each unit consists of two GaAs wells of different thicknesses, nominally 70 and 110 Å, and a $\text{Al}_{0.35}\text{Ga}_{0.65}\text{As}$ barrier. The total width of the intrinsic region is 6080 Å. The sample is processed into an array of diode-mesas (area=200x200 μm^2 , height=4 μm) with gold electrical contacts on top of each mesa and a common contact on the substrate side. The current-voltage characteristics of the p-i-n diodes features low reverse bias current of less than 100 pA (in the dark) and breakdown voltages in excess of 20 V. The processed sample is mounted on a sapphire disk and placed in thermal contact with a cold finger (~20 K) inside an optical cryostat.

Short optical pulses of 750 fs duration tunable over the range of 7200 to 8000 Å are generated at a 82 MHz rate by synchronously pumping a dye-laser (Styryl 8) with the compressed and frequency doubled output of a mode-locked CW Nd-YAG laser. Time-resolved luminescence is realized by the energy up-conversion in a LiIO_3 crystal of a photon from the luminescence with a photon of a delayed pump laser pulse [4]. The photoluminescence is excited at a photon energy of 1.71 eV; the areal carrier density is estimated to be $6 \times 10^{10} \text{ cm}^{-2}$ per pulse.

In Fig. 2, we show luminescence decay traces for two values of the applied electric field. The lower electric field corresponds to an energy separation between the two lowest subband states of less than an optical phonon energy while for the higher value it is larger. The decay time in the latter case is thus shortened from 480 ps to 160 ps. Because of the quantum confined Stark effect, which decreases the energy of the luminescence as the electric field is

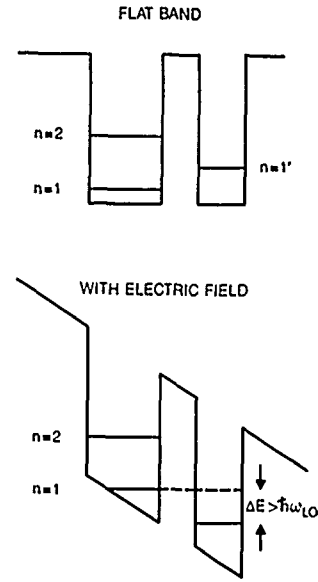


Figure 1: Schematic diagram of the energy levels in a double quantum well structure for two values of the applied electric field (a continuous line indicates a subband state mainly confined in one well).

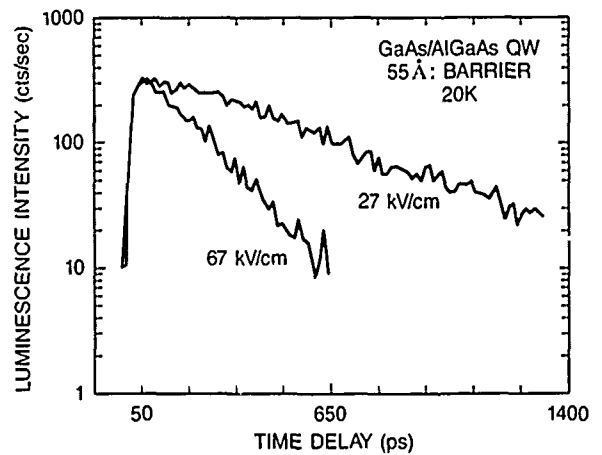


Figure 2: Decay curves of the luminescence intensity from the wide well for two values of the electric field ($h\nu=1.552 \text{ eV}$ at 27 kV/cm). The decrease of the decay time is the result of tunneling.

increased, we measure the luminescence intensity at its spectral peak. In this instance, the peak position had shifted by 5 meV when the field was increased from 27 kV/cm to 67 kV/cm.

The electric field dependence of the wide well luminescence decay times is summarized in Fig. 3. These data exhibit the expected behavior for phonon-assisted tunneling processes. Below a field of 40 kV/cm, the energy separation between the $n=1$ subband in the wide well and the $n=1'$ subband in the narrow well is less than an optical phonon energy and the decay time of the luminescence is nearly unchanged. At a field of about 50 kV/cm the decay time is strongly reduced because of the onset of phonon assisted tunneling processes. Beyond a field of 60 kV/cm, we observe a continuous increase of the decay time presumably due to the reduced overlap of the electronic wavefunction in adjacent wells. These results are, we believe, the first experimental evidence of phonon-assisted tunneling between two coupled quantum wells.

One result of this study remains however unresolved: the lack of structure in the luminescence decay time of the narrow well. We did not observe a corresponding increase of the luminescence decay time of the narrow well when the lowest energy levels in adjacent wells were brought into resonance. This result is rather surprising since a similar lifetime is expected for the luminescence in both wells.

For a phonon-assisted tunneling process, the optical phonons are likely to be emitted from the barrier layer since the overlap of the electronic wavefunctions is strongest there. Because AlGaAs exhibits a two-mode behavior, the scattering of a longitudinal optical phonon will occur at two distinct frequencies: approximately 35 and 47 meV for 35% Aluminum

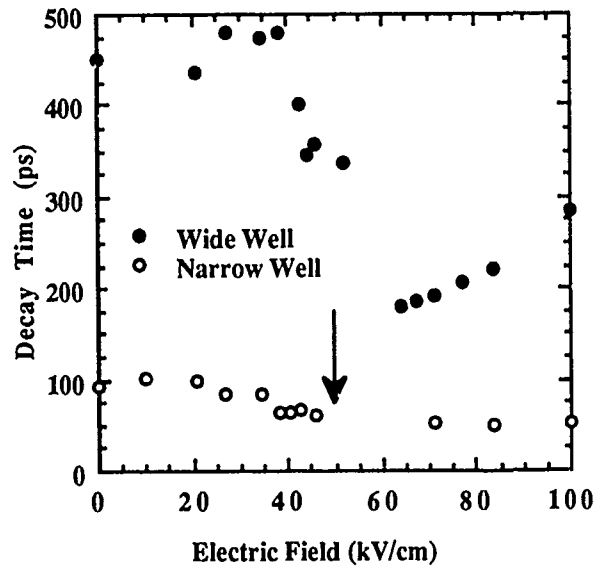


Figure 3: Electrical field dependence of the luminescence decay times. The large decrease of decay time in the wide well occurs at the onset for optical phonon-assisted tunneling (calculated value of field at which resonance is expected for a 37 meV phonon is indicated by an arrow).

content [5,6]. The onset of optical phonon-assisted tunneling has however not been resolved separately for these two phonon modes. From our complementary C-V measurement a background impurity density of $7 \times 10^{15} \text{ cm}^{-3}$ has been estimated inside the intrinsic region. For this reason, the electric field is not uniform across the eight periods of the double quantum well structure. Our estimate of the field inhomogeneity is consistent with the experimental broadening of the onset of phonon-assisted tunneling.

Preliminary calculations of intersubband scattering rates in this asymmetric coupled quantum well structure predict decay times which are longer (about 360 ps for a 55 Å barrier thickness). The model needs to be revised however to include confined optical phonon modes and

the exact wavefunction of the electronic subbands in the coupled quantum wells.

In conclusion, we have performed a time-resolved luminescence study of electron tunneling in coupled asymmetric quantum wells. These results demonstrate the existence of phonon-assisted tunneling in this system when the energy separation of the two lowest energy subbands exceeds one optical phonon energy.

We would like to thank D. A. B. Miller for many stimulating discussions.

1. V. J. Goldman, D. C. Tsui and J. E. Cunningham, "Evidence for LO-Phonon-Assisted Tunneling in Double-Barrier Heterostructures", *Phys. Rev.* **B36**, 7635-7637 (1987).
2. N. S. Wingreen, K. W. Jacobsen, and J. W. Wilkins, "Resonant Tunneling with Electron-Phonon Interaction: an Exactly Solvable Model", *Phys. Rev. Lett.* **61**, 1396-1399 (1988).
3. F. Capasso, K. Mohammed, and A. Y. Cho, "Resonant Tunneling through Double Barriers, Perpendicular Quantum Transport Phenomena in Superlattices, and their Device Applications", *IEEE J. of Quantum Electron.* **QE-22**, 1853-1869 (1986).
4. J. Shah, "Ultrafast Luminescence Spectroscopy using Sum Frequency Generation", *IEEE J. Quantum Electronics* **QE-24**, 276-288 (1988).
5. R. Tsu, H. Kawamura, and L. Esaki in *Proceedings of the Eleventh International Conference on the Physics of Semiconductors, Warsaw 1972*, edited by M. Miasek, p.1135.
6. B. Jusserand and J. Sapriel, "Raman Investigation of Anharmonicity and Disorder-Induced Effects in Ga- $_{1-x}$ Al $_x$ As Epitaxial Layers", *Phys. Rev.* **B24**, 7194-7205 (1981).

New Equivalent-Circuit Model for Resonant Tunneling Diodes

E. R. Brown, C. D. Parker, and T. C. L. G. Sollner

*Lincoln Laboratory, Massachusetts Institute of Technology,
Lexington, Massachusetts 02173*

C. I. Huang and C. E. Stutz

*Wright Research and Development Center,
Wright-Patterson Air Force Base, Ohio 45433*

ABSTRACT

It is shown that a "quantum-well inductance" can account for the effect of quasibound-state lifetime on the speed of resonant-tunneling diodes. This is demonstrated theoretically using a linear-response analysis of the conduction current through a double-barrier diode. The inductance is then incorporated into a new equivalent circuit that is used to predict the oscillation characteristics of a diode designed to make the quasibound-state lifetime longer than any other speed-limiting time constant in the device.

INTRODUCTION

Resonant-tunneling diodes have recently been demonstrated as high-frequency oscillators [1] and high-speed switches [2,3]. An important reason for these developments is that the current density and the capacitance of these diodes are largely independent and thus can be separately optimized for high-speed operation. For oscillators this optimization has heretofore entailed minimizing the RC time constant τ_{RC} in the negative differential conductance (NDC) region of the current-voltage (I-V) curve. This time constant is given by $\tau_{RC} = C(-G/R_S - G^2)^{-1/2}$, where C is the capacitance of the active region of the diode, G is the differential conductance and R_S is the series resistance outside the active region.

This paper deals with a different speed-limiting mechanism that is intrinsic to the process of electron transport through a quasibound state of a resonant-tunneling structure. Any such state is characterized by a lifetime τ_N that is approximately the time required for an electron initially occupying the Nth state to escape. If the resonant-tunneling process is coherent (i.e., collisionless), τ_N is also close to the time required for the Nth quasibound-state wavefunction to build-up and decay during the passage of a wavepacket through the structure. Thus τ_N should be a measure of the time delay of the probability or electrical current in response to an ac voltage applied across the structure. In theory the magnitude of τ_N depends strongly on the barrier parameters in such a way that it decreases exponentially with increasing barrier thickness and has a somewhat weaker dependence on barrier height. In our fastest devices to date, resonant tunneling occurs through the ground state (i.e., $N=1$) and $\tau_1 \cong 100$ fs, compared to $\tau_{RC} \sim 200$ fs. As resonant-tunneling diodes continue to be developed, τ_{RC} should be reduced to values less than or equal to τ_1 . Thus it is useful to combine the effect of these time constants in predicting the ultimate speed of these devices.

THEORETICAL ANALYSIS

One way to incorporate the effect of the quasibound lifetime into the RC circuit model is outlined diagrammatically in Fig. 1. First, an expression is inferred for the conduction current through a double-barrier structure in response to an applied step voltage, $\Delta V\theta(t)$, where $\theta(t)$ is the unit step function and ΔV is small enough that G is essentially constant over the range of the step. This involves the use of the "sudden approximation" [5], which is valid when the quasibound energy level shifts with the applied voltage on a time scale so much shorter than τ_1 that it can be assumed to occur instantaneously. We further assume that the response of the current $i_c(t)$ to the voltage step occurs exponentially with time, and that the relevant

time constant is τ_1 , i.e.,

$$i_c(t) = I_1\theta(-t) + [I_2 + (I_1 - I_2)\exp(-t/\tau_1)]\theta(t),$$

where I_1 and I_2 are the dc currents shown in Fig. 1(b) at $t < 0$ and $t > 0$, respectively.

The second step of the derivation is to apply linear response theory to obtain the small-signal admittance $Y_C(\omega)$ for the conduction current. This admittance can be calculated as the Fourier transform of the response of the current to an impulse in voltage. In view of the fact that i_c is the response to a voltage step, Y_C is given by

$$Y_C(\omega) = \frac{1}{\Delta V} \int_{-\infty}^{\infty} \frac{di_c}{dt} \exp(-i\omega t) dt = \frac{G}{1+i\omega\tau_1}. \quad (1)$$

The result is equivalent to the series combination of G and a "quantum-well inductance," $L_{QW} = \tau_1/G$, as shown in Fig. 1(c).

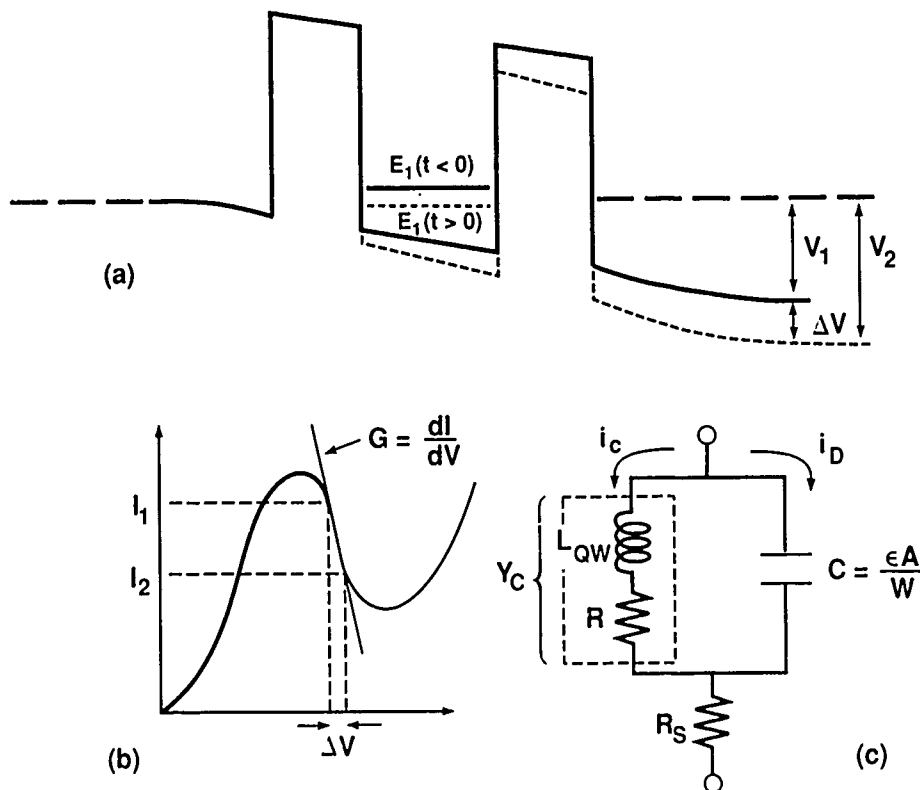


Fig. 1. (a) Diagrammatic outline of the response of the double-barrier structure to an applied voltage step $\Delta V = V_2 - V_1$. $E_1(t < 0)$ and $E_1(t > 0)$ are the quasibound ground-state energies before and after the applied potential step, respectively. (b) Current-voltage curve of a double-barrier diode showing the range of both the applied voltage step and the conduction current response in the negative differential conductance region. (c) Equivalent-circuit model for the double-barrier diode where G is the differential conductance, C is the capacitance, R_S is the series resistance and L_{QW} is the quantum-well inductance.

Physically, this inductance represents the temporal delay of conduction current with respect to ac voltage, analogous to the delay that occurs across inductors in lumped-element circuit theory. Note that this is a *negative inductance* in the NDC region of the I-V curve, and that the analysis is not valid near the peak or valley points that bound the NDC region since the second-order contribution, $(d^2I/dV^2)(\Delta V)^2$, to $i_c(t)$ cannot be neglected near these points.

Equation (1) is the central result of this paper. An important application of this result is to synthesize a new equivalent circuit for the double-barrier diode [6]. As shown in Fig. 1(c), this circuit includes a capacitance C to represent the displacement current i_D that flows through the active region of the device. When G is negative, this circuit will oscillate up to a frequency at which the real part of the terminal impedance vanishes. This frequency is found to be

$$\omega_{RCL} = \left\{ \frac{(1 - C/2LG^2)}{LC} \left[1 - \left[1 - \frac{(GR_S + 1)/GR_S}{(C/2LG^2 - 1)^2} \right]^{1/2} \right] \right\}^{1/2}.$$

In the limit that $L \rightarrow 0$ or equivalently $\tau_1 \rightarrow 0$, this solution reduces to the usual result $\omega_{RC} = 2\pi f_{RC} = C^{-1}(-G/R_S - G^2)^{1/2}$ for the RC model used in previous analyses. In the opposite limit $\tau_1 \gg \tau_{RC}$, ω_{RCL} can be approximated by

$$\omega_{LC} = \left[\frac{1}{LC} \left(1 - \sqrt{-1/(GR_S)} \right) \right]^{1/2}.$$

DEVICE ANALYSIS

Prior to the present study, all of the double-barrier diodes tested in our oscillator experiments demonstrated a maximum measurable oscillation frequency within 50% of f_{RC} . This behavior is consistent with our calculations that these diodes have barriers thin enough so that $\tau_1 \leq \tau_{RC}$. To examine the validity of the quantum-well inductance, it is better to test a diode for which $\tau_1 \geq \tau_{RC}$. Under this condition, the maximum oscillation frequency should be significantly below f_{RC} . A double-barrier structure that satisfies this condition is represented in Fig. 2. It consists of two 4.9-nm-thick undoped

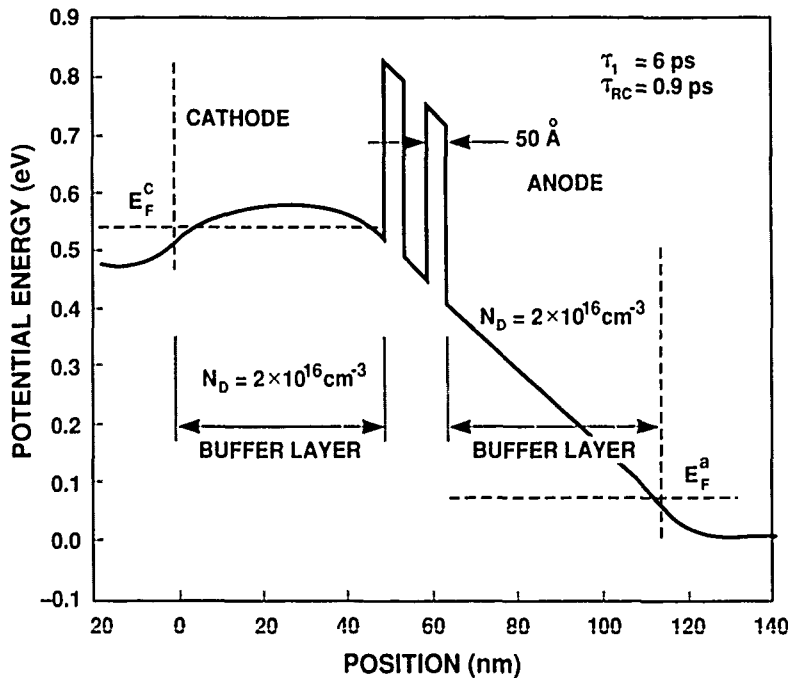


Fig. 2. Band-bending diagram of the double-barrier structure used to make diodes in which the quasibound-state lifetime, $\tau_1 = 6$ ps, is significantly longer than the RC time constant $\tau_{RC} = 0.9$ ps.

$\text{Al}_{0.42}\text{Ga}_{0.58}\text{As}$ barriers separated by a 5.1-nm-thick GaAs quantum well. Outside of each barrier is a 50-nm-thick buffer layer with doping $N_D = 2 \times 10^{16} \text{ cm}^{-3}$, and n^+ epilayers that extend beyond each buffer layer to the substrate and to the top contact. The band bending displayed in Fig. 2 is obtained from a numerical solution to Poisson's equation for a total bias voltage of 0.45 V, the peak of the experimental I-V curve shown in Fig. 3.

The band diagram is used to estimate two of the parameters needed for the calculation of ω_{RCL} . The differential capacitance is obtained from the expression dQ/dV where Q is the space charge on either side of the double-barrier structure. It is found that $C = 77 \text{ fF}$ for an 8- μm -diameter diode at the peak bias voltage. The quasibound-state lifetime is found from the transmission probability function, which results from a numerical solution to Schrödinger's equation in the effective-mass approximation. It is found that $\tau_1 = 6.0 \text{ ps}$ at the peak bias voltage. To demonstrate that the transmission probability function is accurate, we have applied it to the calculation of the dc current. This is carried out with the stationary-state tunneling

formalism [4], and the results for an 8- μm -diameter device at room temperature are shown in Fig. 3. The experimental and theoretical peak currents differ by only about 35%. Since τ_1 and τ_{RC} will be shown below to differ by almost a factor of seven, this accuracy is sufficient to confirm the effect of the quantum-well inductance.

Although the stationary-state formalism provides satisfactory agreement with measured peak current, it poorly predicts the differential conductance in the middle of the NDC region because it greatly underestimates the valley-current density. Thus we obtain G from a phenomenological fit to the experimental I-V curve [1], as shown in Fig. 3. The final parameter that we require for calculating ω_{RCL} is the series resistance. Because of the number and complexity of the components of R_s , we elected to determine this parameter experimentally. It was extracted from a value of the one-port reflection coefficient that was measured by a network analyzer at a bias voltage just above the valley point. A minimum value of $R_s = 5 \Omega$ was obtained for a number of different diodes. This leads to $f_{\text{RC}} = 177 \text{ GHz}$ ($\tau_{\text{RC}} = 0.9 \text{ ps}$), and

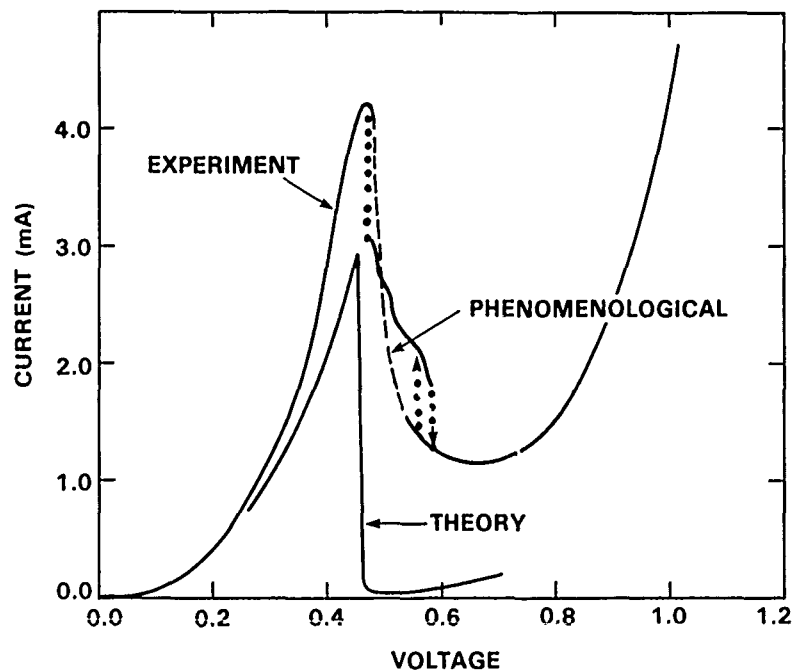


Fig. 3. Experimental, theoretical and phenomenological (dashed) I-V curves for an 8- μm -diameter diode at room temperature. The dotted regions of the experimental curves denote switching behavior.

$f_{RCL} = (2\pi)^{-1}\omega_{RCL} = 51$ GHz. The negative conductance used for this calculation, $G = -48$ mS, is the maximum magnitude and occurs near the center of the NDC region in the phenomenological curve. Implicit in this calculation is that C and τ_1 are constant throughout the entire NDC region, which is a reasonable supposition insofar as both of these parameters vary slowly with bias voltage.

OSCILLATION RESULTS

The experimental oscillation results for an 8- μ m-diameter diode are given in Fig. 4. Each point represents the maximum power measured as a function of bias voltage in one of several resonators spanning the frequency range from about 1 to 40 GHz. The highest-frequency oscillation was 38 GHz and the measured power at this point was about 1 μ W. Notice that the line connecting the measured data points falls toward zero well below f_{RC} . The observed rolloff is obviously more consistent with the value $f_{RCL} = 51$ GHz predicted by the new equivalent circuit. This circuit has recently

been generalized to apply under large-signal conditions, so that theoretical estimations of maximum oscillation power can be made [6]. The results for the present diode are shown in Fig. 4. Again, the new RCL circuit model yields much better agreement with experiment than the RC circuit model. This comparison also indicates that at the lowest frequencies the double-barrier diode generates an absolute power within about 50% of the theoretically-expected value. Before concluding, it is important to mention that the observed rolloff behavior could also be explained with no inductance (i.e., $L_{QW} = 0$) and a larger value of series resistance $R_S \approx 18 \Omega$, which could occur if the quality of the top ohmic contacts were poor. However, in the present experiment an $R_S = 5 \Omega$ was measured for the same diode that oscillated up to 38 GHz.

In summary, a new equivalent circuit has been derived for the resonant-tunneling diode, and it has been used to satisfactorily predict the maximum oscillation frequency of a double-barrier device. The novel feature of the new circuit is a "quantum-well inductance" that represents the temporal delay

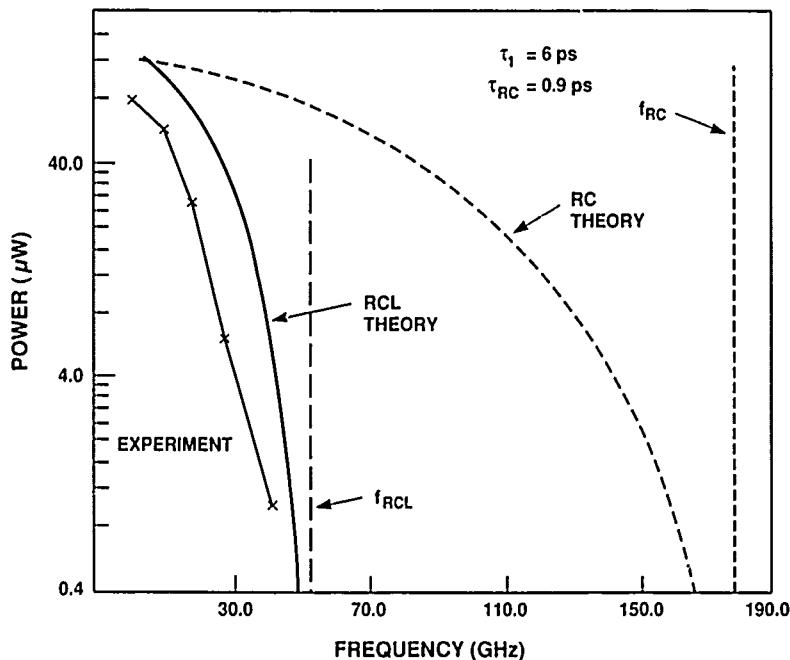


Fig. 4. Comparison of experimental and theoretical oscillation power versus frequency for an 8- μ m-diameter double-barrier diode. The vertical dashed lines denote the maximum oscillation frequencies f_{RC} and f_{RCL} according to the lumped-element RC and RCL circuit models, respectively.

associated with the charging time of the quasibound level of the quantum well. This effect should apply to all resonant-tunneling devices including multiple-barrier superlattice diodes and double-barrier transistors. It should also influence the speed of resonant-tunneling switches, but the analysis given here is not suitable for predicting the actual switching speed since it does not apply near the peak or valley regions of the I-V curve.

ACKNOWLEDGMENTS

We thank C.L. Chen and K.M. Molvar for assistance in fabrication, and L. Cociani for aid in network analysis. We gratefully acknowledge A.L. McWhorter and R.A. Murphy for useful comments on the manuscript. This work was supported by the Air Force Office of Scientific Research, the U.S. Army Research Office, and by NASA.

REFERENCES

- [1] E.R. Brown, W.D. Goodhue and T.C.L.G. Sollner, *J. Appl. Phys.* **64**, 1519 (1988).
- [2] J.F. Whitaker, G.A. Mourou, T.C.L.G. Sollner and W.D. Goodhue, *Appl. Phys. Lett.* **53**, 385 (1988).
- [3] S.K. Diamond, E. Ozbay, M.J.W. Rodwell, D.M. Bloom, Y.C. Pao and J.S. Harris, *Appl. Phys. Lett.* **54**, 153 (1989).
- [4] R. Tsu and L. Esaki, *Appl. Phys. Lett.* **22**, 562 (1973).
- [5] L.I. Schiff, *Quantum Mechanics*, 3rd ed. (McGraw-Hill, New York, 1968), p. 292.
- [6] E.R. Brown, C.D. Parker and T.C.L.G. Sollner, *Appl. Phys. Lett.* **54**, 943 (1989).

Electric-Field Dependence of the Tunneling Escape Time of Electrons from a Quantum Well

T. B. Norris*

*Laboratory for Laser Energetics and Department of Physics and Astronomy,
University of Rochester, 250 E. River Road, Rochester, New York 14623*

X. J. Song, G. Wicks, W. J. Schaff, and J. Eastman

The School of Electrical Engineering, Cornell University, Ithaca, New York 14850

G. A. Mourou*

Laboratory for Laser Energetics, University of Rochester, Rochester, New York 14623

ABSTRACT

Using time-resolved photoluminescence we have directly measured the rate at which electrons tunnel from a quantum well through a thin barrier in the presence of an applied electric field.

Tunneling of electrons through thin barriers in semiconductor heterostructures is usually studied via the tunnel current through multiple barrier structures.[1,2] Time-resolved photoluminescence has also been used to investigate the tunneling escape rate of an electron from a quantum well (QW) bounded on each

side by a thin barrier.[3] We have applied the same technique to investigate the electric field dependence of this tunneling.[4]

The sample nominally consisted of a single 30 Å GaAs QW bounded on the top by a thick $\text{Al}_x\text{Ga}_{1-x}\text{As}$ barrier and on the bottom by a thin barrier, as shown in Fig. 1. The thickness b of this barrier was set so that the tunneling decay time would be between the recombination time (subnanosecond) and the experimental temporal resolution (20 ps). The samples studied in the experiments reported here had barrier width $b=85, 111, \text{ and } 121 \text{ Å}$ for Al composition $x=0.3$, and $x=0.38$ and 0.5 for $b=86 \text{ Å}$. The tunneling structure was situated in the intrinsic region of a p-i-n diode so that the effect of an electric field applied along the growth direction could be studied. The samples were held in a cryostat at a temperature of 6 K.

Electron-heavy-hole pairs were generated in the QW by a picosecond pulse from a synchronously pumped dye laser. The QW photoluminescence was filtered by a monochromator and detected with a synchroscan streak camera. The luminescence decay was fitted by a single exponential; the decay time versus electric field is shown in Fig. 2 for the set of samples with $x=0.3$, and in Fig. 3 for the set of samples with $b=86 \text{ Å}$.

The solid lines of Figs. 2 and 3 are from a simple semiclassical model. The tunneling time under flat band conditions is expressed as $\tau_T(0)=(vT)^{-1}$, where v is the oscillation frequency of the electron in the well, and T is the transmission coefficient of the barrier. We find that for the $x=0.3$ samples $\tau_T(0)=809, 277, \text{ and } 17 \text{ ps}$ for $b=121, 111, \text{ and } 85 \text{ Å}$ respectively. For the $b=86 \text{ Å}$

| | | |
|-------|---------------------------------------|-----------------|
| p^+ | $\text{Al}_x\text{Ga}_{1-x}\text{As}$ | 2000 Å |
| i | $\text{Al}_x\text{Ga}_{1-x}\text{As}$ | 2000 Å |
| i | GaAs | 30 Å |
| i | $\text{Al}_x\text{Ga}_{1-x}\text{As}$ | b |
| i | GaAs | 1000 Å |
| n^+ | GaAs | 1 μm |

S.I. Substrate

Figure 1. Sample structure used in this study.

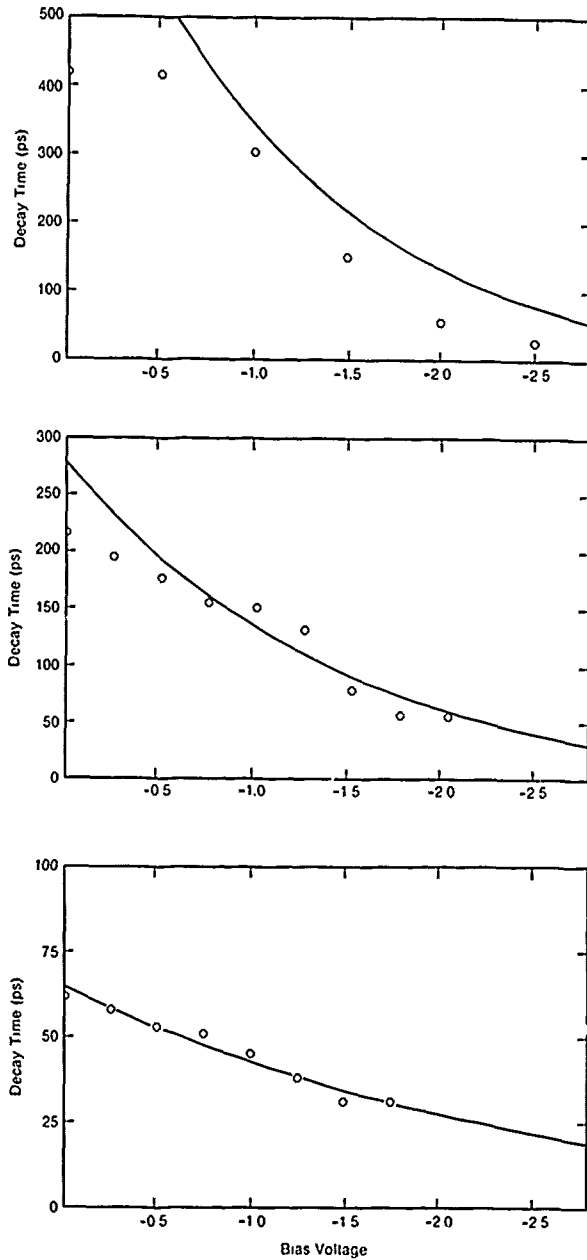


Figure 2. Luminescence decay rate versus applied bias for samples with Al composition $x=0.3$ for barrier widths (a) 121 Å, (b) 111 Å, and (c) 85 Å.

samples, $\tau_T(0) = 143$ ps and 3.4 ns for $x=0.38$ and 0.5, respectively. The field dependence is expressed as

$$\tau = c \exp \left(\frac{2}{\hbar} \int_0^b \sqrt{2m(V-E-eFz)} dz \right)$$

where b is the barrier thickness, F is the field, and c is a constant obtained from the tunneling time at zero field.

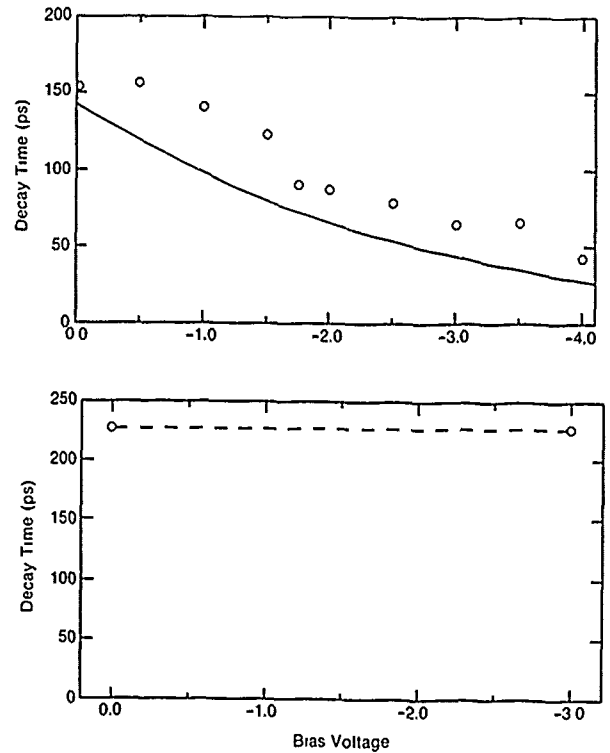


Figure 3. Luminescence decay rate versus applied bias for samples with barrier width $b = 86$ Å and Al composition (a) $x = 0.38$, and (b) $x = 0.5$.

The agreement with experiment is reasonably good, except for the 85 Å barrier zero-field decay time.

Therefore we have plotted that theoretical curve with $\tau_T(0) = 65$ ps. For the sample with $b = 86$ Å and $x = 0.5$, the tunneling rate is much slower than the recombination rate, and the luminescence decay time is expected to be independent of the applied bias, consistent with experimental results. Evidently the field-dependence of the tunneling rate is properly given by the expression above. It is important to note that it is extremely difficult to fit the data quantitatively because small variations in the assumed sample parameters will result in large differences in the calculated tunneling rate, due to the exponential dependence of the rate on the barrier height, thickness, and effective mass.

We have also measured the Stark shift of the luminescence line versus applied field. We found that the luminescence peak shifts to the blue with applied field for all samples which displayed tunneling. This blue shift reached a maximum of about 3 meV for fields in the range $2-4 \times 10^4$ V/cm. The origin of this effect is not presently understood.

In conclusion, we have directly observed the tunneling escape of electrons from a quantum well through a thin barrier in the presence of an electric field,

and have found reasonable agreement with a simple theory. The results of this experiment are particularly relevant for the complete understanding of resonant tunneling diodes and other multiple-barrier structures.

ACKNOWLEDGMENT

This work was supported by the sponsors of the Laser Fusion Feasibility Project at the Laboratory for Laser Energetics and by the U.S. Air Force under contract F49620-87-C-0016.

*Dr. Norris is at the Department of Electrical Engineering and Computer Science and the Department of Applied Physics, University of Michigan, Ann Arbor, MI 48109-2122, and Thomson-CSF Laboratoire Central de Recherches, Domain de Corbeville, BP10,

Orsay, France. Dr. Mourou is at the Department of Electrical Engineering and Computer Science, University of Michigan, Ann Arbor, MI 48109-2122.

REFERENCES

1. T. C. L. G. Sollner, W.D. Goodhue, P. E. Tannenwald, C. D. Parker, and D. D. Peck, *Appl. Phys. Lett.* **43**, 588 (1983).
2. F. Capasso, K. Mohammed, and A. Y. Cho, *IEEE J. Quant. Electron.* **QE-22**, 1853 (1986) and references therein.
3. M. Tsuchiya, T. Matsusue, and H. Sakaki, *Phys. Rev. Lett.* **59**, 2356 (1987).
4. T. B. Norris, X. J. Song, W. J. Schaff, L. F. Eastman, G. W. Wicks, and G. A. Mourou, *Appl. Phys. Lett.* **54**, 60 (1989).

Electron Tunneling Time Measured by Photoluminescence Excitation Correlation Spectroscopy

M. K. Jackson, M. B. Johnson, D. H. Chow, J. Soderstrom, and T. C. McGill

*T. J. Watson, Sr., Laboratory of Applied Physics, California Institute of Technology,
Pasadena, California 91125*

C. W. Nieh

*Keck Laboratory of Materials Engineering, California Institute of Technology,
Pasadena, California 91125*

Abstract

The tunneling time for electrons to escape from the lowest quasi-bound state in the quantum wells of GaAs/AlAs/GaAs/AlAs/GaAs double-barrier heterostructures with barriers between 16 Å and 62 Å has been measured at 80 K using photoluminescence excitation correlation spectroscopy. The decay time for samples with barrier thicknesses from 16 Å (≈ 12 ps) to 34 Å (≈ 800 ps) depends exponentially on barrier thickness, in good agreement with calculations of electron tunneling time derived from the energy width of the resonance. Electron and heavy-hole carrier densities are observed to decay at the same rate, in contrast to resonance-width calculations that indicate that heavy-hole tunneling times should be much longer than those for electrons. Reasons for this observation are discussed. Similar measurements in biased structures showing negative differential resistance are described.

Introduction

The electrical properties of the double-barrier heterostructure (DBH) have been of great interest since its proposal by Tsu and Esaki.[1] The desire to characterize the high frequency behavior of the DBH stems from interest in its use as an oscillator[2] and as a switching element.[3,4] However, the time associated with the tunneling of electrons has been the subject of more than 20 years of discussion.[5-9] Experimental measurements of tunneling times have required the development of high-speed measurement techniques. Recently there have been several experimental studies of the temporal response of double barrier heterostructures. Whitaker and co-workers[10] have used electro-optic sampling mea-

surements to study a single tunnel device. Tsuchiya *et al.*[11] used the photoluminescence (PL) from carriers in the quasi-bound states in the quantum well to study the decay of the electron population in the quantum well as a function of the barrier thickness. Jackson *et al.*[12] used photoluminescence excitation correlation spectroscopy (PECS) to extend the results of Tsuchiya *et al.* to significantly shorter times.

In this paper, we report a study of the decay of photo-excited carriers in double-barrier heterostructures as a function of the thickness of the barrier layers. We have studied undoped DBH's with pure AlAs barriers ranging in thickness from 16 to 62 Å. We have also studied an undoped DBH with superlattice barriers, and a doped structure showing negative differential resistance.

Experimental Technique

The PECS experimental technique has been described previously.[13] A colliding pulse mode-locked ring dye laser is used to generate a train of pulses 200 fs full width at half maximum (FWHM), at a repetition frequency of 120 MHz. The laser output is centered at 6200 Å and has a spectral width of 20 Å FWHM. The pulse train is equally divided into two separate beams which are independently chopped at $f_1 = 1600$ and $f_2 = 2100$ Hz and delayed with respect to one another by time γ ($-500 \leq \gamma \leq 500$ ps) before being recombined and focused to a 25 μm diameter spot on the surface of the sample. The typical average power used was 1 mW per beam before chopping. The PL is spectrally resolved, and then detected by a GaAs photomultiplier tube (PMT). After amplification, the PMT signal is synchronously detected by a lockin amplifier at either the fundamental frequency f_1 or the sum frequency

$f_{\text{sum}} = f_1 + f_2$. All of the results reported here were taken with the sample temperature between 80 and 5 K.

In Fig. 1, we present a schematic diagram of the processes of excitation, tunneling from the well, and the radiative recombination of carriers within the well. Recent observations of the times for thermalization of electrons between subbands have given times less than 200 fs.[14] Hence, we will assume the thermalization of electrons and holes to the lowest subband to be fast compared to the times of interest here.

The information about the tunneling escape times for electrons and heavy holes is derived from the variation of the sum-frequency signal I_{sum} with delay γ . The sum-frequency signal is monitored at a wavelength corresponding to the lowest confined electron to heavy-hole transition. If the lowest-energy confined electron and heavy-hole carrier densities are n and p , respectively, then the photoluminescence detected by the PMT is $I_{\text{PL}} \propto \int np dt$, where the integration is over times long compared to the tunneling processes of interest here, but short compared to the chopping periods. Since the laser excitation is periodic with period T_{rep} it is natural to consider $I_{\text{sum}}(\gamma)$ in terms of the integrated photoluminescence detected in one period T_{rep} . We assume that each optical pulse creates an equal density g of electron and holes. The optical generation function is then given by

$$G_{\text{chop}}(t, \gamma) = g \sum_m [S_{f_1}(t)\delta(t - mT_{\text{rep}}) + S_{f_2}(t)\delta(t - \gamma - mT_{\text{rep}})],$$

where $S_{f_1}(t)$ and $S_{f_2}(t)$ are unit amplitude square waves at the chopping frequencies f_1 and f_2 , respectively. Because of this chopping, during the

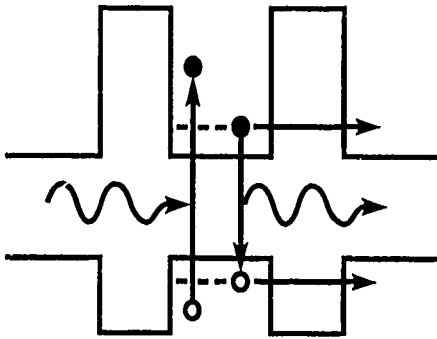


Figure 1. Schematic diagram of relevant carrier processes involved in the double barrier samples during the experiment. Shown are photo-excitation of carriers in the well, tunneling of carriers out of the well, and recombination of carriers in the well. Used with permission from Ref. [12].

experiment the sample is exposed to zero, one, or two optical pulse trains at various times, depending upon the instantaneous values of $S_{f_1}(t)$ and $S_{f_2}(t)$. To allow calculation of the expected sum-frequency signal, $I_{\text{sum}}(\gamma)$ can be simply expressed in terms of the integrated PL detected in these three cases. We can express the integrated PL detected in one period in the form of a truth table as:

| $I_{\text{PL}}(S_{f_1}(t), S_{f_2}(t)):$ | | $S_{f_1}(t)$ | |
|--|---|--------------|---------------|
| | | 0 | 1 |
| $S_{f_2}(t)$ | 0 | 0 | I_1 |
| | 1 | I_1 | $I_2(\gamma)$ |

By considering the component of the PL response at the sum chopping frequency, it can be shown that $I_{\text{sum}}(\gamma)$ is simply given by

$$I_{\text{sum}}(\gamma) \propto [I_2(\gamma) - 2I_1]. \quad (1)$$

In Eq. (1), $I_1 = \int_0^{T_{\text{rep}}} np dt$ is the integrated PL corresponding to the unchopped one-pulse-train optical generation function

$$G_1(t) = g \sum_m \delta(t - mT_{\text{rep}}).$$

Similarly, $I_2(\gamma) = \int_0^{T_{\text{rep}}} np dt$ is the integrated PL corresponding to the unchopped two-pulse-train optical generation function

$$G_2(t, \gamma) = g \sum_m [\delta(t - mT_{\text{rep}}) + \delta(t - \gamma - mT_{\text{rep}})].$$

Eq. (1) is completely general, depending only on the nature of the synchronous detection, and allows the calculation of the sum-frequency signal in any case in which the populations $n(t)$ and $p(t)$ are known. For our case, considering radiative recombination and tunneling, the evolution of the electron and hole populations in the quantum well is given by

$$\frac{dn}{dt} = -\frac{n}{\tau_e} - Bnp + G(t, \gamma), \quad (2a)$$

$$\frac{dp}{dt} = -\frac{p}{\tau_{hh}} - Bnp + G(t, \gamma). \quad (2b)$$

In Eqs. (2), B is a constant giving the strength of the radiative recombination, and $G(t, \gamma)$ is the appropriate optical generation function. The two times τ_e and τ_{hh} are the tunneling decay times for the electrons and heavy holes, respectively. In the

general case Eqs. (2) can be solved numerically for the case $G(t, \gamma) = G_1(t)$ to get I_1 , and for $G(t, \gamma) = G_2(t, \gamma)$ to get $I_2(\gamma)$. Then Eq. (1) is used to find $I_{\text{sum}}(\gamma)$. In the simpler case where the electron and hole populations created by an optical pulse are $n_i(t)$ and $p_i(t)$, the populations created by two optical pulses are independent, and $n_i(T_{\text{rep}})$ and $p_i(T_{\text{rep}})$ are small compared to g , the sum frequency signal is proportional to the cross correlation[13]

$$I_{\text{sum}}(\gamma) \propto \int_0^{T_{\text{rep}}} [n_i(t)p_i(t-\gamma) + n_i(t-\gamma)p_i(t)] dt.$$

This signal is due to the recombination of electrons created by the first pulse with holes created by the second pulse, and vice versa. In the tunneling-dominated case, the electron and heavy-hole densities decay exponentially with time constants τ_e and τ_{hh} , respectively, and the sum frequency signal is proportional to the sum of two exponentials

$$I_{\text{sum}}(\gamma) \propto [\exp(-|\gamma|/\tau_e) + \exp(-|\gamma|/\tau_{hh})]. \quad (3)$$

In the radiative-recombination dominated case, the sum frequency signal is zero.[13] To determine the applicability of Eq. (3) to the intermediate region between the radiative-recombination-dominated and tunneling-dominated cases, equations (1) and (2) have been numerically integrated for various values of τ_e , τ_{hh} , and B . It was found that in the case of a recombination-dominated case, where $\tau_e \gg T_{\text{rep}}$ and $\tau_{hh} \gg T_{\text{rep}}$, that the sum frequency signal is a constant, independent of delay, γ . Thus in the case where tunneling becomes negligible, we do not expect to see $I_{\text{sum}}(\gamma)$ decay with the radiative lifetime, but rather with the shortest non-radiative lifetime in the problem. In the case where $\tau_e \ll T_{\text{rep}}$ and $\tau_{hh} \ll T_{\text{rep}}$, it was also found that even when radiative recombination significantly affects the evolution of the populations, and the problem is not tunneling dominated, Eq. (3) closely approximates the exact solution. It does not become inaccurate until the radiative recombination time becomes much shorter than the tunneling times τ_e and τ_{hh} . Thus we have used equation (3) as the basis for interpreting our data.

Undoped Structures

Double-barrier heterostructures were grown on (100) GaAs substrates by molecular beam epitaxy in a Perkin-Elmer 430 system at 600°C. After growth of 0.5 μm of GaAs, a superlattice buffer layer consisting of 5 periods of (50 Å $\text{Al}_{0.35}\text{Ga}_{0.65}\text{As}$, 500 Å GaAs) was grown. This was followed by growth of a 0.7 μm layer of GaAs, which provided a high quality layer on which to grow the DBH, and eliminated any

optical effects from the superlattice. Then a symmetrical GaAs/AlAs/GaAs/AlAs/GaAs DBH was grown, with a well thickness of 58 Å. The final layer was a 300 Å GaAs cap. All layers were nominally undoped with an estimated residual carbon acceptor concentration of 10^{14}cm^{-3} . Seven samples were studied, with bulk growth rate information predicting barrier thicknesses of 16, 22, 28, 34, 34, 48, and 62 Å. High resolution transmission electron microscopy confirmed the barrier thicknesses of the 16 Å sample and one of the 34 Å samples, within an uncertainty of 2 monolayers. We estimate an uncertainty in barrier thickness of 2 monolayers for all of the samples. One undoped superlattice-barrier sample was grown on a 0.5 μm undoped GaAs buffer grown directly on the GaAs substrate, and had a GaAs well of width 49 Å. The barriers were superlattice barriers each composed of three 8.5 Å AlAs layers, separated by two 8.5 Å GaAs layers. Again, the final layer was a 300 Å GaAs cap. This structure corresponds to the doped structure reported [15] to have a peak-to-valley ratio of 21.7 at 77 K, the highest reported value for a pure GaAs/AlAs heterostructure.

In Fig. 2, we present typical photoluminescence spectra taken at 80 K at the fundamental and sum chopping frequencies, for the 28 Å barrier sample. The spectrum at the fundamental frequency consists of a single distinguishable feature centered at 7650 Å. The wavelength of the feature in the fundamental frequency spectrum is in approximate agreement with the calculated position of 7730 Å for the transition from the lowest electron subband to

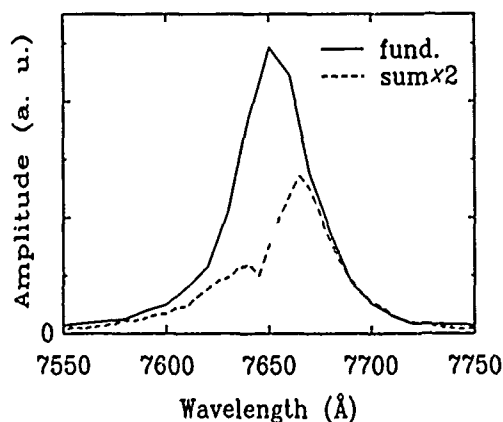


Figure 2. Typical excitation correlated luminescence for 28 Å barrier sample at 80 K. Shown are luminescence signals at the fundamental chopping frequency (solid line) and the sum frequency (dashed line). Both scans were taken with delay $\gamma = 0$. The sum frequency spectrum has been multiplied by 2.

the lowest heavy-hole subband in a 58 Å quantum well. The peak of the corresponding feature in the sum frequency spectrum is shifted slightly to longer wavelengths.

In Fig. 3, we present a semilogarithmic plot of a typical scan of the photoluminescence at the sum chopping frequency as a function of the time delay γ between the two pulses. The scan was taken at 80 K and at a wavelength of 7665 Å, the peak of the sum PL spectrum shown in Fig. 2. This delay scan consists of a peak at zero delay with wings extending to much longer times. The single point at $\gamma=0$ is a coherence peak due to the optical interference of the two incident pulses on the sample, and is not resolved in this scan. A single exponential fits the wings in the sum frequency delay scan shown in Fig. 3. Fits to this sum frequency delay data using a single exponential are shown as dashed lines in Fig. 3. The coherence peak is not included in fitting the delay scans.

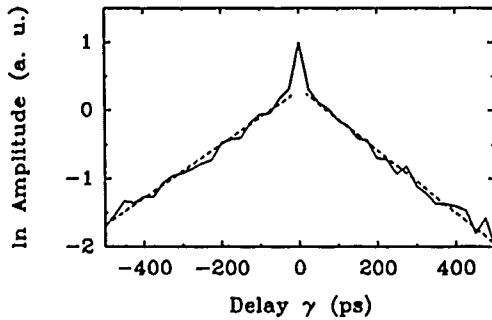


Figure 3. Semilogarithmic plot of the variation of the sum-frequency luminescence signal (solid line) with delay γ . The temperature is 80 K, and the sample is the same as in Fig. 2. The scan was taken at 7665 Å, the peak of the sum frequency spectrum. The coherence peak at $\gamma=0$ is not resolved in this scan. The dashed lines are the fits discussed in the text, which give a decay time of 236 ± 20 ps. Used with permission from Ref. [12].

In Fig. 4, we have plotted the exponential decay time at 80 K as a function of barrier thickness for the seven samples described above. The decay time depends exponentially on barrier thickness for barriers up to approximately 34 Å. Over this range of exponential dependence the decay time varies by two orders of magnitude. For thicker barriers the decay time seems to approach a value that is independent of the barrier thickness, which may be some nonradiative lifetime unrelated to tunneling. Due to the 120 MHz repetition rate of the excitation pulses, and the -500 to 500 ps range for the delay, γ , there is an upper limit on the order of 2 ns to the decay times that can be measured ac-

curately with our technique. Consequently, the result for the sample with a barrier thickness of 62 Å should be viewed with some caution. Our measured decay times are about a factor of 4 longer than those of Tsuchiya *et al.*[11]. The decay time for the superlattice-barrier structure was 350 ± 60 ps at 80 K.

In Fig. 4, we have also plotted the times calculated for electrons, heavy holes, and light holes to tunnel out of the quantum well. The solid, dashed, and dot-dashed lines are the electron, heavy-hole, and light-hole tunneling times, respectively. From Ref. [7] the time for a particle to tunnel out of a quasi-bound state in the quantum well is related to the energy width of the corresponding resonance in the transmission probability by $\tau = \hbar / \Delta E_{\text{FWHM}}$. The transmission probability is calculated using the transfer matrix approach of Kane,[16] modified to account for the different effective masses of the particle in the quantum well and in the barrier.

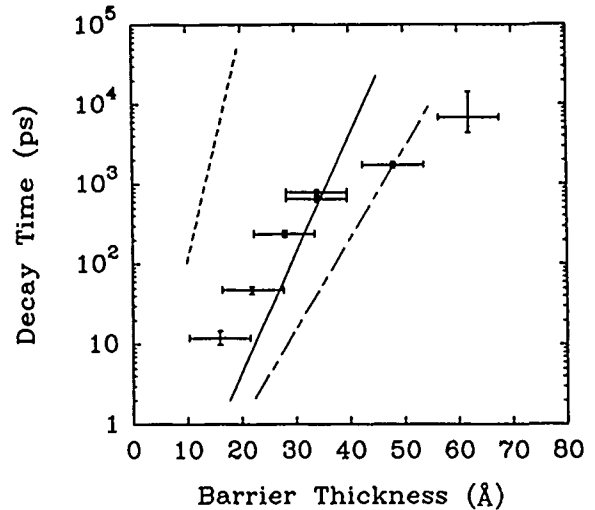


Figure 4. Measured decay times at 80 K as a function of barrier thickness. The data points are the measured decay times, with error bars on the thickness based on uncertainty in the barrier thickness and error bars on the decay times from uncertainties in the fits to the delay scans. The solid, dashed, and dot-dashed lines are the electron, heavy-hole, and light-hole tunneling times, respectively, calculated from the widths of the lowest-energy transmission resonances.

For electrons, we have considered only Γ -point barriers. It is appropriate to use a simple one-band expression for the wavevector in the well, $k = (2m_w^* m_e E / \hbar^2)^{1/2}$, where m_w^* is the effective mass in the GaAs well, m_e is the free electron mass, and E is the energy of the particle with respect to the GaAs band edge. However, with the pure AlAs bar-

riers in our samples, the lowest quasi-bound electron state has an energy far from the band edge in the AlAs barriers, and the one-band model overestimates the wavevector in the barriers. Thus we have used a two-band model[17] to calculate the electron wavevector in the barriers. The barrier height used in these calculations was 1.07 eV, corresponding to a valence band offset of 0.55 eV,[18] and an AlAs band gap of 3.13 eV. The effective masses in the well and the barriers were taken to be $0.067m_e$ and $0.15m_e$, respectively.[19] For the light holes, we also use a two-band model for the barrier wavevector, and for the heavy holes, we use a one-band expression to estimate the wavevector in the barriers. From the theoretical curves in Fig. 4, we can see that the tunneling time for electrons is much shorter than that for heavy holes, and the light-hole tunneling time is shorter than that for the electrons.

Comparing these theoretical estimates of the tunneling times with the decay times observed experimentally, we note that the decay times agree well with the tunneling time of the electrons. In contrast, if we expected Eq. (3) to explain the data, then we should observe two decay times, a short one near zero delay and a longer time at much longer delays. We might expect the longer decay time to be that for the heavy holes. There are a number of phenomena that could contribute to the observation of a single time that is close to the electron tunneling time. The first is the mixing of the light-hole and heavy-hole bands due to confinement in the quantum well. The hole tunneling time calculations shown in Fig. 4 are appropriate for states at the zone center. However, for any finite population of holes, the heavy-hole band will be filled to some non-zero parallel wavevector, and for non-zero parallel wavevector, the confined heavy-hole states are composed of a mixture of bulk light-hole and heavy-hole wavefunctions. The estimated densities of electrons and heavy holes produced by each optical pulse in our experiment are of the order of 10^{11} cm^{-3} . By considering the effect of the finite occupation of the heavy-hole band to densities of the order of 10^{11} cm^{-3} , at a temperature of 80 K, calculations of the average tunneling time for heavy holes indicate that the times decrease drastically,[20] to times very close to the calculated electron tunneling times.

Another important effect is that of charge accumulation in the quantum well during photoexcitation. With differing decay rates for electrons and heavy holes, it is very likely that the quantum well becomes charged. Rapidly escaping electrons could leave slowly decaying holes behind. The areal densities of holes and electrons produced in our experiment are roughly 10^{11} cm^{-2} which are high compared to the background doping of 10^8 cm^{-2} . These areal densities produced by the photo-excitation

could result in very substantial amounts of band bending. First we would expect the potential across the barriers due to charging created by the differences in escape rates to increase the tunneling escape rate for holes. This effect would tend to make the electron and hole densities in the well follow each other and produce a decrease in the tunneling time for holes. Second, if we couple the finite spot size of the laser with the variations in decay rates, we might expect density gradients and electric fields to develop in the plane of the quantum wells. These density gradients and electric fields could act to make the hole density follow the electron density by inducing hole transport in the plane of the quantum well.

To attempt to see the heavy-hole zone-center tunneling time, the decay time was measured for the 28 Å sample, at temperatures from 80 to 5 K. The hole band-mixing effect is expected to be less pronounced for lower temperatures, and lower carrier densities, and the long lifetime of the zone-center heavy holes may be observable under such conditions. The laser power for this experiment was reduced to an average power per beam of 0.3 mW (80 W/cm^2) before chopping, and one measurement was taken at 5 K at an average power per beam of 0.16 mW (80 W/cm^2). The laser pulsewidth for these measurements was 300 fs FWHM. Over this range the sum-frequency signal dependence on delay was exponential, with a single decay time, and the decay time increased slightly with decreasing temperature. The failure to observe the long zone-center heavy-hole tunneling time may be attributable to the large excess energy per photoexcited carrier created by the CPM laser excitation at 2 eV. This results in carriers that have initial temperatures well in excess of the lattice temperature, and which may dominate any effect of changing the sample temperature. The observation of the long zone-center heavy-hole tunneling time may be possible using a tunable pulsed laser source operated at an energy to create carriers with low excess energy.

A detailed understanding of the escape of the photo-excited holes from the quantum well is important to understand the results of all of the measurements reported to date that are based on optical excitation. In particular, the tacit assumption made in previous photoexcitation studies of such structures that heavy-hole escape from the quantum well is a slow process leads one to conclude that enormous densities of holes are accumulated in the quantum well of the DBH. From our observations, we conclude that heavy holes escape rapidly from the quantum well, at the same rate as electrons, providing evidence that heavy-hole escape from the quantum well is not a slow process.

Biased Structures

As the double barrier heterostructure's application is in electrical circuits where it is normally operated in the negative differential resistance (NDR) region, it is of interest to measure the speed of the device under electrical bias. The dependence of tunneling escape time from a quantum well under the influence of an electrical bias has recently been reported by Norris *et al.*[21] However, these experiments were performed on samples that did not show NDR. In order to attempt to measure the tunneling escape time in a device showing NDR, operating with significant tunneling flow of current, a doped structure was grown. The sample was grown on an n^+ GaAs substrate. After growth of $0.5\mu\text{m}$ of n^+ GaAs, 500 \AA of lightly n -doped GaAs, and a 25 \AA undoped GaAs spacer layer were grown. This was followed by 34 \AA AlAs, 58 \AA GaAs, and 34 \AA AlAs barrier, well, and barrier layers. Then another 25 \AA undoped GaAs spacer layer, 275 \AA of lightly n -doped GaAs, and 300 \AA of n^+ GaAs were grown. The n^+ doping was $5 \times 10^{18}\text{ cm}^{-3}$, and the n -type doping was $2 \times 10^{16}\text{ cm}^{-3}$. A 60 \AA layer of Au/Ge was evaporated to form the top contact, and mesas were etched. The bottom of the substrate was used as the back contact. Wire bonds were made to the top of the mesas, which varied from 150 to $250\mu\text{m}$ in diameter. The current-voltage characteristics of a $250\mu\text{m}$ device is shown in Fig. 5 for reverse biases, corresponding to flow of electrons into the top

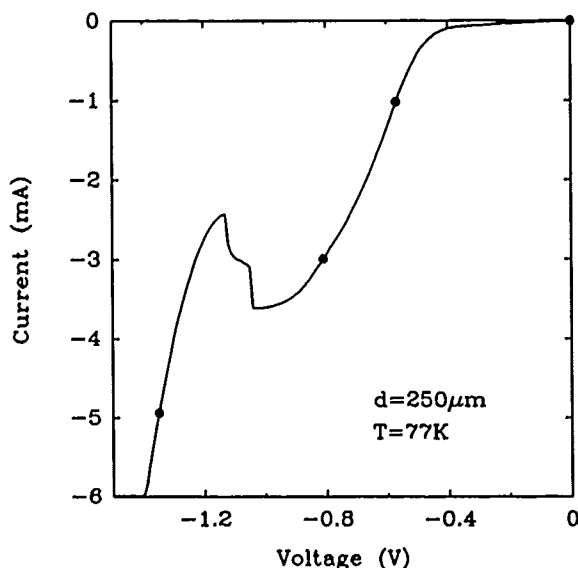


Figure 5. Current-voltage characteristic for $250\mu\text{m}$ diameter mesa sample. Negative bias corresponds to the flow of electrons into the top of the mesa. The solid circles indicate the electrical biases at which photoluminescence decay time measurements were made.

contact. This device only shows NDR in reverse bias, but others show NDR in both forward and reverse bias, indicating that the top metal contact is behaving as an ohmic contact.

To make the photoluminescence measurement under electrical bias, the laser spot was focused on an area of the mesa not obscured by the wire bond. Electrical bias was provided by a constant-current source, and decay-time measurements were made at biases of 0 , -1 , -3 , and -5 mA , indicated by the solid circles in Fig. 5. At zero bias we observe a decay time of the order of 1 ns , comparable to that observed in the undoped DBH with the same 34 \AA barriers. At -1 , -3 , and -5 mA , the sum-frequency signal is constant with delay, showing no appreciable decay over the -500 to 500 ps range of delay time available. This absence of any decay in the presence of an electric field and in the presence of current flow may be due to the flow of photo-generated carriers created in the electrodes into the quantum well.

Conclusions

In summary, the tunneling time for electrons to escape from the lowest quasi-bound state in the quantum wells of GaAs/AlAs/GaAs/AlAs/GaAs double-barrier heterostructures has been measured at 80 K using photoluminescence excitation correlation spectroscopy (PECS). Results are in good agreement with calculations of electron tunneling time based on the energy width of the resonance in the transmission coefficient. The electrons and heavy holes are observed to escape at the same rate, indicating a link between the two escape processes. The role of tunneling escape of photo-excited holes in such structures is important to understand the results of photo-excited measurements of tunneling escape times.

Acknowledgments

The authors would like to thank E. Yu, R. Miles, Y. Rajakarunanayake, D. Ting, and A. T. Hunter for helpful discussions. This work was supported in part by the Office of Naval Research under contract No. N00014-84-K-0501, the Defense Advanced Research Projects Agency under contract No. N00014-84-C-0083, and the National Science Foundation under grant No. NMR8421119. Two of us (MKJ and DHC) would like to acknowledge financial support from the Natural Sciences and Engineering Research Council of Canada, and International Business Machines Corporation, respectively.

M. B. Johnson is presently at: IBM T. J. Watson Research Center, Yorktown Heights, NY 10598.

References

1. R. Tsu and L. Esaki, "Tunneling in a finite superlattice," *Appl. Phys. Lett.* **22**, 562 (1973).
2. T. C. L. G. Sollner, W. D. Goodhue, P. E. Tanenwald, C. D. Parker, and D. D. Peck, "Resonant tunneling through quantum wells at frequencies up to 2.5 THz," *Appl. Phys. Lett.* **43**, 588 (1983).
3. T. K. Woodward, T. C. McGill, H. F. Chung, and R. D. Burnham, "Applications of Resonant-Tunneling Field-Effect Transistors," *IEEE Electron Device Lett.* **9**, 122 (1988).
4. F. Capasso, K. Mohammed, and A. Y. Cho, "Resonant Tunneling Through Double Barriers, Perpendicular Quantum Transport Phenomena in Superlattices, and Their Device Applications," *IEEE J. Quantum Electron.* **QE-22**, 1853 (1986).
5. K. K. Thornber, T. C. McGill, and C. A. Mead, "The Tunneling Time of an Electron," *J. Appl. Phys.* **38**, 2384 (1967).
6. M. Büttiker and R. Landauer, "Traversal Time for Tunneling," *Phys. Rev. Lett.* **49**, 1739 (1982).
7. N. Harada and S. Kuroda, "Lifetime of Resonant State in a Resonant Tunneling System," *Jpn. J. Appl. Phys. Pt. 2* **25**, L871 (1986).
8. S. Collins, D. Lowe, and J. R. Barker, "The quantum mechanical tunnelling time problem - revisited," *J. Phys. C* **20**, 6213 (1987).
9. H. Guo, K. Diff, G. Neofotistos, and J. D. Guntton, "Time-dependent investigation of the resonant tunneling in a double-barrier quantum well," *Appl. Phys. Lett.* **53**, 131 (1988).
10. J. F. Whitaker, G. A. Mourou, T. C. L. G. Sollner, and W. D. Goodhue, "Picosecond switching time measurement of a resonant tunneling diode," *Appl. Phys. Lett.* **53**, 385 (1988).
11. M. Tsuchiya, T. Matsusue, and H. Sakaki, "Tunneling Escape Rate of Electrons From Quantum Well in Double-Barrier Heterostructures," *Phys. Rev. Lett.* **59**, 2356 (1987).
12. M. K. Jackson, M. B. Johnson, D. H. Chow, T. C. McGill, and C. W. Nieh, "Electron tunneling time measured by photoluminescence excitation correlation spectroscopy," *Appl. Phys. Lett.* **54**, 552 (1989).
13. M. B. Johnson, T. C. McGill, and A. T. Hunter, "Picosecond time-resolved photoluminescence using picosecond excitation correlation spectroscopy," *J. Appl. Phys.* **63**, 2077 (1988).
14. K.-K. Choi, B. F. Levine, C. G. Bethea, J. Walker, and R. J. Malik, "Multiple quantum well 10 μm GaAs/Al_xGa_{1-x}As infrared detector with improved responsivity," *Appl. Phys. Lett.* **50**, 1814 (1987).
15. C. I. Huang, M. J. Paulus, C. A. Bozada, S. C. Dudley, K. R. Evans, C. E. Stutz, R. L. Jones, and M. E. Cheney, "AlGaAs/GaAs double barrier diodes with high peak-to-valley current ratio," *Appl. Phys. Lett.* **51**, 121 (1987).
16. E. O. Kane, "Basic Concepts of Tunneling," in *Tunneling Phenomena in Solids*, E. Burstein and S. Lundqvist, eds. (Plenum, New York, 1969) p. 1.
17. E. O. Kane, "The $\mathbf{k} \cdot \mathbf{p}$ Method," in *Physics of III-V Compounds*, Vol. 1, A. C. Beer and R. K. Willardson, eds. (Academic, New York, 1966), p. 75.
18. J. Batey and S. L. Wright "Energy band alignment in GaAs:(Al,Ga)As heterostructures: The dependence on alloy composition," *J. Appl. Phys.* **59**, 200 (1986).
19. S. Adachi "GaAs, AlAs, and Al_xGa_{1-x}As: Material parameters for use in research and device applications," *J. Appl. Phys.* **58**, R1 (1985).
20. E. T. Yu, M. K. Jackson, and T. C. McGill, "Hole tunneling times in GaAs/AlAs double barrier structures," to be published.
21. T. B. Norris, X. J. Song, W. J. Schaff, L. F. Eastman, G. Wicks, and G. A. Mourou, "Tunneling escape time of electrons from a quantum well under the influence of an electric field," *Appl. Phys. Lett.* **54**, 60 (1989).

Part 5
Transistors and Transport

Silicon FETs at 0.1- μ m Gate Length

G. A. Sai-Halasz

IBM Research Division, T. J. Watson Research Center, Yorktown Heights, New York 10598

Abstract

Results are being presented from a work aimed at demonstrating the feasibility of silicon FET technology in the 0.1 μ m gate length regime. Self-aligned, n-channel polysilicon gated MOSFETs were designed for operation at 77°K, with reduced power-supply levels. Noteworthy results of the exercise were: observing clear manifestation of velocity overshoot which resulted in extrinsic transconductance of over 940 μ S/ μ m at 0.07 μ m gate-length, measuring 13ps delay per stage in 0.1 μ m gate length ring oscillators, with simulations showing potential for below 5ps performance.

Introduction

Silicon (Si) FETs are the most common components of integrated electronics. Their fabrication process is the simplest, the material quality of silicon is superior to any other, and the power consumption of FETs is relatively low. Consequently, integration reached its highest levels by employing FET devices and circuits. However, Si FETs did not occupy such a prominent position in the arena of performance. For speed one looked for materials other than Si and devices different than FETs. The work to be presented here was partly aimed at demonstrating that Si FETs are not necessarily low performance components. FETs have a well established scaling path [1], which leads concomitantly to smaller dimensions and increased performance. Indeed, the past two decades have seen the relentless march of FET technology along the prescribed path. If FETs could stay on track, their performance eventually could

better that of other devices. Also, Si turns out to be a very attractive material for realistic high performance devices at the smallest dimensions and highest field strengths [2,3].

Whether the miniaturization process of Si FETs is approaching an end is the subject of much current interest. In the deeply submicron regime one faces a variety of nonscaling parameters and associated detrimental effects. Among others, these include mobility degradation, inversion-layer broadening, tunneling through the gate insulator, and in general the onset of velocity saturation. The technological difficulties like linewidth and alignment control, thin insulator reliability, shallow junction fabrication, the limitations of contact and spreading resistivities, and many others, can also stand in the path of improving performance. Although theoretical treatments abound on the perceived limits of Si FET technology, relatively little experimental work has been performed in the deeply submicron regime. In search for the scaling limits of FETs an investigation has been undertaken on the feasibility of FETs in the 0.1 μ m gate-length regime [4,5]. An overview of the work will be presented here, with emphasis on performance, showing that Si FETs can belong in the high speed arena.

Design and Fabrication

O₁ - voltage cannot be indefinitely decreased with dimensions because of non-scalable parameters and noise margins. As a result, one is forced to work with higher voltage levels than dictated by ideal scaling. This becomes most detrimental once performance saturates at less than the operating voltage, due to velocity saturation type characteristics. In

such an environment, higher voltage leads only to increased power consumption without an accompanying increase in performance. Thus the measure of a good design lies in achieving operation at the lowest feasible voltage. The requirement of low voltage operation naturally leads to a low temperature (LT), 77°K, design. At LT subthreshold conduction and threshold shifts due to temperature changes, are drastically reduced. Since these two effects are the main obstacles in lowering the threshold, and thus operating voltage, LT affords a design point which is not reachable at room temperature (RT). It is doubtful that any worthwhile RT design could be found for 0.1 μm gate length FETs. LT operation entails further advantages [6]: improved performance, mainly due to lower interconnect resistance, and better punch through behavior.

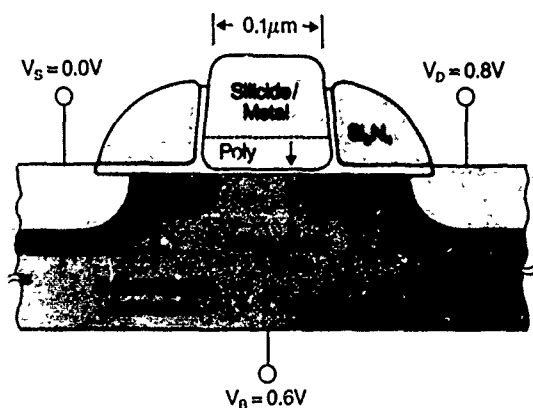


Figure 1. Schematic device cross section and bias levels.

The lowest threshold regarded to be practical even at LT was 150mV, the same as proposed for a 0.25 μm 77°K design [7]. This threshold value then leads to a 0.6-0.8V power supply voltage, (V_{dd}). In order to minimize geometry effects in short channel devices it is necessary to reduce depletion layer widths as much as possible. Such a reduction can be facilitated at 77°K by slightly forward biasing the junctions. In contrast to the RT case, at LT this forward bias does not necessarily cause unacceptable leakage. A reasonable compromise between the desire to reduce depletion layers and the detrimental effects of leakage, is an ~0.6V forward bias between the substrate and the sources.

As a first feasibility study at the 0.1 μm gate length level the efforts were directed toward NMOS. The basic device structure followed the source/drain (S/D) extension type device practiced earlier at 0.5 μm dimensions [8]. This device structure provides reduced geometry effects, low parasitic resistance

and allows for formation of self-aligned metal on the diffusions and gate. A schematic cross section of the device is shown on Fig. 1.

Seven different chips were assembled with a variety of test structures. Three of the chips contained inverter chains or ring oscillators (R/O), four chips housed various parametric test sites, like capacitors, very large devices, linewidth, alignment and bias monitors, contact and sheet-resistivity measurement sites. The test sites were typically repeated several times to give versions with different gate lengths at the design level. The actual fabricated gate lengths on the chips ranged from a maximum 0.275 μm down to a minimum of 0.07 μm . Fig. 2 shows the picture of one such chip. Fig. 3 shows an SEM micrograph of 0.07 μm long gates in an inverter, following the removal of metal and oxide.

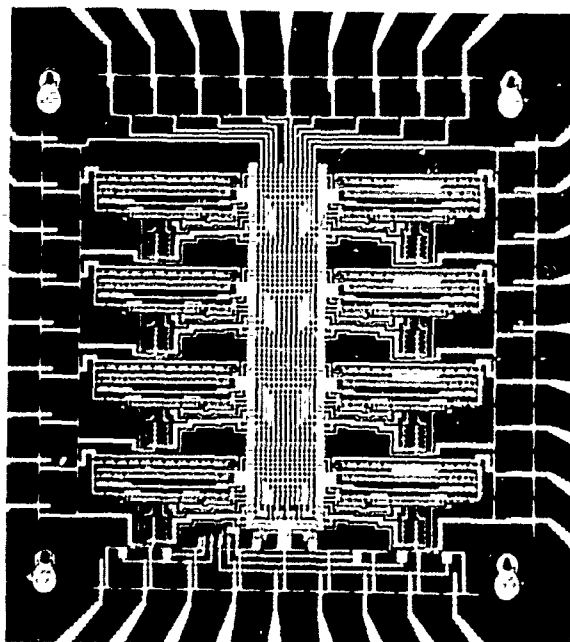


Figure 2. Chip containing ring oscillators. The various oscillators differ from each other gate length. The shortest gates are 0.07 μm long.

Five lithographic levels, including one for alignment, were all done by direct-write electron beam exposure. The scanning electron beam system, designed specifically for nanolithography, had a capability of a few tens of nm features, with an overall overlay accuracy of better than 30nm, inside a 0.25x0.25mm² field [9]. The work was partly directed toward exploring how far conventional processing techniques can be extended. Accordingly, an attempt was made to use well established process steps whenever possible. In this spirit a conventional semi-recessed oxide was used for device isolation. This type of isolation, however, allowed to scale the

ground rules of the diffusion level only to $0.25\mu\text{m}$ instead of $0.1\mu\text{m}$.



Figure 3. SEM micrograph of an inverter after stripping metal, interelectrode oxide, and semi-recessed isolation oxide. The spacers are made of Si_3N_4 .

Vertical scaling and doping levels were attempted to be fully consistent with a $0.1\mu\text{m}$ gate length. The exception was gate oxide, where for reliability reasons the thickness was increased to 3.3nm on one wafer and to 4.5nm on all others. Full scaling would have called for $\sim 2.5\text{nm}$ oxide thickness. The detailed processing steps, some of the reasons behind them, and the significant experimental variations can be found described elsewhere [4,5], only some of the more important features will be pointed out here. Much attention was paid to assure low S/D resistance. It was determined, borne out by measurements, that the S/D resistance is the single most important factor, more so than, for instance, low field mobility, in determining transconductance in the $0.1\mu\text{m}$ gate length regime. (When transconductance is mentioned, as such, the measured extrinsic value is meant without adjustment for parasitic effects.) To achieve low S/D resistance antimony was used in some of the S/D extensions, since for very shallow junctions antimony has advantages over arsenic [10]. Self-aligned silicidation turned out to be the processing step which was most difficult to execute with satisfactory results.

Approximately 75% of all-tested structures were operational. This percentage included some sites that depended on the operation of many devices, such as inverter chains and ring oscillators. Quite a few of

the structures, however, had higher than expected junction or gate leakage. Such leakages occurred in random fashion, independently of gate length. Considering the experimental nature of the work, which entailed no special provisions for cleanliness, such a yield could be considered quite satisfactory.

Not surprisingly, no "generic" $0.1\mu\text{m}$ device behavior was found. Extrinsic characteristics strongly depended on the processing variations introduced during fabrication. In order to show the fundamental device and circuit behavior at these dimensions as clearly as possible, all the results to be presented from now on were taken on a single wafer. In this manner fundamental properties, for instance, correlation of characteristics with gate length, are automatically separated from incidental ones, which are mainly due to processing details. This particular wafer had 4.5nm gate oxide, antimony S/D extensions, and self aligned titanium-silicide on the S/D and gate. Unless RT is specifically indicated, all data and discussion refer to LT. First, device behavior will be presented together with relevant parameters and evidence for velocity overshoot. In the following section circuit performance will be discussed.

Device Characteristics and Velocity Overshoot

Fig. 4 shows the LT terminal characteristics of the $0.07\mu\text{m}$ and $0.1\mu\text{m}$ gate-length devices.

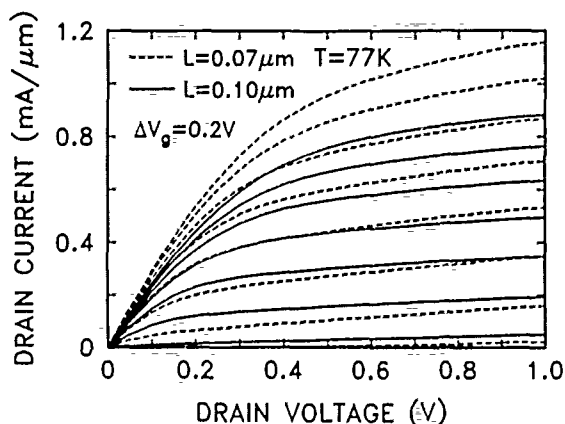


Figure 4. Device characteristics. Maximum V_G is 1.5V , substrate is biased at 0.6V . The $0.07\mu\text{m}$ device at $V_D = 1\text{V}$ has a maximum transconductance of over $940\mu\text{S}/\mu\text{m}$.

As can be seen the device characteristics are excellent, and it is also clear that transconductance is significantly improving with decreasing gate-length even at these dimensions.

The question of transconductance will be taken on later, first some of the important device parameters are being presented. A detailed discussion on the intrinsic parameter extraction can be found in [11], only the results are given here. At LT the total, source plus drain, resistance was found to be between 250 and 270 $\Omega \cdot \mu\text{m}$. Of this $\sim 200 \Omega \cdot \mu\text{m}$ was due to the S/D edges. The RT value was $\sim 440 \Omega \cdot \mu\text{m}$. However, the large difference between the RT and LT resistance was mainly due to the test sites, where thin metal lines were leading to large width-to-length ratio devices. At LT the metal resistance dropped sufficiently to have only a minor influence on the measurements. Without this spurious effect the RT S/D resistance would have been $\sim 20\%$ higher than the LT one. With $(V_G - V_T) = 0.6\text{V}$ gate bias, the low field mobilities were $720\text{cm}^2/\text{V} \cdot \text{sec}$ at LT, and $390\text{cm}^2/\text{V} \cdot \text{sec}$ at RT. V_G , V_D , and V_T have their usual meaning as the gate, drain, and threshold voltage.

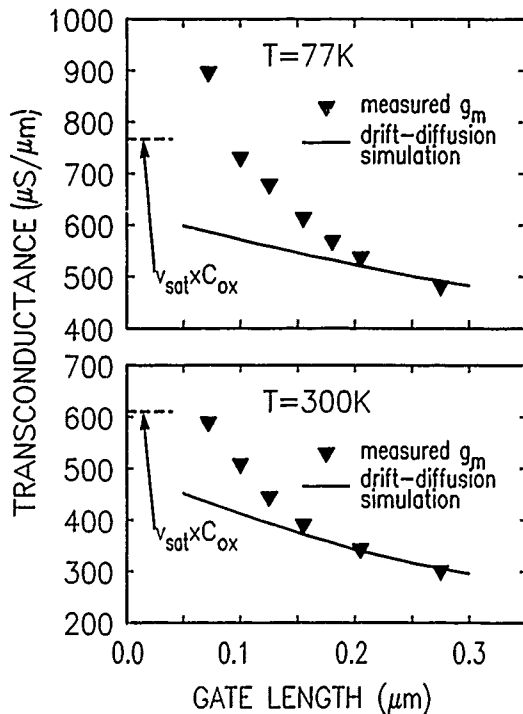


Figure 5. Measured and calculated transconductance at two temperatures. The solid lines show results of conventional two-dimensional simulations. The limit on the intrinsic transconductance $v_{\text{sat}} \cdot C_{\text{ox}}$, is also indicated.

We are now returning to the question of transconductance and the nature of transport. The $0.07\mu\text{m}$ device has a maximum transconductance of over $940\mu\text{S}/\mu\text{m}$, while the $0.1\mu\text{m}$ has $770\mu\text{S}/\mu\text{m}$.

The room temperature transconductance of these devices with 0V substrate bias is 590 and 505 $\mu\text{S}/\mu\text{m}$ respectively. Both the LT and RT transconductances are the highest ones measured to date in FETs.

Fig. 5 gives transconductance as function of gate-length, and shows the clear manifestation of velocity overshoot. The plot was made for $V_D = 0.8\text{V}$, and for each gate-length at that V_G where the transconductance peaked. This typically occurred at $(V_G - V_T) \sim 0.6\text{V}$. The evidence for velocity overshoot is twofold. First, there is the sheer size of transconductance in the shortest devices. If carriers were not capable of exceeding a saturation velocity, v_{sat} , then there would exist an unattainable upper limit for the intrinsic transconductance, namely $v_{\text{sat}} \cdot C_{\text{ox}}$, with C_{ox} being the oxide capacitance per unit area. This limit is marked on Fig. 5, and as can be seen, even the measured, extrinsic, transconductance exceeds this limit set for the intrinsic value. The second manifestation of velocity overshoot is in the trend of transconductance with gate-length. The solid line in Fig. 5 is transconductance obtained by a conventional two-dimensional simulator (FIELDAY). The curve thus shows how transconductance would have behaved in the absence of velocity overshoot. The deviation of the data from the steady state transport curve is a clear sign of velocity overshoot [12,13].

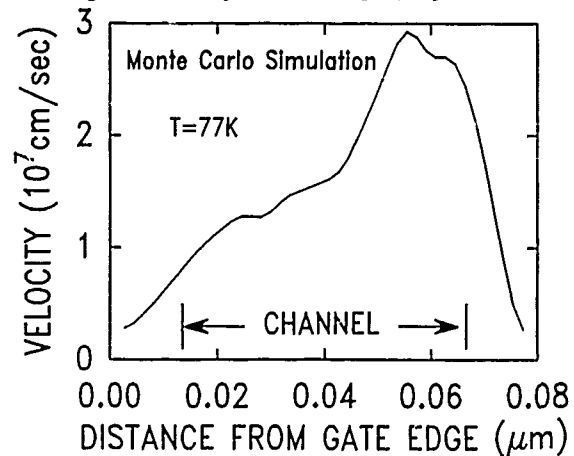


Figure 6. Carrier drift velocity as obtained by a two-dimensional self-consistent Monte Carlo simulator for the $0.07\mu\text{m}$ gate length device. Biases are. $V_D = 0.6\text{V}$, $V_G = 0.8\text{V}$, 0V on substrate. (Courtesy of S. E. Laux and M. V. Fischetti, IBM)

In the overshoot regime a non-local approach to transport is necessary. Fig. 6 shows the velocity as obtained in a self-consistent Monte Carlo simulation, which is non-local, and accounts for the full band structure of silicon [2,3]. According to the

modeling, the carriers reach speeds that are more than double that of v_{sat} .

In fact, velocity overshoot can be seen at a glance from Fig. 4. First, there is an increase in output conductance. This is a consequence of the fact that at higher drain voltage the relevant carrier velocity is higher, and more current is flowing. The second and most important feature is simply the huge transconductance. Indeed, higher output conductance is a small price to pay for the increased transconductance, since this latter leads to better performance in dense circuits. As mentioned in the introduction, the conventional outlook for miniaturization in the deeply submicron regime is one of diminishing performance returns. However, at really small dimensions, velocity overshoot can increasingly counteract this trend. As such, it provides an additional incentive to continue on the path of miniaturization.

Circuit performance

To measure delay times, 21 stage unloaded R/O and open ended inverter chains have been fabricated. An enhancement mode device, with its gate tied to an independent power supply, served as the load element. For the type of device behavior observed at these dimensions, namely roughly constant transconductance in the saturation region, the load device acted as a resistor. The width of the active devices was $5\mu\text{m}$, that of the load devices $1.25\mu\text{m}$. The output of each R/O was buffered into either a push-pull circuit or a source-follower for driving off chip. The gate length in these support circuits was $0.25\mu\text{m}$. The inverter chains had the same dimensions and layout as the R/O, but instead of forming a ring they had one input and two output points. The redundancy in fabricating R/O as well as various chains was done for two reasons. First, the capability to cross check results obtained from these two different circuit configurations was deemed useful. The second reason was to assure a sufficient number of functioning circuits. Successful operation of almost fully-scaled circuits on the $0.1\mu\text{m}$ scale was not assured. Although these were quite simple circuits, nonetheless they were the first ones fabricated at this dimension.

An oscilloscope trace of a $0.1\mu\text{m}$ gate length R/O output is shown in Fig. 7. The delay per stage is 13.1ps. The amplitude does not show the internal signal of the R/O, it is only the output of the on-chip flip-flop driver into a low impedance load. The swing of the driver unfortunately was limited by the fact that its power was supplied through a silicided polysilicon line, and as it will be discussed later, the

resistivity of such lines in this run turned out to be higher than expected. Thus, in spite of the appearance of the output the R/O internally had the full voltage swing.

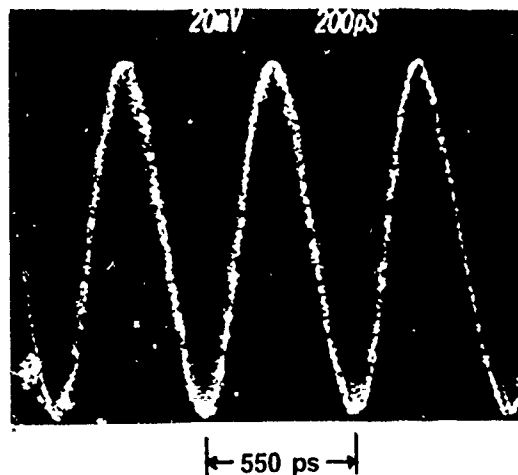


Figure 7. Oscilloscope trace of a 21 stage $0.1\mu\text{m}$ gate-length unloaded ring oscillator. $T=77^\circ\text{K}$, $V_D=1.7\text{V}$, 0.6V on substrate.

Since the program was exploratory, the dose and energy of the threshold adjust implant was also varied. This particular wafer has a higher threshold, 0.3V with 0.6V bias on the substrate, than our nominal design called for. For this reason the R/O performed best at relatively high voltage levels. Fig. 8 shows switching time versus power. At each applied power-supply voltage the load current was adjusted to obtain the highest speed. As can be seen, the curve is quite flat. A power increase of over a factor of 4 resulted in only 15% delay improvement. This is expected since the devices exhibit transconductance saturation in most of their operational range. Had the threshold of these devices been the nominal design value of 0.15V , then at the optimal V_{dd} level of $0.6\text{--}0.8\text{V}$ one would have already obtained maximum performance. As it is, the power-delay product of a device in this R/O at the $0.9\text{V } V_{dd}$ point is 1.1fJ per μm of channel width. (As a reminder, a $1\mu\text{m}$ wide device in this technology has a width to length ratio of 10 to 1.)

The fastest per-stage switching delays measured at selected gate lengths, always on the same wafer, were as follows [14]: 19.5ps at $0.20\mu\text{m}$, 17.8ps at $0.16\mu\text{m}$, 16ps at $0.13\mu\text{m}$, and 13.1ps at $0.10\mu\text{m}$. Except for the $0.1\mu\text{m}$ gate length discussed in detail above, these switching times were typically measured at a V_{dd} of $1.4\text{--}1.5\text{V}$, with a power consumption of $\sim 0.14\text{mW}$ per μm of gate-width. For the $0.1\mu\text{m}$ gate length R/O the shortest room temperature de-

lay was found to be 17.7ps at $V_{dd} = 1.3\text{V}$ with 0.12mW of power consumption per μm of gate width. The switching times measured on the 0.1 μm gate length R/O are the shortest ones ever obtained in any kind of silicon device including bipolars [15], at both 77°K and RT [16]. Measurements on the inverter chains gave consistent values with the R/O.

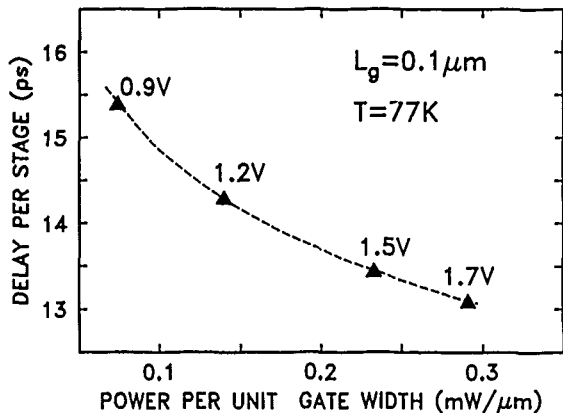


Figure 8. Delay versus power for the 0.1 μm gate length ring oscillators at liquid nitrogen temperature. The power supply voltage is given next to each point.

Detailed circuit simulations (ASTAP), in which the measured device characteristics were used as input, have also been performed. These showed that the measured delay times were longer than what they should have been based on device performance. The discrepancy was caused by a particular processing problem of this run: the resistivity of the silicide on top of polysilicon was too high. Furthermore, it was discovered that for the thinnest silicided polysilicon lines the specific sheet resistance increased significantly over the value measured on wide lines. This resulted in the anomaly that the 0.07 μm gate length circuits were actually the slowest of all. The results of the ASTAP simulations, giving delay as function of silicide resistivity, is shown in Fig 9. As can be seen if the RC time-constant associated with the gate resistance had not limited switching performance, the 0.1 μm gate length R/O would have reached 7ps delay per stage. In a fully-scaled version of the 0.1 μm gate length circuits, fabricated for instance with shallow trenches where junction capacitance is decreased, per-stage delays can be below 5ps.

As a final note, a few comments may be useful on the various possible trade-offs regarding the S/D junction edges in the case of transport far from

equilibrium. In the discussed devices the gate overlap of the S/D was only $\sim 10\text{nm}$ per side [11]. Such a short overlap is advantageous because it reduces the interelectrode capacitances. With a larger gate overlap the transconductance of the devices would have been even higher, but the delay time in the circuits slower. In dense circuits, where wiring capacitance is significant, one might want to fabricate devices with slightly larger gate to S/D overlap in order to gain in transconductance through S/D resistance reduction, even at the expense of some gate capacitance increase. These type of trade-offs occur at any gate length, however at 0.1 μm dimensions they become more complicated because details of the transport that can safely be neglected for longer channels become significant around 0.1 μm .

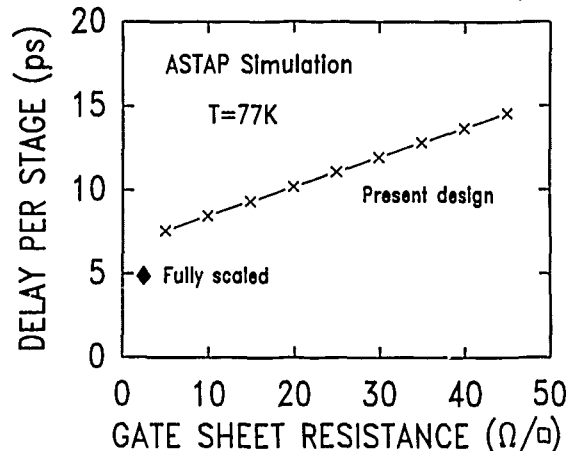


Figure 9. Effect of the silicide sheet resistivity on delay. The effect is due to an RC time constant associated with the gates.

For instance, the distance it takes for carriers to accelerate [2] is a factor which needs to be considered. This distance depending on field strength, can be 10-20nm, which is not negligible in comparison to channel length. Such considerations have direct bearing on the transconductance. The slowest carrier speed in the channel, found at the source edge, determines the current and transconductance of the device. Consequently, it is important for the carriers to enter the channel already with high velocity instead of having to accelerate there. It follows that either the acceleration must take place inside the source, or some other means must be applied by which carriers can be injected into the channel at high velocity. Understanding of such details is needed in order to fabricate an optimal S/D for any specific applications.

Conclusions

It appears that a LT 0.1 μm gate length FET technology is possible without abandoning the mainline processing approaches. The measured and projected delay times give confidence that LT FETs can be contenders even for the highest speed circuits.

Acknowledgments

The work presented in this article was an effort of many people in our laboratory. My closest collaborators were M. R. Wordeman, D. P. Kern, S. A. Rishton, E. Ganin, T. H. P. Chang and R. H. Dennard. I'd like to draw attention to the authors of references [2], [4], [9], [11], and [14] from where many of the results and discussions given here were derived. S. E. Laux and M. V. Fischetti are acknowledged for allowing the use of their unpublished work in Fig. 6. H. Luhn is thanked for his help with photographs.

* Present address: IBM, General Technology Division, East Fishkill, Hopewell Junction, NY 12533

References

- 1 R.H. Dennard, F.H. Gaensslen, L. Kuhn, and H.N. Yu, IEEE IEDM Tech. Dig., p. 344 (1972).
- 2 S. E. Laux and M. V. Fischetti, IEEE Electron Device Lett. EDL-9, 467 (1988).
- 3 M. V. Fischetti and S. E. Laux, Phys. Rev. B, 38, 9721 (1988).
- 4 G. A. Sai-Halasz, M. R. Wordeman, D. P. Kern, E. Ganin, S. Rishton, D. S. Zicherman, H. Schmid, M. R. Polcari, H. Y. Ng, P. J. Restle, T. H. P. Chang, and R. H. Dennard, IEEE Electron Device Lett. EDL-8, 463 (1987).
- 5 G. A. Sai-Halasz, M. R. Wordeman, D. P. Kern, E. Ganin, S. A. Rishton, H. Y. Ng, D. Zicherman, D. Moy, T. H. P. Chang, and R. H. Dennard, IEEE IEDM Tech. Dig., 397 (1987).
- 6 F. H. Gaensslen, V. L. Rideout, E. J. Walker, and J. J. Walker, IEEE Trans. Electron Dev., ED-24, 218 (1977).
- 7 G. Baccarani, M.R. Wordeman, and R.H. Dennard, IEEE Trans. on Electron Dev., ED-31, 452 (1984).
- 8 M. R. Wordeman, A. M. Schweighart, R. H. Dennard, G. A. Sai-Halasz, and W. W. Molzen, IEEE Trans. Electron Devices ED-32, 2214 (1985).
- 9 S. A. Rishton, H. Schmid, D. P. Kern, H. E. Luhn, T. H. P. Chang, G. A. Sai-Halasz, M. R. Wordeman, E. Ganin, and M. Polcari, J. Vac. Sci. Technol. B6, 140 (1988).
- 10 G. A. Sai-Halasz and H. B. Harrison, IEEE Electron Device Lett. EDL-7, 534 (1986).
- 11 G. A. Sai-Halasz, M. R. Wordeman, D. P. Kern, S. Rishton, and E. Ganin, IEEE Electron Device Lett. EDL-9, 464 (1988).
- 12 J. G. Ruch, IEEE Trans. Electron Devices. ED-19 652 (1972).
- 13 R. S. Huang and P. H. Ladbroke, J. Appl. Phys., 48, 4791 (1977).
- 14 G. A. Sai-Halasz, M. R. Wordeman, D. P. Kern, S. Rishton, E. Ganin, H. Y. Ng, D. Moy, T. H. P. Chang, and R. H. Dennard, IEEE Electron Device Lett. EDL-9, 633 (1988).
- 15 K. Y. Toh, C. T. Chuang, T. C. Chen, J. Warnok, G. P. Li, K. Chin, T. H. King, IEEE ISSCC Digest, 224 (1989).
- 16 T. Kobayashi, M. Miyake, Y. Okazaki, M. Sato, D. Defuchi, S. Ohki, and M. Oda, IEEE IEDM Tech. Dig., 881 (1988).

GaAs MESFET and HBT Technology in Picosecond Electronics

Kazuyoshi Asai and Tadao Ishibashi

*NTT LSI Laboratories, 3-1, Morinosato Wakamiya, Atsugi-shi,
Kanagawa 243-01, Japan*

ABSTRACT

Ultra-high-speed signal processing with a bit rate of over 10 Gbit/s will soon be available in GaAs MESFET and HBT integrated circuits. Such remarkable progress in the device performances is based on the scaling down for MESFET and near ballistic transportation for HBT. Propagation delay times of inverters have been reduced to 6.7 ps/gate and 1.9 ps/gate, and maximum toggle frequencies of flip-flop circuits have reached 31.4 GHz and 22.15 GHz, respectively. Wide-band amplifiers with a band width of about 10 GHz have also been obtained. This paper reviews recent progress in the speed performance of these devices.

1. INTRODUCTION

In the past few years, GaAs MESFET and HBT technologies have made rapid progress [1,2]. To achieve high MESFET performance, along with the gate length shortening, the channel and n^+ -contact layers should be effectively scaled down. The short channel effect is a problem in ion-implanted MESFET [3]. To a scale down the FET structure in a way that suppresses the short channel effect, a thin and highly doped active channel layer is essential. A new WSiN metal cap annealing technique can enhance the carrier concentration to suppress GaAs surface degradation due to As out-diffusion [4]. A 96-GHz cutoff frequency has been achieved for a 0.2- μ m-gate MESFET. Low power characteristics of a 0.3- μ m-gate DCFL ring oscillator have been reported, specifically a t_{pd} of 6.7 ps/gate with

a power consumption of 16 mW/gate was reported [1]. These basic MESFET characteristics are comparable to those of high-speed HEMT devices [5,6].

AlGaAs/GaAs HBT design and fabrication techniques have also made rapid progress in the last few years. Improvements have been made by reducing parasitic elements as emitter resistance, base resistance and base/collector capacitance by implementing a non-alloy InGaAs emitter cap, a graded base, and a self-aligned structure [7]. Furthermore, the intrinsic delay time at the collector has been reduced by applying a Ballistic Collection Transistor (BCT) [2]. It is possible to realize near-ballistic transport in the collector depletion layer by controlling electron energy. The BCT structure successfully increased the cutoff frequency to about 100 GHz. A t_{pd} value of 1.9 ps/gate with a power consumption of 44 mW/gate has been observed in an ECL ring oscillator [8].

This paper reviews these remarkable developments in GaAs MESFET and AlGaAs/GaAs HBT performance that have been in our Laboratories. A number of other circuits such as frequency dividers and wide band amplifiers aiming at over 10 Gbit/s signal processing are also reviewed for basic digital and analog applications.

2. MESFET TECHNOLOGY

2.1 MESFET Structure and Device Concept

The typical MESFET structure is illustrated in Fig. 1. The n-channel, n^+ -source and -drain regions are all Si ion implanted in semi-insulating GaAs (100) substrate. Be ions for the p-type dopant are implanted under the channel to prevent the short

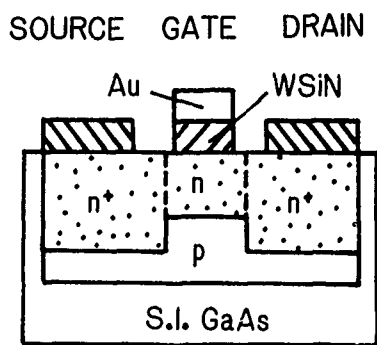


Fig. 1. MESFET schematic structure. "Reproduced with permission from Ref. 12. Copyright 1988 IEEE."

channel effect, mainly caused by substrate leakage current. A newly developed refractive WSiN film has been adopted for both the Schottky gate and the activation annealing cap. To obtain low gate resistance, a Au/WSiN bilayer gate structure is applied. The gate sheet resistance of $0.3 \mu\Omega/\text{cm}$ is sufficient for this gate to be applied to analog circuits.

The scaling we have achieved with our MESFET is shown in Table 1. Along with gate length shortening from $0.5 \mu\text{m}$ to $0.2 \mu\text{m}$, the channel thickness is scaled down from 90 nm to 15 nm . This scaling is achieved by lowering the ion implantation energy from 30 keV to 10 keV and utilizing Rapid Thermal Annealing [9] which minimizes excess thermal diffusion. For circuit applications, the $0.3\text{-}\mu\text{m}$ -gate shown in the Table 1. is utilized.

To realize such scaling by ion implantation technology, As out-diffusion during activation annealing should be suppressed. This is because the implanted Si ions could cause p-type conversion in the As vacancies. We have found that sputtered WSiN film suppresses As out-diffusion. The crystalline phase of this WSiN film maintains amorphous phase even after 800°C annealing. The Secondary Ion Mass Spectroscopy (SIMS) results shown in Fig. 2, explain the suppression of As out-diffusion. This sample was prepared on a GaAs surface by CVD SiO_2 , sputtered WSiN, CVD SiO_2 and WSiN films. It was then annealed at 800°C for one hour. In the first SiO_2 film, the As signal is clearly observed and accumulates at the SiO_2/WSiN interface. In the second SiO_2 film, however, no As signal exists. The same phenomenon is confirmed even for the 20-nm -thick WSiN film. These results prove that the

Table 1. Utilized MESFET scaling.

| Gate Length (μm) | Implant Energy (keV) | Activation Anneal | Channel Thickness (μm) |
|-------------------------------|----------------------|--|-------------------------------------|
| 0.5 | 30 | Furnace ($800^\circ\text{C}/10 \text{ min}$) | 0.09 |
| 0.4 | 30 | Lamp ($900^\circ\text{C}/2 \text{ sec}$) | 0.07 |
| 0.3 | 20 | Lamp ($900^\circ\text{C}/2 \text{ sec}$) | 0.06 |
| 0.2 | 10 | Lamp ($900^\circ\text{C}/2 \text{ sec}$) | 0.045 |

WSiN film successfully suppresses As out-diffusion.

Another very important characteristic is that the WSiN film remains in amorphous phase even after 800°C annealing. Other refractory metals such as WSi [10] and WN [11] recrystallize at such high-temperature treatment. Thus, fine gate patterning down to $0.1 \mu\text{m}$ can be realized by WSiN film.

2.2 MESFET Basic Characteristics

Figure 3 shows the improvement in FET characteristics that accompanies the scaling shown in Table 1. Typical transconductance (gm) and threshold voltage shifts (ΔV_T) for the MESFET are plotted against the gate length (L_g). These values are chosen from the normalized threshold voltage of 0 V which enables good comparisons with any kind of FET. In this figure, each line corresponds to each scaled down channel. If there is no channel scaling, gm and threshold voltage shift rapidly go down along with the gate length shortening. These degradations are caused both by substrate leakage current flowing between the source-drain n^+ regions

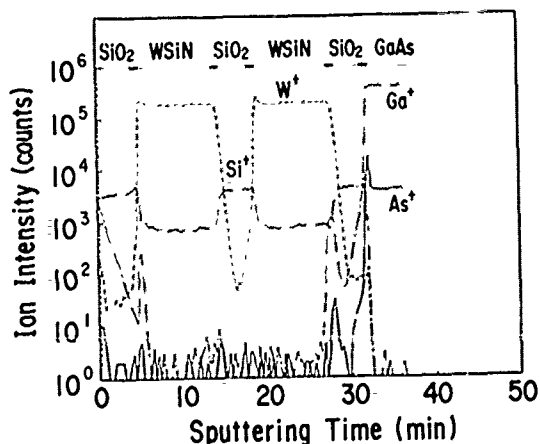


Fig. 2. Suppression of As out-diffusion by WSiN film.

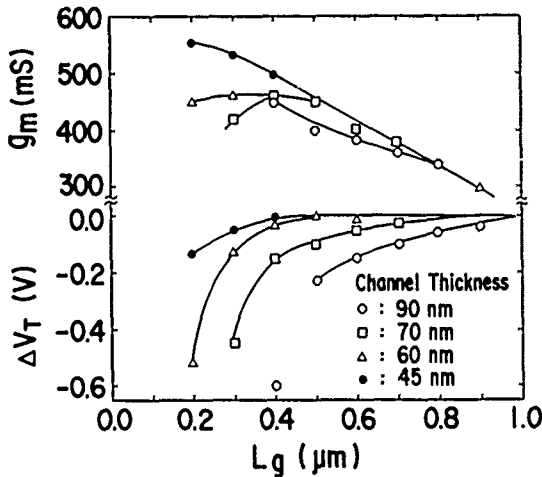


Fig. 3. Transconductance (g_m) and threshold voltage shift (ΔV_T) against gate length (L_g).

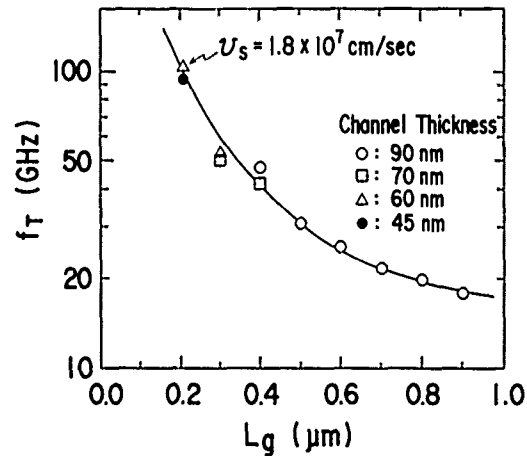


Fig. 4. Cutoff frequency (f_T) dependence on gate length.

and by the two dimensional electric field effect under the gate electrode. Optimal scaling results in the best g_m of 630 mS/mm and suppresses the threshold voltage shift to only -140 mV at the 0.2- μm gate length [12].

One of the most important electronic characteristics is the cutoff frequency (f_T). In Fig. 4, the scaled-down MESFETs' cutoff frequencies are plotted against gate lengths. The cutoff frequencies are measured for a 2-V drain voltage and a 0.5-V gate bias. The cutoff is accurately determined by extrapolating the current gain from 7 to 10 GHz. It should be noted that the f_T does not depend on channel scaling but strongly depends on gate length shortening. At the same gate length, the same f_T is obtained even if the channel thicknesses are different. The highest cutoff of 96 GHz is obtained at a gate length of 0.2 μm . At this cutoff frequency, the electron velocity of 1.8×10^7 cm/s is estimated which is due to the electron velocity overshoot effect [13,14]. The circuitry described below has a gate length of 0.3 μm . The cutoff frequency of the 0.3- μm MESFET measured from 50 to 60 GHz.

2.3 MESFET Circuit Performance

The first circuit is a ring oscillator which gives the FET's switching speed. The measured propagation delay time is plotted against the dissipated power, as shown in Fig. 5. Direct Coupled FET Logic (DCFL) is implemented with a combination of Enhancement- and Depletion-mode (E/D) FETs, and a combination of Enhancement-mode FET and

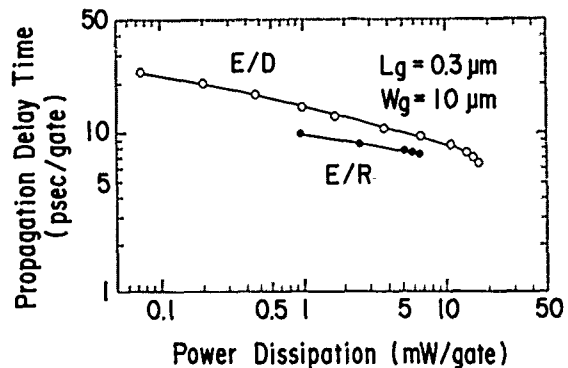


Fig. 5. Switching speed vs. dissipated power for 0.3- μm -gate MESFET ring oscillators.

resistor (E/R). The ring oscillator has 23 stages. The implemented MESFET's gate length is 0.3 μm and the gate width is 10 μm . These MESFETs' current density is 4.4×10^5 A/cm² at the gate bias of +0.7 V. Switching speed below 10 ps/gate are obtained by both types of ring oscillators. The E/R type ring oscillator exhibits lower power dissipation and the E/D type shows higher speed performances. The E/R type operates at 10 ps/gate dissipating only 1 mW/gate. The fastest data was obtained by the E/D type ring oscillator at 6.7 ps/gate. The fastest switching time is theoretically related to the inverse of $(\pi \times f_T)$. From this measured switching speed, the FET's average f_T is estimated to 47.5 GHz [1]. This value is nearly equal to that derived from the S-parameter measurement described ear

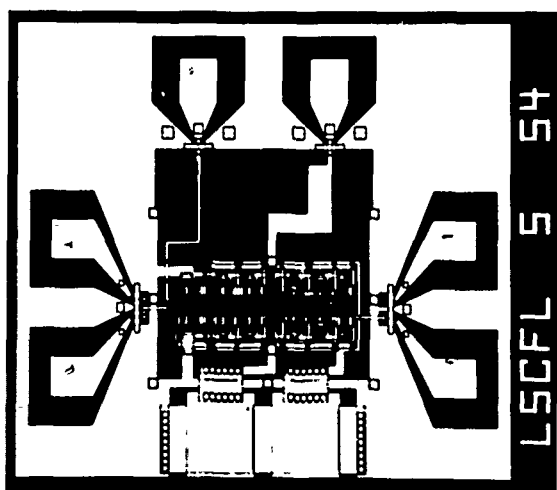


Fig. 6. Microphotograph of MESFET static frequency divider. "Reproduced with permission from Ref. 15. Copyright 1989. 'IEICE Japan'."

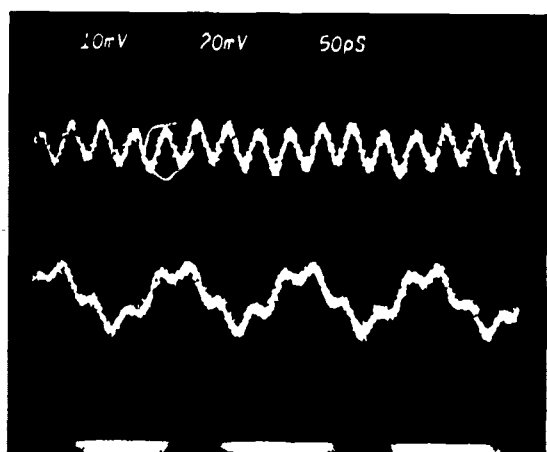


Fig. 7. 31.4 GHz toggling operation of MESFET static frequency divider. "Reproduced with permission from Ref. 15. Copyright 1989. 'IEICE Japan'."

lier.

The next circuit we will consider is a frequency divider. A microphotograph of the chip is shown in Fig. 6. The chip size is 1.2 mm \times 1.3 mm. The gold base two-level interconnection utilizes SiN as an isolation film. This frequency divider is implemented by Low Power Source Coupled FET Logic (LSCFL). The 1 \div 4 static frequency divider is constructed by two Toggling Flip-Flops (T-FF) and 3 buffer FETs. The maximum toggling operation [15]

is shown in Fig. 7. The upper trace is the input toggle of 31.4 GHz and the lower trace is the output waveform divided by 4. This is the fastest data ever reported. The dissipated power is 150 mW/T-FF. The implemented FET's threshold voltage is 110 mV and the transconductance is 505 mS/mm and the cutoff frequency is 53 GHz.

Aside from these digital applications, MESFETs also have advantages for analog circuit applications based on their very high maximum operating frequency (f_{max}). Our 0.3- μ m-gate MESFET realizes a f_{max} of over 100 GHz. Moreover, in the dc wide band amplifier application, it is confirmed to operate at up to 10 GHz with a 20-dB gain.

3. HBT TECHNOLOGY

3.1 Device Concept of BCT

Schematic band diagrams of a BCT and a conventional HBT are compared in Fig. 8. The difference between a BCT and HBT is clearly revealed in the collector region. The collector layer consists of i - p^+ - n^+ multi-layers instead of the n -layer used in conventional HBTs. A planar doped p^+ -layer elevates the i -layer, so that electron transport is confined to the Γ -valley. This effect makes it possible to realize near-ballistic transport [16] over a wide collector depletion layer in a certain collector voltage region. Since ionized impurity scattering with unscreened donors is suppressed in the i -layer, electron momentum relaxation time can be maximized [8].

The BCT structure and its epitaxial layer parameters are shown in Fig. 9. All epitaxial layers are grown by MBE. From the top layer, the graded

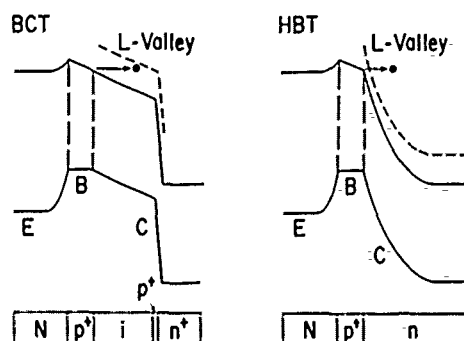


Fig. 8. Schematic band diagram of BCT compared with conventional HBT. "Reproduced with permission from Ref. 8. Copyright 1988 IEEE."

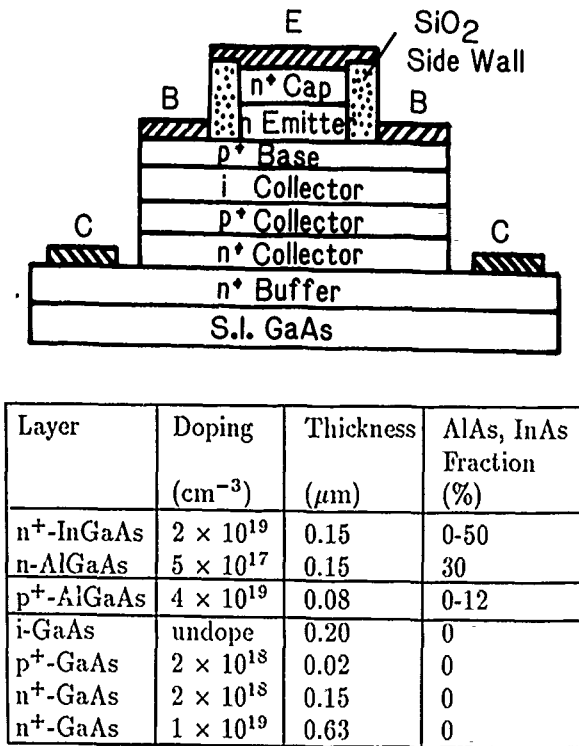


Fig. 9. BCT structure and epitaxial layer parameters. "Reproduced with permission from Ref. 8. Copyright 1988 IEEE."

emitter cap with n⁺-InGaAs/n⁺-GaAs is used as non-alloy contact emitter. Also, the graded base with 12 % AlAs fraction has a grading that is over 800 Å thick. Because of the relatively high substrate temperature of 650 °C during growth, the actual base thickness might be extended to about 1100 Å. This grading generates a quasi-field intensity of 20 kV/cm. In the collector portion, an i-layer is 2000 Å thick and a p⁺-layer is 200 Å thick with doping levels of 10¹⁸ cm⁻³. A heavily Sn-doped collector buffer layer reduces the collector resistance [17]. The devices were fabricated with the self-aligned process [7]. Typical width of the emitter mesa is 2 μm and the width of base/collector junction is 3-10 μm.

3.2 HBT Basic Characteristics

These new concepts clearly reflected in the characteristics of high frequency cutoff [2]. The cutoff frequency dependence on collector bias voltage is shown in Fig. 10. Each curves were measured under the same collector current conditions. The highest f_T of 105 GHz is obtained at a collector current of 5×10^4 A/cm². It is easily recognized that all

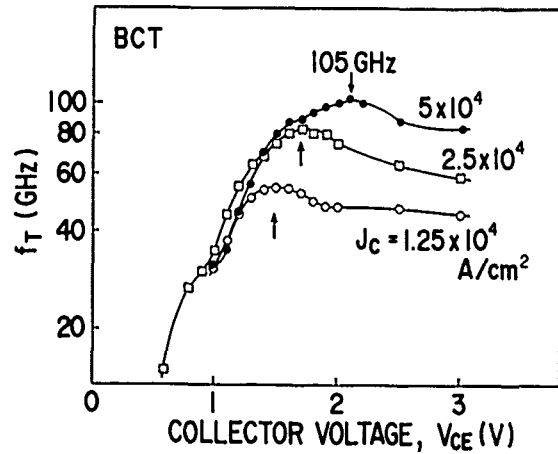


Fig. 10. Cutoff frequency dependence on collector bias voltage. "Reproduced with permission from Ref. 16. Copyright 1988 IEEE."

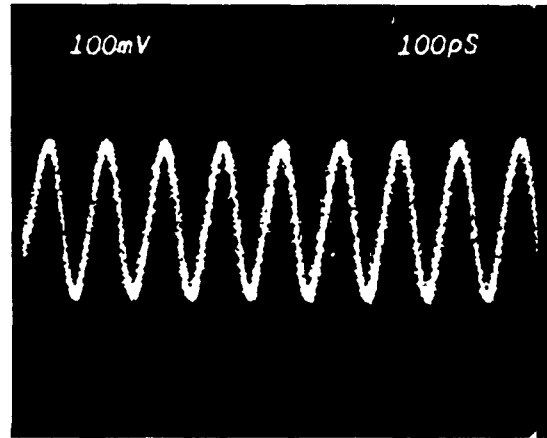


Fig. 11. 1.9 ps/gate ring oscillator waveform. "Reproduced with permission from Ref. 8. Copyright 1988 IEEE."

curves have peaks in the f_T . This implies that the electron velocity changes with potential change in the i-collector. The average electron velocity in the depleted collector is estimated to be 4×10^7 cm/s. This value is 3 to 6 times larger than that of a conventional HBT.

3.3 HBT Circuit Performance

To investigate BCT characteristic as digital circuit elements, ECL ring oscillators and 1 ÷ 4 frequency divider were fabricated. The output waveform of the fastest ring oscillator is demonstrated [8] as in Fig. 11. An outstanding propagation delay time of

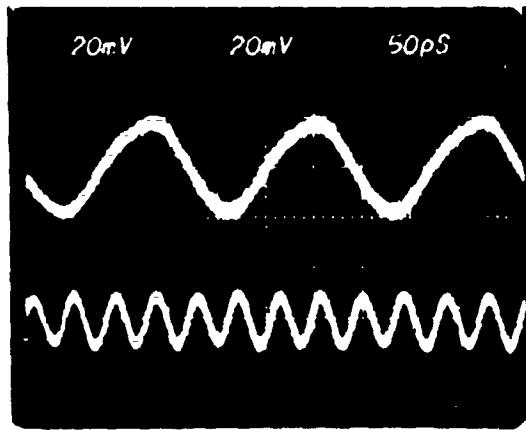


Fig. 12. 22.15-GHz HBT frequency divider operation. "Reproduced with permission from Ref. 18. Copyright 1987. 'IEE'."

1.9 ps/gate was observed in a 31-stage ring oscillator with $[f_{in}] = [f_{out}] = 1$. Here, the logic swing is about 400 mV. Smaller device size with emitter dimensions of $2 \mu\text{m} \times 3 \mu\text{m}$ were used in the circuits to lower power dissipation. The power consumption is 44 mW/gate at a power supply voltage of 7 V. The highest collector current density for current switch transistors is $5.5 \times 10^4 \text{ A/cm}^2$. At this collector current, f_T is estimated to be about 80 GHz.

High-speed digital switching is also confirmed by the frequency divider [18]. The operating waveforms of the $1 \div 4$ frequency divider is shown in Fig. 12. The lower trace is the input toggle of 22.15 GHz and the upper is the output waveform divided by 4. The total dissipated power is 712 mW. The logic swing is 400 mV at a supply voltage of 9 V. A low minimum input power of 0 dBm was also achieved. The divider circuit consists of a series gate T-type flip-flops and buffer circuits operating as level shifters. For the level shifters, Darlington connections are employed to provide stable voltage shift operations.

HBTs were also applied to a direct-coupled differential amplifier [19]. This circuit is very important for various applications because of its de to high-frequency-range coverage. The differential amplifier circuit employing HBTs is illustrated in Fig. 13. There are two basic differential amplifiers. In the output part of the circuit, the HBTs with their collectors connected to bases are implemented as level shift diodes. The typical supply voltages V_{CC} , V_{EE} and V_{BB} are +5 V, -5 V and -3 V. The nega-

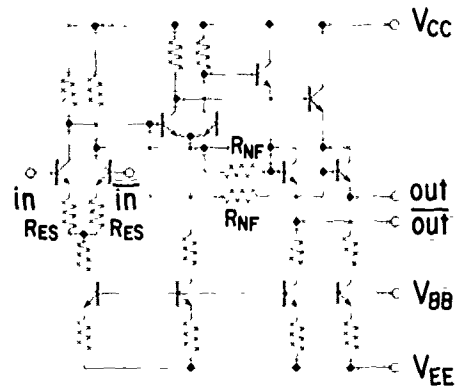


Fig. 13. HBT differential amplifier circuit. "Reproduced with permission from Ref. 19. Copyright 1988. 'IEE'."

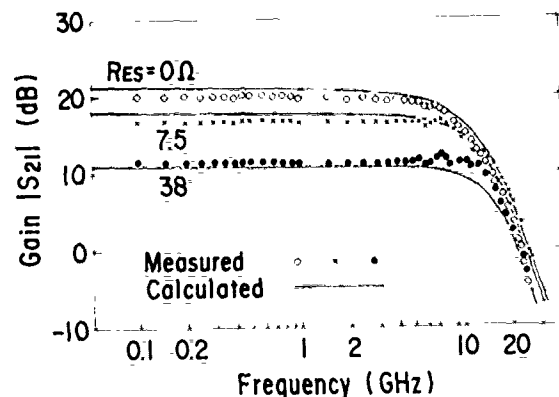


Fig. 14. Performance of HBT differential amplifier. "Reproduced with permission from Ref. 19. Copyright 1988. 'IEE'."

tive feedback resistance R_{NF} can be optimized independently of circuit bias to obtain the maximum gain-bandwidth product of the circuit.

This circuit performance is shown in Fig. 14. This figure shows frequency dependencies of differential amplifier gain. The emitter series resistance R_{ES} is at the parameters 0, 7.5 and 38 Ω . The open circles, crosses and solid circles indicate measured characteristics with flat gains of 20, 16 and 11 dB for each R_{ES} . The corresponding 3-dB gain reduction bandwidths are 9, 12 and 15 GHz. The implemented HBT's emitter area is $2 \mu\text{m} \times 5 \mu\text{m}$. And the cutoff frequency of this HBT is 70-GHz in the operation at the bias point of the circuits.

Table 2. MESFET and HBT technologies and performances.

| Device | | MESFET | HBT |
|---------------------|-------------|--|--|
| Design Concept | | Scaling Down | Ballistic Collection |
| Technology | | Ion Implantation n ⁺ Self-Align WSiN Metal Cap Anneal Buried p-Layer | MBE Base Electrode Self-Align Non-Alloy Emitter Graded Base |
| Size | | 0.2 μ m Gate | 2 μ m \times 5 μ m Emitter |
| Device Performance | gm | 630 mS/mm | |
| | f_T | 96 GHz | 105 GHz |
| | f_{max} | 100 GHz | 80 GHz |
| Circuit Performance | Ring Oscil. | 6.7 ps/gate (16 mW/gate) | 1.9 ps/gate (44 mW) |
| | Freq. Div. | 31.4 GHz (150 mW/T-FF) | 22.15 GHz |
| | D. C. Amp. | 10 GHz/20 dB | 9 GHz/ 20 dB |

4. SUMMARY

The MESFET and HBT technologies described and their performances are summarized in Table 2. The remarkable progress in the device performances is based on scaling for the MESFET, and the near ballistic collector concept for the HBT. The current densities are of the order of over 5×10^4 A/cm², which is almost the same for the two devices. This fact suggests the possibility of high field electron transport in the Γ -valley. Then, both devices would exhibit electron velocity overshoot. The MESFET utilizes conventional ion implantation technology and WSiN metal cap-annealing to suppress As out-diffusion. The HBT utilizes a non-alloy emitter cap, graded base and ballistic collector fabricated by MBE growth. Both devices achieved very high cutoff frequencies of about 100 GHz. Circuit performances corresponded well with these high frequency cutoff values. Minimum switching speeds are 6.7 ps/gate and 1.9 ps/gate and maximum toggling frequencies are 31 and 22 GHz for the MESFET and HBT. The dc wide-band amplifiers operate at up to 10 GHz with a 20-dB gain.

The advantages of MESFETs are their simple process, low power and low noise; those for HBTs are high speed and high gain. By taking advantages of these strengths, high-frequency signal processing applications will expand from 10 to 20 Gbit/s, for example, wide-band amplifiers, MUX/DMUX, LD drivers and decision circuits, for optical links and fiber communications.

ACKNOWLEDGMENTS

The authors would like to thank Drs. A. Ishida, K. Yamamoto and K. Hirata for their valuable suggestions and continuous encouragement.

REFERENCES

1. M. Tokumitsu, K. Onodera and K. Asai, "High Performance Short Channel MESFET's with WSiN Gate Suppressing As-Outdiffusion," in Extended Abstracts in the 46th Device Research Conference (IEEE Electron Device Society, Boulder, CO, 1988) VA-2.
2. T. Ishibashi and Y. Yamauchi, "A Novel AlGaAs/GaAs HBT Structure for Near-Ballistic Collection," in Extended Abstracts in the 45th Device Research Conference (IEEE Electron Device Society, Santa Barbara, CA, 1987), IVA-6.
3. K. Yamasaki, N. Kato and M. Hirayama, "Buried p-Layer SAINT for Very High Speed GaAs LSI's with Submicrometer Gate Length," IEEE Trans. Electron Devices, ED-32, 2420-2425 (1985).
4. K. Asai, H. Sugahara, Y. Matsuoka and M. Tokumitsu, "Reactively Sputtered WSiN Film Suppresses As and Ga Out-Diffusion," J. Vac. Sci. Technol. B6, 1526-1529 (1988).
5. J. F. Jensen, U. K. Mishra, A. S. Brown, R. S. Beaubien, M. A. Thompson and L. M. Jelloian, "25 GHz Static Frequency Dividers in AlInAs-GaInAs HEMT Technology," in Digest of Technical Papers of 31st International Solid-State Circuits Conference (IEEE, San Francisco, CA, 1988) 268-269.
6. Y. Awano, M. Kosugi, T. Mimura and M. Abe, "Performance of a Quarter-Micrometer-Gate Ballistic Electron HEMT," IEEE Electron Device Lett.

- EDL-8, 451-453 (1987).
7. K. Nagata, O. Nakajima, T. Nittono, Y. Yamauchi, H. Ito and T. Ishibashi, "Self-Aligned AlGaAs/GaAs HBT with Low Emitter Resistance Utilizing In-GaAs Cap Layer," *IEEE Trans. Electron Devices* ED-35, 2-7 (1988).
 8. T. Ishibashi, O. Nakajima, K. Nagata, Y. Yamauchi, H. Ito and T. Nittono, "Ultra-High Speed AlGaAs/GaAs Heterojunction Bipolar Transistors," in *Technical Digest of International Electron Devices Meeting*, (IEEE Electron Devices Society, San Francisco, CA, 1988) 826-829.
 9. S. Sugitani, K. Yamasaki and H. Yamazaki, "Characterization of a Thin Si-Implanted and Rapid Thermal Annealed n-GaAs Layer," *Appl. Phys. Lett.* 51, 806-808 (1987).
 10. T. Ohnishi, N. Yokoyama, H. Onodera, S. Suzuki and A. Shibatori, "Characterization of WSi_x /GaAs Schottky Contacts," *Appl. Phys. Lett.* 43, 600-602 (1983).
 11. N. Uchitomi, M. Nagaoka, K. Shimada, T. Mizoguchi and N. Toyoda, "Characterization of Reactively Sputtered WN_x Film as a Gate Metal for Self-Alignment GaAs Metal-Semiconductor Field Effect Transistors," *J. Vac. Sci. Technol.* B4, 1392-1397 (1986).
 12. K. Onodera, M. Tokumitsu, S. Sugitani, Y. Yamane and K. Asai, "A 630-mS/mm GaAs MESFET with Au/ $WSiN$ Refractory Metal Gate," *IEEE Electron Device Lett.* EDL-9, 417-418 (1988).
 13. A. Yoshii, M. Tomizawa and K. Yokoyama, "Accurate Modeling for Submicrometer-Gate Si and GaAs MESFET's Using Two-Dimensional Particle Simulation," *IEEE Trans. Electron Devices*, ED-30, 1376-1380 (1983).
 14. M. B. Das, "Millimeter-Wave Performance of Ultra-submicrometer-Gate Field-Effect Transistors. A Comparison of MODFET, MESFET, and PBT Structures," *IEEE Trans. Electron Devices*, ED-34, 1429-1440 (1987).
 15. M. Tokumitsu, K. Onodera and K. Asai, "A 31 GHz Static Frequency Divider Employing GaAs MESFETs," in *Japanese Technical Report of the Institute of Electronics, Information and Communication Engineers*, IEICE ED88-147 (1989).
 16. T. Ishibashi and Y. Yamauchi, "A Possible Near-Ballistic Collection in an AlGaAs/GaAs HBT with a Modified Collector Structure," *IEEE Trans. Electron Devices*, ED-35, 401-404 (1988).
 17. H. Ito and T. Ishibashi, "Heavily Sn-Doped GaAs Buffer Layers for AlGaAs/GaAs HBTs," *Jpn. J. Appl. Phys.* 27, L707-L709 (1988).
 18. Y. Yamauchi, K. Nagata, O. Nakajima, H. Ito, T. Nittono and T. Ishibashi, "22 GHz 1/4 Frequency Divider using AlGaAs/GaAs HBTs," *Electronics Lett.* 23, 881-882 (1987).
 19. H. Nakajima, Y. Yamauchi and T. Ishibashi, "Wideband Direct-Coupled Differential Amplifiers Utilizing AlGaAs/GaAs HBTs," *Electronics Lett.* 24, 1178-1179 (1988).

Electron-Hole Effects on the Velocity Overshoot in Photoconductive Switches

R. Joshi, S. Chamoun, and R. O. Grondin

*Center for Solid State Electronics Research, Arizona State University,
Tempe, Arizona 85287-6206*

Abstract

The role of the electron-hole interaction on the transient velocity of photoexcited carriers in bulk GaAs is investigated using a bipolar Ensemble Monte Carlo approach. The dependence of the intervalley transfer on the photoexcitation energy, intensity and operating temperature is also discussed. The results show that under appropriate conditions, the electron-hole interaction can enhance the velocity overshoot. Some recent experimental observations can also be better explained by including this interaction. Influence of the non-equilibrium phonons remains negligible even at low temperatures.

Introduction

The use of subpicosecond laser pulses has been an important experimental tool in probing the carrier dynamics and in understanding the physics of the ultrafast processes. There already exists a rich literature on various interesting aspects of nonequilibrium phenomena involving hot phonons [1-3], femtosecond energy relaxation mechanisms [4-6], power loss rates [7-9], transient mobilities [10] and intervalley scattering times [11,12]. The modelling of the transient velocity is also essential for understanding recent photoconductive experiments [13,14]. These experiments typically, use electro-optic sampling to achieve subpicosecond resolution for the measured voltage transients across microstrip lines. In such structures, the analysis is complicated because both transient transport and space charge

effects occur simultaneously.

Our present focus is mainly on the velocity overshoot in bulk semiconductors resulting from the relaxation of a nonequilibrium photo generated carrier distribution. In contrast with other Monte Carlo studies [15,16], we here include the features needed to examine high excitation experiments. In particular, electron-hole scattering in a bipolar plasma and the hot phonon effect have been incorporated. Recent experiments on the transient carrier transport have already indicated that electron-hole interactions are important. Degani et al. [17] observed that minority electrons in p-type InGaAs do not exhibit an overshoot. Shah et al. [18] obtained negative absolute electron mobilities in GaAs quantum wells, while Tang et al. [19] noted a sharp reduction in the minority electron mobility in Si at low fields. These results all emphasize the importance of the electron-hole scattering. The time scale over which such interactions are dominant is typically in the femtosecond range, underscoring the need to properly include the electron-hole interaction while modelling ultrafast transients.

The electron-hole scattering provides an alternative channel for the hot electron energy loss which has the following effects. Firstly, it cools the electrons and tends to keep them in the central valley. Secondly, intervalley transfer rates are affected, leading to changes in the temporal evolution of the valley populations. To investigate these effects, we shall simulate the transient carrier velocity for various excitation levels and photogeneration densities.

In high excitation experiments, nonequilibrium or hot phonon effects are

often important. They are included here as well. In particular, varying the temperature as a parameter is fruitful, as hot phonons are more important at low temperatures, while the electron-hole interaction is relatively insensitive. Such a comparison becomes useful in resolving questions about the experimental transient mobility data. For example, Nuss et al. [10], obtained a carrier density dependence of the mobility rise time which was believed to have been a result of the hot phonon effect.

Monte Carlo Approach

We study the transient response of the photogenerated electron-hole plasma in an uniform field through Monte Carlo simulations. The method is superior to the drift-diffusion models often used [15], because it correctly includes all the non-linearities, builds in the memory effects and incorporates the nonequilibrium nature of the distribution function. The structure under study here corresponds to a reverse biased PIN device with the perturbative fields associated with the charge separation assumed to be small compared to the external bias. This is valid since the time scales under consideration remain extremely short. A three valley electron and a three band hole model has been used. Initial optical generation and distribution of the carriers in *k*-space takes into account anisotropic distributions. Carrier degeneracy has been suitably included through a rejection technique proposed by Lugli et al. [20].

The bipolar EMC includes all the relevant carrier-phonon and electron-hole interactions. Only single mode LO and TO couplings have been considered and all plasmon-phonon interactions ignored for the present. A static but time evolving screening model, proposed by Ferry et al. [21], has been used for all the polar interactions. Only intraband electron-hole processes have been included, leaving out possible multiband scattering as discussed by D'yakonov et al [22].

Hot phonon effects are treated using the EMC algorithm proposed by Lugli et al [23]. Both PO and intervalley phonon populations have been modified since the photoexcitation levels and electric field strengths cause large Γ -L transfer. This can lead to significant perturbations in the intervalley phonon population despite the large wavevectors of the zone boundary phonons and the big volume of phase space associated with it. Finally, as shown in the next section, simulations are also performed for AlGaAs.

This large band gap material is used to investigate the Jones-Rees effect [24] and the bias dependence of the initial velocity rise [16]. For this case, two LO phonon modes are used and the relative interaction strengths chosen according to the hot phonon data of Kash et al. [25].

Results

The results of an EMC simulation of the transient electron velocity, in GaAs at 300K, are shown in Fig. 1 for carrier densities of 10^{16} and 10^{18} cm⁻³. The photoexcitation energy was 2 eV, the pulse width 30 fs FWHM, and the electric field 10 KV/cm. An energy of 2 eV was chosen since it has been used in recent photoconductive experiments [14]. Three important features are evident from the curves shown. Firstly, the steady state value for the higher density is lower. This is due to net transfer of momentum from the electrons to the holes via the electron-hole scattering. The effect is especially pronounced at this high field because the L valley, in the steady state, is sufficiently populated. Given the high density of states and the smaller mass mismatch in the L valley, the electron-hole interaction works to decrease the steady state velocity.

The second effect seen is a density dependence in the delay of the initial velocity rise time. This delay as discussed previously [16], is related to the Jones-Rees effect and is also bias dependent. For the bandgap at 300K, the laser energy places the photogenerated electrons from both the heavy and light hole bands above the threshold for intervalley transfer. The ratio of the populations generated from the heavy, light and split-off hole bands is roughly 2:1:1. As a result, about 75 percent of the initial electron population can transfer over to the L valley. This has two effects. First, the transfer to the heavy mass valley makes the rise time more sluggish. Secondly, the positive electrons in the central valley gain energy from the electric field increasing the probability of an intervalley transfer, while the negative velocity electrons lose energy to the field and get trapped in the Γ valley. The overall outcome is a higher percentage of negative velocity electrons in the central valley which delays the velocity rise. The above effect is less pronounced at higher carrier concentrations since stronger electron-hole scattering provides greater electronic energy loss to the holes and reduces the intervalley transfer.

The third noticeable feature is that the peak velocity at the two different concentrations is almost identical even

though the steady state values are different. This is a result of several competing processes. A strong electron-hole interaction tends to keep the electron distribution in the Γ valley. In addition, the electron-hole scattering decreases the time required for transfer back from the L valley. Without the electron-hole interaction, the electrons would undergo more L-L, X-X and L-X transitions because of the higher density of states. Finally, greater electron-hole scattering at the expense of the PO interaction leads to a greater streaming motion because of small angle scattering [26]. All the above mechanisms keep the peak velocity at 300K for the 2 eV excitation almost equal for the two carrier concentrations.

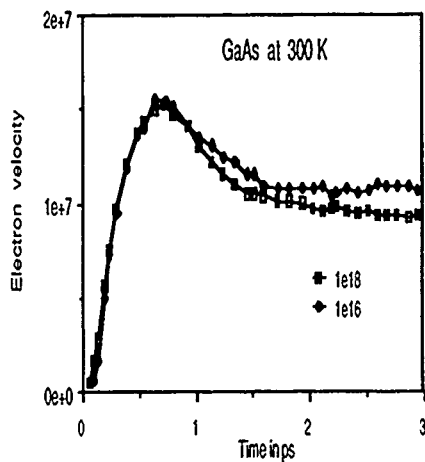


Figure 1. Electron velocity curves following laser excitation for carrier densities of 10^{16} and 10^{18} cm^{-3} . The laser pulse width was 30fs FWHM, the energy 2eV and the electric field 10KV/cm.

In order to emphasize the role of the electron-hole scattering, the transient velocities at a lower temperature of 4K are shown in Fig. 2. At this temperature the phonon absorption processes are shut off, while the higher band gap allows only the electrons generated from the heavy hole band to be above the intervalley transfer threshold. Since the carrier-phonon rates are drastically reduced, the effect of electron-hole scattering is stronger.

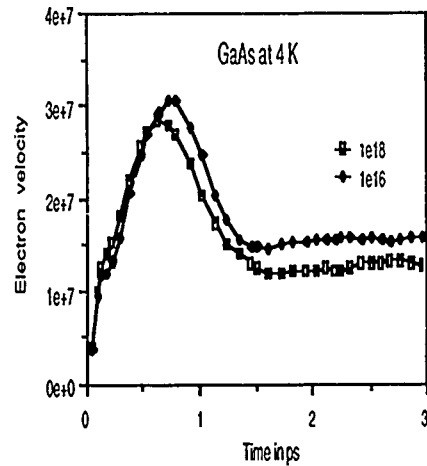


Figure 2. The curves for the electron velocity in GaAs at 4K following a subpicosecond laser pulse. All other parameters are as given in Fig. 1.

The final steady state velocity is lower at the higher concentration as expected. Furthermore, a comparison between the two curves shows a small bump at about 250 fs. This, we believe, is due to the onset of rapid electron transfer from the Γ valley to the X valley for the low density case. As shown in Fig. 3, this point corresponds to the time when electrons begin to appear in the X valley. The effect is prominent for a carrier concentration of 10^{16} cm^{-3} . Since absorption processes are weak, the electrons need time to pick up the required energy from the field. The bump is not as prominent at a density of 10^{18} cm^{-3} since the fraction of electrons having the requisite energy for transfer is reduced by the electron-hole scattering. Reduction of intervalley transfer also leads to a slightly higher velocity during the initial stage. Finally, the peak velocity with strong electron-hole scattering, is lower and occurs at an earlier time. This behaviour can be explained in terms of the two following mechanisms. As the average kinetic energy increases, the inverse screening length is reduced leading to stronger electron-hole scattering. Furthermore, as the difference between the net electron and hole momentum increases, so does the momentum randomization associated with the scattering. The net result is a lower peak occurring at an earlier time.

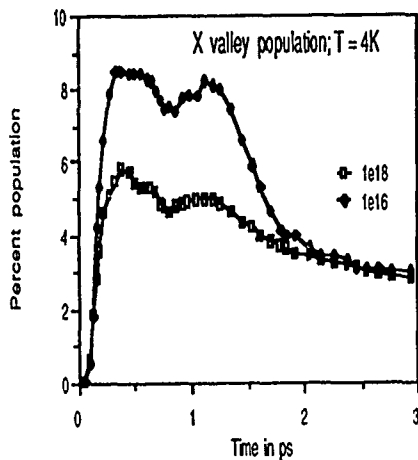


Figure 3. The time dependent X valley population for the simulation at 4K. The laser excitation and electric field corresponds to that shown in Fig. 2 for carrier densities of 10^{16} and 10^{18} cm^{-3} .

Results showing the effects of the non-equilibrium phonons are presented in Fig. 4. A temperature of 4 K with a carrier density of 10^{18} cm^{-3} was used to allow for strong hot phonon amplification. As is evident from the figure, the low wavevector modes are amplified more strongly. There are two reasons for this behaviour. Firstly, the polar electron-LO phonon scattering strength being inversely proportional to the phonon wavevector, favours an increase in the low q values. Secondly, given the electronic band structure any emission/absorption process at a higher energy has a lower wavevector associated with it. A high energy electron distribution would, therefore, contribute more towards low wavevector amplification. In the present situation, the 10 KV/cm field provides the energy driving the electrons to higher energy states. Even to start with, the electron population photogenerated from the heavy hole band is large, leading to a bigger fraction of relatively higher energy electrons. Finally, unlike the unbiased cases examined previously [11], the phonon population reaches its peak well after 3 ps.

The results for the corresponding electron velocity are given in Fig. 5. These curves show that the increased phonon population leads to an enhanced intervalley transfer. This is brought about indirectly because of an increase in the intravalley absorption process. The intravalley absorption feeds energy back into the electron system. The carriers, therefore, are able to acquire energy beyond the intervalley threshold. The

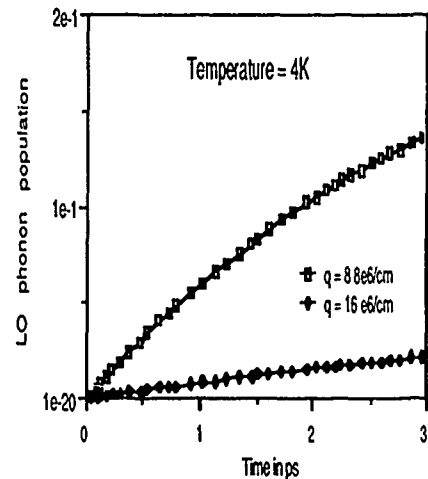


Figure 4. The LO phonon population following the photoexcitation at 4K in GaAs for a carrier density of 10^{18} cm^{-3} . Two phonon modes are shown.

influence of the higher intervalley transfer rate becomes more apparent at times beyond 1 ps when the carrier velocity values are slightly lower by comparison. A similar decrease in the velocity at longer times was obtained by Rieger et al. [27] for n-type GaAs. The magnitude of the changes obtained with the hot phonon effect are not very significant showing that the carrier-carrier scattering is more important for transient transport. By the same reasoning, the density dependence of the mobility rise times obtained by Nuss et al. [10] are probably not due to hot phonon effects alone, but additionally affected by carrier-carrier and anti-screening [28] effects. The rise times mentioned in their experiment are not long enough, nor the operating temperature low enough for significant phonon heating effects.

In order to experimentally verify the hypothesis that the density and bias dependent delay is due to a Jones-Rees mechanism, we need to shut off the intervalley scattering. This can be done by switching material systems. In particular, we choose $\text{Al}_{0.3}\text{Ga}_{0.7}\text{As}$ and show the transient velocity curves in Fig. 6 for the same parameters as used for Fig. 1. The interesting point about these curves is the absence of a delay in the initial rise time. This is a result of the larger band gap of this material which prevents the Jones-Rees like behaviour discussed previously [16,24]. The carriers tend to remain in the Γ valley longer showing a greater velocity overshoot. Furthermore, both the peak and the steady state values are lower than those shown in Fig. 1 because of additional phonon modes and

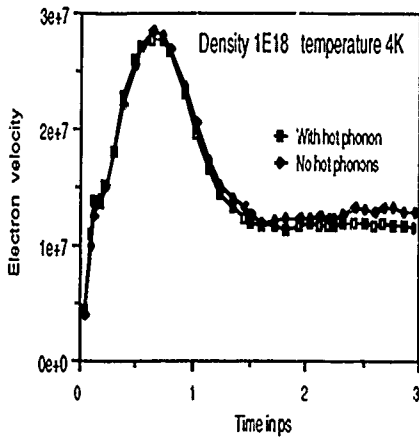


Figure 5. The effects of hot phonons on the electron velocities. The electron velocities are obtained for GaAs at 4K and a carrier density of 10^{18} cm^{-3} . The parameters are the same as before.

increased effective mass related scattering rates. Two phonon like modes have been used in the simulation. The relative strengths and energies of the GaAs-like and AlAs-like modes were taken from the Raman studies of Kash et al. [25]. The relative intensity of the hot phonon spectra yields the desired information about the two dominant modes. With strong electron-hole scattering, the steady state value is lower at the higher carrier density, but the peak shows an increase. The occurrence of a higher peak is similar to that seen in GaAs for low excitation energies [29] or high fields [30]. The electron-hole scattering tends to retain the electrons in the central valley at the early times. Once the electrons have transferred to the L valley, the velocity fall off is faster for AlGaAs than for GaAs. This occurs because the smaller mass mismatch between the electrons and the heavy holes leads to more effective electron-hole scattering than in GaAs.

Summary

The results from Monte Carlo simulations indicate that the inclusion of the electron-hole effect is very important for correctly modelling the transient carrier velocities of photoconductive switches. In certain situations, often encountered in actual experiments, the electron-hole interaction can lead to an enhancement of the velocity overshoot. In all cases, the interaction influences the intervalley transfer effects. Finally, the role of the

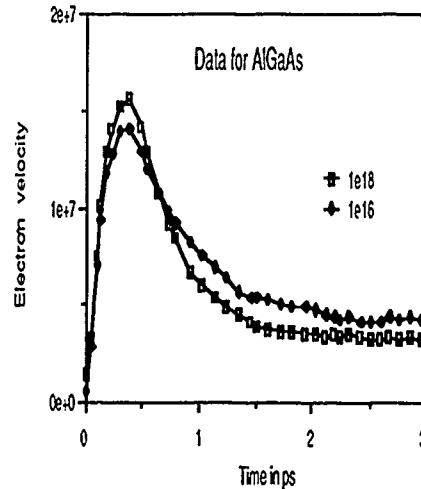


Figure 6. The electron velocity curves for $\text{Al}_{0.3}\text{Ga}_{0.7}\text{As}$ following the laser excitation. A lattice temperature of 300K and a field of 10KV/cm is used here.

nonequilibrium phonons is probably not very significant for the initial portion of the transient situations, but can cause longer time tails in the response.

Acknowledgments

This work was supported by a grant from the Air Force Office of Scientific Research. The authors are indebted for helpful discussions with D. K. Ferry, K. Meyer and G. Mourou.

References

1. J. A. Kash, J. C. Tsang, and J. M. Hvam, Phys. Rev. Lett. **54**, 2151 (1985).
2. W. Potz and P. Koccar, Phys. Rev. **B28**, 7040 (1983).
3. K. T. Tsen, R. P. Joshi, D. K. Ferry, and H. Morkoc, Phys. Rev. **B39**, 1446 (1989).
4. F. W. Wise, I. A. Walmsley, and C. L. Tang, Appl. Phys. Lett. **51**, 605 (1987).
5. W. Z. Lin, J. G. Fujimoto, E. P. Ippen, and R. A. Logan, Appl. Phys. Lett. **51**, 161 (1987).
6. P. Becker, H. Fragnito, C. Brito Cruz, R. Fork, J. Cunningham, J. Henry, and C. V. Shank, Phys. Rev. Lett. **61**, 1647 (1988).
7. S. Das Sarma, J. K. Jain, and R. Jalabert, Phys. Rev. **B37**, 1228 (1988).
8. C. H. Yang, J. M. Carlson-Swindle, S. A. Lyon, and J. M. Worlock, Phys. Rev. Lett. **55**, 2359 (1985).

9. J. Shah, A. Pinczuk, A. C. Gossard, and W. Wiegmann, *Phys. Rev. Lett.* **54**, 2045 (1985).
10. M. C. Nuss, D. H. Auston, and F. Capasso, *Phys. Rev. Lett.* **58**, 2355 (1987).
11. D. K. Ferry, R. P. Joshi, and M. J. Kann, *Proc. SPIE* **942**, 2 (1988).
12. P. C. Becker, H. L. Fragnito, C. Brito Cruz, J. Shah, R. Fork, J. E. Cunningham, J. E. Henry, and C. V. Shank, *Appl. Phys. Lett.* **53**, 2089 (1988).
13. C. V. Shank, R. L. Fork, B. Greene, F. K. Reinhart, and R. A. Logan, *Appl. Phys. Lett.* **38**, 104 (1981).
14. K. Meyer, M. Pessot, G. Mourou, R. O. Grondin, and S. Chamoun, *Appl. Phys. Lett.* **53**, 2254 (1988).
15. A. Evan Iverson, G. M. Wysin, D. L. Smith, and A. Rodendo, *Appl. Phys. Lett.* **52**, 2148 (1988).
16. R. O. Grondin and M. J. Kann, *Solid State Elect.* **31**, 567 (1988).
17. J. Degani, R. F. Leheny, R. Nahory, and J. P. Heritage, *Appl. Phys. Lett.* **39**, 569 (1981).
18. R. A. Hopfel, J. Shah, P. A. Wolff, and A. C. Gossard, *Phys. Rev. Lett.* **56**, 2736 (1986).
19. D. D. Tang, F. F. Fang, M. Scheuermann, and T. C. Chen, *Appl. Phys. Lett.* **49**, 1540 (1986).
20. P. Lugli and D. K. Ferry, *IEEE Trans. Elec. Dev.* **ED-32**, 431 (1985).
21. M. A. Osman and D. K. Ferry, *J. Appl. Phys.* **61**, 5330 (1987).
22. M. D'yakonov, V. I. Perel and I. N. Yassievich, *Sov. Phys. Semicond.* **11**, 801 (1977).
23. P. Lugli, C. Jacoboni, L. Reggiani, and P. Kocevar, *Appl. Phys. Lett.* **50**, 1521 (1987).
24. D. Jones and H. D. Rees, *J. Phys. C* **6**, 1781 (1973).
25. J. A. Kash, S. S. Jha, and J. C. Tsang, *Phys. Rev. Lett.* **58**, 1869 (1987).
26. N. Takenaka, M. Inoue, and Y. Inuishi, *J. Phy. Soc. Jpn.* **47**, 861 (1979).
27. M. Rieger, P. Kocevar, P. Bordone, P. Lugli, and L. Reggiani, *Solid State Elec.* **31**, 687 (1988).
28. A. El-Ela, F. Riddoch, M. Davis, and B. K. Ridley, *Proc. Int. Conf. Semiconductor Phys.*, 1567 (1986).
29. M. A. Osman and H. L. Grubin, *Proc. SPIE* **942**, 18 (1988).
30. K. Sadra, C. M. Mazier, B. G. Streetman, and D. S. Tang, *Appl. Phys. Lett.* **53**, 2205 (1988).

Role of Electron-Electron Scattering on the Ultrafast Relaxation of Hot Photoexcited Carriers in GaAs

M. J. Kann and D. K. Ferry

*Center for Solid State Electronics Research, Arizona State University,
Tempe, Arizona 85287-6206*

Abstract

The femtosecond relaxation of photoexcited carriers in semiconductors is investigated by the use of ensemble Monte Carlo calculations coupled with a molecular dynamics approach for the carrier-carrier interaction, to probe various scattering mechanisms and the dynamic screening of hot carriers in semiconductors. The results indicate that the initial rapid relaxation occurs on a time scale of tens of femtoseconds in GaAs decreasing with increasing carrier density.

INTRODUCTION

Advances in ultrashort laser pulse techniques have led to the generation of laser pulses as short as 6 fs, which have made it possible to measure experimentally the polarization dephasing rate [1], and the initial exponential decay time constant for carriers in the excitation volume (in phase space) in semiconductors [1-6]. As the dimensions of electronic devices reach the submicron region, the energy and momentum losses due to carrier-carrier interactions begin to play a crucial role in device performance [7].

Investigations of hot photoexcited carrier relaxation in semiconductors have shown that a quasi-equilibrium energy distribution is developed in less than 1 ps. However, the initial stages of carrier relaxation occurs through an interplay of both carrier-carrier and carrier-phonon scattering, so that the understanding of the initial rapid cooling observed experimentally requires the knowledge of how this thermalization is established on the femtosecond time scale. For this purpose, careful ensemble Monte Carlo (EMC) calculations are required.

It is known that these EMC calculations are appropriate techniques for studying the transient femtosecond dynamics. We have shown previously that, in the absence of carrier-carrier scattering, the decay of electrons from the initial excitation volume in phase space occurs no faster than about 75-80 fs [8], which agrees well with the experimental results of Shank's group [6], who probe the fast scattering of carriers out of the central valley using pump-probe techniques with two 6 fs pulses centered at 2 eV. The time resolution of the ultrashort 6 fs laser pulse has made it possible for them to investigate directly the dynamics of intervalley scattering in GaAs. Shah's group reports [9] a slow rise of luminescence in GaAs after excitation by a subpicosecond laser pulse, due to a slow return of electrons from the L valley to the central valley. By fitting the data with an EMC calculation, they determine the Γ -L deformation potential to be $(6.5 \pm 1.5) \times 10^8$ eV/cm, which confirms the value we use (7×10^8 eV/cm). Transfer of the carriers to the satellite valleys represents the storage of energy, which is reintroduced to the system when those carriers return to the central valley. The electrons returning to the central valley act as a source of heating for the photoexcitation plasma and thus slow down the cooling of the electron gas.

Experiments in which faster decay rates are observed must entail another process, such as carrier-carrier scattering. With techniques of increased time resolution, Becker *et al.* [1] report the first observation of femtosecond photon echoes from direct transitions in GaAs. The echo decay time constant was found to vary from 11 down to 3.5 fs for carrier density ranging from 1.5×10^{17} to 7×10^{18} cm⁻³. This allowed them to determine the polarization dephasing rate (which is four times the echo decay time constant).

The carrier density dependence of the dephasing rate indicates that carrier-carrier scattering is the dominant dephasing mechanism in the rapid initial stage of relaxation and yields previously unavailable information on Coulomb screening in the nonequilibrium plasma. Collisions involving both electrons and holes can dephase the polarization of an electron-hole pair. At high carrier densities the carrier momentum loses phase coherence primarily due to the screened Coulomb interaction between carriers.

MONTE CARLO AND MOLECULAR DYNAMICS

Most analytical approaches with carrier-carrier scattering do not fully incorporate the energy scattering inherent in this process, and are handicapped by approximations to detailed time-dependent screening. The dynamical screening of nonequilibrium carriers in semiconductors can be studied by inclusion of the electron-electron interaction directly via a molecular dynamics (MD) approach within the EMC technique. In this paper, we utilize a novel MD approach to calculate the inter-carrier Coulomb forces [10], which allows us to examine the details of this process directly, as well as to study the buildup of screening dynamics. Treating a large number of particles via a MD approach in a computer is very time-consuming. However, we have carried out calculations for 2000 particles using a vectorized program, and these calculations can be performed in reasonable time. In these calculations, each particle interacts simultaneously with all other particles in the ensemble through a real space Coulomb potential. The details of the structure of the process are similar to that reported previously for Si [10], in which two basic boxes, of a size determined by the number of particles and the simulated electron density, are used in real space. One box is used to set the laboratory reference frame and has periodic boundary conditions imposed upon it, while the second is a moving box, in which the MD forces are evaluated, centered on each particle. This latter box ensures that we evaluate the net force by summing through the set of shortest equivalent particle vectors in the Ewald sum [11]. By utilizing the MD approach, we thus can treat the inter-carrier potentials exactly and avoid any assumptions on the form of the dielectric function which is used in the screening process.

The use of a molecular dynamics approach to treat the inter-electronic scattering in real space assures that energy can be exchanged between interacting carriers. This follows since

the net force exerted on one carrier by the remaining members of the ensemble assures that it can be accelerated or decelerated. Thus, we account directly for the energy exchange among members of the electron ensemble. On the other hand, we deal only with the electrons here, and leave to later work a study of the role of electron-hole scattering. While this is a drawback of the present work, earlier work on the role of the electron-hole interaction on the psec time scale suggests the results are valid, in that the dominant part of the distribution relaxation occurred by electron-electron scattering [7].

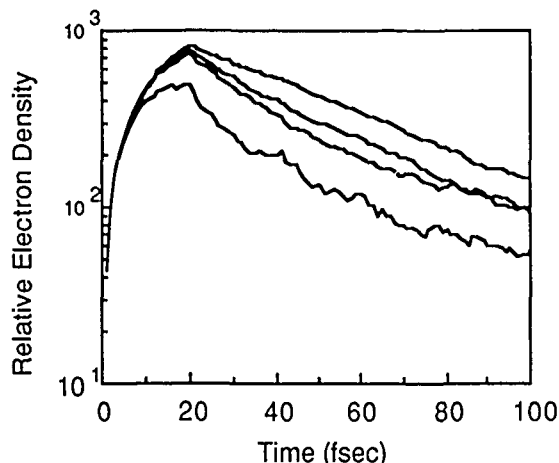


Figure 1. The build-up and decay of the population in the excitation volume. The curves are for 0.05 , 0.5 , 1.0 , and $7 \times 10^{18} \text{ cm}^{-3}$ (decreasing order down the figure). The pulse length is assumed to be 20 fs.

RESULTS

In the studies reported here, we report initial results treating just the dynamics of the electrons at 300 K. In Fig. 1, we show the population of electrons in the central valley that remain in the initial excitation volume after being excited from the heavy hole band. The scattering out of this initial optically excited state is basically dominated by a single exponential decay at short times (we use a 20 fs excitation pulse). In Fig. 2, this single exponential time constant determined from such curves is plotted as a function of the density of excited electrons. The values shown in this latter figure agree well with those inferred from the dephasing experiments of Becker *et al.* [1] and also give good agreement with the values cited by Tang *et al.* [3] for the various time constants. This time is almost totally dominated by the electron-electron scattering process, as suggested by the former authors. Only at the lower values of electron density does the decay rate become sufficiently slow that the intervalley

scattering process becomes a significant part of the total rate.

The data shown in Fig. 2 suggest that there is a knee in the time constant for the decay of the initial state. Clearly, for densities beyond about $2 \times 10^{17} \text{ cm}^{-3}$, the time constant for decay of the number of particles in the excitation volume decreases rapidly with increasing density. On the logarithmic scale shown here, this decay is almost linear in nature. We return to this point later. Below this critical density, however, the time constant does not seem to vary much with the excitation density, which suggests that the lifetime is dominated by phonon scattering processes. In previous work [8], we analyzed the population build-up in the L and X valleys and ascertained that the lifetime for scattering to the L valleys was of the order of 75-80 fs. Similar analysis of the X valley population, presented in this earlier work, suggests that the lifetime for scattering to the X valleys was of the order of 45-50 fs. On the other hand, if these two time constants are this short, the total rate of scattering out of the excitation volume to the satellite valleys would produce a lifetime of the order of 30 fs. Clearly, the data presented in Fig. 2 suggest that the phonon lifetime is longer than this, and should be of the order of 40 fs.

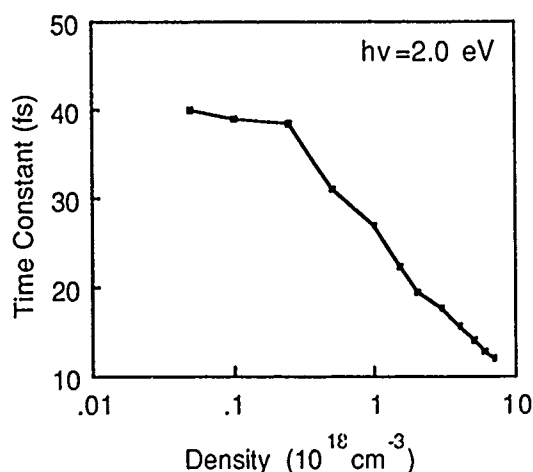


Figure 2. The lifetime for scattering out of the excitation volume for a 2.0 eV photon excitation. The decay is dominated by electron-electron scattering.

The long lifetime at low density suggests that we may have to re-evaluate the lifetimes for scattering to the satellite valleys. If the total rate leads to a lifetime as short as 40 fs, and the lifetime for scattering to the X valleys is as short as 50 fs, then this would mean that the lifetime for scattering to the L valleys could be no less than 200 fs, which is too slow for the actual phonon scattering rates. On the other hand, if the lifetime

for scattering to the L valley is as long as 100 fs, then this would suggest that the lifetime for scattering to the X valleys could be no faster than 65 fs, which does not fit well to the data of Becker *et al.* [6]. One way out of the dilemma lies in the fact that the measurements of the latter authors on the lifetime for scattering to the L valleys were done with the transfer to the X valleys cut off. The calculations done here, and in our earlier work [8] were not done in this fashion, so that the populations of the various valleys, and of the excitation volume, are carried out in the presence of complicated Γ -X-L processes, and the electron-electron scattering, so that the population of the L valley includes electrons that have arrived there after passing through the X valley. Moreover, the scattering lifetimes are affected by the presence of the electron-electron scattering. We examine this in the next paragraph.

Although the curve in Fig. 2 appears to support a decrease of the lifetime as $-\ln(N)$, it should be pointed out that a fit to a power law in N , as suggested by Becker *et al.* [1] gives just as good an agreement, and the exponent is $-1/3$ as suggested by these latter authors. However, we note that this fit uses all of the data in Fig. 2, a point we return to below. It is suggested by these latter authors that this value of the exponent may be understood in terms of a cut-off of the electron-electron interaction on length scales of $1/q_{TF}$. However, this cut-off would lead to an exponent of $-2/3$, rather than $-1/3$. In fact, the results of the present calculation can be interpreted to support an exponent of $-2/3$. To show this, we need to look only at that part of the data corresponding to the electron-electron scattering lifetime, i.e. the data for densities higher than the "knee" in Fig. 2. To investigate this, we have modified the data of Fig. 2, in order to separate out the constant lifetime at low densities, which we interpret as due to intervalley processes. We do this by a simple Matthiessen's rule summation for the various lifetimes. These net lifetimes are plotted in Fig. 3.

The above argument suggests that the interaction, in momentum space, is cut off at a maximum value of q given approximately by the Fermi-Thomas screening wave vector, which leads to this power law behavior. A cut-off of the screened Coulomb interaction for electron-electron interactions has been discussed previously in ensemble Monte Carlo approaches to transport [13]. As we mentioned, this would lead to a $-2/3$ behavior. The data of Fig. 3 have a dependence which is best fit with an exponent of -0.75 ± 0.05 , which while not $-2/3$ is quite close and probably within the accuracy of both the simple screening theory and these calculations.

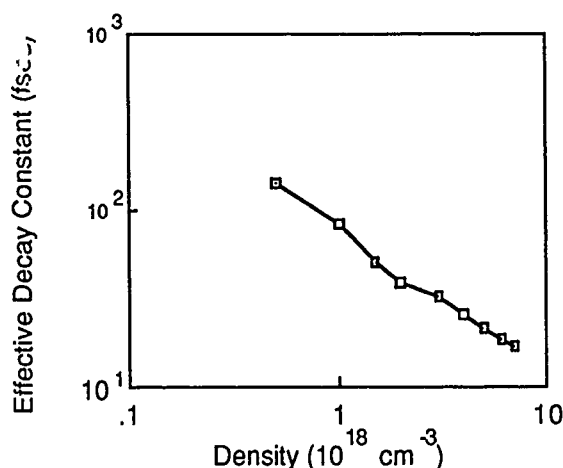


Figure 3. The effective lifetimes for electron-electron processes (with the intervalley contributions removed).

It must be pointed out here, that there is an incongruity in the data presented by Becker *et al.* in refs. [1] and [6]. The data of Figs. 2,3 fit very well the measurements of the former reference [1]. On the other hand, it must be pointed out that the measurements of Becker *et al.* [6], which were made for excitation densities in the range $3\text{--}6 \times 10^{18} \text{ cm}^{-3}$, exhibit a lifetime of 33 fs and their measured lifetime was *independent of the density*, which neither agrees with the results found here nor with the dephasing experiments also carried out by Becker *et al.* [1]. In fact, however, they fit well to the data of the Cornell group [2,3], which gives 33-34 fs at the lower end of this density range. This variation in the measurements, and with the current theory, is puzzling, and warrants further investigation.

Let us now return to the question of lifetime for scattering to the satellite valleys. In Fig. 4, we plot the populations of the satellite valleys in terms of the fraction of the total electrons photo-excited. It is clear that the population of the X-valley is dramatically increased by the presence of the electron-electron scattering, as this latter mechanism excites carriers out of the excitation volume to both higher and lower energy states. These higher energy electrons have a higher scattering probability to the X-valleys. This is reflected also by a longer tail in the L-valleys, which must arise from $\Gamma\text{-X-L}$ scattering processes. Thus, the determination of a lifetime from the population data, such as shown in Fig. 4, must be done quite carefully to unfold such multiple pass-through processes. This applies to both theory and experiment.

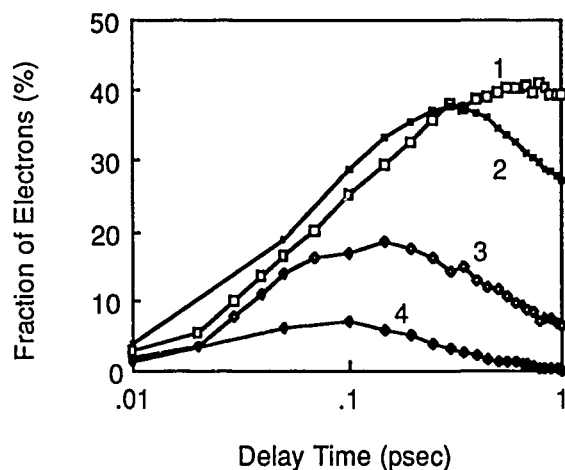


Figure 4. The populations of the satellite valleys. The open symbols (curve 1 for the L valley and 3 for the X valley) are the populations in the presence of electron-electron scattering, while the closed symbols (curve 2 for the L valley and 4 for the X valley) are for its omission.

SUMMARY

In summary, we find the fast initial decay of carriers from the excitation volume occurs predominantly by electron-electron scattering. We found earlier that the $\Gamma\text{-L}$ scattering rate is 75-80 fs (for 2 eV excitation) and the $\Gamma\text{-X}$ scattering rate is about 50 fs. These results agree well with recent measurements [1,6], but disagree with conclusions drawn by others [2,3,12], that would suggest somewhat faster rates. The cause of the disagreement may lie in the use of coupling constants, by the latter authors [12], that overestimate the strength of the scattering from Γ to L. Here, we use coupling constants that have been confirmed by several measurements (by different techniques) [9,14]. Even so, these numbers tend to be even faster than supported by careful calculation of the lifetime for carrier scattering out of the excitation volume done here. At a density for which the GaAs is degenerate (in equilibrium), the scattering out of the excitation volume is dominated by electron-electron scattering alone, and this lifetime decreases with increasing density. This decrease also agrees both in lifetime magnitude and in density dependence with recent experimental measurements [1].

This work was supported by the Office of Naval Research. The authors are indebted for helpful discussions with P. Lugli, S. M. Goodnick, A. M. Kriman, and R. Joshi.

References

1. P. Becker, H. Fragnito, C. Brito Cruz, R. Fork, J. Cunningham, J. Henry, and C. Shank, *Phys. Rev. Letters* **61**, 1647 (1988).
2. M. J. Rosker, F. W. Wise, and C. L. Tang, *Appl. Phys. Letters* **49**, 1726 (1986).
3. F. W. Wise, I. A. Walmsley, and C. L. Tang, *Appl. Phys. Letters* **51**, 605 (1987).
4. R. W. Schoenlein, W. Z. Lin, E. P. Ippen, and J. G. Fujimoto, *Appl. Phys. Letters* **51**, 1441 (1987).
5. W. Z. Lin, J. G. Fujimoto, E. P. Ippen, and R. A. Logan, *Appl. Phys. Letters* **51**, 161 (1987).
6. P. C. Becker, H. L. Fragnito, C. H. Brito Cruz, J. Shah, R. L. Fork, J. E. Cunningham, J. E. Henry, and C. V. Shank, *Appl. Phys. Letters* **53**, 2089 (1988).
7. M. A. Osman and D. K. Ferry, *Phys. Rev. B* **36**, 6018 (1987).
8. D. K. Ferry, R. P. Joshi, and M. J. Kann, *Proc. SPIE* **942**, 2 (1988).
9. J. Shah, B. Deveaud, T. C. Damen, W. T. Tsang, A. C. Gossard, and P. Lugli, *Phys. Rev. Letters* **59**, 2222 (1987).
10. P. Lugli and D. K. Ferry, *Phys. Rev. Letters* **56**, 1295 (1986).
11. D. J. Adams and G. S. Dubey, *J. Comp. Phys.* **72**, 156 (1987).
12. D. W. Bailey, C. J. Stanton, M. A. Artaki, K. Hess, F. W. Wise, and C. L. Tang, *Sol.-State Electron.* **31**, 467 (1988).
13. P. Lugli and D. K. Ferry, *Appl. Phys. Letters* **46**, 594 (1985).
14. K. Kash, P. A. Wolff, and W. A. Bonner, *Appl. Phys. Letters* **42**, 173 (1983).

Intersubband Relaxation of Electrons in $\text{Al}_x\text{Ga}_{1-x}\text{As}/\text{GaAs}$ Quantum Wells During Photoexcitation

Stephen M. Goodnick

Department of Electrical and Computer Engineering, Oregon State University, Corvallis, Oregon 97331

Paolo Lugli

Dipartimento di Ingegneria Meccanica, II Università di Roma, Via O. Raimondo, 00173 Roma, Italy

ABSTRACT

Using an ensemble Monte Carlo simulation of coupled electrons and nonequilibrium slab mode polar optical phonons in single and multiple quantum well systems, we have studied the relaxation of photoexcited carriers in ultra-fast optical intersubband relaxation experiments. Here we study intersubband relaxation in three different types of systems: i) wide wells in which the intersubband separation is less than the optical phonon energy, ii) narrow wells in modulation doped multi-quantum well structures, and iii) coupled asymmetric quantum wells. Simulated results using self-consistent envelope functions in the quantum well system show the importance of nonequilibrium hot phonons and self-consistency in explaining the experimental results from time resolved Raman, intersubband absorption, and photoluminescence spectroscopy.

INTRODUCTION

Ultra-fast optical techniques have proved quite successful in probing hot carrier phenomena in semiconductor quantum well systems [1]. Recently, investigations in such systems have focused on the relaxation of hot carriers via intersubband transitions between the bound states of the quantum well [2-4]. Generally, the intersubband transition rate is reduced compared to intrasubband scattering due to the large change in momentum for intersubband scattering and the orthogonality of the subband wavefunctions themselves. In III-V semiconductors, the dominant intersubband scattering mechanism is believed to be the emission of polar optical phonons for photoexcited carriers injected below the threshold energy of intervalley scattering. Other scattering mechanisms such as acoustic phonons, piezoelectric phonons, impurity and

electron-electron (e-e) interactions may also contribute to transferring electrons from one subband to another. In our previous calculations of the influence of e-e interaction in quantum well systems [6], we found that the intersubband intercarrier scattering rate is quite small although the energy transfer rate is quite efficient so that a quasi-equilibrium in the carrier temperatures is achieved after a few picoseconds.

Studies of the intersubband relaxation in multi-quantum well structures using pump and probe intersubband Raman spectroscopy [2] and far infra-red intersubband absorption spectroscopy [3] have shown unusually long intersubband relaxation times; much longer than that which would be indicated by the intersubband polar optical phonon scattering rate [7]. Oberli et al. [2] studied relaxation in narrow wells (116 Å) and relatively wide wells (215 Å) and saw significantly different results between the two cases. While depopulation of the upper subband was observed to occur quite rapidly in the narrow well case, a depopulation time of several hundred picoseconds was indicated by the rise time of the intersubband Raman spectrum for wide wells. Since the spacing between the ground and first excited subband of the wide well was less than the energy of the polar optical phonon (27 meV compared to a phonon energy of 36 meV), it was argued that a carrier bottleneck develops due to suppression of the intersubband optical phonon scattering. In contrast, Seilmeier et al. [3] found that in narrow, 50 Å modulation doped wells, depopulation times were on the order of 11-14 ps, much longer than the intersubband POP scattering rate which is about 1 ps. In the following sections, we have modeled these two sets of experiments using ensemble Monte Carlo techniques discussed below.

More recently, time resolved photoluminescence (PL) experiments have been performed on coupled asymmetric quantum wells separated by thin AlGaAs barriers [4]. In these experiments, the decay of the

PL intensity due to luminescence from the narrower well (shorter wavelength) measures the transfer of electrons and holes from subband states localized in the narrow well to the lowest subband localized mainly in the wider well. In the coupled QW case, transfer occurs through intersubband scattering as in the single quantum well case. However, the intersubband scattering rate for the coupled well situation may be arbitrarily controlled by the thickness of the barrier which determines the overlap integral between initial and final subband states. We have modeled this case as well using the Monte Carlo model described below and find the time constants in agreement with experimental values.

MONTE CARLO MODEL

The Monte Carlo model used here has been described in detail elsewhere [7-9]. This model simulates the carrier dynamics of photogenerated electrons and holes using the computer random number generator to generate the stochastic collision times and final states of these carriers as they interact among themselves and with the lattice through optical phonon scattering. We simultaneously simulate an ensemble of several thousand particles in order to study the transient behavior of the electronic system during and after photoexcitation. For the present work, we have restricted ourselves to simulation of intersubband relaxation in the electron system alone without the presence of holes. Preliminary calculations including the valence band system have not shown dramatic changes in the basic results presented here, although subtle effects may exist. The basic model for the quantum well system in the present article contains scattering mechanisms due to polar optical and intervalley phonons as well as e-e scattering, calculated numerically using the envelope function states of the quantum well system as described previously [6]. The e-e scattering rate is calculated using a screened Coulomb potential with the use of a static screening constant which is updated during the simulation to account for the time dependent density and temperature of the electron system during photoexcitation. In order to account for effects observed in the ultra-fast optical experiments described above, we have improved the model to additionally include self-consistent solutions of the quantum well states to account for the effect of modulation doping in n-type samples and we have considered nonequilibrium polar optical phonons described by slab mode envelope functions described in more detail below. To model optical generation of carriers due to intraband transitions, we have simply added carriers to the simulation with an excess energy above the lowest conduction band edge appropriate to the experimental photon energy. Photogeneration is assumed to occur according to a phenomenological model for the temporal dependence of the pump pulse and the energy spread of the pulse [6].

INTERSUBBAND RELAXATION IN WIDE QUANTUM WELLS

In the experiments of Oberli et al. [2], rapid relaxation occurred in narrow wells while for wide wells, a long time constant was observed for the population in the first excited subband. To model their results, we used a simple square well potential to represent the eigenstates of the system neglecting self-consistent effects in the potential due to doping. Well widths of 120 Å and 230 Å were used in our calculations to match the experimental intersubband separations. We assume a total injected carrier population of $4 \times 10^{11}/\text{cm}^2$ at a lattice temperature of 5 K. A pulse duration of 1 ps is assumed with the pulse peaking 1 ps into the simulation. The injection energies are chosen so that carriers are excited below the optical phonon energy in the upper subband in accordance with the experimental parameters [2].

It is well known both experimentally and theoretically [9] that the polar optical phonon distribution is driven out of equilibrium due to the emission of phonons from photoexcited hot carriers. To simulate this effect in semiconductor quantum wells, we have modified the polar optical phonon scattering rate to account for confinement of the phonons in the quantum well. Such slab modes have been calculated previously by Riddoch and Ridley [7] and contain both quantized bulk modes and surface modes. For well widths greater than 100, the dominant contribution is due to the quantized bulk modes, and so we neglect the contribution of surface modes for simplicity in the present calculation. To account for hot phonon effects, we employ the algorithm previously employed by us for bulk modes [8] in which the population of phonons is calculated by a detailed balance of phonon emission and absorption events with the electron system. The excess phonon population is also assumed to decay phenomenologically due to anharmonic interactions with a time constant of 7 ps [8]. The dynamic population of excess phonons is used to recalculate the electron-phonon scattering rate at each time step of the simulation, strongly coupling the electron and phonon systems.

Our simulated results are in agreement with the experimental results for narrow wells. For narrow wells (120 Å), the decay of the population in the first excited subband is found to be quite rapid, occurring with a time constant of a few picoseconds. Here, the separation of the subbands is several times larger than the optical phonon energy and, hence, no bottleneck is expected to occur as discussed above. For the wide well case, we see a long time tail in the depopulation of the first excited subband as shown in Fig. 1 where we plot the occupancy and average carrier temperature as a function of time after the peak of the pump pulse at $t = 1$ ps. However, this long time constant tail is found to be associated with hot phonon heating of the carrier distribution rather than a bottleneck in the scattering rate as shown in Fig. 1 by the second set

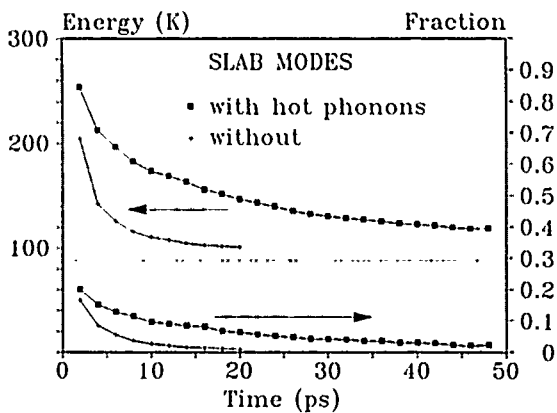


Figure 1. Simulated average energy and fraction of carriers in 2 as a function of time for a 230 Å well with and without hot phonons.

of curves in which we selectively 'turn off' the hot phonon effect by forcing the phonon population to remain in its equilibrium Bose-Einstein distribution. In this case, we see that the decay of the population is quite rapid with a decay time on the order of 5-10 ps. In fact, the population in the upper subband with the presence of hot phonons is found to be very close to that which one would expect for the average energies shown in Fig. 1 versus time in which the thermal tail of the heated Maxwell Boltzmann like distribution overlaps the second subband maintaining the population there. Thus, the conclusion from this study is that intersubband bottlenecks are not present in the relaxation in wide wells, and that experimental studies are showing strong effects due to phonon heating which keeps the upper level occupied for long times.

INTERSUBBAND RELAXATION IN NARROW MODULATION DOPED QUANTUM WELLS

As discussed previously, Seilmeier et al. [3] found relatively long time constants for the relaxation time of carriers out of excited subband states in narrow modulation doped structures. This result is somewhat surprising at first since even for a narrow 50 Å well, the intersubband optical phonon scattering rate is sufficiently high that the upper subbands should be depopulated a few picoseconds after the pump pulse is completed. In fact, our simulated results for a simple finite square well system shown by the upper curve in Fig. 2 show exactly that. Here we plot the percentage of carriers in the lowest subband as a function of time at 300 K. Seilmeier et al. [3] used a pump pulse tuned to the intersubband separation of the ground and first excited subband energies. To model this, we take particles from the lowest subband and promote them to the upper subband conserving the k vector of the electron in the process (vertical

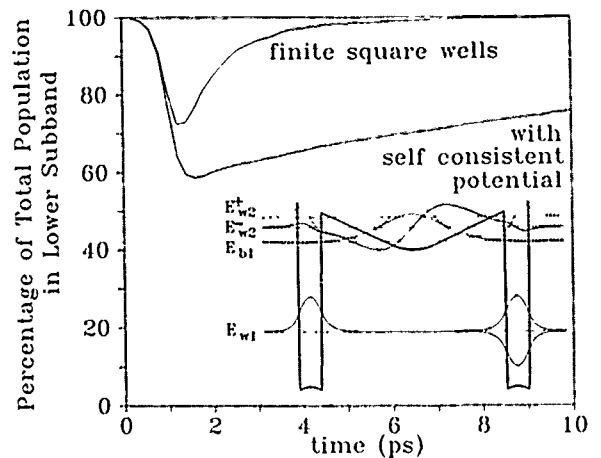


Figure 2. Population of the lowest subband after intersubband excitation using finite square wells versus self consistent solutions. The inset shows the self-consistent conduction band profile and wavefunction for 50 Å GaAs wells separated by 400 Å of modulation doped $\text{Al}_{0.35}\text{Ga}_{0.65}\text{As}$.

transitions). The pump pulse duration was taken as 1 ps which peaks at $t = 1$ ps in Fig. 2. The initial sheet carrier density in the well is $5 \times 10^{11}/\text{cm}^2$, and we assume that half of these electrons are excited to the second subband according to the temporal evolution of the pump pulse. The recovery of the subband population in E_{w1} (the lowest subband energy) for the finite square well appears exponential in nature with a time constant of about 2 ps, much less than the value of 10 ps measured experimentally.

To account for the long experimental time constant, we included the effects of modulation doping on the quantum well potential. In modulation doping, the barrier of the material is heavily doped, with an undoped spacer layer separating the ionized impurities from the free carriers residing in the wells. In the multiple quantum well structures used experimentally [6], the well widths were about 50 Å while the barrier was 400 Å thick with a 100 Å doped region in the center of the barrier. To approximate this structure, we used self-consistent solutions of the coupled Schrodinger and Poisson equations [10] for two wells separated by a 400 Å barrier as shown by the inset of Fig. 2. The lowest lying state in the well is actually two quasi-degenerate states due to the presence of two identical wells. The potential due to ionized donors in the barrier creates a potential well and hence bound states localized in the barrier rather than the well region. The lowest state in the barrier (E_{b1}) is completely localized in that region with very little effect due to the presence of the well. The higher states contain some of the symmetry of the well states as seen in Fig. 2, and thus we label them E_{w2}^+ and E_{w2}^- to identify them as the bonding and antibonding states

associated with the coupled well states. The effect of such bound states on the intersubband scattering rate is pronounced, as the overlap integral between well and barrier states is small.

The ground subband population versus time using self-consistent solutions is found to have a very long time constant as seen in Fig. 2. This is due to the trapping of photoexcited carriers in the E_{b1} state of the barrier, and the attenuated intersubband scattering rate between this state and the E_{w1} state. In fact, the simulated time constant appears even longer than 11-14 ps value measured experimentally. Part of the reason for this overestimation arises because we have neglected to account for the change in the subband eigenstates and self-consistent potential as carriers are promoted from the ground subband to barrier states. The effect of localized electrons in the barrier states will be to compensate the ionized impurity charge in that region and hence reduce the potential well existing in the barrier. As the well barrier decreases, the overlap of the barrier states with the well states will increase and intersubband scattering will be increased. Therefore, our simulated results represent an upper bound on the relaxation time in the modulation doped structure. The basic conclusion of our study of this system remains the same, however: the long time constant for intersubband relaxation is due to trapping of photoexcited carriers in barrier states and not reduced intersubband scattering due to having a narrow well.

INTERSUBBAND RELAXATION IN COUPLED QUANTUM WELLS

Recently, time resolved PL has been used in the study of intersubband relaxation in coupled asymmetric quantum wells [4,5]. A schematic of the energy band diagram for such a system is shown by the insert in Fig. 3 where the distance b represents the thickness of an AlGaAs barrier which separates two wells of different thicknesses. The slope on the conduction band edge represents the experimental situation in which the coupled wells are located in the intrinsic region of a p-i-n diode which controls the electric field across the wells and modulates the subband energies. For the results of Fig. 3, a field of 20 kV/cm was assumed corresponding to studies by Oberli et al. [4]. Wells widths of 60 and 88 Å were used and barrier thicknesses ranging from 25 to 60 Å were simulated in correspondence with experimental parameters [4]. The subband eigenstates were calculated using numerical solutions to Schrodinger's equation. Two sets of subbands arise, those primarily localized in the wide well (the unprimed system in Fig. 3) and those localized in the narrower well (the primed system). During photoexcitation by the pump pulse (here taken as 1 ps in duration peaking at 1 ps), excess carriers are excited with equal populations in the narrow and wide wells below the energy of E_2 of the wide system.

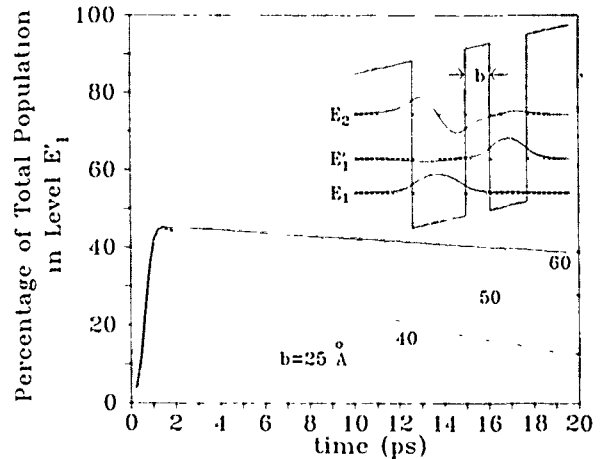


Figure 3. Population in the first excited level E_1' for coupled 88 and 60 Å undoped GaAs wells under applied bias for various $\text{Al}_3\text{Ga}_{.7}\text{As}$ barrier widths after a pulse peaked at 1 ps.

In Fig. 3 we plot the percentage of the total electron concentration residing in the lowest (E_1') subband of the narrow well as a function of time before and after photoexcitation. Since the intersubband scattering rate depends on an overlap integral between different subbands, it is apparent from Fig. 3 that the rate of transitions between states in the same well will be much stronger than transitions between different well states. The main overlap (i.e., regions in which both wavefunctions are non-zero) occurs in the barrier region as shown in Fig. 3 and, therefore, is very sensitive to the height and width of the barrier. This fact is reflected in the strong dependence of the upper subband population versus time on the barrier thickness shown in Fig. 3. Here we see almost exponential decay in the subband population. For narrow barriers (25 Å), the time constant of this decay is about 5 ps while for the 60 Å barrier, simulation times of 115 ps were necessary to approach the $1/e$ value of the initial population. These numbers appear to agree quite well with the values obtained from PL experiments for the same structure.

SUMMARY

We have compared recent pump and probe intersubband relaxation experiments in quantum well systems using an ensemble Monte Carlo simulation. By selectively adding or subtracting different interactions into the simulation, we are able to explain some of the features observed in these experiments. In particular, for wells in which the intersubband separation is less than the optical phonon energy, we find that hot phonons and not an intersubband bottleneck appear to be the mechanism responsible for a long time constant population of upper subbands. For narrow

modulation doped samples, long times in the intersubband relaxation are found to be due to trapping of the carriers in barrier states due to modulation doping. Finally, simulation of intersubband relaxation in coupled wells shows that the relaxation time is critically dependent on the barrier thickness separating the wells as is observed experimentally.

ACKNOWLEDGMENTS

The authors would like to express their deep appreciation to J. Lary for help in the calculations presented here. We would like to express our appreciation to Stellar Computer for the donation of computer resources. One of the authors (SMG) acknowledges support of this work under the U.S. Office of Naval Research Contract No. N00014-87-0686.

REFERENCES

1. J. Shah, "Hot Carriers in Quasi-2-D Polar Semiconductors," *IEEE J. Quantum Elec.* **QE-22**, 1728-1743 (1986).
2. D.Y. Oberli, D.R. Wake, M.V. Klein, J. Klem, T. Henderson, and H. Morkoc, "Time-Resolved Raman Scattering in GaAs Quantum Wells," *Phys. Rev. Lett.* **59**, 696-699 (1987).
3. A. Seilmeier, H.J. Huebner, G. Abstreiter, G. Weimann, and W. Schlapp, "Intersubband Relaxation in GaAs-AlGaAs Quantum Well Structures Observed Directly by an Infrared Bleaching Technique," *Phys. Rev. Lett.* **59**, 1345-1348 (1987).
4. D.Y. Oberli, J. Shah, T.C. Damen, C.W. Tu, and D.A.B. Miller, "Electron Tunneling Times in Coupled Quantum Wells," to be published.
5. T.B. Norris, N. Vojdani, B. Vinter, C. Weisbuch, and G.A. Mourou, "Charge-Transfer State Photoluminescence in Asymmetric Coupled Quantum Wells," to be published.
6. S.M. Goodnick and P. Lugli, "Effect of Electron-Electron Scattering on the Nonequilibrium Transport in Quantum-Well Systems," *Phys. Rev. B* **37**, 2578-2588 (1988).
7. F.A. Riddoch and B.K. Ridley, "Electron Scattering Rates Associated with the Polar Optical Phonon Interaction in a Thin Ionic Slab," *Physica* **134B**, 342-346 (1985).
8. P. Lugli and S.M. Goodnick, "Nonequilibrium Longitudinal-Optical Phonon Effects in GaAs-AlGaAs Quantum Wells," *Phys. Rev. Lett.* **59**, 716-719 (1987).
9. S.M. Goodnick and P. Lugli, "Influence of Electron-hole Scattering on Subpicosecond Carrier Relaxation in $\text{Al}_x\text{Ga}_{1-x}\text{As}/\text{GaAs}$ Quantum Wells," *Phys. Rev. B* **38**, 10135-10138 (1988).
10. F. Stern and S. Das Sarma, "Electron Energy Levels in GaAs-GaAlAs Heterojunctions," *Phys. Rev. B* **30**, 840-847 (1984).

Phonons and Phonon Interactions in Layered Semiconductors

G. Mahler

*Institut für Theoretische Physik, Universität Stuttgart, Pfaffenwaldring 57,
D-7000 Stuttgart 80, Federal Republic of Germany*

A. M. Kriman and D. K. Ferry

*Center for Solid State Electronics Research, Arizona State University,
Tempe, Arizona 85287-6206*

Abstract

Continuum models are developed which describe the optical as well as the acoustic displacements in polar media, including corrections to the harmonic approximation. These lead to simple phonon modes in locally isotropic media, and confirm a previously conjectured dispersion relation. They are used to study phonon lifetimes and the effects of heterostructure confinement. It is found that the lifetime of confined LO phonons decaying into delocalized acoustic phonons is substantially independent of size of the confining region.

INTRODUCTION

In semiconductor heterostructures, the eigenmodes of phonon as well as electron fields are expected to exhibit confinement effects, and these should also influence the respective transition rates induced by external perturbations. Despite the complexity of any detailed treatment of a realistic interface, simplified interface models in terms of boundary conditions, like the infinite barrier model for electrons in quantum wells, have proven useful in providing intuitive understanding and even quantitative estimates. For acoustic and optical phonon fields no such interface models exist, and while models of coupling to the electron field are well established, the anharmonic interaction appears to be very involved: No attempt has been made to date to study the influence of phonon confinement. In this paper, we describe the first attempts to do so, in a framework useful for studies of picosecond excitation in quantum wells.

Within a systematic continuum approach [1], we derive generalized equations of motion for the acoustic and optical displacement fields. As our immediate interest is in the interactions, rather than in the details of the dispersion relations, we specialize these equations to isotropic symmetry and retain gradients up to second order, in which case both fields decouple into

longitudinal and transverse parts. In this way, the *ad hoc* model proposed in Refs. [2,3] can be derived systematically.

For specific point symmetries, we then derive explicit analytical anharmonic coupling models. We use these to study low temperature phonon lifetimes. The wave vector (q) dependence of phonon lifetimes is found for acoustic phonons, as well as the q dependence of different processes contributing to the relaxation of optical phonons. Coupling coefficients are estimated from scaling arguments [4], yielding lifetimes in satisfactory agreement with picosecond experiments [5-7].

We have modeled heterojunctions by interface boundary conditions, and found conditions which lead to confined modes but which nevertheless preserve the longitudinal or transverse character of phonons. This simplifies greatly the form of modes in the presence of interfaces, even for polar displacement fields. Using these modes, we find that the lifetime of *confined* LO phonons decaying into *delocalized* acoustic modes does not depend significantly on the confinement length.

MODEL

Quadratic Lagrangian

Our approach begins from the Lagrangian [8]

$$L = \int dr \mathcal{L}, \quad (1)$$

where we write dr for a differential volume element. The Lagrangian density \mathcal{L} depends only on first order time derivatives and low order spatial derivatives of various continuum fields. The fields that will be the main focus of this study are the multiphase displacement fields $u_i^{\nu}(\mathbf{r}, t)$ of condensed matter systems. [We will use standard index conventions for the subscripts: repeated indices are summed over (e.g., $\psi_{ii} = \psi_{11} + \psi_{22} + \psi_{33}$), and subscripts following a

comma denote differentiation ($\phi_{ij} = \partial \phi / \partial r_j$, etc.).] In a microscopic description, the superscript index v would be an atomic species label. In particular, for a crystalline solid, one may regard the label v as indicating an element in the basis of a unit cell. Each component v has a mass density $\rho_v \equiv M_v/v_c$, with M_v the atomic mass and v_c the cell volume. In most continuum treatments, there is only a single displacement field. (See, however, [1].)

In the present study the Lagrangian will include the following four general kinds of terms:

$$L = L^{uu} + L^{ue} + L^{ee} + L^{uuu}. \quad (2)$$

The first part, L^{uu} , is the usual quadratic Lagrangian which describes the noninteracting phonon modes:

$$L^{uu} = L_{\text{kin}}^u - V^{uu}, \quad (3a)$$

$$L_{\text{kin}}^u = \frac{1}{2} \int dr \sum_v \rho_v \dot{u}_i^v \dot{u}_i^v, \quad (3b)$$

$$V^{uu} = \frac{1}{2} \iint dr dr' \sum_{v,v'} \beta_{ii'}^{vv'}(r,r') u_i^v(r) u_{i'}^{v'}(r'). \quad (3c)$$

The second term in Eq. (2) describes the interaction of the continuum with a static electric field. In this paper we shall not include any externally applied field, so L^{ue} includes only the piezoelectric self-interaction of the medium with its own "internal" electric field \mathcal{E} . In order to determine this field, it becomes necessary to include the self-interaction of the electric field,

$$L^{ee} = \frac{1}{8\pi} \int dr (\epsilon_{\infty} - 1) \mathcal{E}_i \mathcal{E}_i. \quad (4)$$

The first three terms in (2), comprising the quadratic Lagrangian, provide the lowest order eigenstates - phonons - that form the basis for more detailed studies. In this paper we will describe the analysis of these terms in some detail, to the point where phonon dispersion relations are found. The last term, L^{uuu} , consists of the third order terms in the deformation energy, and describes modifications of the phonon modes and transitions among them. The use of these terms to find phonon lifetimes will be discussed below.

From the form of the deformation potential energy (3) it is clear that only the symmetric part of the interaction contributes, so we set

$$\beta_{ii'}^{vv'}(r,r') = \beta_{i'i}^{v'v}(r',r) \quad (5)$$

without loss of generality. We expect the interaction potential (3c) to couple fields strongly only for nearby points. Taylor expansion of the fields then leads to a gradient series for $\beta^{vv'}$:

$$\beta_{ii'}^{vv'}(r,r') = \delta(r-r') \times \quad (6)$$

$$\left[B_{ii'}^{vv'} + C_{ijl}^{vv'} \frac{\partial}{\partial r_j} + C_{iil'}^{vv'} \frac{\partial}{\partial r_{j'}} + \right.$$

$$+ D_{ijkl}^{vv'} \frac{\partial^2}{\partial r_j \partial r_k} + D_{ijl'j'}^{vv'} \frac{\partial^2}{\partial r_j \partial r_{j'}} + D_{iil'jk'}^{vv'} \frac{\partial^2}{\partial r_{j'} \partial r_{k'}} +$$

$$\left. + E_{ijkli'}^{vv'} \frac{\partial^3}{\partial r_j \partial r_k \partial r_{l'}} + \dots + F_{ijklmli'}^{vv'} \frac{\partial^4}{\partial r_j \partial r_k \partial r_{l'} \partial r_m} + \dots \right]$$

The tensors $B^{vv'}$, $C^{vv'}$, $D^{vv'}$, etc. are the local parameter fields of the problem. From Eq. (5) it is clear that

$$D_{ijl'j'}^{vv'} = \frac{\partial^2 L}{\partial u_{i,j}^v \partial u_{i',j'}^{v'}} = D_{i'j'ij}^{v'v}, \quad (7)$$

with the derivative evaluated at the point where all the fields and all their derivatives are zero. By a similar calculation, it is clear that the two $C^{vv'}$ tensors in Eq. (6) are equivalent, but that there are two independent $D^{vv'}$ tensors: $D_{...l}$ and $D_{...l'}$. In general, we shall omit the vertical bar which separates subscripts corresponding to different superscripts, and the identity of the tensor will be clear from the primes on the indices or from context.

In addition to (7) and related identities, other constraints follow from geometric invariance principles. For example, translation invariance leads to constraints such as

$$\sum_v B_{ii'}^{vv'} = \sum_{v'} B_{ii'}^{vv'} = 0. \quad (8)$$

We shall consider the consequences of rotation invariance below.

The most commonly studied semiconductors (Si and Ge, and the III-V compound semiconductors) have crystal lattices (diamond and Zincblende, respectively) with two-atom bases. We therefore specialize to the case in which v takes two values, and we introduce the center-of-mass field

$$s_i(r,t) = \sum_v \frac{\rho_v}{\rho_0} u_i^v(r,t), \quad (9)$$

with

$$\rho_0 = \sum_v \rho_v, \quad (10)$$

and the relative displacement field

$$w_i(r,t) = u_i^{(1)} - u_i^{(2)}. \quad (11)$$

These two fields do *not*, in general, decouple. Indeed, they are not generally the normal modes even of L^{uu} alone. Nevertheless, they are the paradigms of acoustic and optical displacement fields that occur in the simplest

models, and they are found to be useful in many electron-phonon coupling models.

In terms of the new fields, the quadratic part of the Lagrangian may be written as

$$L^{uu} = L_{\text{kin}}^s + L_{\text{kin}}^w - V^{ss} - V^{sw} - V^{ww}, \quad (12)$$

where

$$L_{\text{kin}}^s = \frac{1}{2\rho_0} \int dr \pi_i^s \pi_i^s, \quad (13a)$$

$$L_{\text{kin}}^w = \frac{1}{2\rho_{\text{eff}}} \int dr \pi_i^w \pi_i^w \quad (13b)$$

Here,

$$\frac{1}{\rho_{\text{eff}}} = \frac{1}{\rho_1} + \frac{1}{\rho_2}, \quad (14)$$

and we introduce the canonical momentum density

$$\pi_i^s(r) = \frac{\delta L}{\delta \dot{u}_i^s(r)} = \frac{\partial \mathcal{L}}{\partial \dot{u}_i^s} = \rho_0 \dot{s}_i \quad (15a)$$

and similarly

$$\pi_i^w = \rho_{\text{eff}} \dot{w}_i. \quad (15b)$$

Keeping only the lowest-order terms in the gradient expansions of each potential, we have

$$V^{ss} = \frac{1}{2} \int dr D_{ijij}^{ss} s_{i,j} s_{i,j} + \frac{1}{2} \int dr F_{ijkijk}^{ss} s_{i,jk} s_{i,jk}, \quad (16)$$

where the D^{ss} and F^{ss} tensors can be expressed as derivatives of the Lagrangian density with respect to $s_{i,j}$ (as in Eq. (7)) and also have simple expressions as

linear combinations of $D^{vv'}$ and $F^{vv'}$. Terms with mixed orders of derivatives are excluded, as they do not contribute to the equation of motion. Similarly,

$$V^{ww} = \frac{1}{2} \int dr B_{iijj}^{ww} w_i w_j + \frac{1}{2} \int dr D_{iijj}^{ww} w_{i,j} w_{i,j}. \quad (17)$$

The expression for V^{sw} to second order contains four terms (one C, two D's and one E) coupling the first two gradients of s with w and its gradient. Under certain circumstances, V^{sw} or its expansion to second order will be zero. In this case, the s and w fields are decoupled and represent exact acoustic and optical modes. Then D^{ss} gives the long-wavelength sound velocity and F^{ss} determines the lowest order corrections to that velocity for finite wavelength.

Turning now to the interaction L^{ue} with the electromagnetic field, we can write an expression similar to (3c),

$$L^{ue} = \iint dr dr' \sum_v \beta_{ii'}^{ve}(r, r') u_i^v(r) \mathcal{E}_{i'}(r'), \quad (18)$$

containing a parameter β^{ve} which has a gradient expansion similar to (6). The field \mathcal{E} consists only of the internal field generated by the medium itself, so a consistent expansion to second order in gradients of the displacement includes only:

$$L^{ue} = \int dr C_{iji'}^{se} s_{i,j} \mathcal{E}_{i'} + \int dr B_{iij'}^{we} w_i \mathcal{E}_{i'}. \quad (19)$$

Here C^{se} is the first order piezoelectric tensor.

Equations of Motion

The classical equations of motion of the combined system of deformable medium and electric field are determined by the usual variational principle. The time integral of the Lagrangian, evaluated for fixed initial and final conditions on the fields, is required to be stationary under any small perturbation of the fields. The resulting Euler-Lagrange equations are

$$\frac{\partial}{\partial t} \frac{\partial \mathcal{L}}{\partial \dot{\phi}_i} - \frac{\partial \mathcal{L}}{\partial \phi_i} + \left(\frac{\partial \mathcal{L}}{\partial \phi_{i,j}} \right)_{,j} - \left(\frac{\partial \mathcal{L}}{\partial \phi_{i,jk}} \right)_{,jk} + \dots = 0, \quad (20)$$

where ϕ is each of the fields s , w , and \mathcal{E} in turn.

The simplest equation results from taking variations of \mathcal{E} , since there is no dependence on the time derivative of the field. The Euler-Lagrange equation is then just the Poisson equation:

$$\mathcal{E}_{i,i} = -4\pi P_{i,i}, \quad (21)$$

where the polarization field \mathbf{P} is the canonical momentum associated with the electric field, and is given by

$$P_i = \frac{\epsilon_\infty - 1}{4\pi} \mathcal{E}_i + B_{ii}^{we} w_i + C_{iji}^{se} s_{i,j}. \quad (22)$$

(Inclusion of retardation and magnetic fields leads to the full set of Maxwell's equations. Omission of these terms is roughly equivalent to neglecting radiative relaxation and absorption.) The first term in (22) is the background polarization due to electron motions not treated in this adiabatic approach. Higher order terms than those appearing in (22) represent corrections associated with phonon dispersion.

The Euler-Lagrange equations for the s and w fields are

$$\begin{aligned} \rho_0 \ddot{s}_i - \left(D_{imij'}^{ss} s_{i',j'} \right)_{,m} + \left(F_{imnij'jk}^{ss} s_{i',jk'} \right)_{,mm'} \\ = S_i^{sw} + S_i^{se} \end{aligned} \quad (23)$$

and

$$\rho_{\text{eff}} \ddot{w}_i + B_{ii'}^{ww} \dot{w}_{i'} - \left(D_{imj'}^{ww} w_{i'j'} \right)_{,m} = W_i^{ws} + W_i^{w\epsilon}, \quad (24)$$

where

$$S_i^{sw} = \left(C_{imj'}^{sw} w_{i'j'} \right)_{,m} + \left(D_{imj'}^{sw} w_{i'j'} \right)_{,m} \quad (25a)$$

$$W_i^{ws} = -C_{ii'}^{sw} s_{i'j'} + \left(D_{imj'}^{sw} s_{i'j'} \right)_{,m} \quad (25b)$$

and

$$S^{s\epsilon} = - \left(C_{imj'}^{s\epsilon} \epsilon_{i'j'} \right)_{,m} + \left(D_{imj'}^{s\epsilon} \epsilon_{i'j'} \right)_{,mm} \quad (26a)$$

$$W^{s\epsilon} = B_{ii'}^{w\epsilon} \epsilon_{i'j'} - \left(C_{imj'}^{w\epsilon} \epsilon_{i'j'} \right)_{,m} \quad (26b)$$

In a treatment of the Schrödinger field by an approach analogous to the present one, it is possible formally to eliminate the internal field from the equations of motion. This is *not* possible, in general, for the deformation field. In the isotropic case to be considered, however, it *is* possible and leads to nontrivial corrections.

Isotropic Approximation

We now specialize to the case of an isotropic medium. The rotational symmetry in this case dramatically reduces the number of independent parameters, particularly for low order tensor terms in the Lagrangian. First, we observe that a simple rotation of the undistorted continuum can be described by

$$u_i^v = \omega_{im} r_m, \quad (27)$$

where ω_{im} is an antisymmetric matrix. The potential energy is unchanged by a rotation of the whole medium, and terms of different orders must be zero independently, so

$$\sum_{v,v'} D_{ijj'}^{vv'} \omega_{ij} \omega_{i'j'} = 0.$$

By considering the full range of antisymmetric real matrices ω_{im} , one finds that

$$D_{ijj'}^{vv'} = D_{jii'}^{vv'} = D_{ijj'}^{v'v}. \quad (28)$$

Identity (28) depends on the possibility of describing rotations as deformations. Another set of constraints follows from the general requirement that the Lagrangian be a scalar, utilizes only the vector

character of the fields s , w , and ϵ , and depends only on the way in which the subscripts are partitioned. For the present study, the most important constraints are

$$A_{..} = 0 \quad (29a)$$

$$B_{.,i} = B \delta_{.,i} \quad (29b)$$

$$C_{.,i} = C_{.,i} = 0 \quad (29c)$$

and

$$D_{ijj'}^{ss} = \lambda \delta_{ij} \delta_{i'j'} + \mu \delta_{ii'} \delta_{jj'} + \nu \delta_{ij} \delta_{j'i'}. \quad (29d)$$

By (28), $\mu = \nu$ for D^{ss} . Similar relations hold for D^{sw} and D^{ww} . Observing that $s_{i,jk}$ is symmetric under interchange of j and k , one also finds

$$D_{ijki'}^{s\epsilon} = D_1^{s\epsilon} \delta_{ij} \delta_{ki'} + D_2^{s\epsilon} \delta_{jk} \delta_{ii'}. \quad (30)$$

Similar expressions, involving four invariants, describe F^{ss} .

Applying these relations to the equations of motion (21)-(24), we find

$$\rho_0 \ddot{s} = \mu \Delta s + (\lambda + \mu) \nabla (\nabla \cdot s)$$

$$- F_A \Delta^2 s - F_B \Delta \nabla (\nabla \cdot s), \quad (31)$$

$$\rho_{\text{eff}} \ddot{w} = -B^{ww} w + B^{w\epsilon} \epsilon + \bar{\mu} \Delta w + (\tilde{\lambda} + \bar{\mu}) \nabla (\nabla \cdot w) \quad (32)$$

and

$$\epsilon_{\infty} \nabla \cdot \epsilon = -4\pi B^{w\epsilon} \nabla \cdot w \quad (33)$$

From these equations there follow a few very useful properties of the isotropic special case of our model:

- The acoustic field s decouples from w and ϵ .
- It is possible to incorporate the internal field ϵ implicitly into the equations of motion for w .
- All the fields may be decoupled into longitudinal (L) and transverse parts (T):

$$\rho_0 \ddot{s}_L = (\lambda + 2\mu) \Delta s_L - (F_A + F_B) \Delta^2 s_L, \quad (34a)$$

$$\rho_0 \ddot{s}_T = \mu \Delta s_T - F_A \Delta^2 s_T, \quad (34b)$$

$$\rho_{\text{eff}} \ddot{w}_L = -B_L^{ww} w_L + (\tilde{\lambda} + 2\bar{\mu}) \Delta w_L, \quad (34c)$$

and

$$\rho_{\text{eff}} \ddot{w}_T = -B^{ww} w_T + \bar{\mu} \Delta w_T, \quad (34d)$$

where

$$B_L^{ww} = B^{ww} + \frac{4\pi}{\epsilon_{\infty}} (B^{w\epsilon})^2. \quad (35)$$

The solutions of (34) are plane waves. The acoustic modes have dispersion relations

$$(\omega_L^s)^2 = v_L^2 q^2 + \frac{F_A + F_B}{\rho_0} q^4, \quad (36a)$$

$$(\omega_T^s)^2 = v_T^2 q^2 + \frac{F_A}{\rho_0} q^4, \quad (36b)$$

with the usual sound velocities

$$v_L^2 = \frac{\lambda + 2\mu}{\rho_0}, \quad v_T^2 = \frac{\mu}{\rho_0},$$

in the long wavelength limit. The optical modes have frequencies given by

$$(\omega_L^w)^2 = \omega_{LO}^2 + \frac{\tilde{\lambda} + 2\tilde{\mu}}{\rho_{\text{eff}}} q^2, \quad (37a)$$

$$(\omega_T^w)^2 = \omega_{TO}^2 + \frac{\tilde{\mu}}{\rho_{\text{eff}}} q^2. \quad (37b)$$

The limiting long wavelength optical frequencies are defined by

$$\omega_{LO}^2 \rho_{\text{eff}} = B_L^{ww}, \text{ and } \omega_{TO}^2 \rho_{\text{eff}} = B^{ww}. \quad (38)$$

Dispersion relations of the form (37) have been proposed previously on an *ad hoc* basis (see, for example, [2,3]). Here we have derived them systematically.

The center of mass and relative deformations can be expanded in a normal mode basis:

$$s(\mathbf{r}, t) = \sum_{\mathbf{q}, \alpha} s_{\mathbf{q}\alpha}(\mathbf{r}, t) [a_{\alpha}(\mathbf{q}) + a_{\alpha}^*(-\mathbf{q})], \quad (39)$$

where α is a mode index that may be LA, TA1 or TA2. With periodic boundary conditions in a box of volume V , and \mathbf{e}_{α} a unit polarization vector, the mode has the form (up to corrections of order q^2 in the normalization)

$$s_{\mathbf{q}\alpha}(\mathbf{r}, t) = \left(\frac{\hbar}{2V\rho_0 v_{\alpha} |\mathbf{q}|} \right)^{1/2} \mathbf{e}_{\alpha}(\mathbf{q}) e^{i\mathbf{q} \cdot \mathbf{r} - i\omega_{\alpha} t}. \quad (40)$$

Similar expressions exist for w .

TRANSITION RATES

Transition rates, in general, are computed after converting from a classical to a quantum mechanical formulation. Quantum mechanical discussions are most commonly couched in terms of the Hamiltonian, which is classically

$$H = \int d\mathbf{r} \mathcal{H}, \quad (41)$$

where

$$\mathcal{H} = \dot{w}_i \pi_i^w + \dot{s}_i \pi_i^s - \mathcal{L} \quad (42)$$

is expressed, with (15), as a function of π^s, π^w , and of s, w , and their spatial derivatives. The conversion to quantum mechanics follows from the usual correspondence

$$\{\bullet, \bullet\} \rightarrow \frac{\hbar}{i} [\bullet, \bullet]. \quad (43)$$

taking the Poisson bracket into the commutator.

In the usual way, the quadratic Hamiltonian $H^{uu} + H^{ue} + H^{ee}$ leads to simple phonon modes formally identical to (40) and its analog for w . The normalization factor in (40) was chosen so that a and a^* would satisfy the usual phonon operator commutation relations.

The lifetime of a phonon is found from its decay rate, which we computed by Fermi's Golden Rule. The interaction which induces the decay is typically the anharmonic coupling L^{uuu} (see (2)) that was neglected earlier in finding the dispersion relations. In analogy with the treatment of harmonic coupling, we expand L^{uu} in an integral expression

$$L^{uuu} = -\frac{1}{3!} \iiint d\mathbf{r} d\mathbf{r}' d\mathbf{r}'' \gamma_{iii}^{vvv}(\mathbf{r}, \mathbf{r}', \mathbf{r}'') \times u_i^v(\mathbf{r}) u_i^v(\mathbf{r}') u_i^v(\mathbf{r}'') \quad (44)$$

resembling (3c). (As this is a potential, $H^{uu} = -L^{uu}$, so for convenience we will continue the discussion in terms of the Lagrangian.) We can likewise make a gradient expansion of γ^{vvv} , the first term of which is

$$\delta(\mathbf{r}-\mathbf{r}') \delta(\mathbf{r}-\mathbf{r}'') C_{iii}^{vvv}. \quad (45)$$

We have studied the effects of this term and of the D terms (which each involve only one partial derivative). Here we touch on some of the main features of the analysis which leads to the phonon lifetimes. (A detailed description will be published elsewhere.)

As before, translation and rotation invariance impose a number of constraints similar to (8) and (28)-(30). Isotropic symmetry further reduces the number of degrees of freedom of the tensor parameters to the values of a small number of invariants. (In particular, it forces $C=0$.)

The cubic Lagrangian can again be broken down into components in varying orders of the center-of-mass and relative fields:

$$L^{uuu} = L^{sss} + L^{ssw} + L^{sww} + L^{www}. \quad (46)$$

It is clear from (38) that the number of times s or w appears as a superscript of L is the number of field (creation or annihilation) operators appearing in the corresponding quantum mechanical term. Thus, the decay of an optical phonon into two acoustic phonons is governed by L^{ssw} .

A major difficulty that arises in determining decay rates within the present model is the need to specify the values of the invariants entering into the expressions for tensor parameters. Our approach is to use a generalization of Grüneisen parameters [4]. We illustrate this method for F^{sss} .

In the isotropic case, F^{sss} is determined by three independent invariants. Two of these enter into the equation of motion for s in forms that lend themselves to linearization. Specifically, we keep only those terms in which the second derivatives (a) also appear as linear terms, and (b) have indices which are independent of those in the accompanying first derivative. Then,

$$\rho_0 \ddot{s}_i = \left(\lambda + \mu + F_1^{sss} \nabla \cdot \mathbf{s} \right) s_{i,ji} + \left(\mu + \frac{1}{2} F_2^{sss} \nabla \cdot \mathbf{s} \right) s_{i,jj} \quad (47)$$

In a mean field approximation,

$$\nabla \cdot \mathbf{s} \rightarrow \Delta V / V \sim \text{const.}$$

Only the terms satisfying the conditions (a) and (b) above will preserve the longitudinal/transverse separation, and yield dispersion relations

$$(\omega_L^s)^2 = v_L^2 q^2 \left(1 + \frac{2F_1^{sss} + F_2^{sss}}{2v_L^2 \rho_0} \langle \nabla \cdot \mathbf{s} \rangle \right) \quad (48)$$

or

$$\frac{\Delta \omega_L^s}{\omega_L^s} \equiv \frac{2F_1^{sss} + F_2^{sss}}{4v_L^2 \rho_0} \langle \nabla \cdot \mathbf{s} \rangle \equiv \gamma_{LA} \langle \nabla \cdot \mathbf{s} \rangle, \quad (49a)$$

and similarly

$$\frac{\Delta \omega_T^s}{\omega_T^s \langle \nabla \cdot \mathbf{s} \rangle} \equiv \frac{F_2^{sss}}{4v_T^2 \rho_0} \equiv \gamma_{TA}, \quad (49b)$$

This allows F_1^{sss} and F_2^{sss} to be defined in terms of the "mode Grüneisen constants" γ .

We also consider less symmetric cases, in particular O_h and T_d symmetry. While the deviation from isotropy causes mostly quantitative corrections to the dispersion relations, it can have major qualitative effects on the decay rates. This can happen in two ways:

- Whole types of interactions, such as piezoelectric coupling, are absent for isotropic symmetry. The corresponding "forbidden" transitions arise precisely from the breaking of isotropic symmetry.
- The wave vector dependence of an isotropic-symmetry-allowed decay process may make it negligible, in some parts of wave vector space, compared to less symmetric contributions.

We have studied terms with O_h or T_d symmetry using model Hamiltonians which lead to Grüneisen-constant formulas similar to (49).

If we use only the interactions whose strengths can be estimated from Grüneisen parameter arguments, then even without making any assumption regarding the precise magnitudes of the mode-Grüneisen parameters, the wave vector dependence of various phonon decay processes may be found.

In particular, for the lifetime of acoustic phonons at low temperature, we confirm the well-known [5,9] result that $\tau \sim q^{-5}$ as $q \rightarrow 0$. For LO phonons, the long wavelength limit is complicated by the existence of two distinct decay mechanisms. In either an isotropic or octahedrally symmetric medium, the rate of decay into two acoustic phonons goes to zero as q , apparently giving $\tau \sim q^{-2}$. However, the rate for emission of one optical and one acoustic phonon remains finite at $q=0$, so τ is bounded as $q \rightarrow 0$.

For typical semiconductor materials of T_d symmetry the $q \rightarrow 0$ LO phonon lifetime is found to vary in the range of 5 psec to 50 psec; the corresponding zone-edge phonon lifetimes are estimated to be shorter by one order of magnitude.

LOCALIZATION BEHAVIOR

If parameters are spatially varying, additional terms appear in Eqs. (31-33), which generally violate the decoupling between longitudinal and transverse modes, even in isotropic material. This usually holds also for abrupt parameter changes at planar interfaces, whose properties are defined by means of boundary conditions. For layered (i.e., quasi-one-dimensional) structures, we may keep periodic boundary conditions in the two dimensions parallel to the interfaces.

A simple example of a layered structure that one may consider is a single layer of one material ("B") sandwiched between two layers of another ("A"). This ABA pattern is the typical one for a heterostructure (electron) quantum well. From the point of view of the phonons, the most important effect is that the optical band, if sufficiently narrow to begin with, will be broken up, with phonons typically confined to either the A or the B regions. Typically also, the acoustic band, because it is broad, will *not* be broken up. (As a convention we will place the surface perpendicular to the z axis.) We consider the question: How does the decay of a phonon localized in the B region depend on the length of the B region along the z direction?

In order to investigate this, we consider a simplified

model of the layered structure, in which the w and \mathbf{E} fields have boundaries at $z = \pm L_w$, and the s field has boundaries at $z = \pm L_s$, with $L_w \ll L_s$. (This is possible because, as we have shown, the s field decouples from

the w and \mathbf{E} fields.) At these real interfaces, it is preferable to impose some more realistic boundary conditions than the periodic ones that define (40), even if it is only to confirm that results are not sensitive to the particular conditions chosen. It should be noted also that the precise number of conditions needed depends on the number of terms retained in the gradient expansion.

Common boundary conditions for the s -field are the "free surface" model, in which the momentum current density T^s , along the z direction is set to zero.

$$T_{3j}^s = 0, \quad (50)$$

and "rigid wall" boundary conditions,

$$s_j = 0. \quad (51)$$

A purely longitudinal or purely transverse wave which approaches such a boundary is generally reflected as a mixture of L and T waves. It is clear from their different bulk dispersion relations that conditions such as these, which do not preserve L/T character,

make it difficult to determine the phonon modes. Certain mixtures of Eqs. (50) and (51), however, *do* preserve L/T character:

$$s_3 = 0; T_{3j} = 0 \text{ for } j=1,2, \quad (52)$$

and

$$T_{33}^s = 0; s_j = 0 \text{ for } j = 1,2. \quad (53)$$

With either of these boundary conditions, one can write down the phonon modes analogous to (40). Similar considerations narrow the choices for boundary conditions on the optical mode fields. Using these, it is possible to repeat the calculations of phonon lifetime for a layered structure. The main result of these calculations is that the lifetime does not depend substantially on the thickness of the confining layer: The reduction of overlap with increasing confinement length is counterbalanced by the weakening of the selection rules governing the coupling. This is reminiscent of the fact that typical radiative lifetimes of "zero-dimensional" electronic states (atomic levels) are usually of the same order of magnitude as the extended states of, for example, direct-gap semiconductors.

CONCLUSION

We have developed a theory of anharmonic phonon coupling by systematically extending the existing continuum models, and included multiple fields (two, without loss of generality) to represent crystals with bases. We used it to show how one can obtain simple analytic phonon modes and dispersion curves, as well as the optical-acoustic phonon coupling.

The wave vector dependences of the phonon lifetimes were found using anharmonic terms appearing in the model. By means of "Grüneisen" scaling methods, the values of high order gradient-expansion parameters needed in the theory were estimated, without the need for additional experimental data. This led to satisfactory numerical agreement with measured lifetimes.

Interaction with a Fröhlicher field can be added without difficulty to the model already described. The general model is therefore applicable to a number of experimental situations, including

- a. Phonon linewidth [10] as seen, e.g., in a Raman experiment,
- b. Electron-hole energy relaxation in bulk semiconductors [11],
- c. Electron-hole energy relaxation in quantum wells [12],
- d. Electron-hole energy relaxation in mixed crystals, in the range where they become indirect [13].

The energy relaxation is dominated by the LO phonon lifetime if that is the slowest process, but still the most effective cooling mechanism. For higher excitation the hot phonon effect [14] limits the cooling rate. This effect is less pronounced if large q -vector phonons are

excited, as is the case for intervalley scattering [13], because of their shorter lifetimes.

Acknowledgments

This work was supported in part by the Deutsche Forschungsgemeinschaft (G.M.), and by the U.S. Office of Naval Research.

References

1. A. Askar, Lattice Dynamical Foundation of Continuum Theories, (World Scientific, Singapore, 1985).
2. M. Babiker, "Longitudinal polar optical modes in semiconductor quantum wells," *J. Phys. C* **19**, 683-697 (1986).
3. C. Colvard, R. Fischer, T. A. Gant, M. U. Klein, R. Merlin, H. Morkoç and A. C. Gossard, "Phonon freedom and confinement in GaAs-Al_xGa_{1-x}As," *Superlatt and Microstr.* **1**, 81-86 (1985).
4. V. L. Gurevich: Transport in Phonon Systems, (North Holland, Amsterdam, 1986).
5. P. Baumgartner, M. Engelhardt and K. F. Renk, "Spontaneous decay of high-frequency acoustic phonons in CaF₂," *Phys. Rev. Lett.* **47**, 1403-1407 (1981).
6. J. Kuhl and W. E. Bron, "Photoluminescence of Epitaxial GaAs grown by close space vapor transport method," *Solid State Commun.* **49**, 939-942 (1984).
7. J. A. Kash and J. C. Tsang, "Secondary emission studies of hot carrier relaxation in polar semiconductors," *Solid State Elec.* **31**, 419-424 (1988).
8. B. S. DeWitt in: Relativity, Groups, and Topology, Les Houches Summer School 1964 ed. by C. DeWitt and B. S. DeWitt, (Gordon and Breach, New York, 1965).
9. A. Berke, A. P. Mayer and R. K. Wehner, "Spontaneous decay of acoustic phonons in Calcium Fluoride and Silicon," *Solid State Commun.* **54**, 395-397 (1985).
10. P. F. Tua and G. D. Mahan, "Lifetime of high-frequency longitudinal-acoustic phonons in CaF₂ at low crystal temperatures," *Phys. Rev. B* **26**, 2208-2215 (1982).
11. J. Shah, "Hot electrons and phonons under high intensity photoexcitation of semiconductors," *Solid State Elec.* **21**, 43-50 (1978).
12. J. Shah, A. Pinczuk, A. C. Gossard and W. Wiegman, "Energy loss rates for hot electrons and holes in GaAs quantum wells," *Phys. Rev. Lett.* **54**, 2045-2048 (1985).
13. K. Leo, Ph.D. Thesis, U. Stuttgart (1988).
14. W. Pötz and P. Kocevar, "Electronic power transfer in pulsed excitation of polar semiconductors," *Phys. Rev. B* **28**, 7040-7047 (1983).

Mobility and Lifetime Measurements on PECVD and Type IIa Diamond

Don Kania and Otto L. Landen

Lawrence Livermore National Laboratory, P. O. Box 5508, M.S. 473, Livermore, California 94550

Lawrence Pan and Piero Pianetta

Stanford Synchrotron Radiation Laboratory, Stanford University, Bin 99, P.O. Box 4349, Stanford, California 94309

K. V. Ravi

Crystallume, Inc., 125 Constitution Drive, Menlo Park, California 94025

Abstract

Photoconductivity measurements were used to get carrier lifetimes and mobilities in three forms of diamond: (i) natural type IIa diamond, (ii) synthetic high-pressure, high-temperature bulk diamond, and (iii) plasma enhanced chemical vapor deposited polycrystalline diamond film. Signals were generated by picosecond ultraviolet laser pulses. We find that the lifetimes of carriers generated in both the thin film and the type IIa diamonds are in the range of 100 to 600 ps, varying from sample to sample. In the thin film material, a much longer lifetime component is also observed on some samples and is attributed to the diamond-like carbon transition layer found in these samples. The data also suggests a grain size dependence in the lifetimes. In the synthetic bulk diamond, there was no fast component and the lifetimes were on the order of 4 ns. Mobilities in the thin film and type IIa were also comparable (around 10 to several hundred $\text{cm}^2/\text{V}\cdot\text{s}$), while in the synthetic bulk material, mobilities were around 30 $\text{cm}^2/\text{V}\cdot\text{s}$.

A number of material properties makes diamond an excellent candidate for electronic applications. Insulating diamond has a high dark resistivity, high dielectric breakdown strength, high thermal conductivity, and high carrier mobilities. There has been growing interest lately in diamond, particularly on the synthesis and applications of chemical vapor deposited (CVD) diamond films. These films offer the ability to obtain more controlled response than natural diamonds and are compatible with integrated circuit technologies. We have done photoconductive measurements on these and bulk diamonds to extract carrier mobilities and lifetimes. These quantities are important for potential electronic applications of the material.

Photoconductive measurements are best made on insulating diamonds. Our samples include natural type IIa

diamonds and two types of synthetic diamond. We will refer to the natural diamond as IIa in this paper. Of the two synthetic forms, the first form is created by a high pressure, high temperature process, which results in bulk diamonds with very low impurity concentrations (referred to hereafter as SB). The nitrogen content in this sample has been measured to be < 5 ppm, as compared to the IIa samples (~ 100 ppm). The second form is chemical vapor deposited films of polycrystalline diamond, of order a micron thick, grown on silicon substrates. Raman spectroscopy has shown that these films consist of a mixture of sp^3 and sp^2 -bonded carbon. It is widely believed that the crystallites are quite pure diamond (sp^3 -bonds), and that the sp^2 is amorphous or graphitic carbon in the grain boundaries [1]. We will abbreviate this form as CVD diamond. With the CVD diamond, we have looked at two different types of films: the first set had large grain sizes ($\sim 1 \mu\text{m}$) and no transition layer between the diamond and the silicon substrate. The second set had much smaller grains (100's Å's) and a significant diamond-like carbon layer (DLC) at the interface. This DLC layer is a random network of mostly sp^3 -bonded carbon, which often exists as a transition layer between the diamond film and the silicon substrate.

Fabrication of the thin film photoconductors consisted of depositing titanium and gold contacts, annealing in N_2 for 30 minutes at 800°C , mounting the films face down on an alumina frame, and backetching the silicon away. This leaves a free-standing diamond film mounted in a 50Ω transmission line, capable of being excited with light from either side.

Because of the low impurity concentrations in these samples, carriers must be excited directly across the bandgap. At room temperature the bandgap is 5.5 eV, making pure diamond insensitive to visible light and suitable for excitation by ultraviolet and x-ray photons.

We have looked at the response to picosecond UV laser light. The photon source is a mode-locked Nd:YAG laser, with a fundamental wavelength of $1.064 \mu\text{m}$, and

pulses of around 0.2 J energy and 100 picoseconds in duration. The fundamental 1ω beam is frequency doubled in a 1 cm KDP crystal, frequency tripled in another KDP crystal and the 2ω and 3ω beams are mixed in a 1 mm β -BaBO₄ crystal to yield 5ω at a wavelength of 213 nm (5.8 eV) [2]. Up to 1 mJ in an estimated 40 ps is available at this energy. The e^{-1} absorption depth at this wavelength is 3.4 μm [3]. For a 1 μm film, approximately 25% of the incident power is absorbed in the film. In the bulk diamonds, all of the radiation is absorbed.

The diamond photoconductor is placed in a 50 Ω transmission line and the change in conductivity with light is measured by recording the change in voltage across the 50 Ω line. Signals are recorded with a Tektronix 7250 oscilloscope. The impulse response of the system is measured with a 60 ps GaAs detector.

Shown in Figs. 1-3 are typical pulses from the three forms of diamond. Fig. 1 is the signal from a IIa diamond ($1 \times 1 \times 3 \text{ mm}^3$), biased to a field of 500 V/cm. Fig. 2 is the signal from a CVD film, also biased to 500 V/cm.

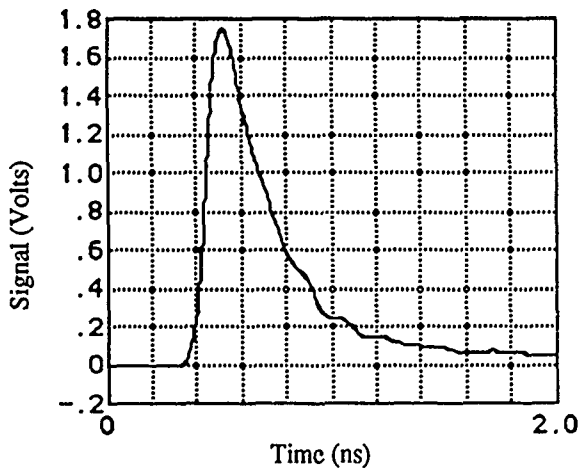


Figure 1. Photoconductive signal from a natural type IIa diamond, excited with a 40 ps laser pulse. The applied field is 500 V/cm.

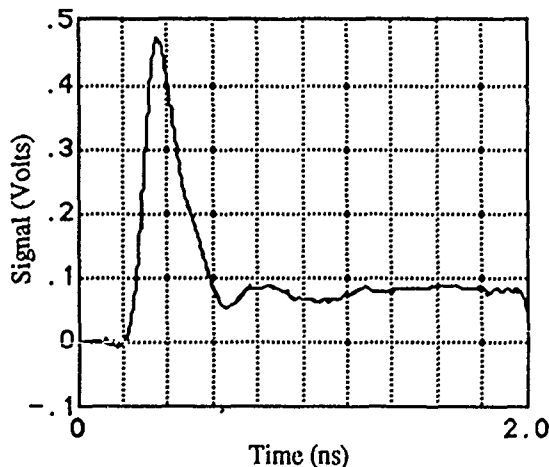


Figure 2. Photoconductive signal from a 1 μm thick polycrystalline diamond film. Applied field is 500 V/cm.

The film was 1 μm thick, with contacts 1 mm apart. Fig. 3 is the signal from a SB diamond ($1 \times 1 \times 1 \text{ mm}^3$), biased to 100 V/cm.

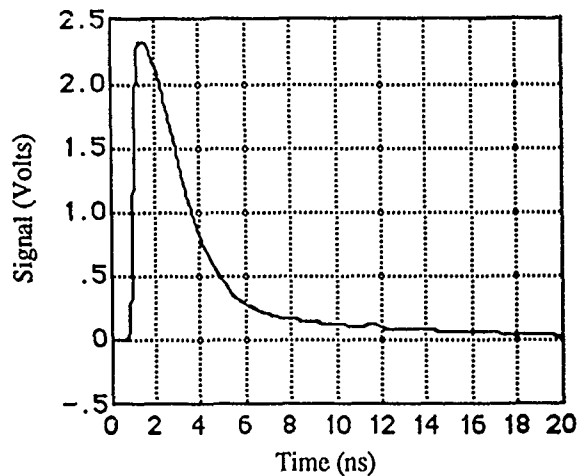


Figure 3. Photoconductive signal from a synthetic bulk diamond. The applied field here is 100 V/cm.

Analysis of the data yields mobility and lifetime values for the excited carriers. The falling tail is fit with a decaying exponential. (See the discussion below.) After subtracting the system response time in quadrature from this exponential time constant, the result is interpreted as the mean carrier lifetime in the material. This is plotted as a function of the applied field and is shown in Fig. 4. The lifetime in the SB diamond is not plotted, but is around 2 ns. Fig. 5 shows the peak voltage obtained as a function of the applied field. Note that they are all fairly linear, and that much of the difference in slopes is due to different incident photon intensities.

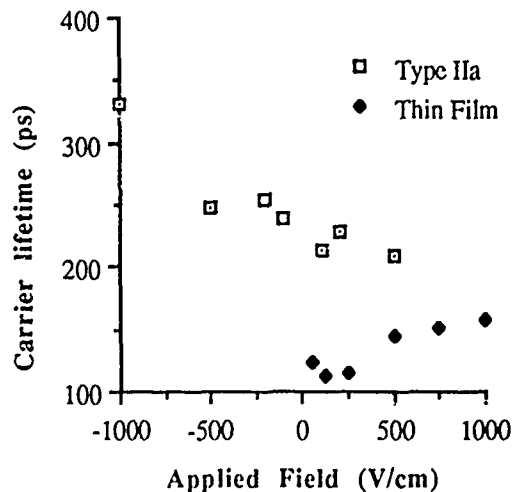


Figure 4. Carrier lifetimes extracted from the decaying exponential tail of the photoconductive pulse. Lifetimes in the SB diamond were around 2 ns, and are not shown.

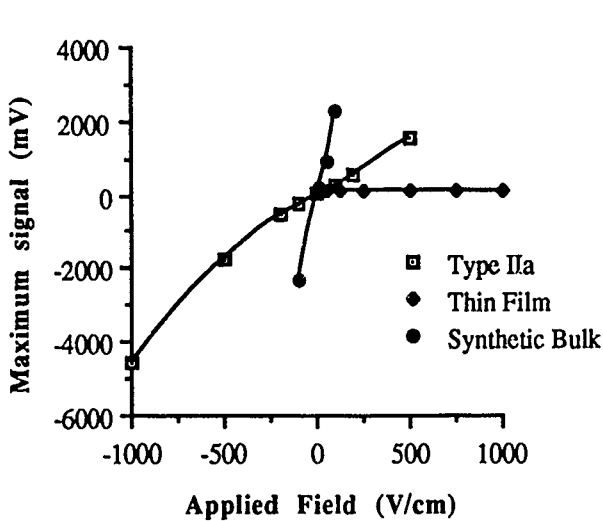


Figure 5. The peak of the photoconductive signal as a function of the applied field. The curves are fairly linear, and the different slopes are mainly due to different amounts of energy in the excitation pulse.

The area under the pulse can be related to the $\mu\tau/\gamma$ product, and knowing τ from the decay, μ can then be determined. We assume that γ , the average energy to form an electron/hole pair, is equal to the photon energy at just above bandgap [4]. This is done in the following manner: The differential equation describing the carrier concentration is:

$$\frac{dn(t)}{dt} = G(t) - \frac{n(t)}{\tau},$$

where $G(t)$ is taken to be a gaussian generation term of FWHM equal to the photon pulse width. The formal

solution to this equation is:

$$n(t) = \frac{E}{\gamma} f_i \quad (1)$$

$$\text{where } f_i = \frac{1}{2} \exp\left(\frac{\sigma^2}{2\tau^2} - \frac{t}{\tau}\right) \left(\operatorname{erf}\left(\frac{1}{\sqrt{2}} \left(\frac{t}{\sigma} - \frac{\sigma}{\tau}\right)\right) + 1 \right)$$

and where E is the energy per pulse absorbed, γ is the average energy per electron/hole pair creation, σ is the standard deviation of the gaussian pulse, and τ is the carrier lifetime. The expression f_i can be viewed as an integration factor, taking into account the finite response time of the material relative to the pulse length. As the pulse gets much shorter than the carrier lifetime, f_i approaches 1.

The sensitivity S of the detector can be measured as the charge collected Q per joule of energy absorbed E . Here Q is given by:

$$Q = \frac{q \left(\int_0^\infty n dt \right) \mu V_b}{l^2}, \text{ where}$$

n is given by Eq. (1), and where q is the electronic charge, μ is the carrier mobility, V_b is the applied bias voltage, and l is the distance between contacts. In the limit as the generation pulse approaches a delta function ($\sigma \ll \tau$), the expression for f_i approaches $e^{-t/\tau}$ (the decaying exponential from which τ is inferred) and the sensitivity S is given by:

$$S = \frac{q \mu \tau V_b}{\gamma l^2}.$$

We use this expression to calculate the carrier mobilities.

Results

Carrier lifetimes in the natural type IIa ranged from 100 to 600 ps. This lifetime is probably influenced by the different impurity concentrations in the natural diamonds. This is consistent with the much longer lifetimes measured in the SB diamond, which is much lower in impurity concentration. Here the decay is of order 2 ns.

In the thin films, an initial fast transient pulse was observed in all of the films. This can be attributed to trapping at either the grain boundaries or at the many defects, such as twins. A slight bias dependence may be seen in the lifetimes of the carriers, as suggested in Fig. 4. This could be due to some velocity-dependent trapping mechanism, such as ionized impurities or defects.

Two additional observations can be made about the films. A slow residual tail is observed in some of the samples. We attribute this to longer lived carriers created in the DLC layer found in these particular samples. This is consistent with the fact that this tail is not observed in the large grain films, which contain no DLC layer. A direct comparison of the two different sides of one particular sample shows the DLC effect even more clearly. Here Fig. 6a shows the pulse due to the illumination incident on side with the DLC layer. Fig. 6b is the pulse due to illumination from the side away from the DLC. A much more significant tail is seen in the first case, consistent with more absorption in the DLC, and therefore more carriers with longer lifetimes.

One further observation is that there may be some grain size dependence on the carrier lifetime. The small grain size film showed lifetimes around 110 ps, while the large grain size film showed lifetimes around 600 ps. The times do not scale directly with the grain sizes, as this ratio is on the order of a hundred.

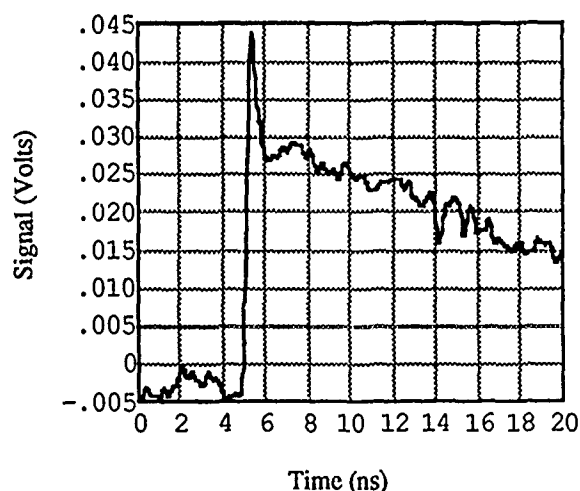


Figure 6a. Light incident on the DLC side of a thin film. The applied field here is 1500 V/cm.

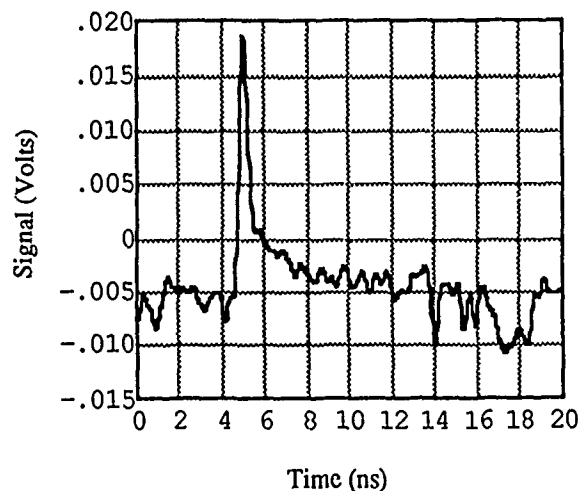


Figure 6b. Light incident on the side away from the DLC. The absence of the slow tail suggests the importance of the DLC layer in observed carrier lifetimes.

Mobility values measured here are lower than those generally reported in the literature. The current values are summarized in Table 1, along with the measured lifetimes. The values reported elsewhere usually lie around 1000 to 2000 $\text{cm}^2/\text{V-s}$ [5-6]. We have also measured similarly higher values in the bulk material, when excited with synchrotron x-rays. No satisfactory explanation exists at this time as to the difference in the single crystal samples (both IIa and SB). One possibility is enhanced surface recombination of the carriers created by wavelengths just above bandgap results in fewer carriers than assumed to be available for conduction. It is not as surprising that the mobility in the polycrystalline films is lower. Such trends are observed in other materials, such

as amorphous silicon [7]. Future work is planned to study the dependence on the absorption depths of the exciting photons.

Conclusions

We have looked at photoconductive signals in three types of diamond, all excited with picosecond ultraviolet laser light. Mobilities and lifetime values have been extracted. The importance of impurities is suggested by the widely different lifetimes in the type IIa and in the SB low nitrogen sample. In the diamond film the slow tail component in the photoconductive response seen in some of films is attributed to the presence of a DLC layer in those films. A weak bias dependence is seen in the

Table 1 Mobilities and lifetimes

| Sample | μ ($\text{cm}^2/\text{V-s}$) | Lifetime | Tail? |
|------------------------------|------------------------------------|------------|-------|
| Type IIa | 10-200 | 100-600 ps | No |
| PECVD Diamond Film | | | |
| Large grain | 20 | 600 ps | No |
| Small grain | 10 | 100-150 ps | Yes |
| Synthetic Bulk Diamond | 30 | 2 ns | No |

lifetimes. Grain sizes also seem to influence the observed lifetimes. Future work will examine the reason for the lower mobilities from those measured with x-rays and also reported elsewhere. Other work will focus on the dependence of the photoconductivity on various parameters of the CVD films, such as grain size and sp^3 to sp^2 ratio. As further experience is gained, this may become a useful analysis technique for examining the structure and quality of a film.

Acknowledgments

We wish to acknowledge Perry Bell at Lawrence Livermore National Laboratories for his help in fabricating the detectors and for his work on the sampling systems. We also wish to thank the Ginzton Microfabrication Laboratory and the Stanford Tube Laboratory, both at Stanford University, for their services. We wish to acknowledge Paul King and R. T. "Skip" Huckaby at Stanford University for their many helpful discussions. This work is supported by the Laser Program at LLNL and by SSRL, which is supported by the Department of Energy, Office of Basic Energy Science.

References

1. K. V. Ravi, Crystallume, Menlo Park, CA.; private communication.
2. M. D. Perry, O. L. Landen, J. Weston, and R. Etlbrick, submitted to Optics Letters.
3. E. L. Palik, ed., Handbook of Optical Constants of Solids (Academic Press, Orlando, FL, 1985), p. 665-673.
4. W. Shockley, Solid-State Electronics, **2** (1), 35-67 (1961).
5. C. Canali, E. Gatti, S. F. Kazlov, P.F. Manfredi, F. Nava, and A. Quirini, Nucl. Instr. and Meth., **160**, 73-77 (1979).
6. E. A. Konorova, and S. A. Shevchenko, Sov. Phys. Semicond., **1** (3), 299 (1967).
7. D. H. Auston, P. Lavallard, N. Sol, and D. Kaplan, Appl. Phys. Lett., **36** (1), 66 (1980).

Part 6
Optical Switches, Detectors, and Applications

Picosecond GaAs-Based Photoconductive Optoelectronic Detectors

F. W. Smith,* H. Q. Le,* M. Frankel,[†] V. Diadiuk,* M. A. Hollis,*
D. R. Dykaar,[†] G. A. Mourou,[†] and A. R. Calawa*

**Lincoln Laboratory, Massachusetts Institute of Technology
Lexington, Massachusetts 02173*

*[†]Laboratory for Laser Energetics, University of Rochester,
Rochester, New York 14623*

ABSTRACT

Picosecond photoconductive-switch performance was demonstrated with a novel material deposited by molecular beam epitaxy at low substrate temperatures using Ga and As₄ beam fluxes. For a photoconductive-gap switch fabricated on a coplanar transmission line, the speed is 1.6 ps (full width at half maximum) and the voltage response is 10 to 100 times greater than that of conventional photoconductive switches. Since LT GaAs is compatible with GaAs device and IC technologies, this photoconductive switch may find extensive use in high-speed device and circuit testing.

INTRODUCTION

In this work we report the development of a GaAs-based high-speed photoconductive detector that exhibits a measured speed of approximately 1.6 ps (full width at half-maximum, FWHM) and a response of the order of a volt using a bias of 10 V and an 80-fs laser pulse of 90-pJ energy. The material appears to be stable for indefinite periods of time and can be easily integrated with GaAs discrete devices and circuits [1]. In fact, the material that is used for this device also offers substantial performance improvements for GaAs devices and circuits [2-5].

The first part of this paper will provide a brief overview of the field of photoconductive switches. The growth and characterization of the low-temperature (LT) GaAs epilayer grown by molecular beam epitaxy (MBE) that is used as the active layer for the photoconductive switch will be discussed. Some of the prior accomplishments achieved using the LT GaAs epilayer in GaAs electronic device applications will be briefly summarized [2-5]. The picosecond photoconductive switch performance of LT GaAs will be demonstrated using the technique of electro-optic sampling [6,7], and the benefits of

this switch for high-speed device and circuit testing will be discussed. Lastly, some of our ongoing work on this material will be presented.

OVERVIEW OF PHOTOCONDUCTIVE SWITCHES

Photoconductive switches are a means of converting ultrafast optical pulses into picosecond electrical pulses. This function is useful in a variety of applications such as picosecond optoelectronic switching and sampling [8,9], high-speed detection for fiber-optic communication and optical-computing systems [10], signal processing [11], and far-infrared spectroscopy [12]. From the perspective of a semiconductor physicist, one of the most important of these is the characterization of high-speed semiconductor devices and circuits.

The ultimate speed of a photoconductive switch is determined both by the properties of the semiconductor material used as the active layer of the device and the configuration of its electrodes. For picosecond speed, short photoexcited carrier lifetimes are required. However, for good sensitivity, high carrier mobilities are needed. Since the damage that is often introduced into the semiconductor to shorten the carrier lifetime also generally reduces the carrier mobility, high speed and good sensitivity are often difficult to achieve in the same detector. The search for materials that can offer high speed with high sensitivity explains the voluminous literature on the subject of photoconductive switches.

Even if the material in question has a short recombination lifetime, the picosecond speed can be masked by slower transients associated with the parasitic capacitance and inductance of the device electrodes. Just as new materials have been investigated as possible active layers of picosecond switches, so too have new electrode configurations been developed to realize these picosecond speeds.

The four most common test configurations of picosecond photoconductive switches are shown in Fig. 1. In the electronic correlation configuration developed by D. H. Auston and shown in Fig. 1(a), one photoconductive gap serves as the pulse generator and a second as the pulse sampler [8]. The gaps are formed in microstrip transmission lines and the measured signal is the electronic correlation of the response of the two gaps. Although widely used, this structure has large parasitic capacitance associated with the photoconductive gaps and suffers from pulse dispersion due to the microstrip transmission lines.

An improved version of the microstrip implementation of the electronic correlation configuration is the photoconductive-gap switch implemented on a coplanar stripline, as shown in Fig. 1(b). Here the picosecond electrical pulse is generated by a photoconductive gap and can be sampled either by using an electronic correlation technique or by electro-optic sampling. In this figure, the electrical pulse is shown

being measured by electro-optic sampling. Although an improvement over the microstrip geometry, this structure is also plagued by the parasitic capacitance of the gap.

The fastest picosecond switching times have been measured using either of the configurations shown in Figs. 1(c) or 1(d). The Hertzian dipole configuration shown in Fig. 1(c) was also pioneered by Auston and operates similarly to the conventional electronic correlation configuration of Fig. 1(a), except that the first photoconductive gap launches the picosecond electrical pulse into free space (or dielectric) and this pulse is then sensed by the second gap [12]. The output is again the electronic correlation of the two switches. Far-infrared spectroscopy measurements are most easily implemented using variations of this configuration [12].

Perhaps the most useful configuration for both the generation and use of picosecond electrical pulses for high-speed device and circuit testing is the sliding-contact switch shown in Fig. 1(d) [13]. The

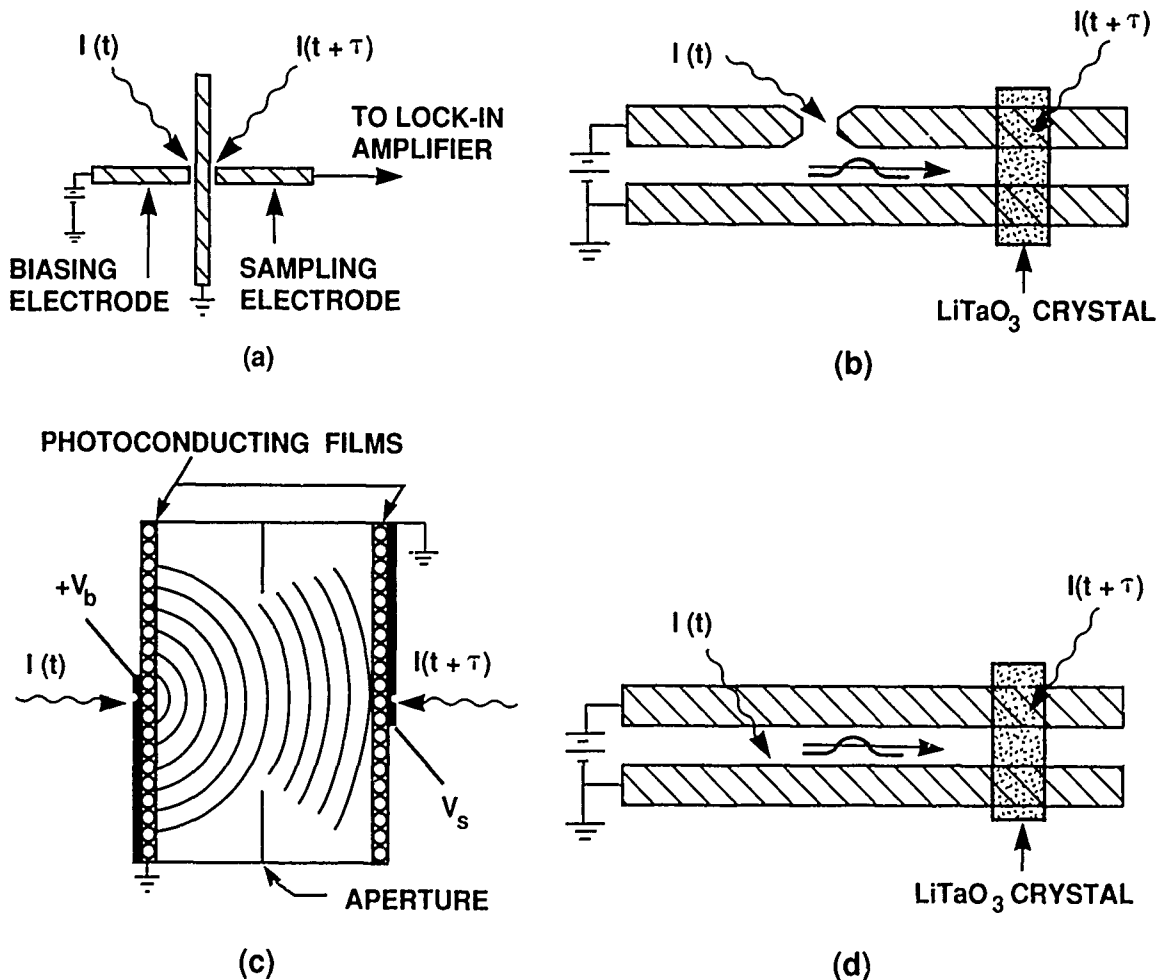


Figure 1. Schematic diagram of commonly used photoconductive switch configurations: (a) Auston's electronic correlation switch (top view), (b) photoconductive-gap switch implemented on a coplanar stripline (top view), (c) Auston's Hertzian dipole electronic correlation switch (cross section), and (d) sliding-contact excitation switch (top view).

only difference between this switch and the switch of Fig. 1(b) is the absence of the photoconductive gap, which reduces the parasitic capacitance. Electrical pulses of FWHM of 0.6 ps have recently been measured using this configuration [14]. In fact, when the photoconductive-gap switch and the sliding-contact switch were used to measure the same material, the photoconductive-gap switch yielded a FWHM of 1.7 ps, while the sliding-contact switch showed a pulse of 1.0 ps FWHM [15]. Clearly the effects of parasitic capacitance can be significant at ultra-high speeds.

The LT GaAs switch results presented below were measured using the photoconductive-gap switch configuration. We intend to report results for the sliding-contact geometry in a future publication [16].

Using either the Hertzian-dipole or sliding-contact configurations, researchers have demonstrated that four different materials exhibit subpicosecond switch performance. The materials are oxygen-implanted silicon-on-sapphire (SOS) [13], implanted and radiation-damaged InP [17], amorphous silicon [9], and polycrystalline CdTe [14]. However, despite the high speeds, these materials have drawbacks which limit their use in high-speed testing applications. The silicon-based and InP-based switches tend to have low mobility, and, hence, exhibit poor sensitivity [14]. In addition, they cannot be easily integrated with the high-speed GaAs-based devices and circuits to be tested. The CdTe-based switch has been demonstrated to have both high speed and sensitivity, but these properties are a function not only of the growth parameters but also the substrate used for deposition [14]. Moreover, the CdTe switch has yet to be monolithically integrated with GaAs-based devices and circuits, although the authors assert that this can be done.

Photoconductive switches based on LT GaAs offer a number of distinct advantages over the switches discussed above. These include fast switching speed (FWHM = 1.6 ps), relatively high sensitivity, the ability to be integrated with high-speed GaAs devices and circuits, and, potentially, the ability to engineer the defects in the material to systematically trade speed for sensitivity. Before discussing these switch results, an overview of this material and some previous device applications of LT GaAs will be presented.

LT GaAs GROWTH AND CHARACTERIZATION

Low-temperature GaAs is grown by MBE using As_4 and Ga beam fluxes at substrate temperatures that are considerably lower than those used for the growth of high-quality, conducting GaAs films (typically between 560 and 600°C). LT GaAs has been grown at temperatures between 150 and 300°C, and then subsequently annealed the material at normal growth temperatures. As will be shown below, the annealing step profoundly changes the characteristics of LT GaAs. All of the device results that will be presented in this paper are for films of LT GaAs

annealed at 600°C for 10 min in an arsenic overpressure

The resistivity of the LT GaAs layer increases as the growth temperature decreases. However, for temperatures near 150°C, the material becomes polycrystalline for layer thicknesses greater than ~0.5 μm . For these reasons, 200°C was chosen as the growth temperature for the films of LT GaAs used in the devices presented here. The LT GaAs grown at 200°C is crystalline and does not exhibit photoluminescence (PL), either near the band gap or from deep levels [4]. However, high-quality, conducting GaAs can be grown at normal growth temperatures upon this insulating layer. The ability to grow high-quality GaAs on top of LT GaAs means that high-performance GaAs devices and circuits can be fabricated on the conducting layer, thereby taking advantage of the improved isolation that the high resistivity buffer layer affords.

The unique properties of LT GaAs can be attributed to excess arsenic in the layer. Auger electron spectroscopy (AES) was used to measure this arsenic excess [4]. A sandwich structure of GaAs and LT GaAs was grown by MBE. The upper and lower GaAs layers were grown at 600°C and are 2000 Å thick. The LT GaAs layer was grown at 200°C and is also 2000 Å thick. The AES signals of Ga and As were measured as the sandwich structure was sputtered at a rate of ~30 Å/min. The results of this measurement are shown Fig. 2. As can be seen, the epitaxial GaAs layers are stoichiometric, whereas the LT GaAs layer contains an excess of arsenic of ~1 at.%. In addition, an excess As content of 1 at.% has also been measured by AES for LT GaAs films that have not been annealed. Although the arsenic content in the film does not change appreciably upon annealing, many of the properties of the material change dramatically after annealing.

In order to better understand and model the properties of LT GaAs, a number of other characterization techniques have been explored. The results of some of these experiments are listed in Table I. The high resistivity of the LT GaAs epilayer is only observed after the anneal. Electron paramagnetic resonance (EPR) experiments have demonstrated that a fraction of the excess arsenic in the unannealed LT GaAs layer is incorporated as EL2, the arsenic antisite defect or complex [18]. However, after annealing, the concentration of EL2 in the LT GaAs layer decreases to levels below the detection limits of the system [18]. Double-crystal x-ray diffraction measurements indicate that the lattice constant of the unannealed LT GaAs epilayer is approximately 0.1% larger than that of GaAs, and that it becomes identical to that of GaAs after annealing, within the experimental resolution [18]. Transmission electron microscopy (TEM) and lattice-imaging TEM demonstrate that the crystal quality of the material is excellent, both before and after annealing [18]. No microscopic precipitates or other inclusions are observed, and the dislocation density observed in these films is comparable to the dislocation density observed for the semi-insulating substrate [18].

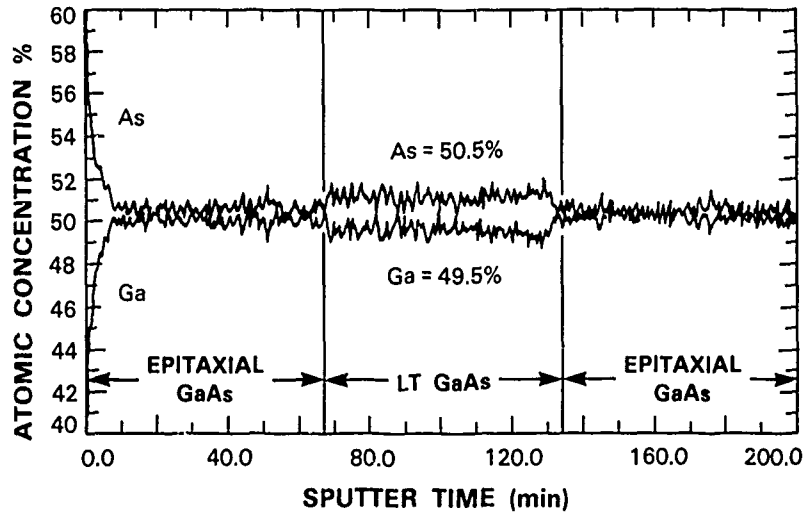


Figure 2. Auger concentration depth profile of an n^+ GaAs/LT GaAs/ n^+ GaAs sandwich structure. The sputtering rate was $\sim 30 \text{ \AA}/\text{min}$. The upper n^+ GaAs layer and the LT GaAs layer are both 2000 \AA thick. Note that the n^+ GaAs regions are stoichiometric, whereas the LT GaAs has a 1 at.% excess of arsenic over gallium.

TABLE I

LT GaAs CHARACTERIZATION

| | LT GaAs | |
|---------------------------------------|--|---|
| | UNANNEALED | ANNEALED AT 600°C |
| RESISTIVITY | LEAKY | $\rho_{\text{LT GaAs}} > \rho_{\text{SI GaAs}}$ |
| AUGER | $\sim 1 \text{ at. \% EXCESS As}$ | $\sim 1 \text{ at. \% EXCESS As}$ |
| EPR | $\sim 5 \times 10^{18} \text{ cm}^{-3} \text{ As}_{\text{Ga}}$ | SIGNAL BELOW DETECTION LIMITS |
| PL (200°C) | NO SIGNAL | NO SIGNAL |
| PL ($300\text{-}450^\circ\text{C}$) | ENHANCED DEEP-LEVEL SIGNAL AS T_s IS REDUCED | |
| RHEED | UNRECONSTRUCTED | TYPICAL GaAs RECONSTRUCTION |
| X-RAY | 2 PEAKS $\sim 0.1\%$ LARGER LATTICE CONSTANT | 1 PEAK GaAs LATTICE CONSTANT |
| TEM | EXCELLENT CRYSTAL QUALITY | EXCELLENT CRYSTAL QUALITY |
| RAMAN | SHIFTED LO PHONON PEAK | TYPICAL GaAs SPECTRA |

At this time, it is hypothesized that the excess As in the LT GaAs creates deep levels, shallow acceptors, and perhaps defect complexes in the GaAs crystal, and that these levels are responsible for the observed electronic, optical, and structural properties of the material [4]. These experiments and others are being pursued to more fully explain the unique properties of LT GaAs.

In the past a number of device applications of LT GaAs were demonstrated [2-5]. DC sidegating effects were eliminated in MESFETs and HEMTs [2,19]. The dielectric breakdown voltage of LT GaAs has been shown to be over an order of magnitude greater than that of GaAs [2]. This result may have implications for the generation of high-voltage picosecond electrical pulses. Submicrometer-gate-length MESFETs that incorporate LT GaAs buffers have demonstrated reduced short-channel effects and improved microwave performance, as compared with identical devices fabricated with undoped GaAs buffer layers [3]. Recently LT GaAs has been shown to substantially improve the isolation between active elements in analog, digital, and microwave integrated circuits (IC's) [4,5], so that LT GaAs can be used to enhance circuit performance and relax layout restrictions.

LT GaAs PHOTOCONDUCTIVE SWITCH

To assess the picosecond performance of the LT GaAs photoconductive switch, a photoconductive-gap switch configuration was used in conjunction with the technique of electro-optic sampling. The device structure is shown in Fig. 3. A 2- μm -thick film of LT GaAs was used as the active layer. Indium metal was patterned into a coplanar transmission line with a width of 50 μm . A square wave of frequency 3.7 MHz and amplitude 10 V was used to bias the structure. The generated electrical pulse was measured at two points, labeled as A and B, along the transmission line by electro-optic sampling.

A schematic diagram of the electro-optic sampling technique is shown in perspective in Fig. 4(a), and a schematic cross section of the LiTaO₃ "finger probe" is shown in Fig. 4(b) [7]. A colliding-pulse mode-locked laser was used to generate 80-fs laser pulses at a 100-MHz repetition rate with a wavelength of 620 nm and an average power of ~ 9 mW (90 pJ/pulse). The picosecond electrical pulse generated by this optical pulse was detected using a "finger probe" of LiTaO₃. The propagating electrical pulse induces a birefringence in the LiTaO₃ crystal. This birefringence is sensed by a second, time-delayed, 80-fs laser pulse. Since both pulses are generated by the same laser, the measurement is jitter-free. The time resolution of the electro-optic sampling technique has been shown to be less than ~ 0.3 ps [7]. The amplitude of the electrical pulse is sensed by the magnitude of the induced birefringence. The absolute amplitude of the pulse was determined by calibrating the tip with fixed values of bias on the transmission line. The birefringence induced for each bias established a calibration for the measurement. The tip position relative to the transmission line and the surface of the LT GaAs epilayer was the same for both the calibration procedure and the picosecond electrical pulse measurement.

The results of the electro-optic sampling measurement are shown in Fig. 5. At both points on the line, a pulse of duration 1.6 ps and amplitude 0.43 V was detected. The FWHM of 1.6 ps translates into a bandwidth of 220 GHz. The slightly longer tail on the pulse detected at point A can be attributed to backplane reflections. Recent measurements of newly fabricated structures have again shown 1.6-ps FWHM pulses, but the voltage amplitude is of the order of ~ 1 V, for a 10 V bias on the transmission line. Preliminary calculations indicate that the actual pulse width of this switch would be less than 1.6 ps if the effects of parasitic capacitance were eliminated. These calculations suggest that it may be possible to measure an electrical response of ~ 0.8 ps duration using the LT GaAs switch in the

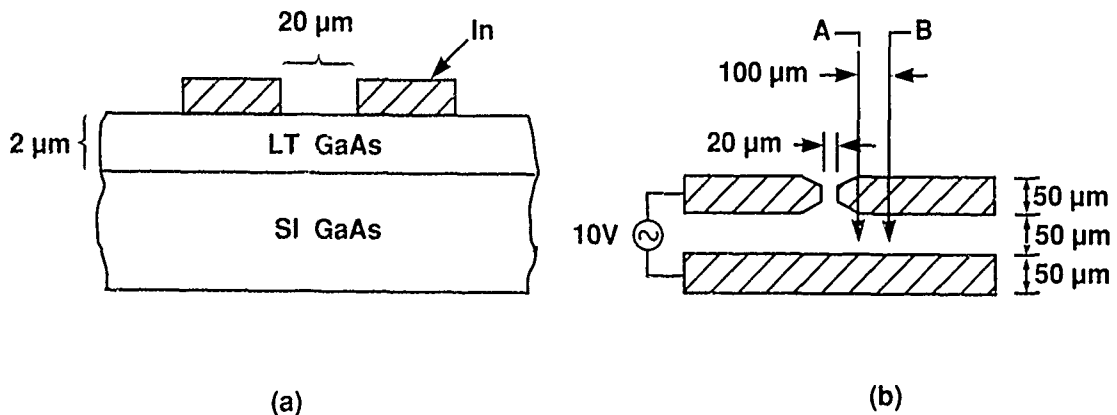


Figure 3. LT GaAs photoconductive-gap switch used for the electro-optic sampling measurement: (a) schematic cross section, and (b) schematic top view. Also shown in (b) are two points on the transmission line labeled as A and B. The electrical impulse is sampled by the probe beam at both points.

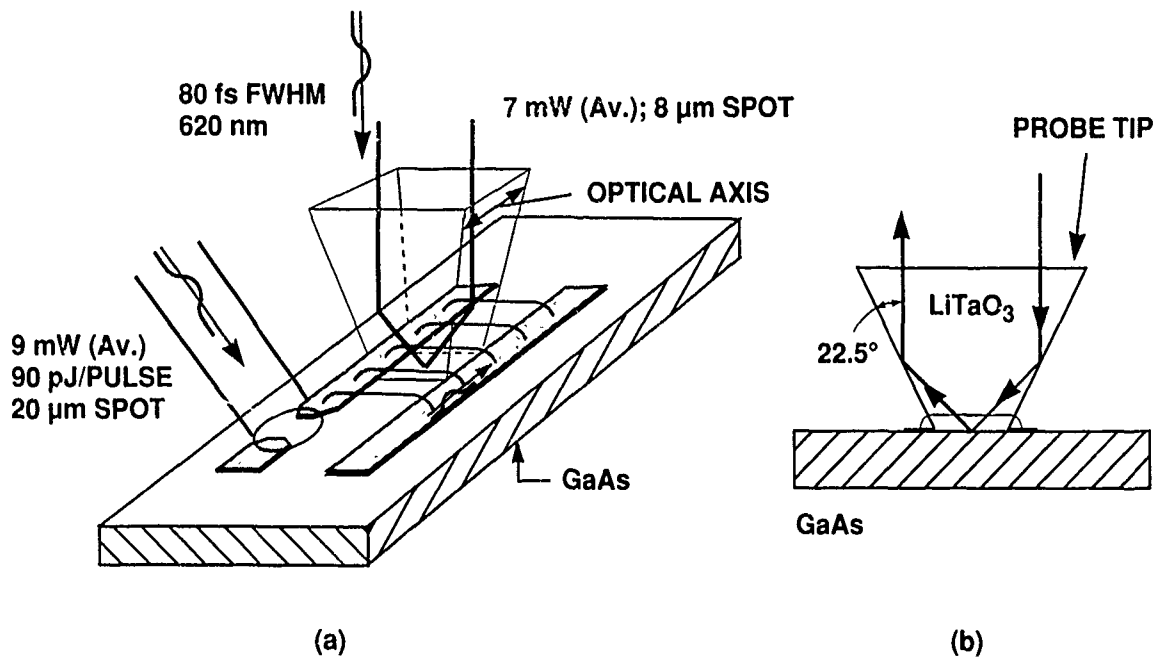


Figure 4. Diagram of electro-optic sampling technique in the finger probe configuration: (a) perspective drawing, and (b) schematic cross section of the LiTaO₃ tip.

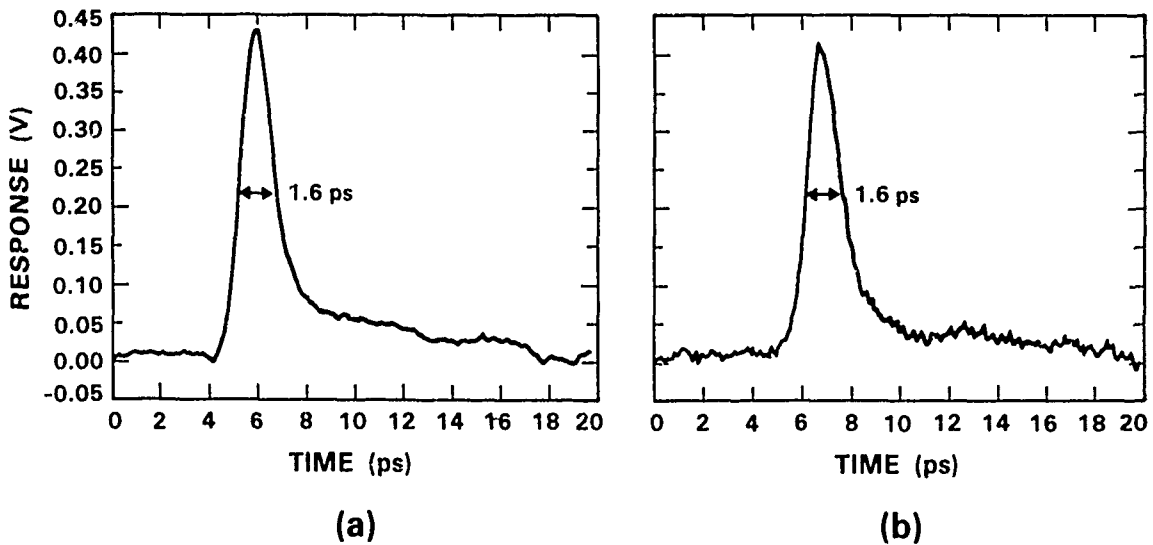


Figure 5. Electrical impulse generated by an 80-fs laser pulse as measured by electro-optic sampling: (a) measured at point A [see Fig. 3(b)], and (b) measured at point B [see Fig. 3(b)].

sliding-contact geometry. Further, preliminary calculations, using the well-known formula of Auston [8,14], indicate the mobility of the photoexcited carrier in this material is of the order of $200 \text{ cm}^2/\text{V}\cdot\text{s}$. We attribute the high speed of the LT GaAs switch to the large excess of arsenic in the crystal and its high mobility and sensitivity to the high degree of crystalline perfection.

CURRENT LT GaAs SWITCH INVESTIGATIONS

In order to more fully characterize LT GaAs as a picosecond switch, we are currently fabricating and testing a number of LT GaAs-based switches. These switches employ the sliding-contact configuration discussed previously. Further, the transmission-line dimensions have been reduced to $10 \mu\text{m}$. The effects of different metallizations are also being investigated.

We intend to study the dependence of the voltage amplitude of the electrical pulse as a function of bias on the transmission line and the laser pulse energy. The goal of this work is to achieve electrical pulses of arbitrary peak height with a temporal response of the order of a picosecond. Pulses of varying peak height would be useful for measuring both the large-signal and small-signal behavior of high-speed electronic devices. We also intend to measure the carrier lifetime by the pulse and probe technique [20]. The results of this investigation will be presented elsewhere.

In addition to improving the switch configuration, we are also investigating the influence of growth parameters on switch performance. The role of arsenic-to-gallium flux ratio, growth temperature, annealing time and temperature, and contact layers in governing the speed and sensitivity of the device will be investigated. A future LT GaAs switch structure that we intend to fabricate in the future is shown in Fig. 6. This structure can be grown on either GaAs or Si substrates and makes use of layered structures of LT GaAs and conducting GaAs. Such layered structures may enhance the sensitivity of the switch without degrading the temporal response.

One of the distinct advantages of LT GaAs as compared with previously reported high-speed switches is the ease with which LT GaAs can be integrated with high-speed GaAs devices and circuits. Using the LT GaAs switch, we can measure, *in situ*, the scattering parameters of high-speed devices, fan-out effects in GaAs circuits, and propagation delays along actual GaAs IC interconnects. By monolithically integrating the LT GaAs switch with the high-speed device or circuit to be tested, we can eliminate spurious reflections that can occur due to the bond wires that are used to connect discrete photoconductive switches with discrete electronic devices and circuits [21]. Further, the use of coplanar stripline in this monolithic configuration can minimize the dispersion of the electrical pulse as it propagates from the generation site to the device under test [22].

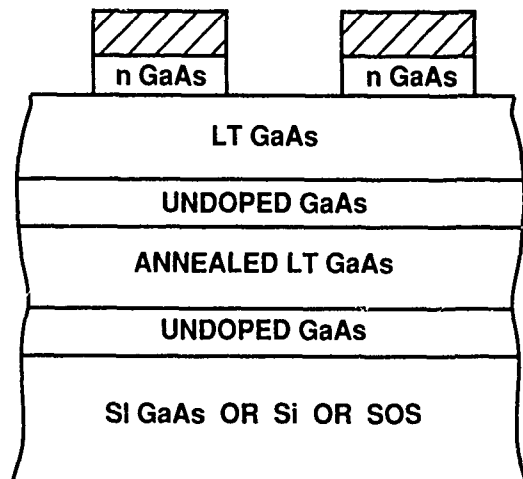


Figure 6. Proposed layered LT GaAs photoconductive switch structure (schematic cross section).

CONCLUSION

We have demonstrated the use of LT GaAs as a picosecond photoconductive switch. A switching speed of 1.6 ps and voltage response of $\sim 1 \text{ V}$ for a 10 V bias have been measured for the LT GaAs switch using the measurement technique of electro-optic sampling. This switch can overcome some of the limitations associated with other high-speed switches. The unique properties of LT GaAs can be attributed to an excess of arsenic in the crystal. Experiments are currently in progress to optimize the LT GaAs switch for speed and sensitivity, and we plan to use this new switch to characterize, with unprecedented temporal response and bandwidth, the time-domain and frequency-domain behavior of high-speed GaAs-based devices and circuits.

ACKNOWLEDGMENTS

The authors thank A. L. McWhorter and R. A. Murphy for helpful discussions. The Lincoln Laboratory portion of this work was sponsored by the Department of the Air Force, in part under a specific program supported by the Air Force Office of Scientific Research. The Laboratory for Laser Energetics is supported in part by the United States Air Force Office of Scientific Research under contract to the Ultrafast Science Center, and by the National Science Foundation. Additional support was provided by the sponsors of the Laser Fusion Feasibility Project at the Laboratory for Laser Energetics. Empire State Electric Corporation, New York State Energy Research and Development Authority, Ontario Hydro, and the University of Rochester.

S. Gupta, M. Frankel, and G. A. Mourou are currently with the Ultra-fast Science Laboratory,

University of Michigan, Ann Arbor, MI 48105. D. R. Dykaar is currently with AT&T Bell Laboratories, Murray Hill, NJ 07974.

REFERENCES

- [1] F. W. Smith, H. Q. Le, V. Diadiuk, M. A. Hollis, A. R. Calawa, S. Gupta, M. Frankel, D. R. Dykaar, G. A. Mourou, and T. Y. Hsiang, *Appl. Phys. Lett.* **54**, 890 (1989).
- [2] F. W. Smith, A. R. Calawa, C. L. Chen, M. J. Manfra, and L. J. Mahoney, *IEEE Electron Device Lett.* **EDL-9**, 77 (1988).
- [3] F. W. Smith, A. R. Calawa, C. L. Chen, L. J. Mahoney, M. J. Manfra, and J. C. Huang, in *Proceedings IEEE/Cornell Conference on Advanced Concepts in High Speed Semiconductor Devices and Circuits*, 1987 (IEEE, New York, 1987), p. 229.
- [4] F. W. Smith, C. L. Chen, G. W. Turner, M. C. Finn, L. J. Mahoney, M. J. Manfra, and A. R. Calawa, in *Technical Digest IEEE International Electron Devices Meeting* (IEEE, New York, 1988), p. 838.
- [5] C. L. Chen, F. W. Smith, A. R. Calawa, L. J. Mahoney, and M. J. Manfra, submitted to *IEEE Trans. Electron Devices*.
- [6] J. A. Valdmanis and G. Mourou, *IEEE J. Quantum Electron.* **QE-22**, 69 (1986).
- [7] J. A. Valdmanis, *Electron. Lett.* **23**, 1308 (1988).
- [8] D. H. Auston, *J. Quantum Electron.* **QE-19**, 639 (1983).
- [9] D. H. Auston, in *Ultrashort Laser Pulses and Applications*, W. Kaiser, ed., Topics Appl. Phys. Vol. 60 (Springer-Verlag, Berlin, 1988), pp. 183-233.
- [10] G. T. Turner, G. M. Metze, V. Diadiuk, B-Y. Tsaur, and H. Q. Le, in *Technical Digest IEEE International Electron Devices Meeting* (IEEE, New York, 1985), p. 468.
- [11] A. G. Foyt and F. J. Leonberger, in *Picosecond Optoelectronic Devices*, C. H. Lee, ed. (Academic, Orlando, 1984), pp. 271-311.
- [12] D. H. Auston, K. P. Cheung, and P. R. Smith, *Appl. Phys. Lett.* **45**, 284 (1984).
- [13] M. B. Ketchen, D. Grischkowsky, T. C. Chen, C-C. Chi, I. N. Duling, III, N. J. Halas, J-M. Halbout, J. A. Kash, and G. P. Li, *Appl. Phys. Lett.* **48**, 754 (1986).
- [14] M. C. Nuss, *Appl. Phys. Lett.* **54**, 57 (1989).
- [15] D. Grischkowsky, C-C. Chi, I. N. Duling, III, W. J. Gallagher, N. H. Halas, J-M. Halbout, and M. B. Ketchen, in *Picosecond Electronics and Optoelectronics II*, F. J. Leonberger, C. H. Lee, F. Capasso, and H. Morkoc, eds. (Springer-Verlag, Berlin, 1987), pp. 11-17.
- [16] S. Gupta, J. A. Valdmanis, G. A. Mourou, F. W. Smith, and A. R. Calawa, to be presented at the Conf. on Lasers and Electro-Optics, Baltimore, MD, April, 1989.
- [17] P. M. Downey and B. Schwartz, *Appl. Phys. Lett.* **44**, 207 (1984).
- [18] M. Kaminska, Z. Liliental-Weber, E. R. Weber, T. George, J. B. Kortright, F. W. Smith, B-Y. Tsaur, and A. R. Calawa, submitted to *Appl. Phys. Lett.*
- [19] B. J. Lin, D. E. Mars, and T. S. Low, presented at the IEEE 46th Annual Device Research Conf., Boulder, CO, 1988.
- [20] M. C. Nuss and D. H. Auston, in *Picosecond Electronics and Optoelectronics II*, F. J. Leonberger, C. H. Lee, F. Capasso, and H. Morkoc, eds. (Springer-Verlag, Berlin, 1987), pp. 72-78.
- [21] D. E. Cooper and S. C. Moss, *IEEE J. Quantum Electron.* **QE-22**, 94 (1986).
- [22] J-M. Halbout, P. G. May, M. B. Ketchen, H. Jackel, G. P. Li, C-C. Chi, M. Scheuermann, and M. Smyth, in *Picosecond Electronics and Optoelectronics II*, F. J. Leonberger, C. H. Lee, F. Capasso, and H. Morkoc, eds. (Springer-Verlag, Berlin, 1987), pp. 36-39.

Interdigitated Metal-Semiconductor-Metal Detectors

D. L. Rogers

IBM Research Division, T. J. Watson Research Center, P.O. Box 218,
Yorktown Heights, New York 10598

Abstract

The Interdigitated-Metal-Semiconductor-Metal (IMSM) detector has recently become one of the more popular detectors for optoelectronic integration. The factors affecting the performance of this type of detector are reviewed particularly in the context of low noise amplification circuitry.

Introduction

The IMSM detector, a simple structure consisting of interdigitated metal fingers deposited on an undoped semiconductor substrate (Figure 1), was proposed originally by Sugeta in 1979¹. This detector has proved to be one of the fastest detectors fabricated to date. Also, due to its lateral structure, as opposed to a vertical structure as found in a PIN or APD detector, it has one of the lowest capacitances.

Recently interest has grown in fiber optic communications for the high receiver sensitivity theoretically possible in fully integrated Opto-Electronic Integrated Circuits (OEICs). To achieve this sensitivity a fast, low capacitance detector compatible with the developed IC technologies is needed. The IMSM detector is ideally suited for this application and has already demonstrated the feasibility of high sensitivity and high speed OEIC receiver designs.

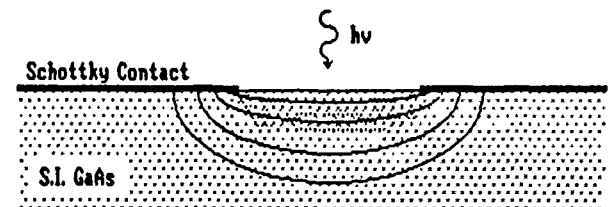


Figure 1. IMSM detector structure

Detector Characteristics

Bandwidth

The bandwidth of the IMSM detector is limited by the transit time between electrode fingers and is limited only by their spacing and the saturation velocity of the holes. Using state of the art lithography finger spacings of .5 micron are easily achieved since in most cases the electrodes are formed with the same metalurgy used to fabricate the short MESFET gates. Figure 2 shows the results of measurements on such a detector with a bandwidth of 105 GHz² making it one of the fastest detectors fabricated today.

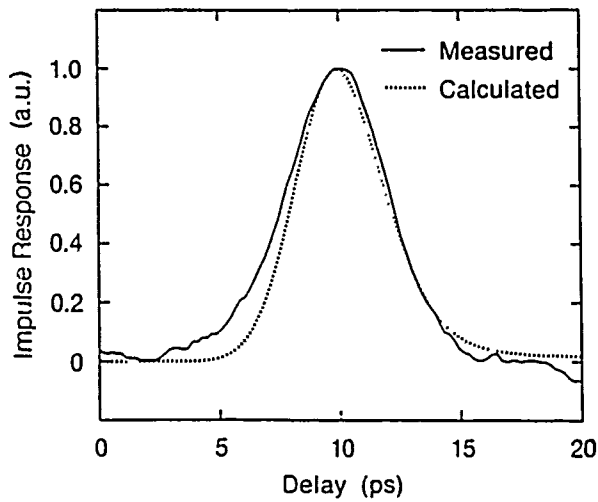


Figure 2. Detector Pulse Response

Capacitance

Due to the two dimensional nature of the IMSM detector and the fact that half of the electric field is not in the semiconductor this type of detector has inherently less capacitance than the parallel plate structure of a PIN diode. Figure 3 shows a plot of capacitance for this type of detector for several finger widths along with that for a comparable PIN detector.

For each finger spacing the intrinsic layer thickness of the PIN detector was chosen the same as the gap spacing in the IMSM detector making the two detector structures similar speed. As can be seen from this plot the capacitance of the IMSM detector is less than half that of a PIN detector of the same bandwidth.

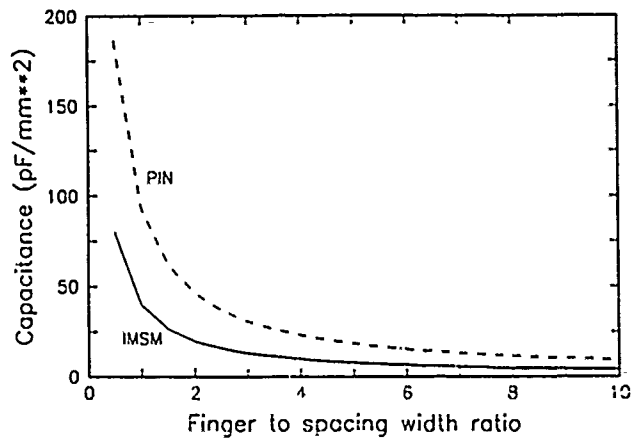


Figure 3. Capacitances of IMSM and PIN detectors.

Responsivity

Even though the IMSM detector may have a responsivity only 50 to 80 percent of an equivalent PIN diode, due to the light blocked by the electrodes, the lower capacitance of the IMSM can actually result in an optical receiver with a higher sensitivity. The reason for this is that the lower capacitance allows, at a given bandwidth, smaller amplification devices to be used in the preamplifier resulting in a lower noise level. Modeling of the noise in such preamplifiers show that in most cases, for a given optimized preamplifier design, the rms input noise current varies as the square root of the photodiode capacitance. The minimum detectable optical power required for a given error rate is related to this noise by the relation:

$$P_S = \frac{Q \langle i_N^2 \rangle}{\eta} \quad [1]$$

where $\langle i_N^2 \rangle$ is the mean square noise current, η is the detector responsivity, and Q is the rms signal to noise ratio which is about 6 for a 10^{-9} bit error rate. Using this relation it is easy to see that the ratio of sensitivities for PIN and IMSM detector systems is:

$$\frac{P_{MSM}}{P_{PIN}} = \frac{\eta_{PIN}}{\eta_{MSM}} \left\{ \frac{C_{MSM}}{C_{PIN}} \right\}^{\frac{1}{2}} \quad [2]$$

The responsivities and capacitances for these geometries can be easily estimated resulting in a sensitivity ratio as plotted in Figure 4 for different IMSM finger spacings. Clearly for spacing to finger width ratios greater than about 2.5 the IMSM detector shows a potential advantage. Recently this potential for high sensitivity was demonstrated in a 250 Mb/s fiber optic receiver operating at a sensitivity of -39.5 dBm³ or only 1900 photons per bit. To our knowledge this is the best sensitivity reported for an optical receiver at this wavelength.

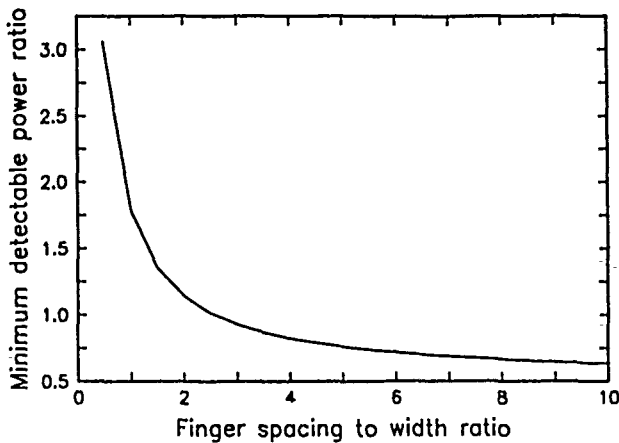


Figure 4. Ratio of minimum detectable power for PIN and IMSM detectors.

Dark Current and Noise

Recently with the use of epitaxial buffer layers² or shallow implants under the detector⁴ it has become possible to reduce or eliminate the problems that affected early versions of the device. These problems included large dark currents, low responsivities, and low frequency gain.

At our lab we have accumulated evidence that these problems are due to a trapping effect. This trapping occurs primarily at the surface and results in an induced charge density which lowers the barrier to tunneling at the detector electrodes. Since the amount of trapping depends on the photocurrent this can give rise to a low frequency photoconductive gain. If no attempt is made to control

this surface trapping we have found the detector's performance to be sensitive to surface conditions and substrate quality. In some cases it has been possible to find a high purity epitaxial layer which yielded good detectors and OEIC preamplifiers have been fabricated using this technique⁵. We have found, however, that such detectors are sensitive to the high temperature processing such as used in doping via implantation.

By using structures that reduce the possibility of the photocurrent being trapped at the surface we have found it possible to greatly reduce the dark current and photoconductive gain. We have found that a thin lightly doped layer under the surface of the detector has not only been effective in eliminating low frequency gain but also has the advantage making the detector insensitive to the high temperature processing steps making it compatible with most high performance MESFET processes.

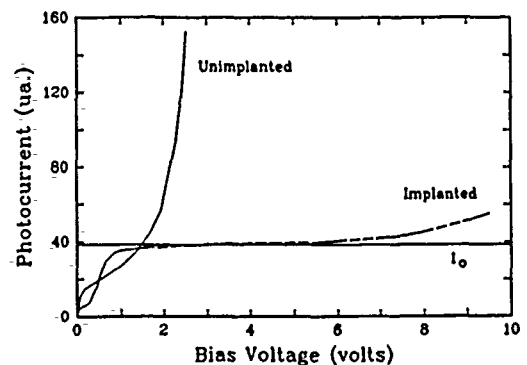


Figure 5. Illuminated IV curves for implanted and unimplanted detectors.

Figure 5 shows the effectiveness of a surface implant in reducing the low frequency gain in this type of device. The flat portion of the curve for the implanted detector corresponds to an internal quantum efficiency very close to 100 percent with very little of the photocurrent coming from trapping effects which generally have a poor frequency response.

Integrated Receivers

Using an implant as described above it has been possible to demonstrate a number of high performance devices including the low noise preamp described above, a 5 GHz preamplifier and for the first time a LSI OEIC. The latter is a 1200 gate chip including all of the high speed circuits necessary for a 1 Gb/sec fiber optic link: optical receiver, clock recovery circuit and 10:1 deserializer⁶. Figure 6 shows a photo micrograph of this circuit along with the coupling to four beveled fibers. This chip has been operated at 950 Mb/sec. and has demonstrated for the first time that all of these functions can be realized on a single chip without serious noise coupling into the sensitive receiver front end.



Figure 6. Photomicrograph of LSI OEIC. The four ovals are the beveled ends of fibers coupled to IMMS receiver circuits.

high circuit densities possible using GaAs IC technology with a detector sensitive to the 1.3 micron wavelength at which fiber dispersion attains a minimum. Almost all semiconductors, however, which absorb at this wavelength are not lattice matched to GaAs. The fact that the IMMS detector does not require a buried electrode allows simpler devices depending only on the quality of the semiconductor near the surface. This makes possible the use of techniques that retain the dislocations in buried layers while maintaining a relatively dislocation free region near the surface. Figure 7 shows the layer structure of such a detector. In this structure a graded InGaAs epitaxial layer at the surface serve both to provide a high schottky barrier and a built in field that repels the photo-generated carrier from the surface preventing trapping there. Using such structures, high performance detectors sensitive to 1.3 micron radiation have been successfully fabricated on GaAs substrates⁷. Such detectors could eventually make possible the realization of long wavelength LSI OEICs similar to those developed for the shorter wavelengths.

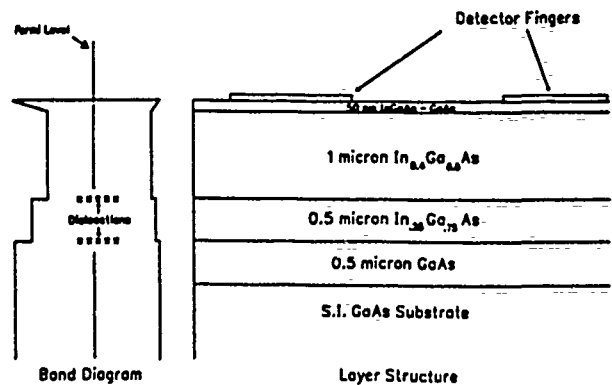


Figure 7. Layer structure of InGaAs-IMMS detector.

Another area where the use of the IMMS detector geometry has been explored is in non-lattice matched devices. There is much interest in the combining the

Summary

In summary the IMSM detector combines being one of the fastest detectors with low capacitance and

compatibility with high performance IC processes. This combination will likely make this the detector the device of choice in many future optical communication applications.

- ¹ T. Sugeta, T. Urisu, S. Sakata and Y. Mizushima, "Metal-Semiconductor Metal Photodetector for High-Speed Optoelectronic Circuits", *Jap. Jour. Appl. Phys.*, V19, Suppl 19-1, 1980, p459-464.
- ² B.J. Van Zeghbroeck, et. al., "105 GHz Bandwidth Metal-Semiconductor- Metal Detectors Fabricated on GaAs Substrates", *Elect. Dev. Lett.*, v9, p527, Oct. 1988.
- ³ R.J. Bates, D.L. Rogers, "A Fully Integrated High Sensitivity PIN/FET Optical Receiver at 250 MBaud", *Proc. Opt. Fiber. Comm. Conf.*, 1988.
- ⁴ D.L. Rogers, "MESFET Compatible IMSM Detectors", *Proc. Picosecond Electronics and Optoelectronics Conf.*, p116, January 1987.
- ⁵ O. Wada, et. al., "Monolithic Four-Channel Photodiode/Amplifier Receiver Array Integrated on a GaAs Substrate", *Jour. Lightwave Tech.*, v LT-4, n 11, p1694, 1986.
- ⁶ J.F. Ewen, et. al., "Gb/s Fiber Optic Link Adapter Chip Set", *GaAs IC. Symp.*, p11, Nov. 1988.
- ⁷ D.L. Rogers, et. al., "High-Speed 1.3 micron GaInAs Detectors Fabricated on GaAs Substrates", *Elect. Dev. Lett.*, v9, n10, p515, 1988.

Coplanar Vacuum Photodiode for Measurement of Short-Wavelength Picosecond Pulses

J. Bokor, A. M. Johnson, W. M. Simpson, and R. H. Storz
AT&T Bell Laboratories, Holmdel, New Jersey 07733

P. R. Smith
AT&T Bell Laboratories, Murray Hill, New Jersey 07974

Abstract

We have fabricated a vacuum photodiode in a coplanar stripline geometry. This device is capable of high quantum efficiency and picosecond response time. It may be particularly useful for diagnostics of picosecond soft X-rays from laser produced plasmas.

Introduction

The first electronic device which involved "ballistic transport" was the vacuum tube. Modern microfabrication technology now makes it possible to implement some of the "classic" vacuum tube devices with microscopic dimensions, thereby achieving high speed operation. As an example of this, we have realized an ultrafast vacuum photodiode detector in a coplanar stripline geometry.

In a vacuum photodiode, photons impinge on a photocathode in vacuum. A nearby anode collects photoelectrons from the cathode and the resulting photocurrent is measured in a suitable external circuit. Such a device is sensitive to photon energies which exceed the photocathode work function in accord with the classical photoelectric effect. Photocathode materials with high quantum efficiency (1-30%) have been developed for use at optical wavelengths shorter than $\sim 1\mu\text{m}$. For vacuum ultraviolet and soft X-ray radiation, photoelectric quantum yields in excess of 50% can be reached.[1] In our device, the two parallel coplanar stripline electrodes themselves serve as the photocathode and anode. With a stripline spacing of a few microns, and a sufficiently high bias potential applied between the strips, the transit-time can be in the range of a few

psec. In order to read out the ultrafast electrical waveform produced on the stripline, a conventional photoconductive sampler is used.

Experiment

A representation of our initial devices is shown in Fig. 1. Gold striplines of $5\mu\text{m}$ width, separated by $5\mu\text{m}$ were deposited on a silicon-on-sapphire substrate. Before the striplines were deposited, the silicon was etched off except in a 2 mm wide strip in the region of the sampling gap so that in the photodiode area of the detector, no silicon remains between the strips. The details of the fabrication of these devices and the initial results have already been described.[2] The apparatus used in testing these devices involves using 266 nm ultraviolet (UV) laser pulses of ~ 500 fsec duration derived from a compressed, mode-locked Nd:YAG laser,[3] and is shown in Fig. 2. The results are reproduced in Fig. 3. The signal was confirmed as photoelectric in origin by venting the vacuum chamber with air and observing the signal disappear due to electron scattering by air molecules. The device was quite sensitive to UV radiation; even our crude cesiated gold photocathode was approximately an order of magnitude more sensitive than the radiation damaged silicon photoconductor.

The signal fall time was found to decrease markedly as the applied cathode-anode bias voltage increased. The bias voltage was applied to the anode with the cathode held at ground potential. With 60 V applied bias, we obtained a 4 psec rise time and a 12 psec fall time. It was not possible to apply a higher bias voltage to this device due to avalanche breakdown of the silicon between the lines. The

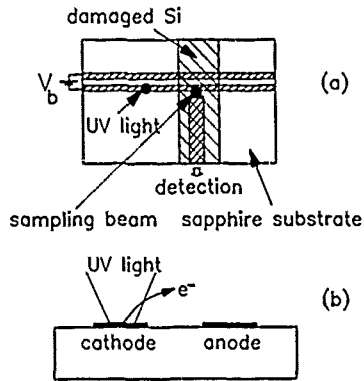


Figure 1. Schematic diagram of the coplanar vacuum photodiode. (a) Top view. (b) Side view. Reproduced with permission from Ref. 2. Copyright 1988, American Institute of Physics.

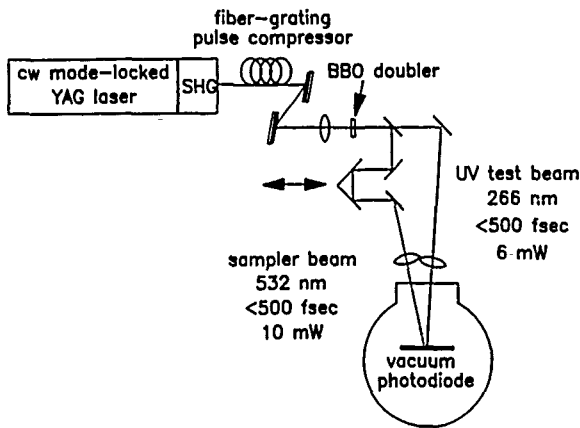


Figure 2. Experimental apparatus used for device testing.

dependence of the rise and fall times on applied bias is shown in Fig. 4. The rise time is seen to be essentially independent of bias while the fall time follows a $1/\sqrt{V_b}$ dependence, where V_b is the bias voltage applied between the strips. This is the expected behavior for electron transit time in a vacuum diode.[4]

In addition to the decreasing fall time with increasing bias, we observed a nearly linear increase in signal magnitude with increasing applied bias, as shown in Fig. 5. We interpret this to be an indication that the emitted cathode current is influenced by space-charge effects. For a vacuum photodiode under constant illumination conditions, one expects the emitted current to increase with applied bias in the space-charge limited regime, and then to saturate when all of the photocurrent is extracted from the cathode. Apparently, at the maximum applied bias of 60 V, saturation was not reached. We estimate the

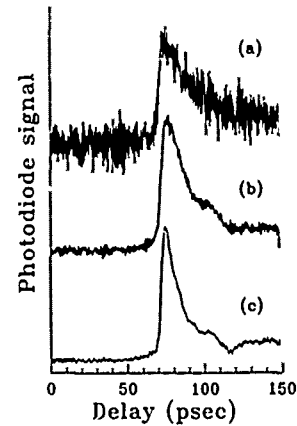


Figure 3. Measured waveforms from the vacuum photodiode - photoconducting sampler device. (a) 5 V bias. 10-90% risetime: 6 psec. 1/e fall time: 36 psec. (b) 20 V bias. Rise time: 5 psec. Fall time: 20 psec. (c) 60 V bias. Rise time: 4 psec. Fall time: 12 psec. Reproduced with permission from Ref. 2. Copyright 1988, American Institute of Physics.

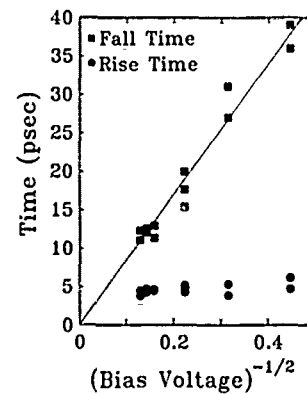


Figure 4. Measured 10-90% rise times and 1/e fall times plotted against $1/\sqrt{V_b}$. Reproduced with permission from Ref. 2. Copyright 1988, American Institute of Physics.

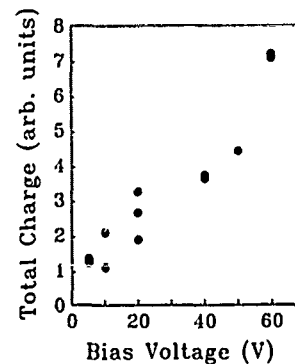


Figure 5. Dependence of signal amplitude on applied bias voltage.

peak cathode current density to be in excess of 200 A/cm^2 .

Analysis

In order to gain a better understanding of what determines the response time of the device, the potential distribution and electron trajectories were calculated using an electron gun design program.[5] An example of the results are shown in Figs. 6, 7 and 8. We see that, due to the large component of electric field normal to the surface of the cathode, the electrons travel out and away from the strips, rather than curving sharply back around to the anode. This behavior is made clearer by displaying the potential distribution as a three dimensional surface as in Fig. 7. Even though the photoelectrons are not collected by the anode, a potential difference

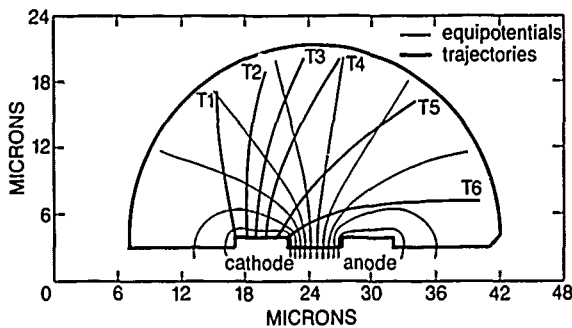


Figure 6. Calculated equipotentials and electron trajectories. The equipotentials are drawn at $0.05 V_b$, $0.15 V_b$, $0.25 V_b$, ..., $0.95 V_b$. Six examples of the electron trajectories are shown labeled T1, T2, ..., T6 for identification.

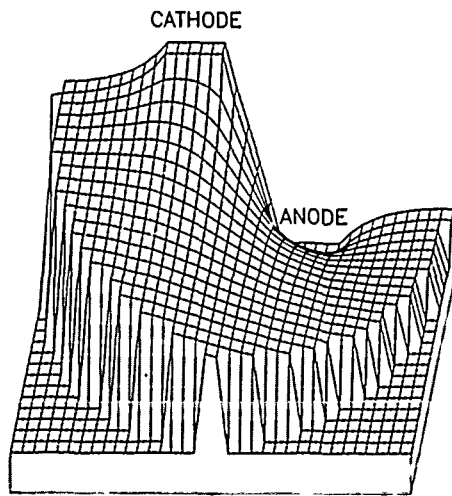


Figure 7. Potential distribution of Fig. 7 displayed as a three dimensional surface.

is induced between the cathode and anode, which is then sensed at the sampling gap. It is clear that the fall time of the pulse generated on the strips will be controlled by the flight time of the electrons through the near-field region. In order to estimate this, we calculated the time required for the electrons to reach the cylindrical boundary shown in Fig. 6, which was somewhat arbitrarily drawn at a radius of $18 \mu\text{m}$ from the midpoint between the strips. The results for several different trajectories are shown in Fig. 8 as a function of the applied bias voltage. The calculated flight times do very nearly follow a $1/\sqrt{V_b}$ dependence, and nearly agree quantitatively with the measured fall times. We therefore conclude that the fall time of the pulse on the strips is determined by the transit time of the photoelectrons out to a distance of several times the strip spacing.

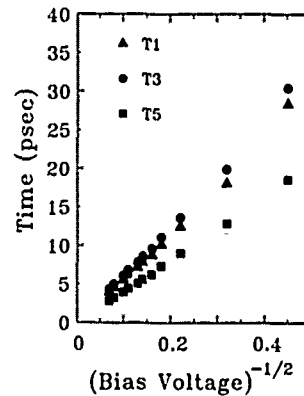


Figure 8. Calculated transit times to the boundary for three of the example trajectories. The calculated transit times for the other trajectories fall between those shown here. Reproduced with permission from Ref. 2. Copyright 1988, American Institute of Physics.

Space-Charge Effects

In order to consider the influence of the space-charge field on the electron transit times, we repeated the above calculations with the emitted cathode current automatically set by the Child-Langmuir law.[4] The results are shown in Figs. 9 and 10. These transit times were virtually identical to those shown in Fig. 8, which were calculated in the low current limit. In a plane-parallel diode, the transit time under space-charge limited conditions is expected to be 50% longer than under non-space-charge limited conditions.[4] However, for our coplanar diode, the calculations show that the space-charge field is much more localized near the cathode than for the plane-parallel case, where the effect of

the space-charge field is felt throughout the cathode-anode space.

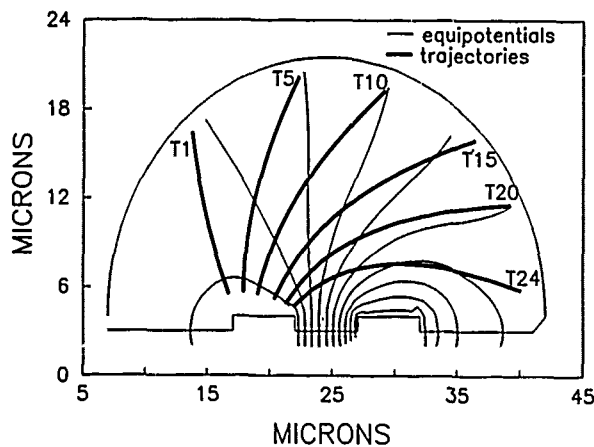


Figure 9. Calculated equipotentials and electron trajectories under conditions of space-charge limited emission.

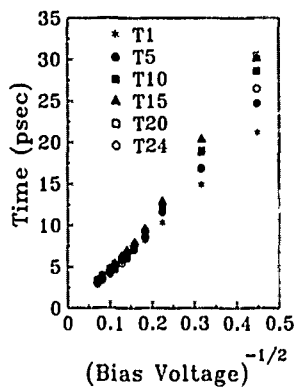


Figure 10. Calculated transit times to the boundary for the trajectories in Fig. 9.

We experimentally investigated the influence of space-charge on the fall time of the diode by holding V_b constant and varying the UV power incident on the diode from 2 to 6 mW. The results are shown in Fig. 11. The signal amplitude varied by a factor of 8, suggesting that there is a significant component of two-photon emission to the signal. Nevertheless, over this range in signal amplitude, the measured rise and fall times remained unchanged, thus confirming our expectations discussed above.

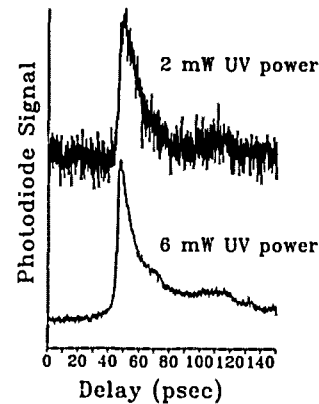


Figure 11. Photodiode response at different UV intensities.

Discussion

This analysis allows us to project that if the bias voltage between the strips could be increased to the 100 - 150 V level, the device fall time could be reduced to <5 psec. As mentioned above, we were limited to 60 V applied bias by avalanche breakdown in the silicon between the strips. Since the silicon is only needed in the sampling gap, it should be possible to fabricate a device capable of sustaining considerably higher bias voltage by eliminating the silicon between the strips.

As shown in Fig. 3, the measured 10-90% rise times were 4-6 psec, with a weak dependence on V_b . Since the distance between the photodiode and the sampler was only ~ 1 mm, we do not expect pulse dispersion on the stripline to contribute on this time scale. The photoconductive sampler was independently measured to have a 2 psec response time. We would therefore expect the limiting risetime of the measured waveform to be ~ 2 psec. Rise times longer than 2 psec would presumably be determined by flight time effects and scale as $1/\sqrt{V_b}$. However, from Fig. 4, the observed limiting risetime is ~ 4 psec. We speculate that the risetime is dependent on the flight paths of the electrons in the immediate vicinity of the cathode. Since this is precisely the region in which the field distribution is strongly influenced by space-charge screening, it then follows that there would be a weak dependence of the risetime on applied bias.

In conclusion, we have demonstrated a new ultrafast radiation detector by incorporating a microfabricated vacuum photodiode into a coplanar stripline geometry. The device shows a 4 psec rise time and a 12 psec fall time. Reduction of the fall time to < 5 psec appears to be straightforward, and further improvements may be possible by optimizing the geometry. We anticipate that this device will be particularly attractive as an ultrafast detector for vacuum ultraviolet and soft X-ray radiation where photocathode materials are available with high quantum efficiency.[1]

References

- [1] J. A. R. Samson, "Techniques of Vacuum Ultraviolet Spectroscopy," (Pied Publications, Lincoln, Nebraska, 1967).
- [2] J. Bokor, A. M. Johnson, W. M. Simpson, R. H. Storz, and P. R. Smith, *Appl. Phys. Lett.* 53, 2599 (1988).
- [3] A. M. Johnson, R. H. Stolen, and W. M. Simpson, *Appl. Phys. Lett.* 44, 729 (1984).
- [4] K. R. Spangenberg, "Vacuum Tubes," (McGraw-Hill, New York, 1948).
- [5] W. B. Herrmannsfeldt, Stanford Linear Accelerator Center report 226, (Stanford University, Stanford, 1978).

20-ps Resolution Single-Photon Solid-State Detector

M. Ghioni, A. Lacaita, S. Cova, and G. Ripamonti

*Politecnico di Milano, Dipartimento di Elettronica and Centro di Elettronica
Quantistica e Strumentazione Elettronica, CNR, Piazza L. da Vinci 32,
20133 Milano, Italy*

Abstract

Single Photon Avalanche Diodes (SPADs) are avalanche photodiodes specifically designed for reverse bias operation above the breakdown voltage (Geiger-mode operation), and used for detecting single optical photons. Studies were performed to relate the attainable timing resolution to the device geometry and operating conditions. A new silicon device structure was designed in order to obtain improved timing performance with respect to previous SPADs.

Extensive tests were carried out in order to ascertain the timing resolution of the device in time-correlated photon counting. The SPAD timing resolution, in terms of its full-width at half-maximum (FWHM) contribution to the overall instrumental response width, is 20 ps with the detector cooled to -65 C, and 28 ps at room temperature. This is the highest resolution so far reported for solid-state single-photon detectors.

Among vacuum tubes, comparable results are obtained only with special microchannel-plate photomultipliers (MCP-PMT). With the excellent timing resolution of the SPAD and the well-known advantages of Time Correlated Photon Counting systems (high sensitivity, linearity etc.), various applications are foreseen in areas so far dominated by streak cameras.

INTRODUCTION

Single Photon Timing techniques have proven to be of considerable interest in various fields. Remarkable performances have been reported in optical fiber characterization by Optical Time-Domain Reflectometry, in laser ranging, in fluorescence and luminescence decay measurements. One of the most interesting properties of the technique is the attainable time resolution,

nowadays in the tens of picosecond range. The main limit to the time resolution lies in the detector. In fact, since the advent of the synchronously pumped dye laser, the generation of light pulses of a few picosecond duration is standard. By proper circuit design, the electronic jitter in the measurement set-up can also be reduced to ≈ 10 ps.

On the detector side, time resolutions of the order of some tens of picoseconds were demonstrated with Photomultiplier Tubes (both discrete-dynode and Microchannel-Plate) [1-3] and also with avalanche photodiodes. Geiger-mode single-photon detectors have been demonstrated in silicon, germanium and III-V compounds [4-7].

In this paper we point out the design strategies aimed at minimizing the time jitter of a single-photon avalanche diode (SPAD). The attainable resolution turns out to depend on a number of specifications, often setting conflicting requirements. Other important parameters of the detector, such as the quantum efficiency and the noise (i.e. the dark-count rate) depend on the same quantities. Therefore trade-offs in the device design must be taken into account.

By exploiting these strategies, we were able to design detectors having better than 20 ps full-width at half maximum (FWHM) resolution.

SINGLE-PHOTON AVALANCHE DIODES

Single-Photon Avalanche Diodes (SPADs) are p-n junctions that operate at reverse bias above the breakdown voltage. In this bias condition, a single carrier can trigger a self-sustaining avalanche current. In case of a photogenerated carrier, the leading edge of the avalanche pulse marks the arrival time of the detected photon. The current will continue to flow until an external quenching circuit [8,9] lowers the bias close to or below the breakdown voltage. The

voltage is then kept low for a finite hold-off interval during which the SPAD cannot retrigger. At the end of this dead time the bias is rapidly restored in order to enable the detection of another photon under well-defined conditions.

The avalanche can also be triggered by thermally generated carriers in the depletion layer of the active junction, that cause the inherent dark-count rate of the device. The dark-count rate is further enhanced by the presence of deep levels in the depletion layer, since they give rise to correlated afterpulses [6]. In order to avoid an excessive dark-count rate, the concentration of deep levels and generation centers must be kept low. Carefully optimized processes with suitable gettering steps must therefore be employed in the fabrication of the SPAD detector.

The prototype SPAD structure has the simple geometry described by Haitz [10,11]. The active junction is formed by a shallow (in our case 0.3 μm) n^+ layer in a p bulk substrate of 0.6 $\text{Ohm}\cdot\text{cm}$. A deep diffused n^- guard ring surrounds the junction in order to prevent edge breakdown. The junction breakdown voltage was about 28 V. The response of the prototype SPAD devices is characterized by a fast peak and a slow tail. The peak is caused by the carriers photogenerated within the depletion layer of the active junction. We observed and reported FWHM values down to 60 ps [6]. The response tail is due to carriers photogenerated in the neutral region below the active junction, some of which reach the active junction considerably delayed, after diffusion. The physics of this diffusion tail is well understood. A Monte Carlo program was previously developed by two of us [12] for computing the time-dependence of this diffusion tail in arbitrary device geometries.

By using a new epitaxial device structure the diffusion tail has been effectively reduced, as is elsewhere reported [13]. The cross section of the new SPADs is outlined in Fig.1.

In order to increase the time resolution of the peak, we have studied both theoretically and experimentally the problem of the build-up of a self-sustaining avalanche. As a result, we achieved an improved resolution of 20 ps FWHM.

TIMING RESOLUTION LIMITS

There are deep differences between the operation of SPADs and that of ordinary APDs biased

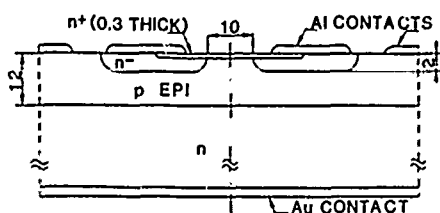


Figure 1. Cross section of the SPAD device.

below breakdown. The criteria derived for APDs from McIntyre's theory [14] cannot be extrapolated to the SPAD design. In fact, in order to achieve high bandwidth and low noise, APDs must have very different ionization coefficients for electrons and holes. For this reason, electric fields in the active region must be as low as possible. In the SPAD, on the contrary, the regenerative feedback due to the ionization of both electrons and holes is an essential feature. An increased electric field is desirable, since it reduces the fluctuations in the avalanche build-up and is therefore expected to improve the timing resolution.

In the following, we shall discuss the main physical points that determine the timing resolution of the SPAD.

Maximum electric field.

In order to evaluate quantitatively the dependence of the attainable timing resolution on the electric field, experiments were performed with samples having different doping i.e. breakdown voltages. Results are shown in Fig. 2 for batch 3, having breakdown voltage $BV = 28$ V, and for batch 9, having $BV = 13$ V. Relevant parameters for these SPADs are shown in Table 1.

Table 1. Active region parameters

| Batch # | Breakdown field (V/cm) | Multiplic. width (micron) | Depleted width (micron) |
|---------|------------------------|---------------------------|-------------------------|
| 3 | 4.6×10^5 | 0.5 | 1.0 |
| 9 | 5.5×10^5 | 0.35 | 0.9 |

The choice of the horizontal scale, that is, the excess electric field above the breakdown one, deserves some comment.

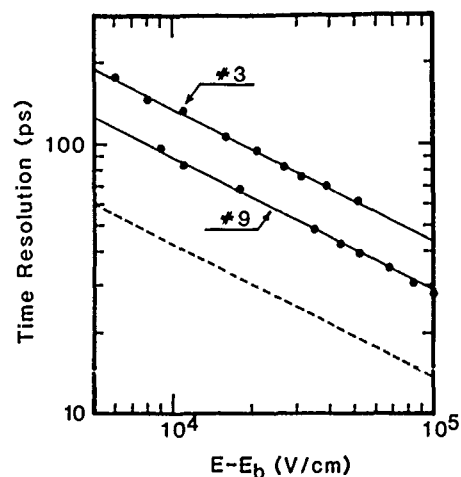


Figure 2. Dependence of the FWHM resolution on the electric field for two SPAD structures. The dashed line indicates a square root dependence.

At the breakdown voltage, the multiplying region can be considered as a positive feedback amplifier having unit loop gain. In this situation the average number of carriers in the multiplying region is constant in time. Since we were comparing samples having different BV, the normalization to the breakdown allows the performance comparison in similar multiplication regimes. The choice of the electric field depends on the consideration that the ionization rate is a strong (exponential) function of the electric field. For this reason, most of the ionizations happen in the highest electric field region. Since the samples have very similar geometries of the multiplying region (a shallow diffused junction), the maximum electric field well defines the multiplication process.

From Fig.2 we can deduce the formula:

$$\text{FWHM} = A (E - E_b)^{-k}$$

where E_b is the maximum electric field at the breakdown voltage; k is 0.5 in shallow diffused junctions; A is a parameter dependent on the device breakdown voltage, that will be discussed in the following [15].

It is evident from Fig.2 that a high excess field, and therefore a bias voltage well above the breakdown, strongly increases the timing resolution. One could also like to increase the voltage as much as possible in order to increase the quantum efficiency.

In a single photon detector, the quantum efficiency is defined as the probability that a photogenerated carrier will succeed in triggering a pulse, that is, a self-sustaining avalanche. Apart from geometrical factors (in particular the depletion region width), the quantum efficiency is known to increase with the electrical field, since the ionization probability increases strongly with the field. The problem was studied by Oldham et al. [16], who found the following relations:

$$dP_e/dx = (1 - P_e) \alpha_e [P_e + P_h - P_e P_h]$$

and:

$$dP_h/dx = - (1 - P_h) \alpha_h [P_e + P_h - P_e P_h]$$

Here the α s are the ionization coefficients, whereas P_e and P_h are the probabilities that an electron and an hole respectively will have an infinite number of descendants, i.e. will trigger an avalanche.

We have studied the avalanche trigger probability for our structures. We obtained the ionization coefficients by using Thornber's formula [17] with Grant's coefficients. The results for the average probability of a carrier generated in the depletion layer to trigger an avalanche are shown in Fig. 3. From Fig. 3 we note that a 80 % triggering probability is possible at the highest electric fields.

Two limits to the maximum field are met in the

SPAD design. The first one is the occurrence of breakdown in regions outside the active region. This can be due to localized breakdown in the edges of the diffusions, or to the breakdown of the guard rings. Edge breakdown, for example, happened in batch 3 at 34 V, thereby limiting the employable excess bias to 6 V. With a correct device design, in particular by using a shallow guard ring and a metal field plate, this limitation can be avoided. In batch 9, for example, the guard ring breakdown was 40 V, thus allowing 27 V excess bias.

However, a second more fundamental limitation to the excess bias is present. It is in fact well-known that at very high electric fields the generation rate is increased due to a number of physical effects, such as the Frenkel-Poole effect and the phonon-assisted tunnelling. Due to these effects, the dark count rate of the SPAD strongly increases with bias. Since the low-breakdown voltage diodes have an higher breakdown electric field, the dark count rate is much higher for these SPADs. In our case, the maximum applicable voltage was limited by guard ring breakdown in batch 3 and by too high a dark count rate in batch 9.

The maximum tolerable dark count rate depends on various considerations. First, a higher dark count rate implies a lower signal-to-noise ratio in single-photon measurements. Second, there is an increasing probability for an avalanche caused by a photon to happen when the diode is recovering from a previous dark avalanche pulse. The timing resolution is in this case impaired.

We have been able to make single-photon experiments with dark count rates up to 100 kpps, by using an active quenching circuit [9] which we developed in our laboratory. If simpler passive quenching circuits were used, the dark count rate must be lower than some kpps.

In order to reduce the dark count rate to a tolerable value, the depleted region volume must be small. For a given doping profile, this means a smaller sensitive area. We experimented with circular active areas of 10 μm diameter.

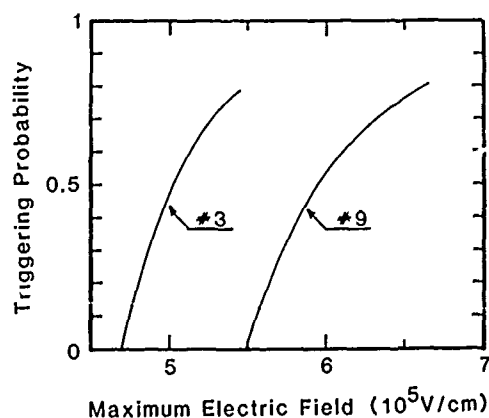


Figure 3. Calculated triggering probability vs. maximum electric field for two SPAD structures.

Note that this value is close to the dimension of a single channel in a microchannel-plate photomultiplier [3].

Multiplying region depth.

As shown in Fig. 2, the best timing resolution was achieved with the diodes having the lowest breakdown voltage, that is, the smallest depth of the multiplying region. The reasons why this happens can only be qualitatively understood at this point.

First, we note that the limit resolution must be of the order of the transit time in the avalanching region (this limit would be attained with a multiplication of such high value, that the number of free carriers rise to a detectable value within the transit time of the photogenerated primary carrier). This consideration suggests that the thinner the multiplication region, the better the timing resolution.

The multiplying region in the SPADs has a field that varies almost linearly with the position. The lower the breakdown voltage, the steeper the slope. In relatively high breakdown voltage devices, the multiplying region with lower field extends longer. If the fluctuations in the ionization process in this lower field region have importance to the overall avalanche build-up statistics, the resolution will be reduced. In order to check this hypothesis, we are developing a Monte Carlo simulation of the process.

In Fig. 4 a typical result of the simulation of the avalanche build-up is shown, as obtained with a first version of the program. The program implements the case of an avalanche region with an uniform field. One can thus simulate the different devices only by changing the multiplying region thickness. The timing resolution can be inferred from the spread of the delay from the photogeneration of the primary carrier to the crossing of a given avalanche current level. The primary carriers are generated at random positions within the depletion layer. Even in this

case, however, we noted a dependence of the timing resolution on the multiplying region thickness. We are now working on a second version of the program that will take into account the actual field profile.

Two main points are worth stressing. First, the absolute maximum resolution of the SPAD appears to be a few picoseconds. Second, it appears possible to improve the resolution beyond 20 ps FWHM by tailoring the field profile.

Active region uniformity.

As previously discussed, there is a trivial limit to the sensitive area, that lies in the dark count rate. In addition, too large a sensitive area could cause other effects that contribute to reduce the timing resolution.

The previously mentioned simulation of the avalanche build-up pointed out that a 10 % non uniformity of the electric field could cause a significant increase of the FWHM resolution. Experiments performed by us with SPADs having different dimensions of the active area confirmed the existence of nonuniformity effects.

Another very important problem, that probably sets a limit in the maximum sensitive area, is the time needed for the propagation of the avalanche pulse over the whole area. This was first found by McIntyre on RCA reach-through avalanche photodiodes [18], and confirmed by us [19]. Whether the horizontal propagation of the avalanche pulse is subbandgap photon assisted, phonon assisted or simply due to the diffusion of the avalanching carriers perpendicular to the electric field, is not yet clear at this point. We are performing experiments to understand this point.

In summary, the sensitive area must be kept small for a number of reasons. A 10 micron diameter was employed in our experiments, and we found no difference of timing resolution on these diodes as compared with devices with even smaller sensitive area that had a lower dark count rate.

Temperature effects.

Finally, the operating temperature was observed to influence the observable resolution. In particular, a better resolution was observed for lower temperatures. We carried out experiments in the temperature range -60 C to +20 C by using a controlled temperature chamber. We noted the well-known temperature dependence of the breakdown voltage, and therefore of the breakdown field, and a timing resolution improvement of ≈ 25 % between the two temperature extremes.

The reason why this change in the attainable resolution is observed lies probably in the greater efficiency of the ionization process at reduced temperature, as compared with other energy-exchanging processes, such as optical phonon emission.

A low temperature is also known to reduce the thermal carrier generation. However, the reduction in the dark-count rate with temperature does

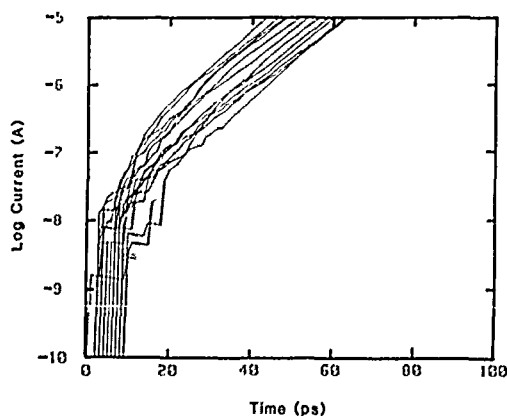


Figure 4. Simulation of the avalanche current build-up. Logarithm of the current vs. time.

not exactly follow the reduction in the generation rate. In fact, deep trap levels release with longer time constants at lower temperature. Therefore, levels filled by an avalanche pulse can release the stored charge at with longer delay time, possibly longer than the hold-off time of the active quenching circuit, thereby increasing the dark count rate [20]. Furthermore, tunnelling effects are not sensitive to temperature, except those assisted by phonons.

EXPERIMENTAL RESULTS

Based on the results of the preceding section, we designed and implemented SPADs having the lowest breakdown voltage compatible with the dark count rate requirement. The aforementioned batch 9 is the result of this design.

The FWHM resolution of the new SPAD is expected to be a few tens of picoseconds. On this time scale, other sources of time dispersion will make significant contributions to the measured overall instrumental FWHM resolution. In order to obtain the true detector resolution, all other contributions must be independently measured and then quadratically subtracted. Errors of the order of a few percent in these terms may well be significant. Possible alternative experimental set-ups were therefore carefully evaluated and results compared, in order to identify individual sources of additional timing jitter and quantify their contribution to the overall instrumental FWHM resolution.

In our standard waveform measurements with a single-photon timing set up employing a synchronously pumped dye laser, the total additional time dispersion was about 35 to 40 ps FWHM, mostly due to the synchronization jitter in the start channel. By using a gain-switched laser diode we estimated a somewhat higher dispersion, due to the width of the optical pulse.

In order to better exploit the ultrashort pulses of the synchronously pumped dye laser, the contribution due to the synchronism jitter was avoided by using two SPADs for the two branches of the single-photon timing set-up, and thus measuring the autocorrelation of the SPAD resolution. In this case we obtained an instrumental additional FWHM of 25 ps.

In the experiments a cavity dumper reduced the pulse repetition rate to 30 kHz. Neutral density filters were used to reduce the signal intensity to below the single photon level. The signal intensity was limited to produce a photon count rate 1.5 kcps (5% of 30 kHz) in order to prevent pulse pile-up effects. Since the dark-count rate of the SPADs exceeds 100 kcps at room temperature, the high dark count rate caused some complication. Dark pulses in the start branch activate the time to pulse height converter (TPHC), causing an increased data collection time. Therefore, in order to avoid most of the useless starts, the TPHC fast gate facility was exploited. Another split off portion of the laser pulse train was

directed to the fast p-i-n photodiode (HP 5082-4220) and constant-fraction discriminator (CFD) normally employed as start branch in the waveform measurements. The CFD output triggered a monostable circuit, that applied to the TPHC gate input a 100 ns square pulse, synchronized with the laser pulse. Start pulses were accepted only if they arrived within this 100 ns window.

Satisfactory histograms were collected in 10 min or less. A 46 ps FWHM autocorrelation curve was obtained, with a data collection time of 600 s. By quadratic deconvolution of the 25 ps contribution of the electronics, the FWHM resolution of the SPAD response at room temperature is therefore demonstrated to be 28 ps.

Extensive experiments were then carried out with fast laser diode pulsers. These results were compared with those obtained in the usual way, with an ultrafast p-i-n photodiodes connected to a sampling oscilloscope. We found results consistent with the SPAD resolution obtained. In fact, the obtained histograms had a lower FWHM value than the ones measured with the sampling oscilloscope.

In order to determine the width of the laser pulse, the 28 ps FWHM of the SPAD, the 16 ps FWHM contributed by the electronic circuitry and the 10 ps jitter of the electrical signal from the laser pulser had to be quadratically subtracted from the measured overall FWHM. A 27 ps laser pulse width is obtained for a 785 nm laser diode (Opto Electronics PPL30K). This is remarkably better than the 38 ps estimated by the manufacturer on the basis of the sampling oscilloscope measurement.

The performance of the SPAD cooled to -65°C was also investigated. In this experiment, the SPAD device was placed in a temperature controlled chamber, the active quenching circuit and the 785 nm laser diode were kept outside the chamber and coupled to the SPAD via coaxial cable and optical fiber respectively. The experimental result is shown in Fig. 5. As before, the SPAD FWHM resolution under these conditions is determined by quadratically subtracting the 27 ps FWHM of the laser pulse (see above), the 16 ps FWHM contributed by the electronic circuits and the 10 ps synchronization jitter of the laser pulser electrical trigger output from the measured 38 ps

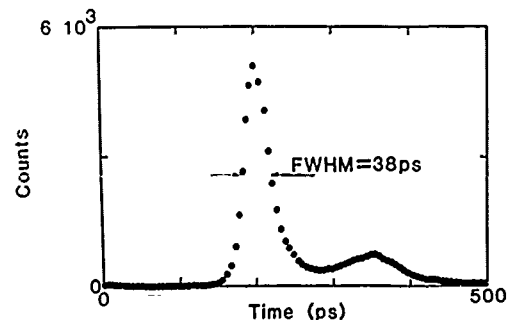


Figure 5. Optical pulse of a laser diode.

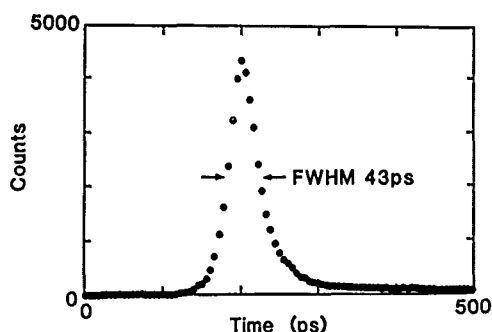


Figure 6. Optical pulse of a laser diode. Note the absence of secondary peaks.

overall FWHM. The FWHM resolution of the epitaxial SPAD at -65°C is thus found to improve down to 20 ps or less. To the best of our knowledge, this is the highest resolution ever reported for solid-state single-photon detectors.

From Fig.5, we note a small secondary peak in the histogram, occurring 150 ps after the principal one. While secondary peaks and ringings are normally present in the current pulse from fast p-i-n diodes, instrumental features of this type are not easily justified in the present type of measurement. The secondary pulse is therefore attributed to the laser and not to the detector. This is further demonstrated by the measurement reported in Fig.6, obtained with a different laser pulser (Hamamatsu CI308). No secondary peak is here noted, thus demonstrating that the secondary peak in Fig.5 is due to light (probably a second, relaxation oscillation in the laser, or Fresnel reflection at the optical fiber entrance).

CONCLUSIONS

We have demonstrated that solid-state single-photon detectors are capable of 20 ps FWHM timing resolution. This result places these detectors at the same resolution level of the fastest available MCP-PMT. Physical quantities that allow to obtain such resolution have been investigated. From these studies, it may be expected that the physical limit to the SPAD resolution is at the level of a few picoseconds.

ACKNOWLEDGMENTS

The authors wish to thank the research and development laboratory of SGS-Thomson Microelectronics, Castelletto-Milano, for the fabrication of the epitaxial devices. This work was supported in part by CNR under programs "PF-MADESS" and "PS Fotorivelazione" and by Ministero della Pubblica Istruzione.

REFERENCES AND NOTES

1. S. Canonica, J. Forrer, and U. P. Wild, "Improved timing resolution using small side-on photomultipliers in single photon counting," *Rev.Sci.Instrum.* **56**, 1754-1758 (1985).
2. D. Babelaar, "Time response of various types of photomultipliers and its wavelength dependence in time-correlated single-photon counting with an ultimate resolution of 47 ps FWHM," *Rev.Sci.Instrum.* **57**, 1116-1125 (1986).
3. H. Kume, K. Koyama, K. Nakatsugawa, S. Suzuki, and D. Fatlowitz, "Ultrafast microchannel plate photomultipliers," *Appl.Opt.* **27**, 1170-1178 (1988).
4. B. F. Levine, and C. G. Bethea, "Single photon detection at 1.3 μm using a gated avalanche photodiode," *Appl.Phys.Lett.* **44**, 553-555 (1984).
5. C. G. Bethea, B. F. Levine, L. Marchut, V. D. Mattered, and L. J. Peticolas, "Photon-counting optical time-domain reflectometer using a planar InGaAsP avalanche detector," *Electron.Lett.* **22**, 302-303 (1986).
6. S. Cova, G. Ripamonti, and A. Lacaita, "Avalanche semiconductor detector for single optical photons with a time resolution of 60 ps," *Nucl.Instr. and Meth.* **A253**, 482-487 (1987).
7. S. Cova, A. Longoni, A. Andreoni, and R. Cubeddu, "A semiconductor detector for measuring ultra-weak fluorescence decays with 70 ps FWHM Resolution," *IEEE J.Quantum El.* **QE-19**, 630-634 (1983).
8. S. Cova, A. Longoni, and G. Ripamonti, "Active quenching and gating circuits for single-photon avalanche diodes" *IEEE Trans. Nucl. Sci.* **NS-29**, 599-601 (1982).
9. Italian patent 22367A/88 pending.
10. R. H. Haitz, "Model for the electrical behavior of a microplasma," *J.Appl.Phys.* **35**, 1370-1376 (1964).
11. R. H. Haitz, "Mechanisms contributing to the noise pulse rate of avalanche diodes," *J.Appl.Phys.* **36**, 3123-3131 (1965).
12. G. Ripamonti, and S. Cova, "Carrier diffusion effects in the time-response of a fast photodiode," *Sol.State Electronics* **2**, 925-931 (1985).
13. A. Lacaita, M. Ghioni, and S. Cova, "Ultrafast single-photon detector with double epitaxial structure for minimum carrier diffusion effects," *Journal de Physique* **49-C4**, 633-636 (1988).
14. R. J. McIntyre, "Multiplication noise in uniform avalanche diodes," *IEEE Trans. on Elect.Dev.* **ED-13**, 164-168 (1966).
15. We also made experiments with commercially available APDs (RCA C30921S) which have completely different structure (reach through avalanche photodiodes), and much higher breakdown voltage, $\approx 200\text{ V}$. We found a similar dependence on the electric field, but much worse resolution, 460 ps FWHM at room temperature. See Ref. [19].
16. W. O. Oldham, R. R. Samuelson, and P. Antognetti, "Triggering phenomena in avalanche

- diodes," *IEEE Trans. on Elect. Dev.* ED-19, 1056-1060 (1972)
17. K. K. Thornber, "Application of scaling to problems in high-field electronic transport," *J. Appl. Phys.* 52, 279-290 (1981).
 18. R. J. McIntyre, RCA, private communication.
 19. A. Lacaita, S. Cova, and M. Ghioni, "Four-hundred-picosecond single-photon timing with commercially available avalanche photodiodes," *Rev. Sci. Instrum.* 59, 1115-1121 (1988).
 20. S. Cova, G. Ripamonti, A. Lacaita, and G. Soncini, "Probe-device detecting single carriers: A new method for deep level characterization with nanosecond resolution," in Technical Digest, IEEE International Electron Device Meeting (IEEE Publishing Service, New York, 1985), pp. 310-313.

Photoconductive and Photovoltaic Picosecond Pulse Generation Using Synthetic Diamond Film

S. T. Feng, J. Goldhar, and Chi H. Lee

*Department of Electrical Engineering, University of Maryland,
College Park, Maryland 20742*

Abstract

Photovoltaic and photoconductive electrical pulse generation was investigated in a composite switching device using thin diamond film. Fast response under high fields was observed with picosecond laser pulses.

Introduction

Recent developments in the field of plasma epitaxial synthetic diamond film growth made it possible to produce high quality thin diamond films on silicon substrates. The diamond films which were used in this work were grown by the Crystallume Corporation. The diamond films are polycrystalline as it can be seen from the electron microscope photograph on figure 1. According to recent study of electrical characteristics of similar films doped with boron, a rectifying junction can be formed between the diamond film and a metal electrode [1]. In our

case the diamond films were not doped and non ohmic contact is formed also between the diamond and the silicon. This junction plays important role in photoresponse of the structure. High intrinsic resistance of the films allowed us to work with relatively high bias voltages on the order of 100 volts, which corresponds to fields of one megavolt per centimeter.

Picosecond photoconductivity effect has been observed when uv light is used, while picosecond photovoltaic effect has been observed when visible or $1.06\mu\text{m}$ laser illuminated the device. Clean picosecond electric waveforms are generated by utilizing, for the first time, the picosecond photovoltaic effect.

Device characterization

Typical structure used in our experiments is shown on figure 2. Semi-transparent thin aluminum electrode (approximately 100 \AA thick) was deposited

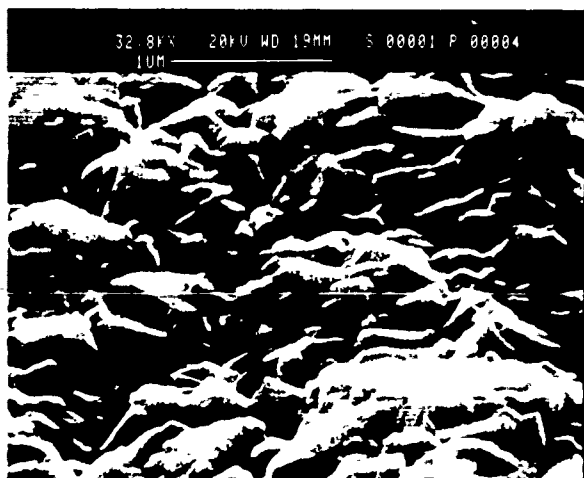


Fig.1 Electron micrograph shows polycrystalline structure of diamond film.

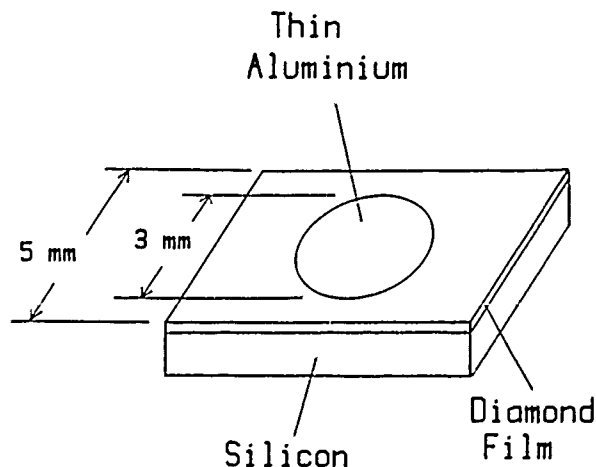


Fig.2 Schematic of diamond film device used in the experiments.

over the diamond film. The substrate, which was heavily doped p-type silicon acted as the other electrode. Figure 3 shows typical dark voltage - current characteristics of such device. Also shown on the same figure is the response of this device to illumination by picosecond pulses at 1.06 microns. Note the generation of photocurrent even when no bias is applied. Here the measurement was performed using Tektronix 7834 oscilloscope on nanosecond time scale. The radiation was produced by a mode locked cw glass laser with a regenerative amplifier operating at 400 Hz with energy output of 10 microjoules in 10 picosecond long pulses [2].

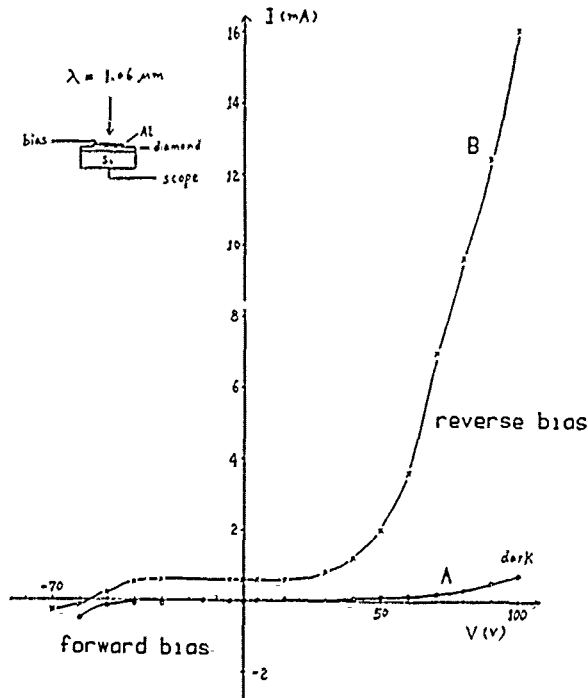


Fig.3 A) Dark, B) illuminated (by 1.06 μm laser) I-V characteristics of the device.

The outstanding feature in this curve is independence of photogenerated current from the bias voltage over sizeable voltage range. In order to better understand this device we measured its photo-response on nanosecond time scale in the visible using dye laser and in uv with KrF laser at 248 nm. Figure 4 shows the response curve observed with 590 nm radiation. Very similar response was observed with blue light at 490 nm. However, when the wavelength was changed to 248 nm a very different response curve was observed as one can see from figure 5.

In order to explain the photo-response we have to consider the band structure of silicon diamond interface. Figure 6a shows qualitatively the bandgap

structure at the heterojunction between diamond and silicon, and between diamond and aluminum

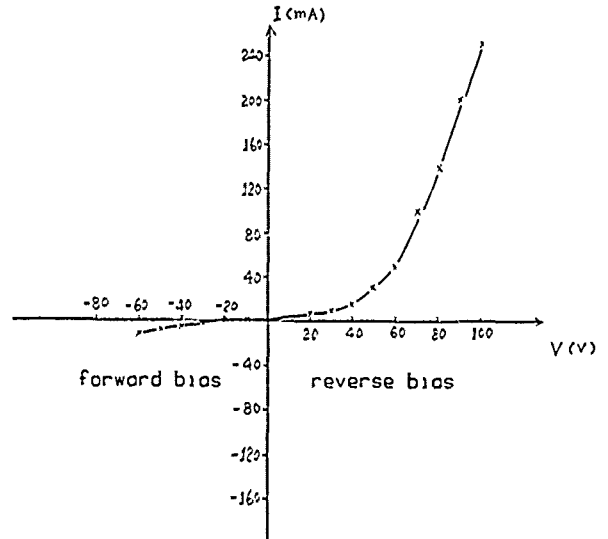


Fig.4 I-V characteristics with 0.59 μm laser illumination shows similar response as with infrared.

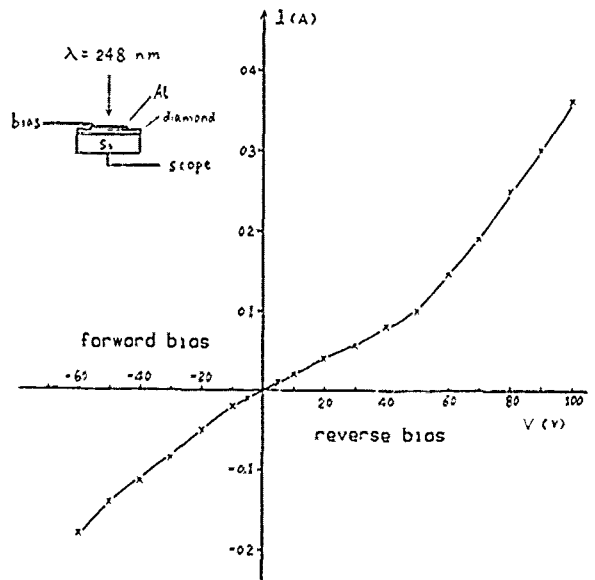


Fig.5 Response observed with UV (248 nm) illumination.

in absence of bias voltage. Diamond film has a large energy band gap of 5.5 eV and an electron affinity around 0 eV [3], whereas silicon possesses the band gap of only 1.1 eV and the electron affinity of 4 eV [4]. The effect of bias field is shown on figures 6b

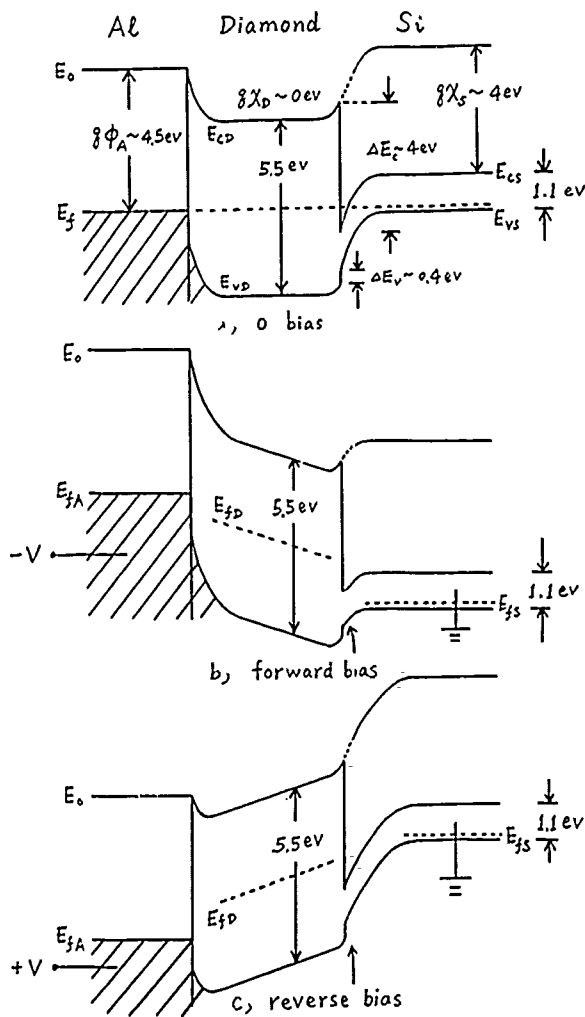


Fig.6 Bandgap diagram of the Aluminum-Diamond-Silicon Device

and 6c. The forward bias corresponding to positive voltage on the silicon side reduces the height of the barrier and the width of the depletion region, and the reverse process occurs for the opposite polarity. At the aluminum - diamond junction we expect to see a diode in the opposite direction to the diode in silicon-diamond interface. Due to high intrinsic resistivity of diamond we expect that most of the bias voltage will actually drop across the diamond film and only a fraction of it will be across either junction.

As it can be seen from the figure 6, the only place that carriers can be generated by the light in the visible or near infrared is at the junction between the silicon and the diamond. This is consistent with

the observation that only when that junction is reverse biased we have strong photo-response.

Picosecond Pulse Shaping

One problem associated with picosecond pulse forming using photoconductive switch is the degradation of bandwidth of the pulse forming network (PFN) by the external biasing circuit. The pulse forming circuits which use photovoltaic effect should be capable of generating particularly clean electrical pulses because there is no need to connect leads for providing bias, as it will be demonstrated below. This effect should be observable with other material junctions, and it could be useful in integrating testing circuits which can be activated by a laser with fast electronic devices.

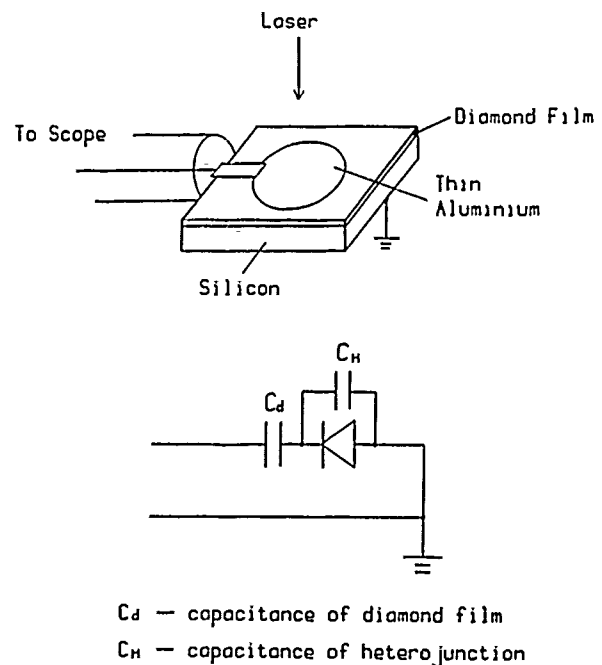


Fig.7 Configuration for generation of step function signal - grounded silicon substrate.

Several pulse forming circuits were tested with the diamond film switch. The Hypres superconducting sampling oscilloscope was used to monitor the electrical pulses. One simple configuration is shown on figure 7. The transparent aluminum electrode on the switch was connected directly through SMA connector to the scope. The silicon side was grounded, thus there was no applied voltage. The photovoltaic signal which was observed is shown in figure 8. It is a good approximation to step function, with the rise time of less than 50 ps, which is due to inductance of the connector.

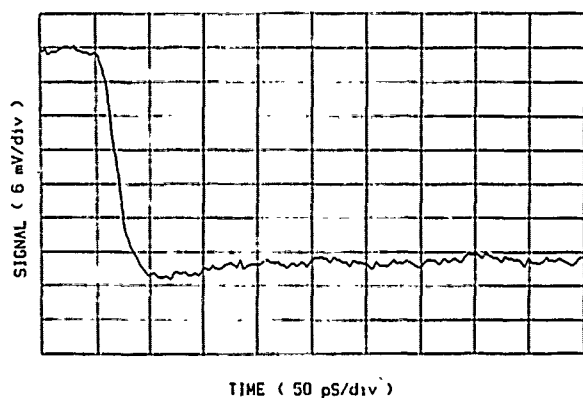


Fig.8 Wave form observed from the device shown on figure 7.

The duration of the voltage pulse is on the order of tens of nanoseconds as it can be observed with a regular oscilloscope. Most likely reason for termination of the pulse is charging up of the capacitance associated with the insulating diamond film which is on the order of 1 nF. For pulses on picosecond time scale this capacitance acts as a short circuit.

If we want to shorten the pulse duration we can insert an external capacitance which is much smaller than that of diamond film. Such circuit shown in figure 9 generates pulses of 60 ps duration as can be seen in figure 10. Note that if instead of a simple

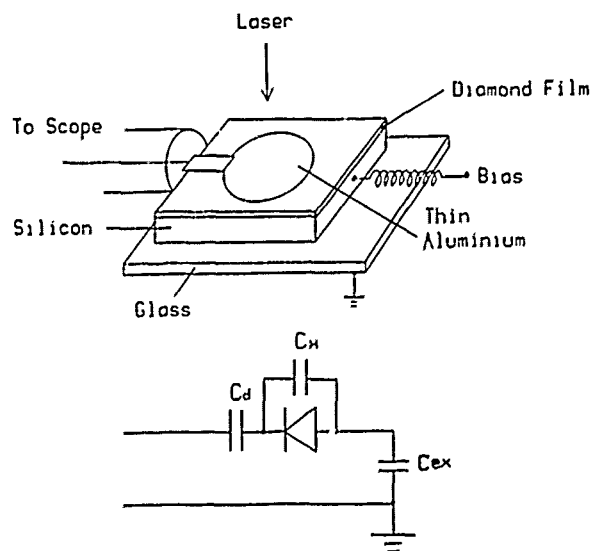


Fig.9 Configuration for short pulse generation-substrate coupled to the ground by a small capacitor (C_{ex}).

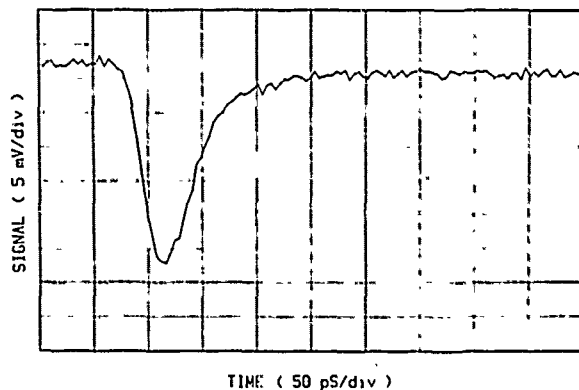


Fig.10 Wave form observed from the device shown on figure 9 - no bias.

capacitor we had used a small transmission line we would have obtained a clean flat top pulse. When a 8 ns coaxial cable was added to the circuit a clean 16 ns flat top pulse was observed as shown in figure 11. Application of bias to the charged line had little effect on the output electrical pulse shape.

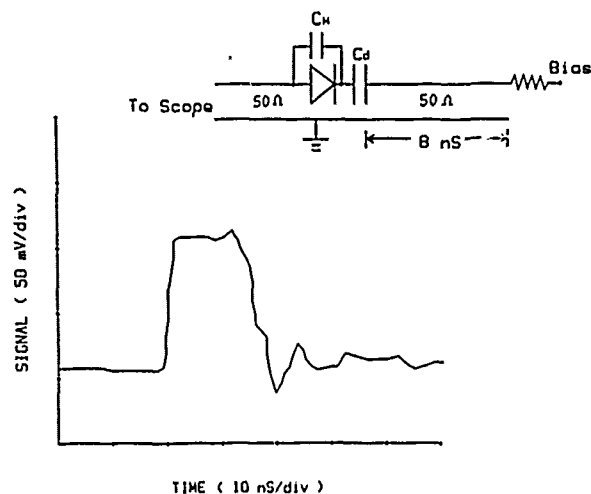


Fig.11 Nanosecond square pulse generated with external transmission line

Conclusion

We demonstrated that thin diamond film on silicon devices generate primarily photovoltaic response when illuminated with near infrared or visible light, and photoconductive response with ultraviolet. Electrical pulses, tens of picoseconds in duration were generated using simple macroscopic circuits. Using microfabrication techniques one should be able to manufacture much shorter duration pulses.

Acknowledgment

We would like to thank Dr. P.-T. Ho for very useful discussions, Hypres Inc. for the loan of their superconducting sampling oscilloscope used in this experiment and Crystallume Corporation for providing the diamond films.

References

1. G. Sh. Gildenblat, S. A. Grot, C. R. Wronski, A. R. Badzian, T. Badzian, and R. Messier, "Electrical characteristics of Schottky diodes fabricated using plasma assisted chemical vapor deposited diamond films," *Appl. Phys. Lett.* **53** (7), 586-588 (1988).
2. L. Yan, J. D. Ling, P.-T. Ho, C. H. Lee, and G. L. Burdge, "An actively mode-locked continuous wave Nd: phosphate glass laser oscillator and regenerative amplifier," *IEEE J. Quantum Electron.* **24** (2), 418-426 (1988). Also, L. Yan, P.-T. Ho, C. H. Lee, and G. L. Burdge, "Generation of high-power, high repetition rate, sub-picosecond pulses by intracavity chirped pulse regenerative amplification," *appl. Phys. Lett.* **54** (8), 690-692 (1989).
3. J. Barnolc and A. Antonelli, "The mechanism of atomic motion in diamond," *SDIO/IST - ONR Diamond Technology Initiative Symposium*, W23 (1988).
4. S. M. Sze, *Physics of Semiconductor Devices* (Wiley & Sons, New York, 1981).

Beryllium-Bombarded $\text{In}_{0.53}\text{Ga}_{0.47}\text{As}$ and InP Photoconductors with High Responsivity and Picosecond Resolution

R. Loepfe, A. Schaelin, and H. Melchior

Institute of Quantum Electronics, Swiss Federal Institute of Technology, Zurich, Switzerland

Abstract

Small size $\text{In}_{0.53}\text{Ga}_{0.47}\text{As}$ and Fe:InP photoconductors with optimized Be^{3+} -ion implantation reach response speeds of 2ps to 4ps, while maintaining responsivities of 0.006A/W and 0.02 A/W. The high speed of these devices is due to the Be-bombardement related introduction of recombination centers. The responsivity is inverse proportional to the speed of response and proportional to the mobility. This mobility appears to be dominated by bombardement related neutral impurity scattering.

The technique of ion bombardement of semiconductor photoconductors has led to detectors with large bandwidths and response times in the picosecond and even subpicosecond range [1,2]. Although these devices show very high speed of response, their sensitivity is severely limited by implantation damage. Of major interest is the improvement of the responsivity while maintaining the response speed.

Two different kinds of photoconductors were investigated: epitaxial $\text{In}_{0.53}\text{Ga}_{0.47}\text{As}$ -layers for the infrared range up to $1.6\mu\text{m}$ and semi-insulating Fe:InP bulk material for the visible to $0.9\mu\text{m}$ range. Thin light absorbing layers of 1 to $2\mu\text{m}$ in thickness on semi-insulating substrates were processed into 4×4 , 8×8 and $16 \times 16\mu\text{m}^2$ mesa structures with $\text{Ni}/\text{Ge}/\text{Au}$ ohmic contacts for $\text{In}_{0.53}\text{Ga}_{0.47}\text{As}$ photoconductors and Au contacts for Fe:InP photoconductors. For extraction of the photoresponse over broad electri-

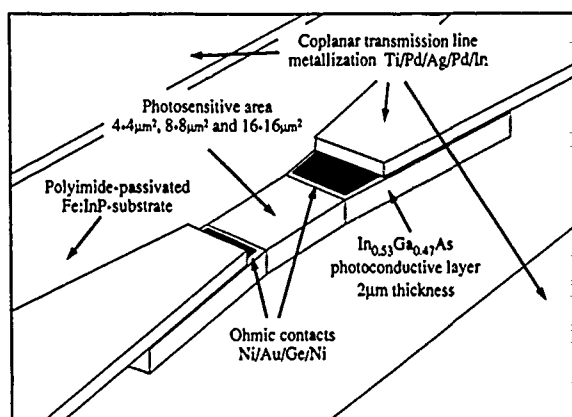


Figure 1: Schematic representation of a high-speed $\text{In}_{0.53}\text{Ga}_{0.47}\text{As}$ -photoconductor on a Fe:InP substrate.

cal bandwidths, these devices were integrated into tapered coplanar 50Ω microwave transmission lines and flip-chip mounted on a sapphire substrate. Response speeds of the as built devices are typically in the low nanosecond range for $\text{In}_{0.53}\text{Ga}_{0.47}\text{As}$ and in the range of 100ps for Fe:InP .

To improve the response speed from the nanosecond range down to the low picosecond range the devices were bombarded with Beryllium ions [2]. Implantation was performed with a tandem accelerator at ion-energies in the MeV range. To reach a broad defect profile over the entire thickness of the active photoconductive layers, ion-energies of 13.9 MeV and 14.6 MeV were chosen and the ions slowed down with a tungsten foil to energies below 800 keV. Doses are scaled between 10^{11}cm^{-2} and 10^{15}cm^{-2} .

For a Be^{3+} dose of 10^{14}cm^{-2} TRIM [3] calculations predict a Be-density of $4 \times 10^{17}\text{cm}^{-3}$ throughout the $2\mu\text{m}$ thick photoconductive layers.

For an evaluation of the speed of response of these devices, we used Carruthers' optical pulse mixing technique [4]. A sequence of two partially overlap-

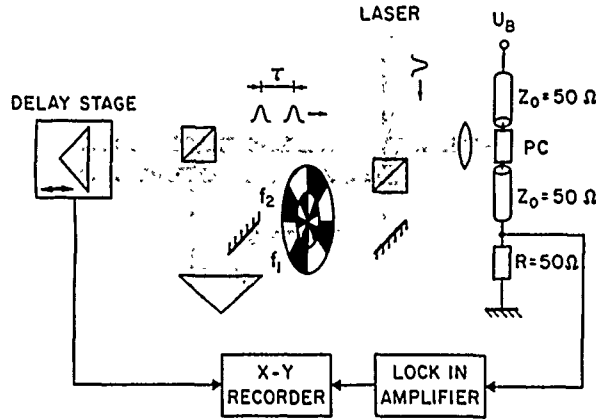


Figure 2: Scheme of the autocorrelation measurement setup. (PC) photoconductor.

ping high-speed laser pulses is directed onto the detector. Relying on the slight nonlinearities inherent in high-speed photoconductors the nonlinear mixing part in the response is then registered in the form of an autocorrelation function. The nonlinearities in our photoconductors are related to bimolecular-type band to band recombination [5]. Considering the carrier dynamics:

$$\frac{\delta p}{\delta t} = g(t) - B \cdot (p^2 + N_D \cdot p) - \frac{p}{\tau_i} \quad (1)$$

$$\frac{1}{\tau} = B \cdot N_D + \frac{1}{\tau_i} \quad (2)$$

the linear photoresponse takes the form:

$$p_{lin}(t) = e^{-\frac{t}{\tau}} \int_0^t g(t') \cdot e^{\frac{t'}{\tau}} \cdot \delta t' \quad (3)$$

with p the photoexcited carrier density, $g(t)$ the optical excitation, N_D the donor concentration, B the bimolecular recombination coefficient, τ_i the impurity recombination lifetime and τ the effective carrier lifetime. For overlapping excitation pulses with delay time Δt the autocorrelation-technique leads to the nonlinearity related pulse charge ΔQ :

$$\Delta Q(\Delta t) = 2BAe\mu \frac{V}{L} \tau \int_{-\infty}^{\infty} p_{lin}(t) \cdot p_{lin}(t + \Delta t) \cdot \delta t \quad (4)$$

with A the contact width \times absorption length, L the gap length, V the bias voltage and μ the electron

mobility. From a measurement of this nonlinearity induced response at different pulse delay, the inherent speed of the response of the photodetectors can be determined.

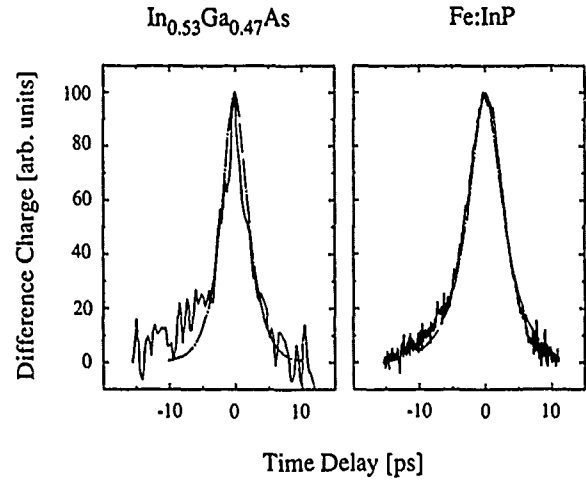


Figure 3: Autocorrelation traces for 10^{14}cm^{-2} Be^{3+} -bombarded $\text{In}_{0.53}\text{Ga}_{0.47}\text{As}$ and Fe:InP photoconductors. Assuming single-sided exponentials the deconvolution leads to photoresponse decay time constants of 1.7ps and 2.8ps respectively.

For the autocorrelation measurement we used a dye laser that emits mode-locked pulses with a repetition rate of 76MHz and pulse energies of 10pJ at a wavelength of 583nm. These pulses take the form of single-sided exponentials with decay time constants of the order 1 ps. This was determined from the second-harmonic autocorrelation, measured by means of a nonlinear electro-optic crystal. Responsivities were measured at 830nm using a semiconductor laser with pulses of 20 ps duration and energies of 30fJ.

The best results for the optimum implantation dose of 10^{14}cm^{-2} show response speeds as low as 2ps and responsivities of 0.02 A/W for $\text{In}_{0.53}\text{Ga}_{0.47}\text{As}$ photoconductors, and 3ps and 0.006 A/W for Fe:InP -photoconductors. In both cases the bias fields were 6.25kV/cm (see Figs. 3, 4 and 5).

Investigations of the relations between implantation dose, response speed and responsivity as well as mobility and dark conductance give an indication of the major scattering and recombination mechanisms in these devices. The shortening of the response speed with Be-bombardement is due to an increase in the density of recombination centers. This can be concluded from a comparison of the photoresponse of unimplanted and implanted photoconductors. While unimplanted detectors show a response that is proportional to the square root of the optical

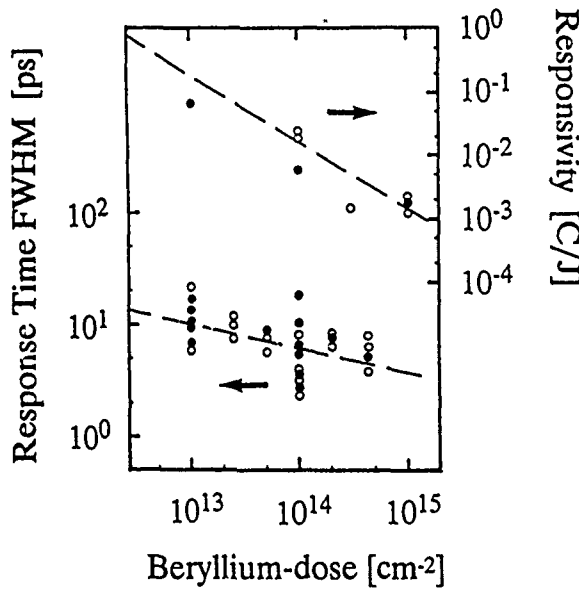


Figure 4: Responsivity and speed of response of Be^{3+} -bombarded photoconductors vs. implantation dose.

energy, the bombarded devices show a response that increases almost proportional with the optical pulse energy. This is in accordance with a change from bimolecular-type band to band recombination to an impurity center related recombination. (see Fig. 5).

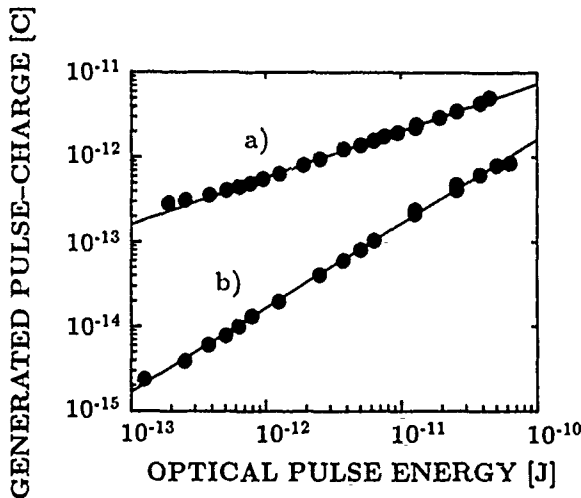


Figure 5: Photogenerated pulse charge vs. optical pulse energy. Comparison between (a) an unimplanted and (b) an implanted device. Their gap lengths are 4 and $8\mu\text{m}$ respectively. The bias field was 6.25kV/cm . The optical excitation at 583nm showed pulse durations of the order 1ps .

The decrease in responsivity with Be-bombardement (see Fig. 4) can be explained by combining both the diminution of the carrier lifetime τ and the carrier mobility μ . Neutral impurity scattering appears to be the dominant additional scattering mechanism that is related to Be-bombardement. We

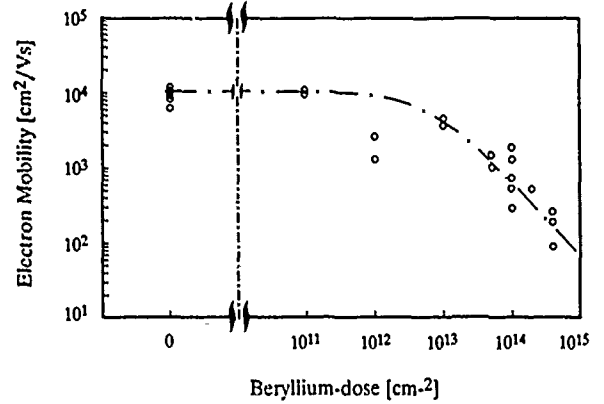


Figure 6: Hall-mobility vs. Be^{3+} -implantation dose in $\text{In}_{0.53}\text{Ga}_{0.47}\text{As}$.

find a best fit of the experimental mobility data for $\text{In}_{0.53}\text{Ga}_{0.47}\text{As}$ (see Fig.6) with Erginsoy's scattering equation [6] and Matthiessen's rule:

$$\mu_N = \frac{8 \cdot \pi^3 \cdot m^* \cdot e^3}{20 \cdot h^3 \cdot \epsilon \cdot N_N} \quad (5)$$

$$\frac{1}{\mu_{eff}} = \frac{1}{\mu_{PO}} + \frac{1}{\mu_A} + \frac{1}{\mu_N} \quad (6)$$

μ_{PO} is the polar optical phonon scattering, μ_A the alloy scattering, μ_N the neutral impurity scattering, N_N the neutral impurity density, ϵ the dielectric constant, m^* the effective electron mass, e the unit charge and h Planck's constant. In these equations the density of the scattering centers N_N , which gives a best fit, is found to be about 2 times higher than the Be-ion density. But this density is also considered to be 250 times lower than the lattice defect density calculated from the implantation profile by the TRIM program.

The C-V profiles obtained from samples which were etched in steps reveal the distribution of the trap density profiles of the photoconductive layers (see Fig. 7). These profiles indicate, that the density of traps is much larger than the doping density of these layers.

In conclusion, we have prepared miniaturized Be^{3+} -bombarded photoconductive $\text{In}_{0.53}\text{Ga}_{0.47}\text{As}$ and Fe:InP detectors with speeds of response in the 2ps to 4ps range and responsivities of 0.006A/W and 0.02A/W respectively. The shortening of the speed of response is due to an increase in the density of re-

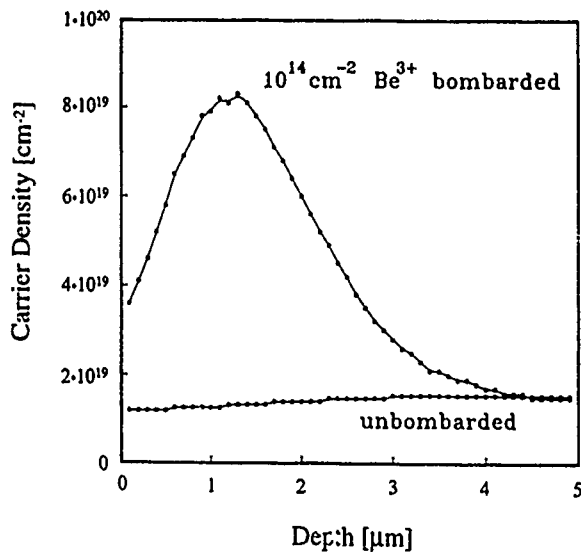


Figure 7: C-V plot of Be^{3+} -bombarded InP. It reveals the distribution of the trap density due to Be-implantation.

combination centers. The diminution of the responsivity of the bombarded photoconductors is related to the combined diminution of the carrier lifetime and the carrier mobility. This mobility appears to be due to the incorporation of neutral impurity scattering centers. Using this model the density of the scattering centers results 2 times higher than the implanted Be-ion density but 250 times lower than the calculated lattice defect density.

This work was supported by the Swiss National Foundation for Research. We wish to thank W.

Woelfli and M. Suter for Be^{3+} -implantations, H. Jaeckel and G. Bona (IBM Research Laboratory, Rueschlikon, Switzerland) for the use of their high-speed laser setup, and M. Blaser for LPE-growth of the $\text{In}_{0.53}\text{Ga}_{0.47}\text{As}$ -layers.

References

1. D. Grischkowsky, C.C. Chi, I.N. Duling III, W.J. Gallagher, N.H. Halas, J.M. Halbout and M.B. Kitchen, "Photoconductive Generation of Subpicosecond Electrical Pulses and Their Measurement Applications", in *Picosecond Electronics and Optoelectronics II*, F.J. Leonberger, C.H. Lee, F. Capasso and H. Morkoc, eds. (Springer, Berlin, 1987).
2. P.M. Downey, J.E. Bowers, C.A. Burrus, F. Mitschke and L.F. Mollenauer, "High-speed, hybrid InGaAs p-i-n/photoconductor circuit", *Appl. Phys. Lett.* **49**, 430 (1986).
3. J.F. Ziegler, J.P. Biersack and U. Littmark, "The stopping and range of ions in solids", Vol. 1, (Pergamon Press, New York, 1985).
4. T.F. Carruthers and J.F. Weller, "Picosecond optical mixing in fast photodetectors", *Appl. Phys. Lett.* **48**, 460-462 (1986).
5. R. Loepfe, A. Schaelin, H. Melchior, M. Blaser, H. Jaeckel and G.L. Bona, "2ps InGaAs photoconductors and their speed-of-response evaluation by optical pulse mixing at inherent nonlinearities", *Appl. Phys. Lett.* **52**, 2130 (1988).
6. C. Erginsoy, "Neutral Impurity Scattering in Semiconductors", *Phys. Rev.* **79**, 1013-1014 (1950)

Photocurrent-Voltage Characteristics of Ultrafast Photoconductive Switches

S. Moss, J. Knudsen, R. Bowman, P. Adams, and D. Smith

*The Aerospace Corporation, PO Box 92957, MS/M2-253,
Los Angeles, California 90009-2957*

M. Herman

*Charles Evans & Associates, 301 Chesapeake Drive,
Redwood City, California 94063*

ABSTRACT

We report measurements of photocurrent-voltage characteristics of ultrafast photoconductive switches fabricated on gallium arsenide, silicon with a buried oxide layer, and silicon-on-sapphire.

INTRODUCTION

Current-voltage characteristics of metal-semiconductor contacts are, in general, nonlinear unless special fabrication procedures are used to form ohmic contacts. Formation of ohmic contacts to semiconductors can be facilitated by fabricating them on a heavily damaged semiconductor surface[1]. Ion-implantation induced damage has been used to reduce surface barrier heights and modify the current-voltage characteristics of metal-semiconductor contacts[2]. It has been suggested that ultrafast photoconductive switches with metallic contacts to semiconductor material amorphized by ion-implantation should exhibit ohmic behavior[3].

We have measured the photocurrent-voltage characteristics (PIV), the dependence of photocurrent upon incident optical intensity, and the dark current-voltage characteristics of ultrafast photoconductive switches (UPS) fabricated on GaAs, Si with a buried oxide layer (SIMOX), and SOS. These switches were fabricated by forming microstrip transmission line structures in a standard optoelectronic autocorrelation configuration with the gaps exposing the photoconductive semiconductor material [4]. These measurements were performed for each material with various ion-implantation dosages to assess the effects of ion-implantation induced damage in the semiconductor material on the linearity of response as well as on the optoelectronic temporal response. We also varied the order of the implantation and the metalization

fabrication steps. Thus, samples implanted before metalization had contacts applied to semiconductor material damaged by the implant. Samples implanted after metalization had contacts applied to fairly crystalline material. The metalization was thick enough that implantation at these energies with these species could not penetrate the metalization. The linearity of response was dependent on the extent of the ion-implantation induced damage and, in this respect, was fairly consistent with reports in the literature [3]. However, the linearity of response was also dependent upon the order of the ion-implantation and metalization processing steps and was inconsistent with recent literature reports [3]. Our measurements show that the dark IV characteristics and the PIV characteristics for UPS with pre-metal implants are nonlinear even for semiconductor material amorphized by the implant. Furthermore, our measurements show that the dark IV characteristics and the PIV characteristics for UPS post-metal implants are linear.

EXPERIMENTAL APPARATUS

The laser system used for these measurements consisted of a Rhodamine 6G dye laser synchronously pumped by an actively modelocked, frequency doubled Nd:YAG laser. The dye laser pulsewidth was 6 ps, the average power was 400 mW, and the repetition rate was 100 MHz. The optical response measurements were obtained by focussing the train of dye laser pulses (mechanically chopped at 326 Hz with a 50 % duty cycle) onto the photoconductive switch to a spot size of approximately 20 μ m (FWHM of intensity). For the PIV measurements, a triangle wave varying linearly from -15 to +15 volts was applied to one sidearm of each of our samples and the photocurrent produced on the central microstrip was taken to a lock-in amplifier referenced to the

chopping frequency. Similarly, the optical intensity dependence of the photocurrent was measured with the sidearm biased while the signal was taken from the central microstrip line to the lock-in amplifier. The incident intensity was varied by rotating a half-wave retardation plate placed in front of a prism polarizer in the dye laser beam path. A small portion of the beam after the polarizer was taken from a beamsplitter to an optical power meter that was calibrated relative to the optical power incident on the switch. The dark current-voltage characteristics were measured by applying the -15 V to +15 V triangle wave to the sidearm of a switch and measuring the current on the central microstrip with a Keithley 405 picoammeter. All signals were stored and processed on a microcomputer system. In the discussion below, samples implanted before metalization are labeled with a "B" and a sample number after the material identifier, e.g., GAB1. Samples implanted after metalization are labeled similarly, but with an "A" after the material identifier, e.g., GAA1.

GALLIUM ARSENIDE SWITCHES

The GaAs wafers were 450 μm thick (100) undoped micro-electronic grade. The Al metalization was 0.5 μm thick, 175 μm wide. The UPS gaps were 20 μm wide. Damage was induced by a quadruple energy implant of 20/50/100/200 keV $^4\text{He}^+$ resulting in total dosages of 7×10^{12} , 7×10^{13} , 7×10^{14} , or 7×10^{15} ions/ cm^2 as shown in

TABLE 1. Implant conditions for GaAs samples.

| SAMPLE/ MATERIAL | ION/ENERGIES/DOSE |
|---------------------|-------------------------------------|
| GAA1/GaAs | $^4\text{He}^+$ /20,50,100,200/7E12 |
| GAA2/GaAs | $^4\text{He}^+$ /20,50,100,200/7E13 |
| GAA3/GaAs | $^4\text{He}^+$ /20,50,100,200/7E14 |
| GAA4/GaAs | $^4\text{He}^+$ /20,50,100,200/7E15 |
| GAB1/GaAs | $^4\text{He}^+$ /20,50,100,200/7E12 |
| GAB2/GaAs | $^4\text{He}^+$ /20,50,100,200/7E13 |
| GAB3/GaAs | $^4\text{He}^+$ /20,50,100,200/7E14 |
| GAB4/GaAs | $^4\text{He}^+$ /20,50,100,200/7E15 |

Table 1. The 200 keV implant was half the dose of each of the other three implants. The results in Figs. 1(a) and 1(b) are for wafers which were implanted before metalization, while those in 1(c) are for wafers which were implanted after metalization. As seen in Fig. 1(a) the low dose pre-metal implants all have qualitatively and quantitatively similar PIV characteristics. We show results for an unimplanted wafer and the 7E13 total dose (sample GAB2). The PIV characteristics for sample GAB1 (7E12 total dose, curve not shown) are qualitatively and quantitatively similar. The photocurrent rises sharply near zero applied bias and becomes sublinear at higher applied bias. The results are

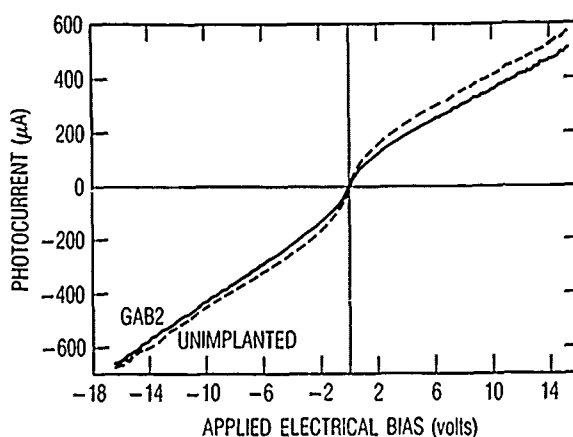


Figure 1(a). GaAs PIV characteristics, pre-metal implants.

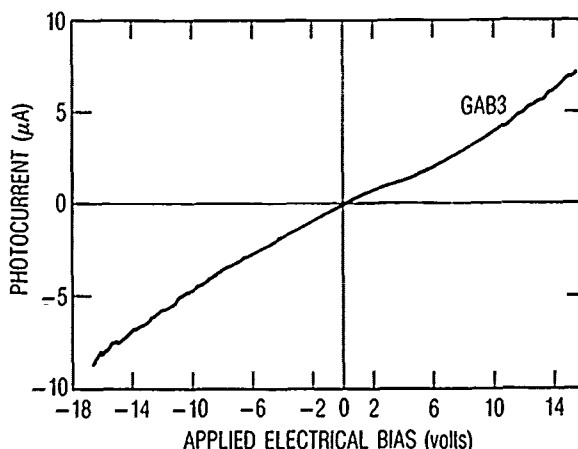


Figure 1(b). GaAs PIV characteristics, pre-metal implant.

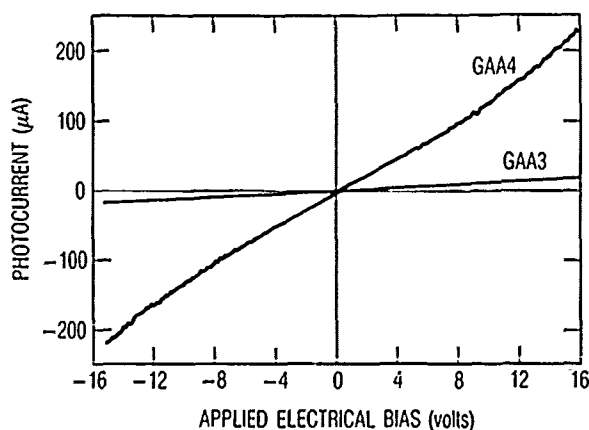


Figure 1(c). GaAs PIV characteristics, post-metal implants.

symmetric about zero applied bias. For the higher dose pre-metal implant (7E14 total dose; sample GAB3), the PIV characteristic shown in Fig. 1(b) is more linear and symmetric about zero applied bias. Switches implanted before metalization display current saturation at higher biases, similar to that reported recently for other GaAs photoconductive devices [5]. For the post-metal implants, samples GAA3 and GAA4, in Fig. 1(c), the PIV characteristics are fairly linear over the entire range of applied bias similar to those obtained previously for UPS fabricated on GaAs in a coplanar waveguide configuration with post-metal implants [6]. The post-metal implants with the lower total dose (GAA1 and GAA2) have a more nonlinear response similar to the low dose pre-metal implants.

Dark IV characteristics for samples implanted before metalization are shown in Fig. 2. The nonlinear nature of the response of these UPS is more pronounced than the PIV. While not shown here the dark IV characteristics of the post-metal implant samples are similar to their PIV characteristics. (NOTE: The results are mislabeled with an "A" instead of a "B".)

The samples' dependence of photocurrent upon incident optical intensity for samples implanted before metalization are shown in Fig. 3(a) while the results for samples implanted after metalization are shown in Fig. 3(b). Samples implanted before metalization have a sublinear response while samples implanted after metalization have a slightly superlinear response. All samples were biased at -15V.

The temporal response of these switches ranged from 200 ps for an unimplanted sample to 15 ps for the 7E15 total dose implants GAB4 and GAA4. The electrical pulsewidth would probably be shorter for samples with thinner substrates and heavier implant dosages.

SIMOX SWITCHES

The SIMOX wafers were 350 μm thick (100) microelectronic grade with a superficial 2200 \AA thick epilayer of Si which covered a buried 3500 \AA thick layer of SiO_2 . The Au metalization was 2.0 μm thick and 175 μm wide on top of a 200 \AA thick barrier layer of Ti/W. As for the GaAs UPS, the gaps were 20 μm wide. Damage was induced by a triple energy implant of 25/75/125 keV $^{28}\text{Si}^+$ at dosages of 1×10^{14} or 3×10^{14} ions/ cm^2 at each energy for a total dose of 3×10^{14} or 9×10^{14} ions/ cm^2 as shown in Table 2. The results in Fig. 4(a) are for wafers which were implanted before metalization, while those in Fig. 4(b) are for wafers which were implanted after metalization. While neither result is linear over the range of applied bias, we again see that the UPS implanted after metalization exhibit a more linear response. The signals from these samples were too weak to measure an optoelectronic autocorrelation width.

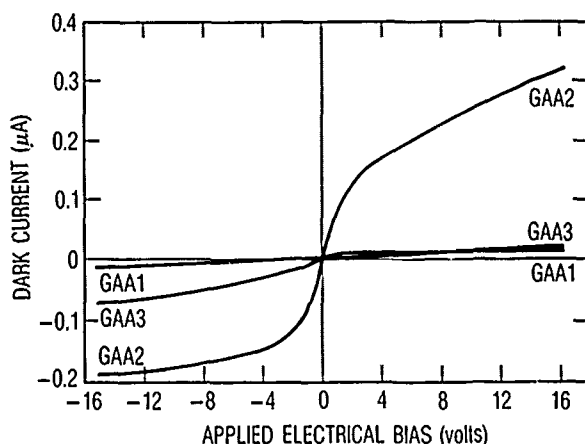


Figure 2. GaAs dark IV characteristics, pre-metal implant.

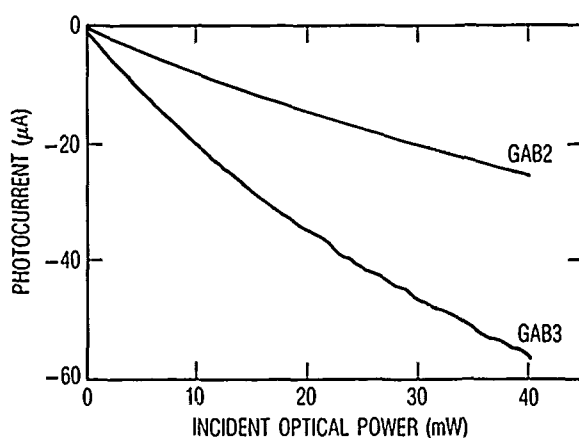


Figure 3(a) Photocurrent vs. incident optical power; GaAs pre-metal implants.

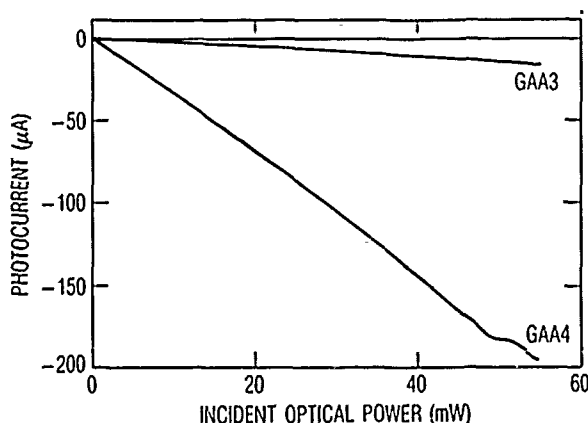


Figure 3(b) Photocurrent vs. incident optical power; GaAs post-metal implants.

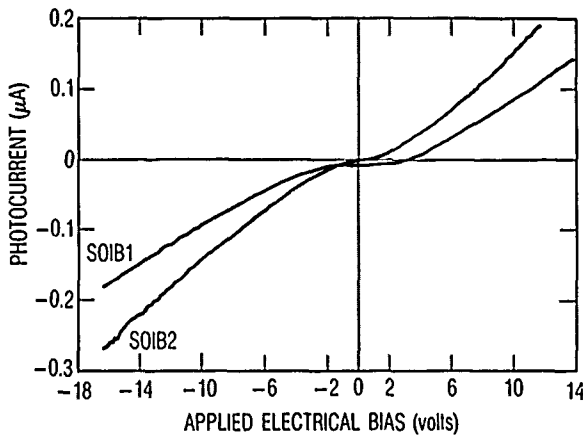


Figure 4(a). SIMOX PIV characteristics, pre-metal implants.

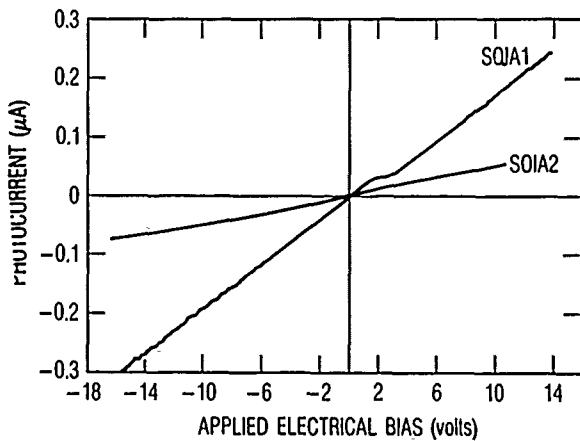


Figure 4(b). SIMOX PIV characteristics, post-metal implants.

Dark IV characteristics for samples implanted before metalization are shown in Fig. 5(a) while the results for samples implanted after metalization are shown in Fig. 5(b). The dark IV characteristics are not symmetric about zero bias and are very different from their PIV characteristics. The response is probably dominated by capacitive effects due to the buried oxide layer and trapping states at the interface of the buried oxide with the Si epilayer. Illumination may eliminate the effects of the trapping states on the PIV characteristics either by filling the trapping states or by screening them.

The samples' dependence of photocurrent upon incident optical intensity (applied bias -15V) is shown in Fig. 6. Results for samples implanted before metalization are shown in Fig. 6(a) while results for samples implanted after metalization are shown in Fig. 6(b). Over this range of incident optical intensity samples implanted after metalization exhibit a more linear photoresponse than samples implanted before metalization.

TABLE 2. Implant conditions for SIMOX samples.

| SAMPLE/ MATERIAL | ION/ENERGIES/DOSE |
|---------------------|------------------------------------|
| SOIA1/SIMOX | $^{28}\text{Si}^+$ /25,75,125/3E14 |
| SOIA2/SIMOX | $^{28}\text{Si}^+$ /25,75,125/9E14 |
| SOIB1/SIMOX | $^{28}\text{Si}^+$ /25,75,125/3E14 |
| SOIB2/SIMOX | $^{28}\text{Si}^+$ /25,75,125/9E14 |

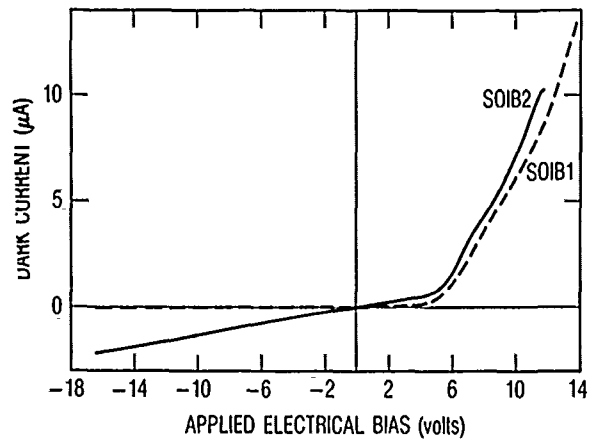


Figure 5(a). SIMOX dark IV characteristics, pre-metal implant.

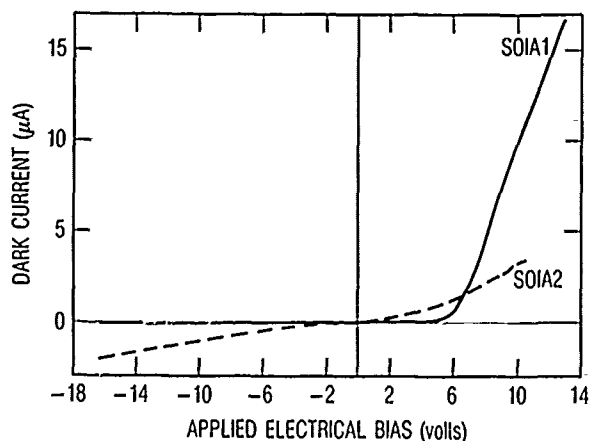


Figure 5(b). SIMOX dark IV characteristics, post-metal implant.

SOS SWITCHES

The SOS wafers were 175 μm thick (1102) sapphire with a 0.5 μm thick (100) Si epilayer. The metalization and UPS gap dimensions were identical to those used for the SIMOX wafers. Damage was induced by a triple energy implant of 100/200/400 keV $^{28}\text{Si}^+$ at dosages of 1×10^{14}

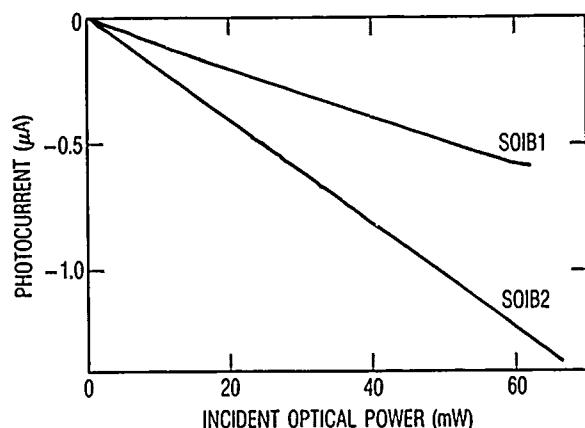


Figure 6(a) Photocurrent vs. incident optical power; SIMOX pre-metal implants.

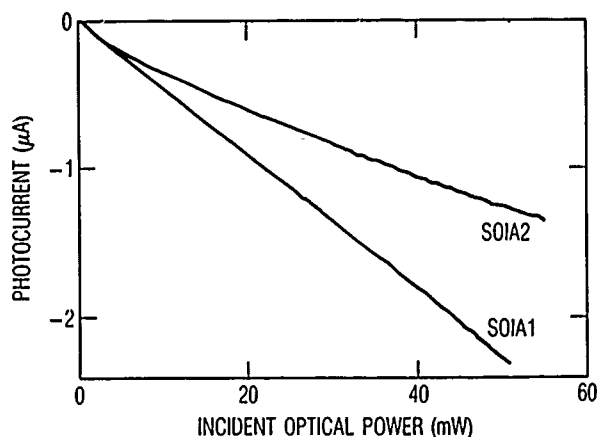


Figure 6(b) Photocurrent vs. incident optical power; SIMOX post-metal implants.

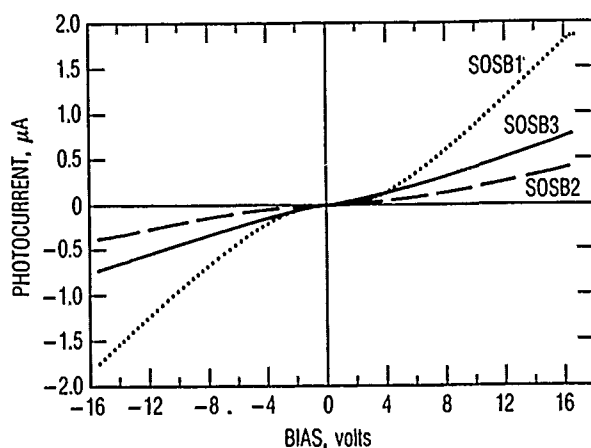


Figure 7(a). SOS PIV characteristics, pre-metal implants.

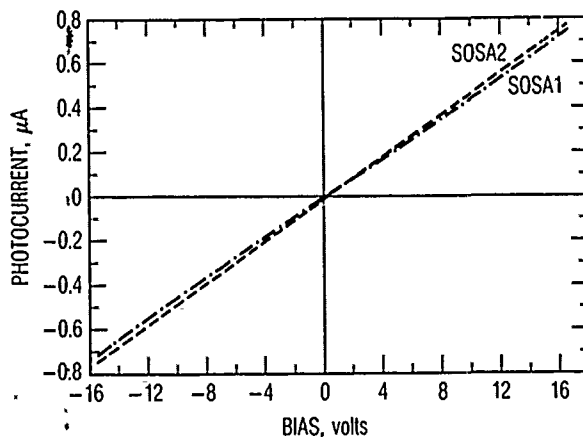


Figure 7(b). SOS PIV characteristics, post-metal implants.

(wafers SOSB2 and SOSA1) or 1×10^{15} (wafers SOSB3 and SOSA2) ions/cm² at each energy as shown in Table 3. Wafer SOSB1 was implanted with a single energy implant of 375 keV at 1×10^{15} $^{28}\text{Si}^+$ ions/cm². The results in Fig. 7(a) are for wafers implanted before metalization, while those in Fig. 7(b) are for wafers implanted after metalization. Wafers implanted before metalization have more linear PIV characteristics at higher levels of ion-implantation induced damage. Conversely, the response of UPS ion-implanted after metalization are quite linear over the entire range of applied bias.

Dark IV characteristics for samples implanted before metalization are shown in Fig. 8(a) while results for samples implanted after metalization are shown in Fig. 8(b). The dark IV characteristics are very similar to the PIV characteristics. Samples implanted before metalization have nonlinear dark IV characteristics while samples implanted after metalization have linear dark IV

characteristics. The nonlinear dark IV characteristics of pre-metal implants are less pronounced than their PIV characteristics but have qualitatively similar features.

TABLE 3. Implant conditions for SOS samples.

| SAMPLE/ MATERIAL | ION/ENERGIES/DOSE |
|---------------------|--------------------------------------|
| SOSA1/SOS | $^{28}\text{Si}^+$ /100,200,400/3E14 |
| SOSA2/SOS | $^{28}\text{Si}^+$ /100,200,400/3E15 |
| SOSB1/SOS | $^{28}\text{Si}^+$ /375/1E15 |
| SOSB2/SOS | $^{28}\text{Si}^+$ /100,200,400/3E14 |
| SOSB3/SOS | $^{28}\text{Si}^+$ /100,200,400/3E15 |

The samples' dependence of photocurrent upon incident optical intensity (applied bias +15V) for samples implanted before metalization are shown in Fig. 9(a) while results for samples implanted after metalization are shown in Fig.

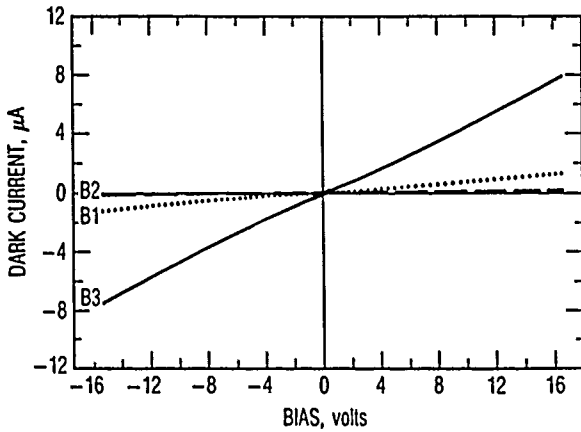


Figure 8(a). SOS dark IV characteristics, pre-metal implant.

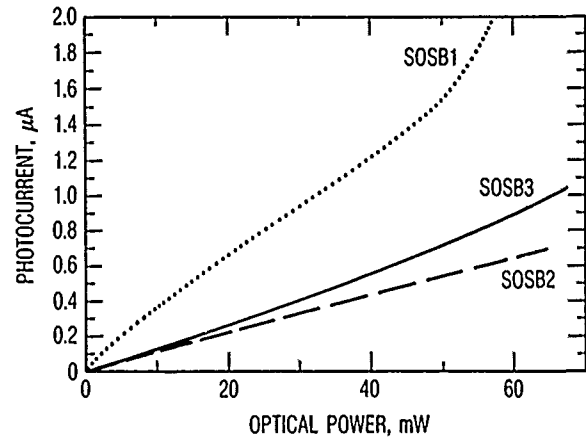


Figure 9(a) Photocurrent vs. incident optical power; SOS pre-metal implants.

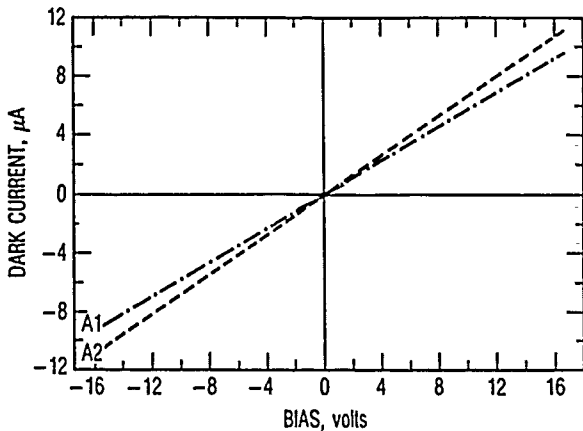


Figure 8(b). SOS dark IV characteristics, post-metal implant.

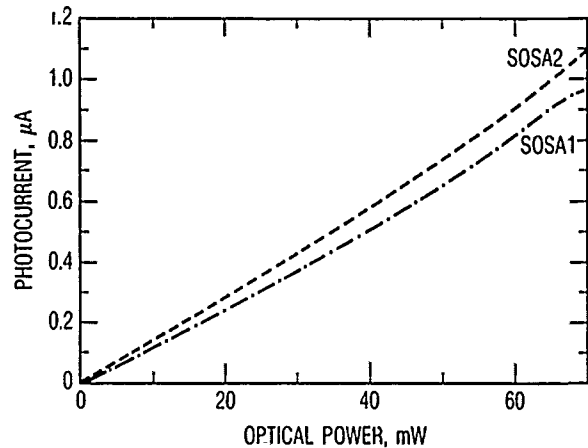


Figure 9(b) Photocurrent vs. incident optical power; SOS post-metal implants.

9(b). The photoresponse of samples implanted before metalization is sublinear at low optical intensities and becomes superlinear at higher intensities. The photoresponse of samples implanted after metalization is linear at low optical intensities but becomes superlinear at higher intensities.

The temporal response of these switches ranged from approximately 200 ps for an unimplanted sample down to approximately 5 ps for the 3E15 total dose implants. The electrical pulsewidth would probably be shorter for samples with thinner substrates, but heavier implant dosages would probably have little effect.

MATERIALS DIAGNOSTICS

Because the response of these UPS is so sensitive to the nature of the metal-semiconductor interface, we have applied a variety of techniques to characterize the structure of the implanted

semiconductor material forming these photoconductive switches. These include Rutherford Backscattering Spectrometry (RBS), Raman spectra, Electron-Beam modulated Electro-Reflectance (EBER), PhotoReflectance (PR), and double-crystal x-ray rocking curves (DCD)[8].

The ion-implanted GaAs was characterized by Raman spectra, EBER, PR, and DCD. The EBER and PR spectra show that modification of the surface region occurs for implant dosages as low as the 7E13 ions/cm² total dose. The EBER and PR spectra for the higher dose samples are featureless indicating that the surface features responsible for the signal are modified to eliminate the signal. This could be taken as an indication of total destruction of electronic order near the surface. However, the Raman spectra indicate that the near surface material is not totally structurally disordered even for the 7E15 ion/cm² total dose. Finally, the DCD results

indicate a buried region of amorphous material near the surface for the $7\text{E}14$ ion/cm² total dose with a significantly strained region further into the sample and, for the $7\text{E}15$ ion/cm² total dose implant, a larger amorphous layer with an even larger strained layer beneath it.

The ion-implanted SIMOX was characterized by RBS. The RBS results show that substantial disorder is produced in the surface Si epilayer by the $3\text{E}14$ ion/cm² total implant dose and that virtually total amorphization of the surface silicon layer occurs for the $3\text{E}14$ ion/cm² implant dose. It also shows that the as-received SIMOX wafers have substantial disorder near the interface of the Si epilayer and the buried oxide layer.

The ion-implanted SOS was characterized by RBS, Raman spectra, and EBER. The RBS, EBER and Raman spectra all show that strong disruption of the surface region occurs for implant dosages as low as the $3\text{E}14$ ion/cm² total dose. The EBER and Raman spectra for the $3\text{E}15$ ion/cm² total dose sample are featureless indicating that the band-bending and Fermi-level pinning, responsible for the signal are modified to eliminate the signal. This indicates near-total destruction of the electronic order near the surface by these implants.

DISCUSSION

We have previously discussed some of the physical mechanisms which affect PIV characteristics of UPS [7]. Carrier transport mechanisms are more likely to produce a nonlinear response in the post-metal implants than the pre-metal implants. Because our measurements are inconsistent with these explanations, we have considered other explanations related to the degree of crystallinity or amorphicity of the semiconductor.

When coupled with the conventional point of view, i.e., that contacts to amorphous semiconductors should yield ohmic response, probing the structural disorder in the pre-metal implants yields results that are at least partially consistent with the observed dark IV and photoresponse results for the pre-metal implants because the response of these UPS become more linear with higher levels of implantation-induced damage. The materials characterization measurements do not, however, offer justification for the linearity of response of the samples which are implanted after metalization. The metallic contacts for these samples are to fairly crystalline material. The response of these switches should be dominated by the barrier at the metal-semiconductor interface so that the response should be nonlinear. However, in the case of the SOS and the SIMOX samples, there are indications in the RBS measurements that the as-received wafers are fairly disordered. The SOS wafers have large densities of dislocations due to microtwins formed at the Si-sapphire interface which have propagated to the surface of the Si.

The SIMOX has pinholes which expose the buried SiO₂ layer as well as a fairly rough surface. Consequently, diffusion of the barrier metals into the semiconductor could occur even though the processing temperatures were kept below 150 °C. Diffusion of these barrier metals into the bulk is known to facilitate formation of ohmic contacts [1]. However, the as-received GaAs wafers have less disorder at the surface than the SIMOX or SOS. Consequently, it is improbable that this mechanism is responsible for the linear response observed for the post-metal implants. Because the contacts are coplanar the response of the switches may be more strongly affected by the very near-surface response than the bulk response. The near surface response of these UPS is probably dominated by perimeter conduction [9]. Consequently, differing contributions of bulk and perimeter conduction may explain the differences in the response characteristics of the pre- and post-metal implants. Further measurements are necessary to understand the observed response.

ACKNOWLEDGMENTS

The authors acknowledge support of the United States Air Force Space Division under contract number F04701-85-C-0086, the technical assistance of S. D. LaLumondiere, and the encouragement of J. A. Gelbwachs and R. Newman.

REFERENCES

1. E.H. Rhoderick and R.H. Williams, Metal-Semiconductor Contacts (Oxford University Press, Oxford, 1988).
2. S. Ashok, K. Giewont, and H. P. Vyas, *Phys. Stat. Sol. (a)* **98**, K99(1986).
3. D. H. Auston, Picosecond Opto-electronic Devices, Ed. C.-H. Lee (Academic Press, New York, 1984).
4. D. H. Auston, A. M. Johnson, P. R. Smith, and J. C. Bean, *Appl. Phys. Lett.* **37**, 371(1980).
5. D. L. Rogers in Picosecond Electronics and Optoelectronics II, Eds. F. J. Leonberger, C.-H. Lee, and H. Morkoc (Springer-Verlag, New York, 1987).
6. H. Schumacher, U. Salz, and H. Beneking, in Picosecond Electronics and Optoelectronics II, Eds. F. J. Leonberger, C.-H. Lee, and H. Morkoc (Springer-Verlag, New York, 1987).
7. S. C. Moss, J. F. Knudsen, R. C. Bowman, and D. D. Smith, *J. Mod. Optics*, Dec. 1988, in press.
8. R. C. Bowman, P. M. Adams, J. F. Knudsen, P. A. Dafesh, D. D. Smith, and S. C. Moss, Proc. MRS Symposium on Ion Beam Processing of Advanced Electronic Materials, to be published (1989).
9. P. D. DeMoulin, S. P. Tobin, M. S. Lundstrom, M. S. Carpenter, and M. R. Melloch, *IEEE Electron Dev. Letts.* **9**, 368(1988).

Use of Tandem Photoconductive Switches for Measuring Picosecond Turn-On Delay of Laser Diodes

P. Blixt

Department of Physics II, Royal Institute of Technology, S-100 44 Stockholm, Sweden

E. Adomaitis and A. Krotkus

Semiconductor Physics Institute of the Lithuanian Academy of Sciences, 232600 Vilnius, Lithuania, USSR

ABSTRACT

A tandem photoconductive switch, producing up to 75 V pulses with 15 ps rise and fall times, were used to characterize a laser diode.

INTRODUCTION

In high bit-rate optical communication systems employing gain-switched laser diodes, the turn-on delay time is a crucial parameter. There have been numerous investigations regarding high-frequency characteristics of laser diodes, and all but a few exceptions rely on small-signal measurements. In pulse-code modulation systems, it is the large-signal behaviour that is important. When high bit-rates [1] approach the bandwidth of the electrical large-signal system, it is hard to discern the intrinsic limitations of the laser diode from the electrical limitations. In order to investigate the turn-on delay of modern laser diodes properly one would need a completely new type of electrical pulse generator that could supply current pulses with rise time that is much shorter than the delay to be measured and with an amplitude that is at least ten times the lasing-threshold current. Conventional pulse generators have been used, based on avalanche transistors and step recovery diodes. Hence, previous investigators, [2,3,4] have had to resort to pulse generators with rise times in the range of 100 to 200 ps. A systematic investigation of large signal switching transients has been performed where some simplified expressions of turn-on and turn-off delays were derived [5]. Here, the rise-time of the current pulse was approximately 90 ps, so turn-on delays shorter than 100 ps were not measured. Further investigations have been made with an experimental set-up incorporating a single-gap photoconductor for measuring the relative turn-on delay dependence on bias level [6], and for measuring chirp on a picosecond time scale [7]. Here the peak current was 70 mA and the rise time around 30 ps.

Turn-on delay measurements have also been employed for estimating the carrier lifetime at threshold, τ [8]. To determine the differential carrier lifetime at threshold, τ' ,

it is sufficient to use moderate injection currents and determine the turn-on delay with nanosecond resolution. Dixon and Joyce have argued theoretically that with high injection currents and an accuracy of tens of picoseconds in the turn-on delay measurements, the radiative lifetime τ_r , and the nonradiative carrier lifetime τ_n , could be deduced as well [9]. However, they erroneously assumed that the spontaneous-recombination coefficient, $B(n)$, is constant. Later it has been shown that a linear approximation, $B(n) = B_0 - B_1 n$, makes a good fit to experimental data, for both GaAs and InGaAsP lasers [10]. Consequently, τ_r and τ_n can still be calculated by the method proposed by Dixon and Joyce [9], provided some justified approximations are made and a fitting parameter, $B_1 n / B_0$, is applied.

The main difficulty in using photoconductive switches to produce short turn-on delays has been the trade-off between the electrical pulse width and amplitude. In order to curtail the fall-time of the switch one must reduce the carrier lifetime, but then the mobility and, consequently, the current will decrease as well [11]. One way to avoid this trade-off is to use a single-gap photoconductor and two different laser wavelengths: a short wavelength to turn the switch on and a long wavelength to shorten the signal to ground [12]. This gives a very limited choice of switch substrate and lasers. Other methods have used passive pulse shaping configurations [13,14,15], but then the pulse width is not variable. In this article we describe a novel technique for measuring turn-on delay utilizing a tandem photoconductive switch made of high-resistivity silicon. Previously, tandem photoconductors made of iron-doped semi-insulating indium phosphide crystals have been investigated in two experiments. An indium phosphide tandem photoconductor has been used as a variable picosecond pulse generator with electrical pulse durations ranging from 40 to 400 ps [16]. Another application of the tandem structure photoconductive switch is as a differential photodetector for accurate laser beam and interference fringe position measurements on a subnanosecond time scale [17].

We will describe an experiment where photoconductive switches were employed to measure turn-on delay of an InGaAsP laser diode down to 60 ps. This novel technique gives turn-on delay times with an uncertainty of 15 ps. Then the carrier lifetimes τ and τ' are evaluated from appropriate plots of the turn-on delays obtained at various injection current levels, and it is shown that τ can be extracted with unprecedented accuracy. Finally, τ_r and τ_n are calculated with the use of a fitting parameter, and the results are compared with those previously obtained by small-signal methods [18,19].

THEORY

The carrier lifetimes τ and τ' can be estimated from plots of the delay time T versus I/I_t and $\ln\{I/(I - I_t)\}$, respectively, where I is the injection current and I_t the threshold current. This possibility is due to the fact that, at the two injection-current extremes, the following two relations apply [9]:

$$T \approx \tau \frac{I_t}{I} \quad \text{when } I \rightarrow \infty \quad (1)$$

and

$$T \approx \tau' \ln\left(\frac{I}{I - I_t}\right) \quad \text{when } I \rightarrow I_t. \quad (2)$$

The different carrier lifetimes are defined by the following relations:

$$\frac{dn}{dt} = \frac{I}{eV} - R(n) = \frac{I}{eV} - \frac{n}{\tau} \quad (3)$$

$$\frac{1}{\tau'} = \frac{\partial R}{\partial n} \quad (4)$$

and

$$\frac{1}{\tau} = \frac{1}{\tau_r} + \frac{1}{\tau_n} \quad (5)$$

where $R(n)$ is the total recombination rate which includes radiative and nonradiative recombination as well as carrier leakage. V is the active volume, e the electronic charge and n the injected minority carrier density. A common expression of $R(n)$ [10] is:

$$R(n) = (B_0 - B_1 n)n(n + p_0) + Cn(n + p_0)^2 + Dn^{5.5} \quad (6)$$

where C is the Auger recombination coefficient and D is the leakage current coefficient. The radiative recombination coefficient $B(n)$ follows the linear approximation, $B(n) = B_0 - B_1 n$. The laser in the experiment was p-doped with $\approx 10^{17} \text{ cm}^{-3}$ of Zn in the active region. Thus, p_0 is neglected in comparison with the carrier density at threshold, n_t . At threshold, the leakage current term, $Dn_t^{5.5}$, contributes only 0.1 mA to the threshold current [19]. Hence, the leakage current is omitted in this analysis.

The carrier dependence of $B(n)$ must be taken into

account. At an injected carrier density of $2 \times 10^{18} \text{ cm}^{-3}$, the decrease in $B(n)$ is of the order of 30 - 40 percent [10]. This gives the following equation:

$$\frac{1}{\tau} = \left(2 - \frac{B_1 n_t / B_0}{1 - B_1 n_t / B_0}\right) \frac{1}{\tau_r} + \frac{3}{\tau_n} \quad (7)$$

EXPERIMENT

A sketch of the experimental set-up is presented in Fig. 1. A passively mode-locked and frequency doubled Nd³⁺:YAG laser ($\lambda = 0.53 \mu\text{m}$) was used for activating the optoelectronic switch. The laser pulse duration was 20 - 25 ps, FWHM, and the pulse energy was 100 μJ . The pulse repetition rate was 12 Hz when a single-pulse selection system was used. The laser beam was split into two parts with equal intensities, each illuminating a photoconductive switch. These switches were made from high-resistivity single-crystal silicon and were connected into the microstrip line structure as shown in Fig. 1. Both switches were biased to voltages of the same magnitude but of opposite polarities. Thus, when the switches were illuminated, two equal step-like current pulses of opposite polarities were launched into the microstrip line. There they were superimposed, so that, when the positive pulse was delayed, a rectangular negative pulse resulted. This delay was accomplished by means of an optical delay line of variable length, which made it possible to change the duration of the electric pulse continuously from approximately 25 ps to 1 ns. The pulse amplitude remained constant, irrespective of the pulse duration, due to the long carrier lifetime in silicon. The rise and fall times were both approximately 15 ps. The switches were fed by two coaxial cables with 50 Ω impedance, matched to the bias power supply and the strip line impedance, Z . Hence, the duration of the step pulse produced by a single switch was determined by the discharge time of the cable, i.e., by its length. To prevent reverse biasing of the laser diode with a very large voltage, we connected the positively biased switch with a cable that was a few centimetres shorter than the one used for the negatively biased switch.

The electric pulses thus obtained were employed to bias the InGaAsP ($\lambda = 1.3 \mu\text{m}$) laser connected in series with a thin film resistor at one end of the main microstrip line branch. This resistor ($R \approx Z$) was intended for impedance matching, i.e. for avoiding pulse reflection. The laser was an LPE-grown, etched-mesa buried-heterostructure diode made by Ericsson Components AB. The p-doping concentration of Zn in the active layer was $\approx 10^{17} \text{ cm}^{-3}$. The threshold current was 24 mA (one facet was antireflection-coated to one percent reflectivity).

The magnitude of the injection current was measured on a high-speed real-time oscilloscope (with 6 GHz resolution) connected to the other end of the main microstrip line branch. An InGaAsP photoconductive switch connected to a boxcar integrator was used to detect the optical signal from the laser diode. The output signal from the boxcar integrator was proportional to the total number of photons emitted by the laser. The integrator was synchronized with the Nd³⁺:YAG laser by means of another photoconductive switch.

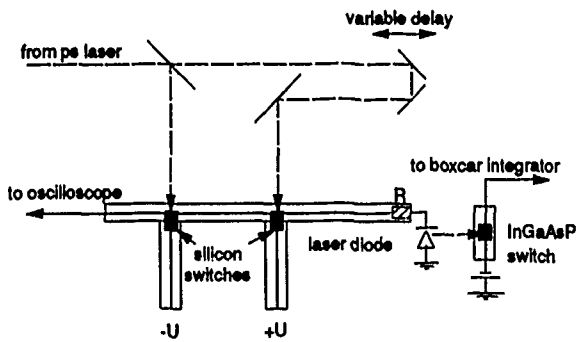


Figure 1. Experimental set-up with photoconductive switches in tandem configuration.

RESULTS

We increased the pulse duration by successive increments and measured the detected signal at each step. The time increments were 4, 10, or 20 ps, depending on the time resolution needed. When the pulse duration became equal to the turn-on delay time, lasing started and the boxcar integrator gave a non-zero signal. By this method it proved possible to measure a turn-on delay time to around 15 ps, the uncertainty primarily stemming from the rise time of the photoconductive switches feeding the laser. Such measurements were made at several different injection current levels, and typical experimental results are shown in Fig. 2. The semiconductor laser turn-on delay time T in each case was established from the onset of the steep increase in output signal. One can see in Fig. 2 that the slopes of the experimental curves increased with the injection current.

Turn-on delay times down to 60 ps were measured, see Fig. 3. Our improved time resolution allowed us to plot the T versus I/I_t dependence at extremely high injection currents ($I/I_t = 62$). This dependence is shown in Fig. 4. Nanosecond delay time data obtained by conventional pulse technique together with the data obtained from tandem photoconductive switch measurements are shown in Fig. 5. It is seen that at both the low and the high injection current limit the experimental points show a good fit to a linear dependence, as predicted by equations (1) and (2). The slopes at these two limits correspond to the overall lifetime $\tau = 3.90$ ns and the differential lifetime $\tau' = 1.87$ ns. Using relations (5) and (7) and assuming that $B_1 n_i / B_0 = 40\%$, we calculated the radiative lifetime τ_r and the nonradiative lifetime τ_n to be 7.1 ns and 8.6 ns, respectively. We then used values for a similar laser obtained from small-signal methods [10] to make a comparison between the different methods. The small-signal method values [20], gave $\tau_r = 9.6$ ns and $\tau_n = 12.3$ ns with $n_i = 2.5 \times 10^{18} \text{ cm}^{-3}$. The rather high estimated n_i is due to the antireflection coating. The values we have found are in reasonable agreement with values reported in Ref. 10.

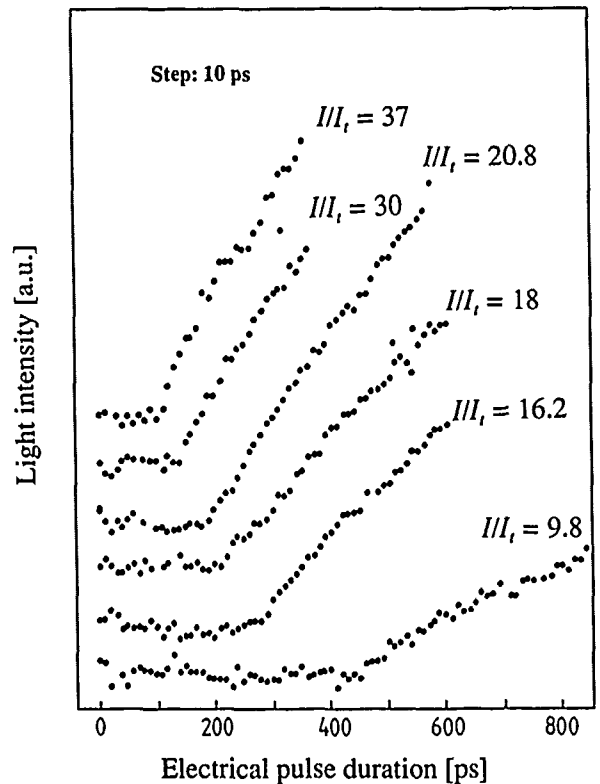


Figure 2. Typical laser-intensity data from the boxcar integrator as a function of the length of the electrical bias pulse. The time increment between adjacent points was 10 ps. The different plots were obtained with different pulse currents, here specified as (I/I_t) .

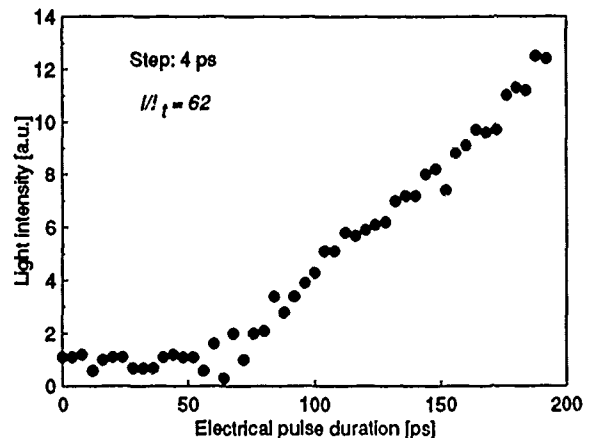


Figure 3. The shortest recorded turn-on delay time, viz. 60 ps. Here, the time increment between adjacent points was 4 ps.

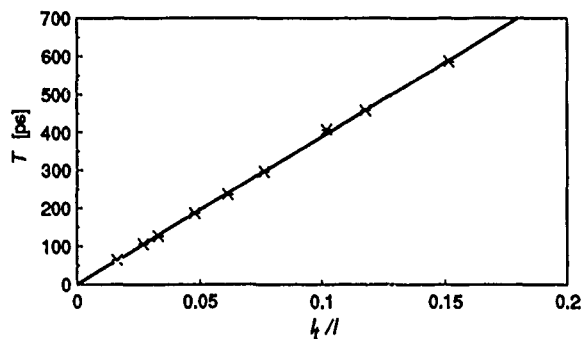


Figure 4. The overall lifetime τ was found by measuring the slope of T vs I^{-1} when $I \rightarrow \infty$.

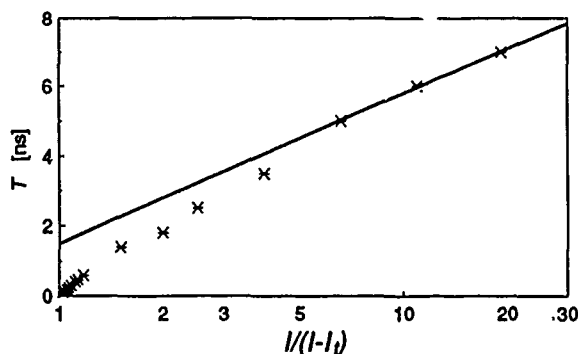


Figure 5. The differential lifetime τ' was found by measuring the slope of T vs $\ln\{I(I-I_0)\}$ when $I \rightarrow I_0$.

CONCLUSION

We have demonstrated a new method to measure turn-on delay times of laser diodes with an accuracy of 15 ps by using tandem photoconductors. This makes it possible to deduce the carrier lifetime at threshold with very good accuracy, even for devices with high threshold. New features of the Si tandem switch are the high pulse magnitude (75 V) and the possibility to vary the pulse duration from 25 ps to 1 ns with constant amplitude and 15 ps rise and fall times. The response of such nearly rectangular pulse excitation is easier to interpret than the corresponding response to the mathematically more complicated pulses produced by single-gap photoconductors or electrical pulse generators. We have also shown that, provided a fitting parameter B_n/B_0 is applied, estimations of radiative and nonradiative carrier lifetimes by this method is in reasonable agreement with the results of well established methods. The main advantage of this new method is that the turn-on delay is measured directly with an uncertainty of 15 ps. It is also possible to measure the dependence of large signal transients, e.g. chirp and relaxation oscillations, on electrical pulse length and overdrive.

ACKNOWLEDGMENT

We wish to thank the National Swedish Board for Technical Development (STU) for support of this work and L. Frank for critical reading of the manuscript. P. Blixt is grateful to the Lithuanian Academy of Sciences for sponsoring his stay.

REFERENCES

1. K.Y. Lau and A. Yariv, "Large-signal dynamics of an ultrafast semiconductor laser at digital modulation rates approaching 10 Gbit/s," *Appl. Phys. Lett.* **47**, 84-86 (1985).
2. D. Bimberg, E.H. Böttcher, K. Ketterer, H.P. Vollmer, H. Beneking and P. Roentgen, "Generation and detection of 15-ps light pulses in the 1.2-1.3- μ m wavelength range by semiconductor lasers and detectors," *Appl. Phys. Lett.* **48**, 83-85 (1986).
3. D. Bimberg, K. Ketterer, H.E. Schöll, and H.P. Vollmer, "Generation of 4 ps light pulses from directly modulated V-groove lasers," *Electron. Lett.* **20**, 343-345 (1984).
4. K.Y. Lau, N. Bar-Chaim, P.L. Derry, and A. Yariv, "High-speed digital modulation of ultralow threshold (<1 mA) GaAs single quantum well lasers without bias," *Appl. Phys. Lett.* **51**, 69-71 (1987).
5. R.S. Tucker, "Large-signal switching transients in index-guided semiconductor lasers," *Electron. Lett.* **20**, 802-803 (1984).
6. J.M. Weisenfeld, R.S. Tucker, P.M. Downey, and J.E. Bowers, "Optical correlation measurement of switching transients in high-speed semiconductor lasers," *Electron. Lett.* **22**, 396-397 (1986).
7. J.M. Weisenfeld, R.S. Tucker, and P.M. Downey, "Picosecond measurement of chirp in gain-switched, single-mode injection lasers," *Appl. Phys. Lett.* **51**, 1307-1309 (1987).
8. K. Konnerth and C. Lanza, "Delay between current pulse and light emission of a gallium arsenide injection laser," *Appl. Phys. Lett.* **4**, 120-121 (1964).
9. R.W. Dixon and W.B. Joyce, "Generalized expressions for the turn-on delay in semiconductor lasers," *J. Appl. Phys.* **50**, 4591-4595 (1979).
10. R. Olshansky, C.B. Su, J. Manning, and W. Powazinik, "Measurement of radiative and nonradiative recombination rates in InGaAsP and AlGaAs light sources," *IEEE J. Quantum Electron.* **QE-20**, 838-854 (1984).
11. D.H. Auston, "Impulse response of photoconductors in transmission lines," *IEEE J. Quantum Electron.* **QE-19**, 639-647 (1983).
12. D.H. Auston, "Picosecond optoelectronic switching and gating in silicon," *Appl. Phys. Lett.* **26**, 101-103 (1975).
13. J.A. Buck, K.K. Li, and J.R. Whinnery, "Optoelectronic switching in a stub transmission line," *J. Appl. Phys.* **51**, 769-771 (1980).
14. W. Margulis and R. Persson, "Coaxial electrical pulse shaper for picosecond electronics," *Rev. Sci. Instr.* **56**, 1586-1588 (1986).
15. V. Brückner, "Picosecond optoelectronic semiconductor switching," *Physica Scripta* **T23**, 214-217 (1988).

16. Y. Hori, J. Paslaski, M. Yi and A. Yariv, "High-speed InP optoelectronic switch with a tandem structure," *Appl. Phys. Lett.* **46**, 749-751 (1985).
17. P. Blixt, A. Krotkus, M. Kull, and J.A. Tellefsen, Jr., "A differential photodetector employing photoconductivity, for subnanosecond laser beam position measurements," *J. Phys. E: Sci. Instr.* **21**, 971-973 (1988).
18. C.B. Su and R. Olshansky, "Carrier lifetime measurement for determination of recombination rates and doping levels of III-V semiconductor light sources," *Appl. Phys. Lett.* **41**, 833-835 (1982).
19. R. Olshansky, J. LaCourse, T. Chow, and W. Powazinik, "Measurement of radiative, Auger, and nonradiative currents in 1.3- μm InGaAsP buried heterostructure lasers," *Appl. Phys. Lett.* **50**, 310-312 (1987).
20. $B_0 = 0.7 \times 10^{-10} \text{ cm}^3/\text{s}$, $B_1/B_0 = 1.7 \times 10^{-19} \text{ cm}^3$, and $C = 1.2 \times 10^{-29} \text{ cm}^6/\text{s}$. The above values were found in Ref.10

Picosecond Optoelectronic Integrated Antennas for Broadband Dielectric Measurements

Y. Pastol, G. Arjavalingam, J.-M. Halbout, and G. V. Kopcsay

IBM Research Division, T. J. Watson Research Center, P.O. Box 218,
Yorktown Heights, New York 10598

ABSTRACT

The picosecond transient electromagnetic radiation from optoelectronically pulsed integrated antennas is used for broadband coherent microwave spectroscopy experiments in the 10-130 GHz frequency range. The apparatus is first characterized using microwave filters of predictable behavior. Measurements of the frequency-dependent absorption coefficient and refractive index of representative materials are also presented.

INTRODUCTION

For accurate design and modelling of high speed electronic devices and circuits, which now operate in the 10-100 GHz frequency range, a detailed knowledge of the dielectric properties of the materials used in their fabrication and packaging is required. Unfortunately, little such information is yet available because most dielectric measurements are carried out at discrete frequencies where sources and related hardware (e.g. waveguides) are available. Moreover, traditional waveguide and closed-cavity methods have some fundamental limitations which are difficult to overcome at millimeter waves, especially in the case of low-loss materials [1]. Here, we present a coherent microwave transient spectroscopy (COMITS) technique which, in a single experiment, yields the complex dielectric constant of a material over a wide frequency range [2]. After a brief description of the spectroscopy apparatus, we show how it was characterized using microwave filters of predictable loss and dispersion

properties. Then, we present measurements of the dielectric properties of fused silica and BK-7 glass performed using this new technique.

SPECTROSCOPY APPARATUS

Exponentially tapered coplanar stripline antennas were fabricated on silicon on sapphire substrates. The uniform, 4 mm long coplanar-strip feedline consists of $5\mu\text{m}$ wide lines separated by a $10\mu\text{m}$ gap, and is terminated at one end by bonding pads. The other end is prolonged by an exponential flare, 3.7 mm long, which forms the antenna part of the structure (Fig. 1). In order to reduce the carrier lifetime, the silicon epilayer is implanted with O^+ ions. Ion doses of 10^{15} cm^{-2} at implant energies of 100 and 200 keV are used.

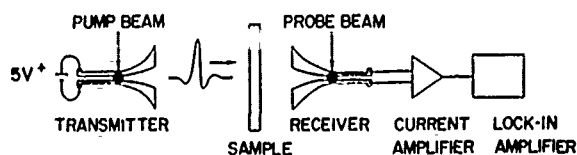


Figure 1. Schematic of the COMITS experimental setup.

The full characterization of the transient radiation properties of the antennas described above (bandwidth, pattern, polarization...) has been presented separately [3]. In the following, we describe how a simple transmission-reception setup can be used for coherent microwave spectroscopy experiments. Two identical antennas, the transmitter and

the receiver, face each other, and are separated by a fixed distance (Fig. 1). A 5V bias is supplied to the transmitter, the receiver is unbiased. Optical pulses of 1.5 ps duration at 240 MHz repetition rate are obtained from a mode-locked, pulse-compressed, and frequency-doubled Nd:YLF laser. The 526 nm wavelength output is split into two beams of equal intensity. The first beam (pump) is focused on the feedline of the transmitter, close to the edge of the antenna part. There it generates an electrical transient which radiates as it propagates in the antenna section. The second optical beam (probe) is delayed with respect to the pump by a variable amount, and is focused at the edge of the antenna part in the receiver. The transient voltage induced by the received field is thus measured as a function of time by photoconductive sampling. A typical waveform, recorded for an antenna separation of 4 cm is shown in Fig. 2. Its prominent feature consists of a 7 ps central pulse of 200 μ V peak amplitude. Numerically Fourier transforming the temporal data yields an amplitude spectrum with frequency components between 0 and 150 GHz, as shown in inset.

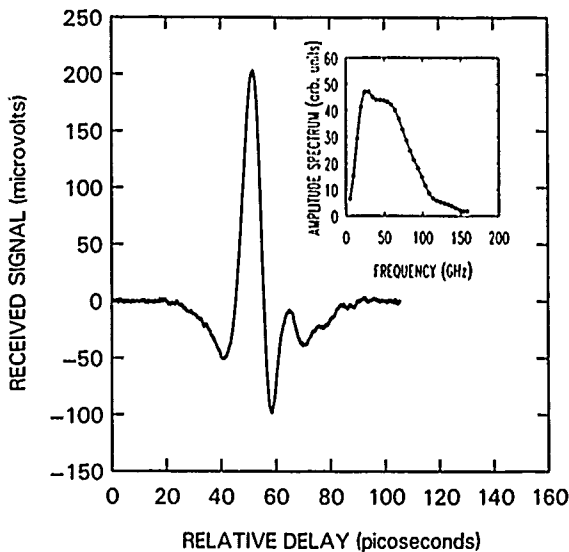


Figure 2. Received waveform with no sample between the transmitter and the receiver. The corresponding amplitude spectrum is shown in inset.

In a COMITS measurement, a reference recording is first taken without any sample between the two antennas. Subsequently the sample, with a cross section exceeding that of the receiving pattern, is introduced close to the receiver and a second waveform is recorded. The complex amplitude

transmission function of the sample is then calculated by dividing the Fourier transform of the second waveform by the Fourier transform of the first [4]. Since the measured voltage is proportional to the received electric field, the amplitude and phase of the transmission function are obtained simultaneously. The former yields the absorption of the sample, the latter gives its dispersion [4]. The spectroscopy apparatus was first characterized using microwave filters of well-known and predictable behavior. Among others, a Fabry-Pérot interferometer, built with two titanium-coated glass slides, was used as a test sample. The transmission function (amplitude and phase) for such an interferometer with the two metallized faces 4 mm apart is shown in Fig. 3. The amplitude spectrum, and the corresponding variations of the phase follow the expected behavior for the electric field transmission function. This is also verified for Fabry-Pérot interferometers with other spacings.

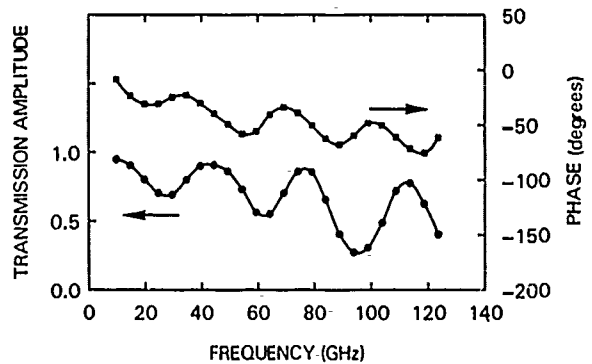


Figure 3. Amplitude and phase of the transmission function of a Fabry-Pérot interferometer with the two reflecting surfaces 4 mm apart.

DIELECTRIC MEASUREMENTS

With the experimental configuration of Fig. 1, the microwave radiation is uncollimated and it is therefore important to correct the experimental data for the refraction occurring inside the samples. In order to avoid this additional step in the data processing, it is desirable to obtain good collimation of the microwave beam. This was achieved using hemispherical glass (BK-7) lenses, as shown in Fig. 4. In addition to the collimation, transmission over longer distances (typically 15 cm) is now possible with very good signal to noise ratio, resulting in an improved versatility of the spectroscopy apparatus.

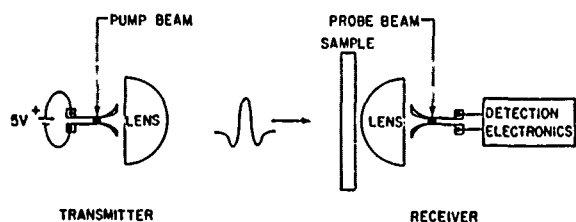


Figure 4. Experimental setup with collimation of the microwave beam.

As a test material, we chose fused silica, which has already been characterized at microwave frequencies [5]. Its refractive index n and electric field absorption coefficient α , measured between 10 and 125 GHz, are displayed in Fig. 5. We find that fused silica exhibits low-loss over the whole frequency range, while n remains constant and equal to 1.96. These results are consistent with earlier data [6,7].

The setup depicted in Fig. 4 was used to measure the frequency-dependent absorption and dispersion properties of numerous low-loss dielectrics between 10 and 130 GHz [8]. As an example we present in Fig. 6 results obtained with BK-7 glass, the material with which the lenses are made of. While α increases with frequency from 0.1 to 1 Np/cm, $n = 2.50$ is constant over the entire frequency range. These results indicate that lenses made of fused silica would be preferable; such lenses have been designed using the data of Fig. 5.

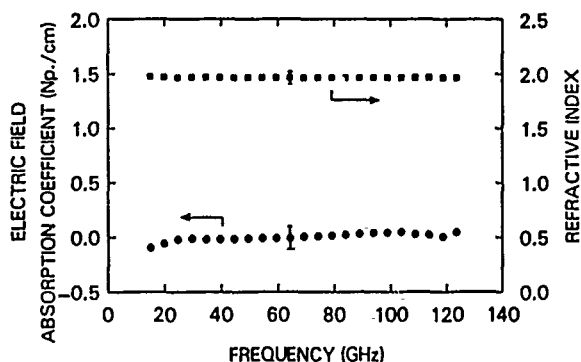


Figure 5. Electric field absorption coefficient and refractive index of fused silica.

CONCLUSION

In conclusion, we have presented a coherent microwave transient spectroscopy (COMITS) technique which, in a single experiment, yields the frequency dependent absorption and dispersion of

a material with continuous frequency coverage between 10 and 130 GHz. Although only transmission experiments are reported, reflection COMITS is also possible and is currently being investigated.

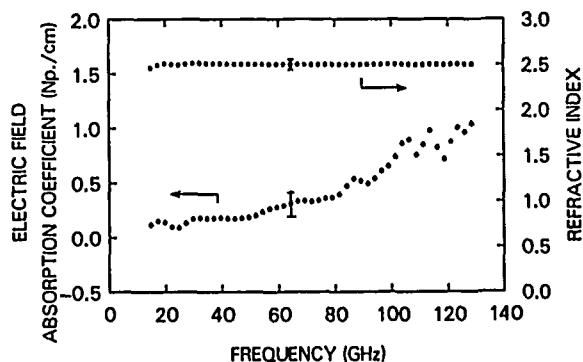


Figure 6. Electric field absorption coefficient and refractive index of BK-7 glass.

REFERENCES

1. F.I. Shimabukuro, S. Lazar, M.R. Chernick, and H.B. Dyson, "A quasi-optical method for measuring the complex permittivity of materials," *IEEE Trans. Microwave Theory Tech.* **32**, 659-665 (1984).
2. Y. Pastol, G. Arjavalingam, J.-M. Halbout, and G.V. Kopcsay, "Coherent broadband microwave spectroscopy using picosecond optoelectronic antennas," *Appl. Phys. Lett.* **54**, 307-309 (1989).
3. Y. Pastol, G. Arjavalingam, J.-M. Halbout, and G.V. Kopcsay, "Characterization of an optoelectronically pulsed broadband microwave antenna," *Electron. Lett.* **24**, 1318-1319 (1988).
4. G. Arjavalingam, Y. Pastol, J.-M. Halbout, and G.V. Kopcsay, submitted for publication.
5. A.R. von Hippel, *Dielectric Materials and Applications* (Wiley, New York, 1954), p. 311.
6. E.D. Palik, ed., *Handbook of Optical Constants of Solids* (Academic Press, Orlando, 1985), p. 763.
7. M.N. Afsar, "Dielectric measurements of millimeter-wave materials," *IEEE Trans. Microwave Theory Tech.* **32**, 1598-1609 (1984).
8. Y. Pastol, G. Arjavalingam, J.-M. Halbout, and G.V. Kopcsay, submitted for publication.

Beams of Terahertz Electromagnetic Pulses

Ch. Fattinger and D. Grischkowsky

*IBM Research Division, T. J. Watson Research Center,
Yorktown Heights, New York 10598*

ABSTRACT

The generation of diffraction limited beams of single-cycle 0.5 terahertz electromagnetic pulses is described. The beams, centimeters in diameter, have a frequency independent divergence of only 15 mrad and have been propagated distances up to 350 cm. The very high collection efficiency of the optical system used for the generation and the detection of these beams provides exceptionally clean and sensitive reception of the transmitted signal. A spectral characterization of water vapor in the intervening ambient air is also presented.

Integrated-circuit Hertzian dipoles, optoelectronically driven by ultrashort laser pulses, have made it possible to generate subpicosecond transients of electromagnetic radiation. The dipole structures have consisted of photoconductive gaps (1), microscopic dipolar antennas (2), and point sources produced by shorting coplanar transmission lines (3,4). An inherent feature of time dependent dipoles on the surface of a dielectric is that most of the radiated power is emitted into the dielectric and only very little power is radiated into the air (5,6). For Hertzian dipoles (point sources) with dimensions small compared to any of the radiated wavelengths the emitted ultrashort radiation pulse can be collimated using optical techniques: By locating the ultrafast point source at the foci of spherical mirrors or lenses contacted to the backside of the chip,

a large fraction of the emitted radiation is captured and can be focused or collimated, providing nearly diffraction-limited imaging of the terahertz radiation (3,4). In addition, the excellent focusing properties preserve the subpicosecond response time of the source. This technique allowed us to produce, for the first time, diffraction limited beams of single-cycle 0.5 terahertz electromagnetic pulses (4). The freely propagating teraHz pulses can be easily measured after propagation distances of several meters using the same optical approach as for their generation: The teraHz radiation is focused on a second integrated-circuit photoconductive gap which is probed by a delayed portion of the laser beam.

The coherent detection of these extremely broadband transients of electromagnetic radiation with subpicosecond time resolution makes this optoelectronic technique an important new tool with many possible applications. The most immediate one is the spectroscopic characterization of materials in the teraHz (far-infrared) regime by time domain spectroscopic techniques (7-9). Here, the measured input and propagated electrical pulses are Fourier analyzed, and because the actual electrical field is measured, both the amplitude and phase of the Fourier components are obtained. Consequently, the frequency dependent absorption and dispersion can be determined for any far-infrared transmitting material. However, the most appropriate use would be time-dependent spectral characterizations after an initiating event.

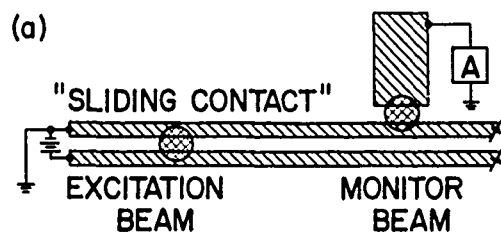
This application is made feasible by the synchronization between the ultrashort light pulses and the teraHz pulses. A completely different type of application would be ranging measurements with a possible precision of better than 100 microns. The fact that millivolt signals are obtained at receivers, allows for possible remote triggering of devices. Finally, it is clear that these beams have tremendous capacity as a communications channel. Unfortunately, the ubiquitous absorption by water vapor will prevent this use in the atmosphere.

In the following we describe an experiment where the optical collimation technique is used to transmit the teraHz pulses over a distance of 350 cm.

The experimental geometry used to generate the transient electric dipole responsible for the teraHz radiation is illustrated in Fig. 1(a). By photoconductive shorting the charged coplanar transmission line with 70 fsec pulses from a colliding-pulse, mode-locked dye laser, a Hertzian dipole is created between the two lines. The 20-mm-long transmission line consisted of two parallel 5 μm wide, 1 μm thick aluminum lines separated from each other by 15 μm . The line was fabricated on an undoped silicon-on-sapphire (SOS) wafer, which was heavily implanted to ensure the required short carrier lifetime (10). The emission of radiation by the subpicosecond dipole created between the two lines is quite efficient, even though the transmission line structure does not act as an antenna for the radiated pulses. The electrical pulses generated on the transmission line were measured by a fast photoconductive switch, probed by the time delayed monitor beam of the same 70 fsec laser pulses. For short propagation distances ($< 300 \mu\text{m}$), the electrical pulse coupled to the transmission line has the same time dependence as the transient current between the two lines responsible for the teraHz radiation (11).

The structure shown in Fig. 1b used to detect the teraHz radiation is simply a photoconductive gap of 5 μm spacing and a width of 25 μm . The length of the two aluminum strips forming the gap was 1 mm. This gap was fabricated as above on a separate SOS chip. A current amplifier is connected across the gap as indicated. As the focused radiation pulse hits the detector a transient voltage appears across the gap. The in-

TERAHZ RADIATION SOURCE



TERAHZ RADIATION DETECTOR

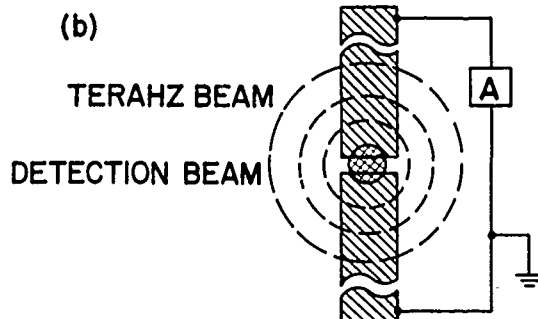


Figure 1. (a) Schematic diagram of the charged coplanar transmission line. The laser excitation beam spot defines the location of the transient electric dipole. The monitor beam measures the electrical pulse coupled to the line. (b) Schematic diagram of the gap detector centered in the concentric focal spots of the incoming teraHz radiation. The laser detection beam spot is centered on the gap.

duced voltage is measured by shorting the gap with the 70 fsec laser pulses in the detection beam and measuring the collected charge (current) versus the time delay between the excitation and detection laser pulses.

The teraHz optics at the radiation source and detector consist of two crystalline sapphire, spherical lenses contacted to the backside (sapphire side) of the SOS chips. The center of the two truncated 9.5 mm dia spheres (lenses) is 2.3 mm above the surface of the chips, so that the radiation source and the detector are at the focus of the refracting spherical surface. As shown in Fig. 2 the angular distribution of the power radiated by the dipole on the surface of the chip is drastically affected by the presence of the sapphire/air interface.

Due to the relatively high dielectric constant of 9.6 for sapphire (12), most of the radiation emitted by the ultrafast dipole is contained within a 60 degree full angle cone normal to the surface of the chip and directed into the substrate material (5,6). The boundary of this cone is indicated by the dashed lines in Fig. 2. This situation gives good collection and collimation of the teraHz radiation, because the central portion of the spherical lens captures most of the emission. Taking into account the reflection loss at the surface of the lens we estimate that 30% of the total emitted power is coupled out by the sapphire lens.

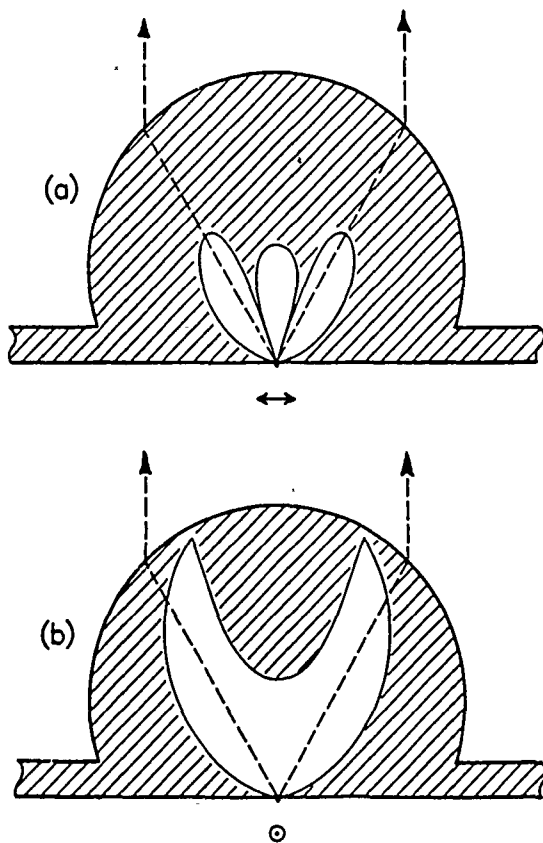


Figure 2. Calculated angular distribution of the power emitted by a Hertzian dipole located on the surface of a dielectric with dielectric constant 9.6. The dipole axis is oriented parallel to the surface. The oscillation of the dipole in (a) is in the plane of the paper, while in (b) the oscillation is perpendicular to (out of) the plane of the paper. The polar diagrams are shown in orthogonal cross-sections of the sapphire lens. The power emitted into the air is indicated on same scale as the little 'dot' below the focal point of the lens.

After collimation we obtain a beam diameter of 5 mm with a diffraction limited divergence. By reciprocity the emission and detection characteristics of an antenna are identical, and Fig. 2 also applies for the angular dependence of the detection efficiency of the receiving dipole.

It is important to note, that sapphire is strongly birefringent for frequencies in the teraHz range (12). Therefore for both lenses the C-axis of the sapphire was perpendicular to the optical axis of the lens, i.e., parallel to the plane face of the spherical segment. For the source lens and the source chip the C-axes were oriented parallel to the transmission line; for the detecting lens and the detecting chip the C-axes were perpendicular to the aluminum strips (parallel to the 25 micron dimension of the gap). Consequently, for both generation and detection the C-axes are perpendicular to the polarization of the teraHz radiation propagating in the direction normal to the surface of the chips. Only for this particular orientation of the C-axes the amplitude of the extraordinary wave cancels at the position of the detector and a clean pulse corresponding to a pure ordinary wave is obtained.

The freely propagating beam pencil, coupled out by the sapphire lens on the source chip, starts out with a frequency independent diameter of about 5 mm, which grows during propagation due to diffraction. As shown in Fig. 3, the diverging beam pencil leaving the sapphire lens can be recollimated with a concave mirror. Our initial set-up is illustrated in Fig. 3a, where the 5 mm diameter diffraction-limited beam from the source lens is emitted at the focal plane of a 25 cm focal-length, spherical, copper mirror with a 50 mm aperture. After recollimation by the mirror, the beam diameter (15-50 mm) is proportional to the wavelength. Therefore the 15 mrad divergence of the collimated beam is the same for all the frequency components in the pulse. The beam then sequentially travels around the numerically indicated rectangular path formed by 4 mirrors of gold coated ($1\text{ }\mu\text{m}$ thick) 5.5 cm diameter silicon wafers. The last gold coated mirror (number 4) reflects the beam back to the spherical mirror which then re-focuses the beam onto the focusing sapphire lens at the detector. This optical path is equivalent to the simpler schematic diagram of Fig. 3b, where the concentric rings indicate the disc-shaped wave packet associated with the freely

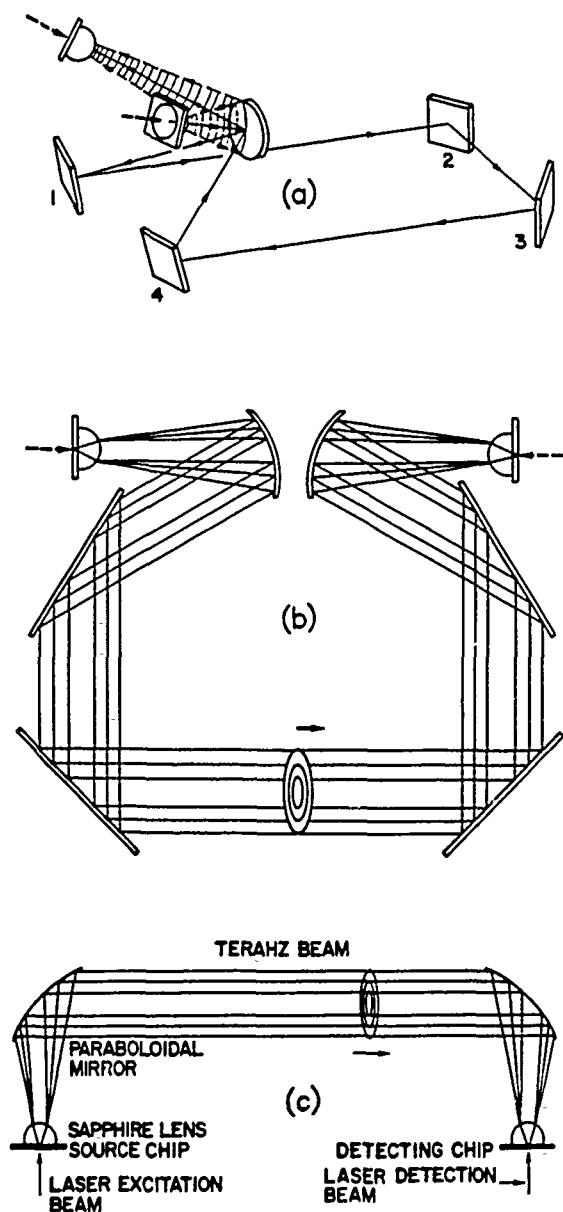


Figure 3. (a) Schematic diagram of the collimating and focusing optics consisting of sapphire lenses in contact with the backside of the SOS chips, located at the focus of a spherical mirror positioned in the center of a delay line defined by 4 flat mirrors. (b) Simplified optical diagram equivalent to (a). (c) Optimal collimating and focusing optics based on paraboloidal mirrors.

propagating teraHz pulse. Inside the smallest ring corresponding to the shortest wavelength, all the frequency components comprising the teraHz pulse are present, and the wave packet has a minimal thickness of only 0.5 mm. After propagating 300 cm to the second identical spherical mirror, the beam is focused on to a second sapphire lens in contact with the detecting chip. Here, all the frequencies are focused to the same 5 mm diameter spot at the entrance to the lens. This lens focuses the beam on to the detection gap, the diameter of the focal spot (200-800 microns) is proportional to the wavelength of the teraHz radiation in sapphire, cf. Fig.1b. The optimal optical arrangement involves the use of paraboloidal mirrors as indicated in Fig. 3c. These mirrors are available commercially in relatively large diameters. Some of our preliminary results with this arrangement gave excellent collimation and focusing together with no loss in time resolution.

Compared to the previous measurements (4) which used only the sapphire lenses facing each other, the addition of the collimating and focusing mirrors provides a dramatically enhanced coupling between the transmitter and the receiver. Above a certain frequency determined by the acceptance angle (aperture) of the spherical mirrors most of the radiation coupled out by the lens on the source chip is collected and focused back on to the lens on the detecting chip. For the setup described here this critical frequency is 0.25 THz. Because of this very high collection efficiency for frequencies above 0.25 THz the power incident on the detecting chip is about 5% of the power generated by the transmitter.

The generated electrical pulse on the transmission line is shown in Fig. 4a. For this measurement the spatial separation between the sliding contact excitation spot and the monitor gap was 150 microns, so that propagation effects were negligible. The measured full width at half maximum is 0.95 psec. Taking into account the response time of the monitor gap, we consider the actual pulse width of the transient current responsible for the teraHz radiation to be 0.6 psec. Figure 4b is the numerical derivative of the pulse on the line (current pulse) and will be used to calculate the limits of the spectral end of the resulting radiation pulse.

The energy of the incident 70 fsec laser pulses coming at a 100 MHz rate in a 5 mW

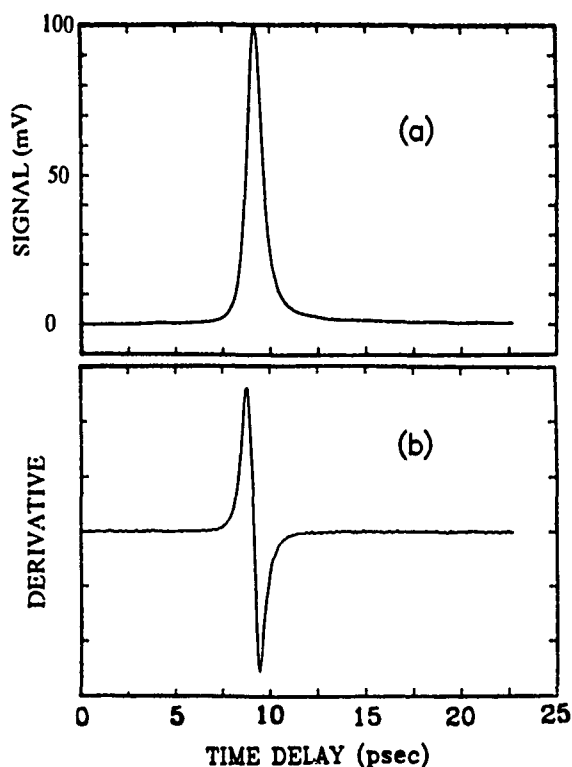


Figure 4. (a) Electrical pulse on the transmission line measured with 150 micron separation between the excitation and monitor beams. (b) Numerical derivative of the measured pulse on the transmission line shown in (a).

beam is 50 picojoules per pulse. With a bias voltage of 20 V, approximately 8000 electrons are transferred between the two lines at the excitation site during one excitation pulse. Knowing this transient current we calculated that 1 attojoule of energy is emitted by the transient dipole moment on the 20 μm wide transmission line (5). Assuming that 20% of the total emitted radiation is found in the freely propagating beam, the resulting energy in the teraHz beam is 0.2 attojoules (approximately 1 eV) per pulse. From the signal strength of 100 mV for the electrical pulse on the coplanar line, knowing that 2 equal and oppositely propagating pulses are generated, and considering the line impedance to be 125 ohms, we calculate approximately 100 attojoules for the electrical pulses coupled to the line. Therefore, the total radiated energy is of the order of 1% of the energy coupled to the transmission line. Another feature is that the conversion of laser en-

ergy to electrical pulse energy on the transmission line and to energy in the teraHz beam radiation is a nonlinear process. For example, if the energy in the laser pulse is increased by 10X, the energy in the pulses on the line and in the teraHz radiation increase by 100X.

An important point concerns the extreme sensitivity of the detection technique. The individual teraHz pulses of energy 0.2 attojoules contain approximately 1000 photons. Our measurement system detects these pulses with a signal-to-noise-ratio of 300:1 for an integration time of 0.1 second. Therefore, in terms of minimum detectable energy, we can measure 0.2 attojoules/(90000). This corresponds to a sensitivity of 1/90 photon per pulse. Of course, our repetition rate of 100 MHz, and our gated detection technique are required for this sensitivity. This exceptional sensitivity corresponds to the capability to detect with a signal-to-noise-ratio of 1:1 and for an integration time of 0.1 sec an incoming average power of 0.2 femtoWatts. In comparison a cryogenic bolometer at liquid helium temperature has the sensitivity of 0.1 picoWatt/(square root Hz) (see Ref. 14) corresponding to 150 femtoWatts for a 0.1 sec integration time. The main reason for this exceptional sensitivity of the optoelectronic technique is that the electric field is detected directly and coherently.

Figure 5a shows a previous measurement (4) of the teraHz radiation pulse, obtained without using any mirrors. The main component of the pulse consists of a single cycle of the electromagnetic field with a time duration from maximum to minimum of less than 1 psec. For this measurement the separation between the two sapphire lenses facing each other was 10 cm. Figure 5b displays the detected teraHz radiation pulse after a total propagation distance of 350 cm in air, measured with the set-up illustrated in Fig. 3a. As can be seen, the main component of the signal (Fig. 5b) measured with the 350 cm long complex optical path is similar to the pulse shown in Fig. 5a. However, the oscillations on the trailing edge dramatically increased. These oscillations are due to the water vapor corresponding to a relative humidity of 30%. In order to see the full extent of these oscillations, the length of the scan was increased to 90 psec as shown in Fig. 5c. Here we see that the ringing persists for more than 50 psec.

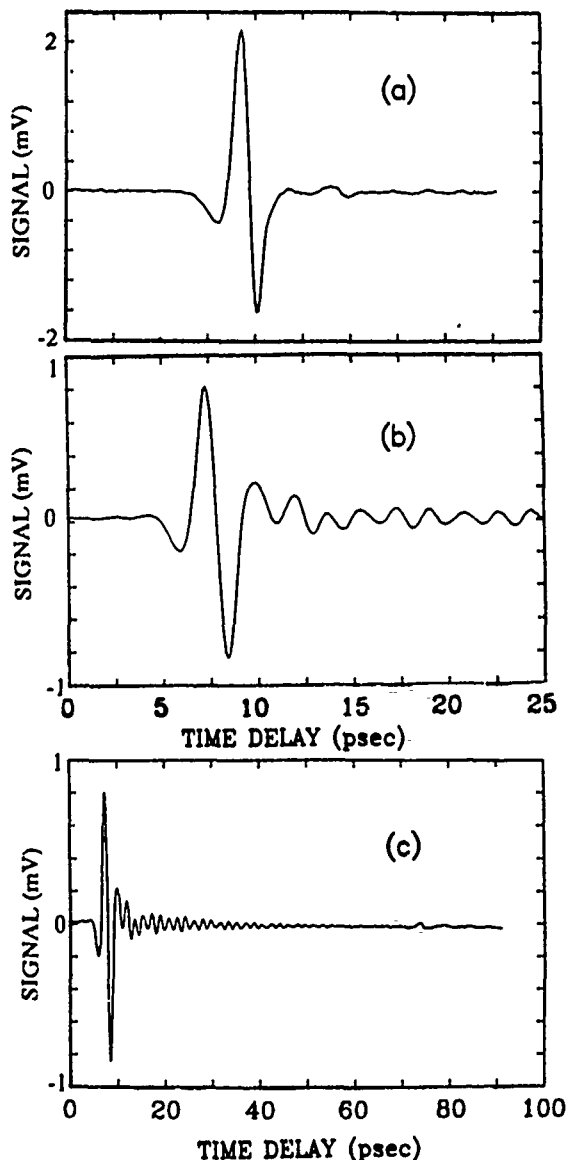


Figure 5. (a) Freely propagating teraHz radiation pulse measured without any mirrors; the separation between the two sapphire lenses facing each other was 10 cm. (b) Radiation pulse of the freely propagating teraHz beam measured with a total propagation path length of 350 cm (cf. Figs. 3a,3b). (c) Longer time scan of (b).

The signal to noise ratio is better than 300:1 for a single 8 min scan of the 90 psec relative time delay between the exciting and probing laser pulses.

The amplitude spectra of the two radiation pulses (Figs. 5a and 5b) are displayed in Figs. 6a and 6b, respectively. Both spectra peak at

approximately 0.4 THz. Apart from a modest decrease of the transmitted bandwidth in spectrum 6b compared to spectrum 6a, the two spectra differ by two significant absorption lines of water vapor at 0.56 and 0.75 THz. (The spike at very low frequency is an artifact and can be ignored.) The two observed absorption lines correspond to transitions between rotational modes of the water molecule and are in agreement with earlier measurements (13).

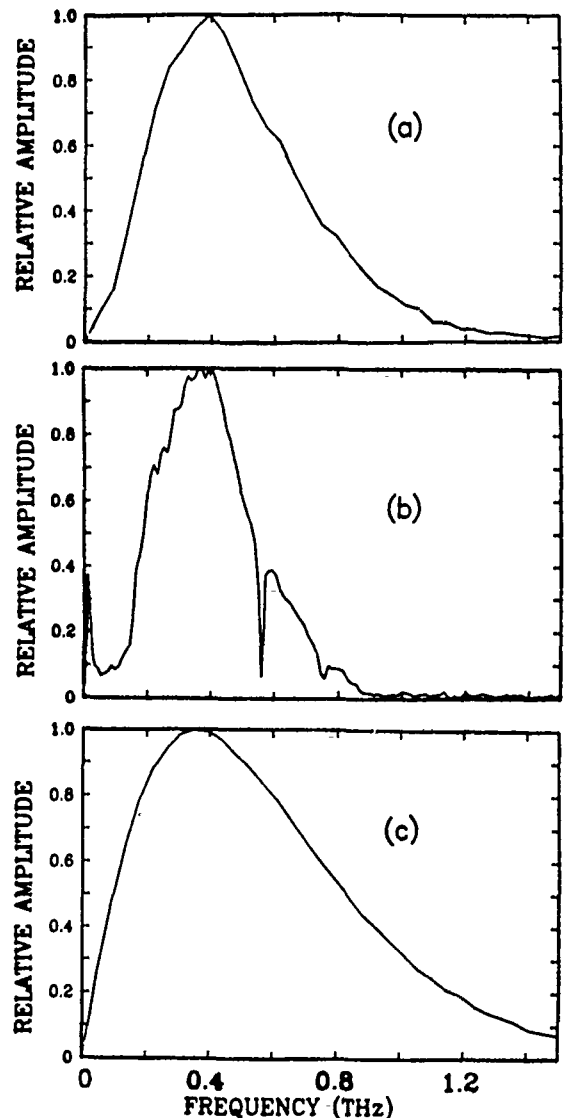


Figure 6. (a) Amplitude spectrum of the pulse shown in Fig. 5a, transmitted over a distance of 10 cm. (b) Amplitude spectrum of the pulse shown in Fig. 5b, transmitted over a total distance of 350 cm. (c) Amplitude spectrum of the numerical derivative of the measured pulse on the transmission line shown in Fig. 4a.

The following argument compares a theoretical lower frequency bandwidth limit for the generated teraHz pulse with the bandwidth of the received signal. In the radiation zone the field of the Hertzian dipole is given by the derivative of the transient current between the two aluminum lines. Figure 4b displays the numerical derivative of the measured electrical pulse on the transmission line shown in Fig. 4a. The amplitude spectrum of this numerical derivative, which is shown in Fig. 6c, provides a lower limit for the true spectral extent of the initially emitted teraHz radiation pulse. This is because the actual transient current at the excitation site is significantly faster than the measured pulse on the transmission line. As can be seen, by comparing Fig. 6c with Figs. 6a and 6b, the lowest and highest frequency components created by the transient dipole on the source chip are not present in the detected radiation pulse. As discussed above, the cut-off for frequency components below 0.25 THz is caused by diffraction.

To explain the observed attenuation of the high frequency components, the following four effects have to be considered: The first and simplest is the frequency dependent reflectivity from the 2 reflections at the copper mirror and the 4 reflections from the gold coated silicon wafers. The second involves the coherent imaging of the teraHz radiation, where wavefront errors due to aberrations of the optical system cause a decrease of the coupling strength between transmitter and receiver. The two off-axis reflections of the THz radiation at the spherical copper mirror induce differences in optical path length between different portions of the beam, which are more severe for the high frequency components of the transmitted signal. The third is the absorption loss in the sapphire lenses which increases with frequency (12). This absorption has a strength such that the total path length of 14mm through the sapphire lenses attenuated the 1 THz component by 1/2. Finally, the 0.8 psec response time of the detector strongly reduces the observed fast time dependence of the received signal.

ACKNOWLEDGMENT

This research was partially supported by the U.S. Office of Naval Research.

REFERENCES

1. D.H. Auston, K.P. Cheung, and P.R. Smith, *Appl. Phys. Lett.* Vol.45, 284 (1984).
2. P.R. Smith, D.H. Auston, and M.C. Nuss, *IEEE J. Quantum Electron.* QE-24, 255 (1988).
3. Ch. Fattinger and D. Grischkowsky, *Appl. Phys. Lett.* Vol.53, 1480 (1988).
4. Ch. Fattinger and D. Grischkowsky, *Appl. Phys. Lett.* Vol.54, 490 (1989).
5. W. Lukosz and R.E. Kunz, *J. Opt. Soc. Am.* Vol.67, 1607 (1977), and W. Lukosz, *J. Opt. Soc. Am.* 69, 1495 (1979).
6. D.B. Rutledge and M.S. Muha, *IEEE Trans. Ant. Propagat.* AP-30, 535 (1982).
7. D. Grischkowsky, C.-C. Chi, I.N. Duling III, W.J. Gallagher, N.H. Halas, J.-M. Halbout, and M.B. Ketchen, in 'Picosecond Electronics and Optoelectronics II', Proceedings of the Second Topical Conference, Incline Village, Nevada, January 14-16, (1987), Editors, F.J. Leonberger, C.H. Lee, F. Cappasso, and H. Morkoc, (Springer-Verlag, New York 1987).
8. D. Grischkowsky, C.-C. Chi, I.N. Duling III, W.J. Gallagher, M.B. Ketchen, and R. Sprik, 'Laser Spectroscopy VIII', Proceedings of the Eighth International Conference, Are, Sweden, June 22-26, (1987), Editors, W. Persson and S. Svanberg, (Springer-Verlag, New York 1987).
9. Y. Pastol, G. Arjavalingam, J.-M. Halbout, and G.V. Kopcsay, *Appl. Phys. Lett.* Vol.54, 307 (1989).
10. F.E. Doany, D. Grischkowsky, and C.-C. Chi, *Appl. Phys. Lett.* Vol.50, 460 (1987).
11. D. Grischkowsky, M.B. Ketchen, C.-C. Chi, I.N. Duling III, N.J. Halas, J.-M. Halbout, and P.G. May, *IEEE J. Quantum Electron.* QE-24, 221 (1988).
12. E.E. Russell and E.E. Bell, *J. Opt. Soc. Am.* Vol.57, 543 (1967).
13. D.E. Burch, *J. Opt. Soc. Am.* Vol.58, 1383 (1968).
14. C. Johnson, F.J. Low and A.W. Davidson, *Optical Engr.*, Vol. 19, 255 (1980).

Characterization of Optically Pulsed Millimeter-Wave Antennas

Charles R. Lutz and Alfred P. DeFonzo

*Department of Electrical and Computer Engineering, University of Massachusetts,
Amherst, Massachusetts 01003*

ABSTRACT

We describe experiments in which optoelectronic sampling techniques are used to investigate the transient response of integrated millimeter wave antenna elements. The internal device characteristics are analyzed by performing wide bandwidth time domain reflectometry measurements over a frequency span exceeding 200 GHz. In addition, we demonstrate a novel approach to measuring the transient far-field radiation patterns emitted from these devices. The far-field patterns in both the E and H Planes are observed to consist of single forward directed lobes which are shown to have a cosine-squared dependence.

1. INTRODUCTION

The availability of picosecond and sub-picosecond lasers and the subsequent development of high-speed photoconductive materials has led to remarkable advances in the area of ultrafast electronics over the last several years. Recent innovations in optoelectronic technology have resulted in the development of photoconductive devices which are capable of producing electrical transients with rise times approaching 100 femtoseconds and pulse durations of less than 500 femtoseconds [1]. The bandwidth of these signals can easily exceed one terahertz making them useful for a variety of applications in the millimeter and far-infrared regions of the electromagnetic spectrum. Instruments based on this technology will be suitable for conducting

investigations of material processes on femtosecond time scales and spectroscopy studies in areas not readily accessible by conventional methods. Potential device applications include high resolution radar, millimeter wave spectroscopy sources [2], and interconnects for transmitting high speed, broadband electrical signals in millimeter-wave integrated circuits [3].

Transient effects become more important as the switching times of electronic devices decrease. For example, researchers have recently observed a variety of phenomena associated with the propagation of picosecond and sub-picosecond transients on integrated microstrip and coplanar transmission line structures [4-6]. These effects can cause dispersion of wide bandwidth waveforms and introduce spurious signals due to scattering and reflections, causing distortion and degradation of the desired signals. A thorough knowledge of the fundamental principles involved in these processes is of considerable interest as this will lead to device designs which are optimized for controlling broadband coherent electrical waveforms. However, in order to explore the underlying physical mechanisms which govern transient processes it is necessary to develop the techniques required for measuring and characterizing propagation and radiation properties well into the terahertz regime. Compared to traditional electronic measurement systems which are limited to resolutions of approximately 25 picoseconds and bandwidths of less than 20 GHz, photoconductive or electro-optic sampling techniques can

be used to characterize the performance of high-speed electronic systems over bandwidths approaching one terahertz, complementing more conventional measurement techniques [7].

In this presentation, we report on the application of optoelectronic techniques to investigate the internal response and the far-field temporal and spatial characteristics of optically pulsed, frequency-invariant antenna structures. These devices are capable of generating and controlling short duration coherent electromagnetic transients in the microwave and millimeter regions and make ideal instruments for studying and utilizing coherent transient electromagnetic radiation [8]. We can obtain information on a number of internal device parameters such as the propagation velocity, dispersion characteristics, and location and magnitude of impedance discontinuities by performing wide bandwidth time domain reflectometry experiments. Employing picosecond photoconductive sampling methods the termination characteristics or impedance variations within the device can be analyzed with sub-millimeter resolution [9].

We also demonstrate novel measurement techniques in which coherent sampling is used to investigate the transient radiation properties of these antennas in the far-field. In these experiments the temporal response and the spatial profile of the radiation emitted from these devices are measured over a frequency range which extends from less than 10 GHz to greater than 80 GHz. Several advantages can be realized by adopting such an approach. First, the large and expensive anechoic chambers traditionally used to suppress unwanted reflection sources from surrounding structures while performing antenna measurements are no longer necessary. In our approach, the sampling process essentially time-gates the waveform of interest while unwanted secondary signals, due to reflections arriving at the receiver delayed with respect to the primary signal, are rejected. The discrimination of signals reflected from structures within a few millimeters of the devices under test can be easily accomplished using sufficiently short sampling pulses. Another benefit of this method is the ability to perform measurements over a large range of frequencies simultaneously, aiding in the rapid

analysis of frequency-dependent effects through the use of numerical and frequency domain analysis techniques.

2. EXPERIMENT

In these experiments an optical pump/probe arrangement is used to coherently generate and sample ultrashort electrical pulses propagating and radiating from integrated planar antenna structures. A schematic representation of our experimental configuration is illustrated in Figure 1. The structures were fabricated from aluminum films deposited on ion bombarded silicon-on-sapphire substrates using conventional photolithographic techniques. The geometry of these devices is similar to that used in previous experiments and is described elsewhere [8]. They consisted of an integrated photoconductive generator/transmission line attached to a flared section of coplanar strip (CPS) transmission line which functioned as a frequency invariant radiating element. Four sampling gates placed symmetrically along the length of the coplanar feedline provided a means for measuring the temporal characteristics of the pulse propagating along the device.

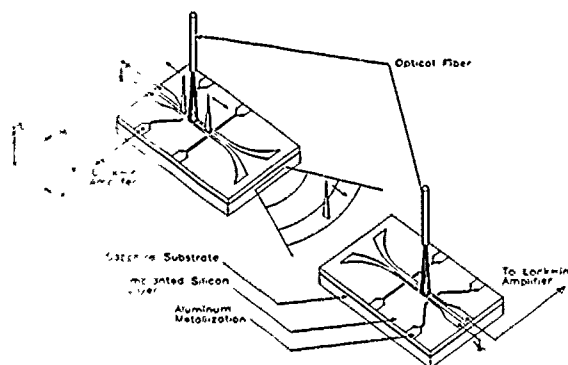


Figure 1. A schematic representation of the experiment. The transmitting antenna radiates a short electrical signal which is received by a second device and photoconductively sampled.

The feedline of the transmitting antenna was dc biased and could be optically shorted with a picosecond laser pulse, via the "sliding contact" method [10], anywhere along its length. This produced a pair of short electrical pulses which propagated in opposite directions along the transmission line as shown

in Figure 1. The lifetime of the free carriers in the semiconductor determined the duration of the electrical pulses and was controlled by high energy ion implantation of the silicon epilayer. In the experiments discussed here, dosages of between 10^{14} to 10^{15} ions/cm² of singly-ionized oxygen atoms were introduced at energies of 100 Kev and 200 Kev. The forward travelling pulse propagated into the antenna region of the device and was subsequently radiated into free-space. The time dependent electric field developed across the gap of the receiving antenna was sampled by illuminating the semiconductor material between the gap with a second picosecond laser pulse. This pulse was derived from the same source as the pump pulse but delayed by a variable time, τ . This resulted in a photo-current induced in the terminals of the receiving device which was directly related to the magnitude of the sampled electric field. By altering the relative path lengths between the pump and probe beams different parts of the waveform were sampled. The temporal dependence of the transmitted signal was mapped out by measuring the change in the average photo-current generated in the receiving device as a function of the delay. The spatial dependence of the far-field radiation patterns was measured by mounting the transmitter on a rotation stage and recording the peak amplitude of the received signal over a range of angles.

The temporal profile of the waveform propagating on the CPS feedline was measured in a similar fashion except that the probe beam was focussed on one of the four sampling gaps located on the transmitter. In this manner it is possible to extract a variety of useful information on device performance such as group velocity, discontinuity location, and dispersive properties. This is accomplished by generating photoconductive transients at several points along the structure and comparing the sampled waveforms.

The source of the ultrashort optical pulses was a mode-locked R6G dye laser in a standard three mirror, astigmatically corrected configuration. The dye laser was synchronously pumped with the frequency doubled output from a CW mode-locked ND:YAG laser operating at 1.06 μ m and a repetition frequency of 100 MHz. These pulses could be continuously tuned in wavelength using frequency selective filters,

with an approximate tuning range of 560 nm to 660 nm. Approximately 15% of the laser output power was diverted to an optical autocorrelator, which used a standard background-free second harmonic generation method to monitor the duration of the laser pulses. The minimum pulse width was measured to be less than 2 ps at a wavelength of 580 nm but could be lengthened by adjusting the cavity parameters. In our experiments, the dye laser cavity was intentionally de-tuned to avoid multiple pulsing which occurred at the shorter cavity lengths. Under these conditions, the typical pulse width measured was approximately 5 ps. The remaining optical energy was divided into two beams as depicted in Figure 1. The first beam was used as the optical excitation or "pump" pulse and generated the photoconductive transient, while the other, sampling or "probe" beam, synchronously detected the voltage induced across the gap of the second device. Each beam was coupled into approximately two meters of single-mode optical fiber which had a core size of 4 μ m. The average optical power in the pump beam was typically 15 mW while a value of approximately 25 mW was measured for the probe beam and a coupling efficiency of nearly 75% was easily obtained. The output of the probe fiber was directed onto the gap of the receiving antenna while the output of the pump fiber illuminated the "sliding contact" gap of the transmitter. The optimum spot size was achieved by adjusting the distance between the device and the fiber. The relative time delay between the pump and probe beams was controlled by mechanically positioning a retroreflector with a computer-controlled stepping motor. The pump beam was mechanically chopped at 2 KHz and a lock-in amplifier was used to detect the sampled photocurrent. The output of the lock-in was digitized and no additional signal averaging of the data was performed.

The radiation pattern measurements were performed by adjusting the relative delay between the pump and probe beams so that a maximum signal was observed on the lock-in amplifier. The transmitting antenna was then rotated by a second stepper motor, while maintaining a fixed time delay between the pump and probe beams. In this manner the peak amplitude of the received signal as a function of pointing angle was determined thereby yielding the

profile of the spatial distribution of the antenna's radiation pattern in the plane of rotation.

3. RESULTS

Correlation traces of the signal propagating along the CPS feedline are shown in Fig. 2 for three different positions of the excitation laser pulse. To facilitate further analysis and eliminate any confusion, the data presented here has been offset in the vertical direction and time-shifted so that the initial peaks coincide. The diagram in the lower half of the figure illustrates the location of the excitation spot for each of the cases shown. The uppermost curve corresponds to the location labeled "pump 1" and for each successive curve the pump beam was advanced toward the antenna region of the device as indicated. The sampled waveforms consisted of an initial short pulse followed by several secondary pulses of increasing duration and decreasing amplitude. The relative positions of these secondary pulses shifted in time with respect to the original transient as the location of the pump spot on the device was altered. This suggests that the source of these additional signals are reflections from discontinuities within the structure.

It is evident that there are three prominent reflection features present in this data which can be easily identified. The first two peaks, which occur less than 100 picoseconds after the main transient, clearly move away from the rear contact as the pump beam is advanced along the structure. These features can therefore be associated with reflections from this general region. The negative peak is the result of the impedance discontinuity encountered when the transient reaches the high impedance-to-low impedance transition of the contact pad while the second peak is a reflection from the SMA connector tab bonded to the pad. These peaks have become stationary with respect to the initial pulse for the final two curves. This is easily explained by noting that as the pump beam is advanced beyond the sampling gate the flight time of the transient from the sampler to the contact region and back remains constant. Therefore, reflections from this region will always occur at a given delay when the excitation point is located in front of the sampler.

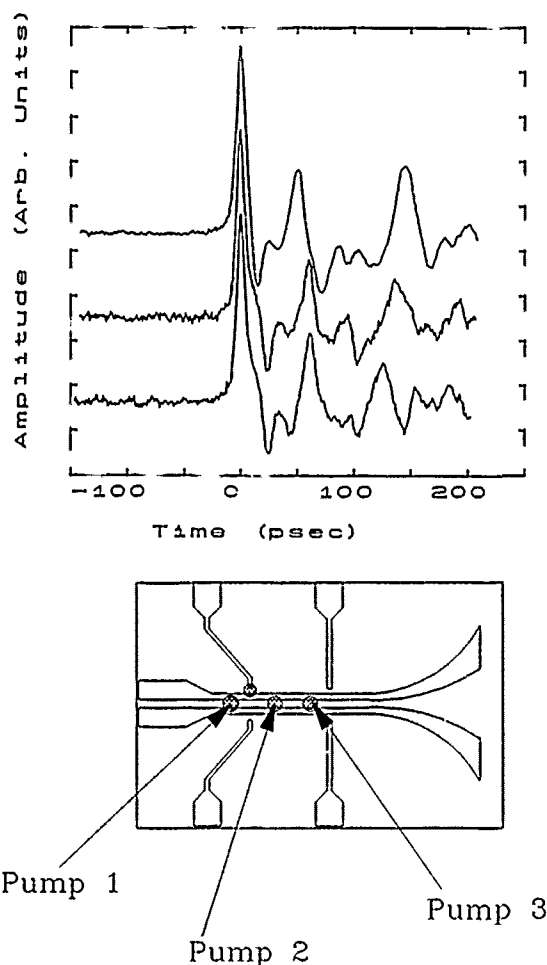


Figure 2. Correlation data of the waveform propagating on the device for several positions of the excitation spot as indicated in the diagram.

The third peak, located at a delay of about 150 picoseconds, can be identified with a reflection from the termination of the radiation structure. As the pump location is moved forward this feature recedes in time to shorter delays reflecting the reduced distance travelled by the initial transient. This feature does not necessarily represent a reflection from an impedance discontinuity but rather a return signal associated with the low frequency cutoff of the antenna. The high frequency content of the initial signal has been radiated into a free-space mode leaving behind the low frequency spectral components. Indeed as would be expected in such a case, the duration of this pulse is significantly longer than that of the initial photoconductive transient.

In Fig. 3, we show a typical radiated signal measured as a

function of time. This waveform consists of a single pulse with "ringing" components which precede and follow the main transient. These features can be attributed to the low frequency roll-off of the antenna's response function. This is a consequence of the requirement that the radiated field amplitude must approach zero as the frequency decreases. An analysis of the amplitude spectrum of the received signal indicates the presence of spectral components with significant amplitude up to at least 80 GHz [9]. The low frequency response falls off below 10 GHz. The value for this cutoff is determined by the maximum dimension of the antenna aperture which, for practical structures, must be truncated at some finite size. The devices used in these experiments had aperture sizes of 10 mm.

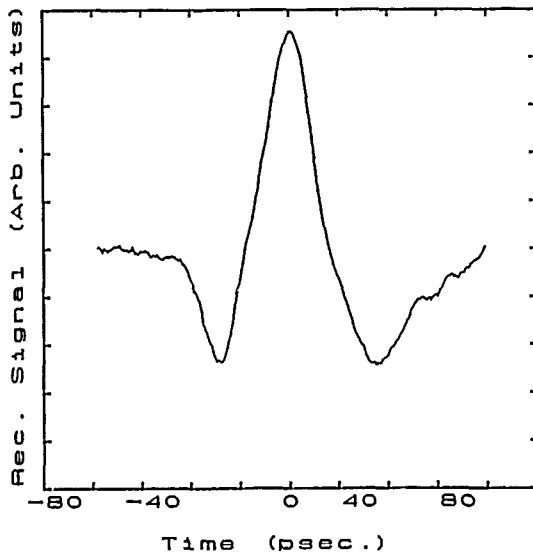


Figure 3. The received waveform with the antennas oriented in an endfire configuration and a separation distance of 36 mm.

In Fig. 4 the dependence of the electric field amplitude in the far-field as a function of direction angle is plotted for the two principle planes. In both cases a zero degree angle corresponds to an endfire orientation. In the E-plane, shown in Fig. 4a, the radiation is emitted in a single "gaussian-like" central lobe with the maximum oriented in the endfire direction. The field amplitude in the E-plane was not measured for angles beyond 90 degrees because the antenna mounting apparatus prevented rotation of the device in this region. For this particular structure the half-power

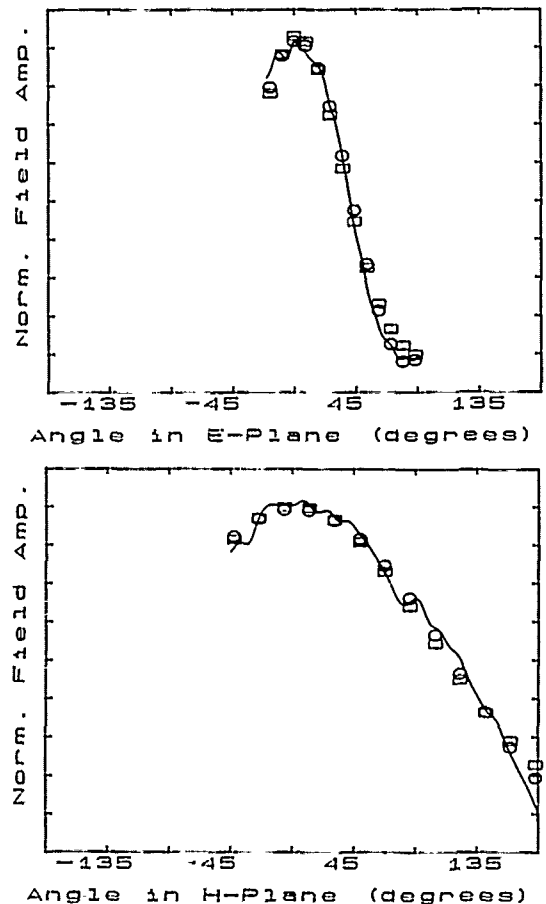


Figure 4. The far-field radiation patterns for the two principle planes. For both cases a gaussian and cosine-squared distribution fit was performed.

a). The E-Plane pattern: The solid trace represents the experimental data while the squares and circles indicate a gaussian and cosine-squared dependence respectively.

b). The data for the H-Plane.

beamwidth (HPBW), assuming a symmetric radiation pattern, is determined to be approximately 62 degrees. This result is indicative of the good directive characteristics for this particular type of antenna geometry. In this experiment the separation between transmitting and receiving antennas was 36 mm. The H-plane pattern is illustrated in Fig. 4b. In this case the antenna separation was approximately 87 mm. Although the signal-to-noise ratio is poor we can still make several observations regarding this data. The distribution of the radiation is much broader in this plane and is slightly asymmetric about the endfire

direction. The beamwidth for this plane is estimated to be 150 degrees. Such a broad spatial extent implies that the distribution of the excitation field in the antenna region is highly localized. The qualitative features of this data are consistent with the general properties of frequency-invariant antenna designs [11].

The measured far-field profiles for both planes were compared to a pair of analytical expressions whose parameters were determined using a least-squares fitting algorithm. These results are also indicated in Fig. 4, the open squares indicating a gaussian fit and the circles representing a cosine-squared dependence. From this graph it is clear that the cosine-squared distribution provides a better overall fit with the observed data particularly for extreme angles away from the endfire direction. A simple equation relating the half-power beamwidths to the directivity or gain of an antenna is given by [12]:

$$G_0 = eD_0 = e \cdot 4\pi / Q_1 Q_2 \quad (1)$$

Where Q_1 and Q_2 are the HPBW angles for the principle planes expressed in radians, e is the antenna's radiation efficiency, and G_0 and D_0 are the gain and directivity respectively. Assuming a radiation efficiency of one, we can establish an approximate value of 5 dB for the gain of our devices. This result is based on the HPBW angles calculated from the curve-fit solutions.

4. CONCLUSION

In conclusion, we have described a versatile technique for measuring the transient far-field radiation properties of integrated optoelectronic antennas using coherent photoconductive sampling. This approach allows both the temporal and spatial characteristics of the transient radiation to be studied in the far-field and should prove to be a useful technique for investigating radiative effects from a variety of picosecond electronic devices. The devices which we have reported on here radiate short electrical pulses with frequency components that extend from approximately 5 GHz to greater than 80 GHz. We have observed that the radiation emitted from these devices forms an "ellipsoidal" far-field pattern with no evidence of secondary sidelobes over the range of angles

investigated. In addition we have analyzed the internal response of these devices and identified the primary reflection sources within the structure. We are currently working on extending the frequency spectrum of the photoconductively generated electrical transients and expect to obtain radiated signals with significant spectral components in the frequency span between 5 GHz and 200 GHz. Additional experiments are underway to further characterize and model the radiation and propagation properties of these broadband antennas.

5. ACKNOWLEDGMENTS

This work was supported by the Air Force Office of Scientific Research under grant number AFOSR-84-0377. Additional support was provided by the National Science Foundation under grant number NSF ECS-8404495.

REFERENCES

- [1]. D. R. Grischkowsky, M. B. Ketchen, C-C. Chi, I. N. Duling, N. J. Halas, J.-M. Halbout, and P. G. May, IEEE J. Quantum Electron., 24, 221, (1988)
- [2]. Y. Pastol, G. Arjavalingam, J.-M. Halbout, and G. V. Kopcsay, Appl. Phys. Lett., 54, 307, (1989)
- [3]. C. R. Lutz, and A. P. DeFonzo, Proc. SPIE, Vol. 947, 85, Newport Beach, Ca., Mar 15, 17, (1988)
- [4]. Ch. Fattering and D. Grischkowsky, Appl. Phys. Lett., 53, 1480, (1988)
- [5]. D.H. Auston, K.P. Cheung, and P.R. Smith, Appl. Lett., 45, 284, (1984).
- [6]. J. R. Karin, P. M. Downey, and R. J. Martin, IEEE J. Quantum Electron., 22, 677, (1986)
- [7]. D. Grischkowsky, I. N. Duling, J. C. Chen, and C-C. Chi, Phys. Rev. Lett., 59, 1663, (1987)
- [8]. A. P. Defonzo and C. R. Lutz, Appl. Phys. Lett., 51, 212, (1987)
- [9]. C. R. Lutz and A. P. Defonzo, (unpublished)

- [10]. M. B. Ketchen, D. R. Grischkowsky, T. C. Chen, C-C. Chi, I. N. Duling, N. J. Halas, J. -M. Halboul, J. A. Kash, and G. P. Li, Appl. Phys. Lett., 48, 751, (1986)
- [11]. C. A. Balanis, Antenna Theory Analysis and Design, Harper & Row, New York, 1982, pp 413-445
- [12]. J. D. Kraus, Antennas, McGraw-Hill, New York, 1950, p. 25

Ultrafast Optical Switching through Virtual Charge Polarization in dc-Biased Quantum-Well Structures

Masamichi Yamanishi

Hiroshima University, Saijyocho, Higashihiroshima 724, Japan

ABSTRACT

An extremely fast modulation of optical properties based on internal field screening due to virtual charge polarization in a dc-biased or built-in asymmetric quantum well structure is discussed with description of relevant optical nonlinearities caused by the virtual charge polarization. A possible device characteristic for electro-static ultrafast switch of quantum interference current through the virtual charge polarization is briefly described, as an application of this modulation scheme to ultrahigh speed optoelectronic devices.

INTRODUCTION

Field-induced modulation of optical properties of quantum wells (QWs) termed quantum confined Stark effect [1] has been attracting a great deal of attention on its uses in high speed optoelectronic devices. The intrinsic response time of the optical properties for the electric field is expected to be extremely short, less than picosecond, determined by coherence dephasing time (T_2 -time) for resonance condition or inverse of detuning frequency ($1/\Delta$) for off-resonance condition. However, in actual cases, the switching time of the devices is limited by modulation speed in the applied field, i.e., by a $C \cdot R$ time constant because the field is controlled by an external voltage. In order to break through the above-mentioned limit on the switching speed, a new modulation scheme based on internal field screening due to virtual pairs excited by an off-resonant light in a dc-biased (or built-in asymmetric) QW has been proposed and discussed by Yamanishi [2] and by Chemla et al.[3], independently of each other. The switching time of this modulation scheme is expected to be short and free from the $C \cdot R$ time constant and from carrier life time. In this paper, we will discuss the extremely fast modulation scheme, named virtual charge-induced optical nonlinearity (VCON) [2], primarily concerned with second order process, i.e., optical rectification, with some comments on the uses of the VCON in ultrahigh speed devices.

VIRTUAL CHARGE-INDUCED OPTICAL NONLINEARITIES

In a dc-biased or built-in asymmetric QW, a net charge polarization would be induced by virtual excitations caused by an off-resonant pump light with a photon energy $\hbar\omega_p$ far below the fundamental excitonic gap of the QW, E_{1e-1h} . The induced virtual charge polarizations may partially screen the original field E_0 , resulting in a decrease E_s of the internal electric field [2,3]. The virtual excitations can last only during the pump light ON period and do not participate in any relaxation process [4,5]. In fact, the virtual population can follow the pump pulse with an intrinsic response time approximately the inverse of the detuning frequency $1/\Delta_{1e-1h}$ where $\Delta = E_{1e-1h}/\hbar - \omega_p$. Also, the field cancellation directly results from the internal charge inside the QW. Therefore, the modulation speed of the internal field is not limited by the recombination life time and $C \cdot R$ time constant.

The charge polarization consists of two kinds of components [6]. As shown in Fig.1, first components (diagonal components) can be written for example, for the lowest exciton (1e-1h exciton) in the presence of an electric field perpendicular to the QW plane,

$$P_z = (-e) \int z \left\{ |\psi_{1e}(z)|^2 - |\psi_{1h}(z)|^2 \right\} dz \cdot N_{1e-1h} \quad (1)$$

where $\psi_{1e}(z)$ and $\psi_{1h}(z)$ are the wavefunctions for the lowest subbands in the conduction and valence bands, respectively, and N_{1e-1h} is the excited virtual pair density given by the transition dipole moment of the exciton μ_{1e-1h} , the optical field amplitude E_p and the detuning frequency Δ_{1e-1h} .

$$N_{1e-1h} \propto \mu_{1e-1h}^2 E_p^2 / \Delta_{1e-1h}^2 \quad (2)$$

Second components (nondiagonal components) can be described as follows. In the dc-biased or built-in asymmetric QW, $\Delta n=0$ selection rule may break. As a result, for example, two electrons at two quantum states

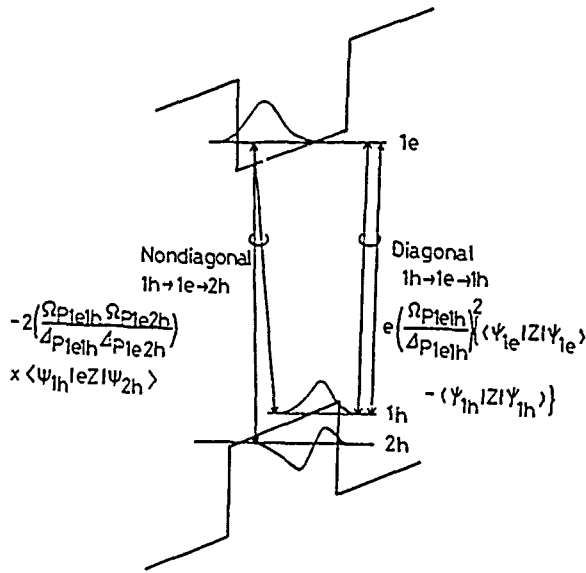


Figure 1. Energy band diagram of QW biased by a dc-electric field. The diagonal and nondiagonal contributions to the virtual charge polarization are illustrated.

in the valence subbands, $1h$ and $2h$ would be coherently excited to a common quantum state in the conduction subband, $1e$. In other words, a hole at a quantum state in the conduction subband $1e$ would be coherent excited to two quantum states in the valence subbands $1h$ and $2h$. This kind of virtual transition may result in the nondiagonal virtual charge polarization,

$$P'_z = (-e) \int \psi_{1h}(z) \psi_{2h}(z) dz \cdot N'_{1h-2h} \quad (3)$$

where

$$N'_{1h-2h} \propto -2\mu_{1e-1h} \cdot \mu_{1e-2h} E_p^2 / \Delta_{1e-1h} \cdot \Delta_{1e-2h} \quad (4)$$

Unfortunately, the nondiagonal components may cancel more or less the diagonal contributions. The over-all polarization can be written as a summation over all the subbands.

Figure 2 shows the numerical result [7] on the averaged screening field E_s (depolarization field), i.e., (the over-all polarization / dielectric constant) estimated with equations (10) and (11) in ref.[6], taking account of the diagonal and nondiagonal contributions. The summation of the diagonal contributions (dashed line) shows a slow tailing with the detuning energy, approximately proportional to the inverse of the detuning energy. As a result, the over-all screening field E_s (solid line) can be fitted by a curve, inversely proportional to the squared detuning energy in spite of the cancellation due to the nondiagonal components. Actually, the detuning energy dependence of the screening field is pretty close to that of contribution of only $1e-1h$ excitons for a GaAs QW with a typical thickness $L_z=120\text{\AA}$ in the presence of a typical electric field, $E_0=80\text{ kV/cm}$, perpendicular to the QW plane.

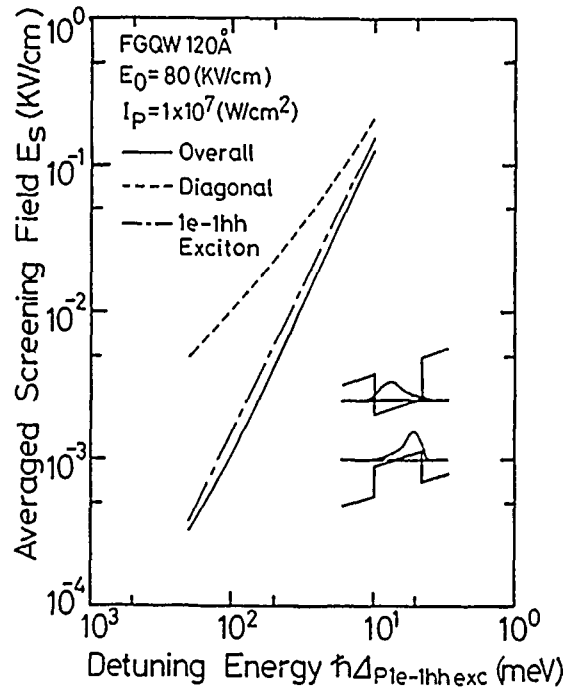


Figure 2. Estimated contributions to screening field E_s as functions of detuning energy in a GaAs QW with a thickness L_z , 120\AA , biased by an electric field E_0 , 80 kV/cm and pumped by an off-resonant light with a power density I_p , $1 \times 10^7 \text{ W/cm}^2$ [7].

This is quite interesting and favorable to our purpose. The field screening due to virtual charge polarization in the QW is proportional to the squared inverse of the detuning energy whereas an optical absorption tail below the excitonic gap is generally described by an exponential function, i.e., $\exp(-\hbar\Delta_{1e-1h}/E)$. Therefore, the virtual processes dominate over the real ones as the detuning energy increases.

The above-mentioned field screening, i.e., optical rectification is described by a second order nonlinear susceptibility $\chi^{(2)}_{zxx}(0;\omega_p, -\omega_p)$ which is estimated to be $5 \times 10^{-3} [\text{esu}]$ for a detuning energy with respect to $1e-1h$ exciton, 15 meV in a GaAs/AlAs QW with a thickness L_z , 120\AA biased by an electric field perpendicular to the QW plane, 80 kV/cm [7]. The value for $\chi^{(2)}_{zxx}(0;\omega_p, -\omega_p)$ in the biased QW is much larger than those due to non-centro symmetry of atomic orientation in bulk GaAs crystals. Refractive index and absorption coefficient would be changed with the internal field modulation. This is illustrated by a third order nonlinear coefficient $\chi^{(3)}_{xxxx}(\omega_p, \omega_p, -\omega_p, \omega_p)$ which is expected to be $\sim 10^{-9} [\text{esu}]$ in a GaAs QW with a thickness L_z , 100\AA , biased by a perpendicular electric field, 60 kV/cm and pumped by an off-resonant light with a detuning energy, 10 meV [6].

VOLTAGE PULSE GENERATION AND CONTROL OF QUANTUM INTERFERENCE CURRENTS

One of the most striking features of this modulation scheme is a possibility of generation of ultrashort voltage

pulses in a diode exhibiting multiple quantum well (MQW) structure [3]. The generation mechanism of voltage pulses is described as follows [8]. When the diode biased by an external voltage is pumped by an off-resonant light with a sub-picosecond pulse width, one can expect partial screening of the electric field, due to virtual charge polarizations, in each QW. The screening can appear and vanish in sub-picosecond regime, resulting in a pulsive change in the capacitance of the diode. In general, the $C \cdot R$ product consisting of the diode capacitance and the series resistance should be much longer than subpicoseconds. As a result, electric charges $\pm Q$ at terminal electrodes of the diode could not respond to such a quick change in the capacitance. Therefore, one may expect a modulation of the voltage across the terminal electrodes. The modulation depth of the voltage during the pump pulse ON-period is approximately written by,

$$\delta V = (E_s L_z) N$$

where E_s , L_z and N are the screening field (depolarization field), the thickness of the QWs and the period of the MQW. Thus, one may generate an extremely short voltage pulse of which width could be much shorter than the $C \cdot R$ time constant. In this view, the modulation scheme for voltage pulse generation can be regarded as free from the $C \cdot R$ time constant. For example, a voltage pulse, ~ 4 mV in a diode involving 50 period MQW structure with a QW thickness L_z , 120 Å, biased by an electric field, 80 kV/cm would be generated with pump light with pump power density I_p , 10 MW/cm² and with a detuning energy, 15 meV. In fact, very recently, such a short (~ 180 femtosecond) voltage pulse has been generated in a GaAlAs MQW structure pumped by an off-resonant light at 250 K although the MQW has been biased by a low electric field, ~ 10 kV/cm parallel to the MQW plane [9].

A possibility of ultrafast electro-static control of quantum interference currents through the voltage pulse generation has been discussed, showing possible operating characteristics such as a switching time, 1 psec and a small power delay product, 200 femtojoule for a specific device structure [4]. Particularly, it should be noted that *many devices stacked and/or integrated on a single chip could be simultaneously driven by a single pump pulse because the virtual process is in principle loss free* [4,5,8]. This is an important advantage of this kind of modulation schemes based on virtual excitations over those on real ones.

The modulation scheme discussed in this paper may open up entirely new opportunities in ultrahigh speed optoelectronics. However, there has been a quite few experimental results on this modulation scheme [9,10]. More experimental efforts regarding this aspect are crucially important to make our knowledge abundant.

ACKNOWLEDGMENTS

The author would like to express his thanks to Prof. Osaka and M.Kurosaki, Hiroshima University, T.Hiroshima, NEC Co. and Prof. S.Datta, Purdue University for their collaboration and fruitful discussions. The work performed at a group of the author was partially supported by a Scientific Research Grant-In-Aid (Project No.61065006) for Specially

Promoted Research from the Ministry of Education, Science and Culture of Japan.

REFERENCES

1. For a review, see D.A.B.Miller, D.S.Chemla and S.Schmitt-Rink, in Optical Nonlinearities and Instabilities in Semiconductors, H.Haug, ed. (Academic, Orlando, 1988) Chap. 13, pp.325-359.
2. M.Yamanishi, "Field-induced optical nonlinearity due to virtual transitions in semiconductor quantum-well structures," *Phys. Rev. Lett.*, **59**, 1014-1017 (1987).
3. D.S.Chemla, D.A.B.Miller and S.Schmitt-Rink, "Generation of ultrashort electrical pulses through screening by virtual populations in biased quantum wells," *Phys. Rev. Lett.*, **59**, 1018-1021 (1987).
4. M.Yamanishi, M.Kurosaki, Y.Osaka and S.Datta, "Ultrafast control of quantum interference currents by virtual charge polarizations in biased quantum well structures," in Proc. 6th Int. Conf. Ultrafast Phenomena, T.Yajima, K.Yoshihara, C.B.Harris and S.Shionoya, eds. (Springer-Verlag, Mt. Hiei, 1988), pp.334-336.
5. M.Yamanishi, "Real and virtual charge polarizations in dc biased low-dimensional semiconductor structures," to be published in Proc. NATO workshop on Optical Switching in Low Dimensional Systems H.Haug and L.Banyai, eds. (Marbella, Spain, 1988).
6. T.Hiroshima, E.Hanamura and M.Yamanishi, "Exciton-exciton interaction and optical nonlinearity in biased semiconductor quantum wells," *Phys. Rev. B*, **38**, 1241-1245 (1988).
7. M.Yamanishi and M.Kurosaki, unpublished.
8. M.Yamanishi, "Ultrafast modulation of quantum states by virtual charge polarization in biased quantum well structures," to be published in Proc. 4th Int. Conf. Superlattices, Microstructures and Microdevices (Trieste, Italy, 1988) : J.Superlattices and Microstructures, J.W.Dow, ed. (Academic Press).
9. W.H.Knox, J.E.Henry, B.Tell, K.D.Li, D.A.B.Miller and D.S.Chemla, "Femtosecond excitonic electroabsorption sampling," presented at topical meeting on Picosecond Electronics and Optoelectronics, (Salt Lake City, 1989) paper No. ThC5-1.
10. H.Q.Le, J.V.Hryniewicz, W.D.Goodhue and V.A.Mims, "Optical nonlinearities in $\text{Al}_x\text{Ga}_{1-x}\text{As/GaAs}$ asymmetric coupled quantum wells," *Optics Lett.* **13** 859-861 (1988).

.

;

Part 7
Digest Summaries

High-Frequency Laser Modulation by Robert Olshansky

**GTE Laboratories Incorporated
40 Sylvan Road
Waltham, MA 02254**

Summary

The commercial application of high speed laser diodes and modulators to lightwave systems is restricted by the limited availability of time-division multiplexing (TDM) circuitry at data rates above 2 Gb/s. The multiplexing of modulated microwave subcarriers is a promising new approach for circumventing this TDM bottleneck and for exploiting the full bandwidth capability of lightwave components.

In a subcarrier multiplexed (SCM) lightwave system, a composite microwave signal is formed by power combining signals from a number of modulated microwave subcarriers. The composite signal can then be used to intensity modulate a high speed laser or an external modulator.

Previously published results have shown that SCM techniques can be used to transmit 120 FM video signals in the 2.8-7.6 GHz band [1], 20 subcarriers in the 2-6 GHz band, each frequency-shift-keyed (FSK) at 100 Mb/s [2], and 2 Gb/s on a single PSK subcarrier[3].

This paper will discuss the extension of SCM techniques to the following areas:

(1) Coherent Transmission of SCM Signals

SCM transmitter electronics can be directly used to drive an external phase modulator for coherent phase-modulated (PM) transmission. After coherent heterodyne detection the transmitted signals can be recovered using the same SCM receiver electronics previously reported for direct detection systems [4].

(2) Multigigabit Direct Detection SCM Systems

By using quadrature-phase-shift-keying (QPSK) efficient bandwidth utilization can be achieved, and 3-4 Gb/s can be transmitted on an individual subcarrier. Using multiple subcarriers, QPSK-SCM systems operating above 8 Gb/s can be built.

(3) Direct Detection with Optical Preamplifiers

Since SCM systems rely on conventional low noise microwave amplifiers with input noise currents of $12 \text{ pA}/\sqrt{\text{Hz}}$ or higher, significant improvement in receiver sensitivity can be achieved using optical preamplifiers. Simple formulae for the improvement in receiver sensitivity will be presented. As an example, the receiver sensitivity of an 8 Gb/s QPSK-SCM system can be improved 8 dB to -30 dBm by using a semiconductor optical preamplifier. A receiver sensitivity of -37 dBm can be achieved with an erbium-doped fiber preamplifier.

This paper will show that subcarrier multiplexing represents an extremely promising alternative to conventional baseband signalling, and provides a versatile approach for exploiting the full bandwidth potential of lightwave technology.

References

- [1] R. Olshansky, P. Hill and V. Lanzisera, Eur. Conf. on Opt. Comm., p. 143, Sept. 11-15, 1988.
- [2] P. Hill and R. Olshansky, Electron. Letts., 24, p. 892, 1988.
- [3] J. Bowers, Electron. Letts., 22, p. 1119, 1986.
- [4] R. Gross, R. Olshansky, and P. Hill, Opt. Fiber Commo. Conf., Houston, TX, Feb. 6-9, 1988.

RECENT DEVELOPMENTS IN HIGH- T_c SUPERCONDUCTING FILMS AND DEVICES

R. A. Buhrman
School of Applied and Engineering Physics
Cornell University
Ithaca, N.Y. 14853-2501

The discovery of high temperature superconductivity (HTS) has created the opportunity for major extensions of current electron device applications of superconductivity, including opening up the possibility of integration of superconductivity with semiconductor devices. However, due to the difficult nature of the presently known HTS materials, the actual realization of this opportunity faces severe challenges. In this talk I will describe recent advances in, and current prospects for, the production of high quality, well-oriented HTS films with acceptable superconducting properties on technologically useful substrates, both insulating and semiconducting. Emphasis will be given to the discussion of new and improved techniques for the lower temperature growth and in-situ formation of the superconducting phase. The stability of current HTS materials will be discussed. I will also report on successful techniques for the formation of very low resistance contacts to HTS films and for the patterning of epitaxial films to micrometer, and possibly submicrometer, dimensions. The most recent results on the microwave and millimeter wave surface losses of high quality HTS material will be presented, as well as results on picosecond pulse propagation experiments on transmission lines formed from epitaxial HTS films.

Optical Detection of Resonant Tunneling of Electrons in Quantum Wells

by

G. Livescu,* A.M. Fox, T. Sizer, W.H. Knox and D.A.B. Miller

AT&T Bell Laboratories, Holmdel, NJ 07733

The investigation of vertical transport in superlattices (SL's) and multiple quantum wells (MQW's) has recently attracted much attention. Intense research was focused on basic quantum effects such as Bloch transport of electrons and holes in minibands,¹ coherent and incoherent, resonant, sequential and Zener tunneling² in double barriers,^{3,4} SL's and MQW's of GaAs/AlAs,^{5,6} GaAs/AlGaAs,⁷ and InGaAs/InP.^{2,8} In addition to the academic interest, the understanding of the mechanisms of escape from and travel through quantum wells is vital for the recently developed and constantly growing family of electro-optical devices using semiconductor quantum wells. Most of them are based on the quantum-confined Stark effect (QCSE), and they include bistable self-electro-optic effect devices (SEED's), tunable detectors, electro-absorption modulators and optical logic elements.⁹ The basic unit of all of these is an epitaxially grown p-i-n diode, with the quantum well layers in the intrinsic region. By reverse biasing the diode, an electrical field is applied on the quantum wells, controlling its optical absorption spectrum. Since operating wavelengths are close to the excitonic absorption peaks, photoexcited charge is created in the quantum wells and is transported to the electrodes. The mechanisms by which this transport occurs are ultimately responsible for the intrinsic maximum speed or operating intensity of these devices.

The techniques used to investigate the dynamics of the photoexcited carriers have included transport (static^{2,4-6} and time-resolved⁴⁻⁶ photocurrent) as well as optical experiments (static^{5,7,8} and time-resolved^{1,3} photoluminescence, as well as time-resolved electroabsorption^{10,11}). For the present work we chose the latter method, in which the picosecond pump-and-probe technique is used to study the photoexcited carrier escape rate, through the voltage changes induced on the electrodes upon their arrival. We find that the rise time of the induced change in absorption is extremely sensitive to the applied DC voltage, varying between 400 ps at low voltages and 25 ps at high voltages. It also exhibits a pronounced minimum at an intermediate voltage, for which the $n=1$ electron level in one quantum well is in resonance with the $n=2$ electron level in the adjacent one.

The sample used was a p-i-n structure grown by MBE, containing in its intrinsic region 75 periods of 65Å/58Å GaAs/Al_{0.26}Ga_{0.74}As quantum wells. Using photolithographic techniques, contacts were made to the doped regions, with 200µm×200µm windows on the p side. The samples were antireflection coated and the substrate was etched away. The transmission spectrum at room temperature (Fig. 1) exhibits the excitonic peaks associated with the allowed $n=1$ and $n=2$ transitions. By applying a voltage (e.g. 10V, as in Fig.1), the allowed peaks shift to lower energy and broaden, while new peaks appear, associated with the forbidden transitions. The shift of the $n=1$ (heavy hole) hh and (light hole) lh excitonic peaks could be followed up to an applied voltage of 30 V (the breakdown voltage was 38V), and were found to be in reasonable agreement with those predicted by the QCSE theory.

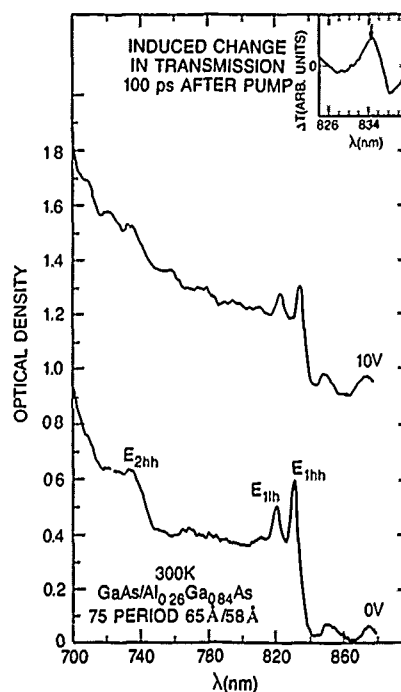


Fig.1. Absorption spectra of the MQW p-i-n modulator (vertically shifted for clarity). Inset: differential transmission at 10 V and 100 ps after the pump. Arrow: wavelength used for time-resolved measurements at 10 V.

For the time-resolved measurements we used a conventional pump-and-probe arrangement, exciting the photocarriers with a short laser pulse (pump), and monitoring the induced transmission changes with a second, time delayed pulse (probe). Both beams were derived from the same synchronously pumped Styryl 9 dye laser (6-10 ps pulse width, 780-870 nm tuning range). The geometry of the measurements is described in more detail elsewhere.¹¹

The two beams were focused to $\sim 25\mu\text{m}$ diameter spots coincident on the sample. The average optical powers were kept relatively low: 20-50 μW (0.24-0.6 pJ per pulse) for the exciting beam, and 5 μW for the probe. The number of photoexcited carriers per pulse was $(2-5)\times 10^{15}\text{cm}^{-3}$. The carriers are created in *all* the wells throughout the sample, although their concentration becomes somewhat smaller as the exciting beam exits the sample. The carriers are generated with very small kinetic energy near the lowest allowed confined level. They are separated by the field, escape from the quantum wells and are swept towards the electrodes. Upon their arrival there (after a time τ) a voltage pulse ΔV is generated on the electrodes, which reduces the bias across the diode locally in the region of the spot, thereby inducing a change in the absorption, through the QCSE. We detected the changes in the intensity of transmitted probe using standard lockin techniques (the pump beam was chopped at 1.5 kHz). An example of the signal one obtains is shown in the inset of Fig. 1. Represented here is $-\Delta T$ (where ΔT is the change in transmission) as a function of wavelength, 100 ps after the exciting pulse. This signal is proportional to $\Delta\alpha$, and its shape indicates a blue shift of the E_{1hh} exciton ($\Delta\alpha < 0$ at long wavelengths), as well as an increase of the peak absorption ($\Delta\alpha > 0$ at shorter wavelengths). A similar, but weaker, signal is obtained also for wavelengths around the E_{hh} exciton. The differential absorption spectrum changes with the applied bias, because of the shift of the excitonic peaks. Therefore, when measuring the time dependence of $\Delta\alpha$ we always chose the wavelength corresponding to the largest positive $\Delta\alpha$ at that voltage. The magnitude of $\Delta\alpha$ is roughly proportional to ΔV , which, in turn, is determined by the total number of photoexcited carriers, thus by the power of the exciting beam. We have checked this proportionality over more than one order of magnitude. One can actually calculate ΔV (thus $\Delta\alpha$) for any exciting power; but the values obtained are at least one order of magnitude larger than the measured ones. We have shown in our previous work¹¹ that the reason for obtaining small $\Delta\alpha$ lies

in the *fast recovery* of the initial voltage, or, in other words the *fast decay* of ΔV in the region of the exciting spot. This is due to the fact that ΔV quickly spreads over the area of the electrodes through a mechanism of diffusive electro-magnetic propagation. The diffusive time constant t_c is determined by the resistivity of the electrodes, the thickness of the intrinsic region of the diode, and the size of the exciting spot. For our sample and spot size, $t_c \sim 5$ ps. The magnitude of ΔV (hence $\Delta\alpha$) is thus the result of these competing processes: the build-up of the voltage pulse at the electrodes during a time τ , and its decay, with a time constant t_c . For $\tau \gg t_c$, ΔV will be much smaller than estimated; it increases for smaller values of τ . This is illustrated in Fig. 2, where the time dependence of the signal is plotted, for different values of τ . The experimental curves were measured at different applied voltages, but are normalized to the same exciting power, and the same value of the absorption coefficient. The dotted curves in Fig. 2 are calculated, using the diffusion model described before,¹¹ with a single set of parameters. Only the "transit times" τ (or "emission rates") are different for each curve, definitely proving that the faster rise time is always associated with a larger signal.

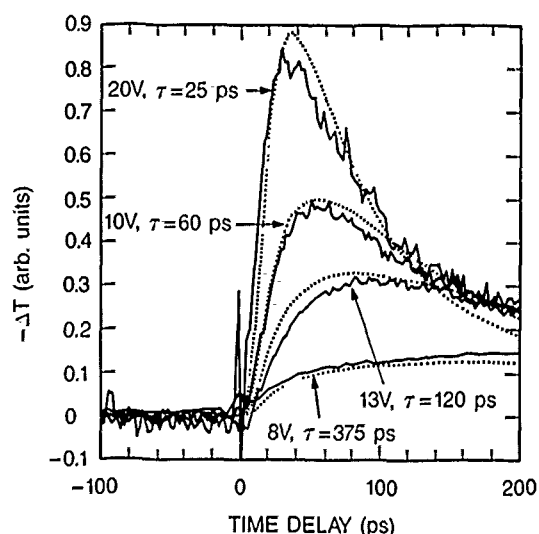


Fig.2. Differential transmission at different applied voltages, vs. time delay after excitation. Full lines: experimental. Dotted lines: calculated.

Our main emphasis in this work is the measurement of the rise times and their dependence on the applied voltage. A key result of our experiment is that the rise times do not depend monotonically on voltage (Fig. 2). We have repeated these measurements over a wider voltage range and in smaller voltage steps, and the results are plotted in Fig. 3. A sharp decrease of the rise times with increasing voltage is observed, with a clear minimum around 10.5V. The tunneling probability of a particle of mass m^* through a square potential barrier of height E_b and width L_b has the form $\exp[-(8m^*E_b/\hbar^2)^{1/2}L_b]$. In the presence of an applied field, the barriers become triangular, with an effective thickness proportional to $1/F$ (F = the applied field). Therefore, a strong increase of the tunneling probability is expected for larger applied fields, i.e. a sharp overall decrease of the "escape time" of the particles. Since the tunneling probability of the electron is about 500 times larger than that of a heavy hole, the electrons are the ones expected to tunnel. The presence of the minimum shows that resonant tunneling occurs, and its position is in agreement with the calculated "alignment" of the $n = 1$ electron level in one well with the $n = 2$ level in the adjacent well. However, the relatively large value of $\tau = 50$ ps cannot be compared with any of the calculated tunneling times. Once a carrier is in the conduction band, it only needs ~ 10 ps to traverse the whole structure at the saturated drift velocity. Assuming sequential tunneling, and assuming that an electron is recaptured in the next well after each successful escape attempt, one may divide this time by the 75 periods, to obtain 0.7 psec, which is a number closer to some theoretical estimates. More work is needed, however, to clarify the nature of this resonance, and the times associated with it. Preliminary low temperature (80K) measurements indicate that the rise times do not become longer, which strongly suggests that the dominant escape mechanism of the carriers is tunneling through the barriers, rather than thermionic emission, as previously proposed.^{10,12}

In conclusion, our time-resolved electroabsorption measurements in a GaAs/AlGaAs p-i-n MQW diode suggest that the main escape mechanism of the photoexcited carriers is tunneling. By studying the dependence of the "sweep out" time on applied bias, we find evidence for resonant tunneling of electrons.

Our thanks are due to A.C. Gossard and J.H. English for the growth of the sample, to F. Beltram for illuminating discussions on resonant tunneling,

and to D. Oberli for sharing with us results of his most recent work on picosecond time resolved luminescence in GaAs/AlGaAs QW's.

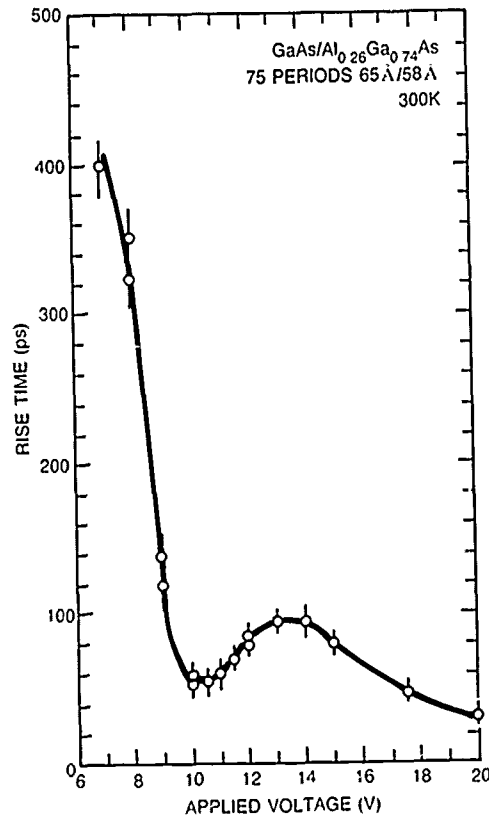


Fig.3. Differential transmission rise time vs. applied voltage.

REFERENCES

- Present address: AT&T Bell Laboratories, Murray Hill, NJ 07974.
- 1. B. Deveaud, J. Shah, T. C. Damen, B. Lambert and A. Regreny, Phys. Rev. Lett. **58**, 2582 (1987).
- 2. See the reviews in IEEE J. of Quantum Electron. **22** (1986) by E. Esaki (p. 1611) and F. Capasso, K. M. Mohammed, and A. Y. Cho (p. 1853).
- 3. M. Tsuchiya, T. Matsusue and H. Sakaki, Phys. Rev. Lett. **59**, 2356 (1987).
- 4. K. K. Choi, B. F. Levine, C. C. Bethea, J. Walker and R. J. Malik, Phys. Rev. Lett. **59**, 2459 (1987).

5. S. Tarucha and K. Ploog, *Phys. Rev. B* **38**, 4198 (1988).
6. H. Schneider, K. von Klitzing and K. Ploog, to be published in *Superlattices and Microstructures* (1989).
7. Y. Horikoshi, A. Fischer and K. Ploog, *Phys. Rev. B* **31**, 7859 (1985).
8. R. Sauer, K. Thonke, W. T. Tsang, *Phys. Rev. Lett.* **61**, 609 (1988).
9. For a recent review of electro-absorption devices see D. A. B. Miller, *Opt. Eng.* **26**, 368 (1987), and G. Livescu and D. A. B. Miller, in "Spatial light modulators and applications II", SPIE, vol.825, p.69 (1987).
10. R. J. Manning, P. J. Bradley, A. Miller, J. S. Roberts, P. Mistry, M. Pate, *Electronic Letters* **24**, 854 (1988).
11. G. Livescu, D.A.B. Miller, T. Sizer, D.J. Burrows, J.E. Cunningham, A.C. Gossard and J.H. English, submitted to *Appl. Phys. Lett.*
12. A. Larsson, P.A. Andrekson, S.T. Eng and A. Yariv, *IEEE J. Quantum Electron.* **24**, 787 (1988).

Optical Evidence of Charge
Accumulation in Double-Barrier Diodes

N.VODJDANI, E.COSTARD, F.CHEVOIR, D.THOMAS, D.COTE, P.BOIS, S.DELAIRE
THOMSON-CSF LCR, Domaine de Corbeville, BP 10
91401 ORSAY Cedex, FRANCE

Tunneling is one of the basic quantum mechanical phenomena which play a key role in many ultra thin semiconductor devices. Besides their potential for applications, double barrier heterostructures are also interesting for the understanding of tunneling-based transport processes (1) and their dynamics. Time-resolved photoluminescence (PL) has been used to determine the tunneling escape rate of electrons from a single quantum well through a thin barrier into a continuum (2) and to determine the electric field dependance of this tunneling rate (3). The charge accumulation in the quantum well can be estimated using magnetotunneling (4) or steady-state photoluminescence (5) as recently demonstrated.

In this work, we present optical studies on Double barrier diode "DBD" samples with large undoped spacer layers on each side of the barriers which are thought to be useful for high frequency operation (6). The increase of the photoluminescence intensity evidences steady-state electron accumulation in the QW and at the same time we observe a crossed optical transition which can occur either between electrons in the collector and holes trapped against the collector side barrier or electrons accumulated against the emitter barrier and holes located in a trough in the emitter.

The sample was grown by molecular beam epitaxy on a $3 \times 10^{18} \text{ cm}^{-3}$ silicon doped substrate and consisted of the following layers : 300 nm GaAs n^+ (10^{18} cm^{-3}) buffer layer, 20 nm non-intentionally doped (nid) spacer, 10 nm (nid) $\text{Al}_{0.39} \text{Ga}_{0.61} \text{As}$ barrier, 4 nm (nid) GaAs Quantum well, 10 nm (nid) $\text{Al}_{0.39} \text{Ga}_{0.61} \text{As}$ barrier, 20 nm (nid) spacer layer and a 300 nm GaAs n^+ (10^{18} cm^{-3}) contact layer. In order to perform optical measurements under applied voltage $500 \mu\text{m} \times 600 \mu\text{m}$ mesas were etched through the structure. AuGeNi-Au alloyed ohmic contacts were realized on the back side and on an annular contact on the mesa. This diode structure was designed to have low current densities compatible with large size mesas.

The sample was mounted in a variable temperature (4 K-300 K) optical cryostat. A 5 mW HeNe laser was focused on the mesa. Bias was applied on the sample using a four probe technique. For high pumping power densities, the effect of the He-Ne laser illumination on the current voltage characteristic is to shift slightly the whole $I(V)$ curve to lower (absolute) voltages and this for both positive (positive bias : electron injection from the substrate) and negative biases. It can be explained in the following way : light creates electron-hole pairs in the whole structure. Electrons (holes) tend to accumulate against the emitter (collector) barrier thus increasing the electric field in the well region. Then the situation in presence of light at a given bias is similar to the one

in the dark at a higher bias. For the experiments presented here care has been taken to work at low excitation power density (0.5 W/cm^2) in order to minimize perturbations due to HeNe illumination.

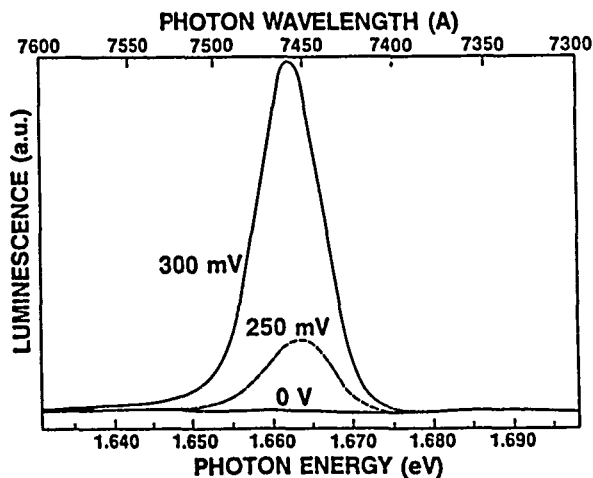


Fig. 1

5K PL spectra of the DBD quantum well under 0 mV, 250 mV and 300 mV applied bias.

At zero bias, the photoluminescence of the QW (around 745 nm) is hardly observable. It has to be noted that the 300 nm n+ GaAs top contacting layer absorbs both the exciting and reemitted light from the QW, but the weakness of this luminescence is also due to the fact that tunneling rate of electrons through the barriers is of the same order than the radiative recombination rate, and therefore in this experiment the main role of the He-Ne illumination is to provide nonequilibrium free holes in the valence band of the QW and spacer layers.

Under applied bias, electrons accumulate in the QW and recombine with the free holes optically injected. As a result the photoluminescence of the QW increases with current by more than two orders of magnitude as illustrated in fig. 1 which shows the Quantum Well photoluminescence for 0 mV, 250 mV and 300 mV at 5 K. The I-V curve of the DBD is shown in fig. 2.

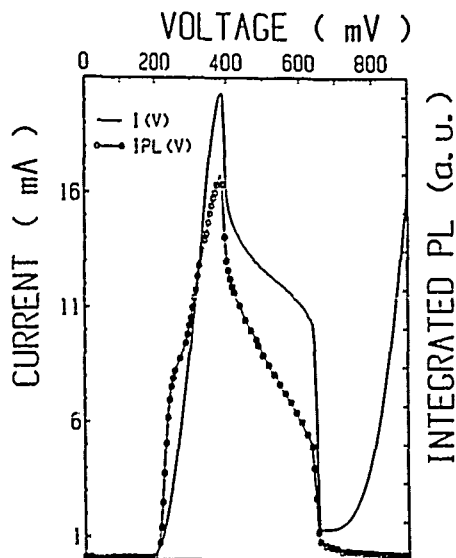


Fig. 2

Current and integrated photoluminescence intensity of the DBD QW as a function of voltage.

For each voltage we have also reported the integrated QW luminescence. It can be seen that :

- (i) At very low optical excitation density (less than 0.5 W/cm^2) the integrated photoluminescence follows closely the current dependence up to 650 mV : however for optical power densities above this value, additional peaks appear around the current peak voltage, in the integrated photoluminescence versus bias curve. These features correspond to similar structures in the photocurrent. This indicates that the relation between QW luminescence intensity, and accumulated charges is not straightforward. It is therefore difficult to derive an accurate estimate of the steady state density of electrons accumulated in the QW and their characteristic escape time versus voltage (5).
- (ii) Above 650 mV the integrated QW luminescence intensity stays at the same level as at 0 bias and does not follow anymore the rise of current. This is because the 4 nm QW has only one electron quasi-bound state and above 650 mV the current rise is due to electrons flowing through extended states. These electrons do not accumulate in the QW and therefore do not contribute to the PL.

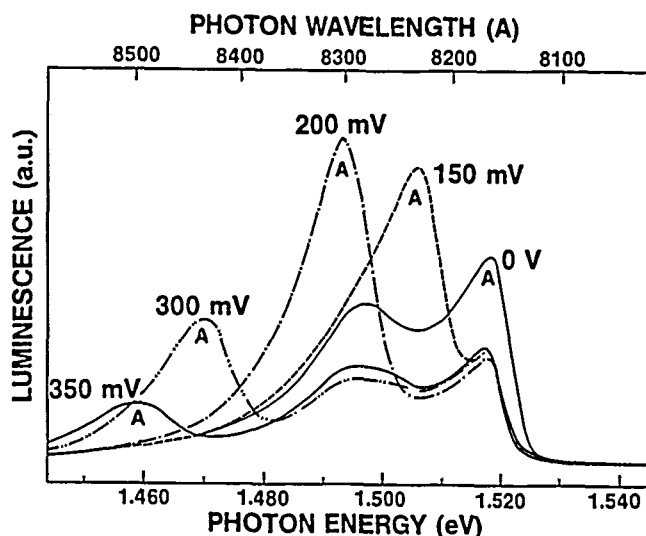


Fig.3
5K PL spectra for the region around GaAs band gap for different voltages.

Fig. 3 shows luminescence spectra in the region around GaAs bandgap for different applied biases. The "A" labelled transition shifts linearly towards lower energies and its intensity fades out with applied bias. The corresponding Stark shift at 350 mV applied voltage is about 60 meV.

To interpret these results, we have calculated the band structure of the device under bias by solving Poisson's equation self-consistently in the spacers. We have included space-charge effects in the well with a sequential tunneling model (7). Quantized state energies are given by resonances in the transmission coefficient. The calculation of the transmission coefficient includes the well, barriers, and the undoped spacer layers where band bending effects are taken into account.

Tunneling Dynamics and Resonant Coupling of Electrons in GaAs/AlAs Coupled Double Quantum-Well Structures under Electric Fields

T. Matsusue^(a), M. Tsuchiya^{(a)*} and H. Sakaki^{(a)(b)}

Institute of Industrial Science, University of Tokyo^(a)

7-22-1 Roppongi, Minato-ku, Tokyo 106, JAPAN

Research Center for Advanced Science and Technology, University of Tokyo^(b)

4-6-1 Komaba, Meguro-ku, Tokyo 153, JAPAN

Resonant tunneling(RT) phenomenon in double-barrier(DB) heterostructure[1,2] has a conceptual similarity to a transmission of optical waves in Fabry-Perot (FP) resonator and involves time delay. Its dynamics should be investigated since they limit the ultimate speed of RT devices. Such a study will also clarify similarities and differences between electronic and optical waves. In our previous work[3], we investigated the tunneling escape process of electrons from AlAs/GaAs/AlAs DBRT structures. The measured escape rate was well explained by the idealized theory of FP-like model, which predicts the tunneling escape time τ in DBRT structures is given by $|t|^2 v_k / L_w$, when $|t|^2 \ll 1$, where t is the transmission coefficient through the barrier, v_k is the group velocity of electrons and L_w is the well width. This predicted escape time is equal to the one calculated by the sequential tunneling model, suggesting that the tunneling escape time is not strongly dependent on the coherency of electron waves. This simple relation may not hold for the tunneling process between quantum wells(QW), where resonant coupling effect plays a more sophisticated role. To clarify the resonant tunneling phenomena between QWs, we report, in this paper, our study on electron dynamics in several different double GaAs QW structures separated by thin AlAs barrier, where the coupling condition between QWs was varied by electric fields. Tunneling process was studied at $\sim 20\text{K}$ by measuring time resolved photoluminescence(PL). Picosecond pulses of a mode-locked dye laser were used to generate electron hole pairs in QWs, and the subsequent PL from particular QWs was monitored by a streak camera to determine the time variation of electron density in the QWs. Note that the electrons are lost either by recombination (radiative[4] and nonradiative) and/or by tunneling process. Since the mass of heavy hole is quite heavy, hole tunneling can be neglected at least in the initial phase of tunneling.

1. Electron Dynamics in Coupled Resonant Tunneling Structures

We investigated first the effect of resonant coupling on tunneling process in coupled QW structures of Fig.1, where $L_{B1}=L_{B2}=31.1\text{\AA}$, $L_{W1}=70.5\text{\AA}$, and $L_{W2}=50.8\text{\AA}$. We measured the variation of tunneling rates at different bias voltage V_a applied to the semi-transparent Schottky contact formed at the surface. The photon energy of laser was chosen to be 1.77eV to generate carriers in both wells. Under the flat band condition ($V_a \sim +0.6\text{V}$), the electrons in QW2 have the highest energy, and therefore, transfer to QW1 or escape rightwards to outside. When the ground levels of QW1 and QW2 are in resonance ($V_a \sim -0.6\text{V}$), interwell tunneling is enhanced. When V_a is made further negative, resonance breaks down, and tunneling from QW1 to QW2 comes to be allowed. In addition, change in potential shape by electric field may affect tunneling process, and radiative recombination lifetime also change gradually with electric field. Measured PL decay time and time-integrated PL intensity I are shown in Fig.2 as a function of V_a . Their variations with V_a indicate large change in tunneling dynamics as will be described below.

*currently at Dept. of Electrical and Computer Engineering, Univ. of California, Santa Barbara, CA 93106, USA

Before the resonance is achieved ($V_a > -0.1V$), the ground level $E_1(QW1)$ of $QW1$ is far lower than that $E_1(QW2)$ of $QW2$. The PL decay time of $QW1$ (τ_1) in this case is 400ps, which is nearly equal to radiative recombination lifetime τ_R . In contrast, the decay time of $QW2$ (τ_2) is 50ps. This decay rate $1/\tau_2$ is equal to the sum of two escape rates $1/\tau_{23}$, $1/\tau_{21}$ which correspond to the tunnel escape from $QW2$ to outside and to $QW1$, respectively. The former (τ_{23}) is estimated to be $\sim 100ps$ by the measured data of Fig.1 with the use of relation $\tau_T \propto L_W^4$. Hence the latter τ_{12} is expected to be also $\sim 100ps$. Note that this tunneling process was clearly observed also in photoluminescence excitation (PLE) spectrum of $QW1$, where the structure associated with $QW2$ exciton appeared. With these time constants, PL efficiency η_1 of $QW1$ and that η_2 of $QW2$ are expected to be ~ 1 and ~ 0.1 , respectively, since $\eta_2 = \tau_2/\tau_R$. The expected values agree well with the data.

When $E_1(QW1)$ and $E_1(QW2)$ are brought close together but slightly separated ($-0.4V < V_a < -0.1V$), $QW1$ and $QW2$ get weakly coupled, which allows a slow electron transfer (injection) from $QW1$ to $QW2$. This leads to the increase in τ_2 . When the two levels are at resonance ($-0.7V < V_a < -0.4V$), interwell tunneling gets frequent and large variations in decay time and PL intensity appeared. The fact that both the PL lifetime $\tau_1 \sim \tau_2$ and the intensity $I_1 \sim I_2$ in this region indicates that the interwell tunneling time τ_{12} is much faster than τ_{23} ($\sim 100ps$). The fact τ_{12} is far smaller than τ_{23} is understood by considering that the tunneling rate is of the order of $\exp(-\kappa L_B)$ [5] for coupled QW and $\exp(-2\kappa L_B)$ for DBRT structures, where κ is electron wave decay constant ($\sqrt{2m(V-E)/\hbar}$) in the barrier and L_B is the barrier thickness. Indeed, when barrier height is 1.13eV, τ_{23} is calculated to be 100ps for $L_W = 7.1nm$ and $L_B = 3.1nm$, while τ_{12} is predicted to be 0.62ps from the calculated energy splitting $\Delta E(\sim \hbar/\tau_{12})$ for coupled QW with $L_{W1} = L_{W2} = 62\text{\AA}$ and $L_{B1} = 31\text{\AA}$.

Hence, under such a condition quasi-equilibrium is reached between N_1 and N_2 , the electron density of each well. The total density $N (= N_1 + N_2)$ is then likely to be dominated mainly by the tunneling escape process and, therefore, written as $dN/dt = -N_2/\tau_{23} = -N/(1+R)\tau_{23}$, where R is the ratio N_1/N_2 of electron densities. This indicates that the lifetimes τ_1 and τ_2 get equal each other and are given by $(1+R)\tau_{23}$, while the PL efficiencies are given $2R\tau_{23}/\tau_R$ for $QW1$ and $2\tau_{23}/\tau_R$ for $QW2$. Therefore, one expects that τ_1 equals τ_2 , and that $\eta_1/\eta_2 (\sim R)$ decreases as V_a decreases. This prediction agrees with the data. Since τ_{23} is expected to change with V_a less sensitively than R does, τ_1 , τ_2 and η_1 should decrease, and η_2 is nearly constant as V_a decreases.

Note here also that τ_R or τ_{NR} (nonradiative recombination lifetime) do not change appreciably with V_a in this region for the following reasons; the measured sum of PL intensity from $QW1$ and $QW2$ in this region varies with V_a in proportion to $\tau_1 (\sim \tau_2)$, indicating that τ_R is nearly constant. In addition, the remarkable increase in PL intensity of $QW2$ at resonance indicates that the non-radiative path remained small here.

When V_a gets more negative beyond the resonance ($V_a < -0.7V$), the tunneling rate from $QW2$ to $QW1$ gets negligible and that from $QW1$ to $QW2$ is also somewhat reduced because of the breakdown of resonance. This mechanism explains the increase in τ_1 and τ_2 , and change in PL intensity. The data indicate τ_{12} increases to $\sim 500ps$ since $\tau_1 (= (1/\tau_R + 1/\tau_{12})^{-1})$ goes up to $\sim 230ps$. The value is reasonable considering the dependence of τ_T on L_W .

2. Electron Dynamics in Coupled Double Quantum Well Structures

To focus mainly on the tunneling process through the interwell barrier, we next investigated the electron dynamics in three different coupled double QW structures which are sandwiched on both ends by thick ($L_{B2} = 100\text{\AA}$) barriers.

These thick barriers prevent the tunneling escape process to outside of the coupled QWs and allow the investigation of interwell coupling only. The thicknesses of the interwell barriers of three samples ranges from 31.1 to 100Å. With the application of electric field, the behavior similar to that in coupled RT structure described in Sec.1 takes place, except for the reduction of escape process to outside. Figure 3 shows PL decay time and the time integrated PL intensity of QW1 and QW2 of three samples as a function of V_a . The physical interpretations are given below.

In the sample with $L_{B1}=31.1\text{Å}$, the PL intensity I_1 and I_2 of QW1 and QW2 show the sharp structure when plotted as a function of V_a . Under the flat band condition and/or before the resonant condition ($V_a > 0\text{V}$), the lifetime τ_1 (~300-400ps) and the PL intensity I_1 are nearly constant, which indicates that electrons in QW1 is not allowed to tunnel into QW2 and that τ_1 is determined by recombination lifetime. As V_a decreases from ~1V to ~0V, I_2 gradually increases and τ_2 decrease, which results from the change in tunneling process from QW2 to QW1. Indeed, at $V_a > 0.8\text{V}$, fast initial decay component, which is ascribed to tunneling process from QW2 to QW1, appeared in time resolved PL from QW2 and was reduced with decrease in V_a . Note that this tunneling process was clearly observed in PLE spectrum of QW1, where the structure associated with QW2 exciton appeared. The gradual increase in I_2 comes from the change in ratio of thermal distribution of N_1 and N_2 .

When V_a goes near the resonant condition, τ_1 and I_1 decreases. Though the measured τ_1 at $V_a = -0.4\text{V}$ is ~70ps, the presence of initial faster transfer process is suggested since the fact that the peak intensity of time resolved PL from QW1 was reduced by factor of ~4 is explained by convoluting the faster decay component ($\tau \sim 20\text{ps}$) with the detection time resolution ($\sigma \sim 30\text{ps}$). As to τ_2 and I_2 , clear dip structure were not observed as a function of V_a ; this suggests that the fast tunneling from QW2 to QW1 occurred even under flat band condition. When the bias is beyond the resonance ($V_a < -0.6\text{V}$), measured τ_1 and I_1 increase again τ_1 reaches up to ~300ps, which indicates tunneling process from QW1 does not play an important role. In contrast, τ_2 and I_2 decrease with decrease in V_a . Although the mechanism of the decrease is not clear, increase in tunneling rate through rightside barrier with strong electric field may take place.

In the sample with $L_{B1}=56.6\text{Å}$, both τ and I showed only the gradual change with V_a without clear resonant behavior. The suppression of resonant coupling was confirmed by the fact that peak associated with QW2 exciton was small in PLE spectrum of QW1. When $V_a < -0.7\text{V}$, however, a small evidence of tunneling component was observed in the time dependence of PL intensity from QW2, where the shoulder of delayed PL component appeared. In the case of $L_{B1}=100\text{Å}$, we observe only gradual change in τ and I and no clear evidence of electron tunneling between QWs.

In all the samples, oscillatory behavior of PL intensity with time predicted by S. Luryi was not observed. This is reasonable since our detection time resolution is about several ten ps, which is much larger than the coherent time.

In summary, electron dynamics in coupled RT and coupled QW structures were investigated. A drastic change in tunneling processes was observed as the coupling condition was varied by applying bias voltage. In the coupled RT structure with barrier thickness of 31.1Å, a large enhancement in interwell tunneling was observed at resonance, where the dynamic processes within two QWs are under quasi-equilibrium. The enhancement was successfully explained by calculating the tunneling rate for coupled QW and DBRT structures. The

tunneling into the other well was observed under the off resonant condition. In coupled QW structures with different barrier thickness, the systematic variation of electron dynamics was demonstrated as a consequence of the varied strength of coupling condition. When $L_{B1} \geq 56.6\text{\AA}$, tunneling rate was found to be small.

References

1. L.L. Chang, L. Esaki, and R. Tsu, *Appl. Phys. Lett.* **24**, 593 (1974)
2. T.C.L.G. Sollner, W.D. Goodhue, P.E. Tannenwald, C.D. Parker, and D.D. Peck, *Appl. Phys. Lett.* **43**, 588 (1983)
3. M. Tsuchiya, T. Matsusue, and H. Sakaki, *Phys. Rev. Lett.* **59**, 1934 (1987)
4. T. Matsusue and H. Sakaki, *Appl. Phys. Lett.* **50**, 1429 (1987)
5. E.O. Kane, "Tunneling Phenomena in Solids", ed. by E. Burstein and S. Lundqvist (Plenum Press, New York, 1969) p.1

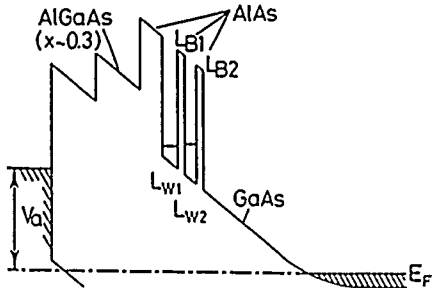


Fig.1 Band diagram of coupled QW structures

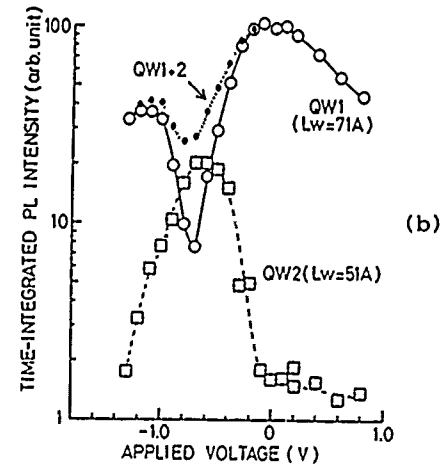
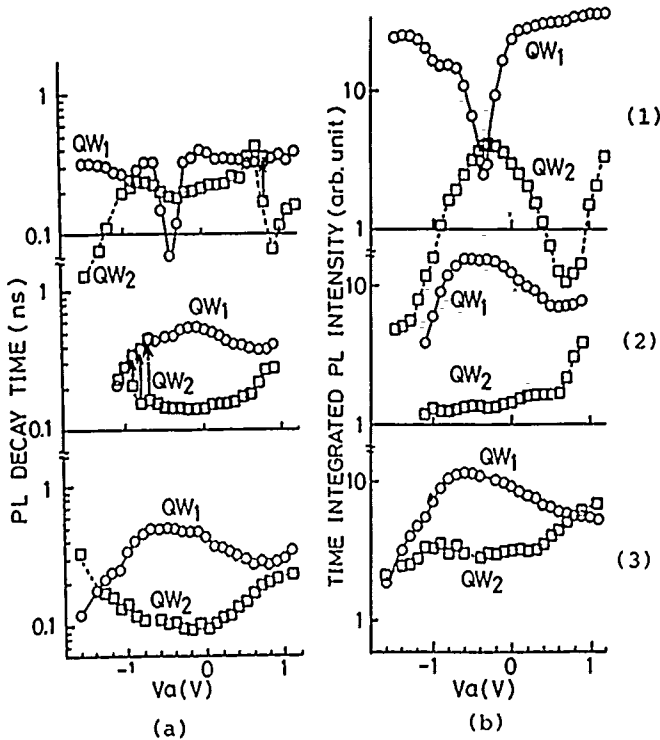
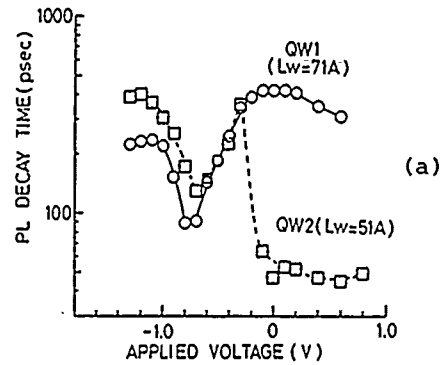


Fig.2 PL decay time(a) and time-integrated PL intensity(b) in coupled resonant tunneling structure as a function of applied voltage

Fig.3 PL decay time(a) and time-integrated PL intensity(b) in coupled QW structures as a function of applied voltage with interwell barrier thicknesses of 31.1Å(1), 56.6Å(2), and 100Å(3). Arrows in (a) indicate presence of two decay components, where decay time changes according to the arrow. Note that relative magnitude of PL intensity between two QWs is arbitrary.

Timing Jitter in Repetitively Pulsed Semiconductor Lasers

by

Ruixi Yuan and Henry F. Taylor
Department of Electrical Engineering
Texas A&M University
College Station, TX 77843

Timing jitter can limit the accuracy of data obtained by optical sampling using repetitively pulsed semiconductor lasers. When the optical sampling is used for real-time analog-to-digital conversion, for example, the maximum allowable jitter is typically 20-40 times less than the maximum permissible pulse width¹. Timing jitter in semiconductor lasers has been studied experimentally^{2,3}, but a predictive model has not heretofore been available.

In this paper, we present results of an analysis of timing jitter in free-running and in external-cavity-coupled semiconductor lasers driven with repetitive current waveforms. The analysis is based upon a quantum amplifier model⁴ of the laser, in which spontaneous emission, stimulated emission, absorption, and scattering of light are treated as Poisson processes which produce random fluctuations in photon and carrier densities. By solving rate equations with appropriate random (Monte Carlo) variables⁵, the temporal variation of output power is simulated. The effect of an external mirror is analyzed by incorporating delayed feedback into the model.

We have studied the effect of variations in key system parameters (facet reflectances, bias current, modulating current waveform, and external cavity length and mirror reflectance) on the average pulse width and the root-mean-square timing jitter. Some representative results are shown in Figs. 1 and 2 for a laser with a 20 mA threshold current. Sinusoidal modulation at a frequency f_m of 2.2 GHz with a peak-to-peak current amplitude of 80 mA is superimposed upon a dc bias of 50 mA. In Fig. 1(a) the full-width at half-maximum of the laser pulse is shown as a function of external cavity length L for front-facet reflectances of .35 (without AR coating) and .01 (with AR coating) and an external mirror reflectance r of .04. As reported by other authors⁶, shortest pulse widths are obtained when the modulation frequency is slightly less than the reciprocal of the round-trip transit time for the external cavity. The results in Fig. 1(b) indicate that timing jitter is very sensitive to external cavity length and that lower jitter (much less than 1 ps) is obtained with the AR-coated laser. Fig. 2 shows a monotonic decrease in pulse jitter with increasing external mirror reflectance r - but at the higher reflectance values the pulses become broadened and distorted.

Results for modulation with short pulses such as those produced by a comb generator will be included in the presentation. In one case, for example, it was found that the laser pulse jitter in an external cavity was less than 1

ps even when a simulated jitter of 4 ps was present in the modulating pulse train.

To summarize, a quantum amplifier model has been applied to the calculation of pulse jitter in semiconductor lasers. The pulse jitter is very sensitive to external cavity length and feedback level. The results suggest that it may be possible to produce optoelectronic "clocks" which show better short-term stability than their all-electronic counterparts.

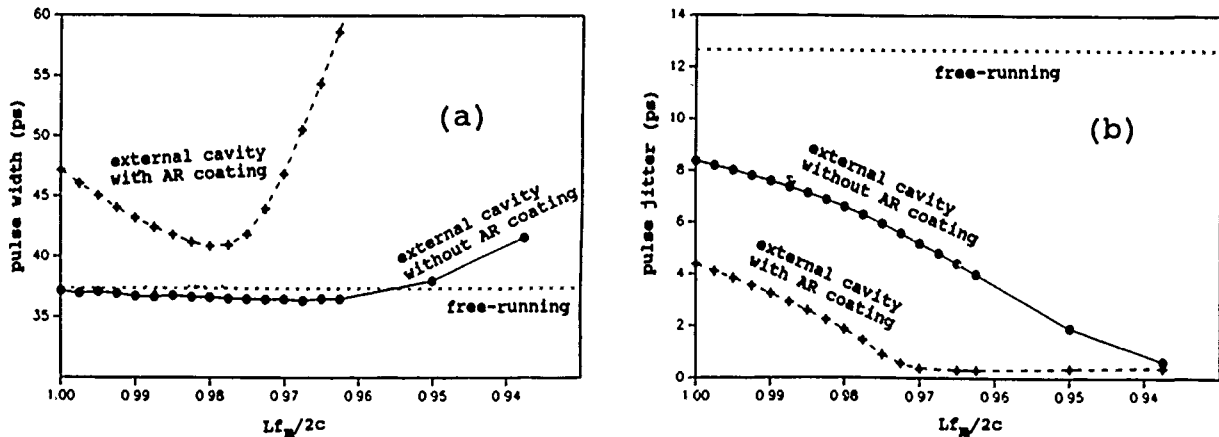
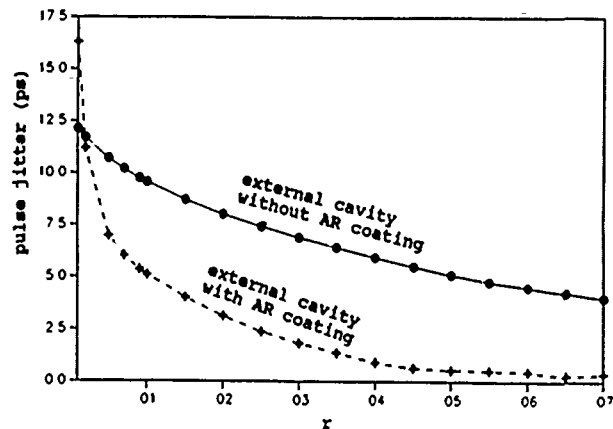


Fig. 1. Dependence of pulse width (a) and pulse jitter (b) on external cavity length, for $r=.04$.

Fig. 2. Dependence of pulse jitter on external mirror reflectance, for $Lf_m/2c = .975$.



REFERENCES

1. H. F. Taylor, IEEE J. Quant. Electron. QE-15, 210 (1979).
2. F. Mengel, C. Lin, and N. Gade, Opt. Commun. 54, 103 (1985).
3. A. J. Taylor, J. M. Wiesenfeld, G. Eisenstein, and R. S. Tucker, Appl. Phys. Lett. 49, 681 (1986).
4. A. M. Yurek, H. F. Taylor, L. Goldberg, J. F. Weller, and A. Dandridge, IEEE J. Quant. Electron. QE-22, 522 (1986).
5. D. Marcuse, IEEE J. Quant. Electron. QE-20, 1139 (1984).
6. J. C. Goodwin and B. K. Garside, IEEE J. Quant. Electron. QE-19, 1068 (1983).

Millimeter Wave AlInAs-GaInAs HEMTs

U.K. Mishra
ECE Department, Box 7911
North Carolina State University
Raleigh, NC 27695-7911
(919) 737-7354

Summary

This paper reports the work done at the Hughes Research Labs in the area of mm-wave AlInAs-GaInAs HEMTs.

Heterostructure FETs based on both GaAs and InP have demonstrated excellent performance in a variety of analog and digital applications. The advantages that heterostructure FETs offer are:

- i) The high electron mobility in modulation doped structures reduces parasitic resistances
- ii) The inherent high aspect ratio in a HEMT structure enables the design of high performance sub-micron devices with good sub-threshold characteristics .
- iii) The probability of velocity overshoot in undoped channels is much higher than in doped channels which leads to higher transconductance and mm-wave gain.

AlInAs-GaInAs HEMTs on InP have several advantages over the GaAs based HEMTs. The mobility at room temperature in GaInAs is much higher than in GaAs ($13000 \text{ cm}^2/\text{V-sec}$ vs. $8000 \text{ cm}^2/\text{V-sec}$). The peak velocity is also substantially higher ($v_p - 2.7 \times 10^7$ vs. $2 \times 10^7 \text{ cm/sec}$). The sheet charge density attainable in the AlInAs-GaInAs system is $- 4 \times 10^{12} \text{ cm}^{-2}$ compared to $- 2 \times 10^{12} \text{ cm}^{-2}$ in the GaAs based system. This high charge density coupled with the high mobility leads to an extremely high conductivity of the two dimensional electron gas which decreases the

parasitic resistances in the device. The electronic properties of the material can be improved further by increasing the Indium composition in the channel. These pseudomorphic structures exhibit both higher mobilities and higher sheet charge densities.

Devices with 0.2 micron and 0.1 micron gate length have been fabricated on lattice-matched and pseudomorphic modulation doped structures. The sheet charge density and mobility in these structures were $\sim 3.5 \times 10^{12} \text{ cm}^{-2}$ and $\sim 9500 \text{ cm}^2/\text{V}\cdot\text{sec}$ respectively. The lattice matched devices demonstrated a transconductance of 800 mS/mm for the 0.2 micron HEMT and a g_m of 1080 mS/mm for the 0.1 micron HEMT. The f_T of the devices were 140 GHz and 170 GHz respectively. 0.1 micron gate length pseudomorphic HEMTs exhibited an f_T of 205 GHz. This is the first demonstration of a transistor with an f_T of > 200 GHz. The f_{max} of the transistor was ~ 300 GHz. The minimum noise figure of single stage amplifiers built with these devices ranged between 0.8 dB and 1.4 dB at 63.5 GHz. These are the best results for low noise amplifiers at V-Band. Ring oscillators built with 0.2 micron gate length HEMTs have demonstrated a minimum propagation delay of 6 pS with a fan-out sensitivity of 2.6 pS per gate at room temperature which is a record for HEMTs. Static frequency dividers have worked at a record frequency of 26.7 GHz. This performance is attributable to the high f_T and drive capability of AlInAs-GaInAs HEMTs.

Future work in AlInAs-GaInAs HEMTs will address epitaxial layer design optimization for mm-wave power applications and integrated circuit designs for mm-wave digital and analog applications.

Picosecond Lasing Dynamics in Quantum-Well Lasers and Its Dependence on the Number of Quantum Wells

Y. Arakawa, T. Sogawa, M. Tanaka, and H. Sakaki

Research Center for Advanced Science and Technology, University of Tokyo

4-6-1 Komaba, Meguro-ku, Tokyo, 153 Japan

Investigation of physics of ultra-fast phenomena in semiconductor lasers is important for high-speed modulation and short pulse generation. It has been recently demonstrated that quantum well (QW) lasers have the advantage to generate shorter light pulses, since the differential gain is enhanced by a factor of four compared to conventional double-hetero structure lasers [1]. In fact, an extremely narrow light pulse (<1.3 psec) was successfully observed in a quantum well laser [2]. This is the shortest pulse so far achieved in the semiconductor lasers without external cavity. However, effects of QW structure-parameters, such as thickness and the number of QWs, on the picosecond pulse dynamics have not been discussed sufficiently. In this paper, we investigate short pulse generation in QW lasers with emphasis on dependence of pulse form on the QW structures. The results demonstrate that the pulse duration strongly depends on the QW structures: The QW laser having a smaller number of QWs generates broader light pulses, which results from in both reduced differential gain and higher quasi-Fermi-energy level of electrons E_{Fc} .

In our experiment, we prepared two GaAs/AlGaAs multi-quantum well (MQW) lasers which consist of 50\AA GaAs QWs separated by 50\AA AlGaAs barriers: One has 16 QWs and the other has 4 QWs, as illustrated in Figures 1 (a) (b). The short pulse generation in the QW lasers was achieved by the gain switching method at room temperature using optical pumping pulses from a dye laser (20 psec, 7000\AA) excited by a Nd^{+} -YAG laser. The optical pumping method makes the experiment free from the electrical RC constant problem. As shown in Figure 1, the photon energy of the dye laser pulse (1.77 eV) is a little higher than $\text{Al}_{0.17}\text{Ga}_{0.83}\text{As}$ optical confinement layer (1.64 eV). Since the total thickness of the optical confinement layer and the QW active layer is the same ($\sim 2000\text{\AA}$) for both lasers, the total number of carriers excited in those layers is the same. As a result, the carrier density (or E_{Fc}) in the QW laser with 4 QWs (QWL4) is much higher than the carrier density in the QW laser with 16 QWs (QWL16), because all excited carriers are relaxed into QWs.

Short pulse generation in those QW lasers were measured by a *single-shot* streak camera. Figures 2 and 3 show measured light pulses from QWL16 and QWL4, respectively. Figure 2 indicates that the estimated pulse duration is less than 2 psec, if the time-resolution of the streak camera is considered. On the other hand, the pulse form of QWL4 is much broader than that of QWL16, as shown in Figure 3. These results demonstrate that the number of QWs has strong

influence on the pulse duration. Since higher carrier density in QWL4 results in energy broadening of carrier distribution, the total relaxation time of carriers into lasing modes is longer. This leads to tailed structures in the pulse form. In addition, under those high carrier density (i.e., high E_{Fc}) condition, the differential gain is also reduced due to the gain flattening effect. Those carrier dynamics were also evidenced by the temporal measurement of spectra through a single shot streak camera with a monochromator. The observed spectra of QWL4 were much broader than that of QWL16.

[References]

- [1] Y.Arakawa, T.Sogawa, M.Nishioka, M.Tanaka, and H.Sakaki, Appl. Phys. Lett. 52, 1295 (1987)
 [2] T.Sogawa, Y.Arakawa, M.Tanaka, and H.Sakaki, Appl. Phys. Lett., October Issue (1988)

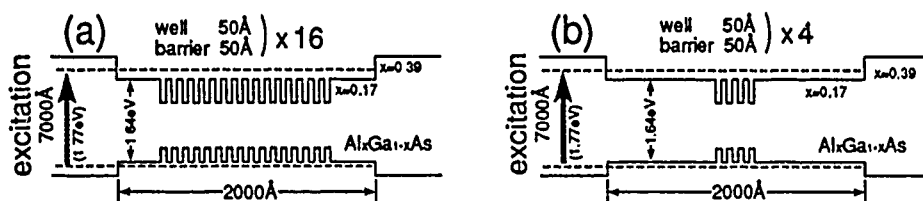


Figure 1: Band diagram for the multi-quantum well (MQW) lasers with (a)16 QWs and (b) 4 QWs

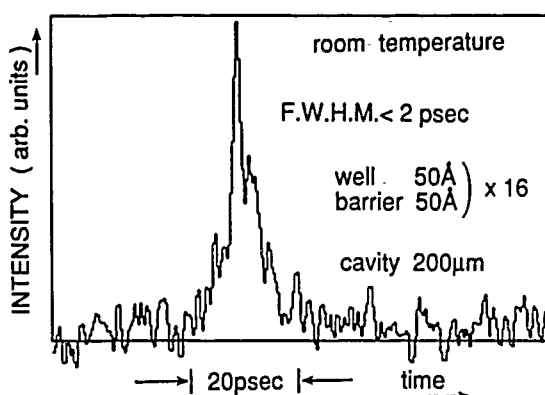


Figure 2: Measured pulse form by a single shot streak camera from the MQW laser with 16 QWs

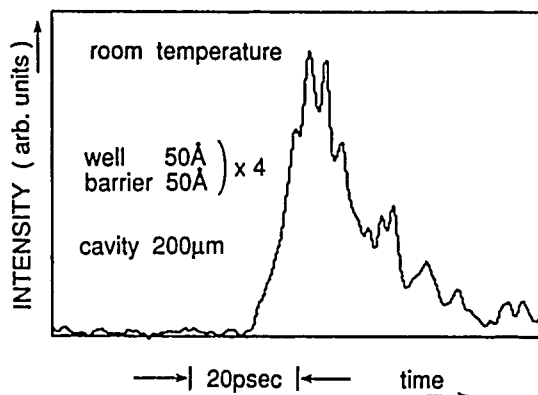


Figure 3: Measured pulse form by a single shot streak camera from the MQW laser with 4 QWs

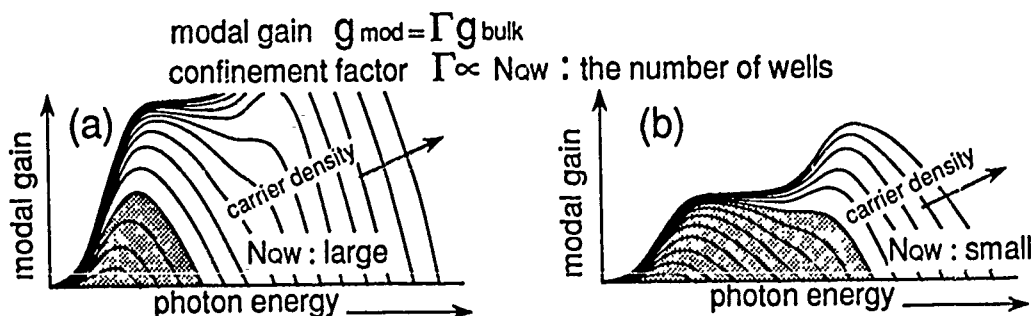


Figure 4: (a) Illustration of the modal gain profile for the MQW laser with 16 QWs; (b) the modal gain profile for the MQW lasers with 4 QWs. Since the total number of carriers excited in the active region is the same, the gain profile of the MQW lasers with 4 QWs is much broader due to the gain flattening effect.

Femtosecond Excitonic Electroabsorption Sampling

W.H. Knox, J.E. Henry, B. Tell, K.D. Li,
D.A.B. Miller and D.S. Chemla

AT&T Bell Laboratories
Holmdel, NJ 07733

Optoelectronic sampling based on the Pockels' effect¹ has become an important technique for the measurement of electrical signals with the highest time resolution, currently at 300 fs. We present first results obtained using a new technique for femtosecond electrical pulse measurement: excitonic electroabsorption sampling (EES). We have previously shown that excitons exhibit a femtosecond electroabsorption response, however the device which was used did not facilitate propagation studies over macroscopic distances². In our new embodiment, a coplanar stripline is fabricated on a GaAs multiple quantum well mesa ridge structure (Fig. 1). We thus obtain optical modulation by parallel-field electroabsorption, which is due to lifetime broadening by field ionization of the excitons³. The detection sensitivity is about 1%/volt in a 10 micron structure. We etch the GaAs substrate down to a 1 micron AlGaAs stop-etch layer in a 1x2 mm area and leave the stripline free-standing on the 1 micron thick film, thus obtaining an extremely low dispersion structure to test the EES concept. We use an infrared dye laser which produces femtosecond pulses at a wavelength of 805 nm⁴ at 82 MHz repetition rate. The exciton energy is temperature-tuned to the laser with a Peletier device, in this case operating at about 5 degrees above ambient temperature. At 300 fs pulsewidth the laser spectrum is already comparable to the exciton linewidth, and we expect that shorter pulses will provide reduced sensitivity relative to the DC response. We expect that time resolution of 100 fs or less may be possible with this technique. We note that electroabsorption is a purely electronic phenomenon, with no ionic lattice contribution such as that of LiTaO₃.

Figure 2 shows the first results, obtained with a generated signal of a few hundred mV at 40 v bias. The signal is detected after about 1 mm of propagation by passing a weak probe beam through the stripline. The pump beam is chopped at a frequency of 1 kHz and the transmitted probe beam is detected with a lock-in amplifier. The 10-90% risetime is 500 fs, which appears to be limited by the 300 fs laser pulsewidth. This signal, accumulated over ten consecutive forward-backward scans appears to show a feature which may be due to a reflection from a small gap in the line at about 2 ps time delay. Further studies of dispersion in this thin film structure and results at higher time resolution are in progress.

.....

- [1] J.A. Valdmanis, G.Mourou and C.W. Gabel, IEEE JQE QE-19, 664 (1983).
- [2] W.H. Knox, D.A.B. Miller, T.C. Damen, D.S. Chemla, C.V. Shank and A.C. Gossard, Appl. Phys. Lett. 48, 864 (1986).
- [3] D.A.B. Miller, D.S. Chemla, T.C. Damen, A.C. Gossard, W. Wiegmann, T.H. Wood and C.A. Burrus, Phys. Rev. B32, 1043 (1985).
- [4] W.H. Knox, JOSA B4, 1771 (1987).

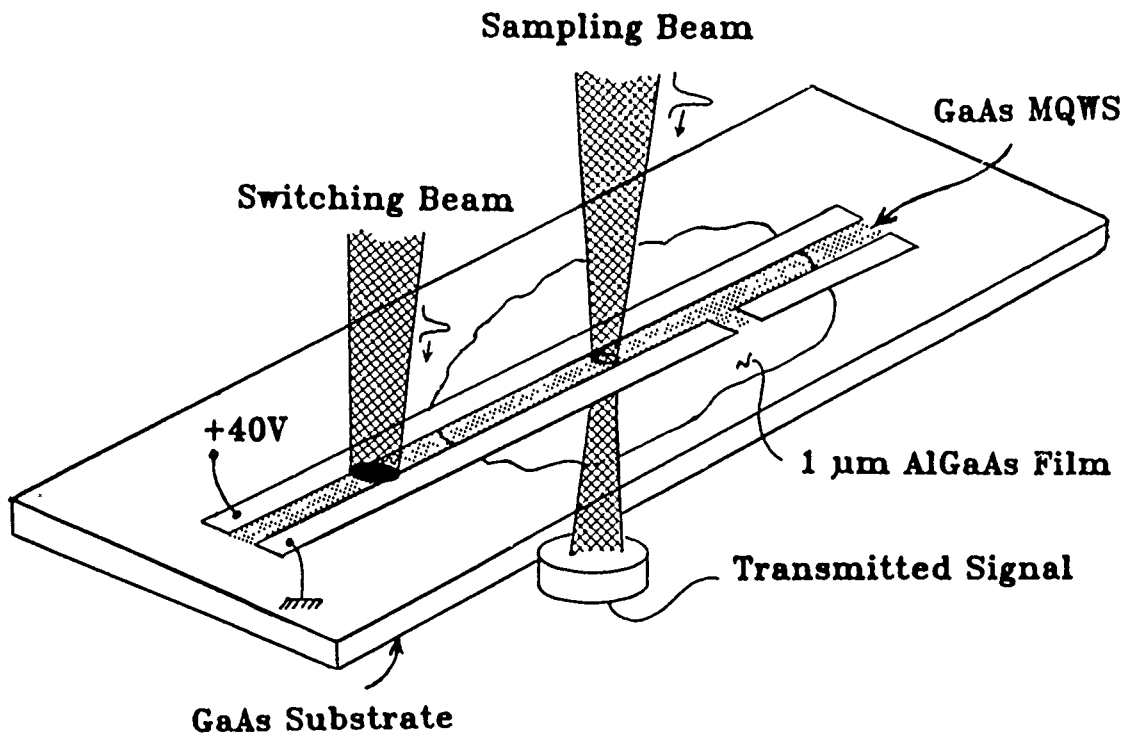


Figure 1. Sample structure showing generation and probing beams.

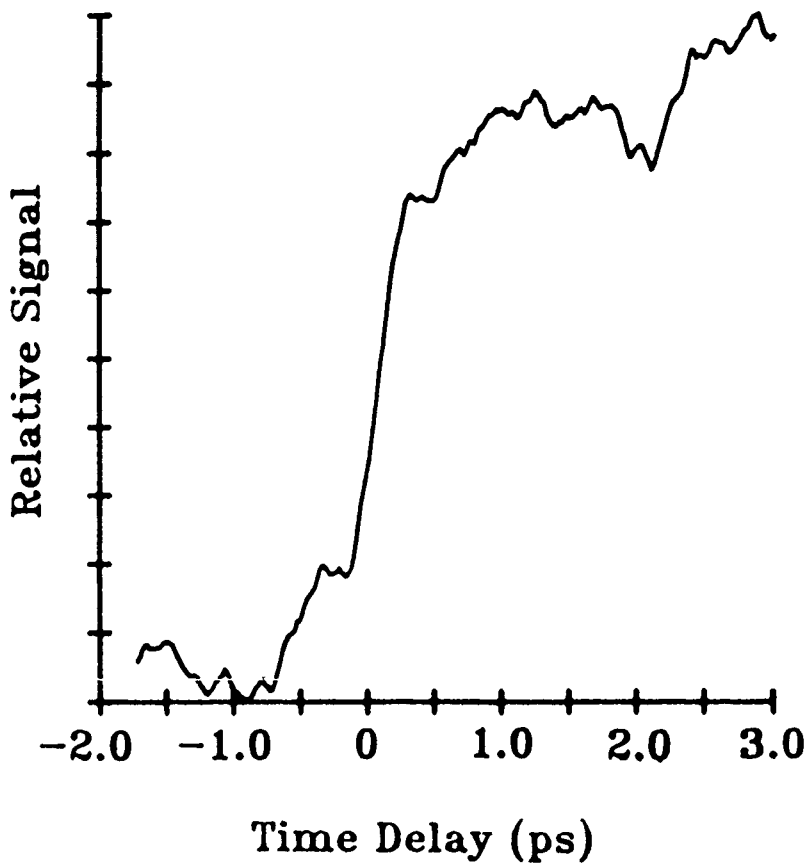


Figure 2. Signal detected after about 1 mm propagation shows 500 fs risetime.

A 10Gb/s-100km OPTICAL FIBER TRANSMISSION EXPERIMENT USING A HIGH SPEED MQW DFB-LD AND A BACK-ILLUMINATED InGaAs-APD

S. FUJITA, M. KITAMURA, T. TORIKAI, N. HENMI, H. YAMADA, T. SUZAKI, I. TAKANO[†], K. KOMATSU and M. SHIKADA

Opto-Electronics Research Laboratories, [†]C&C Systems Research Laboratories, NEC Corporation, Kawasaki, Japan

INTRODUCTION Several high-speed, long-span optical fiber transmission experiments have been reported up to 10Gb/s to explore the feasibility for future ultra high speed trunk line systems.¹⁻³ These experiments indicated that the system suffered insufficient device frequency response, LD wavelength chirping and low receiver sensitivity to realize a high speed, long span transmission. We have confirmed feasibility of 10Gb/s optical transmissions using a high speed and low chirping MQW DFB-LD and a high quantum efficiency back-illuminated InGaAs-APD. Improved characteristics in frequency response, chirping and quantum efficiency made it possible to transmit 10Gb/s signal over 100km.

THE EXPERIMENTAL SYSTEM ARRANGEMENT The experimental setup shown in Fig. 1 is similar to the one we have reported before.² We have constructed a 10Gb/s return to zero (RZ) signal from a 5Gb/s pseudorandom (PN, $2^{15}-1$) data stream. A MQW DFB-LD was directly modulated with 10Gb/s RZ signal with 60 mAp-p current. Received 10Gb/s data streams by a back-illuminated InGaAs-APD were demultiplexed to 5Gb/s. The electric circuits were made by GaAs-FET hybrid integration.

The laser diode utilized is the 1.5 μ m $\lambda/4$ shifted MQW DFB-DC-PBH LD⁴. The MQW active layer consisted of 10 InGaAs wells (75 Å thick) and InGaAsP barriers (150 Å thick). The LD indicated 1.5 times higher relaxation oscillation frequency, as shown in Fig. 2, compared with a regular bulk DFB-LD, which made the MQW DFB-LD possible to operate under $I_b = I_{th}$ LD bias condition (Fig. 3), while the bulk DFB-LD operated at $I_b = 1.3I_{th}$ condition.² Moreover, the spectral chirping observed for the MQW DFB-LD (7Å at -20dB width) is 20-40% narrower than the bulk DFB-LDs. (Fig. 4)

A thin absorption layer of the APD realizes high speed response, but it brings lower quantum efficiency. We have improved the quantum efficiency of a high speed APD from 50%² to 80% by introducing back-illumination and high reflection mirror configuration without reducing the response speed. The measured gain bandwidth product for the back-illumination APD was 60 GHz, and the receiver sensitivity of -23.5dBm (BER 10^{-9}) was obtained.

TRANSMISSION EXPERIMENTS The power penalty dependence on total dispersion was measured using a conventional optical fiber for both bulk and MQW DFB-LD. The results shown in Fig. 4 indicates that the dispersion tolerance for the MQW DFB-LD (48ps/nm @0.5dB penalty) is 1.6 times larger than for the bulk DFB-LD. From these results, we have conducted a long span transmission experiment using a 100.1km dispersion shifted (DS) optical fiber. The total dispersion for the DS fiber was 37ps/nm at the DFB-LD wavelength

(1.549 μ m), so that a 100.1km transmission have been realized with no dispersion power penalty as shown in Fig. 5.

REFERENCES 1)A. H. Gnauck, et al., OFC'86, PD9, 1986. 2)S. Fujita, et al., OFC'88, PD-16, 1988. 3)J. L. Gimlett, et al., OFC'89, PD16, 1989. 4)T. Sasaki, et al., Electron. Lett., vol. 24, No. 23, pp1408, 1988.

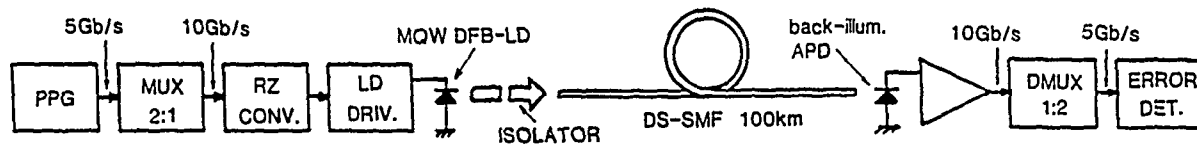


Fig. 1 Block diagram of the 10 Gb/s transmission experimental setup

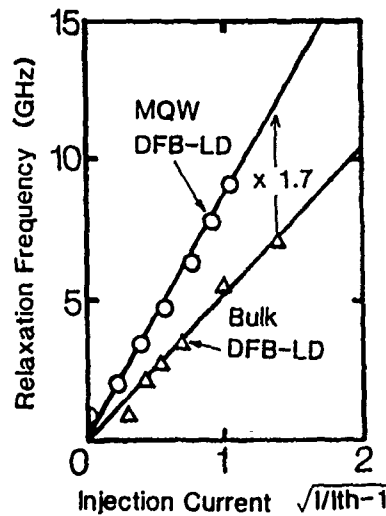
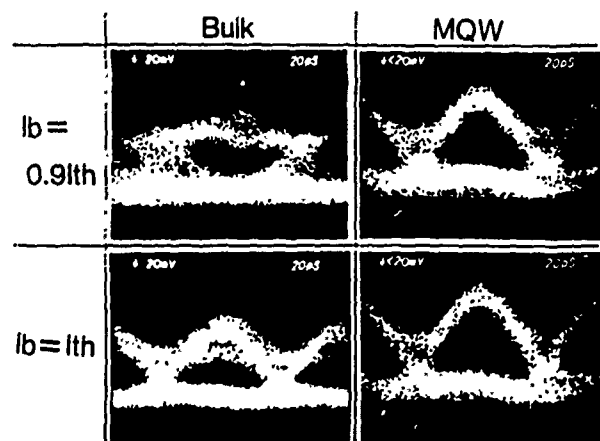


Fig. 2 DFB-LD resonant frequency dependence on injection level



(Monitor: high-speed PIN-PD)

Fig. 3 DFB-LD output waveforms at 10Gb/s

MQW DFB-LD spectrum

10Gb/s
 $I_b = I_{th}$

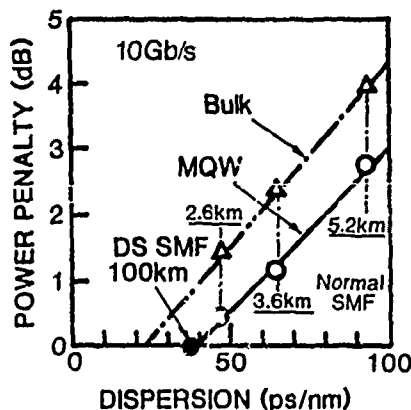
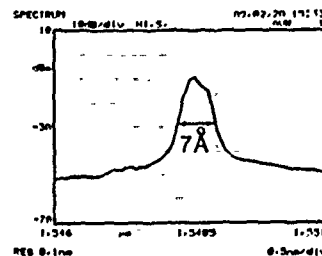


Fig. 4 Power penalty dependence on total fiber dispersion

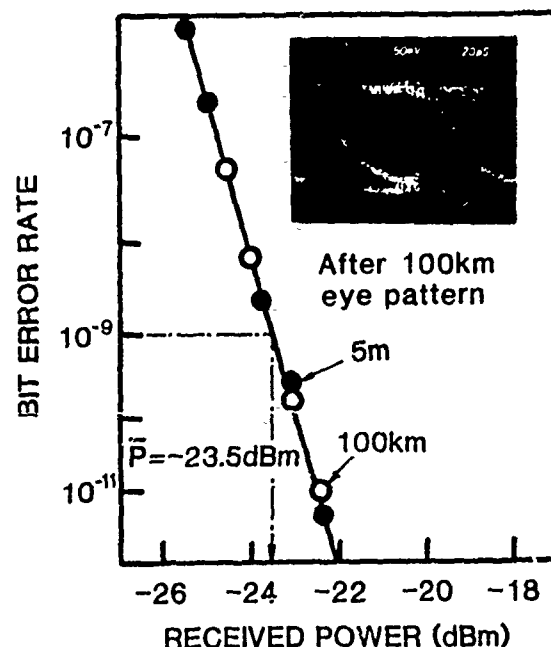


Fig. 5 Bit error rate characteristics of 10Gb/s-100.1km transmission

Author Index

- Adams, P., 210
 Adomaitis, E., 217
 Arakawa, Y., 262
 Arjavalingam, G., 222
 Asai, Kazuyoshi, 139
- Bar-Joseph, I.**, 27
 Basu, Santanu, 68
 Blixt, P., 217
 Bloom, D. M., 16, 31, 101
 Bois, P., 251
 Bokor, J., 189
 Bowers, J. E., 87
 Bowman, R., 210
 Brown, E. R., 115
 Buhrman, R. A., 246
 Burrus, C. A., 27
- Calawa, A. R.**, 176
 Chamoun, S., 147
 Chang, T. Y., 27
 Chauchard, E., 52
 Chemla, D. S., 27, 264
 Chevoir, F., 251
 Cho, Y., 36
 Chow, D. H., 124
 Corzine, S. W., 87
 Costard, E., 251
 Cote, D., 251
 Cova, S., 194
- Damen, T. C.**, 94, 111
 De Lucia, F. C., 57
 DeFonzo, Alfred P., 232
 Delaitre, S., 251
 Deveaud, B., 94
 Diadiuk, V., 176
 Diamond, S. K., 101
 Dolfi, David W., 76
 Dykaar, D. R., 176
- Eastman, L. F.**, 121
 Eisenstein, G., 73
- Fattinger, Ch.**, 225
 Feng, S. T., 201
 Ferry, D. K., 153, 163
 Fox, A. M., 247
 Frankel, M., 176
 Fujita, S., 266
- Ghioni, M.**, 194
 Gnauck, Alan H., 2
 Goldhar, J., 201
 Goodnick, Stephen M., 158
 Grischkowsky, D., 225
 Grondin, R. O., 147
 Guenther, B. D., 57
 Gupta, S., 176
- Halbout, Jean-Marc**, 22, 68, 222
 Hall, K. L., 73
 Hamana, M., 36
 Harris, J. S., 101
 Harvey, G. T., 48
 Heinrich, H. K., 62
 Helkey, R. J., 87
 Henmi, N., 266
 Henry, J. E., 111, 264
 Herman, M., 210
 Heutmaker, M. S., 27, 48
 Hollis, M. A., 176
 Huang, C. I., 115
 Huang, H. C., 52
 Hung, H.-L. A., 52
- Ippen, E. P.**, 73
 Ishibashi, Tadao, 139
- Jackson, M. K.**, 124
 Johnson, A. M., 189
 Johnson, M. B., 124
 Joshi, R., 147
- Kanda, M.**, 36
 Kania, Don, 170
 Kann, M. J., 153
 Ketchen, M., 22
 Kimura, A., 36
 Kitamura, M., 266
 Knox, W. H., 247, 264
 Knudsen, J., 210
 Kobayashi, Tetsuro, 81
 Komatsu, K., 266
 Kopcsay, G. V., 222
 Kopf, R. F., 111
 Krizan, A. M., 163
 Krotkus, A., 217
 Kuo, J. M., 27, 111
- Lacaita, A.**, 194
 Landen, Otto L., 170
 Le, H. Q., 176
 Lee, Chi H., 52, 201
 Li, K. D., 264
 Livescu, G., 247
 Loepfe, R., 206
 Louis, Thomas A., 39
 Lugli, Paolo, 158
 Lutz, Charles R., 232
- Madden, C. J.**, 16
 Mahler, G., 163
 Majidi-Ahy, R., 31
 Mark, J., 73
 Marsland, R. A., 16
 Matsusue, T., 254
 May, Paul G., 68
 McGill, T. C., 124
 Melchior, H., 206
 Miller, D. A. B., 247, 264
 Mishra, U. K., 260
 Morimoto, Akihiro, 81
 Morton, P. A., 87
 Moskowicz, P. A., 22
 Moss, S., 210
 Mourou, G. A., 106, 121, 176
- Nieh, C. W.**, 124
 Norris, T. B., 106, 121
 Nuss, M. C., 48
- Oberli, D. Y.**, 94, 111
 Olshansky, Robert, 244
 Ozbay, E., 101
- Pan, Lawrence**, 170
 Pao, Y. C., 101
 Parker, C. D., 115
 Paslaski, J., 46
 Pastol, Y., 222
 Pianetta, Picro, 170
 Polak-Dingels, P., 52
- Ravi, K. V.**, 170
 Ripamonti, G., 194
 Rodwell, M. J. W., 16, 101
 Rogers, D. L., 184
- Sai-Halas, G. A.**, 132
 Sakaki, H., 254, 262
 Saruwatari, Masatoshi, 7
 Schaelin, A., 206
 Schaff, W. J., 121
 Scheuermann, M., 22
 Shah, Jagdeep, 94, 111
 Shikada, M., 266
 Simpson, W. M., 189
 Sizer, T., 247
 Smith, D., 210
 Smith, F. W., 176
 Smith, P. R., 48, 189
 Soderstrom, J., 124
 Sogawa, T., 262
 Sollner, T. C. L. G., 115
 Song, X. J., 121
 Sprik, R., 22
 Storz, R. H., 189
 Stutz, C. E., 115
 Suzuki, T., 266
 Swartz, J. C., 57
- Takano, I.**, 266
 Tanaka, M., 262
 Taylor, Henry F., 258
 Tell, B., 264
 Thomas, D., 251
 Torikai, T., 266
 Treacy, G., 52
 Tsuchiya, M., 254
- Umeda, T.**, 36
- Valdivia, V.**, 16
 Valdmanis, J. A., 48
 Vinter, B., 106
 Vodjdani, N., 106, 251
- Webb, K.**, 52
 Weisbuch, C., 106
 Wicks, G., 121
 Wiesenfeld, J. M., 27
 Wolak, E., 101
- Yamada, H.**, 266
 Yamanishi, Masamichi, 239
 Yariv, A., 46
 Yuan, Ruixi, 258

Subject Index

AlGaAs-GaAs quantum wells, intersubband relaxation, 158

AlGaAs lasers, charge-density modulation, 62

All-optical multiplexing-demultiplexing, 7

Amplifiers

InGaAsP diode laser, 73

28 GHz, monolithic, 52

Antennas, millimeter wave, characterization, 232

Broadband dielectric measurements, 222

Bulk photoconductors, 46

Charge accumulation in double-barrier diodes, 251

Charge-density modulation, detection, 62

Charge polarization, ultrafast switching, 241

Charge-transfer state, in double quantum wells, 106

Colliding pulse mode-locked lasers, timing jitter, 48

Coupled quantum wells, electron tunneling times, 111

Detectors

GaAs based, photoconductive, 176

metal-semiconductor-metal, 184

Diamond, type IIa, 170

Diamond films, synthetic, 201

Dielectric measurements, broadband, 222

Differential sampling, 46

Diode laser amplifiers, InGaAsP, 73

Diode lasers, injection current modulated, 68

Diodes

double barrier, 251

resonant tunneling, 115

fabrication, 101

Double-barrier diodes, charge accumulation, 251

Double quantum wells, luminescence observation, 106

Electroabsorption sampling, femtosecond, 264

Electromagnetic pulses, terahertz, 225

Electro-optic sampling, versus photoconductive, 52

Electro-optical synthesizing, 81

Electron-electron scattering, 153

Electron-hole effects, 147

Electron tunneling time

by photoluminescence, 124

in quantum wells, 111

Electrons

resonant tunneling, 247

tunneling escape time, 121

Excitonic electroabsorption sampling, femtosecond, 264

Femtosecond excitonic electroabsorption sampling, 264

FETs, silicon, 132

Frequency-domain techniques, 57

GaAs/AlAs coupled double quantum-well structures, 254

GaAs-based detectors, photoconductive, 176

GaAs MESFET, 139

GaAs monolithic integrated circuits, 16

Gallium arsenide

electron-electron scattering, 153

time-resolved photoluminescence, 39

HBT technology, 139

HEMTs, InGaAs/InAlAs, high-speed performance, 260

High- T_c superconducting films and devices, 246

InGaAs APD, back illuminated, 266

InGaAs/InAlAs HEMTs, high-speed performance, 260

InGaAs/InAlAs MODFET, measurements, 27

InGaAs photoconductors, Be bombarded, 206

InGaAsP diode laser amplifiers, 73

Injection current modulated diode lasers, 68

InP photoconductors, Be bombarded, 206

Integrated antennas, 222

Integrated circuits, GaAs monolithic, 16

Interdigitated detectors, 184

Intersubband relaxation of electrons, 158

Laser modulation, high frequency, 244

Lasing dynamics, picosecond, 262

Lifetime measurements, type IIa diamond, 170

Lightwave systems, high speed, 2

Luminescence, time-resolved observation, 106

MESFET, GaAs, 139

Metal-semiconductor-metal detectors, 184

Millimeter-wave antennas, characterization, 232

Mobility measurements, type IIa diamond, 170

Mode-locked lasers, timing jitter, 48

Mode-locked semiconductor lasers, pulse formation, 87

Modulators, spread spectrum integrated, 76

Monolithic integrated circuits, GaAs, 16

Multiplexing-demultiplexing techniques, 7

Optic modulators, spread spectrum integrated, 76

Optoelectronic probes, ultrahigh bandwidth, 22

Perpendicular transport, 96

Phase-space absorption quenching, 27

Phonons, in layered semiconductors, 163

Photoconductive detectors, GaAs based, 176

Photoconductive picosecond pulse generation, 201

Photoconductive sampling, versus electro-optic, 52

Photoconductive switches

tandem, 217

ultrafast, 210

velocity overshoot, 147

Photoconductors

- bulk, 46
- with high responsivity, 206

Photocurrent-voltage characteristics, 210

Photodiodes, coplanar vacuum, 189

Photoexcitation, intersubband electron relaxation, 158

Photoluminescence, time resolved, 39

Photoluminescence excitation correlation spectra, 124

Photon counting, picosecond pulse observation, 36

Picosecond lasing dynamics, 262

Picosecond pulses

- generation, 201
- low-power-level, 36

Probes

- 120-GHz active wafer, 31
- optoelectronic, ultrahigh bandwidth, 22

Propagation delays, measurement, 27

Pulse formation, subpicosecond, 87

Pulsed lasers, tuning, 57

Quantum wells

- coupled, electron tunneling times, 111
- resonant tunneling of electrons, 247
- tunneling escape from, 121

Quantum-well lasers, picosecond lasing dynamics, 262

Quantum-well structures

- dc biased, 239
- GaAs/AlAs coupled, 254

Relaxation oscillations, 68

Resonant tunneling diodes

- equivalent-circuit mode, 115

Resonant tunneling diodes—*Continued*

fabrication, 101

Resonant tunneling of electrons, 247

Semiconductor lasers

- repetitively pulsed, 258
- timing jitter, 258

Semiconductor microstructures, transport, 96

Semiconductors, layered, phonon interactions, 163

Short-wavelength picosecond pulses, measurement, 189

Silicon FETs, 132

Single-photon solid-state detector, 194

Solid-state detector, single photon, 194

Superconducting films and devices, 246

Tandem photoconductive switches, 217

Terahertz electromagnetic pulses, 225

Time-resolved photoluminescence, 39

Timing jitter, 48, 258

Transmission experiment, 10 Gb/s-100 km, 266

Tuning, frequency-domain techniques, 57

Tunneling, 96

- dynamics, 254

Tunneling escape, electric-field dependence, 121

Turn-on delay, measuring, 217

Ultrafast optical switching, 239

Ultrafast photoconductive switches, 210

Vacuum photodiode, coplanar, 189

Velocity overshoot, electron-hole effects, 147

Wafer probes, 120-GHz, 31